Environmental Science

Jaime Klapp
Gerardo Ruíz Chavarría
Abraham Medina Ovando
Abel López Villa
Leonardo Di G. Sigalotti *Editors*

Selected Topics of Computational and Experimental Fluid Mechanics

Springer

Environmental Science and Engineering

Environmental Science

More information about this series at http://www.springer.com/series/3234

Jaime Klapp · Gerardo Ruíz Chavarría
Abraham Medina Ovando
Abel López Villa · Leonardo Di G. Sigalotti
Editors

Selected Topics of Computational and Experimental Fluid Mechanics

Springer

Editors
Jaime Klapp
Instituto Nacional de Investigaciones Nucleares
Ocoyoacac
Mexico

and

Cinvestav-Abacus
Mexico, D.F.
Mexico

Gerardo Ruíz Chavarría
Facultad de Ciencias
National Autonomous University of Mexico
Mexico, D.F.
Mexico

Abraham Medina Ovando
SEPI ESIME Azcapotzalco
National Polytechnic Institute
Mexico, D.F.
Mexico

Abel López Villa
SEPI ESIME Azcapotzalco
National Polytechnic Institute
Mexico, D.F.
Mexico

Leonardo Di G. Sigalotti
Departamento de Ciencias Básicas
Universidad Autónoma Metropolitana-Azcapotzalco
Mexico, D.F.
Mexico

and

Instituto Venezolano de Investigaciones Científicas (IVIC)
Caracas
Venezuela

ISSN 1863-5520 ISSN 1863-5539 (electronic)
Environmental Science and Engineering
ISSN 1431-6250
Environmental Science
ISBN 978-3-319-11486-6 ISBN 978-3-319-11487-3 (eBook)
DOI 10.1007/978-3-319-11487-3

Library of Congress Control Number: 2015930006

Springer Cham Heidelberg New York Dordrecht London

Printed on acid-free paper

Springer International Publishing AG Switzerland is part of Springer Science+Business Media (www.springer.com)

Preface

Fluid dynamics is a highly developed branch of science that has been the subject of continuous and expanding research activity both theoretically and experimentally for more than a century and a half. In particular, the relatively recent development of fluid dynamics has been strongly influenced by its numerous applications in a plethora of research fields as well as industrial and technological processes. Current research in physics, biology, engineering, medicine, and environmental sciences rely more and more on the use of the principles of fluid mechanics. While improvements to the nineteenth-century technologies were possible on the basis of common sense, the new technologies require the knowledge of fluid flow behavior under conditions that go beyond our everyday experience.

This book presents recent experimental and theoretical advances in fluid dynamics applied to physics and engineering. It includes invited lectures given during the International Enzo Levi Spring School held at Cinvestav-Abacus, Estado de México, Mexico, May 15–16, 2013, and seminars presented at the XIX National Congress of the Fluid Dynamics Division of the Mexican Physical Society, held at the Mexican Institute of Water Technology, Jiutepec, Morelos, Mexico, November 13–15, 2013.

The Spring School is organized every year in honor of Prof. Enzo Levi, a well-known Mexican scientist, who dedicated his research to the study of fluids. He was one of the founders of the Instituto de Ingeniería (Engineering Institute) of the Universidad Nacional Autónoma de México (UNAM), and of the Instituto Mexicano de Tecnología del Agua (Mexican Institute for Water Technology) of the National Water Commission. He was the mentor of several generations of Mexican Engineers.

The 2013 Enzo Levi School was held at Cinvestav-Abacus, a recently created Centre for Applied Mathematics and High Performance Computing (HPC) that from early 2015 will host one of the largest supercomputers in Latin America, where scientists and engineers in Mexico and other countries will be able to develop projects on Computational Fluid Dynamics requiring very large HPC facilities.

During the Cinvestav-Abacus two-day school, lectures were given by well-known national and international scientists. The meeting was attended by about 50 researchers and about a hundred graduate and undergraduate students.

A wide variety of topics were presented that included asymptotic methods in fluids, convection, computational methods applied to biological systems, interfacial fluid dynamics, colloidal dispersions, and fluid flow in fractured porous media. Among the lectures we want to mention a very interesting description of *Bubble dynamics with biomedical applications* and *Using computers to study fluid dynamics* by Timothy Colonius of the Mechanical and Civil Engineering Department of the California Institute of Technology, two lectures on the *Fluid mechanics of bio-inspired swimming and flying* and *Some problems on the physics of insect-inspired flapping wings* by Ramiro Godoy Diana of the École Supérieure de Physique et de Chimie Industrielles (ESPCI), Paris, France, and Claudio Pastorino of the Departamento de Física, Centro Atómico Constituyentes, CAN-CONICET, Buenos Aires, Argentina, with the two lectures *Polymer brushes exposed to liquid flow: cyclic dynamics, collective behavior and coarse-grained* and *DPD model to simulate soft matter systems in equilibrium and under flow*. Other interesting lectures were *Smoothed Particle Hydrodynamics for free-surface flows: Implementation (CPU and GPU)* and *DualSPHysics code and applications* by Anxo Barreiro, Universidad de Vigo, Spain, *Numerical simulation of multiphase flow* by Leonardo Di G. Sigalotti of the Universidad Autónoma Metropolitana-Azcapotzalco (UAM-A), Mexico and the Instituto Venezolano de Investigaciones Científicas (IVIC), Caracas, Venezuela, *Modeling the dependence of interfacial tension with temperature and ionic strength in mixtures of solvents, organic and water by dissipative particle dynamics* by Estela Mayoral-Villa, ININ, Mexico, and *Surface waves in the vicinity of a singularity* by Gerardo Ruíz Chavarría, FCUNAM, Mexico. Several of these lectures were included in Part I of the book.

The Annual Fluid Dynamics Congress has a different format compared to its previous episodes. In 2013, it lasted three days and was composed of six plenary lectures and many short oral presentations of students and researchers.

In Part I we also included the plenary lectures given during the congress by national and international well-known invited speakers and some of the most interesting short oral contributions. Among the plenary lectures we can mention the following: *Flow coherence: Distinguishing cause from effect* by F.J. Beron Vera of the University of Miami, Florida, USA, *Flows from bins: New Results* by Abraham Medina of ESIME-IPN, Mexico, *Numerical modeling of the extratropical storm Delta over Canary Islands: Importance of high resolution*, by José M. Baldasano of the Barcelona Supercomputing Center, Barcelona, Spain, *Compositional Flow in Fractured Porous Media: Mathematical Background and Basic Physics*, by Leonardo Di G. Sigalotti of the UAM-A, Mexico and IVIC, Venezuela, *Some aspects of the turbulence role in oceanic currents* by Angel Ruiz Ángulo, UNAM, Mexico, and finally *Alya Red CCM: HPC-based cardiac computational modeling* by Mariano Vázquez of the Barcelona Supercomputing Center, Barcelona, Spain.

The other short presentations are organized by topics: Multiphase flow and Granular Media (Part II), Convection and Diffusion (Part III), Vortex, Oceanography and Meteorology (Part IV), and General Fluid Dynamics and Applications (Part V).

In Part II, Multiphase Flow and Granular Media, we have focused on petroleum-related applications, where we can find interesting contributions on the tracer transport and natural and forced convection with applications to oil recovery, mixed convection around a heated horizontal cylinder and viscous dissipation, characterization of a bubble curtain for PIV measurements, numerical simulations of gas-stirred ladle with applications to metallurgy, and a study of fluid flow through polymeric complex structures using multiscale simulations.

Convection and Diffusion can be found in Part III, with interesting contributions on conjugate convection in an open cavity, and heat transfer in biological tissues. We can also find two applications on fracture-porous media systems in oxygen transport and combustion, and an interesting study of solidification in the presence of natural convection in a Hele-Shaw cell and of thermal convection in a cylindrical enclosure with a wavy sidewall.

In Part IV, Vortex, Oceanography and Meteorology, we can find three contributions on numerical simulations of the flow past a pair of magnetic obstacles, steady and unsteady vortex flow generated by electromagnetic forcing, as well as numerical simulations of the span-wise vortex in a periodic forced flow, of erosion and deposition of particles in a periodic forced flow and of singularities in surfaces waves.

Finally, in Part V, General Fluid Dynamics and Applications, we find several contributions of fluid dynamics applied to various fields such as biopolymers processes, friction stir welding, dynamical behavior of a drop on a vertically oscillating surface, and critical phenomena of a drop through a stratified fluid.

The book is aimed at fourth year undergraduate and graduate students, and at scientists in the field of physics, engineering, and chemistry who have interest in fluid dynamics from the experimental and theoretical points of view. The material includes recent advances in experimental and theoretical fluid dynamics and is adequate for both teaching and research. The invited lectures are introductory and avoid the use of complicated mathematics. The other selected contributions are also adequate for fourth-year undergraduate and graduate students.

The editors are grateful to the institutions that made possible the realization of the International Enzo Levi Spring School 2013 and the XIX National Congress of the Fluid Dynamics Division of the Mexican Physical Society, especially the Consejo Nacional de Ciencia y Tecnología (CONACYT), the Sociedad Mexicana de Física, the Universidad Autónoma Metropolitana-Azcapotzalco (UAM-A), the Instituto Mexicano de Tecnología del Agua, Jiutepec, Morelos, the Universidad Autónoma de México (UNAM), the ESIME of the Instituto Politécnico Nacional (IPN), Cinvestav-Abacus, and the Instituto Nacional de Investigaciones Nucleares (ININ).

We acknowledge the help of the Editing Committee: Carlos A. Vargas, Salvador Galindo Uribarri, Catalina Stern, Mario Alberto Rodriguez Meza, Estela Mayoral-Villa, Armando Gama, Máximo Pliego Díaz, Leonardo Trujillo, and, in particular, Fernando Aragón and Ruslan Gabbasov for their important and valuable contribution to the final manuscript.

Mexico City, January 2015

Jaime Klapp
Gerardo Ruíz Chavarría
Abraham Medina Ovando
Abel López Villa
Leonardo Di G. Sigalotti

Acknowledgments

The production of this book was sponsored by the Consejo Nacional de Ciencia y Tecnología (CONACYT), the Universidad Autónoma Metropolitana-Azcapotzalco (UAM-A), the ESIME-Azcapotzalco of the Instituto Politécnico Nacional (IPN), the Instituto Nacional de Investigaciones Nucleares (ININ), the Instituto Mexicano de Tecnología del Agua (IMTA), the Centre for Applied Mathematics and High Performance Computing of the Centro de Investigación y de Estudios Avanzados of the Instituto Politécnico Nacional (Cinvestav-Abacus), the Facultad de Ciencias of the Universidad Nacional Autónoma de México (FCUNAM), and the Sociedad Mexicana de Física (SMF).

Contents

Contributors

J. Aguado-Sierra Barcelona Supercomputing Center, Barcelona, Spain

R.O. Vargas Aguilar ESIME Azcapotzalco, Instituto Politécnico Nacional, México, D.F., Mexico

C.G. Aguilar-Madera Instituto Mexicano del Petróleo, Eje Central Lázaro Cárdenas 152, Mexico, D.F., Mexico; Now at Facultad de Ciencias de la Tierra, Universidad Autónoma de Nuevo León, Linares, N.L., Mexico

F. Aguilar-Gastelum Instituto Mexicano del Petróleo (IMP), Mexico, D.F., Mexico

C.E. Alvarado-Rodríguez Departamento de Ingeniería Química, DCNyE, Universidad de Guanajuato, Mexico, Guanajuato, Mexico

S. Álvarez ESIME Zacatenco, Instituto Politécnico Nacional, Mexico, D.F., Mexico

V. Álvarez González Departamento de Física, Facultad de Ciencias, Universidad Nacional Autónoma de México, Mexico, Mexico

F. Aragón Instituto Politécnico Nacional, Sección de Estudios de Posgrado e Investigación, Escuela Superior de Ingeniería Mecánica y Eléctrica, Unidad Profesional Adolfo López Mateos, Mexico, D.F., Mexico

R. Arís Barcelona Supercomputing Center, Barcelona, Spain

G. Arreaga-García Departamento de Investigación En Física de la Universidad de Sonora, Hermosillo, Sonora, Mexico

A. Arrieta Departamento de Física y Matemáticas, Universidad Iberoamericana, Mexico, D.F., Mexico

A. Aviles Departamento de Matemáticas, Cinvestav Del Instituto Politécnico Nacional (IPN), Mexico, D.F., Mexico

J.M. Baldasano Earth Sciences Department, Barcelona Supercomputing Center-Centro Nacional de Supercomputación (BSC-CNS), Barcelona, Spain; Environmental Modelling Laboratory, Technical University of Catalonia (UPC), Barcelona, Spain

M.A. Balderas Altamirano Instituto de Física, Universidad Autónoma de San Luis Potosí, Mexico, San Luis Potosí, Mexico

A. Barreiro EPhysLab Environmental Physics Laboratory, Universidad de Vigo, Ourense, Spain

A. Beltrán Instituto de Investigaciones en Materiales, Unidad Morelia, Universidad Nacional Autónoma de México, Morelia, MICH, Mexico

A. Bencomo Escuela de Ingeniería Metalúrgica y Ciencia de los Materiales, Facultad de Ingeniería, Universidad Central de Venezuela, UCV, Caracas, Venezuela

F.J. Beron Vera Department of Atmospheric Sciences, RSMAS, University of Miami, Miami, FL, USA

M.E. Bravo Departamento de Ingeniería Química, Facultad de Química, Universidad Nacional Autónoma de México (UNAM), México, D.F., Mexico

J.C. Cajas Barcelona Supercomputing Center, Barcelona, Spain

I. Carvajal Instituto Politécnico Nacional, Sección de Estudios de Posgrado e Investigación, Escuela Superior de Ingeniería Mecánica y Eléctrica, Unidad Profesional Adolfo López Mateos, Mexico, D.F., Mexico

O. Cazarez-Candia Instituto Mexicano del Petróleo, Eje Central Lázaro Cárdenas 152, Mexico, D.F., Mexico

M. Centeno Physique et Mécanique des Milieux Hetérogènes (PMMH, UMR 7636), CNRS; ESPCI ParisTech; UPMC (Paris 6); Univ. Paris Diderot (Paris 7), Paris, Cedex 5, France; Facultad de Ciencias, Universidad Nacional Autónoma de México, Mexico City, Mexico

M.S. Centeno-Sierra Departamento de Física, Facultad de Ciencias, Universidad Nacional Autónoma de México, México, México

J.L. Cervantes-Cota Instituto Nacional de Investigaciones Nucleares, ININ, Mexico, Mexico

A.E. Chávez Departamento de Ingeniería Química, Facultad de Química, Universidad Nacional Autónoma de México (UNAM), México, D.F., Mexico

J.E. Cisneros Renewable Energy Institute, Universidad Nacional Autónoma de México, Temixco, Mor, Mexico

P. Córdoba Barcelona Supercomputing Center, Barcelona, Spain

M. Coronado Instituto Mexicano del Petróleo (IMP), México D.F., Mexico

A.J.C. Crespo EPhysLab Environmental Physics Laboratory, Universidad de Vigo, Ourense, Spain

E. Cuevas Izaña Atmospheric Research Center, Meteorological State Agency of Spain (AEMET), Santa Cruz de Tenerife, Spain

S. Cuevas Instituto de Energías Renovables, Universidad Nacional Autónoma de México, Temixco, Morelos, Mexico

P. De Jesús Sánchez ESIME Azcapotzalco, Instituto Politécnico Nacional, México, D.F., Mexico

E. De la Cruz-Sánchez Instituto Nacional de Investigaciones Nucleares, Carretera México-Toluca S/N, La Marquesa, Estado de Mexico, Ocoyoacac, Mexico

S. de Santiago ESIME Azcapotzalco, Instituto Politécnico Nacional, Mexico, D.F., Mexico

Leonardo Di G. Sigalotti Departamento de Ciencias Básicas, Universidad Autónoma Metropolitana-Azcapotzalco, Delegación Azcapotzalco, Mexico, D.F., Mexico; Instituto Venezolano de Investigaciones Científicas, IVIC, Caracas, Venezuela

J.M. Domínguez EPhysLab Environmental Physics Laboratory, Universidad de Vigo, Ourense, Spain

C. Echeverría Arjonilla Departamento de Física, Facultad de Ciencias, Universidad Nacional Autónoma de México, Ciudad Universitaria, D.F., Mexico

T. Espinosa Universidad Autónoma Chapingo, Chapingo, CP, Mexico

B. Estela García Rojas Departamento de Ingeniería y Ciencias Químicas, Universidad Iberoamericana, México, D.F., Mexico

V.H. Ferrer L. ESIME Azcapotzalco, Instituto Politécnico Nacional, México, D.F., Mexico

A. Figueroa Facultad de Ciencias, Universidad Autónoma del Estado de Morelos, Cuernavaca, Morelos, Mexico

F. Flores Galicia Departamento de Física, Facultad de Ciencias, Universidad Nacional Autónoma de México, Ciudad Universitaria, D.F., Mexico

E. Fonda New York University, New York, USA

R. Gabbasov Instituto de Ciencias Básicas E Ingenierías, Universidad Autónoma de Pachuca, Ciudad Universitaria, Pachuca, Hidalgo, Mexico

A. Gama Goicochea Instituto de Física, Universidad Autónoma de San Luis Potosí, Mexico, San Luis Potosí, Mexico

O. García-Feal EPhysLab Environmental Physics Laboratory, Universidad de Vigo, Ourense, Spain

M. Gómez Gesteira EPhysLab Environmental Physics Laboratory, Universidad de Vigo, Ourense, Spain

R. Godoy-Diana Physique et Mécanique des Milieux Hetérogènes (PMMH, UMR 7636), CNRS; ESPCI ParisTech; UPMC (Paris 6); Univ. Paris Diderot (Paris 7), Paris, Cedex 5, France

A. Gómez López ESIME Azcapotzalco, Instituto Politécnico Nacional, México, D.F., Mexico

F.I. Gomez-Castro Departamento de Ingeniería Química, DCNyE, Universidad de Guanajuato, Mexico, Guanajuato, Mexico

A. Gómez-Villanueva Instituto Tecnolgico de Toluca, Avenida Tecnolgico S/N Fraccionamiento la Virgen, Metepec, CP, Mexico

A. Gonzalez Department of Physics, Universidad Autonoma Metropolitana-Iztapalapa, Mexico, D.F., Mexico

F.G. Haro Velázquez Departamento de Física, Facultad de Ciencias, Universidad Nacional Autónoma de México, Ciudad Universitaria, D.F., Mexico

C.A. Hernández C. ESIME Azcapotzalco, Instituto Politécnico Nacional, México, D.F., Mexico

G. Hernández Cruz Renewable Energy Institute, Universidad Nacional Autónoma de México, Temixco, Mor, Mexico

S. Hernández Zapata Facultad de Ciencias, Universidad Nacional Autónoma de México, Mexico, D.F., Mexico

J.A. Hernández Zarate Depto. de Metal Mecánica y Mecatrónica, Instituto Tecnológico de Veracruz, Veracruz, Col. Formando Hogar, Mexico

J.R. Hernández-Pérez Instituto Mexicano del Petróleo, Del. Gustavo A. Madero, Mexico, D.F., Mexico

E. Diaz Herrera Department of Physics, Universidad Autonoma Metropolitana-Iztapalapa, Mexico, D.F., Mexico

E.C. Herrera-Hernández Centro de Ingeniería y Desarrollo Industrial, Querétaro, Qro., Mexico

F.J. Higuera ETSI Aeronáuticos, Universidad Politécnica de Madrid, Madrid, Spain

G. Houzeaux Barcelona Supercomputing Center, Barcelona, Spain

M. Iniguez Coordinación de Riego y Drenaje. Instituto Mexicano de Tecnología del Agua., Jiutepec, Morelos. CP, Mexico

P. Jain Physique et Mécanique des Milieux Hetérogènes (PMMH, UMR 7636), CNRS; ESPCI ParisTech; UPMC (Paris 6); Univ. Paris Diderot (Paris 7), Paris, Cedex 5, France; Indian Institute of Technology, Kharagpur, India

A. Jara ESIME Azcapotzalco, Instituto Politécnico Nacional, Mexico, D.F., Mexico

O. Jorba Earth Sciences Department, Barcelona Supercomputing Center-Centro Nacional de Supercomputación (BSC-CNS), Barcelona, Spain

J. Klapp Instituto Nacional de Investigaciones Nucleares, Carretera México-Toluca S/N, La Marquesa, Ocoyoacac, Estado de Mexico, Mexico; Departamento de Matemáticas, Cinvestav del I.P.N., Mexico, D.F., Mexico; and Departamento de Física, Instituto Nacional de Investigaciones Nucleares, Ocoyoacac, Estado de México, Mexico

C.G. Lara Instituto de Energías Renovables, Universidad Nacional Autónoma de México, Temixco, Morelos, Mexico

M. López Barcelona Supercomputing Center, Barcelona, Spain

A. López Villa ESIME Azcapotzalco, Instituto Politécnico Nacional, México, D.F., Mexico

E.J. López-Sánchez Facultad de Ciencias, Universidad Nacional Autónoma de México, Ciudad Universitaria, Mexico, D.F., Mexico

J.C. Luna Sánchez Departamento de Física, Instituto Nacional de Investigaciones Nucleares, Mexico, D.F., Mexico; Departamento de Física y Matemáticas, Universidad Iberoamericana, Mexico, D.F., Mexico

O. Luongo Instituto de Ciencias Nucleares, Universidad Nacional Autónoma de México (UNAM), Mexico, D.F., Mexico; Dipartimento di Fisica, Università di Napoli Federico II, Naples, Italy; Instituto Nazionale di Fisica Nucleare (INFN), Naples, Italy

C. Marrero Izaña Atmospheric Research Center, Meteorological State Agency of Spain (AEMET), Santa Cruz de Tenerife, Spain

S. Martínez Martínez Facultad de Ingeniería Mecánica y Eléctrica, Universidad Autónoma de Nuevo León, San Nicolás de los Garza, NL, México

L.A. Martínez-Suástegui ESIME Azcapotzalco, Instituto Politécnico Nacional, México, D.F., Mexico

E. Mayoral-Villa Instituto Nacional de Investigaciones Nucleares, Carretera México-Toluca S/N, La Marquesa, Estado de Mexico, Ocoyoacac, Mexico

A. Medina ESIME Azcapotzalco, Instituto Politécnico Nacional, Santa Catarina, Mexico, D.F., Mexico

S. Méndez Díaz Facultad de Ingeniería Mecánica y Eléctrica, Universidad Autónoma de Nuevo León, San Nicolás de los Garza, NL, México

R. Méndez-Fragoso Departamento de Física, Facultad de Ciencias, Universidad Nacional Autónoma de México, México, México

R. Mercado Coordinación de Riego y Drenaje. Instituto Mexicano de Tecnología del Agua., Jiutepec, Morelos. CP, Mexico

Eduardo Nahmad-Achar Instituto de Ciencias Nucleares, Universidad Nacional Autónoma de México, Mexico, D.F., Mexico

W. Ojeda Coordinación de Riego y Drenaje. Instituto Mexicano de Tecnología del Agua., Jiutepec, Morelos. CP, Mexico

S.L. Ovando Chacon Depto. de Química y Bioquímica, Instituto Tecnológico de Tuxtla Gutiérrez, Tuxtla Gutiérrez, Chiapas, Mexico

G.E. Ovando Chacon Depto. de Metal Mecánica y Mecatrónica, Instituto Tecnológico de Veracruz, Veracruz, Col. Formando Hogar, Mexico

C. Pastorino Departamento de Física de la Materia Condensada, Centro Atómico Constituyentes, CNEA and CONICET, Buenos Aires, Argentina

E. Pérez Instituto de Física, Universidad Autónoma de San Luis Potosí, Mexico, San Luis Potosí, Mexico

M. Pliego Dpto. CB, ITQ Av. Tecnológico Esq. Gral. M. Escobedo, Querétaro, QRO, Mexico

D. Porta Zepeda Departamento de Física, Facultad de Ciencias, Universidad Nacional Autónoma de México, Ciudad Universitaria, D.F., Mexico

J.C. Prince Avelino Depto. de Metal Mecánica y Mecatrónica, Instituto Tecnológico de Veracruz, Veracruz, Col. Formando Hogar, Mexico

H. Quevedo Instituto de Ciencias Nucleares, Universidad Nacional Autónoma de México (UNAM), Mexico, D.F., Mexico; Dipartimento di Fisica and ICRA, Università di Roma La Sapienza, Rome, Italy

G. Ramírez Renewable Energy Institute, Universidad Nacional Autónoma de México, Temixco, Mor, Mexico

R.G. Ramírez de la Torre Departamento de Física, Facultad de Ciencias, Universidad Nacional Autónoma de México, México, México

H.G. Ramírez Hernández Facultad de Ingeniería Mecánica y Eléctrica, Universidad Autónoma de Nuevo León, San Nicolás de los Garza, NL, México

E. Ramos Renewable Energy Institute, Universidad Nacional Autónoma de México, Temixco, Mor, Mexico

G. Rangel Paredes Departamento de Física, Facultad de Ciencias, Universidad Nacional Autónoma de México, Ciudad Universitaria, D.F., Mexico

J.A. Moreno Razo Department of Physics, Universidad Autonoma Metropolitana-Iztapalapa, Mexico, D.F., Mexico

M. Rivero Barcelona Supercomputing Center, Barcelona, Spain

T. Rodriguez Luna Facultad de Ciencias, Universidad Nacional Autónoma de México, Mexico, D.F., Mexico

M.A. Rodríguez-Meza Instituto Nacional de Investigaciones Nucleares, Carretera México-Toluca S/N, La Marquesa, Estado de Mexico, Ocoyoacac, Mexico

A. Rojano Universidad Autónoma Chapingo, Chapingo, CP, Mexico

F. Rojano EPHOR Lab. Agrocampus Ouest. 2, Angers, France

G. Rojas Altamirano Departamento de Metalmecánica, Instituto Tecnológico de Zacatepec, Zacatepec de Hidalgo, MOR, Mexico

M.A. Chavez Rojo Facultad de Ciencias Quimicas, Universidad Autonoma de Chihuahua, Nuevo Campus Universitario, Circuito Universitario, Chihuahua, Mexico

J. Román Instituto de Energías Renovables, Universidad Nacional Autónoma de México, Morelos, México

U. Romero Ortiz ESIME Azcapotzalco, Instituto Politécnico Nacional, México, D.F., Mexico

A. Ruiz Angulo Centro de Ciencias de la Atmósfera, Universidad Nacional Autónoma de México, Mexico city, México

G. Ruíz Chavarría Facultad de Ciencias, Universidad Nacional Autónoma de México, Ciudad Universitaria, Mexico, D.F., Mexico

C. Ruiz-Ferrel Universidad Tecnológica del Valle de Toluca, Carretera del Departamento del D.F. km 7.5, Lerma, Mexico

M. Sánchez Instituto Politécnico Nacional, Escuela Superior de Ingeniería Mecánica y Eléctrica, Unidad Profesional Azcapotzalco, Mexico, D.F., Mexico

I. Sánchez Calvo González Facultad de Ciencias, Universidad Nacional Autónoma de México, Ciudad Universitaria, Mexico, D.F., Mexico

F.A. Sánchez Cruz Facultad de Ingeniería Mecánica y Eléctrica, Universidad Autónoma de Nuevo León, San Nicolás de los Garza, NL, México

N.Y. Sánchez Torres Facultad de Ciencias, Universidad Nacional Autónoma de México, Mexico, D.F., Mexico

M. Sandoval Department of Physics, Universidad Autonoma Metropolitana-Iztapalapa, Mexico, D.F., Mexico

A. Santiago Barcelona Supercomputing Center, Barcelona, Spain

D.A. Serrano ESIME Zacatenco, Instituto Politécnico Nacional, México, D.F., México

A. Servin Martínez Depto. de Metal Mecánica y Mecatrónica, Instituto Tecnológico de Veracruz, Veracruz, Col. Formando Hogar, Mexico

F. Sanchez Silva ESIME Zacatenco, Instituto Politécnico Nacional, México, D.F., México

E. Sira Centro de Física, Instituto Venezolano de Investigaciones Científicas, IVIC, Caracas, Venezuela

K.R. Sreenivasan New York University, New York, USA

C. Stern Forgach Departamento de Física, Facultad de Ciencias, Universidad Nacional Autónoma de México, México, México

B. Thiria Physique et Mécanique des Milieux Hetérogènes (PMMH, UMR 7636), CNRS; ESPCI ParisTech; UPMC (Paris 6); Univ. Paris Diderot (Paris 7), Paris, Cedex 5, France

A. Torres Coordinación del Posgrado, Instituto Mexicano del Petróleo, Mexico, D.F., Mexico

L. Trujillo Centro de Física, Instituto Venezolano de Investigaciones Científicas, IVIC, Caracas, Venezuela

C.A. Vargas UAM Azcapotzalco Mexico, Mexico, D.F., Mexico

D.C. Vargas-Ortega Departamento de Física, Facultad de Ciencias, Universidad Nacional Autónoma de México, México, México

M. Vázquez Barcelona Supercomputing Center, Ed. Nexus I, Campus Nord UPC, Barcelona, Spain; IIIA-CSIC, UAB Campus Bellaterra, Barcelona, Spain

P.V. Verazaluce-Barragán Instituto Mexicano del Petróleo, Del. Gustavo A. Madero, Mexico, D.F., Mexico

P. Villamil Sapien Facultad de Ciencias, Universidad Nacional Autónoma de México, Ciudad Universitaria, Mexico, D.F., Mexico

A. Weinreb Physique et Mécanique des Milieux Hetérogènes (PMMH, UMR 7636), CNRS; ESPCI ParisTech; UPMC (Paris 6); Univ. Paris Diderot (Paris 7), Paris, Cedex 5, France

H. Zambrano Facultad de Ingeniería, Universidad Central de Venezuela, UCV, (Doctorado Individualizado), Caracas, Venezuela

A. Zarazúa Cruz Departamento de Física, Facultad de Ciencias, Universidad Nacional Autónoma de México, Mexico, Mexico

Part I
Invited Lectures

Compositional Flow in Fractured Porous Media: Mathematical Background and Basic Physics

Leonardo Di G. Sigalotti, Eloy Sira, Leonardo Trujillo and Jaime Klapp

Abstract This chapter presents an overview of the equations describing the flow of multiphase and multicomponent fluids through fractured and unfractured porous media using the framework of continuum mixture theory. The model equations and constraint relationships are described by steps of increasing level of complexity. We first describe the governing equations for multiphase flow in both undeformable and deformable porous media. This model is extended to include the transport of chemical species by first describing the flow of a multicomponent, single-phase fluid and then of a compositional (multiphase and multicomponent) fluid in a porous medium. Finally, the equations governing the flow of compositional fluids in fractured porous media are described. The proposed methodology is suitable for modelling any type of fractured media, including dual-, triple-, and multiple-continuum conceptual models.

L. Di G. Sigalotti
Departamento de Ciencias Básicas, Universidad Autónoma Metropolitana-Azcapotzalco,
Av. San Pablo 180, Delegación Azcapotzalco, 02200 México, D.F., Mexico
e-mail: leonardo.sigalotti@gmail.com

E. Sira (✉) · L. Trujillo
Centro de Física, Instituto Venezolano de Investigaciones Científicas, IVIC,
Apartado Postal 20632, Caracas 1020-A, Venezuela
e-mail: esira.ivic@gmail.com

L. Di G. Sigalotti
Instituto Venezolano de Investigaciones Científicas, IVIC,
Apartado Postal 20632, Caracas 1020-A, Venezuela

L. Trujillo
e-mail: leonardo.trujillo@gmail.com

J. Klapp
Instituto Nacional de Investigaciones Nucleares, ININ, Km. 36.5, Carretera México-Toluca,
La Marquesa 52750, Ocoyoacac, Estado de México, Mexico
e-mail: jaime.klapp@inin.gob.mx

J. Klapp
Departamento de Matemáticas, Cinvestav del I.P.N., 07360 México, D.F., Mexico

J. Klapp et al. (eds.), *Selected Topics of Computational and Experimental Fluid Mechanics*, Environmental Science and Engineering,
DOI 10.1007/978-3-319-11487-3_1

1 Introduction

Multiphase and multicomponent fluid flow in fractured rocks occurs in a variety of subsurface flows and transport processes, including contaminant subsurface migration, saltwater intrusion in coastal aquifers, geothermal hydrotransport, subsurface sequestration of CO_2, and oil production and recovery from underground reservoirs, just to mention but a few. In particular, the transport of compositionally complex fluids in fractured porous media has been the subject of extensive research over the past three decades because of its practical interest in petroleum reservoir engineering. Whereas the occurrence of naturally fractured reservoirs over the world is well acknowledged, more than 20 % of the world's oil reserves are estimated to reside in naturally fractured formations (Firoozabadi 2000).

In contrast to crystalline rocks in which any void space is due to fractures, void space in fractured porous media is predominantly formed by pores, which manifest themselves as microscopic perforations of the fracture matrix interface that alter in-plane flow when fracture aperture is less than or equal to the grain size (Mätthai and Belayneh 2004). Although above a certain aperture and length, fractures may become preferential flow pathways that dominate fluid transport throughout the reservoir (Phillips 1991), their actual impact on the transport is in general difficult to predict because multiple fractures may exhibit self-similar and fractal properties in a wide range of scales, with different orientations and intersecting each other. The problem of compositional (i.e., multiphase and multicomponent) flow in fractured porous rocks becomes even more complex owing to the strong nonlinear couplings among viscous, gravitational, and capillary forces in the reservoir which manifest themselves differently in the fracture and rock matrix domains.

The physics of multiphase flows in porous media seems to be reasonably well established and it has been mostly developed in the framework of continuum mixture theory (Allen 1985; Bear 1988; Adler and Brenner 1988; Miller et al. 1998; Chen et al. 2006), where a multiphase mixture is treated as a set of overlapping continua called constituents. In porous media a multiphase fluid mixture consists of several phases if on the scale of typical pore apertures they are separated by sharp interfaces. If, on the other hand, the fluid mixture consists of several chemical species, or components, in which their spatial segregation is only observable at intermolecular length scales, we call it a multicomponent mixture. In underground petroleum reservoirs, we deal in general with multiphase flows in which each phase comprises several chemical species and so we refer to them as multiphase and multicomponent flows, or simply, as compositional flows. In recent years, research efforts have gone mostly into modelling compositional flow in fractured porous media in order to optimize the recovery of hydrocarbons. The partial differential equations governing this type of flows were presented already in 1960 by Barenblatt et al. (1960), and since then they have undergone little modifications. However, their solution still remains a challenge owing to the nonlinear couplings among the variables, the scale-varying heterogeneity of the fractured porous medium, and the large variations in key material properties. At present, there is no a general satisfactory methodology for quantitatively describing flow and reactive transport in multiscale media.

The key issue for simulating flow in fracture rocks, however, is how to handle fracture-matrix interaction under different conditions. For instance, under multiphase and nonisothermal conditions, a critical aspect involves the interaction of mass and thermal energy at fracture-matrix interfaces. In general, most mathematical models rely on continuum approaches and involve developing conceptual models. They incorporate the geometrical information of the fracture-matrix system, define mass and energy conservation equations for the fracture-matrix domains, and solve a number of discrete nonlinear algebraic and constitutive equations, which express relations and constraints of physical processes, variables, and parameters as functions of primary unknowns. Conceptual models employed to represent fractured porous media include: the discrete fracture and matrix models (DFM) (Lichtner 1988; Steefel and Lichtner 1998a, b; Stothoff and Or 2000), the effective-continuum method (ECM) (Wu 2000), the dual-continuum methods, including double- and multi-porosity, dual-permeability models, and the more general Multiple Interacting Continuum (MINC) approach (Barenblatt et al. 1960; Barenblatt and Zheltov 1960; Warren and Root 1963; Pruess and Narasimhan 1985; Wu and Pruess 1988; Bai et al. 1993). A dual porosity model of multidimensional, compositional flow in naturally fractured reservoirs as derived by the mathematical theory of homogenization was presented by Chen (2007). The dual-continuum model, such as the double-porosity and the dual-permeability concept, has been the most widely used approach for modelling fluid flow, heat transfer, and chemical transport through fractured reservoirs because of its computational efficiency and its ability to match many types of field-observed data. A unified scheme based on the dual-continuum method has been recently reported by Wu and Qin (2009), which can be used with different fracture-matrix conceptual models. The mathematical formulation of dual-continuum models as used in industrial simulators and the-state-of-the-art modelling of the physical mechanisms driving flows and interactions/exchanges within and between fractures and matrix media have been described in two separate papers by Lemonnier and Bourbiaux (2010a, b).

Fluid motion in a petroleum reservoir is governed by the laws of conservation of mass, momentum, and energy. These physical laws are often represented mathematically on the macroscopic level by a set of partial differential or integral equations, referred to as the governing equations. As long as compressible or multiphase flow or heat transfer is involved, these equations are inherently nonlinear. A mathematical model for describing the flow and transport processes in fractured porous media consists of these equations, together with appropriate constitutive relations and a set of boundary and/or initial conditions. In this paper we intend to develop such a model by steps of increasing level of complexity. We first describe in Sect. 2 the equations governing the simultaneous flow of two or more fluid phases within a porous medium. In Sect. 3 we write down the equations used to model the transport of multicomponents in a fluid phase in a porous medium. This model is extended in Sect. 4 to describe compositional flow in a general fashion, where each phase may involve many components and mass transfer between the phases is an important effect. Chemical flooding, i.e., the injection of chemical components in production wells is an important technique employed in enhanced oil recovery to reduce the fluid mobility and increase

the sweep efficiency of a reservoir. In view of its practical importance in petroleum engineering, Sect. 5 extends the equations of Sect. 4 to describe chemical flooding compositional flows in a porous medium. The equations for modelling compositional flow in a fractured porous medium are introduced in Sect. 6. The proposed methodology is suitable for modelling any type of fractured reservoirs, including double-, triple-, and other multiple-continuum conceptual models.

2 Multiphase Flow in Porous Media

In fluid mechanics, multiphase flow is treated as a generalization of the modelling of a two-phase immiscible flow, where the two fluids are not chemically related and coexist in contact separated by well-defined interfaces at the microscopic scale. In reservoir simulations, we are typically interested in the simultaneous flow of two or more fluid phases coexisting within the porous solid matrix. In principle, the physics of such flows can be described using the framework of continuum mixture theory for the development of the governing equations, in which the various phases are considered as distinct fluids with individual thermodynamic and transport properties and with different flow velocities. The transport phenomena are mathematically described by the basic principles of conservation for each phase separately and by appropriate kinematic and dynamic conditions at the interfaces. Whereas the detailed structure of these interfaces and the fluid volumes bounded by them are in general inaccessible to macroscopic observation, their geometry influences the dynamics of the multiphase mixture. To cover this difficulty, mixture theory makes use of the *volume fraction* ϕ_α of phase α, which is defined as a scalar function of position $\mathbf{x}$ and time t such that $0 \leq \phi_\alpha \leq 1$. Therefore, for any volume $\mathscr{V}$ in the mixture, the integral

$$\int_{\mathscr{V}} \phi_\alpha(\mathbf{x}, t) d\mathbf{x}, \tag{1}$$

gives the instantaneous fraction of volume $\mathscr{V}$ that is occupied by the fluid phase α. Another quantity which is important in the description of multiphase flow is the phase *saturation* S_α, defined as the fraction of void space of a porous medium that is filled by phase α,

$$S_\alpha = \frac{\phi_\alpha}{\phi}, \tag{2}$$

where ϕ denotes the skeletal *porosity* of the solid matrix, which is the sum of the fluid volume fractions in a saturated porous medium. In other words, it is the total fraction of void space in the material that can be occupied by the fluid phases.

2.1 Undeformable Porous Media

Consider first a porous medium that is statistically homogeneous and undeformable, and assume that the system has four phases: a solid phase (R) and three fluid phases, namely water (W), gas (G), and oil (O). The water phase wets the porous medium more than the oil phase, and so it is called the *wetting phase*. In general, water is the wetting fluid relative to oil and gas, while oil is the wetting fluid relative to gas. Each phase has its own intrinsic mass density ρ_α, velocity $\mathbf{v}_\alpha$, and volume fraction ϕ_α, with the latter obeying the constraint

$$\sum_\alpha \phi_\alpha = 1. \tag{3}$$

The mass conservation equation for phase α can be written as

$$\frac{\partial\left(\phi_\alpha \rho_\alpha\right)}{\partial t} + \nabla \cdot \left(\rho_\alpha \mathbf{v}_\alpha\right) = I_\alpha, \tag{4}$$

where I_α is an interfacial mass transfer rate from all other phases to phase α. In the absence of any external mass source or sink, the reaction rates must satisfy the constraint

$$\sum_\alpha I_\alpha = 0 \tag{5}$$

in order to ensure mass conservation in the overall mixture. In addition, the fact that all fluid phases jointly fill the void space in the solid matrix implies the further relation

$$\sum_\alpha S_\alpha = 1, \qquad \text{or} \qquad S_W + S_O + S_G = 1. \tag{6}$$

Using relations (2) and (3) and noting that $\phi + \phi_R = 1$, Eq. (4) can be expressed in terms of the saturation and porosity as

$$\frac{\partial\left(\phi S_\alpha \rho_\alpha\right)}{\partial t} + \nabla \cdot \left(\rho_\alpha \mathbf{v}_\alpha\right) = I_\alpha, \tag{7}$$

for the fluid phases, and

$$\frac{\partial\left[\left(1-\phi\right)\rho_R\right]}{\partial t} + \nabla \cdot \left(\rho_R \mathbf{v}_R\right) = I_R, \tag{8}$$

for the solid (rock) phase. If the rock phase is chemically inert, $I_R = 0$. In addition, if the solid medium is immobile then $\mathbf{v}_R = 0$ and Eq. (8) reduces to $\rho_R = const$.

The momentum conservation equation for any phase α obeys the form

$$\frac{\partial\left(\rho_\alpha \mathbf{v}_\alpha\right)}{\partial t}+\nabla\cdot\left(\frac{\rho_\alpha \mathbf{v}_\alpha \mathbf{v}_\alpha}{\phi_\alpha}\right)=-\nabla p_\alpha+\nabla\cdot\mathbf{T}_\alpha+\phi_\alpha\rho_\alpha\mathbf{F}_\alpha+\mathbf{M}_\alpha, \tag{9}$$

where p_α is the mechanical pressure in fluid α, $\mathbf{T}_\alpha$ is the viscous stress tensor, $\mathbf{F}_\alpha$ is a body force, and $\mathbf{M}_\alpha$ is the rate of momentum exchange from all other phases to phase α. The term $\nabla\cdot\mathbf{T}$ represents the viscous transfer per unit volume from the pore walls to the pore spaces. In most reservoir applications, the flow in porous media is characterized by low Reynolds numbers (Re <1), i.e., the viscous forces dominate over the inertial ones causing the fluids to move slowly. Under these conditions the inertial terms on the left-hand side of Eq. (9) can be neglected. In addition, taking the average of the right-hand side of Eq. (9) over the volume of fluid phase α within a representative elementary volume and assuming that gravity is the only body force acting on fluid α (i.e., $\phi_\alpha\mathbf{F}_\alpha=g\nabla z$, where g is the magnitude of the gravitational acceleration and z is a reference depth), it can be demonstrated that the momentum balance reduces to the well-known Darcy's law (Bear 1988)

$$\mathbf{v}_\alpha=-\mathbf{K}_\alpha\cdot\left(\nabla p_\alpha-\rho_\alpha g\nabla z\right), \tag{10}$$

where the tensor

$$\mathbf{K}_\alpha=\mathbf{k}\frac{k_{r\alpha}}{\mu_\alpha}, \tag{11}$$

is the *mobility* of fluid phase α. In this expression $\mathbf{k}$ is the absolute permeability tensor of the porous medium, which measures its ability to transmit the fluid, $k_{r\alpha}$ is the relative permeability of phase α, which describes the effects of the other fluid phases in obstructing the flow of fluid α, and μ_α is the dynamic viscosity of phase α. In any particular rock-fluid system, the mobility $\mathbf{K}_\alpha$ accounts for much of the predictive power of Darcy's law. In general, constitutive relations for $\mathbf{K}_\alpha$ are largely phenomenological and an expression of common use in many applications is just that given by Eq. (11), where the mobility is proportional to the product of the absolute and relative permeabilities. If the medium is isotropic, the absolute permeability is diagonal, i.e., $\mathbf{k}=k\mathbf{I}$, where $\mathbf{I}$ is the identity tensor. Otherwise, we say that the porous medium is anisotropic.

Equation (10) can be modified into a momentum conservation for the multiphase mixture. To do so we first define the kinematic viscosity of phase α as $\nu_\alpha=\mu_\alpha/\rho_\alpha$ and introduce the following definitions

$$\nu=\left(\sum_\alpha\frac{k_{r\alpha}}{\nu_\alpha}\right)^{-1}, \tag{12}$$

$$\lambda_\alpha=\frac{k_{r\alpha}}{\nu_\alpha}\nu, \tag{13}$$

where ν is the kinematic viscosity of the mixture and λ_α is the mobility of each phase in the multiphase mixture, which is commonly referred to as the fractional flow function. It must obey the constraint

$$\sum_\alpha \lambda_\alpha = 1. \tag{14}$$

Using the definitions (12)–(14) into Eq. (10) and summing up over all phases, we obtain the momentum conservation equation of the multiphase mixture

$$\rho \mathbf{v} = \sum_\alpha \rho_\alpha \mathbf{v}_\alpha = -\frac{\mathbf{k}}{\nu} \cdot \left(\nabla p - \gamma_\rho \rho g \nabla z\right) \tag{15}$$

where

$$\nabla p = \sum_\alpha \lambda_\alpha \nabla p_\alpha, \tag{16}$$

and

$$\gamma_\rho = \frac{\sum_\alpha \lambda_\alpha \rho_\alpha}{\phi \sum_\alpha S_\alpha \rho_\alpha}, \tag{17}$$

are, respectively, the mixture gradient pressure and the density correction factor (Starikovičius 2003). The definition of the mixture pressure according to Eq. (16) is somewhat non-conventional. For instance, it is satisfied only for homogeneous cases, while for heterogeneous, multidimensional, multiphase systems it is not always possible to define such function.

In multiphase flow the function $k_{r\alpha}$ indicates the tendency of phase α to wet the porous medium. In practical applications, the relative permeabilities are assumed to be known functions of the phase saturations, which must be empirically determined (Morel-Seytoux 1969). The simplest correlations used for the relative permeabilities are power functions of the phase saturations, which for a gas-liquid system are

$$k_{rl} = s_l^n, \qquad k_{rg} = (1 - s_l)^n, \tag{18}$$

where s_l is a normalized liquid saturation defined by

$$s_l = \frac{S_l - S_{lr}}{S_{lm} - S_{lr}}, \tag{19}$$

with S_{lr} being the residual or irreducible liquid saturation and S_{lm} the maximum achievable liquid saturation, which in many cases is less than unity. At the irreducible saturation, the liquid becomes immobile since no interpore connections of liquid exist. Identical forms to Eq. (18) with $n = 3$ are widely used in petroleum and nuclear safety engineering, porous heat pipes (Wyllie 1962). However, this picture of relative permeabilities is quite simplistic. In nature relative permeabilities often

exhibit significant hysteresis, and the verification of an appropriate model in the presence of multiphase fluids (with three or more phases) (Stone 1973) or compositional effects (Bardon and Longeron 1980; Amaefule and Handy 1982) are still not clear. According to Eq. (10), each fluid phase has its own pressure at any point in the reservoir. At the microscopic scale, the effects of interfacial tension and pore geometry on the curvatures of fluid-fluid interfaces lead to capillary effects, which at the macroscopic scale can be quantified in terms of the capillary pressure, defined as the difference between the pressures of two adjacent phases α and β in a porous medium

$$p_{c\alpha\beta} = p_\alpha - p_\beta. \tag{20}$$

In simple models, the capillary pressure is also assumed to be a function of saturation. However, in general it is a function of the pore geometry, the physical properties of the fluids, and the phase saturations (Parker 1989), i.e.,

$$p_{c\alpha\beta} = f(\phi, \sigma_{\alpha\beta}, S_1, S_2, \ldots, S_P), \tag{21}$$

where $\sigma_{\alpha\beta}$ is the interfacial tension at the α-β interface and where it has been assumed the presence of P phases. In actual flows the capillary pressure is generally multivalued, exhibits hysteretic behaviour (Hoa et al. 1977), and depends on fluid composition (Coats 1980). If P phases coexist, then $P - 1$ independent capillary pressure functions will appear in the system.

The most restrictive hypothesis concerning Eq. (10) is the one that considers the flow laminar and the fluid movement as dominated by viscous forces. It is therefore valid when the velocities of the fluids are small. As the flow rate increases, deviations from Darcy's law occur due to inertia, turbulence, and other high-velocity effects (Chen et al. 2006; Mei and Auriault 1991). Although Darcy's law is valid for $\mathrm{Re} < 1$, its upper limit of validity can be extended to $\mathrm{Re} = 10$ (Bear 1988), approximately at the border between the linear and nonlinear laminar flow regimes. For $\mathrm{Re} > 100$, in the turbulent regime, a correction to Darcy's law can be described by the quadratic relation (Forchheimer 1901)

$$(\mu_\alpha \mathbf{I} + \beta_\alpha \rho_\alpha |\mathbf{v}_\alpha| \mathbf{K}_\alpha) \cdot \mathbf{v}_\alpha = -\mathbf{K}_\alpha \cdot (\nabla p_\alpha - \rho_\alpha g \nabla z), \tag{22}$$

where β_α is a factor including the inertial or turbulence effects and $|\mathbf{v}_\alpha|$ is the modulus of the velocity of phase α. This relation is commonly known as Forchheimer's law and incorporates laminar, inertial, and turbulence effects (Chen et al. 2006; Amiri and Vafai 1994). A formal derivation of the Forchheimer's equation from volume-averaging the microscopic momentum balance equation is given by Whitaker (1996). However, much more fundamental research on multiphase flow in porous media is needed to rigorously include these non-Darcian effects into the model.

If the flow is nonisothermal, we must add a balance equation for the energy, which introduces the temperature as an additional dependent variable to the system. In a reservoir, the average temperature of the solid matrix and the fluids in a porous medium may not be the same and so heat conduction may occur between the solid and

the fluids. Furthermore, heat conduction may also occur between the coexisting fluid phases. For simplicity in the exposition, we may invoke local thermal equilibrium in the fluid and assume that the temperature is the same in all fluid phases. In addition, some variables such as porosity, density, and viscosity may depend on temperature. We start by defining the internal energy of the composite system, consisting of the flowing multiphase mixture and the solid matrix, as

$$\phi\rho U = \phi \sum_{\alpha} \rho_\alpha S_\alpha U_\alpha + (1-\phi)\rho_R C_R T, \tag{23}$$

where U_α, C_R, and T are the specific internal energy of phase α, the heat capacity of the rock, and the common temperature, respectively. The overall density is given by

$$\phi\rho = \phi \sum_{\alpha} \rho_\alpha S_\alpha + (1-\phi)\rho_R. \tag{24}$$

From the statement of the first law of thermodynamics in a differential volume occupied by phase α, we can derive the internal energy balance equation of phase α as

$$\frac{\partial(\phi\rho_\alpha S_\alpha U_\alpha)}{\partial t} + \nabla\cdot(\rho_\alpha H_\alpha \mathbf{v}_\alpha) = \nabla\cdot\left(\phi S_\alpha k_{T,\alpha}\nabla T\right) - \varepsilon_r \sigma_{SB} T^4 + Q_\alpha, \tag{25}$$

where H_α is the specific enthalpy of phase α given by

$$H_\alpha = U_\alpha + \frac{p_\alpha}{\rho_\alpha}, \tag{26}$$

$k_{T,\alpha}$ is the thermal conductivity of phase α, ε_r is a radiation emissivity factor, σ_{SB} is the Stefan-Boltzmann constant, and Q_α is the interphase heat transfer rate associated with phase α. Here,

$$Q = \sum_{\alpha} Q_\alpha, \tag{27}$$

where Q includes all external volumetric heat sources and sinks. Noting that $U_\alpha = C_\alpha T$, where C_α is the heat capacity of fluid phase α, and using the mass conservation equation (4) and the enthalpy definition (26), Eq. (25) can be rewritten in terms of the temperature T as follows

$$\begin{aligned}\phi\rho_\alpha S_\alpha C_\alpha \frac{\partial T}{\partial t} + \rho_\alpha C_\alpha \mathbf{v}_\alpha\cdot\nabla T + C_\alpha I_\alpha T = -\nabla\cdot(p_\alpha \mathbf{v}_\alpha)\\ + \nabla\cdot\left(\phi S_\alpha k_{T,\alpha}\nabla T\right) - \varepsilon_r\sigma_{SB}T^4 + Q_\alpha.\end{aligned} \tag{28}$$

Sometimes it is useful to define the diffusive mass flux of phase α within the multiphase mixture as

$$\mathbf{J}_\alpha = \rho_\alpha \mathbf{v}_\alpha - \lambda_\alpha \rho \mathbf{v}, \tag{29}$$

with the constraint

$$\sum_{\alpha} \mathbf{J}_{\alpha} = 0, \tag{30}$$

which can be used to decompose the phase velocity in Eq. (28). Summing up Eq. (28) for all fluid phases and solid matrix and using the constraint (27) along with Eq. (29), we finally obtain

$$\begin{aligned}[\phi\rho C + (1-\phi)\rho_R C_R]\frac{\partial T}{\partial t} + \gamma_C \rho C \mathbf{v}\cdot\nabla T + \left(\sum_{\alpha} C_{\alpha} I_{\alpha} + C_R I_R\right) T \\ = -\nabla\cdot(p_{\alpha}\mathbf{v}_{\alpha}) + \nabla\cdot\left(k_{T,\text{eff}}\nabla T\right) - \left(\sum_{\alpha} C_{\alpha}\mathbf{J}_{\alpha}\right)\cdot\nabla T \\ - \varepsilon_r \sigma_{SB} T^4 + Q,\end{aligned} \tag{31}$$

for the energy balance equation of the multiphase mixture, where ρC is the heat capacity of the multiphase fluid mixture defined as

$$\rho C = \sum_{\alpha} \rho_{\alpha} S_{\alpha} C_{\alpha}, \tag{32}$$

$k_{T,\text{eff}}$ is an estimation of the effective thermal conductivity of the composite system given by

$$k_{T,\text{eff}} = (1-\phi)k_{T,R} + \phi \sum_{\alpha} S_{\alpha} k_{T,\alpha}, \tag{33}$$

and γ_C is the correction factor for energy advection defined as

$$\gamma_C = \frac{\rho \sum_{\alpha} \lambda_{\alpha} C_{\alpha}}{\sum_{\alpha} \rho_{\alpha} S_{\alpha} C_{\alpha}}. \tag{34}$$

To complete the mathematical description of multiphase flow and heat transfer in non-deformable porous media, the above equations need to be supplemented with a number of constitutive equations. As expressed by relations (18) and (21), the relative permeabilities, capillary pressures, and thermal conductivity in most applications are assumed to be functions of the fluid saturations, while the phase density and dynamic viscosity are treated as functions of the pressure and temperature (Wu and Qin 2009). Equations (7), (10), and (31) provide $2P + 1$ differential equations, while there are $3P + 1$ independent variables: S_{α}, $\mathbf{v}_{\alpha}$, p_{α}, and T. The additional P relations to determine a solution of the system are provided by the constraint (6) and the $P - 1$ independent capillary pressure functions.

2.2 Deformable Porous Media

If the porous medium is deformable, additional equations are needed for a closed system. Here we shall assume that the porous medium is heterogeneous and composed of elastic material. A mesoscopic model of deformation of a porous elastic solid is provided by the theory of elasticity modified to account for micro-structural disorder. In this way, the heterogeneity of the solid matrix can be characterized by the spatial variations of the local elastic constants. The mechanics of deformation of heterogeneous media is largely based on studies of wave propagation (Karal and Keller 1964; Frisch 1968; Weaver 1990; Ryzhik et al. 1996; Larose 2006), and it is in this context that we shall derive the general formalism to be implemented here.

The analysis of deformation of a heterogeneous solid body can be handled mathematically by introducing the concept of a continuum medium. In this idealization, we assume that the properties of the medium averaged over a mesoscopic scale are continuous functions of position and time. However, the presence of heterogeneities at the microscopic scale, implying preferred force paths within the medium, have been used as an empirical argument against an isotropic continuum description of inhomogeneous materials. Nonetheless, recent findings on the stress distribution response to local and global perturbations have shed some light on the validity of a continuum theory (Ellenbroek et al. 2009).

For multiphase flow through a deformable porous medium, a new dependent variable, say $\mathbf{w}_R(\mathbf{x}, t)$, must be introduced for the displacement field of the solid matrix. Furthermore, we shall assume that the deformations are small. While this assumption limits the range of applicability of the theory, it is physically reasonable for poroelastic materials under strong static compression like underground soil rocks. We note that for infinitesimal deformations both the displacements and their gradients are much smaller than unity. With this provision and using index notation, the components of the strain tensor of the solid can be defined up to linear order as

$$\varepsilon_{ij} = \frac{1}{2}\left(\frac{\partial w_{R,i}}{\partial x_j} + \frac{\partial w_{R,j}}{\partial x_i}\right), \tag{35}$$

where $\varepsilon_{ij} = \varepsilon_{ji}$, $\mathbf{w}_R = \{w_{R,i}\} = (w_{R,1}, w_{R,2}, w_{R,3}) = (w_{R,x}, w_{R,y}, w_{R,z})$, and $\mathbf{x} = \{x_i\} = (x_1, x_2, x_3) = (x, y, z)$ in Cartesian coordinates. Strain and stress are linked by a stress-strain or constitutive relationship. The most general relationship between the stress and strain tensors can be written as

$$\Sigma_{ij} = C_{ijkl}\varepsilon_{kl}, \tag{36}$$

where C_{ijkl} is a fourth-rank stiffness tensor having 81 components and $\Sigma_{ij} = \Sigma_{ji}$. Because of the symmetry of the stress and strain tensors, C_{ijkl} has only 21 independent components, which are necessary to specify the stress-strain relationship for the most general form of the elastic solid. If the properties of such a solid vary with direction, the material is termed anisotropic. In contrast, the properties of an

isotropic solid are the same in all directions. Although anisotropy is important in some regions of the Earth's interior, isotropy has proven to be a reasonable first-order approximation for most parts. Therefore, if we assume isotropy, C_{ijkl} will be invariant with respect to rotation and the number of independent parameters reduces to two parameters only so that

$$C_{ijkl} = \hat{\lambda}\varepsilon_{kk}\delta_{ij} + 2\hat{\mu}\varepsilon_{ij}, \tag{37}$$

where δ_{ij} is the Kronecker delta, and $\hat{\lambda}$ and $\hat{\mu}$ are called the Lamé parameters of the material, which characterize the rigidity of the solid. These two parameters completely describe the linear stress-strain relation within an isotropic solid. $\hat{\mu}$ is termed the shear modulus and is a measure of the resistance of the material to shearing, while the other parameter, $\hat{\lambda}$, does not have a simple physical explanation. In the case of pure shear, the elastic constant that comes into play is $\hat{\mu} = G$, while for isotropic compression the strain tensor is proportional to the identity tensor. The elastic constant relating the pressure to the decrease of volume is $K = \hat{\lambda} + 2\hat{\mu}$, where K is called the compressibility modulus.

Mathematically, a heterogeneous material is represented by a *random medium* $\mathscr{M}$, i.e., a family of media $\mathscr{M}(\omega)$ whose members differ slightly from the homogeneous (reference) medium $\mathscr{M}_0$, where ω is a point in the sample space Ω (space of events). In probability theory Ω consists of all possible outcomes ω of an experiment or observation. To close the statistical description we must provide the mathematical model with a probability distribution over the members $\mathscr{M}(\omega)$. However, most heterogeneous materials are nonequilibrium, quenched disordered media and so we have no access to a true statistical ensemble. Thus, theory and experiment can only be connected through some kind of ergodicity. The equivalence between theoretical and observational averaging in heterogeneous media is an open problem and will not be addressed here. Therefore, our description of a heterogeneous system as a random medium is based on a heuristic model for the local spatial variations.

Rigorous methods are mostly limited to the study of simple models. In particular, we model the heterogeneous medium by introducing spatial fluctuations of the material density and Lamé coefficients, i.e.,

$$\begin{aligned} \rho_R(\mathbf{x}) &= \rho_{R,0} + \varepsilon\rho_{R,1}(\mathbf{x}), \\ \hat{\lambda}(\mathbf{x}) &= \hat{\lambda}_0 + \varepsilon\lambda_1(\mathbf{x}), \\ \hat{\mu}(\mathbf{x}) &= \hat{\mu}_0 + \varepsilon\mu_1(\mathbf{x}), \end{aligned} \tag{38}$$

where

$$\begin{aligned} \rho_{R,0} &= \langle\rho_R(\mathbf{x})\rangle, \\ \hat{\lambda}_0 &= \langle\hat{\lambda}(\mathbf{x})\rangle = K - \frac{2}{3}G, \\ \hat{\mu}_0 &= \langle\hat{\mu}(\mathbf{x})\rangle = G, \end{aligned}$$

are constant values representing an equivalent averaged effective medium. The average expectation values with respect to the corresponding probability distribution are denoted by $\langle\cdot\rangle$. Here ε is a measure of the departure of the medium from homogeneity. The fluctuations in relations (38) are assumed to be independent and identically distributed functions with zero mean values

$$\langle \rho_{R,1}(\mathbf{x})\rangle = \langle \hat{\lambda}_1(\mathbf{x})\rangle = \langle \hat{\mu}_1(\mathbf{x})\rangle = 0. \tag{39}$$

In addition, we assume that the fluctuations are homogeneous and isotropic with respect to $\mathbf{x}$. Thus, there would be nine autocorrelation functions defined as

$$\begin{aligned}
R_{\rho_{R,1}\rho_{R,1}}(\mathbf{x}|\mathbf{x}') &= \langle \rho_{R,1}(\mathbf{x})\rho_{R,1}(\mathbf{x}')\rangle, \quad R_{\rho_{R,1}\hat{\lambda}_1}(\mathbf{x}|\mathbf{x}') = \langle \rho_{R,1}(\mathbf{x})\hat{\lambda}_1(\mathbf{x}')\rangle,\\
R_{\rho_{R,1}\hat{\mu}_1}(\mathbf{x}|\mathbf{x}') &= \langle \rho_{R,1}(\mathbf{x})\hat{\mu}_1(\mathbf{x}')\rangle;\\
R_{\hat{\lambda}_1\rho_{R,1}}(\mathbf{x}|\mathbf{x}') &= \langle \hat{\lambda}_1(\mathbf{x})\rho_{R,1}(\mathbf{x}')\rangle, \quad R_{\hat{\lambda}_1\hat{\lambda}_1}(\mathbf{x}|\mathbf{x}') = \langle \hat{\lambda}_1(\mathbf{x})\hat{\lambda}_1(\mathbf{x}')\rangle,\\
R_{\hat{\lambda}_1\hat{\mu}_1}(\mathbf{x}|\mathbf{x}') &= \langle \hat{\lambda}_1(\mathbf{x})\hat{\mu}_1(\mathbf{x}')\rangle;\\
R_{\hat{\mu}_1\rho_{R,1}}(\mathbf{x}|\mathbf{x}') &= \langle \hat{\mu}_1(\mathbf{x})\rho_{R,1}(\mathbf{x}')\rangle, \quad R_{\hat{\mu}_1\hat{\lambda}_1}(\mathbf{x}|\mathbf{x}') = \langle \hat{\mu}_1(\mathbf{x})\hat{\lambda}_1(\mathbf{x}')\rangle,\\
R_{\hat{\mu}_1\hat{\mu}_1}(\mathbf{x}|\mathbf{x}') &= \langle \hat{\mu}_1(\mathbf{x})\hat{\mu}_1(\mathbf{x}')\rangle;
\end{aligned}$$

which are a measure of the spatial scale. For simplicity we shall assume that the covariances are given by Gaussian random processes such that

$$R_{ab}(\mathbf{x}|\mathbf{x}') = 2C\eta(|\mathbf{x}-\mathbf{x}'|), \tag{40}$$

where a and b stands for ρ_R, $\hat{\lambda}$, and $\hat{\mu}$.

We note that from the thickness of geological porosity logs (Hewett 1986), it is reasonable to expect a fractal character in the distribution of the micro-mechanical properties of deformable porous media. Therefore, the concepts regarding fractal geometry can be also applied for modelling the heterogeneity of oil reservoirs (Srivastava and Sen 2009). For instance, general forms for the self-affine fractal distributions of the bulk density, elastic moduli, and wave velocities of heterogeneous materials can be modelled using the statistics of either a fractional Gaussian noise (fGn) or a fractional Brownian motion (fBm) (Sahimi and Tajer 2005). For example, for a fBm, η in expression (40) is expressed as:

$$\begin{aligned}
\eta(x,\omega) = \eta_0 + \frac{1}{\Gamma(H+1/2)}\Bigg[&\int_{-\infty}^{0} dB(s,\omega)\left[(x-s)^{H-1/2} - (-s)^{H-1/2}\right]\\
&+ \int_0^x dB(s,\omega)(x-s)^{H-1/2}\Bigg],
\end{aligned} \tag{41}$$

for $x > 0$, where $\eta_0 = \eta(0,\omega)$, H is the Hurt exponent, $B(x,\omega)$ is the Bachelier-Wiener-Lévy process, and Γ is the gamma function. For $H > 1/2$ ($<1/2$) the spatial

correlation is positive (negative), while for $H = 1/2$ the correlation is random and follows a Brownian motion.

For the heterogeneous porous medium described above, the equation of motion for the elastic displacement $\mathbf{w}_R(\mathbf{x}, t)$ can be written in vector notation as follows

$$\begin{aligned}\rho_R(\mathbf{x})\frac{\partial^2}{\partial t^2}\mathbf{w}_R(\mathbf{x},t) = &\left[\hat{\lambda}(\mathbf{x}) + 2\hat{\mu}(\mathbf{x})\right]\nabla\left[\nabla\cdot\mathbf{w}_R(\mathbf{x},t)\right]\\ &- \hat{\mu}(\mathbf{x})\nabla\times\nabla\times\mathbf{w}_R(\mathbf{x},t) + \nabla\hat{\lambda}(\mathbf{x})\nabla\cdot\mathbf{w}_R(\mathbf{x},t)\\ &+ \left[\nabla\hat{\mu}(\mathbf{x})\right]\times\left[\nabla\times\mathbf{w}_R(\mathbf{x},t)\right] + 2\left[\nabla\hat{\mu}(\mathbf{x})\cdot\nabla\right]\mathbf{w}_R(\mathbf{x},t)\\ &+ \mathbf{F}(\mathbf{x},t),\end{aligned} \tag{42}$$

where $\mathbf{F}$ is an external force per unit volume. If we assume mechanical equilibrium, the governing equation for the total stress in the bulk material can be obtained from Eq. (42) by setting

$$\rho_R(\mathbf{x})\frac{\partial^2}{\partial t^2}\mathbf{w}_R(\mathbf{x},t) = 0. \tag{43}$$

The effects of the hydrostatic compression exerted by the fluid on the solid matrix enter in Eq. (42) through the body force term as

$$\mathbf{F} = \phi p\mathbf{I}, \tag{44}$$

where p denotes the mean pore pressure exerted by the fluid phases on the solid grains, defined by

$$p = \sum_{\alpha} S_\alpha p_\alpha. \tag{45}$$

If the system is in thermodynamical equilibrium, the fluid is at rest and p is constant throughout the body. We note that Eq. (42) with the body force as given by relation (44) is equivalent to the concept of the modified effective stress employed in the mechanics of partially saturated porous media to take into account the compressibility of the solid matrix. According to experimental observations, it is this modified effective stress that governs the major deformation of the solid skeleton (Khoei and Mohammadnejad 2011).

If we define the displacement vector of the fluid phase α as $\mathbf{w}_\alpha$, the displacement vector of the fluid phase relative to the solid is $\mathbf{w}'_\alpha = \mathbf{w}_\alpha - \mathbf{w}_R$ and the variation in the fluid phase content ξ_α can be defined as

$$\xi_\alpha = -\nabla\cdot\left[\phi\left(\mathbf{w}_\alpha - \mathbf{w}_R\right)\right] = -\nabla\cdot\left(\phi\mathbf{w}'_\alpha\right), \tag{46}$$

where ξ_α is the variation of the volume of fluid phase α per unit pore volume. It is the difference between the strain of the pore space and the strain of the volume of fluid α in the pore space and it is therefore a dimensionless quantity. In order to complete the description of multiphase flow in a deformable, heterogeneous porous medium,

Darcy's law (10) must be generalized according to

$$\mathbf{v}'_\alpha = \mathbf{v}_\alpha - \mathbf{v}_R = -\mathbf{K}_\alpha \cdot (\nabla p_\alpha - \rho_\alpha g \nabla z)\,, \tag{47}$$

where $\mathbf{v}_R = \dot{\mathbf{w}}_R = \partial \mathbf{w}_R/\partial t$, $\mathbf{v}_\alpha = \dot{\mathbf{w}}_\alpha = \partial \mathbf{w}_\alpha/\partial t$, and $\mathbf{v}'_\alpha$ is the relative velocity of fluid phase α with respect to the solid phase. In the presence of a deformable medium, the mass balance equation for the fluid phases is given by Eq. (7) with $\mathbf{v}_\alpha$ replaced by $\mathbf{v}'_\alpha + \mathbf{v}_R$, while the mass balance equation for the solid phase is given by Eq. (8). Similarly, the energy balance equation is identical to Eq. (31) with the following changes:

$$\mathbf{v} \to \mathbf{v}' = \frac{1}{\rho}\sum_\alpha \rho_\alpha \mathbf{v}'_\alpha, \tag{48}$$

$$\mathbf{v}_\alpha \to \mathbf{v}'_\alpha + \mathbf{v}_R, \tag{49}$$

$$\mathbf{J}_\alpha \to \mathbf{J}'_\alpha = \rho_\alpha \mathbf{v}'_\alpha - \lambda_\alpha \rho \mathbf{v}'. \tag{50}$$

3 Multicomponent Flow in a Single Fluid Phase

In this section, we consider the transport of multicomponents (i.e., multispecies) in a fluid phase that occupies the entire void space in a porous medium. We identify each component in the fluid in terms of its volumetric concentration function (or volumetric mass fraction) $c = c(\mathbf{x}, t)$, such that c_k denotes the concentration of the kth species. The sum of the concentrations of all species residing in the fluid must obey the constraint

$$\sum_{k=1}^{n} c_k = 1, \tag{51}$$

where n is the total number of species in the fluid. Each species has its own intrinsic mass density ρ_k, measured as the mass of component k per unit volume of the fluid, and velocity $\mathbf{v}_k$. Using these basic quantities, we may introduce the following definitions:

$$\rho = \sum_{k=1}^{n} \rho_k, \tag{52}$$

as the overall density of the fluid and

$$\mathbf{v} = \frac{1}{\rho}\sum_{k=1}^{n} \rho_k \mathbf{v}_k, \qquad \mathbf{u}_k = \mathbf{v}_k - \mathbf{v}, \tag{53}$$

as the barycentric fluid velocity and the diffusion velocity of species k in the fluid for which

$$\sum_{k=1}^{n} \mathbf{u}_k = 0. \tag{54}$$

In single-phase flow through a porous medium, the diffusive flux of a component with respect to the barycentric fluid velocity is called *hydrodynamic dispersion*. Each component k has its own mass and momentum conservation equations, which by analogy with Eqs. (4) and (10) are given by

$$\frac{\partial (\phi \rho_k)}{\partial t} + \nabla \cdot (\rho_k \mathbf{v}_k) = I_k, \tag{55}$$

and

$$\mathbf{v} = -\frac{\mathbf{k}}{\mu} \cdot (\nabla p - \rho g \nabla z), \tag{56}$$

where ϕ and $\mathbf{k}$ are the porosity and absolute permeability of the porous medium. Since the species velocities are typically inaccessible to measurement, it is more convenient to rewrite Eq. (55) as

$$\frac{\partial (\phi c_k \rho)}{\partial t} + \nabla \cdot (\rho c_k \mathbf{v}) = -\nabla \cdot \mathbf{d}_k + I_k, \tag{57}$$

where we have used the relations: $\rho_k = c_k \rho$ and $\mathbf{v}_k = \mathbf{u}_k + \mathbf{v}$. In the above equation $\mathbf{d}_k = \rho c_k \mathbf{u}_k$ is the dispersive mass flux of species k, which we assume to obey Fick's law, i.e.,

$$\mathbf{d}_k = -\mathbf{D} \cdot \nabla c_k, \tag{58}$$

where $\mathbf{D}$ is the diffusion-dispersion tensor given by (Peaceman 1966)

$$\mathbf{D} = \phi \rho \zeta_m \mathbf{I} + \rho |\mathbf{v}| \left[\zeta_l \mathbf{E}(\mathbf{v}) + \zeta_t \mathbf{E}^{\perp}(\mathbf{v}) \right]. \tag{59}$$

The coefficient ζ_m is the molecular diffusivity (in units of volume rate per unit length), while ζ_l and ζ_t (having units of length) are the longitudinal and transversal dispersivities, respectively, $|\mathbf{v}|$ is the Euclidean norm of $\mathbf{v}$, i.e., $|\mathbf{v}| = \sqrt{v_x^2 + v_y^2 + v_z^2}$, $\mathbf{I}$ is the identity tensor, and the tensor $\mathbf{E}(\mathbf{v})$ is the orthogonal projection along the velocity

$$\mathbf{E}(\mathbf{v}) = \frac{1}{|\mathbf{v}|^2} \mathbf{v} \cdot \mathbf{v}^t, \tag{60}$$

where the superscript ^{t} means transposition and $\mathbf{E}^{\perp}(\mathbf{v}) = \mathbf{I} - \mathbf{E}(\mathbf{v})$. Summing up the contributions of all species in Eq. (58), we obtain the further constraint

$$\sum_{k=1}^{n} \mathbf{d}_k = 0. \tag{61}$$

A common approach in oil reservoir simulations is to assume that hydrodynamic dispersion is a small enough effect that the diffusion-dispersion fluxes in the component mass balance equations are negligible (Allen 1985).

In Eq. (57) the term I_k is a source/sink term for the kth component. It can result from injection and/or production of a particular component by external means. However, it can also stem from various other processes within the fluid, such as chemical reactions among species, radioactive decay, biodegradation, and growth due to bacterial activities, that may cause the mass fraction of the components to increase or decrease. In particular, for a reactive flow the term I_k can be expressed as

$$I_k = q_k - l_k c_k, \tag{62}$$

where q_k and l_k are the chemical production and loss rates, respectively, of the kth species.

By analogy with Eq. (25), we can write the internal energy equation of component k as

$$\frac{\partial(\phi\rho c_k U_k)}{\partial t} + \nabla\cdot(\rho c_k U_k \mathbf{v}_k) + \nabla\cdot(p_k \mathbf{v}_k) = \nabla\cdot\left(\phi k_{T,k}\nabla T\right) - \varepsilon_r \sigma_{SB} T^4 + Q_k, \tag{63}$$

where $k_{T,k}$ is the heat conductivity associated with species k and Q_k is a heat source or sink term for the kth component. We assume thermodynamic equilibrium among all fluid components k so that $T_k = T$. Using relations (53), introducing the following definitions:

$$U = \sum_{k=1}^{n} c_k U_k, \tag{64}$$

$$p = \sum_{k=1}^{n} p_k, \tag{65}$$

$$H_k = U_k + \frac{p_k}{\rho c_k}, \tag{66}$$

$$k_T = \sum_{k=1}^{n} k_{T,k}, \tag{67}$$

for the total specific energy, the total pressure, the specific enthalpy of species k, and the total heat conductivity, respectively, summing up Eqs. (57) and (63) over all components, and combining the resulting equations, we obtain the temperature equation for the multicomponent fluid

$$\phi\rho C\frac{\partial T}{\partial t}+\rho C\mathbf{v}\cdot\nabla T=-\nabla\cdot\left(\sum_{k=1}^{n}H_k\mathbf{d}_k\right)-\nabla\cdot(p\mathbf{v})+\nabla\cdot(\phi k_T\nabla T)-\varepsilon_r\sigma_{SB}T^4+Q, \tag{68}$$

where C is the multicomponent fluid heat capacity, defined as

$$C=\frac{1}{\rho}\sum_{k=1}^{n}\rho_k C_k. \tag{69}$$

The first term on the right-hand side of Eq. (68) describes the heat generated due to diffusion of one species into another, while the last one accounts for the heat generated by chemical reactions and the kinetic energy generated when one component chemically changes into another. For the composite system consisting of the multicomponent fluid and the solid porous matrix, Eq. (68) is still applicable by making

$$\phi\rho C\rightarrow\phi\rho C+(1-\phi)\rho_R C_R, \tag{70}$$

and

$$\phi k_T\rightarrow(1-\phi)k_{T,R}+\phi\sum_{k=1}^{n}k_{T,k}. \tag{71}$$

To complete the description of the multicomponent flow system, Eqs. (57) and (68) are complemented by the mass balance equation for the single-phase fluid, namely

$$\frac{\partial(\phi\rho)}{\partial t}+\nabla\cdot(\rho\mathbf{v})=0, \tag{72}$$

in the absence of external sources or sinks. If Darcy's velocity (56) is replaced into Eqs. (57), (68), and (72), we have a coupled set of $n+2$ equations for the n concentrations c_k, the temperature T, and the pressure p, where the density and dynamic viscosity are known functions of p, T, and c_k:

$$\rho=\rho(p,T,c_1,c_2,\ldots,c_n), \tag{73}$$

$$\mu=\mu(p,T,c_1,c_2,\ldots,c_n), \tag{74}$$

while the heat conductivity is a function of temperature and chemical concentration.

4 Compositional Flow in a Porous Medium

In this section, we consider multiphase and multicomponent flow, i.e., compositional flow, in a porous medium. In this type of flows there may be several coexisting fluid phases in which a finite number of chemical species may reside. As before, the subscript α is chosen for the fluid phases, R for the solid phase, and k, with

$k = 1, 2, 3, \ldots, n$, for the species (or components). Therefore, each pair (k, α) is a constituent. We assume thermal equilibrium among the species in a given phase and among all phases so that $T_{k\alpha} = T$.

We start by stating that each constituent (k, α) has its own intrinsic mass density $\rho_{k\alpha}$, measured as the mass of component k per unit volume of phase α, and its own velocity $\mathbf{v}_{k\alpha}$. By analogy with Eq. (4) we can write the mass balance equation for each constituent (k, α) as

$$\frac{\partial \left(\phi_\alpha \rho_{k\alpha}\right)}{\partial t} + \nabla \cdot \left(\rho_{k\alpha} \mathbf{v}_{k\alpha}\right) = I_{k\alpha}, \tag{75}$$

where $I_{k\alpha}$ represents the sources and sinks of component k in phase α. In the absence of injection and production of this component by external means, the exchange terms $I_{k\alpha}$ must obey the restriction

$$\sum_{k=1}^{n} \sum_{\alpha \neq R} I_{k\alpha} = 0. \tag{76}$$

Using relation (2) together with the definitions

$$\rho_\alpha = \sum_{k=1}^{n} \rho_{k\alpha}, \tag{77}$$

$$c_{k\alpha} = \frac{\rho_{k\alpha}}{\rho_\alpha}, \tag{78}$$

$$c_k = \frac{1}{\rho} \sum_{\alpha \neq R} S_\alpha \rho_\alpha c_{k\alpha}, \tag{79}$$

$$\mathbf{v}_\alpha = \frac{1}{\rho_\alpha} \sum_{k=1}^{n} \rho_{k\alpha} \mathbf{v}_{k\alpha}, \tag{80}$$

$$\mathbf{u}_{k\alpha} = \mathbf{v}_{k\alpha} - \mathbf{v}_\alpha, \tag{81}$$

$$\mathbf{d}_{k\alpha} = \rho_\alpha c_{k\alpha} \mathbf{u}_{k\alpha}, \tag{82}$$

where ρ_α is the intrinsic mass density of phase α, $c_{k\alpha}$ is the concentration of species k in phase α, c_k is the total volumetric concentration of species k in the mixture, $\mathbf{v}_\alpha$ is the barycentric velocity of phase α, $\mathbf{u}_{k\alpha}$ is the diffusion velocity of species k in phase α, and $\mathbf{d}_{k\alpha}$ is the diffusive flux of constituent (k,α), the mass balance equation (75) can be rewritten in the more convenient form

$$\frac{\partial \left(\phi S_\alpha \rho_\alpha c_{k\alpha}\right)}{\partial t} + \nabla \cdot \left(\rho_\alpha c_{k\alpha} \mathbf{v}_\alpha\right) = -\nabla \cdot \mathbf{d}_{k\alpha} + I_{k\alpha}. \tag{83}$$

The effective diffusive flux $\mathbf{d}_{k\alpha}$ can be written in Fickian form by simply extending Eq. (58) to multiphase flows, i.e.,

$$\mathbf{d}_{k\alpha} = -\mathbf{D}_{k\alpha} \cdot \nabla c_{k\alpha}, \tag{84}$$

where the diffusion-dispersion tensor $\mathbf{D}_{k\alpha}$ is defined as

$$\mathbf{D}_{k\alpha}(\mathbf{v}_\alpha) = \phi_\alpha \rho_\alpha \zeta_{k\alpha} \mathbf{I} + \rho_\alpha |\mathbf{v}_\alpha| \left[\zeta_{l\alpha} \mathbf{E}(\mathbf{v}_\alpha) + \zeta_{t\alpha} \mathbf{E}^{\perp}(\mathbf{v}_\alpha) \right], \tag{85}$$

where now $\zeta_{k\alpha}$ is the molecular diffusivity of component k in phase α, $\zeta_{l\alpha}$ and $\zeta_{t\alpha}$ are, respectively, the longitudinal and transversal dispersivities of phase α, and $|\mathbf{v}_\alpha|$ is, as before, the Euclidean norm of the phase velocity. The orthogonal projections along the phase velocity are as given by relation (60) with $\mathbf{v} \to \mathbf{v}_\alpha$.

Summing Eq. (83) over all phases, using relations (29) and (84), and the correction factor for species advection

$$\gamma_{kc} = \frac{\rho \sum_\alpha \lambda_\alpha c_{k\alpha}}{\sum_\alpha \rho_\alpha S_\alpha c_\alpha}, \tag{86}$$

where we have made use of relation (79), we obtain the species mass conservation equation for the multiphase mixture

$$\frac{\partial (\phi \rho c_k)}{\partial t} + \nabla \cdot (\gamma_{kc} \rho \mathbf{v} c_k) = \nabla \cdot \left(\sum_\alpha \mathbf{D}_{k\alpha} \cdot \nabla c_{k\alpha} \right) - \nabla \cdot \left(\sum_\alpha c_{k\alpha} \mathbf{J}_\alpha \right). \tag{87}$$

In passing from Eq. (83) to (87), we have assumed that

$$\sum_\alpha I_{k\alpha} = 0, \tag{88}$$

since the production of component k in phase α must be accompanied by destruction of this component in other phases. However, if there is an external generation of components due to chemical or biological reactions the sum of $I_{k\alpha}$ over all phases does not vanish and so this term should appear in Eq. (87). Moreover, since $\mathbf{v}_\alpha$ and $\mathbf{v}$ are needed in Eqs. (85) and (87), the momentum conservation equation is given by Darcy's law in the form given by Eqs. (10) and (15).

When heat transfer is important, we must write a further equation for the specific internal energy. In analogy with Eqs. (25) and (63), the energy balance equation for each constituent (k, α) will read as follows

$$\frac{\partial (\phi_\alpha \rho_{k\alpha} U_{k\alpha})}{\partial t} + \nabla \cdot (\rho_{k\alpha} U_{k\alpha} \mathbf{v}_{k\alpha}) + \nabla \cdot (p_{k\alpha} \mathbf{v}_{k\alpha}) = \nabla \cdot \left(\phi k_{T,k\alpha} \nabla T \right) - \varepsilon \sigma_{SB} T^4 + Q_{k\alpha}. \tag{89}$$

Using relations (2), (29), (78), (81), and (82) into the above equation and combining the result with the mass balance equation (83), we obtain the energy equation in terms of the common temperature

$$\phi S_\alpha \rho_\alpha c_{k\alpha} C_{k\alpha} \frac{\partial T}{\partial t} + c_{k\alpha} C_{k\alpha} \left(\lambda_\alpha \rho \mathbf{v} + \mathbf{J}_\alpha\right) \cdot \nabla T + C_{k\alpha} \left(I_{k\alpha} - \nabla \cdot \mathbf{d}_{k\alpha}\right) T = -\nabla \cdot \left(p_{k\alpha} \mathbf{v}_\alpha + H_{k\alpha} \mathbf{d}_{k\alpha} - \phi k_{T,k\alpha} \nabla T\right) - \varepsilon \sigma_{SB} T^4 + Q_{k\alpha}, \tag{90}$$

where we have used the definitions

$$U_{k\alpha} = C_{k\alpha} T, \tag{91}$$

$$H_{k\alpha} = U_{k\alpha} + \frac{p_{k\alpha}}{\rho_{k\alpha}}, \tag{92}$$

for the specific internal energy and enthalpy of constituent (k,α). Summing up over all species, making use of the definitions

$$U_\alpha = \sum_{k=1}^{n} c_{k\alpha} U_{k\alpha}, \tag{93}$$

$$C_\alpha = \sum_{k=1}^{n} c_{k\alpha} C_{k\alpha}, \tag{94}$$

$$p_\alpha = \sum_{k=1}^{n} p_{k\alpha}, \tag{95}$$

for the specific internal energy, heat capacity, and pressure of phase α, together with relation (34) for the correction factor for energy advection, and then summing up over all phases, we obtain the temperature equation for the compositional flow

$$\phi \rho C \frac{\partial T}{\partial t} + \left(\gamma_C \rho C \mathbf{v} + \sum_\alpha C_\alpha \mathbf{J}_\alpha\right) \cdot \nabla T = -\nabla \cdot \left(\sum_\alpha p_\alpha \mathbf{v}_\alpha - \sum_{k=1}^{n} \sum_\alpha H_{k\alpha} \mathbf{D}_{k\alpha} \cdot \nabla c_{k\alpha} - \phi k_T \nabla T\right) - T \sum_{k=1}^{n} \sum_\alpha C_{k\alpha} \left[I_{k\alpha} + \nabla \cdot (\mathbf{D}_{k\alpha})\right] - \varepsilon \sigma_{SB} T^4 + Q. \tag{96}$$

Using relations (70) and (71) into Eq. (96) we recover the form of the temperature equation for the composite system (i.e., the solid and the fluid phases). For a reactive solid phase, a term of the form

$$- T \sum_{k=1}^{n} C_{kR} I_{kR} \tag{97}$$

must be added on the right-hand side of Eq. (96).

To formally close this system of equations, we need some supplementary constraints. One class of supplementary constraints consists of thermodynamic relationships for the phase densities, saturations, and concentrations as functions of the phase pressure and fluid mixture composition (Allen 1985), which can be written as

$$c_{k\alpha} = c_{k\alpha}\left(\rho_\alpha, c_1, c_2, \ldots, c_n\right), \tag{98}$$

$$\rho_\alpha = \rho_\alpha\left(p_\alpha, T, c_{1\alpha}, c_{2\alpha}, \ldots, c_{n\alpha}\right), \tag{99}$$

$$S_\alpha = S_\alpha\left(p_\alpha, c_1, c_2, \ldots, c_n\right). \tag{100}$$

The actual form of these constraints may imply simultaneous sets of nonlinear algebraic equations giving the phase densities, concentrations, and saturations implicitly. In particular, this occurs when we use fugacity functions for the components in the fluid phases in conjunction with an equation of state to solve for local thermodynamic equilibria. In compositional flows, mass transfer between adjacent fluid phases is characterized by the variation of mass distribution of each species in these phases. In general, the coexisting fluid phases are assumed to be in equilibrium, which is a reasonable physical condition because the interchange of mass between adjacent phases occurs much faster than the fluid flow in the porous medium. Therefore, the distribution of component k into two adjacent phases, say α and β, is subject to the condition of stable thermodynamic equilibrium, which results from minimizing the Gibbs free energy of the compositional system. This condition can be expressed by demanding that the fugacities of component k in the two phases be equal:

$$F_{k\alpha}(p_\alpha, T, c_{1\alpha}, c_{2\alpha}, \ldots, c_{n\alpha}) = F_{k\beta}(p_\beta, T, c_{1\beta}, c_{2\beta}, \ldots, c_{n\beta}). \tag{101}$$

The other class of supplementary relations includes constitutive relations for the capillary pressures and relative permeabilities as functions of the phase saturations. Equation (87), Darcy's law for the phase velocities $\mathbf{v}_\alpha$, and Eq. (96) provide $n+P+1$ differential equations for $n+(n+3)P+1$ independent variables for S_α, p_α, $\mathbf{v}_\alpha$, c_k, $c_{k\alpha}$, and T. The $(n+2)P$ remaining relations needed to solve the problem are given by the saturation constraint (6), the $(P-1)$ capillary pressures (21), the n constraints (79), the $n(P-1)$ equal-fugacity constraints (101), and the P constraints

$$\sum_{k=1}^{n} c_{k\alpha} = 1, \tag{102}$$

for the mass fraction balance.

5 Chemical Flooding Compositional Flow in Porous Media

In the previous section we have described the equations governing the flow of compositional fluids in a porous medium in the absence of sources and/or sinks of chemical components by external means. It is a common practice in the oil industry to use

chemical flooding as a method to improve the recovery rates of oil fields and to get the oil trapped in the pores of rocks. In secondary oil recovery water is injected to move out the oil (water flooding). The injection of surfactants (surfactant flooding) to reduce the interfacial tension between the oil and the aqueous phases, thus allowing the recovery of oil trapped in small pores, has also been suggested (Lake 1996). As before, this type of compositional flow can be modelled using a mass balance equation for each component, Darcy's law for the phase velocities, and an energy balance equation. Under the assumption of thermal equilibrium among the components and fluid phases, this latter equation can be written in terms of the common temperature. In contrast to the exposition of previous section, an overall mass conservation or continuity equation for the pressure of the acqueous phase must be added, where the effects of the slight compressibility of the solid and coexisting fluid phases can be incorporated.

The mass conservation equation of component k can be expressed in terms of the total concentration of this component in the multiphase fluid per unit pore volume. This equation is similar in form to Eq. (87)

$$\frac{\partial\left(\phi\rho c_k\right)}{\partial t}+\nabla\cdot\left(\gamma_{kc}\rho\mathbf{v}c_k\right)=\nabla\cdot\left(\sum_{\alpha}\mathbf{D}_{k\alpha}\cdot\nabla c_{k\alpha}\right)-\nabla\cdot\left(\sum_{\alpha}c_{k\alpha}\mathbf{J}_{\alpha}\right)+\mathscr{I}_k, \quad (103)$$

except that now

$$\mathscr{I}_k=\sum_{\alpha}\mathscr{I}_{k\alpha}=\phi\sum_{\alpha}S_{\alpha}r_{k\alpha}+(1-\phi)r_{kR}+L_k, \quad (104)$$

where $r_{k\alpha}$ and r_{kR} are the chemical reaction rates of component k in the fluid phase α and rock phase, respectively, and L_k is the injection/production rate of the same component per unit volume, and

$$c_k=\left(1-\sum_{i=1}^{m}\hat{c}_i\right)\sum_{\alpha}S_{\alpha}c_{k\alpha}+\hat{c}_k, \quad (105)$$

where c_k is the overall concentration of component k, including the adsorbed phases, m is the number of volume-occupying components, $\hat{c}_k$ is the adsorbed concentration, and the term between parentheses represents the reduction of the pore volume due to adsorption effects. In order to ensure mass conservation, the following constraints must hold for each phase

$$\sum_{k=1}^{m}r_{k\alpha}=\sum_{k=1}^{m}r_{kR}=0, \qquad \sum_{k=1}^{m}\mathbf{D}_{k\alpha}\cdot\nabla c_{k\alpha}=0, \quad (106)$$

where the summations are taken over the total number of adsorbed components.

The phase velocity is given by the extended Darcy's law (10) for multiphase flow and the temperature equation has the same form of Eq. (96) with $I_{k\alpha}$ replaced by $\mathscr{I}_{k\alpha}$. In the calculation of chemical flooding, a pressure equation for the acqueous phase, say A, will be needed to account for the effects of adsorption. This equation can be derived from Eq. (57) by replacing I_k by $\mathscr{I}_k$ and summing up over all volume-occupying components. Noting from Eq. (105) that

$$\sum_{k=1}^{m} c_k = 1, \tag{107}$$

and using the constraints (61) and (106), and making $\rho \rightarrow \rho_A$ and $\mathbf{v} \rightarrow \mathbf{v}_A$, we obtain the mass balance equation

$$\frac{\partial (\phi \rho_A)}{\partial t} + \nabla \cdot (\rho_A \mathbf{v}_A) = \sum_{k=1}^{m} L_k. \tag{108}$$

The compressibility of the flooding phase and rock requires introducing the following definitions:

$$\mathscr{C}_A = \frac{1}{\rho_A} \frac{\partial \rho_{kA}}{\partial p_A}, \tag{109}$$

at a fixed temperature, for the acqueous phase, and

$$\mathscr{C}_R = \frac{1}{\phi} \frac{d\phi}{dp_A}, \tag{110}$$

for the rock. Assuming that the fluid and rock compressibilities are constant over a certain range of pressures, the above equations can be readily integrated to give

$$\rho_A \approx \rho_0 + \rho_0 \mathscr{C}_A (p_A - p_0), \tag{111}$$

$$\phi \approx \phi_0 + \phi_0 \mathscr{C}_R (p_A - p_0), \tag{112}$$

where we have used Taylor series expansions to approximate the exact solutions of Eqs. (109) and (110). Here ρ_0 and ϕ_0 are the density and porosity at the reference pressure p_0 of the acqueous phase. Expanding the time derivative in Eq. (108), using relations (106) and (107), and replacing $\rho_A \mathbf{v}_A$ by Darcy's law written in the form

$$\rho_A \mathbf{v}_A = -\lambda \mathbf{k} \cdot \nabla p_A - \sum_{\alpha} \lambda_\alpha \mathbf{k} \cdot (\nabla p_{c\alpha A} - \rho_\alpha g \nabla z), \tag{113}$$

where λ_α is the phase mobility defined as

$$\lambda_\alpha = \frac{k_{r\alpha}}{\mu_\alpha} \sum_{k=1}^{n} \rho_k c_{k\alpha}, \tag{114}$$

and $p_{c\alpha A}$ is the capillary pressure function

$$p_{c\alpha A} = p_\alpha - p_A, \tag{115}$$

which is used to evaluate all other phase pressures, we obtain the pressure equation

$$\phi \mathscr{C} \frac{\partial p_A}{\partial t} - \nabla \cdot (\lambda \mathbf{k} \cdot \nabla p_A) = \nabla \cdot \left[\sum_\alpha \lambda_\alpha \mathbf{k} \cdot (\nabla p_{c\alpha A} - \rho_\alpha g \nabla z) \right] + \sum_{k=1}^{m} L_k, \tag{116}$$

where $\mathscr{C}$ is the total compressibility defined as

$$\mathscr{C} = \frac{\phi_0}{\phi} \sum_{k=1}^{m} \rho_{k0} c_k \left(\mathscr{C}_{kA} + \mathscr{C}_R \right). \tag{117}$$

We note that relation (111) is actually a sum over all volume-occupying components, with

$$\rho_A \mathscr{C}_A = \sum_{k=1}^{m} \rho_{kA} \mathscr{C}_{kA}. \tag{118}$$

This problem involves $P(n+3)+n+m+1$ independent variables: c_k, $\hat{c}_k$, $c_{k\alpha}$, $\mathbf{v}_\alpha$, p_α, S_α, and T, while Eqs. (103) and (116), Darcy's law for the phase velocity, and the energy balance provide $n+P+2$ differencial equations. The other $(n+2)P+m-1$ relations are provided by the constraints (6), (79), (101), (107), (115), (118), and

$$\sum_{k=1}^{m} c_{k\alpha} = 1, \qquad \hat{c}_k = \hat{c}_k \left(c_1, c_2, \ldots, c_k \right), \tag{119}$$

for the phase concentration and adsorption constraints.

6 Compositional Flow in Fractured Porous Media

A *fractured porous medium* has throughout its extent a system of interconnected fractures dividing the medium into a number of essentially disjoint blocks of porous rocks, called the *matrix blocks*. The fractured medium has two main length scales of interest: the microscopic scale of the fracture thickness ($\sim 10^{-4}$ m) and the macroscopic scale of the average distance between fracture planes, which is the size of the matrix blocks (from $\sim$0.1 to $\sim$1 m). Since the entire medium is about 10^3–10^4 m across, the flow can be numerically simulated only in some average sense. The analysis of fluid flow through fractures in rocks is a process that is relevant in many areas of the geosciences, ranging from ground-water hydrology to oil production. For

instance, in most petroleum reservoirs and some tight sands, natural fractures play a critical role in controlling fluid flow and hence production in recovery processes.

There are major differences between recovery performance of fractured and non-fractured oil reservoirs. The high contrast of capillarity between the solid matrix and the fractures is the main cause of these differences. For instance, high rate wells in the early life of the field is one main characteristic of fractured reservoirs due to the high effective single-phase permeability of the combined matrix-fracture porous media (Firoozabadi 2000). Depending on their matrix/fissure permeabilities and matrix block sizes, fractured reservoirs can be produced using several recovery processes, which include primary recovery, gas drive, waterflood, miscible or immiscible gas-flood, and enhanced oil recovery methods, such as gas injection combined with water injection, chemical, and thermal methods (Manrique et al. 2007).

In view of its important applications in the oil industry, several conceptual models have been developed for describing fluid flow in fractured porous media. Basically, each method can be distinguished on the basis of the storage and flow capabilities of the porous medium and fracture. The storage characteristics are associated with porosity, while the flow characteristics are associated with permeability. Out of the several existing conceptual models, the double-porosity/dual-permeability concept has been the most widely used approach for modelling fluid flow, heat transfer, and chemical transport through fractured reservoirs (Lemonnier and Bourbiaux 2010a, b). In addition, multiple-interacting continua and multi-porosity/multi-permeability conceptual models have been also developed (Sahimi 1995). Further distinctions among the models can be drawn on the basis of the spatial and temporal scales of integration, or averaging, of the flow regime. For instance, scales of concern in fracture flow include: (a) the very near field, where flow occurs in a single fracture and porous medium exchange is possible; (b) the near field, where flow occurs in a fracture porous medium and each fracture is described in detail; (c) the far field, where flow occurs in two overlapping continua with mass exchanged through coupling parameters; and (d) the very far field, where fracture flow occurs, on average, in an equivalent porous medium (Bear and Berkowitz 1987). However, state-of-the-art reservoir simulation packages employed in the oil industry often do not take into account the complex random geometry of real fractured systems that can vary from one grid-block to another, and sometimes even within a single grid-block. The are two reasons for this: first, there exists no technology as yet to image the micro-fractures in-situ, and second, most of the existing software does not use micro-scale flow equations to calculate the change of flow variables.

6.1 Dual-Continuum Model

In particular, dual-continuum models are based on an idealized flow medium consisting of a primary porosity created by deposition and lithification and a secondary porosity created by fracturing, jointing, or dissolution. The basis of these models is the observation that unfractured rocks account for much of the porosity (storage) of

the medium, but little of the permeability (flow). In contrast, fractures may have negligible storage, but high permeability. So, the porous medium and the fractures are envisioned as two separate but overlapping continua and fluid mass transfer between these two continua occurs at the fracture-porous medium interface (Barenblatt et al. 1960; Barenblatt and Zheltov 1960; Warren and Root 1963; Lemonnier and Bourbiaux 2010a).

Before writing down the governing equations of compositional flow in naturally fractured reservoirs in the framework of the dual-porosity/dual-permeability concept, we must introduce the following definitions. First, we define the matrix porosity ϕ_m and the fracture porosity ϕ_f as the pore volume of the matrix blocks and fractures, respectively, divided by unit volume of both media. Second, we must distinguish between quantities in the matrix and fractures. For instance, $c_{m,k\alpha}$, $S_{m,\alpha}$, $\rho_{m,\alpha}$, and $\mathbf{v}_{m,\alpha}$ denote the concentration of component k, saturation, density, and velocity of phase α in the matrix blocks, while $c_{f,k\alpha}$, $S_{f,\alpha}$, $\rho_{f,\alpha}$, and $\mathbf{v}_{f,\alpha}$ are the same variables in the fracture system. Now, using Eq. (83), the mass balance equation for each component k, including water, in the matrix blocks, after summing over all phases, is expressed as

$$\frac{\partial}{\partial t}\left(\phi_m \sum_\alpha S_{m,\alpha}\rho_{m,\alpha}c_{m,k\alpha}\right) + \nabla\cdot\left(\sum_\alpha \rho_{m,\alpha}c_{m,k\alpha}\mathbf{v}_{m,\alpha} + \mathbf{d}_{m,k\alpha}\right) = \sum_\alpha \mathscr{I}_{m,k\alpha} - \mathscr{F}_{mf,k\alpha}, \tag{120}$$

while in the fracture system, the same equation will read as follows

$$\frac{\partial}{\partial t}\left(\phi_f \sum_\alpha S_{f,\alpha}\rho_{f,\alpha}c_{f,k\alpha}\right) + \nabla\cdot\left(\sum_\alpha \rho_{f,\alpha}c_{f,k\alpha}\mathbf{v}_{f,\alpha} + \mathbf{d}_{f,k\alpha}\right) = \sum_\alpha \mathscr{I}_{f,k\alpha} + \mathscr{F}_{mf,k\alpha}, \tag{121}$$

where the volumetric source/sink terms $\mathscr{I}_{m,k\alpha}$ and $\mathscr{I}_{f,k\alpha}$ are as defined by relation (104) and $\mathscr{F}_{mf,k\alpha}$ is the matrix-fracture mass flow rate of component k in phase α per unit bulk volume of the reservoir. The molecular diffusion and dispersion flux of component k in phase α in medium M, i.e., $\mathbf{d}_{\mathrm{M},k\alpha}$, where M$= f, m$, can be written in Fickian form using relation (84), with the diffusion-dispersion tensor in each medium having the same form of relation (85). As in Eq. (104), the terms $\mathscr{I}_{\mathrm{M},k\alpha}$ contain the chemical reaction rates of component k in the fluid phases and rock phase and the injection/production rate of the same component per unit volume, which can be written as

$$L_{\mathrm{M},k\alpha} = \rho_{\mathrm{M},\alpha}c_{\mathrm{M},k\alpha}\mathscr{Q}_{\mathrm{M},\alpha}, \tag{122}$$

where $\mathscr{Q}_{\mathrm{M},\alpha}$ denotes the volumetric injection/production rate of phase α in medium M$= f, m$ per unit volume of the reservoir. This rate is positive in production and negative in injection.

The phase velocity in both media $\mathbf{v}_{\mathrm{M},\alpha}$ is expressed using Darcy's law (10) with the mobility tensor of phase α as defined by relation (11). However, we note that the absolute permeability of the medium $\mathbf{k}$ is the equivalent permeability of the flow continuum under consideration, that is, the permeability of the medium that is scaled up to the simulated flow scale. For instance, in the dual-continuum model of (Warren and Root 1963), the permeability of the fracture large-scale continuum is obtained by homogenizing the transport equations on the fracture network, assuming impervious boundaries. On the other hand, if heat transfer is important, we need to add two additional equations for the specific internal energy $U_{\mathrm{M},k\alpha}$ in each medium. These equations have the same form of Eq. (89), except that now the term $Q_{\mathrm{M},k\alpha}$ is a source/sink or fracture-matrix interaction term for energy. If we assume thermal equilibrium between the fluids and the media, these two equations can be combined into a single equation for the common temperature T. To close the system, additional equations must be added to the flow equations. These are the two saturation constraints

$$\sum_{\alpha} S_{\mathrm{M},\alpha} = 1, \tag{123}$$

the $2P$ composition constraints

$$\sum_{k=1}^{n} c_{\mathrm{M},k\alpha} = 1, \tag{124}$$

the $2P - 2$ capillary pressure relationships

$$p_{\mathrm{M},c\alpha\beta} = p_{\mathrm{M},c\alpha} - p_{\mathrm{M},c\beta}, \tag{125}$$

and the $2n(P - 1)$ equilibrium conditions of the form given by relation (101) for M$= m, f$.

The matrix-fracture transport flux $\mathscr{F}_{mf,k\alpha}$ in Eqs. (120) and (121) can be expressed either by the direct application of Darcy's law between matrix and fractures with the explicit input of matrix block dimensions or the input of a shape factor that takes into account the size and shape of the matrix blocks. For instance, considering a single-phase, quasi-steady-state flow, Warren and Root (1963) expressed $\mathscr{F}_{mf}$ as

$$\mathscr{F}_{mf} = -\Lambda k_m \frac{\rho}{\mu} \left(p_f - p_m \right), \tag{126}$$

where k_m is the matrix permeability (assumed to be isotropic), p_f and p_m the fracture and matrix pressures, ρ the fluid density, μ the fluid viscosity, and Λ the shape factor. This factor is a constant matrix-fracture exchange factor that depends only on the geometry and characteristic size of the matrix blocks assuming a

steady-state matrix-fracture transfer. Its dimension is the inverse of a squared length. For instance, assuming a cubic block of size a, Warren and Root (1963) derived the following expression for the shape factor

$$\Lambda = \frac{4N(N+2)}{a^2}, \tag{127}$$

where N is the number of flow dimensions.

In most modern simulators the expression for $\mathscr{F}_{mf,k\alpha}$ is based on a simplified representation of the dual-medium fractured system, where fracture and matrix grids are identical and superposed. Each cell is a discretized element of volume including both fracture and matrix blocks and contains a number of identical matrix blocks, which are assumed to be parallelepipeds of volume abc. Therefore, an expression for the matrix-fracture transfer flux per unit volume of matrix rock is

$$\mathscr{F}_{mf,k\alpha} = \frac{1}{abc}\sum_{i=1}^{6} f_{i,k\alpha}, \tag{128}$$

where the $f_{i,k\alpha}$ represent the mass flux of component k in phase α through each of the six faces of the block. This term is usually split up into two contributions due to convection-diffusion and diffusion-dispersion effects (Sarda et al. 1997). Since the matrix-fracture flow rate is governed by the matrix permeability, the absolute permeability used for the calculation of these flow rates is given by $k_{m,i}$, the matrix permeability in the face direction i, which allows for permeability anisotropy through different values of $k_{m,i}$ in each direction. An expression for the fluxes $f_{i,k\alpha}$ is given by Sabathier et al. (1998), where for the anisotropic case the matrix-fracture coupling transmissibility between a cell of the matrix grid and the corresponding one of the fracture grid is defined as

$$\Lambda k_{m,i} = 4\left(\frac{k_{m,x}}{a^2} + \frac{k_{m,y}}{b^2} + \frac{k_{m,z}}{c^2}\right). \tag{129}$$

If deformation of the matrix-fracture system is important, the body force term in Eq. (42) for the solid displacements is of the form

$$\mathbf{F} = \left(\phi_m p_m + \phi_f p_f\right)\mathbf{I}, \tag{130}$$

where p_m and p_f are, as in Eq. (126), the mean pressure exerted by the fluid on the pore matrix and pore fractures, respectively. A description of deformation-dependent flow models of various porosities and permeabilities relevant to the characterization of naturally fractured reservoirs is given by Bai et al. (1993).

6.2 Triple-Continuum Model

The dual-continuum models are suitable for the simulation of a fractured reservoir with low-permeability matrix blocks. However, for severely fractured reservoirs where a dominant fracture system intercepts a less pervasive and nested fracture network, which in turn is set within a porous matrix, dual-porosity/dual-permeability models may not be appropriate. An immediate extension of the dual-porosity conceptualization is to triple porosity. For a triple-porosity/dual-permeability system, matrix pores are interwoven with non-percolating fissures and they interact with open cracks through fluid exchange among different phases. While these models are suitable for severely fractured reservoirs with moderate permeability, in reservoirs with high permeability an extension of the model to a triple-porosity/triple-permeability concept would be required. One important difference is that the triple-permeability model allows each fluid phase α to carry its own permeability.

Another example of fractured reservoirs where the extension to a triple-continuum model is important concerns the existence of vugs (i.e., empty holes or cavities) in naturally fractured reservoirs. Typical fractured vuggy reservoirs consist of a large and well connected fractured, lower-permeable rock matrix with a large number of cavities, or vugs, of irregular shapes and sizes ranging from millimetres to metres in diameter. Many of the small-sized cavities appear to be isolated from fractures. Therefore, conceptual models for vugs include: (a) vugs that may be indirectly connected to fractures through small fractures or microfractures; (b) vugs that are isolated from fractures or separated from fractures by the rock matrix; and (c) the case where some vugs are connected to fractures and some others are isolated. Triple-porosity models for flow in vuggy matrix-fracture systems have been presented by Liu et al. (2003), Kang et al. (2006) and Wu et al. (2007).

Irregular and stochastic distributions of small (f) and large fractures (F) can also be handled using a triple-continuum model. For example, experimental observations show that in typical fractured rocks there may be many more small fractures than large ones (Liu et al. 2000). Therefore, in a triple-continuum model the fracture-matrix system can be conceptualized as consisting of a single porous rock matrix and two types of fractures: large globally connected fractures and small fractures that are locally connected to the large fractures and the rock matrix. As before, compositional fluid flow and heat-transfer processes can be described using a continuum approach for the two types of fractures and the matrix. We have now three transport equations describing mass conservation for each component k in the multiphase mixture within each of the three continua, which can be written by analogy with Eqs. (120) and (121) as follows:

$$\frac{\partial}{\partial t}\left(\phi_m \sum_\alpha S_{m,\alpha}\rho_{m,\alpha}c_{m,k\alpha}\right) + \nabla\cdot\left(\sum_\alpha \rho_{m,\alpha}c_{m,k\alpha}\mathbf{v}_{m,\alpha} + \mathbf{d}_{m,k\alpha}\right) = \sum_\alpha \mathscr{I}_{m,k\alpha} - \mathscr{F}_{mf,k\alpha} - \mathscr{F}_{mF,k\alpha}, \quad (131)$$

$$\frac{\partial}{\partial t}\left(\phi_F \sum_\alpha S_{F,\alpha}\rho_{F,\alpha}c_{F,k\alpha}\right) + \nabla\cdot\left(\sum_\alpha \rho_{F,\alpha}c_{F,k\alpha}\mathbf{v}_{F,\alpha} + \mathbf{d}_{F,k\alpha}\right) = \sum_\alpha \mathscr{I}_{F,k\alpha} + \mathscr{F}_{mF,k\alpha} + \mathscr{F}_{fF,k\alpha}, \quad (132)$$

$$\frac{\partial}{\partial t}\left(\phi_f \sum_\alpha S_{f,\alpha}\rho_{f,\alpha}c_{f,k\alpha}\right) + \nabla\cdot\left(\sum_\alpha \rho_{f,\alpha}c_{f,k\alpha}\mathbf{v}_{f,\alpha} + \mathbf{d}_{f,k\alpha}\right) = \sum_\alpha \mathscr{I}_{f,k\alpha} + \mathscr{F}_{mf,k\alpha} - \mathscr{F}_{fF,k\alpha}, \quad (133)$$

where ϕ_m, ϕ_F, and ϕ_f are the porosities of the matrix blocks, the large fractures, and the small fractures, respectively. Under the assumption of quasi steady-state flow, the mass transfer flux terms can be defined according to Eq. (126) as

$$\mathscr{F}_{mF} = -\Lambda_{Fm}k_m\frac{\rho}{\mu}\left(p_F - p_m\right), \quad (134)$$

$$\mathscr{F}_{mf} = -\Lambda_{fm}k_m\frac{\rho}{\mu}\left(p_f - p_m\right), \quad (135)$$

$$\mathscr{F}_{fF} = -\Lambda_{fF}k_f\frac{\rho}{\mu}\left(p_F - p_f\right), \quad (136)$$

for large fracture-matrix, small fracture-matrix, and large fracture/small fracture interactions. Following Warren and Root (1963), $\Lambda_{Fm} = \Lambda_{fm} = \Lambda$, while for the f-F interaction, the shape factor for one-dimensional small fractures is defined by (Wu et al. 2004)

$$\Lambda_{fF} = \frac{A_{fF}}{d_{fF}}, \quad (137)$$

where A_{fF} is the total large-fracture and small-fracture connection area per unit volume of rock and d_{fF} is the characteristic distance between large and small fractures. Again the phase velocity in each medium $\mathbf{v}_{\mathrm{M},\alpha}$, for $\mathrm{M} = m, F, f$, is given by Darcy's law (10). An energy conservation equation for each medium is also required if the effects of heat transfer are important. However, these equations can be combined into a single equation for the temperature if thermal equilibrium is assumed for the entire system. This gives a total of $3(n+P)+1$ differential equations. The system is closed by adding to the flow equtions 3 saturation constraints, $3P$ concentration constraints, $3P-3$ capillary pressure relationships, and $3n(P-1)$ equilibrium conditions as given by relations (123), (124), (125), and (101), respectively. As a final remark, for deformation-dependent flows, the body force in Eq. (42) will have the form

$$\mathbf{F} = \left(\phi_m p_m + \phi_F p_F + \phi_f p_f\right)\mathbf{I}, \quad (138)$$

where p_m, p_F, and p_f are the pressures exerted by the fluid on the pores of the three media. The extension of the present triple-continuum model to a unified

multiporosity/multipermeability model can be done using the formulation proposed by Bai et al. (1993), which permits the generalization of porosity- or permeability-oriented models to any degree. Such models are suitable for the characterization of a large variety of formation types.

Acknowledgments This work has been partially supported by the Consejo Nacional de Ciencia y Tecnología of Mexico (CONACyT) under the project CONACyT-EDOMEX-2011-C01-165873.

References

Adler PM, Brenner H (1988) Multiphase flow in porous media. Annu Rev Fluid Mech 20:35–59
Allen MB (1985) Numerical modelling of multiphase flow in porous media. Adv Water Res 8:162–187
Amaefule JO, Handy LL (1982) The effect of interfacial tensions on relative oil/water permeabilities of consolidated porous media. Soc Pet Eng J 22:371–381
Amiri A, Vafai K (1994) Analysis of dispersion effects and non-thermal equilibrium, non-Darcian, variable porosity incompressible flow through porous media. Int J Heat Mass Transf 37:939–954
Bai M, Elsworth D, Roegiers J-C (1993) Multiporosity/multipermeability approach to the simulation of naturally fractured reservoirs. Water Resour Res 29:1621–1633
Bardon C, Longeron DG (1980) Influence of interfacial tensions on relative permeability. Soc Pet Eng J, 391–401
Barenblatt GI, Zheltov IP (1960) Fundamental equations of filtration of homogeneous liquids in fissured rocks. Sov Phys-Doklady 5:522–525
Barenblatt GI, Zheltov IP, Kochina IN (1960) Basic concepts in the theory of seepage of homogeneous liquids in fissured rocks. J Appl Math Mech 24:1286–1303
Bear J (1988) Dynamics of fluids in porous media. Dover, New York
Bear J, Berkowitz B (1987) Groundwater flow and pollution in fractured rock aquifers. In: Novak P (ed) Development of hydraulic engineering, vol 4. Elsevier Applied Science, Oxford
Chen Z (2007) Homogenization and simulation for compositional flow in naturally fractured reservoirs. J Math Anal Appl 326:12–32
Chen Z, Huan G, Ma Y (2006) Computational methods for multiphase flows in porous media. SIAM, Philadelphia
Coats K (1980) An equation-of-state compositional model. Soc Pet Eng J, 363–376
Ellenbroek WG, van Hecke M, van Saarloos W (2009) Jammed frictionless disks: connecting global and local response. Phys Rev E 80:061307
Firoozabadi A (2000) Recovery mechanisms in fractured reservoirs and field performance. J Can Pet Technol 39(11):13–17
Forchheimer P (1901) Wasserbewegung durch Boden. Zeitschrift des Vereines Deutscher Ingenieure 45:1736–1741
Frisch U (1968) Wave propagation in random media. In: Bharucha-Reid AT (ed) Probabilistic methods in applied mathematics. Academic Press, New York, pp 75–198
Hewett TA (1986) Fractal distributions of reservoir heterogeneity and their influence on fluid transport. In: 61st annual technical conference and exhibition of the society of petroleum engineers, SPE Paper 15386, New Orleans, Louisiana, 5–8 October 1986
Hoa NT, Gaudu R, Thirriot C (1977) Influence of the hysteresis effect on transient flows in saturated-unsaturated porous media. Water Resour Res 13:992–996
Kang Z, Wu YS, Li J, Wu Y, Zhang J, Wang G (2006) A triple-continuum numerical model for simulating multiphase flow in naturally fractured vuggy petroleum reservoirs. In: SPE annual technical conference and exhibition. SPE Paper 102356, San Antonio, Texas, 24–27 September

Karal FC, Keller JB (1964) Elastic, electromagnetic, and other waves in a random medium. J Math Phys 5:537–547
Khoei AR, Mohammadnejad T (2011) Numerical modeling of multiphase flow in deforming porous media: a comparison between two- and three-phase models for seismic analysis of earth and rockfill dams. Comput Geotech 38(2):142–166
Lake LW (1996) Enhanced oil recovery. Prentice-Hall, New Jersey
Larose E (2006) Mesoscopics of ultrasound and seismic waves: application to passive imaging. Annales de Physique 31(3):1–126
Lemonnier P, Bourbiaux B (2010a) Simulation of naturally fracture reservoirs. State of the art. Part 1. Physical mechanisms and simulator formulation. Oil Gas Sci Technol - Rev IFP 65(2):239–262
Lemonnier P, Bourbiaux B (2010b) Simulation of naturally fracture reservoirs. State of the art. Part 2. Matrix-fracture transfers and typical features of numerical studies. Oil Gas Sci Technol - Rev IFP 65(2):263–286
Lichtner PC (1988) The quasi-stationary state approximation to coupled mass transport and fluid-rock interaction in a porous media. Geochimica et Cosmochimica Acta 52:143–165
Liu HH, Ahlers CF, Cushey MA (2000) Analysis of hydrologic properties. Report ANL-NBS-HS-000002. Berkeley, California: Lawrence Berkeley Laboratory. Las Vegas, Nevada: CRWMS M&O
Liu JC, Bodvarsson GS, Wu YS (2003) Analysis of pressure behavior in fractured lithophysal reservoirs. J Contam Hydrol 62–63:189–211
Manrique EJ, Muci VE, Gurfinkel ME (2007) EOR field experiences in carbonate reservoirs in the United States. SPE Reser Eval Eng 10(6):667–686
Mätthai SK, Belayneh M (2004) Fluid flow partitioning between fractures and a permeable rock matrix. Geophys Res Lett 31(7):7602–7606
Mei CC, Auriault J-L (1991) The effect of weak inertia on flow through a porous medium. J Fluid Mech 222:647–663
Miller CT, Christakos G, Imhoff PT, l, McBride JF, Pedit JA et al.(1998) Multiphase flow and transport modeling in heterogeneous porous media: challenges and approaches. Adv Water Res 21(2):77–120
Morel-Seytoux HJ (1969) Introduction to flow of immiscible liquids in porous media. In: De Weist RJM (ed) Flow through porous media. Academic Press, New York, pp 456–516
Parker JC (1989) Multiphase flow and transport in porous media. Rev Geophys 27:311–328
Peaceman DW (1966) Improved treatment of dispersion in numerical calculation of multidimensional miscible displacements. Soc Pet Eng J 6:213–216
Phillips OM (1991) Flow and reactions in permeable rocks. Cambridge University Press, Cambridge
Pruess K, Narasimhan TN (1985) A practical method for modeling fluid and heat flow in fractured porous media. Soc Pet Eng J 25:14–26
Ryzhik L, Papanicolaou G, Keller JB (1996) Transport equation for elastic and other waves in random media. Wave Motion 24:327–370
Sabathier JC, Bourbiaux B, Cacas MC, Sarda S (1998) A new approach of fractured reservoirs. In: SPE international petroleum conference and exhibition. SPE Paper 39825, Villahermosa, Mexico, 3–5 March 1998
Sahimi M (1995) Flow and transport in porous media and fractured rock: from classical methods to modern approaches. VCH, Weinheim
Sahimi M, Tajer SE (2005) Self-affine fractal distribution of the bulk density, elastic moduli and seismic wave velocities of rocks. Phys Rev E 71:046301
Sarda S, Bourbiaux B, Cacas MC, Sabathier JC (1997) An innovative procedure to compute equivalent block size in a dual-porosity model. Paper presented at the 9th European symposium on improved oil recovery. The Hague, The Netherlands, 20–22 October
Srivastava RP, Sen MK (2009) Fractal-based stochastic inversion of poststack seismic data using very fast simulated annealing. J Geophys Eng 6:412425
Starikovičius V (2003) The multiphase flow and heat transfer in porous media. Report Fraunhofer-Institut für Techno- und Wirtschaftsmathematik ITWM 55, 30 pp

Steefel CI, Lichtner PC (1998a) Multicomponent reactive transport in discrete fractures: I. Controls on reaction front geometries. J Hydrol 209:186–199

Steefel CI, Lichtner PC (1998b) Multicomponent reactive transport in discrete fractures: II. Infiltration of hyperalkaline groundwater at Maqarin, Jordan, a natural analogue site. J Hydrol 209:200–224

Stone HL (1973) Estimation of three-phase relative permeability and residual oil data. J Can Pet Technol 12(4):53–61

Stothoff S, Or D (2000) A discrete-fracture boundary integral approach to simulating coupled energy and moisture transport in a fractured porous medium. In: Faybishenko B, Witherspoon PA, Benson SM (eds) Dynamics of fluids in fractured rocks, concepts, and recent advances, vol 122. AGU Geophysical Monograph. American Geophysical Union, Washington, pp 269–279

Warren JE, Root PJ (1963) The behavior of naturally fractured reservoirs. Soc Pet Eng J 3:245–255

Weaver RL (1990) Diffusivity of ultrasound. J Mech Phys Solids 38:55–86

Whitaker S (1996) The Forchheimer equation: a theoretical development. Transp Porous Media 25:27–61

Wu YS (2000) On the effective continuum method for modeling multiphase flow, multicomponent transport and heat transfer in fractured rock. In: Faybishenko B, Witherspoon PA, Benson SM (eds) Dynamics of fluids in fractured rocks, concepts, and recent advances, vol 122. AGU Geophysical Monograph. American Geophysical Union, Washington, pp 299–312

Wu YS, Pruess K (1988) A multiple-porosity method for simulation of naturally fractured petroleum reservoirs. SPE Reserv Eng 3:327–336

Wu YS, Qin G (2009) A generalized numerical approach for modeling multiphase flow and transport in fractured porous media. Commun Comput Phys 6(1):85–108

Wu YS, Liu HH, Bodvarsson GS, Zellmer KE (2004) A triple-continuum approach for modeling flow and transport processes in fractured rocks. J Contam Hydrol 73:145–179

Wu YS, Ehlig-Economides C, Qin G, Kang Z, Zhang W, Babatunde A, Qingfeng T (2007) A triple-continuum pressure-transient model for a naturally fractured vuggy reservoir. In: SPE annual technical conference and exhibition. SPE Paper 110044-MS, Anaheim, California, 11–14 November

Wyllie MRJ (1962) Relative permeability. In: Frick TC (ed) Petroleum production handbook, Chap. 25. McGraw-Hill, New York

Turbulent Thermal Convection

Enrico Fonda and Katepalli R. Sreenivasan

Abstract Turbulent thermal convection is a phenomenon of crucial importance in understanding the heat transport and dynamics of several natural and engineering flows. Real world systems such as the Earth's atmosphere—its oceans as well as the interior—and the interior of stars such as the Sun, are all affected to various degrees by thermal convection. The simplified physical model used to understand this ubiquitous heat transport mechanism is the Rayleigh-Bénard convection, which is a fluid flow driven by a temperature difference between the top and bottom plates of an experimental cell with adiabatic sidewalls. Despite the long history of the subject and the recent progress in theoretical, numerical and experimental domains, many questions remain unresolved. We report some recent results and discuss a few open issues.

1 Introduction

The density of fluids in general decreases with increasing temperature. A temperature difference can then drive a flow via buoyancy force. This ubiquitous phenomenon, called convection, has a history that goes back to the 18th century with the work of Hadley, Lomonosov, Thompson and others, but is still the subject of active research (e.g., Ahlers et al. 2009a; Lohse and Xia 2010; Chillà and Schumacher 2012; Xia 2013). The possibility that convection greatly enhances heat transport compared to thermal conduction makes it basic for heat transfer engineering—for example, ovens, nuclear reactors, ventilation systems, crystallization processes and casting. In natural phenomena, motion due to non-uniform heating is perhaps the most widespread kind of fluid motion in the universe.

E. Fonda (✉) · K.R. Sreenivasan
New York University, New York, USA
e-mail: enrico.fonda@gmail.com

K.R. Sreenivasan
e-mail: katepalli.sreenivasan@nyu.edu

J. Klapp et al. (eds.), *Selected Topics of Computational and Experimental Fluid Mechanics*, Environmental Science and Engineering,
DOI 10.1007/978-3-319-11487-3_2

On the Earth's surface, convection plays a fundamental role in weather and climate, driving the oceans (Marshall and Schott 1999) as well as the atmosphere (Hartmann et al. 2001). In the Earth's interior, convection plays a role both in the outer core (Cardin and Olson 1994) and in the mantle (Schubert et al. 2001). The convective liquid metal flows in the core are thought to be responsible of the Earth's magnetic field through a dynamo mechanism (Buffett 2000). The convective mantle motion is related to the phenomenon of plate tectonics (Tackley 2000); even when planets do not show plate tectonics, as in the case of Venus or Mars, mantle convection is important because of its role in transporting heat from the planet interior to the surface. In giant planets, which have a hot interior, convection occurs when conduction and radiation are not sufficient to transport all the heat (Guillot 2005).

In the Sun, the nuclear energy generated at the core is transported by the convective motion in the outer 30 % of the radius. This motion shows cellular structures on different scales, distinguished usually as granular (2,000 km), mesoscale (5,000–10,000 km), supergranular (3×10^4 km) and giant ($1–2 \times 10^5$ km) cells (Nordlund et al. 2009). Cellular structures driven by convective motions are also evident in the atmosphere (see Fig. 1).

Many basic questions relating to these diverse systems are similar. How do we predict the heat transfer due to the convective motion? Conversely, what flow structure is needed to transport a given amount of thermal energy? How important are the macroscopic large scale structures? What is their dynamics? What are the properties of the small scale turbulence? How does the small scale motion relate to large scales? And so forth.

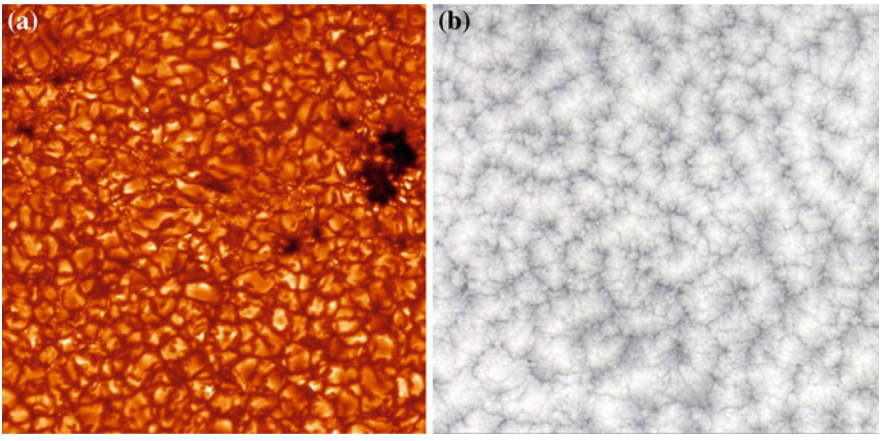

Fig. 1 Cellular convective structures in natural phenomena. **a** Sun's granular structure where each cell is on the order of 1,000 km. Image from Swedish 1-m Solar Telescope (SST)—Royal Swedish Academy of Sciences—Oddbjorn Engvold, Jun Elin Wiik, Luc Rouppe van der Voort. **b** Closed cells structures in a layer of marine stratocumulus over the southeastern Pacific Ocean. Each cell is on the order of 5 km. Image by NASA/GSFC/LaRC/JPL, MISR Team

Even though all convective flows share similarities, they are also different from each other in detail, and include additional physical processes such as rotation, stratification, salinity, pressure gradients, gravity gradients, phase changes, and magnetic fields. These effects complicate what is already one of the most challenging problems in nature, namely turbulence. It is thus useful, indeed essential, to study an idealized form of thermal convection in order to gain basic physical understanding. This idealized flow is the Rayleigh-Bénard convection (RBC).

2 Rayleigh-Bénard Convection

In Rayleigh-Bénard convection the flow is confined to a cylindrical container of height H and diameter D; $\Gamma = D/L$ is called the aspect ratio. The sidewalls are adiabatic and the bottom and top walls are conducting. The fluid motion is driven by the temperature difference between the bottom hot plate and the cold top plate (see Fig. 2).

The dual-name assigned to the flow acknowledges the work of Henri Bénard and Lord Rayleigh. Bénard's contribution started with his Ph.D. thesis from 1901, in which he observed the famous hexagonal cells (see Fig. 3) on a thin layer of spermaceti (whale oil) placed on a heated metallic plate. For lack of theoretical insight, these seminal observations were received with some reserve by the thesis committee presided by the (future) 1908 Nobel laureate, Gabriel Lippman, who stated "...though Bénard's main thesis was very peculiar, it did not bring significant elements to our knowledge. ... the thesis should not to be considered as the best of what Bénard could produce" (Wesfreid 2006).

One who did not miss the theoretical insight was Lord Rayleigh, who first solved the linearized stability problem in 1916. Under the Boussinesq approximation, which assumes that the fluid properties are constant except in the buoyancy term, the equations that describe the system are relatively simple. For these equations the only

Fig. 2 The image on the *left* shows a diagram of a Rayleigh-Bénard convection cell. The shadowgraph images from Xi et al. (2004) show the structure of the thermal plumes and the mean wind into which they organize

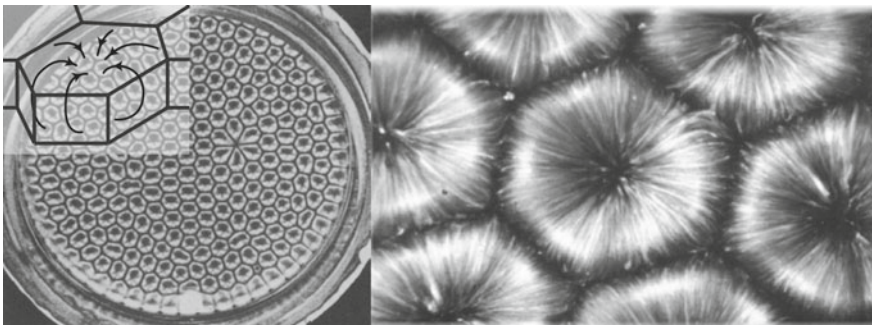

Fig. 3 The images show the hexagonal convective cells similar to those observed by Bénard in his experiments. Bénard was informed that the cells, now known to be due to the temperature dependence of surface tension, resembled the pattern of the solar granulation photographed by Janssen. Images from Van Dyke (1982): *left* photograph by Koschmieder (1974) and *right* photograph by Velarde et al. (1982). The sketch of the hexagonal flow structure in a Rayleigh-Bénard cell is inspired by Getling (1991)

dimensionless numbers necessary for dynamic similarity, given the geometry, are the Rayleigh number Ra, and the Prandtl number Pr. Here,

$$Ra = \frac{\alpha g \Delta T H^3}{\nu \kappa}, \quad Pr = \frac{\nu}{\kappa},$$

where α is the isobaric thermal expansion coefficient, g is the acceleration of gravity, ν is the kinematic viscosity, κ is the thermal diffusivity, and ΔT is the temperature difference between the top and bottom plate. Rayleigh found that the fluid starts to move when the dimensionless temperature difference, expressed by Ra, exceeds the critical value. For a detailed treatment of the linearized stability problem, see the classic text by Chandrasekhar (1961); for a general introduction, see Tritton (1988).

The RBC flow just beyond the onset of convection has been used as a paradigm for studying flow instabilities, chaotic systems and pattern formation (e.g., Busse 1978; Cross and Hohenberg 1993; Bodenschatz et al. 2000).

When the convective flow is strong enough, and the Rayleigh number is on the order of 10^5, the flow is characterized by thermal plumes, mushroom-shaped features of hot (cold) fluid detaching from the bottom (top) thermal boundary layer (e.g. Zocchi et al. 1990). At higher Rayleigh numbers, the plumes organize into a large scale motion linked synergistically with the turbulent flow (Qiu and Tong 2001; Xi et al. 2004). At very large Rayleigh numbers, the mean wind may itself be destroyed (Niemela et al. 2001; Sreenivasan et al. 2002).

The Rayleigh number, which can be interpreted as the ratio of buoyancy to viscous and thermal dissipation, is of the order $Ra \sim 10^{18} - 10^{22}$ in the atmosphere ($Pr \sim 0.7$), $Ra \sim 10^{20}$ in the ocean ($Pr \sim 7$), $Ra \sim 10^{20} - 10^{24}$ in the Sun ($Pr \sim 10^{-7} - 10^{-3}$), and $Ra \gtrsim 10^{20}$ for most astrophysical phenomena (see Sreenivasan and Donnelly 2001). These values indicate the upper end of the Rayleigh number in which we are interested.

3 High *Ra* and Ultimate Regime

Studying flows at Ra comparable to those of natural phenomena is challenging: numerical simulations and experiments cannot yet reach the parameter limits, and extrapolating the behavior from the dynamics at lower Ra is not always an option, in particular because different theories suggest different scenarios. Hence, answering even the apparently simple question of how much thermal energy is carried by the flow for a stipulated temperature difference is very hard when the temperature difference is large. This question can be formalized by looking for the dependence of the Nusselt number, the dimensionless heat transfer coefficient, on the Rayleigh number. The Nusselt number is defined as $Nu = hH/k$, where h is the measured heat transfer coefficient and k is the thermal conductivity of the fluid.

Several scaling theories have been proposed over the years. The oldest is the marginal stability theory by Malkus (1954), in which $Nu \sim Ra^{1/3}$. Written out in detail, this means that the heat transport is independent of the container height. The experiment with cryogenic helium in Chicago from the late 80s (Castaing et al. 1989) led to theories where the scaling exponent was 2/7. Additional and more precise experiments and simulations have made it clear that none of these theories could explain all the observations (though there have been suggestions in favor of the 1/3 power, see Urban et al. (2014)). A phenomenological theory that tries to account for the observed results is that of Grossmann and Lohse (2000). In this theory, there are two coupled equations for the Nusselt number and the flow Reynolds number, with six free parameters fitted to experimental and numerical data (for the updated prefactors based on the latest experiments and simulations, see Stevens et al. (2013)). The theory divides the $Pr - Ra$ parameters space into several regions in which either the bulk or the boundary layer dominates the dissipation rates (see Fig. 4).

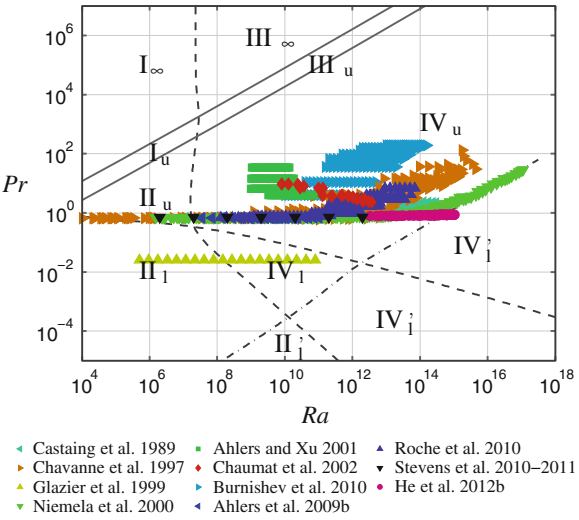

Fig. 4 Rayleigh-Bénard convection phase diagram in the $Ra - Pr$ space for $\Gamma = 1/2$ where the different regimes are from the Grossmann-Lohse theory. There is a dearth of data from experiments and simulation for the so-called ultimate regime (IV_l'), in which the kinetic boundary layer is assumed to be "completely" turbulent. The figure is adapted from Stevens et al. (2013)

The regime that is still very puzzling is the asymptotic regime for high Ra, denoted in Fig. 4 by IV_l', corresponding to "completely" turbulent boundary layers, dubbed also as the ultimate or Kraichnan regime. Indeed, Kraichnan (1962) predicted that, when the Rayleigh number exceeds some large value (for which he provided preliminary estimates), the boundary layer becomes "completely" turbulent, leading to an enhancement of heat transport; in this regime, he predicted that the Nusselt number scales as $Nu \sim Ra^{1/2}/(\log Ra)^{3/2}$.

A regime in which $Nu \sim Ra^{1/2}$ has been attained in configurations with no top and bottom boundaries, in simulations by Lohse and Toschi (2003) and in experiments in a vertical open-ended channel by Cholemari and Arakeri (2009) and Gibert et al. (2006). However, the experimental confirmation of the ultimate regime in the presence of boundary layers on solid boundaries, as one has in the classical RBC, is still awaited. For contradictory points of view on the ultimate regime, one may consult Chavanne et al. (1997), Niemela and Sreenivasan (2003, 2010), Roche et al. (2010), He et al. (2012a), Ahlers et al. (2012) and Urban et al. (2014), and references therein. One hopes that this issue will soon be resolved satisfactorily.

4 Large Aspect Ratio and Large Scales

Most experiments at high Ra are performed so far for $\Gamma = 0(1)$. However, most natural phenomena are not constrained laterally in this way, with Γ on the order $10 - 10^2$. Unfortunately, little is known for high-Ra turbulent convection in containers of large aspect ratio, and, in general, also for different geometries. Theories do not account for the aspect ratio explicitly; and while geometry effects were discussed briefly in Grossmann and Lohse (2003), only qualitative predictions are known for Γ larger than unity. Historically, convection theories have been guided by empirical results, hence the lack of data prevented a proper theoretical formulation of geometrical effects. Just recently data for Γ significantly different from order unity at high Ra are starting to appear both at moderately large aspect ratios ($\Gamma \sim 10$)—see Hogg and Ahlers (2013), du Puits et al. (2013)—and small aspect ratios, $\Gamma \sim 1/10$—see Huang et al. (2013). We should call attention to experiments by Niemela and Sreenivasan (2006) for $\Gamma = 4$, covering Rayleigh numbers up to 10^{15}, the highest to-date. Several experiments studied the convection in large aspect ratio, $\Gamma \sim 100$, using pressurized gas, and using a shadowgraph visualization technique. However, almost all the studies were done near the onset of convection (see, for example, de Bruyn et al. (1996), Bodenschatz et al. (2000)). The reason that the high Ra-high Γ parameter space is largely unexplored is that it is very challenging: while keeping all other quantities constant, we find that $Ra \propto \Gamma^{-3}$.

From available data, it would seem that the dependence of the Nusselt number Nu on the aspect ratio Γ is rather weak. Indeed, there is a strong indication that the mean wind may become weaker with increasing Rayleigh numbers (Sreenivasan et al. 2002). No major change in the Nusselt number scaling was observed in the process. This points to the likelihood that the mean wind may not play a particularly

fundamental role in determining the heat transport. Further, the flow structure and the mean wind are affected by the geometry of the system. Yet, the mean wind is interesting in its own right. This large-scale mean flow was first observed experimentally by Krishnamurti and Howard (1981) and, in experiments with helium, by Sano et al. (1989) up to 10^{12} and by Niemela et al. (2001) up to 10^{13}. The importance of the aspect ratio for the mean wind was evident already in the experiments of Niemela and Sreenivasan Niemela and Sreenivasan (2003, 2006, 2010) for aspect ratios 1/2, 1 and 4, all other aspects remaining the same. Other experiments have examined different aspects of the mean wind. Several studies characterized the dynamics of these large scale motions (Ciliberto et al. 1996; Qiu and Tong 2001; Xi et al. 2004; Brown and Ahlers 2007; Funfschilling et al. 2008) in cells of aspect ratio $\Gamma \simeq 1$ and moderate Ra. One important observation is that, once in a while, the mean wind reverses direction. Such dramatic phenomenon has fascinating analogies. Statistics of the wind reversal in convection experiments show the same statistical signature as solar flare activity, which is driven by Sun's outer layer convective motion (Sreenivasan et al. 2002), and the abrupt changes in mean flow direction in large-scale atmospheric winds (van Doorn et al. 2000). Another important analogy is the reversal of Earth's magnetic field which, despite the data from past reversals obtained from geological footprints, lacks full understanding with predictive power (even for a short time).

As for Nusselt number scaling, meager amount of data is available for the case of high aspect ratio and high Ra. For $\Gamma \simeq 10$ and moderate Rayleigh numbers, simulations show the presence of cellular coherent structures (Cattaneo et al. 2001; Hartlep et al. 2003; Parodi et al. 2004; Shishkina and Wagner 2005; von Hardenberg et al. 2008). In particular, recent direct numerical simulations up to $Ra = 10^8$ (Bailon-Cuba et al. 2010) detected polygonal structures that resemble those observed right above the onset of convection. Experimentally it would be a challenging task to visualize these structures at high Ra. See Fig. 5.

The work of Niemela and Sreenivasan (2006) for $\Gamma = 4$ suggests the presence of a single coherent mean wind over the whole container, consistent with the observations of Krishnamurti and Howard (1981) at much lower Rayleigh numbers. However, at very high Ra the former authors reported the absence of the wind, a result confirmed

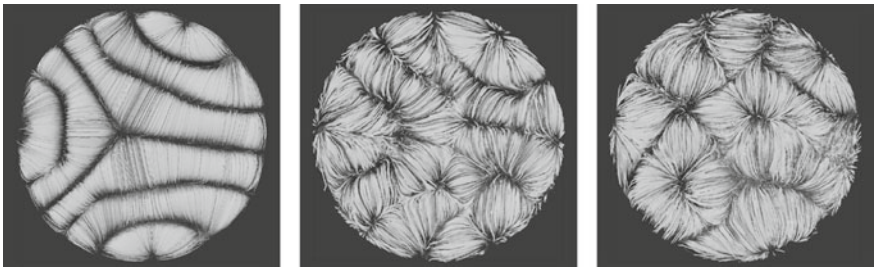

Fig. 5 Images from Bailon-Cuba et al. (2010) showing the polygonal structures of the time-averaged streamlines of the direct numerical simulations in a Rayleigh-Bénard cell with $\Gamma = 8$ for $Ra = 6{,}000$, 10^7, and 10^8, respectively

subsequently by du Puits et al. (2007). The absence of wind could be either a consequence of a completely random motion, or due to the formation of more complex structures. Resolving this kind of questions experimentally requires the visualization of the global flow structure. To our knowledge, the highest Rayleigh number in a large aspect ratio experiment is $\sim 10^9$ for $\Gamma = 9$ in the air experiments by du Puits et al. (2013). If we consider only the experiments that visualized the global flow structures, the maximum Rayleigh number is $Ra = 2 \times 10^7$ in the $\Gamma = 11$ cell by Hogg and Ahlers (2013). More experiments at large aspect ratios and large Ra are therefore needed, in particular with capabilities for visualizing the flow structures (see Fig. 6).

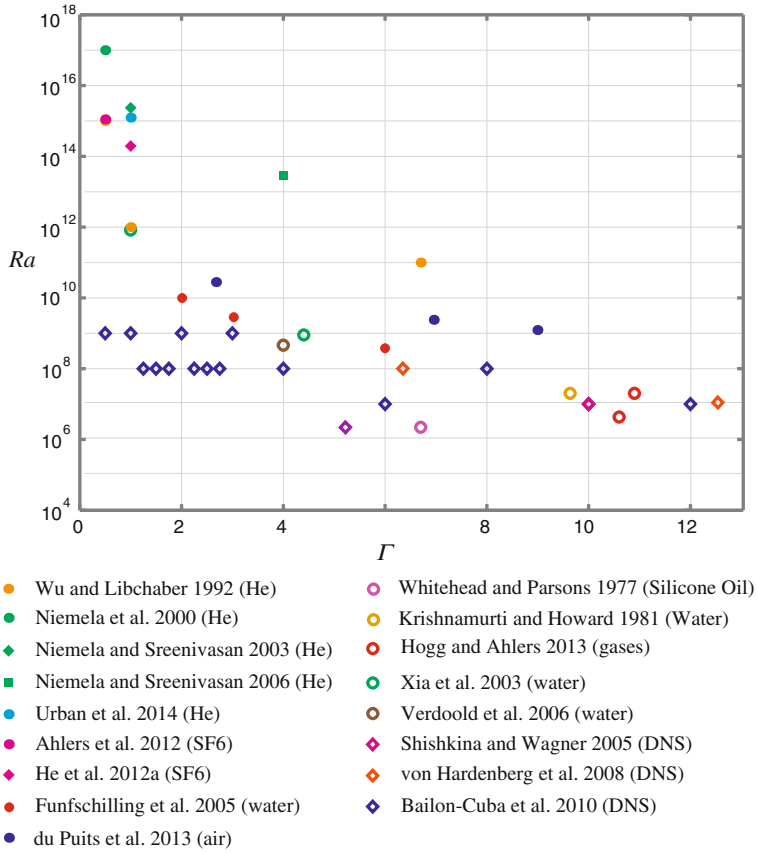

Fig. 6 The plot shows the maximum Rayleigh numbers achieved by some selected experiments and simulations for different values of the aspect ratio. Open symbols denote conditions for possible visualization

Understanding the dynamics of these flow structures, besides being of interest to the RBC community, is also of interest for the Solar Physics community. Indeed, with the exception of solar granulation, the cellular structures of the Sun are still not completely understood (Rieutord and Rincon 2010). It is worth noting that despite the traditional view that separates the scales into discrete features with different names, there is some evidence for a continuous spectrum of motion (Nordlund et al. 2009).

The appearance of discrete wavelengths or the presence of a continuous spectrum in RBC at high Ra and high Γ is still unexplained. As already mentioned, simulations at moderately high Ra show the presence of coherent structures but there are no data available at very high Ra. The appearance of regular structures from the random turbulence motion is a fascinating phenomenon that seems to go against the classical notion of turbulence, and can be seen more broadly in the context of self-organization of a system far from equilibrium (Nicolis and Prigogine 1977). In hydrodynamic turbulence such regular structures have been observed in the Taylor-Couette flow (Lathrop et al. 1992), the von Kármán flow (La Porta et al. 2001) and the pipe flow (Hof et al. 2004). In general, there is a renewed interest in the role of coherent structures in turbulent flows (Ouellette 2012), also thanks to the new tools for detecting Lagrangian coherent structures (Haller 2015). It will be interesting to see the role that RBC will play in this context in the years to come.

5 Conclusions

Turbulent convection has been studied more extensively in recent years, and much more sophisticated data have become available in both experiment and simulation. Unprecedented ranges of parameters have been explored. However, many of the old questions are still open—for example, the basic heat transport law for asymptotically large Ra. We discussed some of the open problems for the simplest case of Rayleigh-Bénard convection. Variations that include rotation, phase change and magnetic fields have also gained a lot of attention recently but are not included in this review for brevity.

One feature of experiments in the last two decades is the effort in achieving higher and higher Rayleigh numbers by building larger and larger facilities, and using different test fluids. The experiments that used cryogenic helium and pressurized SF_6 are currently the record holders for the highest Rayleigh number achieved in controlled laboratory experiments. An alternative to helium and its increasing price, or to large storage and compressing facilities of SF_6, could be the use of cryogenic nitrogen (Fonda et al. 2012), which we believe could be the fluid of choice for a landmark facility with the goal of reaching $Ra \sim 10^{20}$.

References

Ahlers G, Grossmann S, Lohse D (2009a) Heat transfer and large scale dynamics in turbulent Rayleigh-Bénard convection. Rev Mod Phys 81(2):503

Ahlers G, Funfschilling D, Bodenschatz E (2009b) Transitions in heat transport by turbulent convection at Rayleigh numbers up to 10^{15}. New J Phys 11(12):123001

Ahlers G, He X, Funfschilling D, Bodenschatz E (2012) Heat transport by turbulent Rayleigh-Bénard convection for $Pr \simeq 0.8$ and $3 \times 10^{12} \leq Ra \leq 10^{15}$: aspect ratio $\Gamma = 0.50$. New J Phys 14(10):103012

Ahlers G, Xu X (2001) Prandtl-number dependence of heat transport in turbulent Rayleigh-Bénard convection. Phys Rev Lett 86(15):3320

Bailon-Cuba J, Emran MS, Schumacher J (2010) Aspect ratio dependence of heat transfer and large-scale flow in turbulent convection. J Fluid Mech 655:152

Bodenschatz E, Pesch W, Ahlers G (2000) Recent developments in Rayleigh-Bénard convection. Annu Rev Fluid Mech 32(1):709

Brown E, Ahlers G (2007) Large-scale circulation model for turbulent Rayleigh-Bénard convection. Phys Rev Lett 98(13):134501

Buffett BA (2000) Earth's core and the geodynamo. Science 288(5473):2007

Burnishev Y, Segre E, Steinberg V (2010) Strong symmetrical non-Oberbeck-Boussinesq turbulent convection and the role of compressibility. Phys Fluids 22(3):035108

Busse FH (1978) Non-linear properties of thermal convection. Rep Prog Phys 41(12):1929

Cardin P, Olson P (1994) Chaotic thermal convection in a rapidly rotating spherical shell: consequences for flow in the outer core. Phys Earth Planet In 82(3–4):235

Castaing B, Gunaratne G, Heslot F, Kadanoff L, Libchaber A, Thomae S, Wu X-Z, Zaleski S, Zanetti G (1989) Scaling of hard thermal turbulence in Rayleigh-Bénard convection. J Fluid Mech 204:1

Cattaneo F, Lenz D, Weiss N (2001) On the origin of the solar mesogranulation. Astrophys J 563(1):L91

Chandrasekhar S (1961) Hydrodynamic and hydromagnetic stability. Dover Publications, New York

Chaumat S, Castaing B, Chilla F (2002) Rayleigh-Bénard cells: influence of the plates' properties. Advances in turbulence IX (ed. IP Castro, PE Hancock, and TG Thomas) CIMNE, Barcelona

Chavanne X, Chilla F, Castaing B, Hebral B, Chabaud B, Chaussy J (1997) Observation of the ultimate regime in Rayleigh-Bénard convection. Phys Rev Lett 79(19):3648

Chillà F, Schumacher J (2012) New perspectives in turbulent Rayleigh-Bénard convection. Eur Phys J E 35(7):58

Cholemari MR, Arakeri JH (2009) Axially homogeneous, zero mean flow buoyancy-driven turbulence in a vertical pipe. J Fluid Mech 621:69

Ciliberto S, Cioni S, Laroche C (1996) Large-scale flow properties of turbulent thermal convection. Phys Rev E 54(6):R5901

Cross M, Hohenberg P (1993) Pattern formation outside of equilibrium. Rev Mod Phys 65(3):851

de Bruyn JR, Bodenschatz E, Morris SW, Trainoff SP, Hu Y, Cannell DS, Ahlers G (1996) Apparatus for the study of Rayleigh-Bénard convection in gases under pressure. Rev Sci Instrum 67(6):2043

du Puits R, Resagk C, Thess A (2007) Breakdown of wind in turbulent thermal convection. Phys Rev E 75(1):016302

du Puits R, Resagk C, Thess A (2013) Thermal boundary layers in turbulent Rayleigh-Bénard convection at aspect ratios between 1 and 9. New J Phys 15(1):013040

Fonda E, Sreenivasan KR, Lathrop DP (2012) Liquid nitrogen in fluid dynamics: visualization and velocimetry using frozen particles. Rev Sci Instrum 83(8):085101

Funfschilling D, Brown E, Ahlers G (2008) Torsional oscillations of the large-scale circulation in turbulent Rayleigh-Bénard convection. J Fluid Mech 607:119

Funfschilling D, Brown E, Nikolaenko A, Ahlers G (2005) Heat transport by turbulent Rayleigh-Bénard convection in cylindrical samples with aspect ratio one and larger. J Fluid Mech 536:145

Getling AV (1991) Formation of spatial structures in Rayleigh-Bénard convection. Sov Phys Usp 34(9):737

Gibert M, Pabiou H, Chillà F, Castaing B (2006) High-Rayleigh-number convection in a vertical channel. Phys Rev Lett 96(8):084501
Glazier JA, Segawa T, Naert A, Sano M (1999) Evidence against 'ultrahard' thermal turbulence at very high Rayleigh numbers. Nature 398(6725):307
Grossmann S, Lohse D (2000) Scaling in thermal convection: a unifying theory. J Fluid Mech 407:27
Grossmann S, Lohse D (2003) On geometry effects in Rayleigh-Bénard convection. J Fluid Mech 486:105
Guillot T (2005) The interior of giants planets: models and outstanding questions. Annu Rev Earth Planet Sci 33(1):493
Haller G (2015) Lagrangian coherent structures. Annu Rev Fluid Mech (August 2014):137
Hartlep T, Tilgner A, Busse F (2003) Large scale structures in Rayleigh-Bénard convection at high Rayleigh numbers. Phys Rev Lett 91(6):064501
Hartmann DL, Moy LA, Fu Q (2001) Tropical convection and the energy balance at the top of the atmosphere. J Clim 14(24):4495
He X, Funfschilling D, Bodenschatz E, Ahlers G (2012a) Heat transport by turbulent Rayleigh-Bénard convection for $Pr \simeq 0.8$ and $4 \times 10^{11} \leq Ra \leq 2 \times 10^{14}$: ultimate-state transition for aspect ratio $\Gamma = 1.00$. New J Phys 14(6):063030
He X, Funfschilling D, Nobach H, Bodenschatz E, Ahlers G (2012b) Transition to the ultimate state of turbulent Rayleigh-Bénard convection. Phys Rev Lett 108(2):024502
Hof B, van Doorne CWH, Westerweel J, Nieuwstadt FTM, Faisst H, Eckhardt B, Wedin H, Kerswell RR, Waleffe F (2004) Experimental observation of nonlinear traveling waves in turbulent pipe flow. Science 305(5690):1594
Hogg J, Ahlers G (2013) Reynolds-number measurements for low-Prandtl-number turbulent convection of large-aspect-ratio samples. J Fluid Mech 725:664
Huang S-D, Kaczorowski M, Ni R, Xia K-Q (2013) Confinement-induced heat-transport enhancement in turbulent thermal convection. Phys Rev Lett 111(10):104501
Koschmieder EL (1974) Bénard convection. Adv Chem Phys 26. Prigogine I, Rice SA (eds). Wiley, Hoboken
Kraichnan RH (1962) Turbulent thermal convection at arbitrary Prandtl number. Phys Fluids 5(11):1374
Krishnamurti R, Howard LN (1981) Large-scale flow generation in turbulent convection. Proc Natl Acad Sci USA 78(4):1981
La Porta A, Voth GA, Crawford AM, Alexander J, Bodenschatz E (2001) Fluid particle accelerations in fully developed turbulence. Nature 409(6823):1017
Lathrop DP, Fineberg J, Swinney H (1992) Transition to shear-driven turbulence in Couette-Taylor flow. Phys Rev A 46(10):6390
Lohse D, Toschi F (2003) Ultimate state of thermal convection. Phys Rev Lett 90(3):034502
Lohse D, Xia K-Q (2010) Small-scale properties of turbulent Rayleigh-Bénard convection. Annu Rev Fluid Mech 42(1):335
Malkus WVR (1954) The heat transport and spectrum of thermal turbulence. Proc R Soc Lond A 225(1161):196
Marshall J, Schott F (1999) Open-ocean convection: observations, theory, and models. Rev Geophys 37(1):1
Nicolis G, Prigogine I (1977) Self-organization in nonequilibrium systems. Wiley, New York
Niemela JJ, Skrbek L, Sreenivasan KR, Donnelly RJ (2000) Turbulent convection at very high Rayleigh numbers. Nature 404(1):837
Niemela JJ, Skrbek L, Sreenivasan KR, Donnelly RJ (2001) The wind in confined thermal convection. J Fluid Mech 449:169
Niemela JJ, Sreenivasan KR (2003) Confined turbulent convection. J Fluid Mech 481:355
Niemela JJ, Sreenivasan KR (2006) Turbulent convection at high Rayleigh numbers and aspect ratio 4. J Fluid Mech 557:411

Niemela JJ, Sreenivasan KR (2010) Does confined turbulent convection ever attain the 'asymptotic scaling' with 1/2 power? New J Phys 12(11):115002
Nordlund AK, Stein RF, Asplund M (2009) Solar surface convection. Living Rev Sol Phys 6
Ouellette NT (2012) On the dynamical role of coherent structures in turbulence. C R Phys 13(9–10):866
Parodi A, von Hardenberg J, Passoni G, Provenzale A, Spiegel E (2004) Clustering of plumes in turbulent convection. Phys Rev Lett 92(19):194503
Qiu X-L, Tong P (2001) Large-scale velocity structures in turbulent thermal convection. Phys Rev E 64(3):036304
Rieutord M, Rincon F (2010) The suns supergranulation. Living Rev Sol Phys 7
Roche P-E, Gauthier F, Kaiser R, Salort J (2010) On the triggering of the ultimate regime of convection. New J Phys 12(8):085014
Sano M, Wu X, Libchaber A (1989) Turbulence in helium-gas free convection. Phys Rev A 40(11):6421
Schubert G, Turcotte DL, Olson P (2001) Mantle convection in the earth and planets. Cambridge University Press, Cambridge
Shishkina O, Wagner C (2005) Analysis of thermal dissipation rates in turbulent Rayleigh-Bénard convection. J Fluid Mech 546:51
Sreenivasan K, Bershadskii A, Niemela J (2002) Mean wind and its reversal in thermal convection. Phys Rev E 65(5):056306
Sreenivasan K, Donnelly R (2001) Role of cryogenic helium in classical fluid dynamics basic research and model testing. Adv Appl Mech 37:239
Stevens RJAM, Lohse D, Verzicco R (2011) Prandtl and Rayleigh number dependence of heat transport in high Rayleigh number thermal convection. J Fluid Mech 688:31
Stevens RJAM, van der Poel EP, Grossmann S, Lohse D (2013) The unifying theory of scaling in thermal convection: the updated prefactors. J Fluid Mech 730:295
Stevens RJAM, Verzicco R, Lohse D (2010) Radial boundary layer structure and Nusselt number in Rayleigh-Bénard convection. J Fluid Mech 643:495
Tackley PJ (2000) Mantle convection and plate tectonics: toward an integrated physical and chemical theory. Science 288(5473):2002
Tritton DJ (1988) Physical fluid dynamics. Clarendon Press, Oxford
Urban P, Hanzelka P, Musilová V, Králík T, Mantia ML, Srnka A, Skrbek L (2014) Heat transfer in cryogenic helium gas by turbulent Rayleigh-Bénard convection in a cylindrical cell of aspect ratio 1. New J Phys 16(5):053042
van Doorn E, Dhruva B, Sreenivasan KR, Cassella V (2000) Statistics of wind direction and its increments. Phys Fluids 12(6):1529
Van Dyke M (1982) An album of fluid motion. Parabolic Press, Stanford
Velarde MG et al (1982) An album of fluid motion, assembled by Van Dyke M. Parabolic Press, Stanford
Verdoold J, Tummers M, Hanjalić K (2006) Oscillating large-scale circulation in turbulent Rayleigh-Bénard convection. Phys Rev E 73(5):056304
von Hardenberg J, Parodi A, Passoni G, Provenzale A, Spiegel E (2008) Large-scale patterns in Rayleigh-Bénard convection. Phys Lett A 372(13):2223–2229
Wesfreid JE (2006) Scientific biography of Henri Bénard (1874–1939). In: Mutabazi I, Wesfreid JE, Guyon E (eds) Dynamics of spatio-temporal cellular structures. Springer tracts in modern physics, vol 207. Springer, New York, pp 9–37
Whitehead JA, Parsons B (1977) Observations of convection at Rayleigh numbers up to 760,000 in a fluid with large Prandtl number. Geophys Astrophys Fluid Dyn 9(1):201
Wu X-Z, Libchaber A (1992) Scaling relations in thermal turbulence: the aspect-ratio dependence. Phys Rev A 45(2):842
Xi H-D, Lam S, Xia K-Q (2004) From laminar plumes to organized flows: the onset of large-scale circulation in turbulent thermal convection. J Fluid Mech 503:47

Xia K-Q (2013) Current trends and future directions in turbulent thermal convection. Theor Appl Mech Lett 3(5):052001
Xia K-Q, Sun C, Zhou S-Q (2003) Particle image velocimetry measurement of the velocity field in turbulent thermal convection. Phys Rev E 68(6):066303
Zocchi G, Moses E, Libchaber A (1990) Coherent structures in turbulent convection, an experimental study. Phys A 166(3):387

Dissipative Particle Dynamics: A Method to Simulate Soft Matter Systems in Equilibrium and Under Flow

C. Pastorino and A. Gama Goicochea

Abstract We provide examples and a concise review of the method of Dissipative Particle Dynamics (DPD), as a simulation tool to study soft matter systems and simple liquids in equilibrium and under flow. DPD was initially thought as a simulation method, which in combination with soft potentials, could simulate "fluid particles" with suitable hydrodynamic correlations. Then DPD evolved to a generic "thermostat" to simulate systems in equilibrium and under flow, with arbitrary interaction potential among particles. We describe the application of the method with soft potentials and other coarse-grain models usually used in polymeric and other soft matter systems. We explain the advantages, common problems and limitations of DPD, in comparison with other thermostats widely used in simulations. The implementation of the DPD forces in a working Molecular Dynamics (MD) code is explained, which is a very convenient property of DPD. We present various examples of use, according to our research interests and experiences, and tricks of trade in different situations. The use of DPD in equilibrium simulations in the canonical ensemble, the grand canonical ensemble at constant chemical potential, and stationary Couette and Poiseuille flows is explained. It is also described in detail the use of different interaction models for molecules: soft and hard potentials, electrostatic interactions and bonding interactions to represent polymers. We end this contribution with our personal views and concluding remarks.

C. Pastorino (✉)
Departamento de Física de la Materia Condensada, Centro Atómico Constituyentes, CNEA and CONICET, Av. Gral Paz 1499, 1650 San Martín, Buenos Aires, Argentina
e-mail: pastor@cnea.gov.ar

A. Gama Goicochea
Instituto de Física, Universidad Autónoma de San Luis Potosí, Av. Álvaro Obregón 64, 78000 Mexico, San Luis Potosí, Mexico
e-mail: agama@alumni.stanford.edu

J. Klapp et al. (eds.), *Selected Topics of Computational and Experimental Fluid Mechanics*, Environmental Science and Engineering,
DOI 10.1007/978-3-319-11487-3_3

1 Introduction

Dissipative Particle Dynamics (DPD) is already a well established simulation method to study particle systems (Frenkel and Smit 2002). In the seminal work by Hoogerbrugge and Koelman (1992) the motivation of developing DPD was to study the hydrodynamic behavior with a particle based method and an integration scheme very similar to that of Molecular Dynamics (MD). While hydrodynamic conditions could be studied theoretically with MD, in practice, performing a simulation with the typical time step of MD, for a large number of particles, so that the Reynolds number of a fluid can be varied considerably, would be prohibitively expensive in computer time, even with current computer systems (Murtola et al. 2009). Additionally, most of the thermostats, which would allow for an isothermal simulation in presence of flow, will perturbe the hydrodynamic correlation between particles (Hünenberger 2005). DPD tackled these two drawbacks to allow particle-based simulations in a scheme very similar to MD (Frenkel and Smit 2002; Allen and Tildesley 1987).

As was originally deviced by Hoogerbrugge and Koelman (1992), Español and Warren (1995), and Groot and Warren (1997), DPD allows for a higher time step than usual MD simulations. This was achieved by defining the so-called "soft potentials" as the interaction model between particles in the original DPD scheme. These quadratic potentials, have linear and small derivatives (repulsive forces), as compared to a typical interaction potential of MD simulation, such as the Lennard-Jones potential. The equations of motion of these "fluid particles" interacting with soft potentials can be integrated with a time step with a factor of 10–100 times higher than that used for the Lennard-Jones potential. This speed-up allows for the simulation of larger systems, and therefore higher Reynolds numbers. The other important contribution of DPD to the simulation of hydrodynamic phenomena is the use of a thermostat that conserves locally linear and angular momentum, which is one of the assumptions of the hydrodynamic continuum formulation of the equations of motion. Either locally or globally, most of the widely used thermostats in MD, such as the Andersen, Nosé-Hoover (Frenkel and Smit 2002) or the Langevin (Hünenberger 2005) thermostats, violate Galilean invariance and momentum conservation, giving rise to screening of hydrodynamic correlations (Soddemann et al. 2003; Dünweg 2006).

The DPD method solves this by establishing a thermostatic process similar to Brownian Dynamics, in which a dissipative and a viscous force are applied over the particles of the fluid. The difference is, however, that in the DPD method these forces are applied in a pair-wise form, and in the direction of the line that connects a pair of particles (see Fig. 1). In this way, the total "external force" on the particles is zero, resulting in local momentum conservation. Additional details will be given in Sect. 2. We can mention other two appealing features of DPD. It can be implemented from a straight-forward modification of a working MD program, from which efficient parallelization strategies have been deviced (Plimpton 1995; Brown et al. 2012). Additionally, it has a great versatility to study complex fluids or other soft matter systems in the hydrodynamics context by adding interactions among particles, for example, harmonic or other spring-like interactions (bonded), to describe polymers,

colloids or amphiphilic molecules (Allen and Tildesley 1987; Frenkel and Smit 2002). Liquid mixtures can be also studied by changing the potential among different kind of particles.

While the original DPD method was thought as a complete simulation procedure, including the soft potentials and the pair-wise thermostat, it was soon realized that they do not need to be used together (Soddemann et al. 2003; Pastorino et al. 2007). One could use a DPD thermostat with any interaction model (potentials) among particles or molecules, and not only with soft potentials. This option of using "hard potentials", such as Lennard-Jones or any other common potential in MD simulations comes, of course, at the price of reducing the time step in the simulations, which is one of the original advantages of DPD. However, the correct description of hydrodynamics can be a highly desirable feature in many physical situations of interest.

DPD has been used for soft matter systems in many contexts and physical situations (Murtola et al. 2009; Binder et al. 2011; Moeendarbary et al. 2010). In this work we review the use of the DPD method with soft and hard potentials for complex fluids and polymeric systems. In Sect. 2, we review the DPD method as a variation of standard MD and Brownian Dynamics simulations. In Sect. 3, we provide details of the use of soft and hard potentials to simulate soft matter systems such as polymeric systems. In this section we also provide various examples of equilibrium DPD simulations with soft potentials. We devote Sect. 4 to give examples of the use of DPD in soft matter systems under flow in order to study the behavior and coupling of these soft matter systems under non-equilibrium conditions. We also show some difficulties concerning temperature conservation in strongly out-of-equilibrium simulations and how to deal with them in Sect. 5. We provide the final comments and conclusions in Sect. 6.

2 Details of the Dissipative Particle Dynamics Method

2.1 Basic Molecular Dynamics Simulation

The DPD simulation scheme can be thought as an extension of the typical MD algorithm (Allen and Tildesley 1987; Frenkel and Smit 2002). The basic idea in MD is integrating numerically the classical equations of motion for a set of N particles. The Newton equation for each particle i is

$$-\frac{\partial V(\mathbf{r})}{\partial \mathbf{r}_i} \equiv \mathbf{f_i} = m_i \ddot{\mathbf{r}}_i, \tag{1}$$

where m_i is the mass of the particle, $\mathbf{f}_i$ is the total force on particle i due to other particles of the system and any external field applied. In a simple bulk simulation, the evolution is done in a box of a certain volume with periodic boundary conditions,

to warrant that all particles will always be in the simulation box. From a physical point of view, this bulk simulation should avoid any surface effect (Frenkel and Smit 2002).

Assuming ergodicity, a time average over the integrated numerical trajectory of the N-particle system of any quantity depending on the dynamical variables positions $\{\mathbf{r}_i\}$ and velocities $\{\mathbf{v}_i\}$ is equivalent to an ensemble average

$$\langle A \rangle_{ens} \equiv \frac{1}{\tau} \int_0^\tau A(\{\mathbf{r}_i(t), \mathbf{v}_i(t)\})dt,$$

where A stands for any physical quantity as a function of the dynamics variables of the system. From the point of view of the statistical mechanics, the simple integrating of the Newton equations corresponds to a micro-canonical ensemble in which the number of particles N, the volume of the system V and the total internal energy of the system E are held constant.

2.2 Simulating at Constant Temperature: The Langevin Thermostat

The microcanonical ensemble, while useful theoretically is not usually used in experiments in which exchange of heat, particles and or volume is usually the case. A typical ensemble in experiments, which is widely used in simulations, is the canonical ensemble, in which the constant thermodynamic variables are the number of particles N, the volume V and the temperature T. Keeping the temperature constant means, of course, fluctuations of the energy of the system due to a heat exchange with a "thermal bath". To simulate the system at constant temperature, some additional terms must be added to the original dynamical equations (1). In the last thirty years, significant effort has been done to extend the Newton equations of a classical system to obtain constant temperature. The different thermostats can be classified conceptually as those which provide constant temperature by *stochastic relaxation* (i.e. Langevin thermostat or Brownian dynamics simulations), *stochastic coupling* (Andersen thermostat), *extended Langrangian schemes* (i.e. Nosé-Hoover thermostat), *temperature constraining* (Woodcock and Hoover-Evans thermostats) and *weak coupling* (Berendsen thermostat) (Hünenberger 2005). All these schemes have advantages and drawbacks and find areas of application according to the systems, physical conditions and phenomena to be addressed. We will not review this, and suggest the excellent review by Hünenberger (2005) and the classical textbooks on MD simulations by Frenkel and Smit (2002), Allen and Tildesley (1987), and Rapaport (2004). We will give some details of the Langevin thermostat, also termed Brownian Dynamics, as a first step, to describe then the DPD thermostat. In this scheme instead of integrating the Newton equation of motion, we integrate a Langevin equation that describes the

dynamics of each particle of the simulation. The integration scheme and most of the MD program implementation remains exactly the same, except that two force terms are added to the conservative forces already present in the MD simulations. The first order equations of motion for the particle i are

$$\dot{\mathbf{r}_i} = \frac{\mathbf{p}_i}{m_i},$$
$$\dot{\mathbf{p}_i} = \mathbf{F^c}_i + \mathbf{F}_i{}^{\mathrm{D}} + \mathbf{F}_i{}^{\mathrm{R}},$$

where $\mathbf{r}_i$ and $\mathbf{p}_i$ are the positions and momenta of the particles. $\mathbf{F}^c$ stands for all the conservative forces of the system, with arbitrary molecular complexity. These are called the molecular interaction model. The Langevin thermostat adds a dissipative and a stochastic force to the conservative forces of the system. It can be rationalized by thinking that a particle is coupled to an implicit fluid, which acts as a thermal bath (Pastorino et al. 2006, 2007). The dissipative force on particle i is given by $\mathbf{F}_i{}^{\mathrm{D}} = -\gamma \mathbf{v}_i$, where γ is a friction coefficient fixed in the simulation, and $\mathbf{v}_i$ is the velocity of the particle. The random force, $\mathbf{F}_i^{\mathrm{R}}$, is chosen such that it has zero mean value and its variance satisfies

$$\langle F_{i\mu}^{\mathrm{R}}(t) F_{j\nu}^{\mathrm{R}}(t') \rangle = \sigma_i^2 \delta_{ij} \delta_{\mu\nu} \delta(t - t'), \tag{2}$$

where σ_i is the noise strength. The relation $\sigma_i^2 = k_B T \gamma / m_i$, couples the friction γ and the noise strength σ_i in a particular way such that the fluctuation-dissipation theorem is satisfied and the system is simulated in the canonical ensemble (*NVT*). An elegant derivation of this can be obtained from a Fokker-Planck equation for this system (Dünweg 2006). This way of thermostating, also known as Stochastic Dynamics, allows particle simulations at constant temperature. However, this algorithm violates Galilean invariance because it damps the absolute velocities of the particles, thus assuming as "special" the laboratory frame. The Langevin thermostat, while allowing the simulation of correct thermodynamic conditions, it is of little use for hydrodynamic phenomena. Taking a simple liquid, it was shown by Dünweg and Kremer (1993) and Dünweg (2006) that this unphysical behavior can be thought as a screening length for the hydrodynamic correlations

$$\xi = \left[\frac{\eta}{\rho \gamma / m} \right]^{1/2},$$

where η is the viscosity of the fluid, ρ the number density, γ the friction constant and m the mass of each particle (Dünweg and Kremer 1993). The propagation of momentum is screened and dampened, as compared to the correct hydrodynamics behavior.

2.3 The Dissipative Particle Dynamics Thermostat

The Dissipative Particle Dynamics thermostat improves the Langevin thermostat and solves the screening problem. In this way, it allows one to simulate hydrodynamics phenomena at the mesoscale in equilibrium and in presence of flows. It is very similar to the Langevin thermostat, described in the previous section. Dissipative and stochastic forces are applied, but to pairs of particles. The thermostat is also Galilean invariant because it damps relative velocities and not the absolute velocity of a single particle. The stochastic forces are applied also to pairs of interacting particles in opposite direction, such that Newton's third law is satisfied. In this way the total "thermostating" (external and non-conservative) force to a pair of particles is zero and the momentum is conserved locally. The new expressions for the dissipative and random forces are

$$\begin{aligned} \mathbf{F}_i{}^{\mathrm{D}} &= \sum_{j(\neq i)} \mathbf{F}_{ij}^{\mathrm{D}} \; ; \; \mathbf{F}_{ij}^{\mathrm{D}} = -\gamma \omega^{\mathrm{D}}(r_{ij})(\hat{\mathbf{r}}_{ij} \cdot \mathbf{v}_{ij})\hat{\mathbf{r}}_{ij}, \\ \mathbf{F}_i{}^{\mathrm{R}} &= \sum_{j(\neq i)} \mathbf{F}_{ij}^{\mathrm{R}} \; ; \; \mathbf{F}_{ij}^{\mathrm{R}} = \sigma_R \omega^{\mathrm{R}}(r_{ij})\theta_{ij}\hat{\mathbf{r}}_{ij}, \end{aligned} \tag{3}$$

where $\mathbf{r}_{ij} \equiv \mathbf{r}_i - \mathbf{r}_j = r_{ij}\hat{r}_{ij}$ and $\mathbf{v}_{ij} \equiv \mathbf{v}_i - \mathbf{v}_j$ are the relative positions and velocities, respectively. γ is the friction constant and σ_R the noise strength. Friction and noise obey the relation $\sigma_R^2 = 2k_B T\gamma$, exactly in the same of way as the Langevin thermostat does. $\omega^D(r_{ij})$ and $\omega^R(r_{ij})$ are weight functions that have to satisfy the relation

$$[\omega^{\mathrm{R}}]^2 = \omega^{\mathrm{D}}. \tag{4}$$

in order to fulfill the fluctuation-dissipation theorem (Español and Warren 1995; Español 1995). θ_{ij} stands for a random variable with zero mean and second moment

$$\langle \theta_{ij}(t)\theta_{kl}(t^{'})\rangle = (\delta_{ik}\delta_{jl} + \delta_{il}\delta_{jk})\delta(t - t^{'}). \tag{5}$$

The standard weight functions found in the literature are:

$$[\omega^{\mathrm{R}}]^2 = \omega^{\mathrm{D}} = \begin{cases} (1 - r/r_{\mathrm{c}})^2, r < r_{\mathrm{c}}, \\ 0, \quad r \geq r_{\mathrm{c}} \end{cases} \tag{6}$$

where r_{c} is the cut-off radius for a given molecular model. It is emphasized that Eq. (6) is just the typical choice when the DPD thermostat is employed in conjunction with "soft" potentials. Any choice satisfying the first equality in Eq. (6) would be a suitable option for the weight functions. In Fig. 1, we present a sketch with the direction of the dissipative and stochastic forces of the DPD thermostat on a pair of fluid particles. The equations of motion including the DPD thermostat are often integrated using

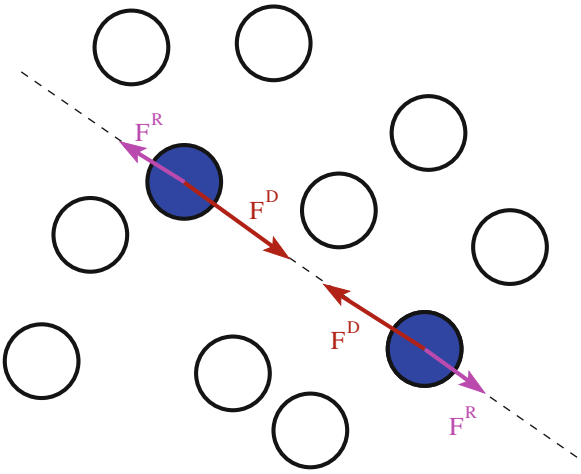

Fig. 1 Sketch of the dissipative and stochastic forces applied in a pair of fluid particles in the DPD thermostat. The forces are applied in the direction connecting both particles in such a way that all added "thermostating" forces vanish

the velocity Verlet algorithm (Murtola et al. 2009; Frenkel and Smit 2002; Allen and Tildesley 1987).

3 Interaction Models: Soft and Hard Potentials

3.1 DPD with Soft Potentials

From the very inception of the DPD method by Hoogerbrugge and Koelman (1992), the spatial dependence of the conservative force ($\mathbf{F}_{ij}^{C}$) was chosen to be a short range, linearly decaying function:

$$\mathbf{F}_{ij}^{C} = a_{ij}\left(1 - \frac{r_{ij}}{R_c}\right)\hat{\mathbf{e}}_{\mathbf{ij}}, \tag{7}$$

where $r_{ij} = r_i - r_j$ is the relative position vector and $\hat{\mathbf{e}}_{ij}$ is the unit vector in the direction of $\mathbf{r}_{ij}$, with r_i being the position of particle i. The constant a_{ij} is the strength of the conservative force between particles i and j and R_c is a cutoff distance. This force becomes zero for $r_{ij} > R_c$. It should be remarked that this choice of the distance-dependent force is not arbitrary, as it has been shown to arise from properly averaged, microscopic interactions, such as the Lennard-Jones potential (Forrest and Suter 1995). As for the interaction constant, a_{ij}, Groot and Warren (1997) have provided a guide to calculate it using the Flory-Huggins model for like-unlike particles, and the isothermal compressibility of water for like-like interactions. The standard procedure to choose the conservative force parameter for particles of the same type, a_{ii}, is given by

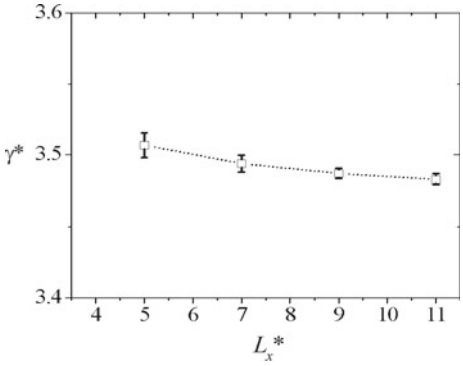

Fig. 2 Dependence of the interfacial tension γ^* between two immiscible model fluids as a function of the size of the simulation *box*. Note that the difference between the values of the interfacial tension for the *smallest* and *biggest boxes* amounts to about 1 %. The axes are drawn in reduced DPD units. Adapted from Velázquez et al. (2006)

$$a_{ii} = \left[\frac{\kappa^{-1}N_m^{-1}}{2\alpha\rho}\right]k_BT, \tag{8}$$

where N_m is the coarse-graining degree (number of water molecules grouped in a DPD particle), $\alpha = 0.101$ is a numerical constant, ρ is the DPD number density and κ is the dimensionless compressibility of the system. It is defined as $\kappa^{-1} = 1/(\rho_0 k_B T \kappa_T)$, where ρ_0 is the number density of molecules and $\kappa_T = (\partial p/\partial\rho_0)_T$ is the usual isothermal compressibility. When one chooses a coarse-graining degree equal to 3, water molecules in a DPD particle and the water compressibility under standard conditions, $\kappa^{-1} \simeq 16$, the DPD force parameter takes the value $a_{ii} = 78.3$. The parameter for different types of particles, a_{ij}, is calculated from the Flory-Huggins coefficient χ_{ij} using the following relation:

$$a_{ij} = a_{ii} + 3.27\chi_{ij}. \tag{9}$$

The χ_{ij} value can be obtained from the solubility parameters. The remaining forces of the model, namely the dissipative force and the random force, are exactly as defined in Eq. (3). Because all the conservative forces are repulsive, the equation of state of DPD is positive definite and it does not have a van der Waals loop (Groot and Warren 1997). Therefore, it cannot predict liquid-vapor phase transitions. However, this limitation can be overcome by introducing a local density dependent attractive term into the conservative force (see Eq. 7), which is useful for predicting surface tension (Pagonabarraga and Frenkel 2001). Among the advantages of the soft potentials used in DPD is the fact that finite size effects are minimal when the appropriate ensemble is used because the potentials are also short ranged (Velázquez et al. 2006). This allows one to perform accurate simulations using relatively small, computationally inexpensive systems, as shown in Fig. 2.

3.2 Selected Examples of Soft Matter Systems in Equilibrium

We provide in this section examples of DPD with soft potentials for equilibrium simulations. When beads are joined through a harmonic potential polymer chains can easily be simulated, as well as other types of molecules such as surfactants, rheology modifiers and others (Groot and Warren 1997). The influence of the characteristics of the harmonic force forming surfactant molecules on the interfacial tension between two immiscible liquids has been studied thoroughly (Gama Goicochea et al. 2007) and it was shown that the predictions follow closely the experimental trends. Most applications of DPD have been carried out at constant temperature although there are plenty of situations of importance for modern research where the influence of temperature is not sufficiently well understood. One of such cases is the dependence on temperature of the interfacial tension between liquids. Very recently, an extension of the DPD model that incorporates the variability of the temperature has been proposed by Mayoral and Gama Goicochea 2013. It is based on the addition of the temperature dependence of the solubility parameters for the pure components in a mixture, which leads to temperature dependent interaction parameters, (see Eqs. 8 and 9). Applying the temperature dependent form of DPD to the interfacial tension between organic solvents and water led to predictions that are in excellent agreement with experimental results (Mayoral and Gama Goicochea 2013). Another important extension of the DPD model is the incorporation of electrostatic interactions through the method of the Ewald sums. Using distributions of charge instead of point charges to avoid the formation of artificial ionic pairs, the behavior of poly-electrolytes in solution under the influence of varying ionic strength has been predicted and compared with similar studies carried out with certain proteins (Alarcón et al. 2013b). In particular, it has been shown that strongly charged poly-electrolytes in aqueous solution experience a contraction followed by a re-expansion as a function of the tetravalent salt content, as shown in Fig. 3.

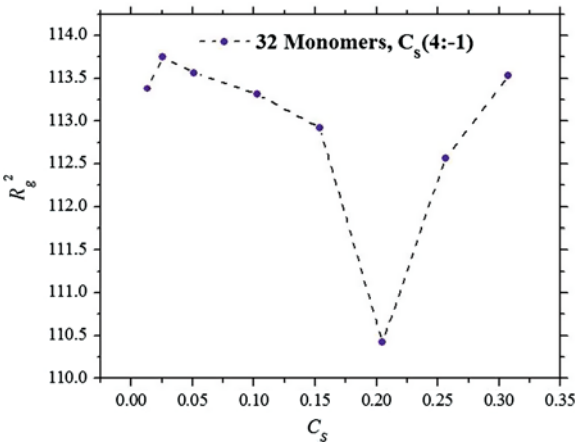

Fig. 3 The squared radius of gyration R_g of a poly-electrolyte made up of 32 equally charged monomers, in aqueous solution with varying ionic strength C_s. The latter is made up of tetravalent ions of Na neutralized with Cl ions. The axes are drawn in reduced DPD units. Adapted from Alarcón et al. (2013b)

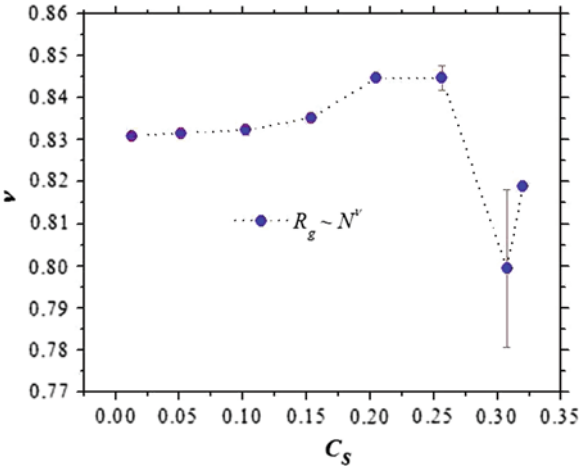

Fig. 4 The scaling exponent of the radius of gyration as a function of the polymerization degree under a varying concentration of Na and Cl ions. The y-axis is dimensionless while the x-axis is shown in reduced DPD units. Adapted from Alarcón et al. (2013b)

The contraction-re-expansion behavior quantified through the radius of gyration R_g of a model poly-electrolyte shown in Fig. 3 is the result of a complex interplay between the electrostatic interaction and the excluded volume effect brought about by the softness of the DPD interaction potential. Moreover, it is by no means an artifact of the DPD model, as it has been obtained using other interaction potentials and has also been observed in experiments with proteins in aqueous solution (Hsiao and Luijten 2006). In fact, using this electrostatic version of DPD it has been possible to predict the scaling exponent of the radius of gyration, defined by the well-known relation $R_g \sim N^\nu$ where N is the polymerization degree and ν is the scaling exponent (Alarcón et al. 2013b). It is known that it depends on the quality of the solvent in which the polymer is immersed, and on the dimension of the system. For neutral polymers in a good solvent it has been shown for some time that $\nu = 0.588$. However, for poly-electrolytes much less is known. To begin with, it is not even firmly established if a scaling relation is obeyed and much less what the value of the scaling exponent should be. Nevertheless, several groups have shown that poly-electrolytes do show scaling characteristics in their radius of gyration, but their scaling exponent is usually larger that its counterpart for neutral polymers.

Figure 4 shows the values of the scaling exponent of the radius of gyration for model linear poly-electrolytes of different polymerization degrees as a function of the ionic strength. Although the results in Fig. 4 were obtained for simulations in which all the interaction parameters between the poly-electrolyte and solvent were kept the same, the values of the scaling exponent are well above the value of 0.588 for neutral polymer in good solvent. These conditions correspond, in the neutral case, to the so-called theta solvent. Therefore, the results shown in Fig. 4 demonstrate that the quality of the solvent can be strongly modified by the electrostatic interactions.

3.3 DPD with Hard Potentials

As it concerns the use of DPD with hard potentials, we mention a widely used polymer coarse-grained model, developed by Grest and Kremer (1986) and Kremer and Grest (1990). It has been applied to a variety of thermodynamic conditions and physical systems as glasses, polymer melts and solutions, and polymer brushes (Grest 1999; Baschnagel and Varnik 2005; Dünweg and Kremer 1993; Binder and Milchev 2012; Kroger 2004). The bonded interaction along the same polymer is modeled by a finite extensible non-linear elastic (FENE) potential:

$$U_{\text{FENE}} = \begin{cases} -\frac{1}{2}k\ R_0^2 \ln\left[1 - \left(\frac{r}{R_0}\right)^2\right] & r \leq R_0 \\ \infty & r > R_0 \end{cases}, \tag{10}$$

where the maximum allowed bond length is $R_0 = 1.5\sigma$, the spring constant is $k = 30\varepsilon/\sigma^2$, and $r = |\mathbf{r}_i - \mathbf{r}_j|$ denotes the distance between neighboring monomers. Excluded volume interactions at short distances and van-der-Waals attractions between beads are described by a truncated and shifted Lennard-Jones (LJ) potential:

$$U(r) = U_{\text{LJ}}(r) - U_{\text{LJ}}(r_c), \tag{11}$$

with

$$U_{\text{LJ}}(r) = 4\varepsilon\left[\left(\frac{\sigma}{r}\right)^{12} - \left(\frac{\sigma}{r}\right)^{6}\right], \tag{12}$$

where the LJ parameters, $\varepsilon = 1$ and $\sigma = 1$, define the units of energy and length, respectively. The temperature is therefore given in units of ε/k_B, with k_B the Boltzmann constant. $U_{\text{LJ}}(r_c)$ is the LJ potential evaluated at the cut-off radius. There are typically two values taken as a cut-off distance: (i) the minimum of the LJ potential $r_c = 2^{1/6}\sigma \simeq 1.12\sigma$ and (ii) twice the minimum of the LJ potential: $r_c = 2 \times 2^{\frac{1}{6}}\sigma \simeq 2.24\sigma$, which allows for poor solvent conditions. In the first case, the interactions between monomers of different chains are purely repulsive. From the point of view of polymer solutions, this means good solvent conditions because the polymer bead is close to the solvent, giving rise to an effective repulsion among polymer beads. In the second case, longer ranged attractions are included (full Lennard-Jones potential), giving rise to liquid-vapor phase separation and droplet formation for adequate thermodynamic conditions (Müller and MacDowell 2001; MacDowell et al. 2000; Servantie and Müller 2008).

4 Selected Examples of DPD in Flow Simulations

4.1 Polymer Brushes with Soft Potentials

There are a number of applications in soft matter systems that require of surfaces covered by polymers to improve factors such as colloidal stability, reduction of interfacial tension for wetting purposes, or improvement of lubrication. The most common procedure to accomplish this is by grafting polymer chains of varying length to surfaces, changing the grafting density also. Within the context of computer simulations, when one is dealing with systems that model colloidal dispersions or surfaces with grafted polymers, to ensure that the confined system is in chemical, mechanical and thermal equilibrium with the non-confined fluid it is necessary to use the so-called Grand Canonical ensemble, which is well-known in statistical mechanics. It requires that the chemical potential, the volume of the system and the temperature be fixed during the simulation. To do so, one needs to perform Monte Carlo simulations, which are relatively demanding from the computational point of view because the number of particles in the simulation box is fluctuating and, as the concentration is increased, the probability of introducing new particles into the system becomes exceedingly small. However, for moderate densities it has been shown to be a very useful tool. Within the context of DPD there are now some works that have explored the properties of fluids confined by surfaces covered with polymers, using the Monte Carlo method in the Grand Canonical ensemble (MCGC). A common approximation consists of substituting the colloidal particles by planar surfaces, given the disparity of sizes between them and the solvent molecules. Also, planar surfaces are useful to model pores or mimic experimental arrangements such as that of the atomic force microscope or the surface force apparatus (Israelachvili 2011). These planar walls have been implemented in DPD through two methods: either by fixing in space some layers of DPD particles, placed at the ends of the simulation box (Goujon et al. 2004), or by introducing an effective wall potential that acts on particles close to the ends of the simulation box (Gama Goicochea 2007). Several models for the wall potential have been proposed; the first one being a linearly decaying force, in the spirit of the other DPD forces, namely (Gama Goicochea 2007):

$$\mathbf{F}_i(z) = a_{w,i}\left(1 - \frac{z}{z_c}\right)\hat{z}. \tag{13}$$

Equation (13) represents the force that acts on the ith-particle in the $\hat{z}$ direction (perpendicular to the plane where the surfaces are placed), $a_{w,i}$ is the interaction strength of such force, and z_c is a cutoff distance, beyond which the force becomes identically zero. For obvious reasons, this model is usually called the "DPD wall" force. Recently, a self-consistent surface force was obtained for DPD particles (Gama Goicochea and Alarcón 2011). It considers an infinite planar wall made up of regularly spaced, identical DPD particles that interact with other particles on the wall and with particles in the fluid through the usual DPD conservative force (see Eq. 7

and Fig. 5). By integrating the contribution to the total wall force from each particle on the surface it is possible to obtain an exact expression for the effective DPD surface force, which is given by the following polynomial (Gama Goicochea and Alarcón 2011):

$$\mathbf{F}_i(z) = a_{w,i}\left[1 - 6\left(\frac{z}{z_c}\right)^2 + 8\left(\frac{z}{z_c}\right)^3 - 3\left(\frac{z}{z_c}\right)^4\right]\hat{z}, \tag{14}$$

where the symbols have the same meaning as in Eq. (13), except that the strength of the interaction is given in this case by the relation:

$$a_{w,i} = \frac{\pi}{12}\rho_w R_c^3 a_{ij}. \tag{15}$$

In Eq. (15) ρ_w is the density of the wall, R_c is the usual cutoff radius, and a_{ij} is the conservative force strength between the particle i in the fluid and j on the wall.

The surface force in Eq. (14) is appealing for several reasons: it is exact, it is soft and short—ranged as the other DPD forces, and its strength is defined through the interaction strength of the conservative force as expressed in Eq. (15). Using this effective surface force, GCMC simulations have been performed to calculate the full solvation force that the walls exert on a simple monomeric DPD fluid. This solvation force, which is equal to the change in the free energy of the system between two compression states, per unit area, is surprisingly of relatively long range, as shown in Fig. 6, even though the surface—fluid particle force is of short range. This phenom-

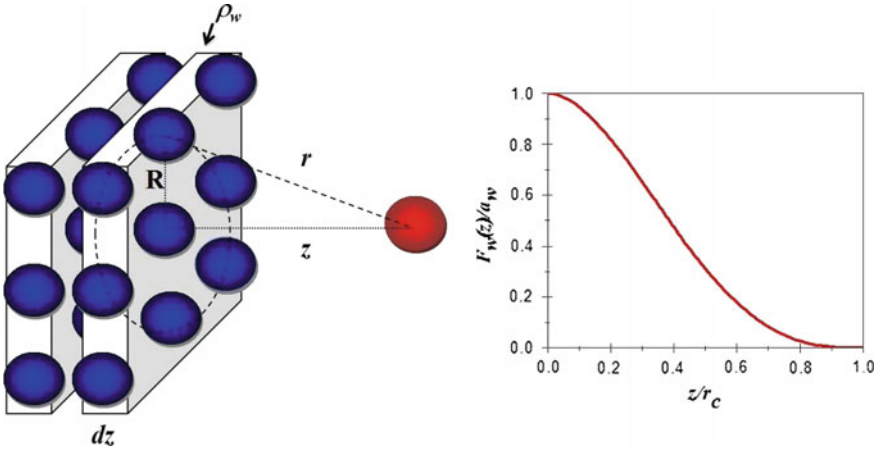

Fig. 5 Model to derive an effective DPD surface force (*left*). The resulting force is a polynomial (see Eq. 14) which is also of short range, as are the other forces that make up the DPD model (*right*). Adapted from Gama Goicochea and Alarcón (2011)

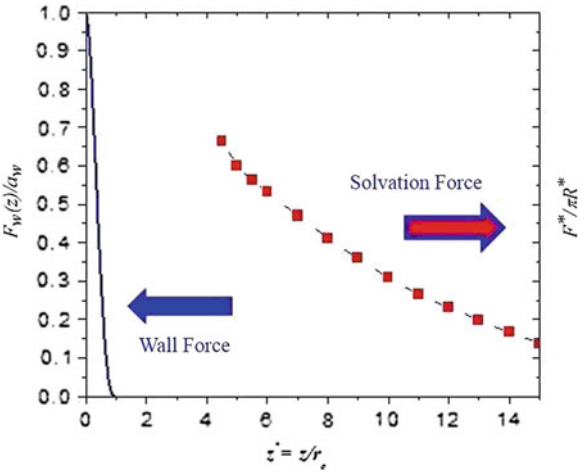

Fig. 6 The exact DPD wall-fluid force (Eq. 14) is shown in *blue*, while the full, many-body solvation force obtained from simulations with the wall force is shown in *red squares*. Both scales on the *y*-axis are shown in reduced DPD units, as is also the *x*-axis. To convert the latter into physical distances it is necessary to multiply z^* by 6.46Å. Adapted from Gama Goicochea and Alarcón (2011)

enon is the result of the collective many—body interactions that carry information about the boundary conditions of the fluid in the direction of the confinement (Fig. 6).

By attaching polymer chains to these effective surfaces it is possible to calculate the force between colloidal particles covered with polymer brushes and compare it with other models, like the well-known Alexander-de Gennes (AdG) model (Alexander 1977; de Gennes 1980), which is based on scaling arguments and assumes that the density profile of the monomers that make up the polymer brushes is a step function. This is known to be inaccurate. It also assumes that the polymer chains do not interact with one another, and that they are immersed in a solvent of good quality (Alexander 1977; de Gennes 1980). The AdG force is then the result of short range repulsion caused by the increased osmotic pressure when the polymer brushes are brought into close contact, and elastic attraction created by the entanglement of polymer chains on opposite brushes. In the left panel of Fig. 7, we present the density profile of the polymer brushes at a given separation between the walls, which shows the beads attached to each surface and the structuring in the density profile of the brushes, which is a consequence of having relatively short chains ($N = 5$ for the case shown in this figure). Notice how this profile is far from resembling a step function. Yet, as shown in the right panel of Fig. 7, the AdG model reproduces fairly well the trend in the full solvation force obtained with GCMC DPD simulations, although the latter are more accurate because the interactions between all particles are accounted for.

The disjoining pressure of a simple monomeric fluid confined by effective linearly decaying wall forces, as the one shown in Eq. (13), has been calculated by means

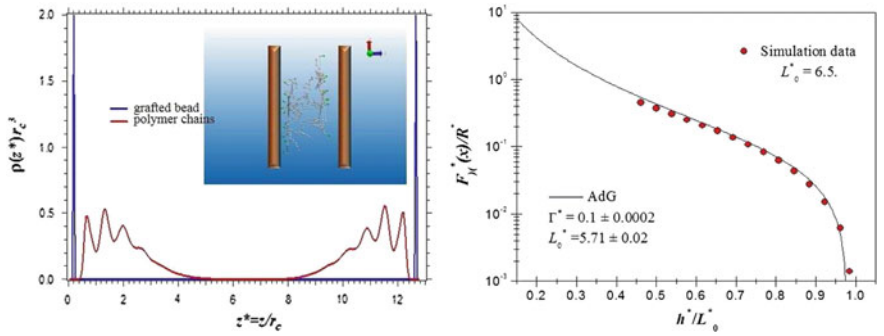

Fig. 7 Density profile for polymer chains with degree of polymerization $N = 5$ (*left*). The inset shows an image from the actual simulations. Full solvation force obtained from GCMC DPD simulations of polymer brushes (*right*). The *line* represents the AdG model. Axes are shown in reduced units. Adapted from Gama Goicochea and Alarcón (2011)

of GCMC-DPD simulations. This is a quantityof importance when studying the properties of confined fluids because it is a measure of the stability of complex fluids under confinement and fixed chemical potential (Gama Goicochea 2007). It is defined as the difference between the pressure tensor component in the direction perpendicular to the confinement (P_N) and the pressure of the bulk (unconfined) fluid, P_B. In Fig. 7, we see the disjoining pressure (Π) as a function of the distance between the walls (L_z), for a monomeric fluid confined by linearly decaying surface forces. There appear intercalated maxima with minima whose interpretation is as follows. The maxima in Π represent thermodynamic states with maximal force between colloidal particles (per unit area) represented by the walls, mediated by the corpuscular nature of the solvent. These maxima are the consequence of an ordered array of the solvent molecules into layers, whose order gets increasingly lost as the separation between the surfaces grows, as should be expected. These states correspond to conditions of optimal stability for the colloidal dispersion. The minima seen in Fig. 8 represent states where there is an attractive (negative) force between the surfaces, therefore they are thermodynamically unstable and would lead to the agglomeration of colloidal particles. It is remarkable that an attractive force can emerge from a model (DPD) where all particle interactions are repulsive, including the wall force. It occurs because of the confinement condition and the corpuscular nature of the solvent, which forces the particles to form orderly layers when the force is at a maximum (see points labeled *a*, *c* and *e* in Fig. 8) and be disordered when the force is minimal (as in states labeled *b* and *d* in Fig. 8).

The behavior shown in Fig. 8 reproduces very well the trends found in experiments and with other calculation methods (Israelachvili 2011), and lends credence to the usefulness of DPD as a precise predicting tool, not only for polymers in solution, but also for confined complex fluids. It is advantageous to perform simulations like these before embarking in laborious, time consuming and expensive experiments, such as those required to determine adsorption isotherms. In the design of new colloidal dispersions for the paint industry, for example, or for the improvement and

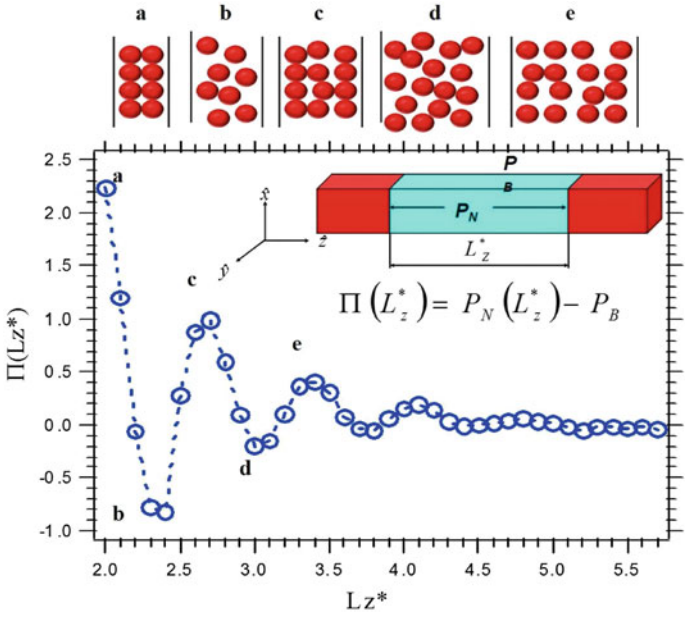

Fig. 8 The disjoining pressure Π of a simple fluid made up of monomers obtained from GCMC–DPD simulations of the fluid confined by linearly decaying wall forces, as a function of the distance separating the surfaces. The *inset* shows a schematic diagram of the system model and how it is calculated. The *top* part of the figure illustrates how the maxima and minima are due to the arrangement of the fluid's molecules. The axes are shown in reduced units. Adapted from Gama Goicochea (2007)

optimization of known formulations, it is usually required to determine the amount of material (polymers, surfactants) that needs to get adsorbed on the surfaces of the colloidal particles. This is traditionally determined from adsorption isotherms, which can take several weeks to measure and interpret. By contrast, the adaptability of computer simulations allows one to calculate adsorption isotherms in a relatively short time, having full control of the thermodynamic variables. For these purposes it is crucial to perform the calculations at constant chemical potential (and at constant volume and temperature). Because of the mesoscopic reach of the DPD model and its success in predicting the behavior of polymers in solution and also confined fluids, it becomes a well suited tool for the study of adsorption of polymers on colloidal particles.

Figure 9 shows adsorption isotherms obtained with GCMC-DPD simulations for two cases. In one case, where the surfaces were implemented as Lennard-Jones (9-3) forces to represent alumina surfaces (Al_2O_3) that are known to have hydrophilic character (Esumi et al. 2001). In the other case, the walls were modeled as soft DPD walls (see Eq. 13). In order to represent the hydrophobic nature of silica (SiO_2) surfaces. The fluid confined by these walls is composed of solvent monomers and a varying number of *PEG* molecules, which are modeled as linear chains with $N = 7$

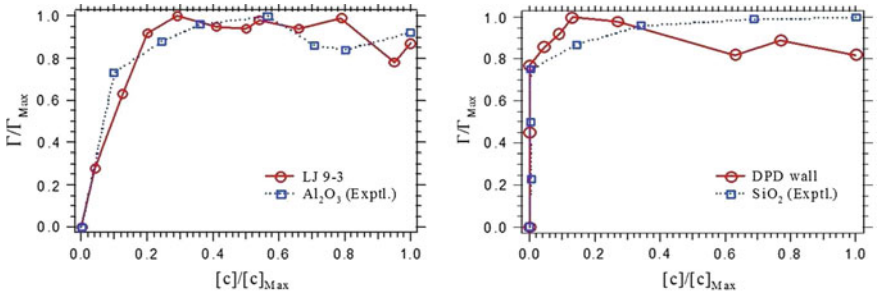

Fig. 9 Adsorption isotherms obtained with GCMC–DPD simulations of fluids confined by a Lennard-Jones (9–3) surface model (*left*), and a linearly decaying, DPD wall force (*right*). The fluid is made up of the monomeric solvent and a varying number of linear polymer chains (N = 7) to represent PEG molecules. *Red circles* represent the simulation results while the *blue squares* are the experimental data as taken from Esumi et al. (2001). The axes are normalized with their maximum value so that both scales range from 0 to 1. The *lines* are only guides for the eye. Adapted from Gama Goicochea (2007)

beads each, joined by harmonic springs. This polymerization degree corresponds to a molecular weight $M_w = 400$ for *PEG* (Gama Goicochea 2007). The predicted adsorption isotherms are compared with the experimental counterparts (Esumi et al. 2001) in Fig. 9. Notice how the DPD methodology correctly reproduces the trends if not the actual values of the isotherms; not only that, it is possible to model different surfaces characteristics by a judicious choice of the wall force model or interaction parameters. Up to this point all the results reported for confined fluids were carried out for neutral systems. However, poly-electrolytes which are charged polymers are ubiquitous in nature and in modern day applications (Holmberg 2003). Many colloids acquire electric charges on their surface when immersed in a polar solvent, like water, and are rich in showing complex phenomena when they are subject to varying ionic strength and pH, as poly-electrolytes are as well. From the point of view of fundamental research, the long range nature of the Coulomb interaction gives rise to behavior that is qualitatively different from neutral systems, which needs to be thoroughly investigated to reach a satisfactory understanding of soft condensed matter systems. Because of these needs it became necessary to adapt the DPD model so that it could handle long range interactions such as the electrostatic one, for confined systems. The natural route was to adapt the Ewald sums method for cases when there is reduced symmetry, as in the confined fluids we have discussed (Alarcón et al. 2013a).

Alarcón and co-workers (2013a) calculated the first adsorption isotherms of poly-electrolytes using the GCMC–DPD algorithm adapted with Ewald sums for confined systems as a function of pH. They studied the adsorption of weakly charged, linear cationic and anionic poly-electrolytes at various values of pH on negatively charged and neutral colloidal surfaces. The adsorption isotherms they obtained for cationic poly-electrolytes adsorbed on neutral surfaces modeled by the exact, self-consistent DPD wall force (see Eq. 14) are shown in the left panel of Fig. 10. For the model poly-

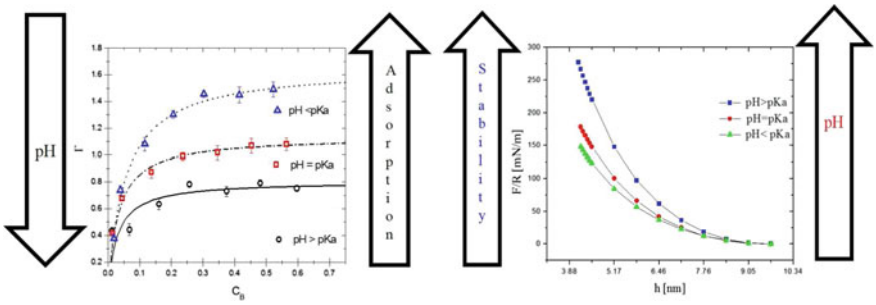

Fig. 10 Fully charged linear cationic poly-electrolyte on neutral surfaces with $N = 7$ beads. Only every other bead is charged. The *left panel* shows the adsorption isotherms obtained at three different pH values. The symbols represent the results of the simulations while the *solid lines* are the best fits to the Langmuir adsorption isotherm model. In the *right panel* of this figure we show the full force between colloidal surfaces mediated by the poly-electrolytes and the solvent, for the same pH values as in the *left panel*. Notice that when the pH is increased so is the surface force, in contrast with the adsorption isotherm trend. The axes in the *left* figure are shown in reduced DPD units while those on the *right* have been appropriately dimensionalized. Adapted from Alarcón et al. (2013a)

electrolyte used in those simulations the adsorption increases as the pH is reduced, which was attributed to the competition between the poly-electrolytes and their counterions for the adsorption sites on the colloids surfaces, because the adsorption of the counterions grows when that of the poly-electrolytes is reduced. This is precisely the trend found in experiments performed on comparable situations (Drechsler et al. 2010). The right panel in Fig. 10 shows the full surface force that neutral colloidal particles, modeled by the exact DPD wall force, exert on each other by means of the cationic poly-electrolytes at different pH values (Alarcón et al. 2013a). This is the first calculation of its kind, not only within the context of DPD simulations. The trend found in the surface force is entirely different from that found in the adsorption isotherms (left panel in the same figure) even though the calculations were performed on the same systems. In other words, when the pH of the cationic poly-electrolyte is increased, it translates into a larger surface force between colloidal particles. What this means is that if one is looking for optimal stability of colloidal dispersions it may be advantageous to add less poly-electrolytes as dispersants, at a basic pH, because the competition of electrostatic interactions between poly-electrolytes and counterions, and the excluded volume interactions with the solvent are enough to increase the many-body surface force so that the colloidal dispersion turns out to be optimally stable, as the right panel of Fig. 10 shows. The results shown in the right panel of Fig. 10 fully reproduce the experiments carried out on poly-electrolytes and characterized using atomic force microscopy at different pH (Drechsler et al. 2010), among others.

Lastly, we comment on some very recent DPD simulations that model complex fluids under stationary flow using soft DPD potentials. The reason for simulations of this type stems from the need to understand phenomena seen in applications such as drug–carrying liposomes in the pharmacological industry, in the processes of

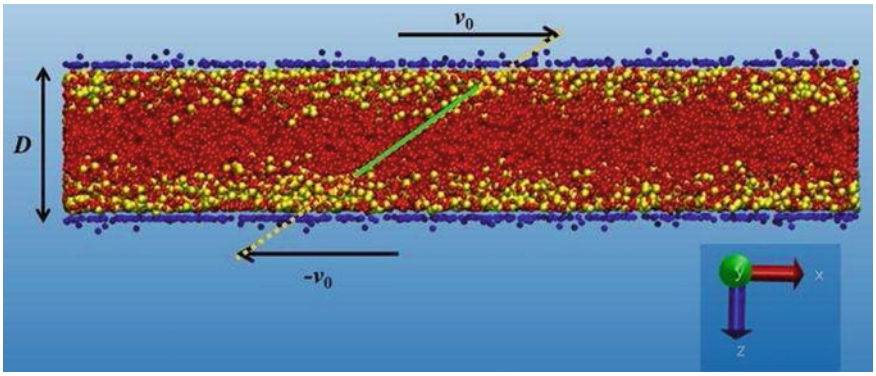

Fig. 11 A system configuration extracted directly from non-equilibrium computer simulations using soft DPD interactions of polymer brushes grafted on soft DPD surfaces. The *blue* particles are the grafted beads which move at constant speed v_0 in the direction indicated by the *arrows*. Those beads drag the rest of the beads forming the polymer chains (in *yellow*) to produce flow of the solvent particles (in *red*). The *green line* indicates the velocity gradient as is expected in stationary Couette flow. Adapted from Gama Goicochea et al. (2014)

enhanced oil recovery, for the design of improved rheology modifiers in the paint industry, as well as lubricants, to mention a few. The idea behind non equilibrium, stationary flow simulations for applications like those mentioned above is as follows: two parallel plates are placed a certain distance apart, say in the z–direction; then a constant force is applied to the top plate and an equal in magnitude but opposite in direction force is applied to the bottom plate. This creates a velocity gradient (or shear rate) which is responsible for creating a steady flow known as Couette flow. We shall have more to say about the details of this type of flow in the next section, but for now we focus on the use of soft DPD potentials in non-equilibrium simulations. Although many works have been published that use computer simulations to study Couette flow, most of them have been carried out using microscopic models, which are accurate but are very time-consuming, even more than equilibrium simulations. Recently, a study of the rheological properties of polymer brushes under theta solvent conditions using only soft DPD interactions has been published (Gama Goicochea et al. 2014). The system consists of two parallel plates on the xy-plane, modeled as soft DPD wall forces separated by a fixed distance D, where a number of polymer chains were grafted at one of their ends and at grafting densities large enough to form polymer brushes. A constant velocity v_0 is applied to the grafted ends of the polymer chains on the top and bottom plates, in opposite directions, so that stationary flow is produced by the collisions of the chains with themselves and with the solvent particles. This gives rise to a mean constant force F_x in each plate, in the stationary regime. The grafted beads on the surfaces move with a constant velocity (v_0) but there is a velocity gradient of constant shear rate $\dot{\gamma}$ along the direction separating the plates. Figure 11 shows a configuration of this system, extracted directly from the simulations.

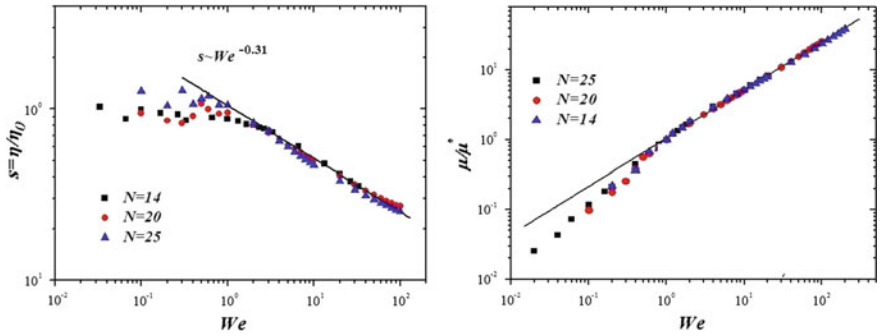

Fig. 12 (*Left*) Viscosity of the grafted beads of polymer chains forming brushes of three different polymerization degrees, as a function of the applied shear rate. In order to use dimensionless units on both axes, the y-axis was normalized with the limiting value of the viscosity at zero shear rate η_0. The x-axis was normalized with the value of the shear rate when the behavior of the applied force changes from linear to sub-linear, so defining the Weissenberg number *We*. The *line* is the predicted scaling law. (*Right*) The friction coefficient is normalized by its value at the transition from linear to sublinear regimes, as a function of *We*. The friction coefficient for all brushes modeled obeys the scaling law $\mu/\mu^* \sim We^{0.69}$. See text for details. Adapted from Gama Goicochea et al. (2014).

One can calculate rheology properties such as the viscosity η for fluids under flow, as the one shown in Fig. 11, using the following relation (Macosko 1994; Pastorino et al. 2006):

$$\eta = \frac{\langle F_x(\dot{\gamma})\rangle / A}{\dot{\gamma}}. \tag{16}$$

In Eq. (16) F_x is the magnitude of the constant force in the x-direction, applied to the planar surfaces of area A and $\dot{\gamma}$ is the shear rate. The brackets represent an average over the entire simulation time (Gama Goicochea et al. 2014; Pastorino et al. 2006). By changing the applied force one can vary the shear rate and then measure the dynamic response of the fluid through the viscosity using Eq. (16). Newtonian fluids are characterized by viscosities that are independent of the shear rate, but most fluids of interests for modern applications, as well as the fluid simulated and shown in Fig. 11, are of the non-Newtonian type, namely they have viscosities that are shear rate dependent (Macosko 1994). Another rheological property of interest for polymer brushes is the friction coefficient between the brushes and the fluid, which is given by the following expression:

$$\mu = \frac{\langle F_x(\dot{\gamma})\rangle}{\langle F_z(\dot{\gamma})\rangle}, \tag{17}$$

where $\langle F_x(\dot{\gamma})\rangle$ and $\langle F_z(\dot{\gamma})\rangle$ represent the mean forces that the grafted beads experience along the direction of the flow ($\hat{x}$) and perpendicularly to it ($\hat{z}$), respectively. The brackets symbolize time averages over all the particles in the simulation box. Clearly, μ is a dimensionless number. Figure 12 shows the predictions for the viscosity and the friction coefficient obtained from DPD simulations of Couette flow for linear polymer brushes of varying polymerization degree under theta solvent

conditions, using Eqs. (16) and (17), respectively (Gama Goicochea et al. 2014). In particular, the viscosity (left panel in Fig. 12) shows what is usually known as "shear thinning", i.e., the viscosity is reduced as the shear rate is increased. As we way see from the figure, the viscosity for brushes of different polymerization degrees N, obeys a universal law for large values of the shear rate. In fact, a scaling law can be extracted, yielding $\eta \sim \dot{\gamma}^{-0.31}$ independently of the value of N. On the other hand, the friction coefficient (right panel in Fig. 12) increases with the shear rate but obeys also a scaling law, which is found to be $\mu \sim \dot{\gamma}^{0.69}$. These scaling exponents are in excellent agreement with those predicted using different arguments (Galuschko et al. 2010) and they are found to be related according to those predictions (Gama Goicochea et al. 2014).

We conclude this section by recalling that there are numerous examples where the application of the soft DPD potentials have yielded novel and accurate predictions which make this model one of the leading current tools to understand phenomena in soft matter systems. Here we have reviewed only some of the recent ones, mostly taken from our own work and expertise.

4.2 Hard Coarse-Grained Potentials

In this section, we provide examples of simulations of flows with the coarse-grained Kremer-Grest model for polymers. The two simplest hydrodynamic flows can be easily set within the MD with DPD thermostat simulations. These two flows are very important to characterize the behavior in operational conditions of microfluidic devices. The small size of the channels that confine the fluid implies a laminar regime, which departs from the turbulent hydrodynamic regime.

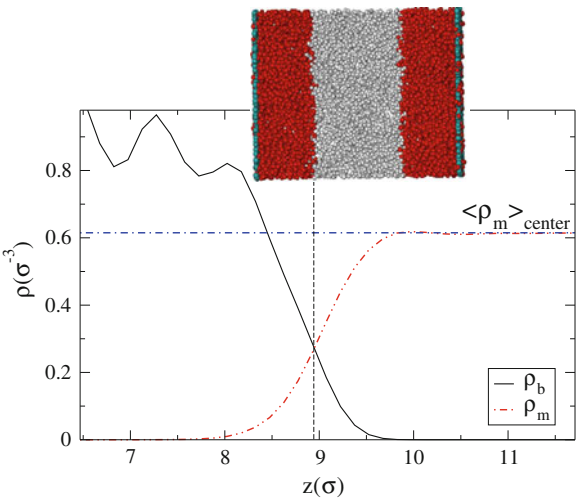

Fig. 13 Density profile of the brush (*full line*) and the melt (*dashed-dotted line*) for $\rho_g = 0.77\sigma^{-2}$. The inset shows a configuration of the simulated system, aligned with the density profile such that the brush-melt interface coincides. Adapted from Pastorino et al. (2009)

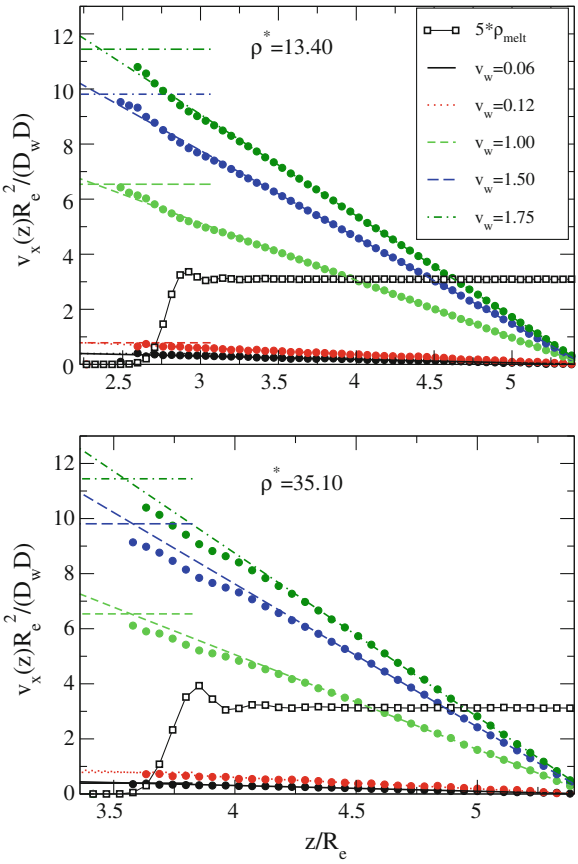

Fig. 14 Velocity profile for the linear Couette flow simulations for different wall velocities (shear rate). The velocity is scaled with the dynamic scale of a polymer melt of the same density as the brush $D_w D/R_e^2$, where D_w is the channel width, D the diffusion coefficient of the equivalent polymer melt and R_e its end-to-end distance. The *open squares* show the density profile of the same system. It should be noted that it is highly independent of the flow conditions. Adapted from Pastorino et al. (2009)

In these examples, the Couette (linear) flow is established by moving the walls of the polymer-coated channel at constant and opposite velocity. This builds up, at stationary regime, a linear velocity profile in the channel with 0 velocity exactly at the center of the channel.

A typical simulation is shown in the inset of Fig. 13. The Figure shows a density profile with the two species in the system: a polymeric liquid of ten-bead chains (gray) which is confined between two layers of end-grafted polymers, a polymer brush (red). The densities show the brush-liquid interfaces clearly defined. The liquid is not able to enter in the brush layer, even when all the interactions are attractive, due to entropic effects (Pastorino et al. 2007, 2009). This corresponds to the well-known case of autophobicity (Pastorino et al. 2006). The brush thickness depends on the grafting density (number of chains per unit area grafted at the wall). This system can be studied in equilibrium and also under flow.

The velocity profiles obtained as a result of moving the wall at constant and opposite velocity are shown in Fig. 14. The linear velocity profiles are clearly observed for two different grafting densities in the brush (upper and lower panels). The density

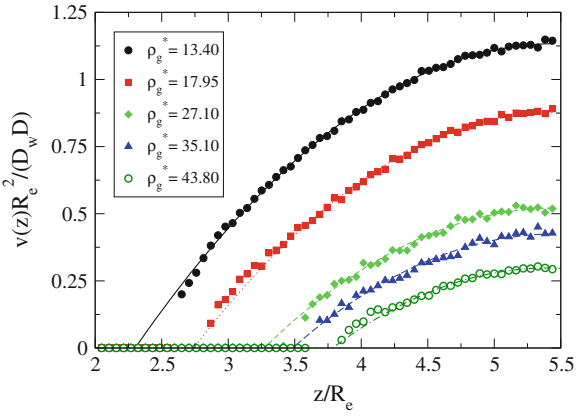

Fig. 15 Symmetrized velocity profile for Poiseuille-flow simulations for different grafting densities. The body force acting in each bead is $f_x = 0.008\varepsilon/\sigma$. The $\hat{x}$-axis is given in units of a measure of the polymer size, the end-to-end radius for these liquid density and temperature is $R_e = 3.66\sigma$. The channel width is $D = 40\sigma$ with the center of the channel in 20σ ($z/R_e = 5.46$). There the velocity profile reaches the maximum. Adapted from Pastorino et al. (2009)

profile is also shown with open circles. Close to the brush-liquid interface, inside the brush layer, deviations from the dominant linear profiles are observed. This has a physical meaning, since the interface properties are not expected to be the same as that of the bulk liquid, in the center of the channel. The mixture of liquid and grafted chains (which do not flow in the wall reference frame) can be understood as an effective liquid of different viscosity, in this zone. It is important to emphasize the difference of this simulation scheme as compared to the one in conventional computational fluid dynamics. In MD with DPD, neither the viscosity of the fluid, nor the boundary conditions (i.e. slip length or slip velocity) are imposed to the system. These two quantities can be measured in the simulations for given flow, thermodynamic conditions and molecular interaction models. Figure 15 shows the Poiseuille-like velocity profile for the same system. It is obtained by applying a constant body force for each particle. This can be understood as a gravity force acting on each particle, or a pressure difference. Only the velocity profile of the polymeric liquid is shown. The brush has a vanishing mean velocity since the molecules are grafted to the hard substrate. The velocity profiles are progressively narrower upon increasing grafting density due to the increased thickness of the brush layer. This smaller effective width of the channel reduces also the flow rate at constant body force (or pressure gradient). The mean viscosity of the polymeric liquid can be extracted from the simulations by just fitting the analytic velocity profile obtained from the integration of the Navier-Stokes equation:

$$v(z) = \frac{\rho f_x}{2\eta}(z - z_0)(D_w - z_0 - z), \tag{18}$$

where ρ is the number density of the fluid at bulk, $f_x = 0.008\varepsilon/\sigma$ is the external body force applied on each bead to produce the flow, D_w is the channel width and z_0 indicates the position at which the velocity profile extrapolates to 0 velocity. The viscosity η is the only parameter in Eq. (18) that is not measured directly from the simulation. It can be obtained from the fit of the profile with Eq. (18).

These examples illustrate the use of DPD with hard potentials, in which the structural properties of the liquid, flow properties (slip length and slip velocity, velocity profile) and rheological properties (viscosity, regions of non-newtonian behavior) of these soft matter systems can be obtained from the simulations using the two simplest hydrodynamic flows, i.e. Couette (linear) and Poiseuille (quadratic) flows. Velocity fields, together with density profiles can be studied globally (Pastorino et al. 2006, 2009; Müller et al. 2009; Léonforte et al. 2011), locally (for example inside a droplet) (Servantie and Müller 2008; Tretyakov et al. 2013; Tretyakov and Müller 2013) or for a given type of molecule (Pastorino and Müller 2014).

5 The Conservation of Temperature in Flow Simulations

Under conditions of high flow, the DPD thermostat can have problems to maintain a constant temperature across the fluid (Pastorino et al. 2007). A particular complicated case takes place for good solvent conditions in polymeric or other soft matter system. An important difference between Langevin and DPD thermostat is that Langevin forces act on every particle, independently of the cut-off radius of the potential or the density of the system. DPD, however, acts on pairs of interacting particles, those that are within the cut-off radius. For systems with short cut-off radii as it is the case of the Kremer-Grest model for polymers in good solvent conditions, the number of thermostated pairs per time step can be pretty low, reducing the ability of the DPD thermostat to extract a given amount of heat per unit time in the system. This behavior is illustrated in Fig. 16 for Poiseuille-flow simulations. Figure 16b shows the velocity profile across the channel for different external forces. There is a quadratic behavior, but some deformation is observed, as compared to Fig. 15. The reason for that can be noticed in Fig. 16a, which shows the temperature profile across the channel.These are extracted from the mean quadratic velocity in the directions without flow ($\hat{y}$ and $\hat{z}$). The equipartition theorem implies $\frac{1}{2}m\langle v_y^2\rangle = \frac{1}{2}k_BT$, from which a local temperature can be extracted. For higher forces, starting in $f_x = 0.014\varepsilon/\sigma$, the temperature is not conserved and heating of the liquid occurs in the regions of higher shear rate. There, the heat production per unit time is higher than the maximum removed by the thermostat and the temperature cannot be maintained at the defined value $k_BT = 1.68\varepsilon$.

In these situations various strategies can be adopted to maintain the constant temperature. The simplest choice would be increasing the friction constant of the thermostat. This can be perfectly done if the short-time dynamics of the molecules is not of interest. This means also increasing the amplitude σ_R of the stochastic force (see Eq. 3). Another alternative is to change the weight functions in the forces of the

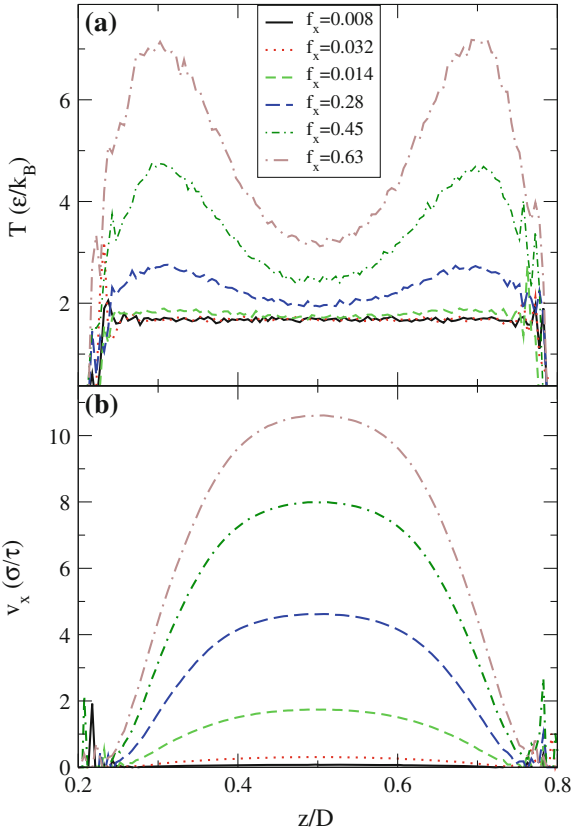

Fig. 16 Panel **a** Temperature and velocity profiles for different external forces for a polymeric liquid of 10-bead chains confined in a brush coated channel. Panel **b** velocity profiles of the Poiseuille flow simulations for the same cases of the Panel **b**. For a high body force the temperature is not conserved across the channel, reaching the maximum deviation in the regions of highest shear rate (local velocity gradient). Adapted from Pastorino et al. (2007)

thermostat. As it was emphasized, they only have to fulfill the requirement of Eq. (4) to warrant the fluctuation-dissipation theorem. Figure 17 illustrates this option. It shows the temperature profile across the channel with exactly the same flow conditions for different weight functions. The usual choice (Eq. 6) has the worst performance with the higher deviation from the desired temperature $k_B T = 1.68\varepsilon$. The usual choice of weight functions fails to keep a constant temperature across the channel (dark full line), while the constant weight functions $\left[\omega^D\right]^2 = \omega^R = \Theta(R_c - r)$ gives much better temperature conservation. The defined temperature is shown with a dashed line. Constant weight functions fulfill temperature conservation at the desired temperature. The last option that we comment here to improve temperature conservation is increasing the number of thermostated pairs of particles by extending the cut-off for the DPD forces. In this case, the cut-off of the conservative forces continues to be of short range, for example $R_c =^6 \sqrt{2}\sigma$ (good solvent for the Kremer-Grest model). But the cut-off for DPD forces is twice as long: $R_c^{(DPD)} = 2 \times^6 \sqrt{2}\sigma$. This option was successfully employed by Pastorino and Müller (2014).

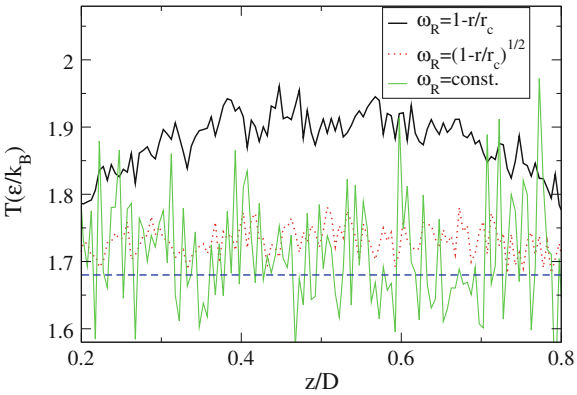

Fig. 17 Temperature profile for different DPD weight functions in a Couette-flow simulation. The walls are moved at $v_w = 3\sigma/\tau$ and the channel width is $D_w = 30\sigma$, with a shear rate of $\dot{\gamma} = 0.3\tau^{-1}$. The usual choice of weight function fails to keep a constant temperature across the channel (*dark full line*). Constant weight functions $\left[\omega^R\right]^2 = \omega^D = \Theta(R_c - r)$ are able to give a temperature profile at the defined temperature (*dashed line*). Θ is the Heaviside function and R_c the cut-off of the forces. Adapted from Pastorino et al. (2007)

This problem of temperature conservation shows up for hard potentials at very short cut-off radius and strong flow conditions. This by no means limits the use of DPD, taking into account the solutions we propose in this section.

6 Concluding Remarks

In this contribution we have reviewed the Dissipative Particle Dynamics method, as a useful simulation technique to study soft matter systems in equilibrium and under flow. We emphasize the role of DPD as a thermostat that takes into account correctly the hydrodynamic correlations in the system, unlike many thermostats used in molecular dynamics. This is a desired property to study stationary flows at the mesoscopic level with coarse-grained models of the molecular degrees of freedom. We give examples of the use of the DPD thermostat with soft potentials and hard potentials for polymeric liquids, polymer brushes and simple liquids. In equilibrium simulations with soft potentials, we also illustrate the use of DPD with Coulomb interactions to model poly-electrolytes, confinement and constant chemical potential simulations in the Grand-Canonical Ensemble (μVT).

We show that DPD is suitable for generating simple flows like Couette and Poiseuille flows and having access to the main velocity of density fields, characteristic of hydrodynamic theories but also to the boundary conditions and dynamics coefficients such as diffusion coefficients or viscosity. The latter are not imposed to the system, but obtained from the simulation itself, for given molecular model and flow conditions. In the studied cases the goal is simulating the system at constant

temperature, though DPD can be modified to perform energy-conserving simulations and explore heat conduction (Español 1997; Avalos and Mackie 1997). For some particular cases of very short-range potentials and strong flow conditions, the ability of DPD to keep the temperature at the fixed value must be verified. We report also some examples in which temperature is not conserved and the workarounds to follow when this is the case.

We have shown that DPD is a powerful and efficient tool to simulate soft matter systems under flow, keeping the dynamics of the individual molecules. This can be exploited in fields where surface-to-volume ratio of the confined liquid or polymeric compound is not negligible and the effects of the interface are important for the whole properties of the system. This would be the case in microfluidic devices, oil-recovery problems in porous media or biological interfaces and vascular systems.

Acknowledgments C.P. thanks Marcus Müller for the enjoyable and fruitful discussions since he started in this exciting topic of simulations of soft matter systems. Kurt Binder and Torsten Kreer are also gratefully acknowledged for the support and scientific discussions in the nice times of Mainz. AGG would like to thank F. Alarcón, M.A. Balderas Altamirano, C. Carmín, E. Mayoral, G. Pérez-Hernández, and E. Pérez for their help and collaborative efforts.

References

Alarcón F, Pérez E, Gama Goicochea A (2013a) Dissipative particle dynamics simulations of weak polyelectrolyte adsorption on charged and neutral surfaces as a function of the degree of ionization. Soft Matter 9(3):777–3788. doi:10.1039/C2SM27332B, http://dx.doi.org/10.1039/C2SM27332B

Alarcón F, Pérez-Hernández G, Pérez E, Gama Goicochea A (2013b) Coarse-grained simulations of the salt dependence of the radius of gyration of polyelectrolytes as models for biomolecules in aqueous solution. Eur Biophys J 42(9):661–672

Alexander S (1977) Adsorption of chain molecules with a polar head a scaling description. J Phys Fr 38(8):983–987

Allen MP, Tildesley DJ (1987) Computer simulations of liquids. Clarendom Press, Oxford

Avalos JB, Mackie AD (1997) Dissipative particle dynamics with energy conservation. EPL (Europhys Lett) 40(2):141

Baschnagel J, Varnik F (2005) J Phys Condens Matter 17:R851

Binder K, Milchev A (2012) Polymer brushes on flat and curved surfaces: how computer simulations can help to test theories and to interpret experiments. J Polym Sci Part B: Polym Phys 50(22):1515–1555

Binder K, Kreer T, Milchev A (2011) Polymer brushes under flow and in other out-of-equilibrium conditions. Soft Matter 7:7159–7172

Brown WM, Kohlmeyer A, Plimpton SJ, Tharrington AN (2012) Implementing molecular dynamics on hybrid high performance computers-particle-particle particle-mesh. Comput Phys Commun 183(3):449–459

de Gennes PG (1980) Conformations of polymers attached to an interface. Macromolecules 13(5):1069–1075

Drechsler A, Synytska A, Uhlmann P, Elmahdy MM, Stamm M, Kremer F (2010) Interaction forces between microsized silica particles and weak polyelectrolyte brushes at varying ph and salt concentration. Langmuir 26(9):6400–6410

Dünweg B (2006) Mesoscopic simulations for problems with hydrodynamics, with emphasis on polymer dynamics. In: Ferrario M, Ciccotti G, Binder K (eds) Computer simulations in condensed matter systems: from materials to chemical biology vol 2, vol 704., Lecture Notes in PhysicsSpringer, Berlin, pp 309–340

Dünweg B, Kremer K (1993) J Chem Phys 99:6983

Español PE (1995) Hydrodynamics from dissipative particle dynamics. Phys Rev E 52:1734

Español P (1997) Dissipative particle dynamics with energy conservation. EPL (Europhys Lett) 40(6):631 http://stacks.iop.org/0295-5075/40/i=6/a=631

Español P, Warren P (1995) Statistical mechanics of dissipative particle dynamics. Europhys Lett 30:191

Esumi K, Nakaie Y, Sakai K, Torigoe K (2001) Adsorption of poly(ethyleneglycol) and poly(amidoamine)dendrimer from their mixtures on alumina/water and silica/water interfaces. Colloids Surf A: Physicochem Eng Asp 194:7–12

Forrest BM, Suter UW (1995) Accelerated equilibration of polymer melts by time coarse graining. J Chem Phys 102(18):7256–7266

Frenkel D, Smit B (2002) Understanding molecular simulation: from algorithms to applications. Academic Press

Galuschko A, Spirin L, Kreer T, Johner A, Pastorino C, Wittmer J, Baschnagel J (2010) Frictional forces between strongly compressed, nonentangled polymer brushes: molecular dynamics simulations and scaling theory. Langmuir 26(9):6418–6429

Gama Goicochea A (2007) Adsorption and disjoining pressure isotherms of confined polymers using dissipative particle dynamics. Langmuir 23(23):11656–11663

Gama Goicochea A, Alarcón F (2011) Solvation force induced by short range, exact dissipative particle dynamics effective surfaces on a simple fluid and on polymer brushes. J Chem Phys 134(1):014703

Gama Goicochea A, Romero-Bastida M, López-Rendón R (2007) Dependence of thermodynamic properties of model systems on some dissipative particle dynamics parameters. Mol Phys 105(17–18):2375–2381

Gama Goicochea A, Mayoral E, Klapp J, Pastorino C (2014) Nanotribology of biopolymer brushes in aqueous solution using dissipative particle dynamics simulations: an application to peg covered liposomes in a theta solvent. Soft Matter 10:166–174

Goujon F, Malfreyt P, Tildesley DJ (2004) Dissipative particle dynamics simulations in the grand canonical ensemble: applications to polymer brushes. ChemPhysChem 5(4):457–464

Grest G (1999) Adv Polym Sci 138:1

Grest GS, Kremer K (1986) Molecular dynamics simulations for polymers in the presence of a heat bath. Phys Rev A 33:3628

Groot RD, Warren PB (1997) Dissipative particle dynamics: bridging the gap between atomistic and mesoscopic simulation. J Chem Phys 107:4423–4435

Holmberg K (2003) Surfactants and polymers in aqueous solution. Wiley, Chichester

Hoogerbrugge PJ, Koelman JMV (1992) Simulating microscopic hydrodynamic phenomena with dissipative particle dynamics. Europhys Lett 19:155

Hsiao P-Y, Luijten E (2006) Salt-induced collapse and reexpansion of highly charged flexible polyelectrolytes. Phys Rev Lett 97:148301

Hünenberger P (2005) Thermostat algorithms for molecular simulations. Adv Polym Sci 173:105

Israelachvili J (2011) Intermolecular and surface forces. Academic Press, Burlington

Kremer K, Grest GS (1990) Dynamics of entangled linear polymer melts: a molecular-dynamics simulation. J Chem Phys 92:5057

Kroger M (2004) Simple models for complex nonequilibrium fluids. Phys Rep-Rev Sect Phys Lett 390:453–551

Léonforte F, Servantie J, Pastorino C, Müller M (2011) Molecular transport and flow past hard and soft surfaces: computer simulation of model systems. J Phys: Condens Matter 23(18):184105

MacDowell L, Müller M, Vega C, Binder K (2000) Equation of state and critical behavior of polymer models: a quantitative comparison between wertheim's thermodynamic perturbation theory and computer simulations. J Chem Phys 113:419–433

Macosko C (1994) Rheology principles, measurements, and applications. VCH, New York

Mayoral E, Gama Goicochea A (2013) Modeling the temperature dependent interfacial tension between organic solvents and water using dissipative particle dynamics. J Chem Phys 138(9):094703

Moeendarbary E, Ng TY, Zangeneh M (2010) Dissipative particle dynamics in soft matter and polymeric applications: a review. Int J Appl Mech 02(01):161–190

Müller M, MacDowell LG (2001) Wetting of a short chain liquid on a brush: First-order and critical wetting transitions. EPL (Europhys Lett) 55(2):221

Müller M, Pastorino C, Servantie J (2009) Hydrodynamic boundary condition of polymer melts at simple and complex surfaces. Comput Phys Commun 180(4):600–604

Murtola T, Bunker A, Vattulainen I, Deserno M, Karttunen M (2009) Multiscale modeling of emergent materials: biological and soft matter. Phys Chem Chem Phys 11:1869–1892

Pagonabarraga I, Frenkel D (2001) Dissipative particle dynamics for interacting systems. J Chem Phys 115(11):5015–5026

Pastorino C, Müller M (2014) Mixed brush of chemically and physically adsorbed polymers under shear: inverse transport of the physisorbed species. J Chem Phys 140(1):014901

Pastorino C, Binder K, Kreer T, Müller M (2006) Static and dynamic properties of the interface between a polymer brush and a melt of identical chains. J Chem Phys 124:064902

Pastorino C, Kreer T, Müller M, Binder K (2007) Comparison of dissipative particle dynamics and langevin thermostats for out-of-equilibrium simulations of polymeric systems. Phys Rev E 76:026706

Pastorino C, Binder K, Müller M (2009) Coarse-grained description of a brush-melt interface in equilibrium and under flow. Macromolecules 42(1):401–410

Plimpton S (1995) Fast parallel algorithms for short-range molecular dynamics. J Comp Phys 117:1–19

Rapaport D (2004) The art of molecular dynamics simulation, 2nd edn. Cambridge University Press, Cambridge

Servantie J, Müller M (2008) Statics and dynamics of a cylindrical droplet under an external body force. J Chem Phys 128:014709

Soddemann T, Dünweg B, Kremer K (2003) Dissipative particle dynamics: a useful thermostat for equilibrium and nonequilibrium molecular dynamics simulations. Phys Rev E 68:046702

Tretyakov N, Müller M (2013) Correlation between surface topography and slippage: a molecular dynamics study. Soft Matter 9:3613–3623

Tretyakov N, Müller M, Todorova D, Thiele U (2013) Parameter passing between molecular dynamics and continuum models for droplets on solid substrates: the static case. J Chem Phys 138(6):064905

Velázquez ME, Gama-Goicochea A, González-Melchor M, Neria M, Alejandre J (2006) Finite-size effects in dissipative particle dynamics simulations. J Chem Phys 124(8):084104

Flow Coherence: Distinguishing Cause from Effect

F.J. Beron Vera

Abstract The geodesic transport theory unveils the especial fluid trajectory sets, referred to as Lagrangian Coherent Structures (LCS), that cause a flow to organize into ordered patterns. This is illustrated through the analysis of an oceanic flow dataset and contrasted with the tendency of a widely used flow diagnostic to carry coherence imprints as an effect of the influence of LCS on neighboring fluid trajectories.

1 Introduction

Flow coherence is manifested by the appearance of ordered patterns in the distribution of any transported scalar. The fundamental cause of flow coherence is attributed to the existence of especial sets of fluid trajectories that dictate the evolution of neighboring ones. In two-space dimensions, time slices of these especial fluid trajectory sets form material lines which are widely referred to as Lagrangian Coherent Structures (LCS), a terminology introduced by Haller and Yuan (2000); cf. Haller (2015) for a recent review.

Since the introduction of the LCS notion, a considerable effort has been devoted to devising techniques capable of diagnosing flow coherence from time-aperiodic flows defined over finite-time intervals that is not obvious from the inspection of velocity snapshots. One such flow diagnostic is the Finite-Time Lyapunov Exponent (FTLE), which characterizes the amount of stretching about fluid trajectories in an objective (i.e., frame-independent) manner. Constructed from fluid trajectories, the FTLE tends to carry flow coherence imprints as an effect of the underlying LCS, which have been heuristically associated with locally extremizing FTLE curves. For a recent review on the wide range of FTLE applications, cf. Peacock and Dabiri (2010). Similar tendency to carry flow coherence imprints has been noted with other flow diagnostics constructed from fluid trajectories. These include objective flow diagnostics, such as relative dispersion (Provenzale 1999), Finite-Size Lyapunov Exponents (FSLE)

F.J. Beron Vera (✉)
Department of Atmospheric Sciences, RSMAS, University of Miami, Miami, FL, USA
e-mail: fberon@rsmas.miami.edu

J. Klapp et al. (eds.), *Selected Topics of Computational and Experimental Fluid Mechanics*, Environmental Science and Engineering,
DOI 10.1007/978-3-319-11487-3_4

(Joseph and Legras 2002), and probabilistic coherence measures (Froyland et al. 2010), and nonobjective flow diagnostics, such as correlation dimension (Rypina et al. 2011), trajectory arclength (Mancho et al. 2013), and operator-theoretical measures of coherence (Mezić 2013).

In contrast with the above flow diagnostics, the recent geodesic transport theory specifically targets LCS as material lines (Haller and Beron-Vera 2012, 2013; Beron-Vera et al. 2013; Farazmand et al. 2014). More specifically, the geodesic transport theory seeks LCS as minimal or stationary solutions to variational principles where the relevant functionals represent appropriate integral objective measures of flow deformation. The resulting LCS are exactly material curves that satisfy explicit ordinary differential equations, describing all possible deformation forms. Here we are concerned with LCS of hyperbolic type, particularly with those that have the property of attracting nearby fluid trajectories. These are finite-time-aperiodic generalizations of classic unstable manifolds of saddle fixed points in the steady flow case.

The purpose of this note is twofold. First, we seek to illustrate the ability of the geodesic transport theory to reveal the fundamental cause of coherence in an oceanic flow dataset, namely, the so-called LCS. Second, using the same oceanic flow dataset, we seek to show that while the FTLE—the most widely used flow diagnostic—can carry flow coherence imprints as an effect of the underlying LCS, it is not successful in revealing them.

Section 2 presents a few dynamical systems notions that are needed to pose the geodesic transport theory, which is briefly described in Sect. 3. The geodesic transport theory is applied to oceanic flow data in Sect. 4 and its results are compared with those from applying an FTLE analysis on the same data. Concluding remarks are made in Sect. 5. Finally, an appendix is reserved for a brief description of the oceanic flow dataset and numerical details.

2 Mathematical Setup

Let $v(x,t)$ be an incompressible two-dimensional velocity field, where position x ranges on some open domain of the plane and time t is defined on a finite interval $[t_-, t_+]$. Fluid particles evolve according to

$$\dot{x} = v(x,t). \tag{1}$$

An objective measure of material deformation is the right Cauchy–Green strain tensor,

$$C^{t_0,t}(x_0) := \mathrm{D}F^{t_0,t}(x_0)^\top \mathrm{D}F^{t_0,t}(x_0), \tag{2}$$

where D stands for differentiation with respect to x_0 and

$$F^{t_0,t}(x_0) := x(t; x_0, t_0) \tag{3}$$

is the flow map that associates times t_0 and t with the positions of fluid particles. (Dependencies on t_0 and t will herein be omitted for notational simplicity.) For any smooth $v(x,t)$, $F(x_0)$ represents a diffeomorphism, which ensures invertibility of $\mathrm{D}F(x_0)$ and thus positive definiteness of $C(x_0)$. Furthermore, incompressibility of $v(x,t)$ implies $\det C(x_0) = 1$. Consequently, eigenvalues and normalized eigenvectors of $C(x_0)$ satisfy:

$$0 < \lambda_1(x_0) < \lambda_2(x_0) \equiv \frac{1}{\lambda_1(x_0)}, \quad \xi_1(x_0) \perp \xi_2(x_0). \tag{4}$$

Normal repulsion to a material line γ_0 at time t_0 with unit normal n_0 is measured by the local normal growth of n_0 (Haller 2011):

$$\rho(x_0, n) := \frac{1}{\sqrt{\langle n_0, C(x_0)^{-1} n_0 \rangle}}, \tag{5}$$

where $\langle \cdot\,, \cdot \rangle$ is the Euclidean inner product. Note that $\rho(x_0, \xi_2(x_0)) \equiv \sqrt{\lambda_2(x_0)} > 1$ and $\rho(x_0, \xi_1(x_0)) \equiv \sqrt{\lambda_1(x_0)} < 1$. Accordingly, a material line everywhere tangent to $\xi_1(x_0)$ [resp., $\xi_2(x_0)$] is referred to as a *squeezeline* (resp., *stretchline*). Squeezelines obtained from backward (resp., forward) time integration and stretchlines obtained from forward (resp., backward) time integration attract (resp., repel) nearby fluid trajectories. These material lines satisfy the following duality property (Farazmand and Haller 2013): squeezelines (resp., stretchlines) at $t_0 = t_+$ obtained from forward integration out to $t = t_-$ map to backward stretchlines (resp., squeezelines) at $t_0 = t_-$ obtained from backward integration out to $t = t_+$.

Finally, material shear across γ_0 is measured by the local tangential growth of n (Haller and Beron-Vera 2012):

$$\sigma(x_0, n_0) := \langle n_0, C(x_0)^{-1} \Omega n_0 \rangle \rho(x_0, n_0), \quad \Omega := \begin{pmatrix} 0 & -1 \\ 1 & 0 \end{pmatrix}. \tag{6}$$

Geometrical representations of the normal repulsion and Lagrangian shear are given in Fig. 1.

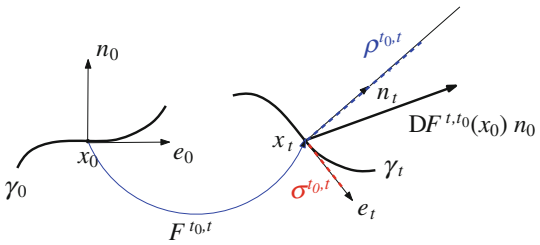

Fig. 1 A material curve γ_0 at time t_0 is advected by the flow $F^{t_0,t}$ to a curve γ_t at time t. At time t_0, normal repulsion, $\rho^{t_0,t}(x_0, n_0)$, and Lagrangian shear, $\sigma^{t_0,t}(x_0, n_0)$, over the interval $[t_0, t]$ are normal and tangential projections onto γ_t of the linearly advected normal to γ_0, $\mathrm{D}F^{t_0,t}(x_0)$

3 Geodesic Transport Theory

The geodesic transport theory seeks LCS as minimal (Haller and Beron-Vera 2012) or stationary (Haller and Beron-Vera 2013; Farazmand et al. 2014) curves of functionals representing appropriate integral objective deformation field measures. Here we are concerned with LCS of hyperbolic type that follow as stationary curves of the integrated material shear functional.

More specifically, for a material line $[s_-, s_+] \ni s \mapsto r(s) \in \gamma_0$, the relevant functional is given by:

$$\mathfrak{S}_\sigma[r] := \int_{s_-}^{s_+} \sigma\left(r, \Omega \frac{r'}{|r'|}\right) \mathrm{d}s, \tag{7}$$

where $|\cdot|$ is the Euclidean norm. Motivated by behavior of classic hyperbolic invariant manifolds, along which material shear is suppressed, Farazmand et al. (2014) propose to seek hyperbolic LCS as exceptional material lines within strips of material lines, which, connecting the same endpoints, have integrated material shears that vary by an order of magnitude less than what the widths of the strips permit. This means that the material lines of interest must be stationary curves of $\mathfrak{S}_\sigma[r]$. Exploiting the symmetry of $\sigma(r, \Omega r'/|r'|)$ under s translations, Farazmand et al. (2014) show that stationary curves of $\mathfrak{S}_\sigma[r]$ coincide with stationary curves of

$$\mathfrak{S}_d[r] := \int_{s_-}^{s_+} d(r', r')(r)\, \mathrm{d}s \equiv 0, \tag{8}$$

where

$$d(\cdot\,, \cdot)(x_0) := \langle \cdot\,, D(x_0)\cdot \rangle, \quad D(x_0) := \tfrac{1}{2}\left(C(x_0)\Omega - \Omega C(x_0)\right). \tag{9}$$

Stationary curves of $\mathfrak{S}_d[r]$ are known as *geodesics*. (More specifically, these geodesics are said to be null because $d(r', r')(r)$, representing a Lorentzian metric, vanishes.) As Farazmand et al. (2014) further demonstrate, such geodesics must coincide with squeezelines or stretchlines, i.e., integral curves of

$$r' = \xi_1(r) \quad \text{or} \quad r' = \xi_2(r), \tag{10}$$

connecting points where $C(x_0) \neq \mathrm{Id}$. The resulting material lines are the sought LCS, which, as we illustrate below through an explicit example, are responsible for causing the flow to organize into ordered patterns.

4 Application to an Oceanic Flow Dataset

The flow dataset considered in the application reported here is produced by ocean velocities inferred using satellite altimetric measurements of sea surface elevation in the Gulf of Mexico. This assumes a geostrophic balance between the Coriolis

and pressure gradient forces with the latter entirely due to differences in sea surface elevation. Specifically,

$$v(x,t) = \frac{g}{f}\nabla^{\perp}\eta(x,t), \tag{11}$$

where $\eta(x,t)$ is the sea surface elevation; f is the Coriolis parameter (twice the local vertical component of the Earth's angular velocity); and g denotes gravity. Oceanic flow data of this type are commonly used to monitor mesoscale variability, i.e., with length and time scales of the order of tens of kilometers and weeks, respectively. For a recent application in the Gulf of Mexico, cf. Olascoaga et al. (2013).

We begin by illustrating in Fig. 2 the role of LCS geodesically extracted from the altimetric velocity data in revealing the cause of coherence in the resulting flow. This figure specifically shows snapshots of the evolution of three fluid patches (blue) along with those of the corresponding *centerpiece LCS* (red). Such attracting LCS snapshots are images under the flow map of stretchlines on t_0 = 12 September 2012 computed in forward time out to t = 22 September 2012. More specifically, out of the entire stretchline foliation, the most stretching stretchline, i.e., that one with the largest average $\sqrt{\lambda_2(r)}$, through each patch is considered. Note that each patch stretches and folds, acquiring a shape dictated by its centerpiece LCS.

We now turn to the FTLE analysis of the altimetric velocity data. The FTLE is defined by

$$\Lambda(x_0) := \frac{1}{|t-t_0|}\log\sqrt{\lambda_2(x_0)}. \tag{12}$$

The FTLE, more precisely the backward FTLE, has a well-documented tendency to carry ordered flow pattern imprints (cf. Peacock and Dabiri 2010, for a recent survey). This is illustrated in left panel of Fig. 3, which shows the patches on t_0 = 22 September 2012 overlaid on a field of FTLE computed in backward time out to t = 12 September 2012. Normalized by its maximum value attained in the domain, the FTLE ranges from 0 (white) to 1 (black). Note the similarity between the shapes acquired by the patches and those evident in the FTLE distribution, particularly as

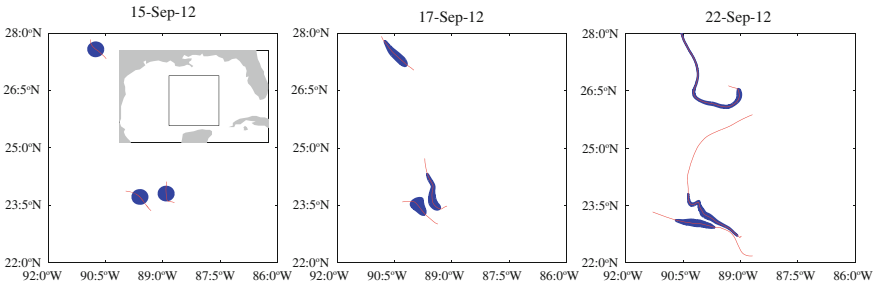

Fig. 2 Selected snapshots of the evolution of fluid patches (*blue*) and corresponding centerpiece LCS (*red*), all computed based on satellite altimetry flow data in a selected region of the Gulf of Mexico (*inset*). Centerpiece LCS correspond to images under the flow map of most stretching stretchlines obtained from forward integration

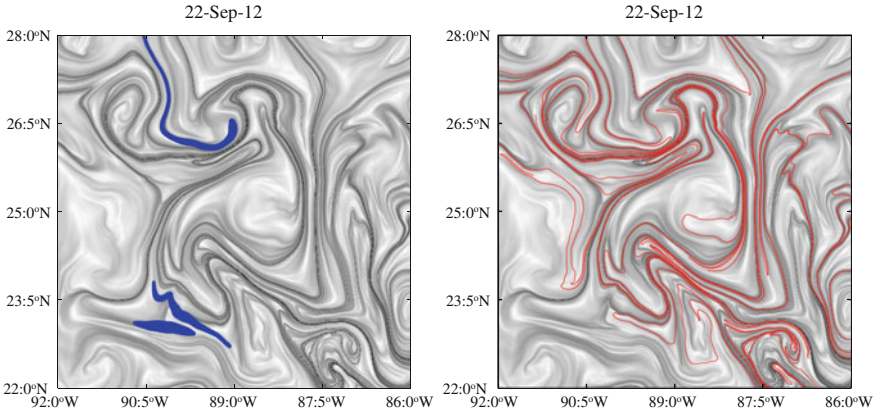

Fig. 3 (*left*) Fluid patches (*blue*) overlaid on backward FTLE normalized by the largest value in the domain (from white to black in a gray scale, the FTLE changes from 0 to 1). (*right*) Backward FTLE with attracting LCS obtained as squeezelines computed in backward time (*red*)

suggested by ridges (locally maximizing curves) of the FTLE field (thin regions of darkest gray tones in the figure). While FTLE ridges cannot be expected to coincide with squeezelines or stretchlines (Haller 2011), they tend to run close to each other, at least over some segments. This is illustrated in the right panel of Fig. 3, which shows the same backward FTLE field shown in the left panel with selected attracting LCS obtained as squeezelines on t_0 = 22 September 2012 computed in backward time out to t = 12 September 2012. These squeezelines are launched on t_0 = 22 September 2012 at locations lying on selected FTLE ridges. Note that, while departures are evident, FTLE ridges run close to LCS over some segments.

The tendency of the FTLE to carry flow coherence imprints should not be taken as implying that this flow diagnostic is capable of revealing the fundamental cause of flow coherence. This is illustrated in Fig. 4, which shows patches and corresponding centerpiece LCS overlaid on backward FTLE computed at each t_0 shown using $|t - t_0| = 10$ days. Note that these LCS are not well represented by nearby FTLE

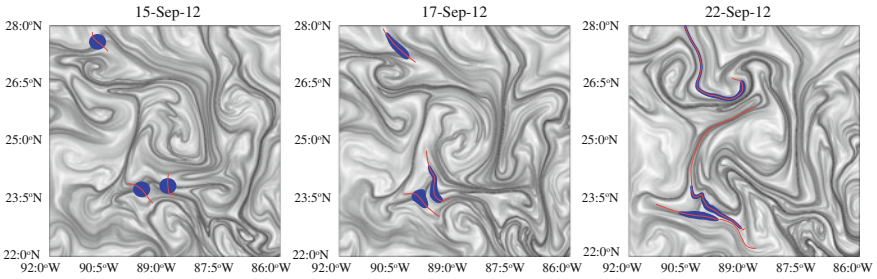

Fig. 4 Selected snapshots of the evolution of fluid patches (*blue*) and centerpiece LCS (*red*), all overlaid on backward FTLE on the corresponding date

ridges, particularly at initial times. Indeed, at initial times patch centerline LCS and nearby FTLE ridges run transversal, almost orthogonal, to each other. At later times, FTLE ridges run closer to the LCS, but this is not a consequence of the LCS being attracted by the FTLE ridges. Rather, it is a consequence of the LCS organizing the flow into ordered patterns, which place their imprints in any scalar that is transported by the flow or flow diagnostic that is constructed from fluid trajectories, such as the FTLE. For instance, the reason for the peculiar pattern shapes in the FTLE field on t_0 = 22 September 2012 is attributed to attracting LCS over t_0 = 12 September 2012 through t = 22 September 2012. Because of the duality between backward squeezelines and forward stretchlines, these LCS are given by images under the flow map of stretchlines on t_0 = 12 September 2012 computed in forward time out to t = 22 September 2012 or, equivalently, squeezelines on t_0 = 22 September 2012 computed in backward time out to t = 12 September 2012.

5 Final Remarks

The geodesic transport theory seeks to reveal the fundamental cause of coherence in flow datasets, manifested by the emergence of ordered patterns in the distribution of any transported scalar. The fundamental cause of flow coherence is found in the existence of special material lines, known as LCS, which control the evolution of neighboring fluid trajectories. In this note we have illustrated the ability of the geodesic transport theory to reveal LCS by analyzing an oceanic flow dataset. Using the same dataset, we showed that while the FTLE, by far the most popular flow diagnostic, tends to carry flow coherence imprints, it is not successful in revealing the LCS that dictate the evolution of the fluid transported. We emphasized that the ability of the FTLE to carry flow coherence imprints is a direct effect of being constructed from fluid trajectories, whose evolution is tied to LCS. Similar tendency to carry flow coherence imprints by other flow diagnostics constructed from fluid trajectories is expected for the same reason.

Acknowledgments The altimeter dataset is distributed by AVISO (http://www.aviso.oceanobs.com). Work supported by a BP/The Gulf of Mexico Research Initiative grant; NSF grant CMG0825547; and NASA grant NX10AE99G.

A Altimetry Data and Numerical Details

The sea surface elevation field, $\eta(x, t)$, consists of background and perturbation components. The background $\eta(x, t)$ component is steady, given by a mean dynamic topography constructed from satellite altimetry data, in-situ measurements, and a geoid model (Rio and Hernandez 2004). The perturbation $\eta(x, t)$ component is transient, given by altimetric sea surface elevation anomaly measurements provided weekly on a 0.25°-resolution longitude–latitude grid. This perturbation component

is referenced to a seven-year (1993–1999) mean, obtained from the combined processing of data collected by altimeters on the constellation of available satellites (Le Traon et al. 1998).

To obtain the flow map, $F(x_0)$, we integrated Eq. (1) with the altimetric velocity field (11) for initial positions, x_0, on a regular 0.5-km-width grid covering the domain of interest. This was done using a stepsize-adapting fourth-order Runge–Kutta method with interpolations obtained using a cubic scheme. The derivative of the flow map, $\mathrm{D}F(x_0)$, was computed using finite differences on an auxiliary 0.1-km-width grid of four points neighboring each point in the above grid. Explicit formulas were used for the eigenvalues and eigenvectors of the Cauchy–Green strain tensor, $C(x_0)$. Finally, to obtain squeezelines (resp., stretchlines), we integrated, using a stepsize-adapting fourth-order Runge–Kutta method and cubic interpolation,

$$r' = \mathrm{sign}\langle r'(s-\Delta), \xi_i(r)\rangle\, \xi_i(r), \quad i = 1\,[\text{resp., } i = 2]. \tag{A.1}$$

The factor multiplying $\xi_i(r)$ removes orientational discontinuities in $\xi_i(r)$ arising from the lack of global orientation of an eigenvector field (Haller and Beron-Vera 2012).

References

Beron-Vera FJ, Wang Y, Olascoaga MJ, Goni GJ, Haller G (2013) Objective detection of oceanic eddies and the Agulhas leakage. J Phys Oceanogr 43:1426–1438

Farazmand M, Blazevski D, Haller G (2014) Shearless transport barriers in unsteady two-dimensional flows and maps. Phys D (in press)

Farazmand M, Haller G (2013) Attracting and repelling Lagrangian coherent structures from a single computation. Chaos 23:023101

Froyland G, Santitissadeekorn N, Monahan A (2010) Transport in time-dependent dynamical systems: finite-time coherent sets. Chaos 20:043116

Haller G (2011) A variational theory of hyperbolic Lagrangian coherent structures. Phys D 240:574–598

Haller G (2015) Lagrangian Coherent Structures. Ann Rev Fluid Mech 47:137–162

Haller G, Beron-Vera FJ (2012) Geodesic theory of transport barriers in two-dimensional flows. Phys D 241:1680–1702

Haller G, Beron-Vera FJ (2013) Coherent Lagrangian vortices: the black holes of turbulence. J Fluid Mech 731:R4

Haller G, Yuan G (2000) Lagrangian coherent structures and mixing in two-dimensional turbulence. Phys D 147:352–370

Joseph B, Legras B (2002) Relation between kinematic boundaries, stirring, and barriers for the Antarctic polar vortex. J Atmos Sci 59:1198–1212

Le Traon P-Y, Nadal F, Ducet N (1998) An improved mapping method of multisatellite altimeter data. J Atmos Oceanic Technol 15:522–534

Mancho AM, Wiggins S, Curbelo J, Mendoza C (2013) Lagrangian descriptors: a method for revealing phase space structures of general time dependent dynamical systems. Comm Nonlin Sci Numer Sim 18:3530–3557

Mezić I (2013) Analysis of fluid flows via spectral properties of the Koopman operator. Ann Rev Fluid Mech 45:357–378

Olascoaga MJ, Beron-Vera FJ, Haller G, Trinanes J, Iskandarani M, Coelho EF, Haus B (2013) Drifter motion in the Gulf of Mexico constrained by altimetric Lagrangian coherent structures. Geophys Res Lett 40:6171–6175

Peacock T, Dabiri J (2010) Introduction to focus issue: Lagrangian coherent structures. Chaos 20:017501

Provenzale A (1999) Transport by coherent barotropic vortices. Annu Rev Fluid Mech 31:55–93

Rio M-H, Hernandez F (2004) A mean dynamic topography computed over the world ocean from altimetry, in situ measurements, and a geoid model. J Geophys Res 109:C12032

Rypina II, Scott S, Pratt LJ, Brown MG (2011) Investigating the connection between complexity of isolated trajectories and Lagrangian coherent structures. Nonlin Proc Geophys 18:1–11

Parametrisation in Dissipative Particle Dynamics: Applications in Complex Fluids

Estela Mayoral-Villa and Eduardo Nahmad-Achar

Abstract A brief overview of mesoscopic modelling for neutral and electrostatically charged complex fluids via Dissipative Particle Dynamics (DPD) is presented, with emphasis on the appropriate parametrisation and how to calculate the relevant parameters for given realistic systems. DPD is a technique that consists of carrying out a coarse-graining of the microscopic degrees of freedom and it is highly dependent on parameters describing the different kinds of force fields and the parametrisation. For this reason, we present here a revision of DPD parametrisation together with applications and comparisons with experimental results. The dependence on concentration and temperature of the interaction parameters for electrostatic and non-electrostatic systems is also considered, as well as some applications in complex fluids.

1 Introduction

In a colloidal dispersion, the stability is governed by the balance between Van der Waals attractive forces and electrostatic repulsive forces, together with steric mechanisms. Being able to model their interplay is of utmost importance to predict the conditions for colloidal stability, which in turn is of major interest in basic research and for industrial applications.

Complex fluids are composed typically at least of one or more solvents, polymeric or non-polymeric surfactants, and crystalline substrates onto which these surfactants adsorb. Neutral polymer adsorption has been extensively studied using mean-field approximations and assuming an adsorbed polymer configuration of loops and tails (de Gennes 1979, 1981, 1982; Méndez et al. 1998). Different mechanisms of

E. Mayoral-Villa (✉)
Instituto Nacional de Investigaciones Nucleares, Carretera México-Toluca S/N, La Marquesa, 52750 Estado de Mexico, Ocoyoacac, Mexico
e-mail: estela.mayoral@inin.gob.mx

E. Nahmad-Achar
Instituto de Ciencias Nucleares, Universidad Nacional Autónoma de México, Apartado Postal 70-543, 04510 Mexico, D.F., Mexico
e-mail: nahmad@nucleares.unam.mx

J. Klapp et al. (eds.), *Selected Topics of Computational and Experimental Fluid Mechanics*, Environmental Science and Engineering,
DOI 10.1007/978-3-319-11487-3_5

adsorption affecting the global stability of a colloidal dispersion, including surface-modifying polymer chains *versus* end-grafted polymer chains, have been studied by Gama Goicochea et al. (2009). Attempts to measure the forces themselves that act in a confined complex fluid in thermodynamic equilibrium with its surroundings have been made using atomic force microscopy (cf., e.g., McNamee et al. (2004)), while it has been argued (Derjaguin and Churaev 1986) that it is more appropriate to use the concept of disjoining pressure, which is the difference between the force (per colloidal particle unit area) normal to the conning surfaces and the fluids bulk pressure. This disjoining pressure allows for a direct determination of the free energy of interaction, hence its importance.

Polyelectrolyte solutions have very different properties from those observed in solutions of uncharged polymers, and their behaviour is less well known (de Gennes 1976; Odijk 1979; Dobrynin et al. 1995). In particular, it is not evident that the scaling of some quantities presents a similar behaviour as that of electrically neutral solutions, or that they present the same or similar scaling exponents. Calculating Langmuir isotherms for polyacrylate dispersants adsorbed on metallic oxides, and their scaling properties as a function of the number of monomeric dispersant units obtained via Dissipative Particle Dynamics (DPD) simulations, it has been shown (Mayoral and Nahmad-Achar 2014; Gonzalez-Melchor et al. 2006) that the critical exponent for the renormalized isotherms agree perfectly well with the scaling theory of Gennes et al. (1976) even though polyelectrolytes have been considered.

Due to the long-range Coulombic repulsion produced by the presence of small mobile counterions in the bulk, the properties of these systems cannot in general be obtained analytically. The most usual systems are even more complex, encompassing various surfactants of different chemical nature and molecular weight (acting as dispersants, wetting agents, rheology modifiers, etc.), pigments, "inert" extenders, and so on. In all these cases there are various different lengths and dynamic scales, every species interacts with all others at a molecular level, in a way which depends on temperature and concentration. Furthermore, there is a competitive adsorption amongst all surfactants present. Ideally, one should have a basic understanding of all interactions, but the main problem is that all colloidal systems are thermodynamically unstable. Empirical methods have been used as well as few and greatly approximated analytic models, and a more recent and promising method is that of *molecular dynamics simulations*. Its basic methodology consists of taking advantage of the fast computing facilities that are nowadays available, to integrate Newton's equations of motion for a large number N of particle (molecules, atoms, or whatever the problem in turn calls for). Thus, one sets initial positions $r_i(t)$ and momenta $p_i(t)$ for each particle i at time t, and uses the force field felt by each one of them

$$F(r) = -\nabla V(r) = m\frac{d^2r}{dt^2}, \tag{1}$$

to find its new position and momentum at time $t + \delta t$ iteratively. The approximation being made is to consider the potential $V(r)$ to be constant during the time step δt which, if taken very small, can make the error negligible. Typical choices for the

force field are the electrostatic interaction $V(r) = k\,q\,q'/r$ and a Lennard-Jones type potential $V(r) = 4\varepsilon\left[(\sigma/r)^{12} - (\sigma/r)^{6}\right]$, where the adjustable parameters $(\varepsilon,\ \sigma,\ k)$ must be obtained by other means (first principles or experimentation). Relevant quantities of the system are computed as time-averages over a macroscopic time interval

$$A = \lim_{t\to\infty} \frac{1}{t} \int_{t_0}^{t_0+t} A\left[r_1(t'), r_2(t'), \ldots, r_N(t');\, p_1(t'), p_2(t'), \ldots, p_N(t')\right] dt' \,. \tag{2}$$

The pieces of information that one can obtain through these simulations are mainly structural and thermodynamic properties: (i) the density profile $\rho(r)$, which in particular may be used to characterise when two phases (e.g., liquid and vapour) coexist; (ii) the radial distribution function $g(r)$ given by

$$\langle\rho\rangle \;= \int \rho(r) g(r)\, dr, \tag{3}$$

which measures the average number of particles in each coordination shell with respect to a given centre (and usually obtained through X-ray or neutron scattering experiments); (iii) the interfacial tension

$$\gamma^* = L_z \left[P_{zz} - \frac{1}{2}\left(P_{xx} + P_{yy}\right)\right], \tag{4}$$

obtained from the pressure tensor components P_{ij} within a box of length L_z; (iv) the radius of gyration of a polymer chain, given by

$$R_g = a_f \mathcal{N}^{\nu}, \tag{5}$$

where ${a_f}^3$ is proportional to the Flory volume, $\mathcal{N}$ is the monomer length of the chain, and ν is the appropriate scaling exponent; (v) phase diagrams; (vi) adsorption isotherms; (vii) disjoining pressures; etc. Figure 1 shows descriptively this methodology.

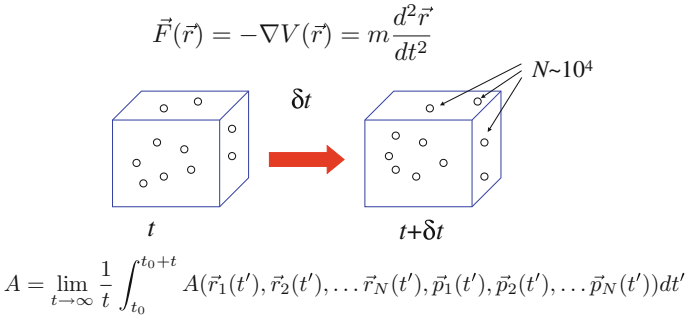

Fig. 1 Descriptive methodology of a *molecular dynamics simulation*. Taken from Gama Goicochea, private communication (see text for details)

By its nature, microscopic molecular dynamics simulations require a great deal of computational resources, the reason being that the integration of the equations of motion require very small time steps when the interaction potential changes significantly over small distances. An alternative that has proven to be very successful is to do mesoscopic modelling via DPD (Hoogerbrugge and Koelman 1992), consisting of carrying out a coarse-graining of the microscopic degrees of freedom. It is highly dependent on parameters describing the different kinds of force fields, whose parametrisation as appears in the literature is not always clear. For this reason, we present here a revision of DPD parametrisation together with applications and comparison with experimental results.

In Sect. 2 we give a brief description of the DPD modelling, including *electrostatic* DPD. Section 3 deals with the appropriate parametrisation and how to calculate the relevant parameters for given realistic systems. The dependence on concentration and temperature of the interaction parameters is also considered. Section 4 presents some interesting applications, and we close with some conclusions.

2 Electrostatic Dissipative Particle Dynamics: A Brief Overview

A good alternative to overcome the difficulties presented by molecular dynamics simulations is to do a coarse-graining of the microscopic degrees of freedom. When done carefully, results can be obtained which approximate very well those obtained through lengthy experimentation (cf. e.g., (Gonzalez-Melchor et al. 2006; Gama Goicochea et al. 2009; Mayoral and Nahmad-Achar 2012; Mayoral et al. 2011) and references therein). DPD as was originally introduced by Hoogerbrugge and Koelman (1992), consists of grouping several molecules, or parts of molecules, into soft mesoscopic "particles". As with molecular dynamics simulations, one integrates the equations of motion to obtain the particle's positions and velocities, but here one distinguishes only between 3 contributions to the total force: *conservative*, *dissipative* and *random*.

Conservative forces account for local hydrostatic pressure and are of the form

$$\boldsymbol{F}_{ij}^{c} = \begin{cases} a_{ij}\omega^{c}(r_{ij})\hat{\boldsymbol{e}}_{ij}, & (r_{ij} < r_c), \\ 0, & (r_{ij} \geq r_c). \end{cases} \tag{6}$$

Here, a_{ij} is a parameter which represents the maximum repulsion between particles i and j, $\boldsymbol{r}_{ij} = \boldsymbol{r}_i - \boldsymbol{r}_j$, $r_{ij} = |\,\boldsymbol{r}_{ij}|$, and $\hat{\boldsymbol{e}}_{ij} = \boldsymbol{r}_{ij}/r_{ij}$ where $\boldsymbol{r}_i$ denotes the position of particle i, and the weight function is given by $\omega^{c}(r_{ij}) = (1 - r_{ij}/r_c)$.

This force, depicted in Fig. 2, derives from a soft interaction potential and there is no hard-core divergence as in the case of the Lennard-Jones potential, which makes more efficient the scheme of integration since it allows for a large time step. In the case of macromolecules, such as polymers, the particles (which can consist of

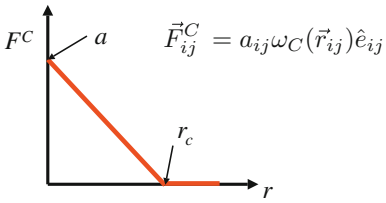

Fig. 2 Form of the conservative force in the DPD methodology

representative monomers or sets of monomers) are joined by springs with a spring constant k, so we have an extra conservative force of the form $\boldsymbol{f}_{ij} = -k\,\boldsymbol{r}_{ij}$ whenever particle i is connected to particle j.

Dissipative forces account for the local viscosity of the medium, and are of the form

$$\boldsymbol{F}_{ij}^{D} = -\gamma\,\omega^{D}(r_{ij})\,\left[\hat{\boldsymbol{e}}_{ij}\cdot\boldsymbol{v}_{ij}\right]\hat{\boldsymbol{e}}_{ij}, \tag{7}$$

where $\boldsymbol{v}_{ij} = \boldsymbol{v}_i - \boldsymbol{v}_j$ is the relative velocity, γ the dissipation constant, and $\omega^{D}(r_{ij}) = (1 - r_{ij}/r_c)^2$ a dimensionless weight function.

Finally, the random (thermal) force disperses heat produced by the dissipative force and invests it into Brownian motion in order to keep the temperature T locally constant. It is of the form

$$\boldsymbol{F}_{ij}^{R} = -\sigma\,\omega^{R}(r_{ij})\,\xi_{ij}\,\hat{\boldsymbol{e}}_{ij}, \tag{8}$$

with $\xi_{ij} = \theta_{ij}\,(1/\sqrt{\delta_t})$, where δ_t is the integration time-step and θ_{ij} is a random Gaussian number with zero mean and unit variance. A dimensionless weight function $\omega^{R}(r_{ij}) = (1 - r_{ij}/r_c)$ also appears.

Not all three forces are independent. The fact that the random force compensates the energy dissipated in order to keep T constant means that it acts as a regulating thermostat. The relation between the dissipative and random forces is

$$\gamma = \frac{\sigma^2}{2\,k_B\,T}, \quad \omega^{D}(r_{ij}) = \left[\omega^{R}(r_{ij})\right]^2, \tag{9}$$

where k_B is Boltzmann's constant. This expression is a consequence of the fulfillment of the *fluctuation-dissipation* theorem (Español and Warren 1995).

When dealing with electrically charged species, such as polyelectrolytes, a problem with the DPD methodology, arising from the fact that the interactions are soft, is the formation of ionic clusters which do not correspond to the real system. Electric charges are usually treated as point charges whose potential diverges at their position in space. In Groot (2003) and Gonzalez-Melchor et al. (2006) this problem is solved by considering charge distributions over the DPD-particles. Suppose that we have a system consisting of N particles, each one with a point charge q_i and a position r_i in

a volume $V = L_x\, L_y\, L_z$. Charges interact according to Coulomb's law and the total electrostatic energy for the periodic system is given by

$$U(r^N) = \frac{1}{4\pi\varepsilon_0\varepsilon_r}\left[\sum_i \sum_{j>i} \sum_{n_x} \sum_{n_y} \sum_{n_z} \frac{q_i\, q_j}{|\boldsymbol{r}_{ij} + (n_x L_x,\, n_y L_y,\, n_z L_z)|}\right], \tag{10}$$

where $\boldsymbol{n} = (n_x,\, n_y,\, n_z)$, $n_x,\ n_y,$ and n_z are non-negative integer numbers, and ε_0 and ε_r are the dielectric constants of vacuum and water at room temperature, respectively. According to Ewald's approach it is convenient to separate this long-range electrostatic interaction into real and reciprocal space, getting a short-ranged sum which may be written as

$$U(r^N) = \frac{1}{4\pi\varepsilon_0\varepsilon_r}\Big[\sum_i \sum_{j>i} q_i\, q_j \frac{\operatorname{erfc}(\alpha_\varepsilon r)}{r} + \frac{2\pi}{V}\sum_{k\neq 0}^{\infty} Q(k)\, S(k)\, S(-k) - \frac{\alpha_\varepsilon}{\sqrt{\pi}}\sum_{i=1}^{N} {q_i}^2\Big], \tag{11}$$

with

$$Q(k) = \frac{e^{-k^2/4\alpha_\varepsilon^2}}{k^2}, \quad S(k) = \sum_{i=1}^{N} q_i\, e^{i\,\boldsymbol{k}\cdot r_{ij}}, \quad \boldsymbol{k} = \frac{2\pi}{L}\,(m_x,\, m_y,\, m_z).$$

Here, α_ε is the parameter that controls the contribution of the real space, k is the magnitude of the reciprocal vector $\boldsymbol{k}, m_x,\ m_y,\ m_z$ are integer numbers, and $\operatorname{erfc}(\alpha_\varepsilon r)$ is the complementary error function (cf. Mayoral and Nahmad-Achar 2012). Equation (11) is a good approach to $1/r$ including the full long-range characteristic of electrostatic interactions.

In the DPD approach the conservative force F_c is mathematically well defined at $r = 0$, making possible the overlap between particles, but the electrostatic contribution diverges at $r = 0$, giving rise to non-natural ionic pairs. A solution of this problem was proposed by Groot (2003) by using charge distributions on DPD particles such as a Slater-type charge density distribution expressed as:

$$\rho(r) = \frac{q}{\pi\lambda^3} e^{-2r/\lambda}, \tag{12}$$

where λ is the decay length of the charge. For this distribution, well-known approximated expressions for the force are available. The reduced interaction potential between two charged distributions separated by a distance r^* from center to center is given by:

$$\frac{4\pi u^*(r^*)}{\Gamma} = \frac{Z_i\, Z_j}{r^*}[1 - (1 + \beta^* r^*)e^{-2\beta^* r^*}], \tag{13}$$

where Z_i is the valence of ion i, e is the electron charge, $\Gamma = e^2/(\kappa_B T \epsilon_0 \epsilon_r R_c)$, and $\beta^* = R_c/\lambda$; $R_c = (\rho^* N_m V_m / N_A)^{1/3}$, N_A is the number of Avogadro, N_m is the number of real water molecules inside of a DPD particle, ρ^* is the reduced density of DPD particles and V_m is the molar volume of water. The magnitude of reduced force between two charge distributions is

$$\frac{4\pi F_{ij}^{*e}}{\Gamma} = \frac{Z_i Z_j}{r^{*2}} \{1 - e^{-2\beta^* r^*} [(1 + 2\beta^* r^* (1 + \beta^* r^*)]\}. \tag{14}$$

The Coulombic term appearing in the equations can be obtained in a simulation using the standard Ewald scheme. The charge distribution is included by removing the divergency of the Coulomb interactions at $r^* = 0$. The energy and the force between two charged distributions are finite quantities in the limit $r^* \to 0$ and are given by:

$$\lim_{r \to 0} \frac{4\pi u^*(r)}{\Gamma} = Z_i Z_j \beta^*, \tag{15}$$

and

$$\lim_{r^* \to 0} \frac{4\pi F_{ij}^{*e}}{\Gamma} = 0, \tag{16}$$

respectively.

The various parameters introduced, viz. a_{ij}, σ, γ, θ_{ij}, contain all the information of the particular system being considered. It is therefore crucial to be able to establish these parameters faithfully in order to make the DPD methodology to work.

3 Parametrisation for Realistic Systems

By far the most important parameter is the one defining the conservative force, a_{ij}, because it contains all the physicochemical information for each component in the system. In contrast, the noise and dissipative parameters correspond to the temperature and fluid viscosity, respectively. In a mono-component system the conservative force parameter for equal species $a_{AA} \equiv a$ relates to the inverse isothermal compressibility (Groot and Warren 1997)

$$\kappa^{-1} = \frac{1}{n\, k_B\, T\, \kappa_T} = \frac{1}{k_B\, T\, (\partial p / \partial n)_T}, \tag{17}$$

where n is the number density of molecules and $\kappa_T = (\partial p/\partial n)_T$ is the usual isothermal compressibility. The pressure p in the system may be obtained using the virial theorem such that $p = \rho k_B T + \alpha\, a\, \rho^2$, where ρ is the density and $\alpha = 0.101$ for $\rho > 2$. We then have $\kappa^{-1} = 1 + 2\alpha\, a\, \rho / k_B T \simeq 1 + 0.2a\, \rho / k_B T$. If N_m is the number of molecules contained in a DPD particle, then $a = k_B T (\kappa^{-1} N_m - 1)/2\alpha\, \rho_{DPD}$, where ρ_{DPD} is the DPD number density for the system and is usually set to

$\rho_{DPD} = 3$ (three water molecules per mesoscopic particle in an aqueous solution, for example). For the mono-component system the virial free energy density f_v is given by $f_v/k_BT = \rho \ln \rho - \rho + 2\alpha\, a\, \rho^2/k_BT$.

When a mixture of 2 components A and B is considered, the virial pressure is given by (Maiti and McGrother 2003)

$$p = \frac{\alpha\, k_B T\, \rho^2}{{r_c}^3} \left[a_{AA}\, \phi^2 + 2\, a_{AB}\, \phi(1-\phi) + a_{BB}(1-\phi)^2 \right], \tag{18}$$

where ϕ is the volume fraction of component A and $(1-\phi)$ that of component B. The virial free energy density for this system is

$$f_v/\rho\, k_B T = \frac{\phi}{N_A} \ln \phi + \frac{(1-\phi)}{N_B} \ln(1-\phi) + \frac{\alpha(2\, a_{AB} - a_{AA} - a_{BB})\rho}{k_B T} \phi(1-\phi) + cte, \tag{19}$$

with $\rho = \rho_A + \rho_B$ and $a_{AB} = a_{BA}$.

The relationship between a_{ij} and the physicochemical characteristics of a real system may be obtained through the Flory-Huggins (FH) theory, based on occupations of a lattice where we have exclusively and uniquely a polymer segment or a solvent molecule per lattice site. In the mean-field approximation this exacting single occupancy is relaxed to a site occupancy probability, which gives a mean-field free energy of mixing constituted by a combinatorial entropy and a mean-field energy of mixing $\Delta F^{MF}_{MIX} = \Delta S^{MF}_{MIX} + \Delta H^{MF}_{MIX}$. The free energy per unit volume for a mixture of two polymers A and B could then be written as

$$\frac{\Delta F^{MF}_{MIX}}{N\, k_B T} = \frac{\phi}{N_A} \ln \phi + \frac{(1-\phi)}{N_B} \ln(1-\phi) + \chi(\phi)(1-\phi), \tag{20}$$

with N_A and N_B the number of monomers of species A and B, respectively, and $N = N_A + N_B$. The first two terms on the right hand side contain the information of the energy of the pure components and correspond to the entropic contribution ΔS^{MF}_{MIX}. The third one involves the excess energy produced by the mixture (ΔH^{MF}_{MIX}). The χ-parameter tells us how alike the two phases are, and is known as the *Flory-Huggins interaction parameter*. In the mean-field theory this parameter is written in terms of the nearest-neighbor interaction energies ϵ_{ij} as $\chi_{12} = z(\epsilon_{11} + \epsilon_{22} - \epsilon_{12})/2k_BT$, where z is the lattice coordination number. It is a phenomenological parameter, and corrections considering an ionisation equilibrium between counterions and electrolyte are needed in the presence of long-range forces. But one can also estimate this quantity by using the Hildebrand-Scatchard regular solution theory (Hildebrand and Wood 1933; Scatchard 1931; Hildebrand and Scott 1950), in which the entropy of mixing is given by an ideal expression, but the enthalpy of mixing is non-zero and is the next simplest approximation to the ideal solution. In this approach one can appropriately consider the Coulombic contribution in the enthalpy of mixing via the activity coefficients in electrolyte solutions (vide infra).

Whereas the FH mean-field theory considers χ_{12} as proportional to T^{-1} but independent of the solute concentration ζ, comparisons with experiments show that the phenomenological χ_{12} contains both energetic and entropic contributions; i.e., $\chi_{12} = \chi_{12}(T, \zeta)$. A correct parametrisation in our electrostatic DPD system must therefore take into account the dependence of the repulsive parameters for the solvated ions a_{ij} with the salt concentration ζ. The way to understand this is as follows: when we perform a coarse graining, the volume of a DPD particle does not usually encompass a full molecule or polymer; thus, for instance, although for dodecane our DPD particle contains only a butane fragment, we do not construct dodecane from the union of butane particles, and the interaction between the DPD dodecane particles and water does not correspond to the χ parameter of butane with water; the χ parameter employed to estimate the DPD repulsive parameter a_{ij} should be that of the full dodecane molecule because its behaviour is that of the global joined units which affect the electronic distribution throughout. In this case, the "monomeric" units, which constitute the dodecane "polymeric" molecule, interact through short-range (covalent bond) forces. When considering a solvated electrolyte, e.g., $N_a{}^+$ or Cl^- ions, their concentration is given precisely by the amount of solvated ionic particles present, which corresponds effectively to the amount of "monomeric" solvated ionic units. These are in effect the individual DPD units, which in this case are not covalently joined but are subject to long-range electrostatic forces. The presence and quantity of "monomeric" solvated ions affect the global properties of the network and their corresponding χ parameter should take into account the whole electrolytic entity, and thus a correct parametrisation of the DPD system forces a dependence of the conservative force parameters a_{ij} on the concentration ζ, through $\chi(T, \zeta)$.

3.1 Concentration Dependence of the DPD Interaction Parameters

For an electrolyte solution in water, $e + w$, the chemical potential $\mu_{w/e}$ for each component (w/e) may be obtained by differentiating the free energy per unit volume of the mixture $e + w$ with respect to the number of molecules $N_{w/e}$ of the component. Thus,

$$\frac{\mu_w}{k_B T} = \ln \phi + \chi(1-\phi)^2, \quad \frac{\mu_e}{k_B T} = \ln(1-\phi) + \chi\phi^2, \tag{21}$$

where ϕ and $1-\phi$ are the volumetric fractions for the w (solvent) and e (electrolyte) components, respectively. The activity coefficient for the electrolyte α_e is defined as

$$\ln(\alpha_e) = \frac{\mu_e - \mu_e^\theta}{R\,T}, \tag{22}$$

where μ_e^θ denotes an arbitrarily chosen zero for the component e and is called the *standard chemical potential* of e. The χ-parameter for the solvent and the electrolyte can be obtained from α_e:

$$\chi = \frac{\ln(\alpha_e) - \ln(1-\phi)}{\phi^2}, \tag{23}$$

and its explicit concentration-dependence comes out by writing $\alpha_e = (x)^x (y)^y (\alpha_e^0 m)^z$, where x and y are the stoichiometric coefficients of the cation and the anion, and $z = x + y$. α_e^0 denotes the *mean* activity coefficient of the electrolyte, and m its molarity. Equation (23) allows one to obtain the Flory-Huggins concentration-dependent parameter if the activity coefficient is known. The scaling of χ with the quantity of ions present has been studied by Mayoral and Nahmad-Achar (2012). The behaviour of this quantity as a function of the concentration ζ follows a power law $\chi \sim \zeta^\tau$ with characteristic scaling exponent τ depending on the kind of salt.

Comparing Eqs. (19) and (20), Groot and Warren (1997) proposed that the repulsive parameters a_{AB} in the DPD simulation can be obtained using the χ-Flory-Huggins parameter as

$$\chi_{AB} = \frac{\alpha\,(2\,a_{AB} - a_{AA} - a_{BB})\,\rho}{k_B\,T}, \tag{24}$$

and using Eqs. (24) and (23) the repulsive DPD parameter a_{ij} depending on the concentration may be obtained as

$$a_{ij} = a_{ii} + 3.27\,\chi_{ij}, \tag{25}$$

with, as before,

$$a_{ii} = \frac{k_B\,T\,(\kappa^{-1} N_m - 1)}{2\,\alpha\,\rho_{DPD}}. \tag{26}$$

Thus, for 3 water molecules per particle ($N_m = 3$) and a compressibility of $\kappa^{-1} \approx 16$ for water at 300 °K and 1 atm, we have $a_{ww} = 78.3$.

3.2 Temperature Dependence of the DPD Interaction Parameters

When the heat of mixing is given by the Hildebrand-Scatchard regular solution theory (Hildebrand and Wood 1933; Scatchard 1931; Hildebrand and Scott 1950; Barton 1975), the χ_{ij}-parameter can be obtained using the solubility parameters $\delta_i(T)$, $\delta_j(T)$ for the pure components in the mixture, which are themselves temperature-dependent. We have

$$\chi_{ij}(T) = \frac{v_{ij}}{R\,T}\left[\delta_i(T) - \delta_j(T)\right]^2, \tag{27}$$

where v_{ij} is the partial molar volume. While this approximation is valid for non-polar components, it has been used in polar systems with reasonable success (Blanks and Prausnitz 1964; Mayoral and Gama-Goicochea 2013). From Eqs. (25) and (27) we have

$$a_{ij}(T) = a_{ii}(T) + 3.27\,\frac{v_{ij}}{R\,T}\,\left[\delta_i(T) - \delta_j(T)\right]^2. \tag{28}$$

The determination of solubility parameters is a difficult and laborious undertaking, but correlations with other physical properties of the substance in question help. For example, writing

$$\delta^2 = \delta_d^2 + \delta_p^2 + \delta_h^2, \tag{29}$$

where δ_d^2 denotes the *dispersion* component of the total solubility parameter, δ_p^2 its *polar* component, and δ_h^2 its contribution from *hydrogen bonding*. The dispersion component δ_d may be very well approximated by using the total solubility parameter of a *homomorphic* molecule, i.e., a non-polar molecule most closely resembling the molecule in question both in size and structure (n-butane is homomorphic to n-butyl alcohol, for example). This is because the solubility parameter of the homomorphic molecule is due entirely to dispersion forces. One still needs to determine either δ_p or δ_h (the other one is obtained by subtraction from the total solubility parameter δ using Eq. (29), when known), and this is done through trial and error experimentation on numerous solvents and polymers and by comparing similar and dissimilar structures according to functional groups and molecular weights.

The total solubility parameter may be calculated from the cohesive energy E_{coh} or, equivalently, from the enthalpy of vaporisation H^{vap}

$$\delta_A = \sqrt{\frac{\Delta E_{coh}}{V_A^0}} = \sqrt{\frac{\Delta H^{vap} - RT}{V_A^0}}, \tag{30}$$

by using atomistic dynamic simulations. To do this, periodic cells of amorphous fluid structures may be constructed using regular available software such as the *Amorphous Cell* program of *Materials Studio*. The dimension of the box is specified (e.g., 25 Å on each side). Interatomic force-field interactions are set as initial conditions, and the system is evolved according to Eq. (1).

The solubility parameter of a mixture of liquids is determined by calculating the volume-wise contributions of the solubility parameters of the individual components of the mixture, i.e., the parameter for each liquid is multiplied by the fraction that the liquid occupies in the blend, and the results for each component added together. In these multicomponent systems the χ-parameters are calculated by pairs. If, for instance, we have a 3-component mixture of water w (or other solvent), electrolyte e, and an organic compound o, we have

$$\chi_{ew} = \frac{v_{ew}}{R\,T}\,\left[\delta_e(T) - \delta_w(T)\right]^2, \tag{31}$$

$$\chi_{wo} = \frac{v_{wo}}{R\,T}\,[\delta_w(T) - \delta_o(T)]^2\,, \tag{32}$$

$$\chi_{eo} = \frac{v_{eo}}{R\,T}\,[\delta_e(T) - \delta_o(T)]^2\,, \tag{33}$$

and, in fact, taking the square root of any two of these equations (say, the first two), adding them together, and assuming $v_{ew} = v_{wo} = v_{eo} \equiv v_m$, we can have a very good estimate for the third one

$$\left[\sqrt{\chi_{ew}} + \sqrt{\chi_{ew}}\right]^2 = \frac{v_m}{R\,T}\,[\delta_e(T) - \delta_o(T)]^2 \equiv \chi_{eo}. \tag{34}$$

Although we have assumed heretofore that DPD particles mix randomly, and that the particles of a given type are indistinguishable, this model predicts very well the major trends in the behaviour of real polymer solutions and is used to predict new behaviour in polymers in current research of (Gama Goicochea et al. 2009; Mayoral and Nahmad-Achar 2014; Gonzalez-Melchor et al. 2006; Mayoral and Nahmad-Achar 2012).

4 Applications

4.1 Interfacial Tension

Interfacial tension arises from the contact between immiscible fluids. It is a measure of the cohesive (excess) energy present, arising from the imbalance of forces between molecules at the interface. This excess energy is called *surface free energy* and is a measurement of the energy required to increase the surface area of the interface by one unit. Equivalently, it may be quantified as a force/length measurement: the force which tends to minimise the surface area. Interfacial tension plays an important role in the formation of colloids or emulsions: as each phase tries to maintain as small an interface as possible, they do not easily mix. Similarly, it is important for the dispersion of insoluble particles in a liquid medium, the penetration of molecules through membranes, adsorption, and stability.

The measure or determination of the interfacial tension then allows us to study the hydrodynamics and morphology of multiphase systems, and this in turn is a most important aspect of the understanding of natural processes and of product design.

The conservative force allows us to calculate the average kinetic energy E_k via the virial theorem

$$2\,\langle E_k\rangle = -\sum_{i=1}^{N} \langle {F_i}^C \cdot r_i\rangle, \tag{35}$$

where ${F_i}^C$ is the total conservative force on DPD particle i: ${F_i}^C = \sum_{j=1}^{N} {F_{ji}}^C$ with ${F_{ji}}^C$ the force applied by particle j on particle i; and from $\langle E_k \rangle$ we may calculate the fluid pressure tensor

$$P_{\alpha\beta} = \frac{1}{V}\left(\sum_{i=1}^{N} m_i\, v_{i\beta}\, v_{i\alpha} + \sum_{i=1}^{N} F_{i\beta}\, \alpha_i\right). \tag{36}$$

Here, m_i is the mass of particle i (which we set equal to 1 in DPD-units) and $v_{i\alpha}$ is the α-component of the velocity of particle i in the volume V. Similarly, $F_{i\beta}$ is the β-component of the force F_i on particle i, α_i is the α-coordinate of particle i, etc. Equation (4) may then be used to calculate directly the interfacial tension γ at the volume boundary, with $\gamma = (k_B\, T/r_c)\, \gamma^*$.

γ depends on temperature. From the mechanical work needed to increase a surface area, $dW = \gamma\, dA$, we have

$$\gamma = \left(\frac{\partial G}{\partial A}\right)_{T,P,n}, \tag{37}$$

with G the Gibbs free-energy and A the surface area. Given that all spontaneous thermodynamic processes follow $\Delta G < 0$, it is easy to understand why the liquid tries to minimise its surface area. From its definition, $G = H - T\, S$ with H the enthalpy and S the entropy of the system. Thus

$$\left(\frac{\partial \gamma}{\partial T}\right)_{A,P} = -\frac{S}{A} \tag{38}$$

so that the normal behaviour of γ is to decrease with temperature.

Results concerning the study of the interfacial tension between immiscible mixtures such as benzene/water and ciclohexane/water at different temperatures, using the parametrisation mentioned above and performing DPD simulations, can be found in Mayoral and Gama-Goicochea (2013). Results taken from this reference are shown in Fig. 3, where the interfacial tension obtained by DPD simulations are compared with experimental data. The excellent agreement confirms that the parametrisation via the use of solubility parameters at different temperatures to obtain the repulsive DPD parameters a_{ij} as functions of T is appropriate for introducing the effect of temperature in DPD simulations.

Additionally, the interfacial tension between two species will change when an electrolyte is added at different concentrations, since the cohesive forces between neighbouring molecules will be altered. Its behaviour with concentration will depend strongly on the type of electrolyte. Figure 4 (top) shows the behaviour of the interfacial tension γ^* between n-dodecane and water with sodium chloride $NaCl$ added, obtained by DPD electrostatic simulations. In this figure $[NaCl]\ M$ denotes the number of DPD ions added as molar concentration. The increase with salt concentration is expected, and the same behaviour is observed when several other inorganic salts are added (Mayoral and Nahmad-Achar 2012). The opposite behaviour is observed,

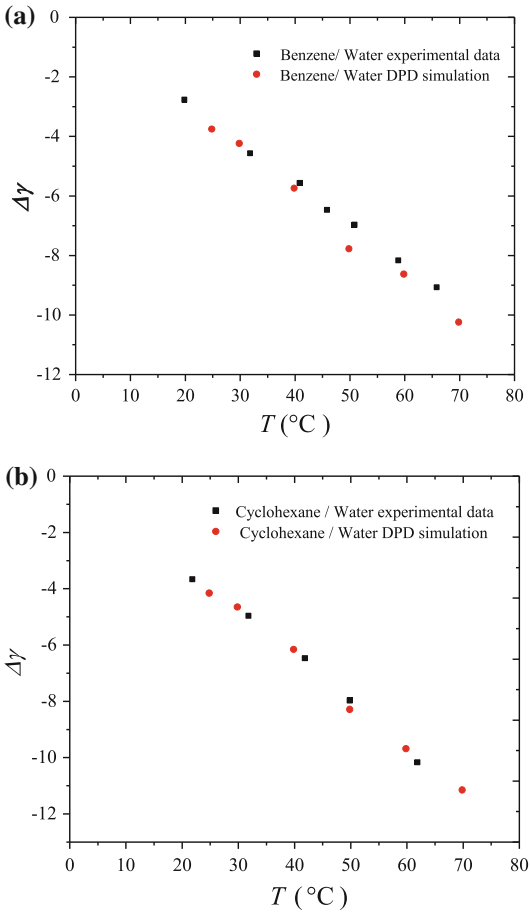

System	Experimental	DPD simulations
Benzene/water	$\gamma_{b/w}[mN/m] = 36.0 - 0.139T\,[°C]$	$\gamma_{b/w}\,[mN/m]=(22.40\pm0.3) - (0.147\pm0.007)T[°C]$
Cyclohexane/water	$\gamma_{c/w}[mN/m] = 52.0 - 0.161T\,[°C]$	$\gamma_{c/w}\,[mN/m]=(27.76\pm0.3) - (0.161\pm0.005)T[°C]$

Fig. 3 Interfacial tension for Benzene/Water and Ciclohexane/Water mixtures at different temperatures using DPD simulations. Taken from Mayoral and Gama-Goicochea (2013)

however, when hydrochloric acid (HCl) is added to the same solvent mixture, as shown in Fig. 4 (bottom). This shows that not only the ionic charge is important in a DPD simulation but also the kind of ionic species in the mixture. This information must be incorporated in the simulation using the a_{ij} parameter because each species has a different activity coefficient and the chemical potential is modified in a different way.

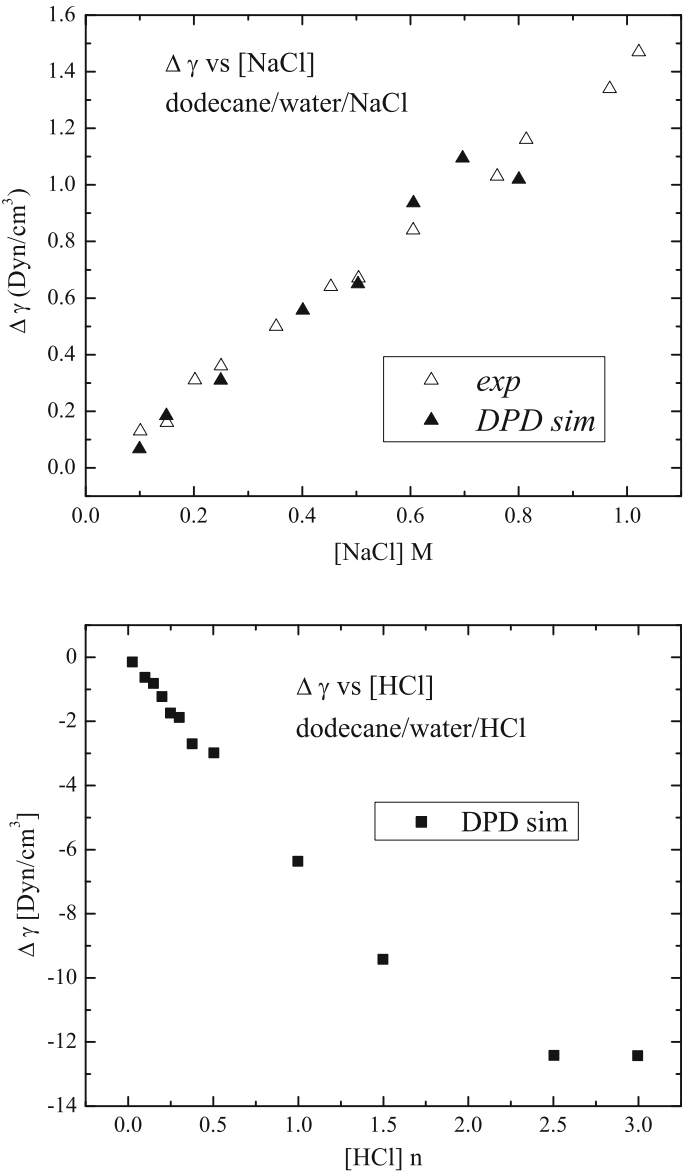

Fig. 4 Experimentally measured interfacial tension is shown with *white triangles* and DPD simulations results are shown in *black triangles* for *n*-dodecane–water with $n[NaCl]$ (*top*) and HCl (*bottom*) added. Results taken from Mayoral and Nahmad-Achar (2012)

4.2 Adsorption Isotherms

The adsorption of polymers onto different surfaces has been the subject of many theoretical and experimental studies. Specifically, the adsorption of polyelectrolytes is a topic of extensive concern because of its practical applications. Many surfactants and additives are polyelectrolytes, and they must be adsorbed with great selectivity on different surfaces in order to have a good performance. This phenomenon is observed in different fields such as water purification where the adsorption of polyelectrolytes could produce flocculation. Other critical examples are emulsifiers in the food and pharmaceutical industries, as well as complex polyelectrolytes for medical science applications, among others. In order to have a good understanding of this phenomenon, more precise information about the conformation of polyelectrolytes adsorbed on a surface and living in the surrounding medium is important. Few theoretical studies have been developed to describe polyelectrolyte adsorption, while experimental studies are laborious. For this reason, numerical simulations seem to be a good alternative. DPD simulations can reproduce the behaviour of this kind of systems but some considerations must be taken.

By construction, the DPD dynamics keep the number of particles N, the cavity volume V, and the temperature T constant. For adsorption isotherms one needs the chemical potential

$$\mu_i = \left(\frac{\partial U}{\partial N_i}\right)_{S,V,N_{j\neq i}}, \tag{39}$$

fixed; i.e., one needs to work in a Grand Canonical Ensemble (μ, V, T). This may be achieved by using a hybrid DPD–Metropolis Criterion (DPD/MC) (Alarcón et al. 2013). In this, after the usual DPD dynamics, one performs a certain number of cycles of particle exchange with the virtual bulk that will return the chemical potential to its initial value $\mu(t_0)$, and calculates the final energy of the system: if equal to or lower than the initial energy, the exchange cycle is accepted; if higher than the initial energy it is rejected and a new exchange cycle is performed. This is followed by another iteration of DPD dynamics together with particle exchange cycle, and so on. By generating separate simulations for different polymer concentrations in this manner, one may calculate the density profile $\rho(z)$ in a box of length L_z, and from it the adsorption Γ as

$$\Gamma = \int_0^{L_z} [\rho(z) - \rho_{\text{bulk}}]\, dz. \tag{40}$$

Adsorption isotherms have been calculated performing DPD simulations in this manner (Alarcón et al. 2013) and checked to coincide with experimental determinations (Mayoral et al. 2011; Huldén and Sjöblom 1990; Esumi et al. 2001). As an example, Fig. 5 displays the results for the simulation of the adsorption of polyacrylic acid (PAA) on explicit TiO_2 surfaces. PAA was mapped considering each DPD bead as one monomeric unit ($-CH_2 - COOH$). The repulsive a_{ij} parameters were obtained according to Sect. 3. The number of independent adsorbed versus

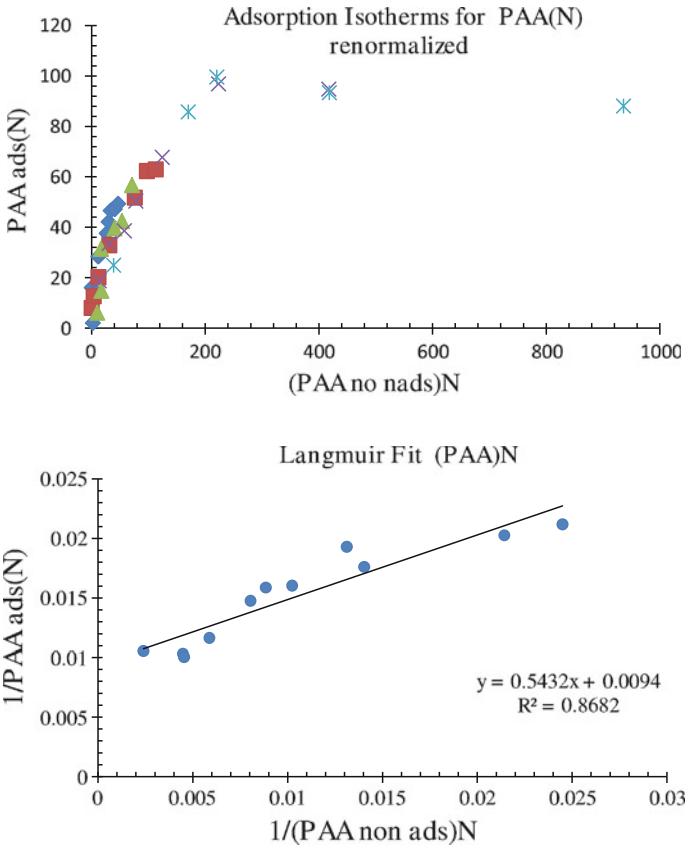

Fig. 5 Adsorption isotherm for *PAA* on TiO_2 via electrostatic DPD simulation. Taken from Mayoral et al. (2011)

non-adsorbed DPD beads is presented. If we assume that only one layer is adsorbed on the surface and all adsorption positions are equivalent, we can extract the maximum concentration at equilibrium and the adsorption-desorption constant, which is given by the Langmuir isotherm. We consider that the ability of one monomeric unit to be adsorbed onto one site of the surface is independent of the occupied sites next to it. The expression for this kind of adsorption model is given by the Langmuir isotherm expressed by

$$\frac{1}{\Gamma} = \left(\frac{1}{\Gamma_M} + \frac{1}{\Gamma_M K C}\right), \tag{41}$$

where $K = K_a/K_d$ and C is the concentration in the bulk, Γ is the adsorbed quantity and Γ_M is the maximum adsorbed quantity. A linear fit for this isotherm is shown in Fig. 5, where it can be seen that $1/\Gamma_M = 0.8829$, $\Gamma_M = 1.13257$ and $K = 6.4476$. Taking into account a surface area for $Ti\,O_2$ of $30.22\,\mathrm{m}^2/\mathrm{g}$, it results in $\Gamma_M = 7.987$

(mg *PAA*/mg TiO_2). This value agrees well with the experimental data of $\Gamma_M = 6.96$ (mg *PAA*/mg TiO_2) reported by Huldén and Sjöblom (1990) and Mayoral et al. (2011).

4.3 Disjoining Pressure

Colloid stability strongly depends on the *disjoining pressure*. For a confined fluid, the pressure component perpendicular to the confining walls P_N is different from the unconfined bulk pressure P_{bulk}. This differential pressure relative to the bulk, which is a function of the separation L_z between the parallel walls is called "disjoining pressure". For a wall perpendicular to the z-direction

$$\Pi(L_z) = P_{zz}(L_z) - P_{bulk}. \tag{42}$$

While P_{bulk} is obtained from the average of the diagonal components of the pressure tensor (cf. Eq. 36), the pressure normal to the wall is calculated from the zz-component, averaged over the length L_z of the simulation box in the direction perpendicular to the walls. The disjoining pressure is a measure of the force, per unit area, needed to bring 2 particles (or a particle and a substrate) together, thus providing a criterion for stability. It has been calculated (Gama Goicochea et al. 2009) for different types of surfactants (those that graft at one end onto a substrate, and those that can adsorb onto the substrate along their full length thus acting as surface modifiers) and for different substrates. The results show that the greater stability attained is not a consequence of the greater molecular weight of the dispersant species itself, as it is so often misinterpreted, but rather of the greater molecule mobility. That is, the entropic gain due to monomers with more mobility capable to sample the configurational space more than polymers (at the same monomer concentration) is the leading mechanism responsible for the higher values of disjoining pressure. This is shown in Fig. 6 for a surface-modifying polymer. In this figure we observe the typical oscillations in Π present in confined fluids (Israelachvili 1992). While the maxima in Π correspond to more stable thermodynamic configurations, the minima represent regions of instability. In this case, molecules with a molecular weight $M_w = 400$ were considered, corresponding to 7 DPD-particles joined by springs. Having 20 such molecules amounts to having 140 monomeric units, a concentration that can also be achieved by considering 10 polymeric molecules of $M_w = 800$ of the same chemical type.

Polyethylene glycol (PEG) of $M_w = 400$ and $M_w = 800$ were used for the results of Fig. 6, with a DPD-particle volume of 90 Å^3 which can accommodate 3 water molecules. The repulsive wall interaction parameter was chosen as $a_{w-monomer} = 60$, when the particle interacting with the wall was a monomer of the polymer molecule, and as $a_{w-sol} = 120$ for solvent molecules (see Gama Goicochea et al. (2009) for details). For particles of the same species $a_{ii} = 78.0$ and for particles of different species $a_{ij} = 79.3$. This parameters reproduce the isothermal compressibility of

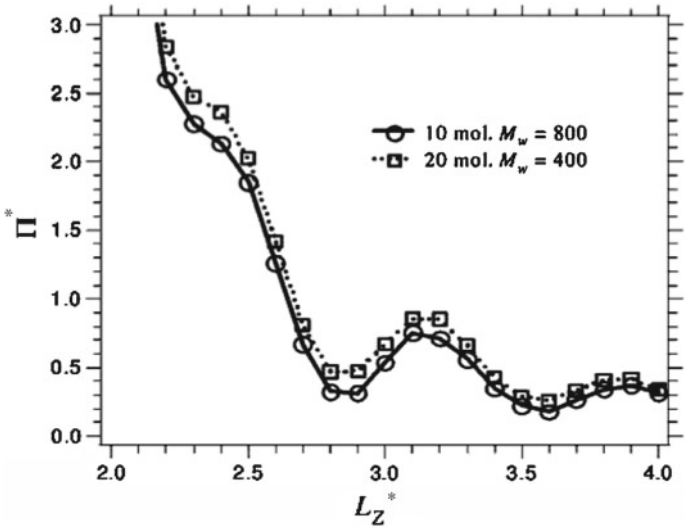

Fig. 6 Disjoining pressure isotherms for 20 molecules of short-chain $M_w = 400$, versus 10 molecules of long-chain $M_w = 800$ surfactant molecules of the PEG-type. Taken from Gama Goicochea et al. (2009)

water at room temperature, and promotes polymer adsorption onto the substrate over solvent adsorption. For the spring constant in the polymer DPD-particles $k = 100$ has been chosen with an equilibrium distance of $r_{eq} = 0.7$. The temperature was kept constant at $T = 300$ K.

It could be observed that shorter polymers are better as dispersants when compared with longer ones at the same monomer concentration. If we multiply the dimensionless Π^* depicted in the figure by $k_B T / {r_c}^3$ (cf. Eq. 18), the disjoining pressure for short polymers can be up to 4.5×10^5 Pa larger than that for the longer chains at certain wall separations. Stability via surface modification is then much better attained through the use of monomeric species than through polymer chains. The same behaviour is found for grafted polymers (cf. Gama Goicochea et al. (2009) for details).

4.4 Radius of Gyration

The radius of gyration is a measure of the size of an object of arbitrary shape. For a polymer chain in solution, however, this is not a very useful definition as it can take many different configurations. One may calculate a *root mean square end-to-end distance* R_{RMS} of the chain as

$$ {R_{RMS}}^2 = \langle (r_N - r_0)^2 \rangle, \tag{43} $$

where we have denoted by r_i, $(i = 0, 1, \ldots, N)$ the positions of the chain joints (i.e., the two ends of the i-th bond are r_{i-1} and r_i). A more useful quantity, however, is the *radius of gyration* R_g of the chain, given by

$$R_g{}^2 = \left\langle \frac{1}{N+1} \sum_{i=0}^{N} (r_i - r_{CM})^2 \right\rangle, \tag{44}$$

where $r_{CM} = \frac{1}{N+1} \sum_{i=0}^{N} r_i$ is the centre of mass of the chain. Loosely speaking, the chain occupies the space of a sphere of radius R_g, i.e., it intuitively gives a sense of the size of the polymer coil. Note that $mR_g{}^2$ (with m the mass of the polymer molecule) is the moment of inertia of the molecule about its centre of mass, and so we can write the equation above as

$$R_g{}^2 = \frac{1}{2} \left\langle \frac{1}{(N+1)^2} \sum_{i,j=0}^{N} (r_i - r_j)^2 \right\rangle, \tag{45}$$

which is useful since it allows us to calculate the radius of gyration of the molecule by using the mean square distance between monomers without calculating r_{CM}. Note also that we have used averages in all the equations above; this is because the possible chain conformations are numerous and constantly change in time, thus we understand the radius of gyration as a mean over time of all the polymer molecules, which by ergodicity principles we calculate as an ensemble average.

The radius of gyration can be easily determined experimentally through light scattering or other alternative methods (neutron scattering, etc.), allowing one to check a theoretical model against reality, and this is what makes it an interesting quantity of study. It has been extensively studied for neutral polymeric species but, as the presence of charges completely changes the possible configurations of the molecules in solution, it is interesting to study the behaviour of R_g in a polyelectrolyte.

One interesting problem is the pH-dependent conformational change of some biopolyelectrolites because it affects directly the mechanism of action in different situations. An example of this is the poly(amidoamine) (PAA) which is used as endosomolytic biopolymer for intracellular delivery of proteins and genes. Bioresponsive behaviour of these kinds of compounds is related to with the structure and conformation in the medium, which could be estimated by the radius of gyration. This is modified by pH and ionic strength effects. Experimental studies of small-angle neutron scattering (SANS) have been published in order to illustrate the pH-dependence and conformational change of PAA ISA 23 (Griffiths et al. 2004). Linear poly(amidoamine) polymers (PAAs) have amido- and tertiary amino-groups along the main polymer, which gives rise to an interesting pH-dependent conformational change and thus offers a perfect prospect for devising polymers that present membrane activity at low pH. The neutral structure of this biopolymer is shown in Fig. 7a.

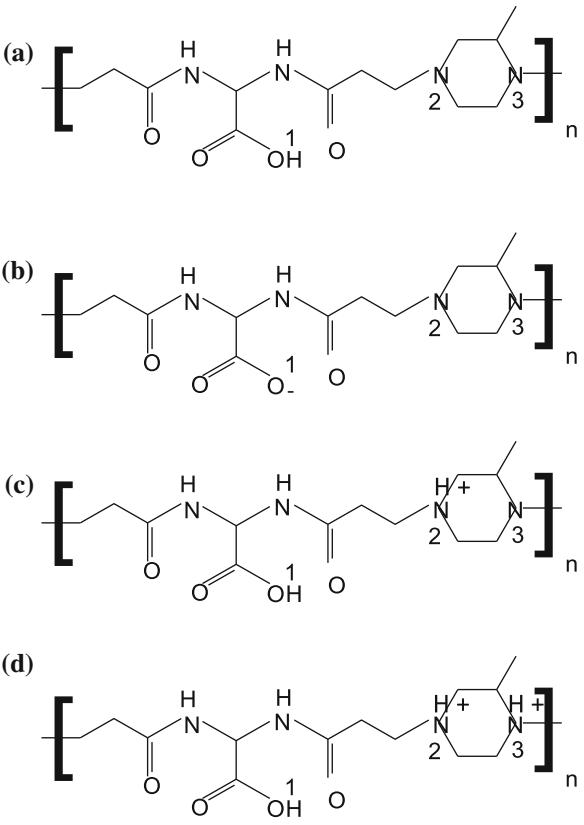

Fig. 7 Neutral and ionised structures of bio-polymer PAA ISA 23. **a** Neutral. **b** pH $<$ pKa$_1$. **c** pKa$_1$ $<$ pH $<$ pKa$_2$. **d** pKa$_2$ $<$ pH $<$ pKa$_3$

The molecular weight of ISA23 is 16,500 g/mol and it has three pKa's: $pKa_1 = 2.1$, $pKa_2 = 7.5$ and $pKa_3 = 3.3$. For this reason, the molecule could be in three different ionisation forms as illustrated in Fig. 7b–d.

Electrostatic DPD simulations have been performed (Mayoral and Nahmad-Achar to be published) in order to study the radius of gyration of this molecule and compare with experimental data reported. The mapping used is shown in Fig. 8. It was established by taking into account the molar volume of each segment or monomeric unit, and considering the volume of each DPD bead as $3V_w$, where $V_w = 30\,\text{Å}^3$ is the molar volume of one water molecule.

ISA23 could be considered as a weak poly-acid and the pH could be modelled considering its ionisation degree over the polymeric structure. Partial charges are introduced over the molecule considering that the B-DPD bead (see Fig. 8) could be neutral or have a charge of 1^- depending on the pH in the solution. The C-DPD beads could be neutral or have a positive charge of 1^+ or 2^+ depending also on the pH of the medium according to the acid-base equilibrium given by

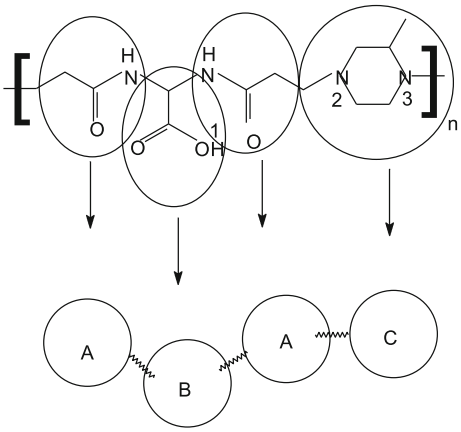

Fig. 8 Mapping of PAA ISA 23 for DPD simulations

$$pH = \begin{cases} \log\left[\frac{\theta}{1-\theta}\right] + pKa_1, & pH < pKa_1, \\ \log\left[\frac{\theta}{1-\theta}\right] + pKa_2, & pKa_1 < pH < pKa_2, \\ \log\left[\frac{1}{1-\theta}\right] + pKa_3, & pKa_2 < pH < pKa_3, \end{cases} \tag{46}$$

where θ is the ratio between the number N^- of protonated-deprotonated monomeric units and the total number N of monomeric units, and pKa_i is the acid-base equilibrium constant. The variation of pH at constant ionic strength makes available the control of the partial charge over the macromolecule. The DPD parameters a_{ij} are calculated as described in Sect. 3 using the solubility parameters obtained by molecular simulation. Ionic strength was fixed to $0.1M$ and the pH was varied according to Eq. (46).

Performing electrostatic DPD simulations at different pH's, the mean radius of gyration was calculated for 25 blocks of 10,000 steps. The size of the system was $L_x = L_y = L_z = 8.5$. Also, $\gamma = 1.6$ and $\sigma = 3$. PAA ISA 23 was represented by 48 DPD beads joined by springs with $k = 2$. The results as a function of pH and θ are shown in Fig. 9.

According to these simulations, the PAA ISA 23 radius of gyration increases to a maximum when the pH decreases. At high pH, and therefore high ionic strengths (because of the counter-ions present in the system), the polymer is negatively charged and adopts a rather compact structure. The conformation is displayed in Fig. 10, showing how the negative counter-ions (violet beads in the figure) are distributed near the extreme of the polymer where the amide group is located and the internal structure is extended at low pH ($\theta = 1.8333$). At high pH ($\theta = -0.75$) the positive counter-ions (orange DPD beads in the figure) are around the carboxyl extreme.

Experimental data reported by Griffiths et al. (2004) shows a very similar but more complex equilibrium in the system: with decreasing pH, the PAA ISA 23 radius of gyration increases to a maximum around pH = 3, after which value a decreasing R_g is

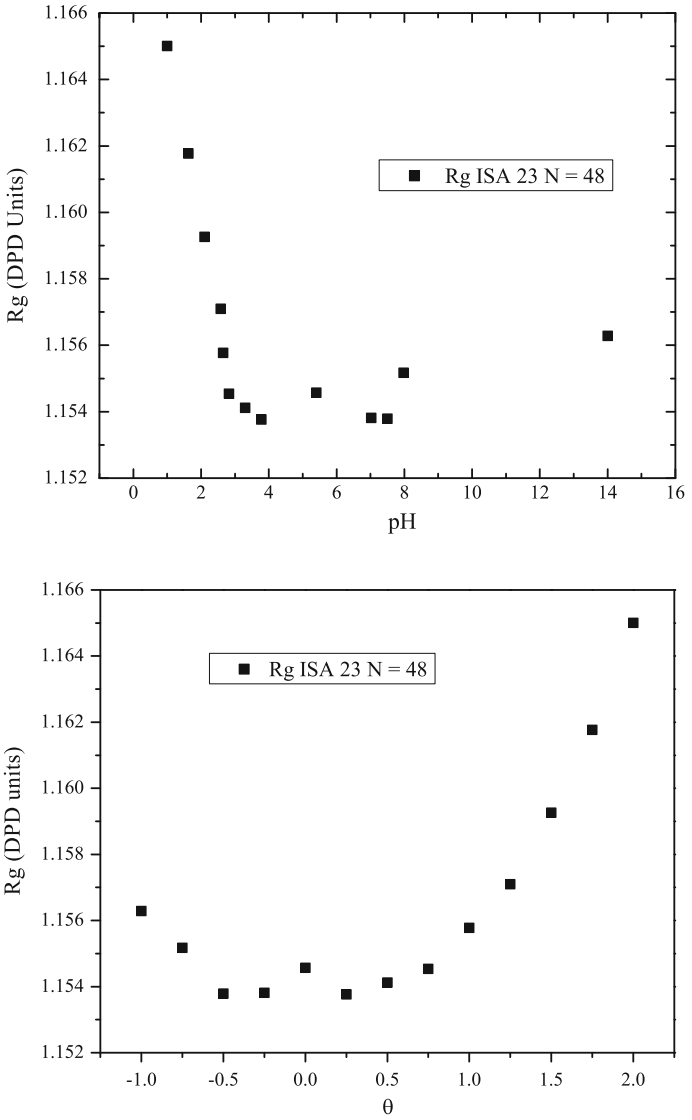

Fig. 9 *Top* R_g versus pH for PAA ISA 23. *Bottom* R_g versus θ for PAA ISA 23

observed when the pH is increased. At high pH the polymer is negatively charged and presents a pretty compact structure presumably. At low pH, the coil again collapses, and the authors suggest that this is almost certainly due to the effects of the high ionic strength; this latter behaviour is not observed in Fig. 9 probably because the ionic strength was fixed at 1 M.

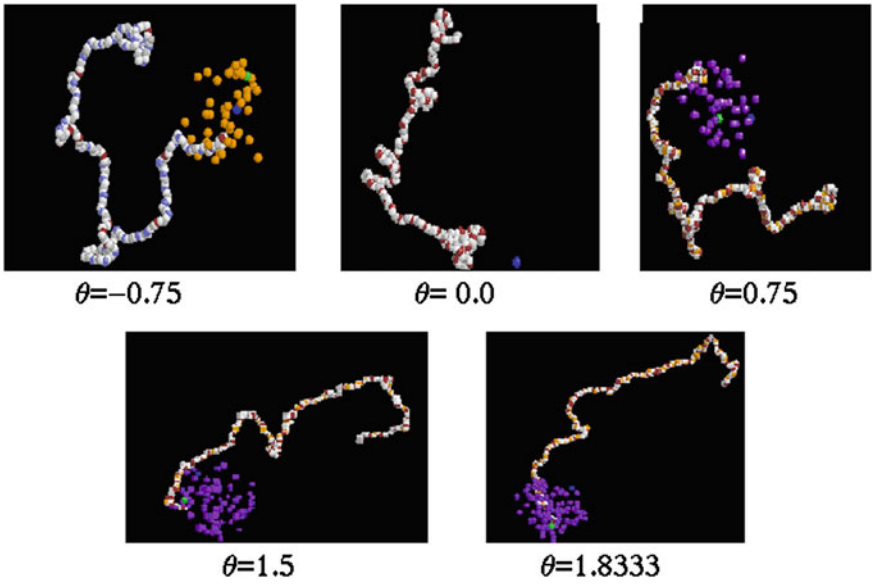

Fig. 10 Conformation of PAA ISA 23 as a function of θ

5 Scaling

Scaling and universality are two amazing properties that collectively have generated the modern theory of critical behaviour appearing in different areas of modern physics, such as condensed matter, field theory, plasma physics, complex systems, dynamical systems, and hydrodynamics (Kadanoff 2000; Cardy 1997). The *universality* quality means that many different systems present the same critical behaviour, while *scaling* is concerned with the fact that in a neighbourhood of a critical point the system is scale invariant. Preserving this symmetry in the system makes it possible to relate physical phenomena which take place at very different length scales. As a consequence, the correct description of systems near their critical points can be described by *power laws* and this kind of behaviour might be analysed by dimensional considerations known as *scaling laws*. Even though the Renormalization Group (RG) approach is a good alternative to obtain in an accurate way the critical exponents (Albert 1982; Le Guillou and Zinn-Justin 1980), in many instances the use of this approach in complex systems is quite difficult. On the other hand, numerical simulations allow one to describe in a simpler and more attractive way different complex systems, but the possibility to use numerical simulations near the critical points of a system is still a topic under discussion. *Coarse graining* is another common concept when we study systems which present scale invariance and, when different scales are involved. The coarse grained simulations have shown to be a very good alternative. DPD (Hoogerbrugge and Koelman 1992) is one such a coarse graining method

and, if correct parametrisations are used, it can reproduce in great detail the scaling properties of different kinds of real systems.

As an example, the scaling exponent observed for the dependence of the interfacial tension γ with temperature T, for several liquid-liquid systems, is given by:

$$\gamma(T) = \gamma_o \left(1 - \frac{T}{T_c}\right)^{\mu}, \tag{47}$$

where γ_0 is a system-dependent constant, T_c is the critical temperature at which the interface becomes unstable, and μ is a critical exponent which has been found experimentally some years ago to be close to 11/9 (Guggenheim 1945). According to the hyper-scaling relationship of Widom (1965); Fisk and Widom (1969), we have $\mu = \nu(d - 1)$ where ν is the scaling exponent for the radius of gyration given in Eq. (5) and d is the dimensionality of the system. More recently, by renormalization group calculations (Albert 1982; Le Guillou and Zinn-Justin 1980; Moldover 1985), more accurate results give $\mu = 1.26$ and $\nu = 0.63$, which for $d = 3$ satisfy the hyper-scaling law. These results have been reproduced by DPD simulations for different systems (Mayoral and Nahmad-Achar 2013; Mayoral and Gama Goicochea 2014) and are presented in Fig. 11 for a dodecane/water mixture.

Another interesting example is the scaling of γ_{max} (maximum adsorption) with the number N of chain units. The number of chains of size N per unit area, Γ_{max}, needed to satisfactorily cover some given amount of material, say 1 mol, can be obtained by performing DPD simulations for the adsorption of polymers with different length

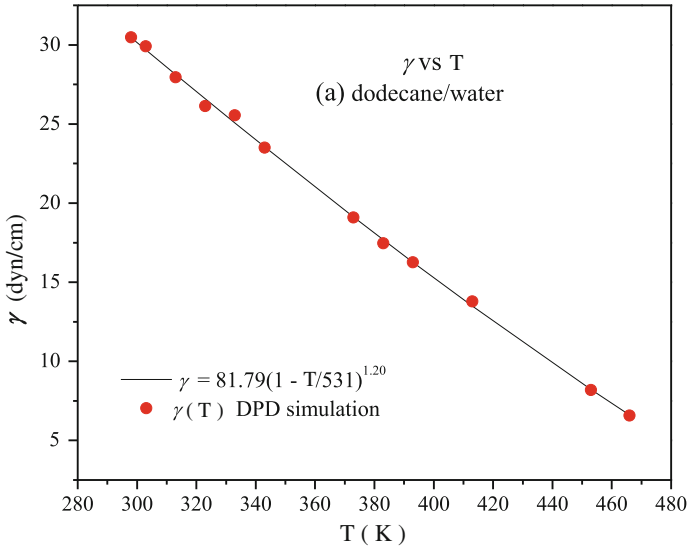

Fig. 11 Scaling exponent observed for the dependence of the interfacial tension γ with temperature T for dodecane/water

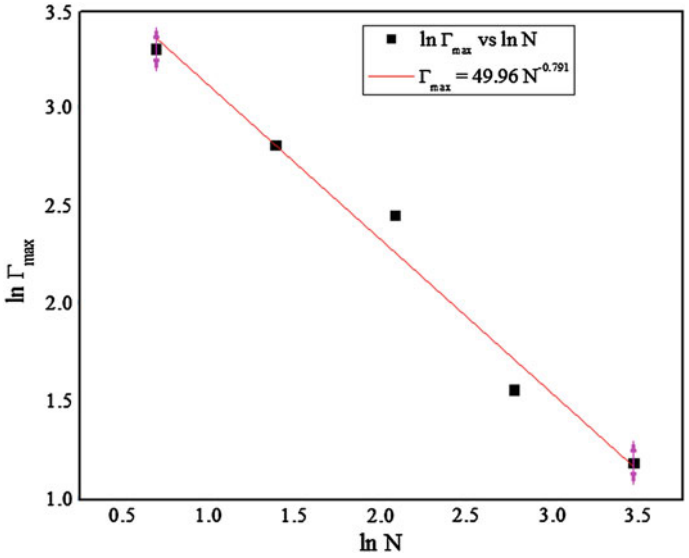

Fig. 12 Scaling of γ_{max} (maximum adsorption) with N for polyacrylic acid on TiO_2 surfaces. Taken from Mayoral and Nahmad-Achar (2014)

N and fitting each simulation to a Langmuir isotherm. When Γ_{max} versus N is plotted, the behaviour shown in Fig. 12 is obtained and the scaling function is $\Gamma_{max} \propto N^{-0.79} \sim N^{-4/5}$. This result is in perfect agreement with the scaling theory in the weak adsorption regime (de Gennes 1976), which indicates that at maximum saturation

$$\gamma_p = \Gamma_{max} N \sim N^{1/5}, \tag{48}$$

where γ_p is the number of monomers adsorbed in the flat plateau of the isotherm. This implies $\Gamma_{max} \sim N^{-4/5} = N^{-0.8}$ as obtained above.

Finally, another important example could be found in Gama Goicochea et al. (2014), where scaling laws for the viscosity (η) and the friction coefficient (μ) were obtained by non-equilibrium DPD simulations.

6 Conclusions

The appropriate parametrisation for the relevant parameters in Dissipative Particle Dynamics (DPD) simulations were presented. A clear methodology has been developed in the last few years to obtain the interaction parameters in great detail for realistic systems, making possible the study of their dependence on concentration and temperature. This work has proven to give predictions in accordance with experimental results. Explicit examples of interfacial tension, adsorption isotherms, disjoining

pressure and radii of gyration are presented. Scaling properties present in different phenomena may also be reproduced in a precise manner using this methodology.

Acknowledgments This work was partially supported by DGAPA-UNAM (under project IN101614). Valuable support in computing resources was obtained from DGTIC-UNAM.

References

Alarcón F, Perez E, Gama-Goicochea A (2013) Soft Matter 9:3777
Albert DZ (1982) Phys Rev B 25:4810
Barton AFM (1975) Chem Rev 75:731
Blanks RF, Prausnitz JM (1964) IEC fundamentals 3:1
Cardy J (1997) Scaling and renormalization in statistical physics. Cambridge University Press, UK
de Gennes PG (1976) J Phys 37:1445
de Gennes PG (1979) Scaling concepts in polymer physics. Cornell University Press, Ithaca
de Gennes PG (1981) Macromolecules 14:1637
de Gennes PG (1982) Macromolecules 15:492
de Gennes PG, Pincus P, Velasco RM, Brochard F (1976) J Phys 37:1461
Derjaguin BV, Churaev NV (1986) In: Croxton CA (ed) Fluid interfacial phenomena. Wiley, New York
Dobrynin AV, Colby RH, Rubinstein M (1995) Macromoleules 28:1859
Español P, Warren P (1995) Europhys Lett 30:191
Esumi K et al (2001) Coll Surf A 194:7
Fisk S, Widom B (1969) J Chem Phys. 50:3219
Gama Goicochea A, Mayoral E, Klapp J, Pstorino C (2014) Soft Matter 10:166
Gama Goicochea A, Nahmad-Achar E, Pérez E (2009) Langmuir 25:3529
Gonzalez-Melchor M, Mayoral E, Velazquez ME, Alejandre J (2006) J Chem Phys 125:224107
Griffiths PC, Paul A, Khayat Z, Wan K-W, King SM, Grillo I, Schweins R, Ferruti P, Franchini J, Duncan R (2004) Biomacromolecules 5:1422–1427
Groot RD (2003) J Chem Phys 118:11265
Groot RD, Warren PB (1997) J Chem Phys 107:4423
Guggenheim EA (1945) J Chem Phys 13:253
Hildebrand JH, Scott RL (1950) Solubility of nonelectrolytes. Reinhold, New York
Hildebrand JH, Wood SE (1933) J Chem Phys 1:817
Hoogerbrugge PJ, Koelman JMVA (1992) Europhys Lett 19:155
Huldén M, Sjöblom E (1990) Progr Colloid Polym Sci 82:28
Israelachvili JN (1992) Intermolecular and surfaces forces. Academic Press, New York
Kadanoff LP (2000) Statistical physics: statics, dynamics and renormalization. Word Scientific Publishing, Singapore
Le Guillou C, Zinn-Justin J (1980) Phys Rev B 21:39767
Maiti A, McGrother S (2003) J Chem Phys 120:1594
Mayoral E, de la Cruz E, Longoria LC, Nahmad-Achar E (2011) Rev Int Contam Ambie 27:253
Mayoral E, Gama Goicochea A (2014) Soft Matter 10:9054
Mayoral E, Gama-Goicochea A (2013) J Chem Phys 138:094703
Mayoral E, Nahmad-Achar E (2012) J Chem Phys 137:194701
Mayoral E, Nahmad-Achar E (2013) In: Klapp J et al (eds) Study of structural properties in complex fluids by addition of surfactants using DPD simulation, in fluid dynamics in physics, engineering and environmental applications. Springer, ISBN 978-3-642-27722-1

Mayoral E, Nahmad-Achar E (2014) Scaling properties in the adsorption of ionic polymeric surfactants on generic nanoparticles of metallic oxides by mesoscopic simulation. In: Sigalotti L, Klapp J, Sira E (eds) Computational and experimental fluid mechanics with applications to physics, engineering and the environment. Springer, Switzerland. doi:10.1007/978-3-319-00191-3
Mayoral E, Nahmad-Achar E (to be published)
McNamee CE, Tsujii Y, Ohshima H, Matsumoto M (2004) Langmuir 20:1953
Méndez JM, Johner A, Joanny JF (1998) Macromolecules 31:8297
Moldover MR (1985) Phys Rev A 31(2):1022
Odijk T (1979) Macromolecules 12:688
Scatchard G (1931) Chem Rev 8:321
Widom B (1965) J Chem Phys 43(11):3892

Smoothed Particle Hydrodynamics for Free-Surface Flows

A. Barreiro, J.M. Domínguez, A.J.C. Crespo, O. García-Feal and M. Gómez Gesteira

Abstract A solver for free-surface flows (DualSPHysics) based on the Smoothed Particle Hydrodynamics (SPH) model is presented. The classical SPH formulation is described along with the governing equations, filters and corrections, boundary conditions and time stepping schemes. The reliability of the DualSPHysics model is discussed by comparing the numerical results with the experimental data for a benchmark test case. The applicability of the code is shown with some examples where wave propagation and wave-structure interaction are simulated.

1 Introduction

Smoothed Particle Hydrodynamics (SPH) is a mesh-free Lagrangian numerical method developed in the 1970s to solve astrophysical problems (Gingold and Monaghan 1977). Lately this method started to be widely applied in the field of fluid mechanics (Monaghan and Kos 1999; Monaghan et al. 1999) due to the simplicity of the Lagrangian numerical models to describe the fluid as a set of points (or particles) that interact with each other according to the conservation laws (Gómez-Gesteira et al. 2010).

SPHysics is a project that sums the effort of researchers at different universities, i.e., the University of Vigo (Spain), the University of Manchester (U.K.), and the

A. Barreiro (✉) · J.M. Domínguez · A.J.C. Crespo · O. García-Feal · M.G. Gesteira
EPhysLab Environmental Physics Laboratory, Universidad de Vigo,
Edificio de Física, Campus As Lagoas s/n, 32004 Ourense, Spain
e-mail: anxo.barreiro@uvigo.es

J.M. Domínguez
e-mail: jmdominguez@uvigo.es

A.J.C. Crespo
e-mail: alexbexe@uvigo.es

O. García-Feal
e-mail: orlando@uvigo.es

M.G. Gesteira
e-mail: mggesteira@uvigo.es

J. Klapp et al. (eds.), *Selected Topics of Computational and Experimental Fluid Mechanics*, Environmental Science and Engineering,
DOI 10.1007/978-3-319-11487-3_6

Johns Hopkins University (U.S.A.). This project is based on the development of an open-source tool that represents accurately the behaviour of a fluid (Gómez-Gesteira et al. 2012a, b). SPHysics has been mainly applied to the study of coastal processes in 2D (Gómez-Gesteira et al. 2005; Dalrymple and Rogers 2006; Narayanaswamy et al. 2010; Rogers et al. 2010) and in 3D (Gómez-Gesteira and Dalrymple 2004; Crespo et al. 2008). The first version in FORTRAN was released in 2007, which was followed by new releases, including a multicore version implemented with Message Passing Interface (MPI). Despite this improvement, the number of particles that the model was able to handle at a reasonable computational time was not high; this means that the applicability of the model was compromised by the size of the domain of study. This issue lead to the development of a new code keeping the same open-source philosophy. DualSPHysics is a new implementation that takes advantage of the computational power of hundreds of cores of the NVIDIA graphic processing units (GPUs).

The DualSPHysics code has been developed by researchers from the University of Vigo (Spain) and University of Manchester (U.K). The model is implemented in C++ language with MPI and CUDA programming platforms to carry out simulations on the CPUs and GPUs, respectively. The new CPU code presents some advantages, such as a more optimised use of the memory. The object-oriented programming paradigm provides means to develop a code that is easy to understand, maintain and modify. Furthermore, additional approaches are implemented, for example particles are reordered to provide faster access to memory, symmetry is considered in the force computation to reduce the number of particle interactions and the best approach to create the neighbour list is implemented (Domínguez et al. 2011). The CUDA library manages the parallel execution of threads on the GPUs. The best approaches were considered to be implemented as an extension of the C++ code, so that the most appropriate optimizations to parallelise particle interactions on GPU were implemented (Domínguez et al. 2013a, b). The first rigorous validations were presented by Crespo et al. (2011).

Due to the aforementioned facts, DualSPHysics is especially well suited to simulate complex engineering problems involving violent collisions between water and coastal structures. Different problems have been analysed with the code such as the computation of forces exerted by large waves on the urban furniture of a promenade (Barreiro et al. 2013) or the study of the run-up in an existing armour block sea breakwater (Altomare et al. 2014). The software is available to free download at www.dual.sphysics.org.

The different formulations implemented in DualSPHysics will be presented in the subsequent sections. A benchmark case to show the capabilities of the code to reproduce the dam-break behaviour and its interaction with coastal structures is described.

2 Theory

The principles of the SPH theory are here described. For a wider and deeper description of the SPH method, the reader is addressed to Monaghan (1982, 1992, 2005), Benz (1990), Liu (2003) and Gómez-Gesteira et al. (2010, 2012a).

2.1 SPH Interpolant

The main principle of the SPH method is that any given function $A(\boldsymbol{r})$ can be approximated by the integral interpolant:

$$A(\boldsymbol{r}) = \int A(\boldsymbol{r}')W(\boldsymbol{r} - \boldsymbol{r}', h)d\boldsymbol{r}' \tag{1}$$

where h is the smoothing length and $W(\boldsymbol{r} - \boldsymbol{r}', h)$ is the weighting function known as the kernel. Applying a Lagrangian approximation to the previous integral leads to a discrete notation of the interpolation at a given point:

$$A(r) = \sum\nolimits_b m_b \frac{A_b}{\rho_b} W(\boldsymbol{r} - \boldsymbol{r}_b, h), \tag{2}$$

with the summation index (b) running over all the particles within the region delimited by the compact support of the kernel function. m_b and ρ_b are the mass and the density of the particle b, respectively, $V_b = m_b/\rho_b$ represents the volume of a particle, $\boldsymbol{r}_b$ its position vector, and $W(\boldsymbol{r}_a - \boldsymbol{r}_b, h)$ is the weighting function or the kernel referred to particles a and b.

2.2 The Smoothing Kernel

The choice of the kernel is crucial for the performance of the SPH method. The weighting function must satisfy the following conditions: positivity, compact support, and normalization. Another property to be satisfied is that the selected function must be monotonically decreasing with the distance from particle a. The kernels are expressed as functions of the non-dimensional quantity $q = r/h$, where r is the distance between particles a and b. The parameter h controls the size of the area around particle a where the contribution of a given particle b cannot be neglected.

The different kernels that the user can choose in DualSPHysics are:

(a) Cubic-Spline:

$$W(r, h) = \alpha_D \begin{cases} 1 - \frac{3}{2}q^2 + \frac{3}{4}q^3 & 0 \le q \le 1, \\ \frac{1}{4}(2 - q)^3 & 1 < q \le 2, \\ 0 & q > 2 \end{cases} \tag{3}$$

(b) Wendland (Wendland 1995):

$$W(r, h) = \alpha_D \left(1 - \frac{q}{2}\right)^4 (2q + 1) \qquad 0 \le q \le 2. \tag{4}$$

The α_D values for the different kernel functions are shown in Table 1.

Table 1 Different values of α_D for 2D and 3D

Kernel	2D	3D
Cubic-spline	$10/(7\pi h^2)$	$1/(\pi h^3)$
Wendland	$7/(4\pi h^2)$	$21/(16\pi h^3)$

2.3 Momentum Equation

The equation of momentum conservation in a continuum field is

$$\frac{\mathrm{d}\boldsymbol{v}}{\mathrm{d}t} = -\frac{1}{\rho}\nabla P + \boldsymbol{g} + \boldsymbol{\Gamma}, \tag{5}$$

where $\boldsymbol{\Gamma}$ refers to the dissipative terms and $\boldsymbol{g}$ is the gravitational acceleration (0, 0, -9.81) $\mathrm{m}\cdot\mathrm{s}^{-2}$. There are several ways to solve the dissipative terms, but the artificial viscosity proposed by Monaghan (1992) has been the most widely used due to its simplicity.

In discrete notation and adding the artificial viscosity, the previous equation can be rewritten as follows:

$$\frac{\mathrm{d}\boldsymbol{v}_a}{\mathrm{d}t} = -\sum\nolimits_b m_b \left(\frac{P_b}{\rho_b^2} + \frac{P_a}{\rho_a^2} + \Pi_{ab}\right)\nabla_a W_{ab} + \boldsymbol{g} \tag{6}$$

where P_k represents the pressure of particle k (with $k = a$ or b). The artificial viscosity term depends on the relative position and motion of the computed particles

$$\Pi_{ab} = \begin{cases} \frac{-\alpha \overline{c_{ab}}\mu_{ab}}{\rho_{ab}} & \boldsymbol{v}_{ab}\cdot\boldsymbol{r}_{ab} < 0 \\ 0 & \boldsymbol{v}_{ab}\cdot\boldsymbol{r}_{ab} > 0, \end{cases} \tag{7}$$

where $\boldsymbol{r}_{ab} = \boldsymbol{r}_a - \boldsymbol{r}_b, \boldsymbol{v}_{ab} = \boldsymbol{v}_a - \boldsymbol{r}_b, \mu_{ab} = h\boldsymbol{v}_{ab}\cdot\boldsymbol{r}_{ab}/(r_{ab}^2+\eta^2), c_{ab} = 0.5(C_a+C_b)$ is the mean value of the speed of sound, $\eta^2 = 0.01h^2$, and α is a free parameter that should be tuned according to the configuration of the problem.

2.4 Continuity Equation

The mass of each particle is constant, so that changes in the fluid density are computed by solving the conservation of mass or continuity equation in SPH form:

$$\frac{\mathrm{d}\rho_a}{\mathrm{d}t} = \sum\nolimits_b m_b \boldsymbol{v}_{ab}\cdot\nabla_a W_{ab}. \tag{8}$$

2.5 Equation of State

Following the work of Monaghan (1994), the fluid is treated as weakly compressible and an equation of state is used to determine the pressure as a function of density.

The compressibility reduces the speed of sound making the time step requirement more reasonable. Another limitation on weak compressibility is to restrict the sound speed to be at least ten times faster than the maximum fluid velocity, thereby keeping density variations to within less than 1 %.

Following Batchelor (1974) and Monaghan et al. (1999), the expression that relates pressure and density is written as:

$$P = B\left[\left(\frac{\rho}{\rho_0}\right)^{\gamma} - 1\right], \tag{9}$$

where the parameter B is related to the compressibility of the fluid; $\rho_0 = 1000.0$ kg/m^3 is a reference density, taken as the density of the fluid at the surface, and γ is the polytropic constant that usually ranges from 1 to 7. The latter value has been adopted in DualSPHysics.

2.6 Moving the Particles

Particles are moved using the XSPH variant (Monaghan 1989):

$$\frac{d\mathbf{r}_a}{dt} = \mathbf{v}_a + \varepsilon \sum\nolimits_b \frac{m_b}{\overline{\rho}_{ab}} \mathbf{v}_{ba} W_{ab}, \tag{10}$$

where $\overline{\rho}_{ab} = \frac{1}{2}(\rho_a + \rho_b)$ and ε is a constant, whose value ranges from zero to unity. Here $\varepsilon = 0.5$ is commonly used.

This method is a correction for the velocity of particle a. This velocity is recalculated taking into account the velocity of the particle and the average velocity of all particles that interact with particle a. Only the closest neighbours will be included, due to the compact support of the kernel. This correction allows particles to be more organized and, for high fluid velocities, helps to avoid particle penetration through the boundaries.

2.7 Time Stepping

The physical magnitudes (velocity, density, position and density) change every time step due to the forces calculated during particle interactions. The time integration scheme to compute the new values of these quantities at the next time step in SPH should be at least of second order to obtain accurate enough results.

Consider the equations of momentum (6), density (8), and position (10) written in the following form:

$$\frac{d\mathbf{v}_a}{dt} = \mathbf{F}_a, \tag{11}$$

$$\frac{d\rho_a}{dt} = D_a \tag{12}$$

$$\frac{d\mathrm{r}_a}{dt} = \mathbf{v}_a \tag{13}$$

These equations are time-integrated in DualSPHysics using one of the two following schemes.

2.7.1 Verlet Scheme

This algorithm was proposed by Verlet (1967) and has two sets of equations. The first one which is used in most of the iterations reads as follows

$$\begin{aligned} \mathbf{r}_a^{n+1} &= \mathbf{r}_a^n + \Delta t \boldsymbol{v}_a^n + 0.5\Delta t^2 \mathbf{F}_a^n, \\ \mathbf{v}_a^{n+1} &= \mathbf{v}_a^{n-1} + 2\Delta t \mathbf{F}_a^n, \\ \rho_a^{n+1} &= \rho_a^{n-1} + 2\Delta t D_a^n, \end{aligned} \tag{14}$$

and the second one is used every certain number of steps, normally once after 50 steps

$$\begin{aligned} \mathbf{r}_a^{n+1} &= \mathbf{r}_a^n + \Delta t \boldsymbol{v}_a^n + 0.5\Delta t^2 \mathbf{F}_a^n, \\ \mathbf{v}_a^{n+1} &= \mathbf{v}_a^n + \Delta t \mathbf{F}_a^n, \\ \rho_a^{n+1} &= \rho_a^n + \Delta t D_a^n. \end{aligned} \tag{15}$$

This prevents time integration divergence since the equations are no longer coupled when considering only (14).

2.7.2 Symplectic Scheme

Symplectic time integration algorithms are time reversible in the absence of friction or viscous effects (Leimkuhler et al. 1996). This method preserves geometric features like energy time-reversal symmetry, leading to improved resolution of long term solution behaviour. In this case, the scheme used is an explicit Symplectic scheme of the form

$$\begin{aligned} \rho_a^{n+\frac{1}{2}} &= \rho_a^n + \frac{\Delta t}{2}\frac{\mathrm{d}\rho_a^n}{\mathrm{d}t}, \\ \mathbf{r}_a^{n+\frac{1}{2}} &= \mathbf{r}_a^n + \frac{\Delta t}{2}\frac{\mathrm{d}\boldsymbol{r}_a^n}{\mathrm{d}t}. \end{aligned} \tag{16}$$

In a second time step $(d(\omega_a \rho_a \mathbf{v}_a)^{n+\frac{1}{2}})/dt$ gives the velocity and the position of the particles at the end of each time step:

$$\begin{aligned} (\omega_a \rho_a \mathbf{v}_a)^{n+1} &= (\omega_a \rho_a \mathbf{v})^{n+\frac{1}{2}} + \frac{\Delta t}{2}\frac{d(\omega_a \rho_a \mathbf{v}_a)^{n+\frac{1}{2}}}{dt}, \\ \mathbf{r}_a^{n+1} &= \mathbf{r}_a^{n+\frac{1}{2}} + \frac{\Delta t}{2}\mathbf{v}_a^{n+1}. \end{aligned} \tag{17}$$

At the end of the time step $d\rho_a^{n+1}/dt$ is calculated using the updated values of $\mathbf{v}_a^{n+1}$ and $\mathbf{r}_a^{n+1}$ (Monaghan 2005).

2.8 Variable Time Step

The time step depends on the flow properties. For example, the time step decreases when the fluid collides with fixed boundaries since the forces increase. In general, the time step depends on the force per unit mass and the Courant condition. A variable time step Δt is calculated according to (Monaghan and Kos 1999):

$$\begin{aligned} \Delta t &= C \cdot min(\Delta t_F, \Delta t_{CV}), \\ \Delta t_F &= min_a \left(\sqrt{h/f_a}\right), \\ \Delta t_{CV} &= min_a \frac{h}{c_s + max_b \left| \frac{h v_{ab} x_{ab}}{r_{ab}^2} \right|}, \end{aligned} \tag{18}$$

here Δt_F is based on the force per unit mass $|f_a|$, and Δt_{CV} depends on the Courant condition and the viscosity of the system. C is a constant that can vary between 0.1 and 0.3.

2.9 Boundary Conditions

The boundary conditions implemented in DualSPHysics are the Dynamic Boundary Conditions (DBCs). The boundary particles (BPs) must satisfy the same equations as the fluid particles (FPs), but they are not free to move in any direction. The movement of these particles is equal to zero or externally imposed such as a flap or a piston in a wave maker or any other kind of moving object (gates, elevators, etc.).

The behaviour of these boundary particles can be summarized as follows. The FPs are free to move and interact with each other but when a FP approaches a boundary and the distance between a FP and the BPs becomes smaller than $2h$, the BPs increase their density, leading to a pressure increase through the equation of state (9). This process modifies the force exerted on the FP due to the pressure term on the momentum Eq. (6). For a more detailed description of the boundaries the reader is referred to the work of Crespo et al. (2007).

2.9.1 Periodic Boundary Conditions

Periodic boundary conditions are also implemented in DualSPHysics. In this case, the particles near an open lateral boundary interact with the particles on the other side of the domain since the area of influence of a particle extends beyond the lateral boundary.

2.9.2 Floating Objects

Assuming that an object has a rigid inner structure, the force on each BP (boundary particle) is computed by summing the contribution of each FP (fluid particle) in the area of influence. The force per unit mass on a given boundary particle k may be expressed as

$$\boldsymbol{f}_k = \sum_{\boldsymbol{a} \in \boldsymbol{FPs}} \boldsymbol{f}_{ka} \tag{19}$$

where $\boldsymbol{f}_{\mathrm{ka}}$ is the force per unit mass exerted by FP a on BP k. Taking into consideration the principle of equal and opposite action and reaction, the force exerted by a FP on each BP is given by

$$m_k \boldsymbol{f}_{ka} = -m_a \boldsymbol{f}_{ak} \tag{20}$$

which allows estimating the force exerted on the moving body.

For the motion of the moving body, the following equations of rigid body dynamics are used:

$$M \frac{\mathrm{d}\boldsymbol{V}}{\mathrm{d}t} = \sum_{k \in BPs} m_k \boldsymbol{f}_k, \tag{21a}$$

$$I \frac{\mathrm{d}\boldsymbol{\Omega}}{\mathrm{d}t} = \sum_{k \in BPs} m_k (\boldsymbol{r}_k - \boldsymbol{R}_0) \times \boldsymbol{f}_k, \tag{21b}$$

where M is the mass of the body, I is the moment of inertia, $\boldsymbol{V}$ is the velocity of the object, $\boldsymbol{\Omega}$ is the rotational velocity and $\boldsymbol{R}_0$ is the position of the centre of mass.

Each boundary particle has a velocity given by

$$\boldsymbol{u}_k = \boldsymbol{V} + \boldsymbol{\Omega} \times (\boldsymbol{r}_k - \boldsymbol{R}_0). \tag{22}$$

The BPs within the rigid body are then advanced in time by integrating Eq. (22).

3 Validation Case

The reliability of DualSPHysics is investigated with a standard free-surface benchmark test for SPH flows, reproducing the SPHERIC Benchmark Test Case #2 (http://wiki.manchester.ac.uk/spheric/index.php/Test2).

The experiment described in Kleefsman et al. (2005) consists of a dam break flow impacting an obstacle. This experiment is considered a valuable benchmark for the SPH free-surface flow community.

The initial setup of the experiment is depicted in Fig. 1. The tank is 3.22 m long, 1m wide and 1 m tall. The volume of water is 1.228 m long, 1m wide and 0.55 m tall and it is initially confined at one end of the tank with a retaining wall that is

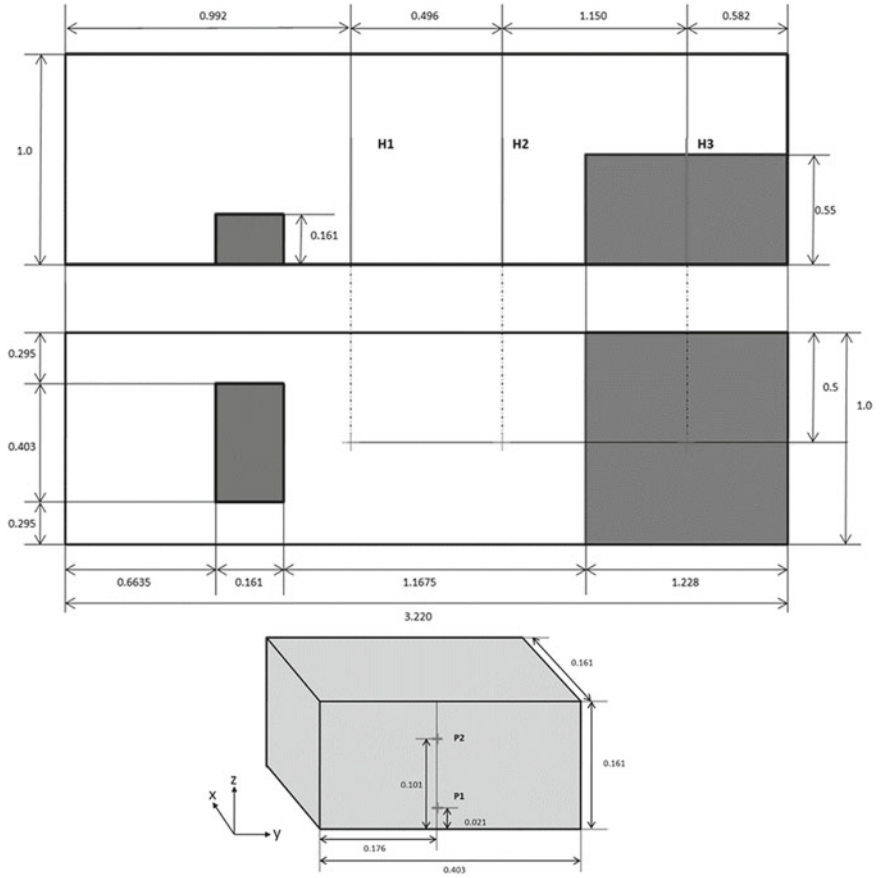

Fig. 1 Experimental setup with water height and pressure gauge position

released instantaneously. There is also an obstacle whose dimensions are shown in Fig. 1. When the water is released, the fluid floods the dry bed of the tank and hits the obstacle. Six seconds of physical time were numerically simulated.

The parameters and key features of the simulation are shown in Table 2.

The experiment provides water heights and pressure measurements at different locations. Three vertical height probes (H1, H2, and H3 in Fig. 1) were used to determine the water height during the experiment. Pressures exerted on the obstacle initially facing towards the water were also sampled to detect the water impacts (P1, P2 in Fig. 1).

Figure 2 shows different instants of the simulation with DualSPHysics of the dam break flow impacting the obstacle. The initial dam release can be observed in the first frame (time = 0.32 s). The second instant (time = 0.40 s) shows the dam break just before the collision with the obstacle. After the impact, the fluid is split in two

Table 2 Parameters of the validation case

Parameter	Value
Kernel function	Wendland
Time-step algorithm	Symplectic
Viscosity treatment	Artificial with $\alpha = 0.05$
XSPH	$\varepsilon = 0.5$
Interparticle distance	0.008 m
Total number of particles	1,151,717
Physical time	6 s
Computation time	2.7 h
Execution device	GTX TITAN Black

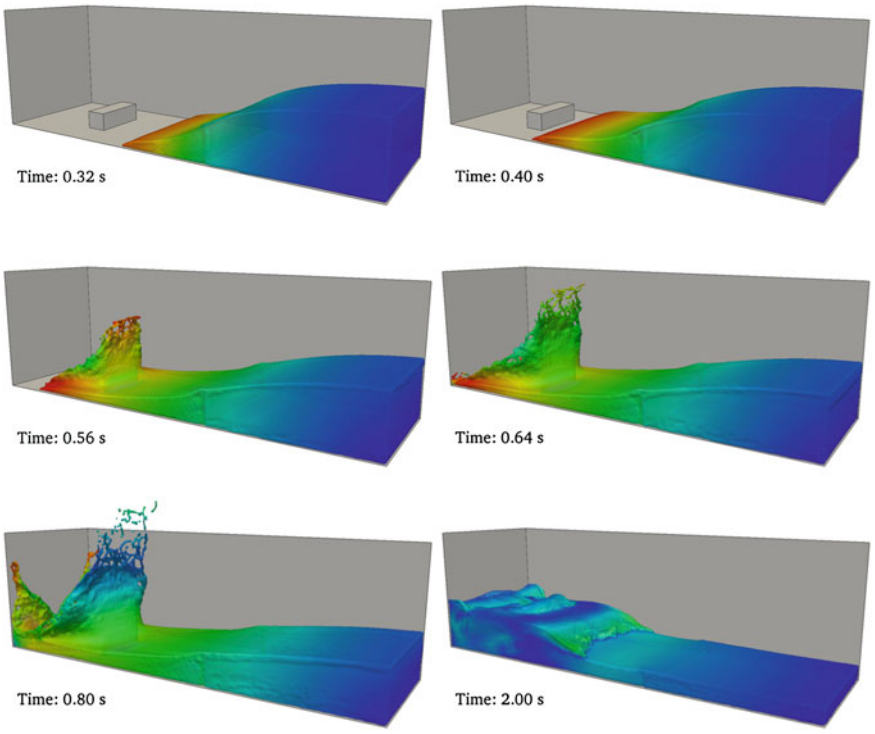

Fig. 2 Different instants of the DualSPHysics simulation for the test case

parts. Most of the fluid surrounds the obstacle and a jet is created (time = 0.56, 0.64, 0.56 s). The last frame (time = 2.0 s) shows the splash due to the reflected wave generated after hitting the left wall of the container.

Numerical depth probes were computed to compare with the experimental measurements. The procedure to numerically compute the wave elevation was previously used by Gómez-Gesteira and Dalrymple (2004) and it is based upon the fact

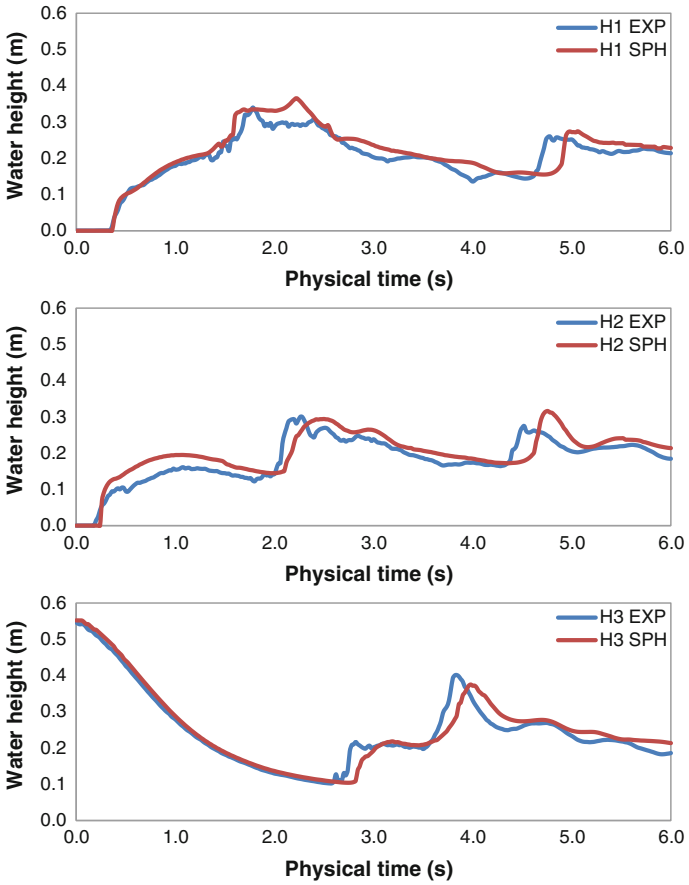

Fig. 3 Experimental and numerical water heights measured at the three probes

that there is an abrupt change in mass at the free surface. Hence, Fig. 3 summarises the experimental and numerical water heights calculated at the three probes located before the obstacle (H1, H2 and H3). The blue line corresponds to the experimental water height data and the red line corresponds to the numerical wave heights. The water column collapse is observed during the first 2 s. This dam break is clearly shown by the probe at H3, where the water level decreases during this period and by the other probes where the water arrives sequentially (first at H2 and then at H1). After 1.75 s the reflected water wave moves to the right after hitting the left wall. The reflected wave hits the right wall and a second incoming wave hits the obstacle for a second time on the right side (a second maximum in the water level is detected by H3 at 3.8 s, later by H2 at 4.6 s and by H1 at 4.8 s). The SPH results reproduce very well the dam evolution observed in the experiment.

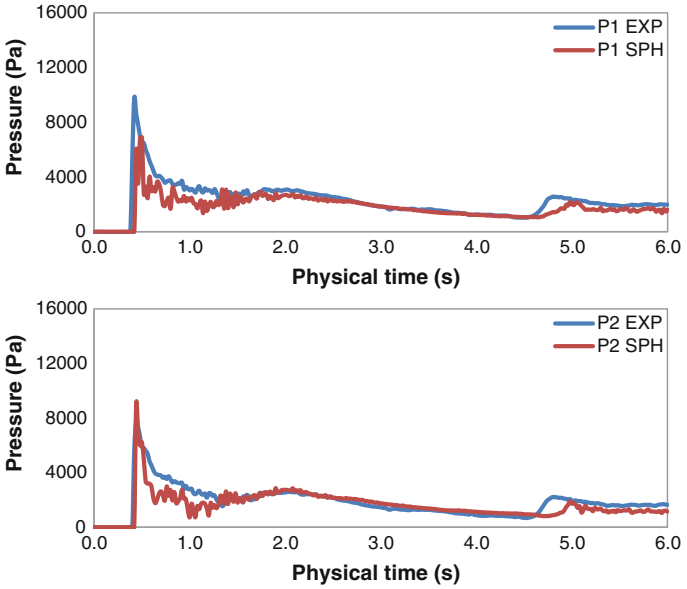

Fig. 4 Experimental and numerical pressures measured at the two gauges

Pressure was also measured experimentally. Different pressure sensors (Fig. 1) were used to collect the experimental pressure on the obstacle. The pressure on the front side of the obstacle (P1 and P2) was computed by DualSPHysics to analyse the validity of the model to predict the forces exerted by the fluid on the structure. Numerical pressures were computed at the positions where the experimental sensors were located. The comparison between experimental and numerical pressures is shown in Fig. 4. A close agreement between both signals can be observed. The maximum experimental and numerical peaks, which correspond to the main water impact on the obstacle, coincide in time. The presence of a secondary peak at approximately 5 s is also detected by the numerical simulation, although there is a slightly delay with respect to the experimental one.

4 DualSPHysics Capabilities

In the following section some examples of the capabilities of the DualSPHysics code are shown, where different functionalities implemented in the code are employed. DualSPHysics is therefore proven to simulate wave propagation and wave-structure interaction impact waves on a large and a complex structure.

4.1 Wave Propagation

DualPSHysics is suitable to study the wave propagation in the vicinity of the coast where the real bathymetry and topography of the shoreline is given. In this first case, large waves approach the shore and impact with a steep coast. On the other hand, any 3D external model with the complex geometry of a protection structure or a promenade can be included in the simulation since these geometries can be easily converted into fixed boundary SPH particles to interact with.

The SPH parameters corresponding to this simulation are shown in Table 3. This simulation was executed in 32 Tesla M2090 (hosted at Minotauro cluster at Barcelona Supercomputing Center, BSC). The multi-GPU parallelisation allows the simulation of very large domains in a reasonable time or to run cases that will not fit in a unique GPU card due to the memory usage.

Different instants of the simulation using DualSPHysics are illustrated in Fig. 5.

4.2 Wave Interaction with a Fixed Complex Structure

In the second case, the importance of the numerical resolution is highlighted. This application consists of the interaction of a large wave with a fixed oil rig using realistic dimensions. The domain size is $172 \times 116 \times 55$ m and the structure includes items with a spatial scale on the order of a few centimetres. Hence, a huge number of particles is required to represent the objects of small size in the oil platform.

As in the previous case, the simulation was performed using 64 GPUs at the BSC facilities and 1 billion particles were simulated (one of the largest simulations with a meshfree model in the field of fluid dynamics). All parameters are summarised in Table 4, and Fig. 6 shows different instants of the simulation with DualSPHysics.

Table 3 Parameters of the wave propagation case

Parameter	Value
Kernel function	Wendland
Time-step algorithm	Symplectic
Viscosity treatment	Artificial viscosity with $\alpha = 0.1$
Interparticle distance	0.1 m
Total number of particles	265 million particles
Physical time	50 s
Computation time	246.3 h
Execution device	32 × Tesla M2090

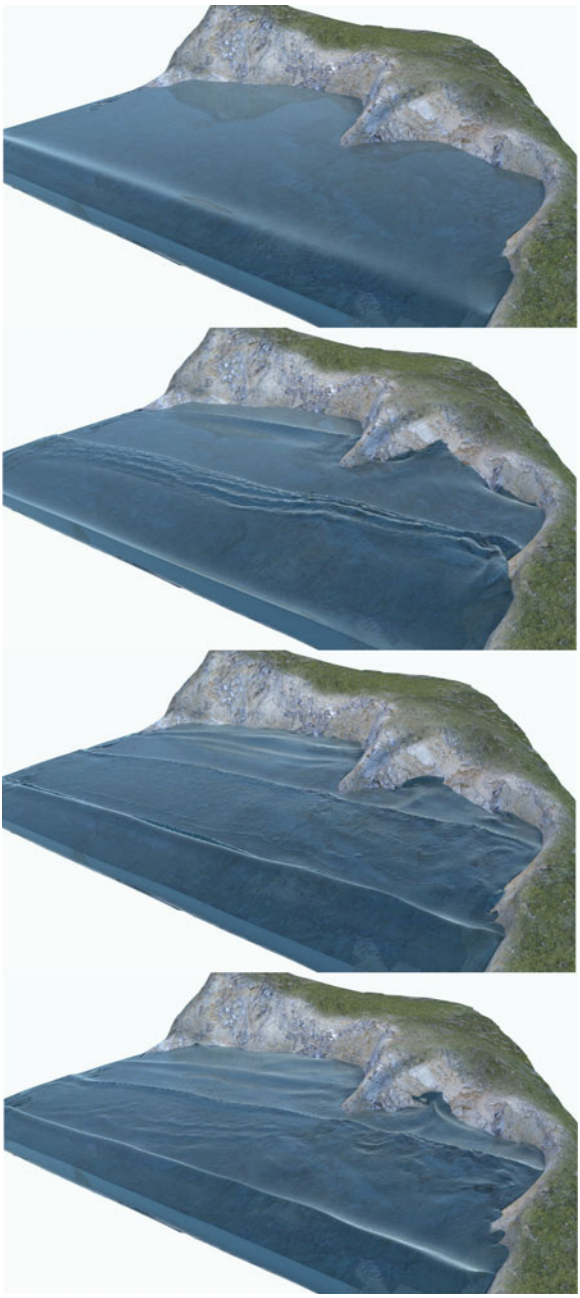

Fig. 5 Wave propagation case at different times: 5.3, 21.4, 36.4 and 55.2 s

Table 4 Simulation parameters of the wave interaction with a fixed complex structure

Parameter	Value
Kernel function	Wendland
Time-step algorithm	Symplectic
Viscosity treatment	Artificial viscosity with $\alpha = 0.3$
Interparticle distance	0.06 m
Total number of particles	10^9 particles
Physical time	12 s
Computation time	79.1 h
Execution device	64 × Tesla M2090

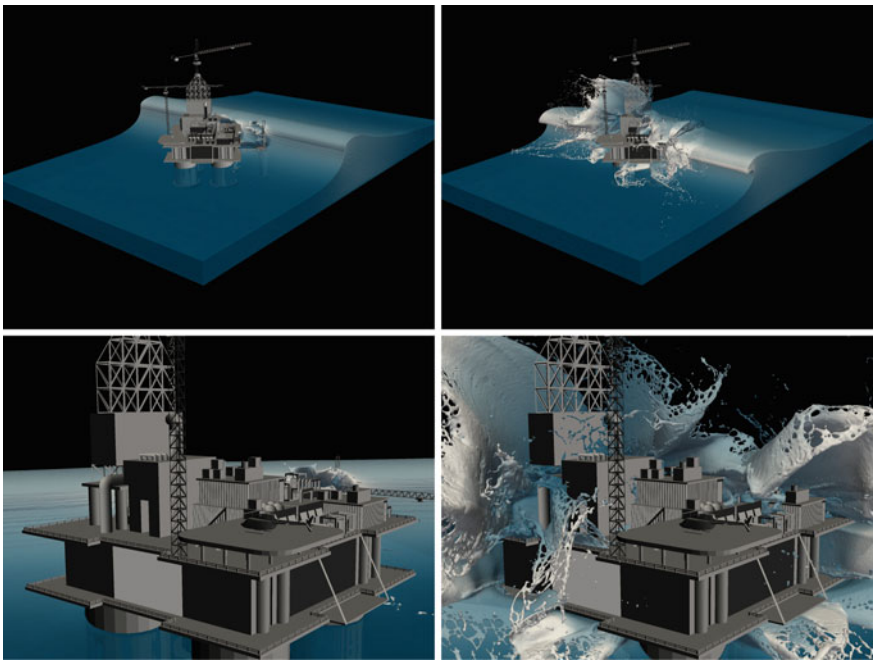

Fig. 6 Instants 2.4 s (*left*) and 3.52 s (*right*) of the wave interaction with a fixed and complex structure. *Bottom panels* show zoomed area

Table 5 Parameters of the wave interaction with a floating object

Parameter	Value
Kernel function	Wendland
Time-step algorithm	Symplectic
Viscosity treatment	Artificial viscosity with $\alpha = 0.2$
Interparticle distance	0.03 m
Total number of particles	6 million
Physical time	10 s
Computation time	41 h
Execution device	GTX Titan

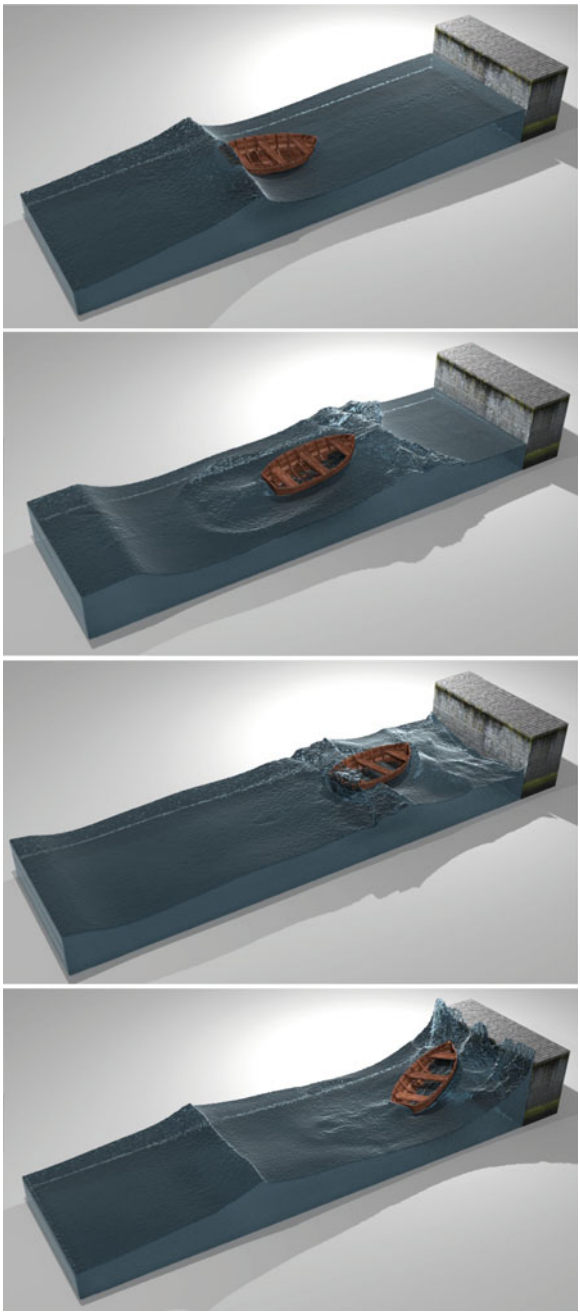

Fig. 7 Four instants (3, 7, 13 and 15 s) of the wave interaction with a floating object

4.3 Wave Interaction with a Floating Object

In this last case, the theory described in Sect. 2.9.1 (periodic boundary conditions) and 2.9.2 (floating objects) is applied for the interaction of waves with a floating object (a boat in this case). Table 5 contains the SPH parameters used in this simulation.

The physics of a fluid-driven object (the boat) is simulated in this case. In this simulation waves propagate pushing the boat that is located close to a dock (Fig. 7), where wave propagation, reflection and breaking play an important role. The moment of inertia, the centre of mass and the total weight of the object are considered to provide a realistic movement of the boat.

5 Conclusions

The DualSPHysics code has been developed to study complex free-surface flows requiring high computational resources.

A complete description of the SPH formalism implemented in DualSPHysics is presented. This work addresses a review of the governing equations such as the momentum and continuity equations, density filters, velocity corrections, time stepping schemes and boundary conditions.

The code is validated with the experimental data of a dam break impacting an obstacle. The experiment is a benchmark for the free-surface flow SPH community (http://wiki.manchester.ac.uk/spheric/index.php/Test2) and provides water elevation and pressure data sampled at different locations. The simulations show a close agreement between the numerical and experimental results both for free-surface elevations and pressures.

Three examples have been shown to illustrate some of the capabilities of the DualSPHysics code to simulate wave propagation, wave interaction with coastal structures and the movement of floating objects.

References

Altomare C, Crespo AJC, Rogers BD, Domínguez JM, Gironella X, Gómez-Gesteira M (2014) Numerical modelling of Armour block sea breakwater with smoothed particle hydrodynamics. Comput Struct 130:34–45

Barreiro A, Crespo AJC, Domínguez JM, Gómez-Gesteira M (2013) Smoothed particle hydrodynamics for coastal engineering problems. Comput Struct 120(15):96–106

Batchelor GK (1974) Introduction to fluid dynamics. Cambridge University Press, Cambridge

Benz W (1990) Smoothed particle hydrodynamics: a review. Numerical modelling of nonlinear stellar pulsations: problems and prospects. Kluwer Academic Publishers, Boston

Crespo AJC, Gómez-Gesteira M (2007) Boundary conditions generated by dynamic particles in SPH methods. CMC: Comput Mater Contin 5(3):173–184

Crespo AJC, Gómez-Gesteira M, Dalrymple RA (2008) Modeling dambreak behavior over a wet bed by a SPH technique. J WaterW Port, Coast, Ocean Eng 134:313–320
Crespo AJC, Dominguez JM, Barreiro A, Gómez-Gesteira M, Rogers BD (2011) GPUs, a new tool of acceleration in CFD: efficiency and reliability on smoothed particle hydrodynamics methods. PLoS ONE 6(6):e20685
Dalrymple RA, Rogers BD (2006) Numerical modeling of water waves with the SPH method. Coast Eng 53:141–147
Domínguez JM, Crespo AJC, Gómez-Gesteira M, Marongiu JC (2011) Neighbour lists in smoothed particle hydrodynamics. Int J Numer Methods Fluids 67(12):2026–2042
Domínguez JM, Crespo AJC, Gómez-Gesteira M (2013a) Optimization strategies for CPU and GPU implementations of a smoothed particle hydrodynamics method. Comput Phys Commun 184(3):617–627
Domínguez JM, Crespo AJC, Rogers BD, Gómez-Gesteira M (2013b) New multi-GPU implementation for smoothed particle hydrodynamics on heterogeneous clusters. Comput Phys Commun 184:1848–1860
Gingold RA, Monaghan JJ (1977) Smoothed particle hydrodynamics: theory and application to non- spherical stars. Mon Not R Astron Soc 181:375–389
Gómez-Gesteira M, Dalrymple RA (2004) Using a 3D SPH method for wave impact on a tall structure. J Waterw Port, Coast, Ocean Eng 130(2):63–69
Gómez-Gesteira M, Cerqueiro D, Crespo AJC, Dalrymple RA (2005) Green water overtopping analyzed with a SPH model. Ocean Eng 32:223–238
Gómez-Gesteira M, Rogers BD, Dalrymple RA, Crespo AJC (2010) State-of-the-art of classical SPH for free surface flows. J Hydraul Res 48:6–27. doi:10.3826/jhr.2010.0012
Gómez-Gesteira M, Rogers BD, Crespo AJC, Dalrymple RA, Narayanaswamy M, Domínguez JM (2012a) SPHysics-development of a free-surface fluid solver-part 1: theory and formulations. Comput Geosci 48:289–299
Gómez-Gesteira M, Crespo AJC, Rogers BD, Dalrymple RA, Domínguez JM, Barreiro A (2012b) SPHysics-development of a free-surface fluid solver-part 2: efficiency and test cases. Comput Geosci 48:300–307
Kleefsman KMT, Fekken G, Veldman AEP, Iwanowski B, Buchner B (2005) A volume-of-fluid based simulation method for wave impact problems. J Comput Phys 206:363–393
Leimkuhler BJ, Reich S, Skeel RD (1996) Integration methods for molecular dynamic IMA volume in mathematics and its application. Springer, New York
Liu GR (2003) Mesh free methods: moving beyond the infinite element method. CRC Press, Boca Raton
Monaghan JJ (1982) Why particle methods work. SIAM J Sci Stat Comput 3:422–433
Monaghan JJ (1989) On the problem of penetration in particle methods. J Comput Phys 82:1–15
Monaghan JJ (1992) Smoothed particle hydrodynamics. Annu Rev Astron Appl 30:543–574
Monaghan JJ (1994) Simulating free surface flows with SPH. J Comput Phys 110:399–406
Monaghan JJ (2005) Smoothed particle hydrodynamics. Rep Prog Phys 68:1703–1759
Monaghan JJ, Kos A (1999a) Solitary waves on a Cretan beach. J Waterw Port, Coast, Ocean Eng 125:145–154
Monaghan JJ, Cas RF, Kos A, Hallworth M (1999b) Gravity currents descending a ramp in a stratified tank. J Fluid Mech 379:39–70
Narayanaswamy MS, Crespo AJC, Gómez-Gesteira M, Dalrymple RA (2010) SPHysics-Funwave hybrid model for coastal wave propagation. J Hydraul Res 48:85–93. doi:10.3826/jhr.2010.0007
Rogers BD, Dalrymple RA, Stansby PK (2010) Simulation of caisson break water movement using SPH. J Hydraul Res 48:135–141. doi:10.3826/jhr.2010.0013
Verlet L (1967) Computer experiments on classical fluids. I. Thermodynamical properties of Lennard-Jones molecules. Phys Rev 159:98–103
Wendland H (1995) Piecewiese polynomial, positive definite and compactly supported radial functions of minimal degree. Adv Comput Math 4:389–396

Numerical Modelling of the Extratropical Storm Delta Over Canary Islands: Importance of High Resolution

O. Jorba, C. Marrero, E. Cuevas and J.M. Baldasano

Abstract The tropical storm "Delta" was formed on November 23, 2005 in a sea zone of the subtropical Atlantic south of the Azores. After days with an erratic movement, the day 27 the storm reinforced their intensity and accelerated its movement towards the Northeast in the direction of the Canary Islands. On 28 and 29, it made a transition to extratropical storm, affecting the Canary Islands with very strong sustained winds with maximum streak of 152 km/h at the airport of La Palma and close to 250 km/h in the Izaña observatory (2,360 m altitude), which caused significant property damage. The aim of this numerical modelling is to reproduce the local effects of Delta storm with high spatial resolution. The WRF-ARW model is applied from 9 to 3 km of horizontal resolution using ECMWF forecasts as IBC. The simulation reproduces the main features that contributed to the high wind speeds observed. Variations in the vertical static stability, vertical wind shear and intense synoptic winds from the southwest part of Delta with a warm core at 850 hPa were the main features that have contributed to the development and amplification of intense gravitational waves, while the large-scale flow interacted with the complex topography of the islands. Nonhydrostatic and hydrostatic experiments were designed taking into account the settings and domain factors. The results associated with changes relative to a controlled simulation showed that the boundary layer, the horizontal resolution, and the nonhydrostatic option have the greatest impact.

O. Jorba · J.M. Baldasano (✉)
Earth Sciences Department, Barcelona Supercomputing Center-Centro Nacional de Supercomputación (BSC-CNS), Barcelona, Spain
e-mail: jose.baldasano@bsc.es

C. Marrero · E. Cuevas
Izaña Atmospheric Research Center, Meteorological State Agency of Spain (AEMET), Santa Cruz de Tenerife, Spain

J.M. Baldasano
Environmental Modelling Laboratory, Technical University of Catalonia (UPC), Barcelona, Spain

J. Klapp et al. (eds.), *Selected Topics of Computational and Experimental Fluid Mechanics*, Environmental Science and Engineering,
DOI 10.1007/978-3-319-11487-3_7

1 Introduction

The Canary Islands are located in the middle-east of the Atlantic Ocean in front of the southern coast of Morocco, between 27–30°N latitude and 19–13°W longitude (see Fig. 1). The complex topography of Canary Islands and the interaction with the large-scale flow associated with extratropical storm Delta on November 28–29, 2005 contributed to the development of the extreme winds observed. The flow was characterized by a warm core around 850 hPa (Beven 2006; Martín et al. 2006; NHC 2006). It represented unusual meteorological phenomena for that region. The highest wind speeds were recorded in meteorological stations located downwind of steep mountain barriers in the western islands. This fact indicates that the strong winds might be related to downslope windstorms (e.g., Lilly and Zipser 1972; Peltier and Clark 1979; Durran 1986) induced by the intense synoptic flow affecting the archipelago. This work analyzes the development of strong downslope winds that were observed in the Canary Islands during the influence of Delta storm.

Several authors have analyzed the sensitivity of numerical weather prediction models under extratropical storm situations, taking into account the impact of the observing system and the initial conditions (Zou et al. 1998; Zhu and Thorpe 2006; Froude et al. 2007) and the model uncertainties such as numerical scheme, horizontal and vertical resolution and physical parameterizations (Orlanski et al. 1991; Prater and Evans 2002; Forbes and Clark 2003; Jung et al. 2006). They have found a clear dependence on the predictability of extratropical cyclones with the initial conditions and model configuration.

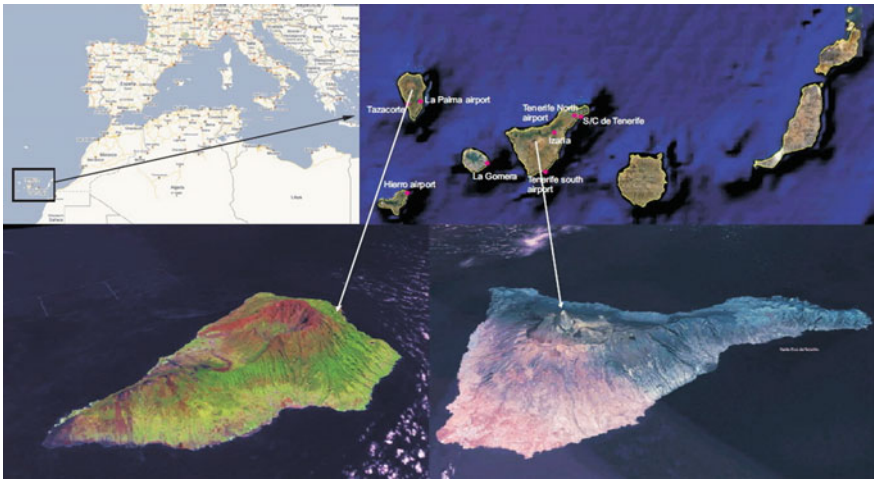

Fig. 1 Location of Canary Islands

The aim of the present work is to reproduce this weather phenomenon using the WRF-ARW NWP model and analyze the sensitivity to the horizontal high-resolution mesoscale meteorological modelling and the nonhydrostatic option.

2 Methods

The Weather Research and Forecasting (WRF) Model v2.1.2 (Michalakes et al. 2005) was used to simulate the wind field over the Canary Islands under the Delta meteorological situation. WRF was configured with the ARW dynamics solver (Skamarock et al. 2005) to integrate the primitive equations. The physical parameterizations used were: single-moment 3-class scheme for the microphysics processes, Kain-Fritsch scheme for cumulus parameterization, the Rapid Update Cycle model Land-Surface scheme with 6 sub-soil layers (Smirnova et al. 1997, 2000), the Yonsei University PBL scheme (Noh et al. 2003), the long-wave radiative processes are parameterized with the Rapid Radiative Transfer Model following Mlawer et al. (1997) and the short-wave radiative scheme based on Dudhia (1989).

Three domains were defined using two-way nesting technique interaction. The domains were centered over the Canary Islands with 300 × 230, 340 × 226 and 337 × 292 grid points for the outer to inner domains, respectively. The location of the meshes is shown in Fig. 2. The horizontal resolutions were 9, 3, 1 km with 40 sigma vertical levels, 11 characterizing the boundary layer. The model top was fixed at 50 hPa. Analysis of the European Center for Medium Weather Forecasts (ECMWF) at 00:00 UTC November 28 was used as the initial condition. The boundary conditions were provided by the ECMWF forecasts at 3 h intervals from 03:00 UTC November 28 to 00:00 UTC November 30. The ECMWF data used a spatial resolution of 25 km derived from the T799 model forecasts.

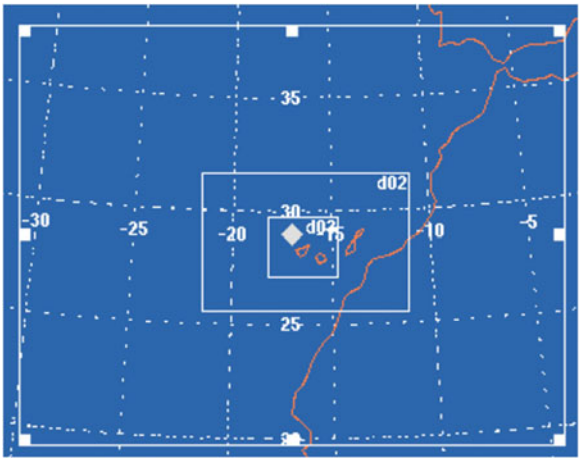

Fig. 2 Definition of the three nested model domains

The boundary conditions (BC) are known to provide a basic limitation to the predictability of local area models (Warner et al. 1997). Several errors produced on BC are mainly propagated into the domain at advective speeds by the mean flow, so in order to minimize these effects in our interest area, the mother domain has been dimensioned by considering HYSPLIT (Draxler and Rolph 2003) backward trajectories results (not shown) with the destination centred in the Canary Islands (28°N 16°W) at several levels in the 48 h model simulation run.

3 Numerical Solution and Results

The numerical simulations for November 28 (Fig. 3a, b) show a mature cyclone with a warm front extending from the centre of the low north-westward following the cyclone shape as shown by absolute vorticity. The structure of the extratropical

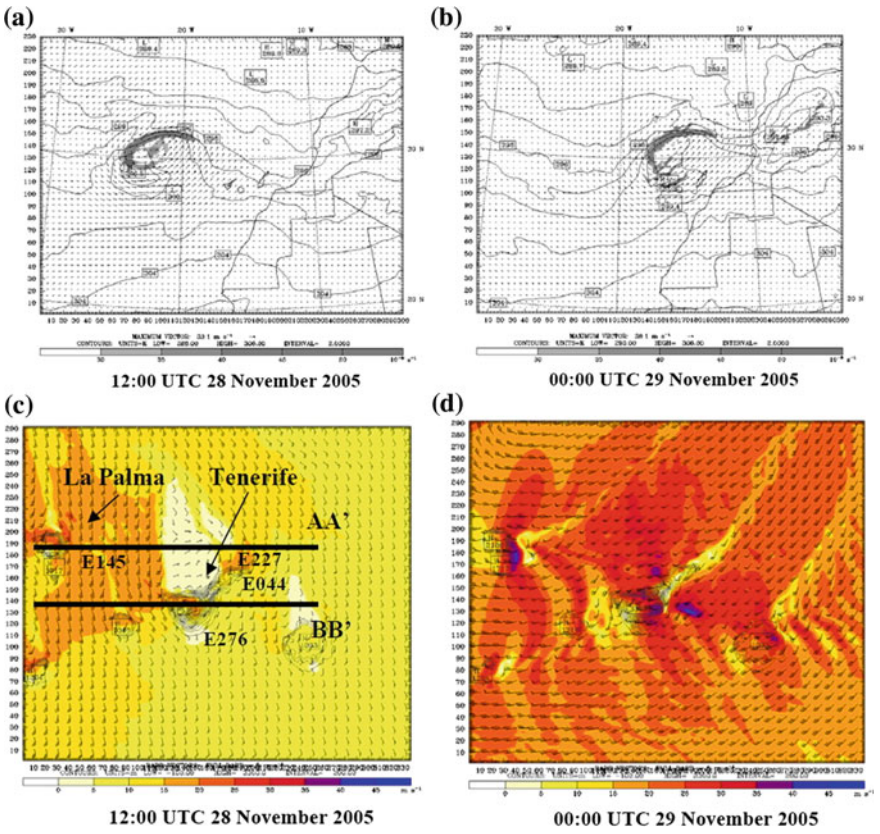

Fig. 3 **a**, **b** Simulated 850 hPa potential temperature, winds and absolute vorticity for November 28–29 2005 from 9 km domain; **c**, **d** 10 m wind field from 1 km domain

storm reaching Canary Islands was analog with the third phase of the Shapiro-Keyser conceptual model (Shapiro and Keyser 1990) for cyclone evolution, with a frontal T-bone and bent-back warm front (Martín et al. 2006). The bent-back front encloses a pool of warmer air at 850 hPa, and contributes to reinforcing the winds in the southwest region of the cyclone.

Figure 3c and d shows the results of the model at 1 km resolution. The surface wind speeds before 12:00 UTC of November 28 remain below 50 km/h over the whole Canary Islands with well-defined wake areas. The wind speed starts to reinforce at 12:00 UTC November 28, while the Delta storm approaches the archipelago with a counterclockwise veering of the synoptic flow to south-western direction. The north-western region of the domain presents the most intense flows, where the maximum wind speed is produced on the lee-side of La Palma, with the wind reaching a speed of 72 km/h. The development of trapped-lee waves starts at 14:00 UTC in the lee-side of La Palma. The vertical structure of the flow is reflected at surface level with regularly spaced regions of intense wind speed above 72 km/h. The synoptic veering of the flow towards south-westerly directions coincides with the flow intensification. The intense westerly warm core of the Delta storm affects the Canary Islands from 20:00 UTC November 28 to 02:00 UTC 29 November. This period is characterized by the development of local strong winds lee-ward of La Palma and Tenerife islands. The maximum surface wind speed is reached at 23:00 UTC November 28 over the lee-side of La Palma, with an intensity of 144 km/h at 10 m agl (Above ground level). In the southeast coast of Tenerife an intense core flow of high wind speeds develops, affecting the sea and part of the coast at 137 km/h at 10 m agl.

A vertical cross section is performed in order to understand the physical mechanisms that lead to the intense wind flows observed and simulated at surface levels for La Palma and Tenerife islands (Fig. 4). At 12:00 UTC the main flow affecting Tenerife presents a marked westerly direction and important vertical wind shear, and an elevated inversion is present around 780 hPa which delimits two different statically stable layers. Under these conditions an internal gravity wave develops aloft Tenerife island as it is shown in the cross section. The wind speed at the lee of the mountain intensifies and the downslope flow enhances. The maximum velocities of the downslope jet flow are of the order of 130 km/h at 100 m agl. The surface wind speed remains lower than 115 km/h. At 24:00 UTC the windstorm has extended downslope and its jet core presents a maximum wind speed of 162 km/h at 100 m agl.

Figure 4 shows the cross section along La Palma and Tenerife islands at different horizontal resolutions (9, 3 and 1 km). The cross section along La Palma shows how the trapped-lee waves do not develop in the simulation at 9 km. The simulation results at 3 and 1 km present good performance in developing the trapped-lee waves. As was noted by Durran (1986), the trapped-lee is not taken into account by the hydrostatic hypothesis, and these fine-scale features will not be captured by the hydrostatic models. The simulation results at 9 km point out the impact of the orography representation in the non-hydrostatic model used; the increase of the horizontal resolution provides a better representation of the orography that lead to the development of the fine-scale features.

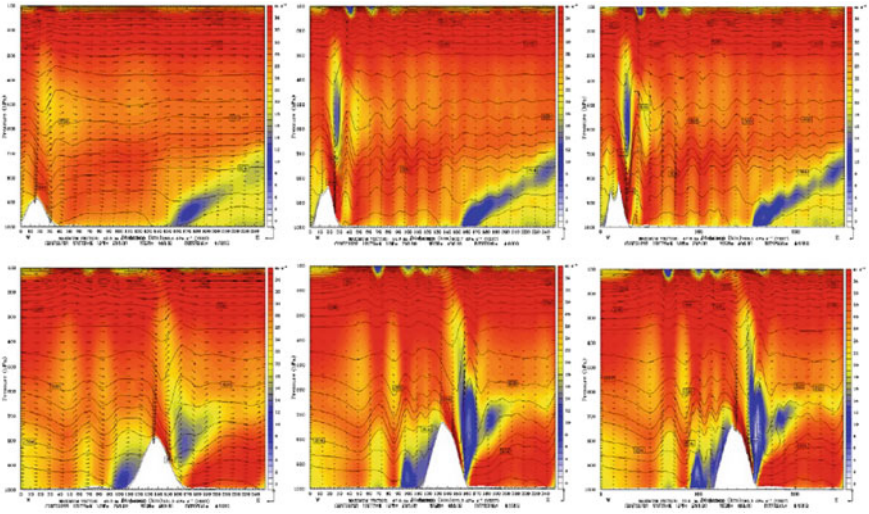

Fig. 4 Vertical cross section of potential temperature and wind field at La Palma (*top*) at 18:00 UTC November 28, 2005 and Tenerife (*bottom*) at 00:00 UTC November 29, 2005 at 9 km resolution (*left*), 3 km resolution (*middle*), and 1 km resolution (*right*). The cross sections are depicted in *bottom-left* of Fig. 3, La Palma: AA', and Tenerife: BB (color map: wind speed (m/s); vector map: wind field; contour map: potential temperature (K))

The increase of the horizontal resolution brings high winds to the bottom of the mountain, in agreement with Durran (1986) who attributes this behaviour to the finite amplitude effects (increase of mountain height), and more in agreement with the often observed strongest winds near the base of a mountain. In summary, if the horizontal resolution is decreased, the mountain wave activity lessens, even though the mountain-top winds present no major differences. As noted by other authors (e.g., Doyle and Shapiro 2000; Zhang et al. 2005) the horizontal resolution of the mesoscale models need to be higher than 9–10 km to develop the details of the wave. In La Palma cross section, it is also noticeable the effect of Tenerife island in the flow, provoking a plume of low wind speed at low levels downwind of La Palma.

Finally, the 10 m hourly wind speeds modelled were compared against meteorological observations available in the area (Fig. 5). Due to power loss of the automatic meteorological stations related to the damage of the energy supply provoked by the intense Delta wind field, the meteorological stations stopped measuring after 22:00 UTC of November 28 and no information is available after then. The model results show a good agreement with the observations in places where the major wind speeds were registered. The stations of La Palma-E145 and Tenerife Sur-E276 reached maximum wind speeds of 90–108 km/h at 10 m agl that are accurately reproduced by the

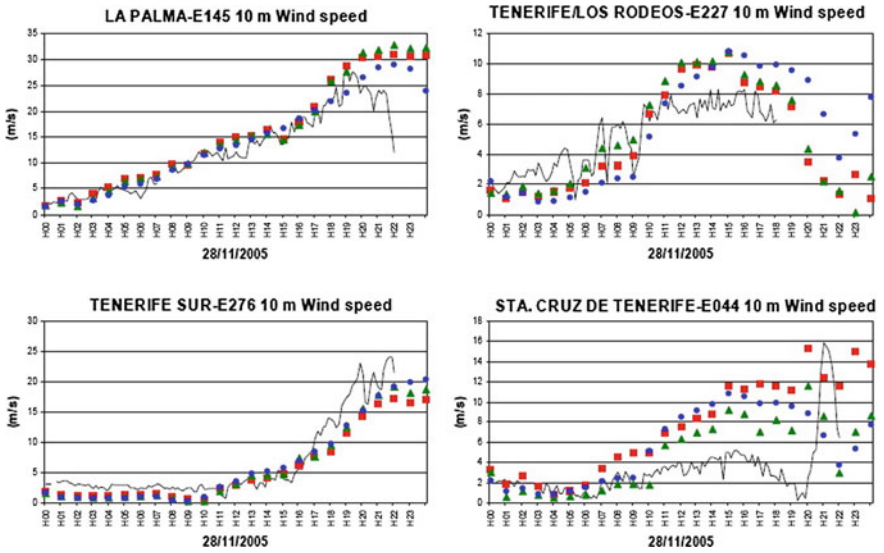

Fig. 5 10 m wind speed comparison of model results versus meteorological observations. Location of surface stations is depicted in the *bottom-left* panel of Fig. 3 (*Black line* 15 min mean surface measurements; *blue circle* 9 km domain; *green triangle* 3 km domain; *red square* 1 km domain)

model results. The model results show a regular increase of the wind speed at 10 m from 18 to 108 km/h in La Palma-E145 station for the period of study. The Santa Cruz de Tenerife-E044 station shows a sudden increase in the wind field, suggesting the presence of mountain wave activity aloft those impacts at surface levels with the development of a downslope wind event (as it has been shown with the model results). The results show how in the Santa Cruz de Tenerife-E044 station the high-resolution simulations (3 and 1 km) reproduce the sudden increase in wind speed reasonably well, improving the 9 km simulation. But it is also where the simulation results show the largest deviations. This is due to the topographic component of the location of the station, at the sea level, and conditioned by the situation bay surrounded by mountains with an important altitude difference.

The use of modelling allows another important and significant finding. We evaluated that the effect of this storm is enhanced due to the existence of a complex topography with high altitudes (the Teide volcano has a height of 3,718 m). Figure 6 shows the results of the different patterns for the three spatial resolutions with and without topography. The dynamic pattern is totally different; and it highlights the need to work at high spatial resolutions. This is especially evident on the Tenerife Island.

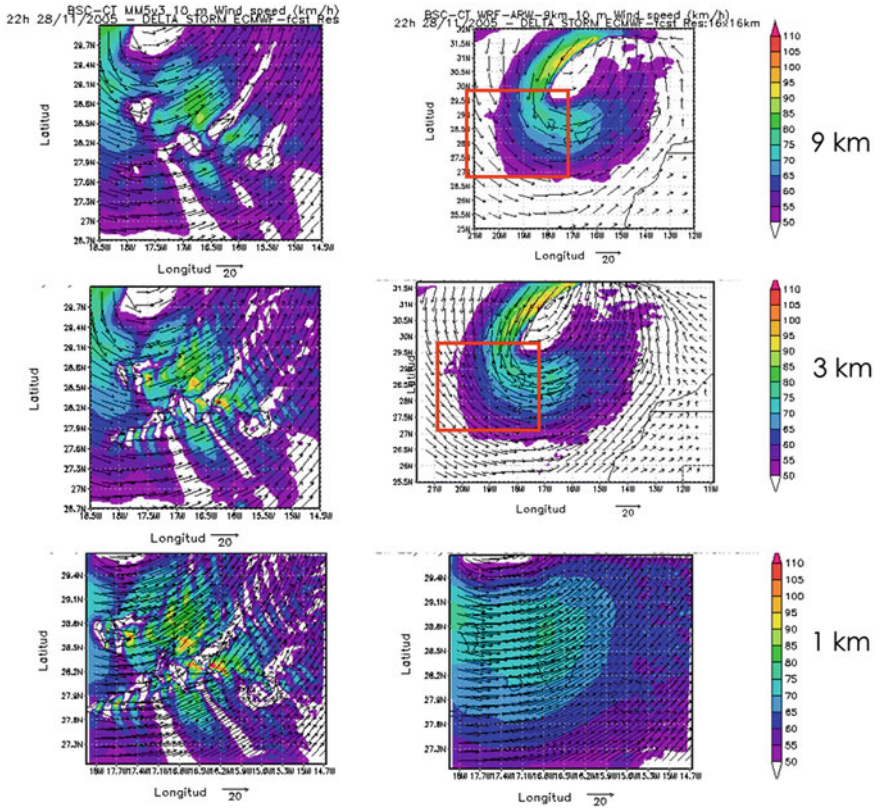

Fig. 6 Patterns at three different resolutions with (*left*) and without (*right*) topography

4 Conclusions

An unusual synoptic situation affected the Canary Islands from November 28 to November 30, 2005 provoking the Delta extratropical storm. The high-resolution simulation using the WRF model has outlined the main features that contribute to the high wind speeds observed in the archipelago of Canary Islands. The presence of the warm core at 850 hPa, near the top of higher mountain peaks and the variations in vertical static stability and important vertical wind shear were the main characteristics that contributed to the development and amplification of intense gravity waves leeward of the major mountain barriers of the western islands of the Canary archipelago that leads to the development of downslope windstorms.

The comparisons with surface observations indicate that the mesoscale model provides a reasonably good performance of the local effects produced in the complex islands orography. The model results may contribute to reinforce the idea that downslope windstorms associated with mountain wave activity developed when the

Delta storm affected the Canary Islands. This was a result of interactions between large-scale airflow (Delta storm) and the complex local topography of the islands.

The development and evolution of the Delta storm was a challenge for forecasters and numerical weather prediction models (e.g., ECMWF, HIRLAM), which underestimated the speed and impact of the storm during its evolution near the Canary Islands. In this sense, high-resolution modelling clearly contributes to understand the physical processes that lead to the observed strong wind speeds and gusts. The analysis of the simulation results shows that most of the modifications of the model parameters had a moderate to strong impact in the 10 m maximum wind speed solution. The greatest positive variations were associated with modifications of the Boundary-Layer and Surface-Layer parameterization, and especially the increase in horizontal resolution.

The results clearly show the importance of working with high spatial horizontal resolution and the need to use a nonhydrostatic mesoscale meteorological model to simulate more correctly this type of meteorological phenomenon in domains with complex or very complex topography.

Acknowledgments The authors wish to thank the AEMET (Spanish Met Office) and the ECMWF for the IFS-ECMWF data and the surface meteorological observations. The simulation was performed with the MareNostrum Supercomputer held by the Barcelona Supercomputing Center-Centro Nacional de Supercomputación.

References

Beven J (2006) Tropical cyclone report on tropical strom delta 22–28 November 2005, NOAA Technical Note TCR-AL292005, Tropical Prediction Center, National Hurricane Center

Doyle JD, Shapiro MA (2000) A multi-scale simulation of an extreme downslope windstorm over complex topography. Meteorol Atmos Phys 74:83–101

Draxler R, Rolph G (2003) HYSPLIT (HYbrid Single-Particle Lagrangian Integrated Trajectory) Model access via NOAA ARL READY Website (http://www.arl.noaa.gov/ready/hysplit4.html), NOAA Air Resources Laboratory, Silver Spring, MD, 15

Dudhia J (1989) Numerical study of convection observed during the winter monsoon experiment using a mesoscale two-dimensional model. J Atmos Sci 46:3077–3107

Durran DR (1986) Another look at downslope windstorms. Part I: On the development of supercritical flow in an infinitely deep, continuously stratified fluid. J Atmos Sci 43:2527–2543

Forbes R, Clark P (2003) Sensitivity of extratropical cyclone mesoscale structure to the parametrization of ice microphysical processes. Q J Roy Meteor Soc 129:1123–1148

Froude L, Bengtsson L, Hodges K (2007) The predictability of extratropical storm tracks and the sensitivity of their prediction to the observing system. Mon Weather Rev 135:315–333

Jung T, Gulev S, Rudeva I, Soloviov V (2006) Sensitivity of extratropical cyclone characteristics to horizontal resolution in the ECMWF model. Geophys Res Abstr 8:03367

Lilly DK, Zipser J (1972) The front range windstorm of 11 January 1972—a meteorological narrative. Weatherwise 25:56–63

Martín F, Alejo C J, de Bustos J J, Calvo F J, San Ambrosio I, Sánchez-Laulhé J M, Santos D (2006) Study of the tropical storm "Delta" and its extratropical transition: meteorological impacts over Canary Islands (27–29 November 2005), Technical Report, Instituto Nacional de Meteorología, Madrid

Michalakes J, Dudhia J, Gill D, Henderson T, Klemp J, Skamarock W, Wang W (2005) The weather research and forecasting model: software architecture and performance. In: Zwiefhofer W, Mozdzynski G (eds) Proceedings of the eleventh ECMWF workshop on the use of high performance computing in meteorology. World Scientific, pp 156–168

Mlawer EJ, Taubman SJ, Brown PD, Iacono MJ, Clough SA (1997) Radiative transfer for inhomogeneous atmosphere: RRTM, a validated correlated-k model for the longwave. J Geophys Res 102(D14):16 663–16 682

National Hurricane Center (2006) 2005 Atlantic Hurricane Season available at: http://www.nhc.noaa.gov/2005atlan.shtml

Noh Y, Cheon WG, Hong SY, Raasch S (2003) Improvement of the K-profile model for the planetary boundary layer based on large eddy simulation data. Bound Lay Meteorol 107:401–427

Orlanski I, Katzfey J, Menendez C, Marino M (1991) Simulation of an extratropical cyclone in the southern hemisphere: model sensitivity. J Atmos Sci 48:2293–2312

Peltier WR, Clark TL (1979) The evolution and stability of finite amplitude mountain waves. Part II: surface wave drag and severe downslope winds. J Atmos Sci 36:1498–1529

Prater B, Evans J (2002) Sensitivity of modeled tropical cyclone track and structure of hurricane Irene (1999) to the convective parameterization scheme. Meteorol Atmos Phys 80:103–115

Shapiro MA, Keyser D (1990) Fronts, jet streams and the tropopause. In: Newton CW, Holopainen EO (eds) Extratropical cyclones, the Erik Palme'n memorial volume. American Meteorology Society, Boston, pp 167–191

Skamarock W C, Klemp J B, Dudhia J, Gill D O, Barker D M, Wang W, Powers J G (2005) A Description of the advanced research WRF version 2, NCAR Technical note NCAR/TN-468+STR

Smirnova TG, Brown JM, Benjamin SG (1997) Performance of different soil model configurations in simulating ground surface temperature and surface fluxes. Mon Weather Rev 125:1870–1884

Smirnova TG, Brown JM, Benjamin SG, Kim D (2000) Parameterization of coldseason processes in the MAPS landsurface scheme. J Geophys Res 105(D3):4077–4086

Warner T, Peterson R, Treadon R (1997) A tutorial on lateral boundary conditions as a basic and potentially serious limitation to regional numerical weather prediction. Bull Am Meteorol Soc 78:2599–2617

Zhang Y, Chen YL, Kodama K (2005) Validation of the coupled NCEP mesoscale spectral model and an advanced land surface model over the Hawaiian islands. Part II: A high wind event, weather forecast 20:873–895

Zhu H, Thorpe A (2006) Predictability of extratropical cyclones: the influence of initial condition and model uncertainties. J Atmos Sci 63:1483–1497

Zou X, Kuo Y, Low-Nam S (1998) Medium-range prediction of an extratropical oceanic cyclone: impact of initial state. Mon Weather Rev 126:2737–2763

Four-Winged Flapping Flyer in Forward Flight

R. Godoy-Diana, P. Jain, M. Centeno, A. Weinreb and B. Thiria

Abstract We study experimentally a four-winged flapping flyer with chord-wise flexible wings in a self-propelled setup. For a given physical configuration of the flyer (i.e. fixed distance between the forewing and hindwing pairs and fixed wing flexibility), we explore the kinematic parameter space constituted by the flapping frequency and the forewing-hindwing phase lag. Cruising speed and consumed electric power measurements are performed for each point in the (f, φ) parameter space and allow us to discuss the problem of performance and efficiency in four-winged flapping flight. We show that different phase-lags are needed for the system to be optimised for fastest flight or lowest energy consumption. A conjecture of the underlying mechanism is proposed in terms of the coupled dynamics of the forewing-hindwing phase lag and the deformation kinematics of the flexible wings.

1 Introduction

Flapping flyers display an extremely rich variety of maneuvers because of the multiple kinematic parameters that rule the unsteady production of aerodynamic forces. From a biological point of view, the case of four-winged flyers capable of out-of-phase motion between forewings and hindwings such as dragonflies is particularly interesting. In the words of Azuma et al. (1985): "Dragonflies can hover, fly at high speed and maneuver skillfully in the air in order to defend their territory, feed on live prey and mate in tandem formation". Their body and wing kinematics

R. Godoy-Diana (✉) · P. Jain · M. Centeno · A. Weinreb · B. Thiria
Physique et Mécanique des Milieux Hetérogènes (PMMH, UMR 7636),
CNRS; ESPCI ParisTech; UPMC (Paris 6); Univ. Paris Diderot (Paris 7),
10 rue Vauquelin, 75231 Paris, Cedex 5, France
e-mail: ramiro@pmmh.espci.fr

P. Jain
Indian Institute of Technology, Kharagpur, India

M. Centeno
Facultad de Ciencias, Universidad Nacional Autónoma de México, Mexico City, Mexico

J. Klapp et al. (eds.), *Selected Topics of Computational and Experimental Fluid Mechanics*, Environmental Science and Engineering,
DOI 10.1007/978-3-319-11487-3_8

have been studied extensively (Alexander 1984, 1986; Azuma and Watanabe 1988; Rüppell 1989; Wakeling and Ellington 1997a, b) and flow visualizations in tethered- and free-flight configurations have demonstrated the crucial role of unsteady mechanisms such as the formation of leading-edge vortices in the production of lift (Thomas et al. 2004). Forewing-hindwing phase-lag has been shown in hovering configurations to be determinant for flight performance (Maybury and Lehmann 2004): optimal efficiencies have been found for out-of-phase beating whereas in-phase motion of forewings and hindwings has been shown to produce stronger force (Wang and Russell 2007; Usherwood and Lehmann 2008). The physical mechanisms behind these differences in performance have nonetheless not yet been completely elucidated, and open questions remain in particular when considering the role of wing elasticity. Wing deformation is important because it can passively modify the effective angle of attack of a flapping wing, thus determining its force production dynamics.

In the present paper we address this problem experimentally using a four-winged self-propelled model mounted on a "merry-go-round". The setup is a modified version of the one used by Thiria and Godoy-Diana (2010) and Ramananarivo et al. (2011), where the thrust force produced by the wings makes the flyer turn around a central axis. A constant cruising speed is achieved for a given wingbeat frequency when the thrust generated is balanced by the net aerodynamic drag on the flyer. These previous works have shown that passive mechanisms associated to wing flexibility govern the flying performance of a flapping wing flyer with chord-wise flexible wings. These determine, for instance, that the elastic nature of the wings can lead not only to a substantial reduction of the consumed power, but also to an increment of the propulsive force. Here we introduce a new parameter using a model with two pairs of wings. In addition to the flapping frequency and wing flexibility, the thrust production is now also determined by the phase lag φ between the forewings and the hindwings.

2 Experimental Setup

Figure 1 shows a sketch of the experimental setup. As in Thiria and Godoy-Diana (2010), the stroke plane is parallel to the shaft linking the flyer to the central bearing of the wheel. In addition to the four-winged instead of two-winged flyer, the setup also differs from Thiria and Godoy-Diana (2010) in that a counterweight has been added using an opposite radial shaft to balance the system. The fluctuating lift force is thus directed radially and absorbed by the shaft. The two wings are driven by a single direct-current motor with a set of gears that allows to fix the phase difference between the forewings and the hindwings. All wings beat thus at the same frequency which was varied between 15 and 30 Hz. We have reduced the parameter space in the experiments reported here by fixing the physical characteristics of the flyer. Namely, the distance between the wings d, the stroke amplitude θ_0 and the chord-wise flexural rigidity of the wings. Of course, it should be noted that these parameters in the present tandem wing configuration, in particular the wing spacing d, should in

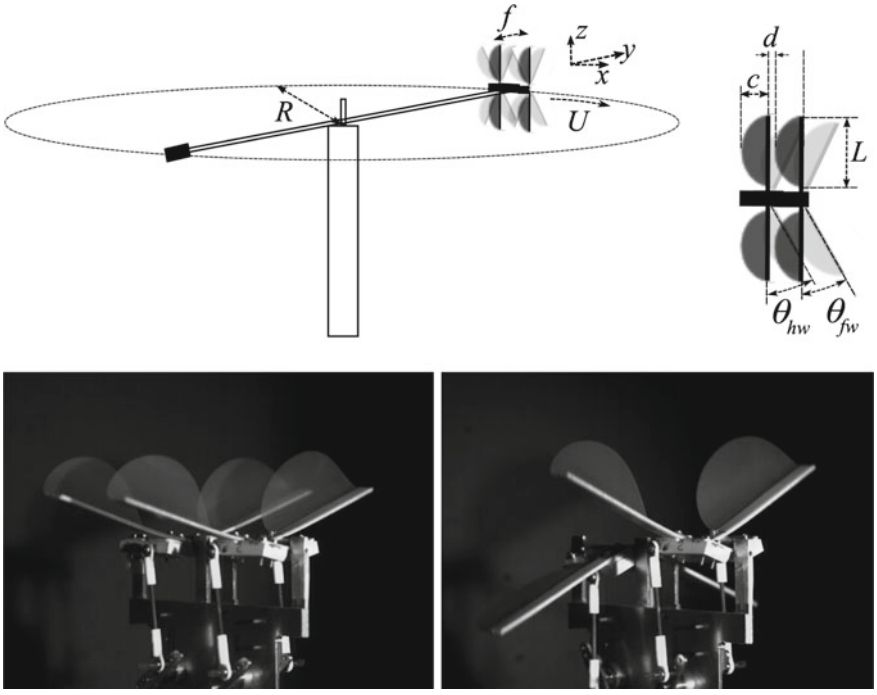

Fig. 1 *Top* sketch of the experimental setup. *Bottom* photos of the flapping flyer with forewing-hindwing phase lags 0 (*left*) and π (*right*). Each wing has a *semi-circular* shape so that $c = 30\,\text{mm}$ and $L = 60\,\text{mm}$. The distance between the wings $d = 1\,\text{mm}$, so that the trailing edge of the forewing and the leading edge of the hindwing almost touch when the wings are aligned without bending; the stroke amplitude $\max(\theta_{fw}) = \max(\theta_{hw}) = \theta_0 = 37°$. Wings are made of 0.05 mm thick Mylar that gives a flexural rigidity $B = 3.3 \times 10^{-5}\,\text{Nm}$ The leading edge is thicker (1 mm) and made of fiberglass so that it can be considered rigid and the deformation exclusively chord-wise

general be analysed simultaneously with the forewing-hindwing phase lag (Maybury and Lehmann 2004; Rival et al. 2011). The motion of the wings is described using the angles of the forewing and hindwing leading edges to the xz-plane, θ_{fw} and θ_{hw}, respectively (see Fig. 1), as

$$\theta_{fw} = \theta_0 \sin(2\pi f t) \quad \text{and} \quad \theta_{hw} = \theta_0 \sin(2\pi f t - \varphi), \tag{1}$$

where f is the flapping frequency and the phase lag φ is varied between 0 and 2π. For $0 < \varphi < \pi$ the forewing is leading, whereas for $\pi < \varphi < 2\pi$ it is the hindwing that leads. The Reynolds number $\text{Re} = Uc/\nu$ based on the cruising speed and the chord length was in the range of 1,000–4,000.

The measured quantities are the cruising flight speed U and the consumed power P_i. In the study of the two winged flyer of Thiria and Godoy-Diana (2010) and Ramananarivo et al. (2011) an additional independent setup was used to measure the thrust force F by holding the flyer in a stationary position. The product of the force

and cruising speed measurements was then an estimate of the aerodynamic power $P_a = FU$. One of the disadvantages of that procedure was that the two measurements did not correspond to the same flight configuration: while U corresponds to self-propelled cruising flight, F measured at a fixed station corresponds to a "hovering" flight configuration. Here we avoid that problem by using an estimate of aerodynamic power obtained only from the velocity measurements, as explained in the next section.

3 Results

(i) Flying performance. The aerodynamic interactions are thus ruled by φ and their effect can be directly measured in the performance parameters of the experiment: the cruising speed U and the consumed power P_i. In order to get a clear picture of the effect of each parameter we first show in Fig. 2 two data series corresponding to different flapping frequencies, where U and P_i are plotted as functions of φ. It can be seen that the phasing between the wings produces a net effect in performance, the fastest cruising flight velocities corresponding to a range around in-phase flapping ($\varphi = 0$), but the picture becomes richer when looking at the consumed power. Indeed, the latter has two peaks around $\varphi \approx 0$ and π. The previous series lie in a regime where increasing the flapping frequency shifts the curves to higher flying speeds and higher consumed power. The observed trend is readily explained using the non-dimensional expressions $p = P_i c/B\omega_f$ and $u = U/A_0\omega_f$ defined by Ramananarivo et al. (2011), where A_0 is the amplitude of oscillation of the leading edge at mid span given by $A_0 = (L/2)\sin\theta_0$ and $\omega_f = 2\pi f$. The insets in Fig. 2 show the behaviour of the dimensionless quantities.

The increase of speed with increasing flapping frequency is not indefinite however, an effect shown in Fig. 3, where U is plotted in coloured contours in a (φ, f)-

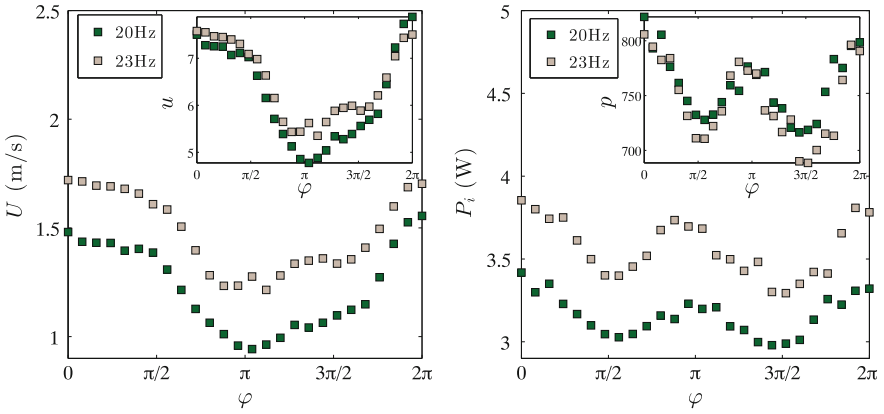

Fig. 2 Cruising speed and consumed power as a function of the forewing-hindwing phase lag for two different flapping frequencies

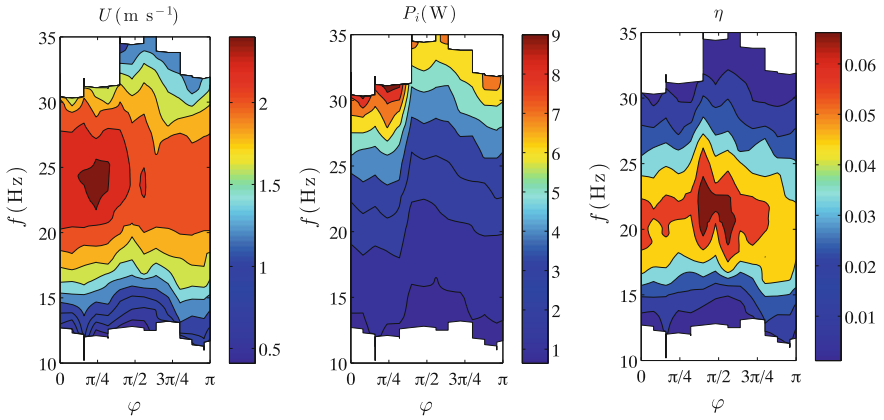

Fig. 3 Cruising speed, consumed power and efficiency (see text) as a function of the forewing-hindwing phase lag and the flapping frequency. Only the first half of the phase-lag φ range, where the forewing is leading, was examined here

space for $\varphi \in [0, \pi]$ and scanning the full range of flapping frequencies available experimentally. For all phase lags, a clear maximum of the attained cruising speed occurs always around 24 Hz. We will discuss in the following that this optimal frequency is related to the elastic properties of the wings. The second plot in Fig. 3 shows the consumed power P_i in the same parameter space. Here the main observation is that, while not surprisingly consumed power increases monotonically with increasing flapping frequency, the effect of the phase lag on energy expenditure, shown previously in Fig. 2, is clearly present regardless the flapping frequency. Because of this effect, the ranges of frequency explored changed for different phase lags, giving, for instance, a maximum frequency for $\varphi = 0$ of around 30 Hz, while at $\varphi \in [\pi/2, 3\pi/4]$ the frequency could reach 35 Hz. We use those two measurements to define the following expression of efficiency, considering that the aerodynamic thrust power is proportional to U^3 (velocity times thrust force, the latter being $\sim U^2$):

$$\eta = \frac{\frac{1}{2}\rho S U^3}{P_i} \tag{2}$$

where S is the effective wing surface. Other definitions of efficiency using purely dynamical parameters (Kang et al. 2011) should give equivalent results to expression (2) chosen here in terms of the measured consumed power P_i. It can be seen that the optimum in terms of efficiency is shifted toward larger phase lags (around $\varphi \approx \pi/2$) than the optimum in terms of maximum cruising speed.

(ii) Wing kinematics. In addition to the performance measurements, the wing motion was recorded using high-speed video in a fixed frame. That is, with the mechanical insect not mounted on the merry-go-round but on a fixed base. Figures 4 and 5 show typical time series for $\varphi = 0$ and 1.3π, respectively. A dark screen was used to mask

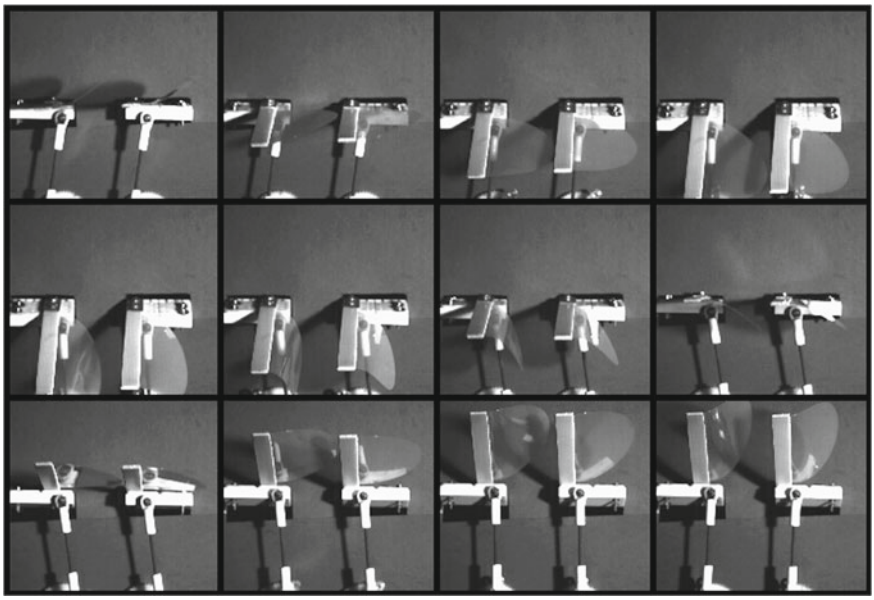

Fig. 4 Sequence showing the kinematics of the flapping wings at $f = 23\,\mathrm{Hz}$ and $\varphi = 0$

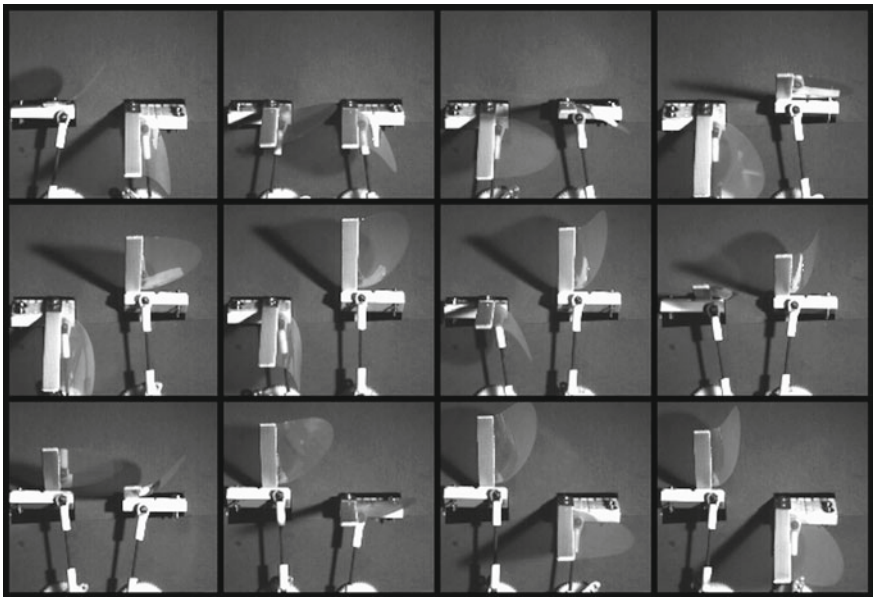

Fig. 5 Sequence showing the kinematics of the flapping wings at $f = 23\,\mathrm{Hz}$ and $\varphi = 1.3\pi$

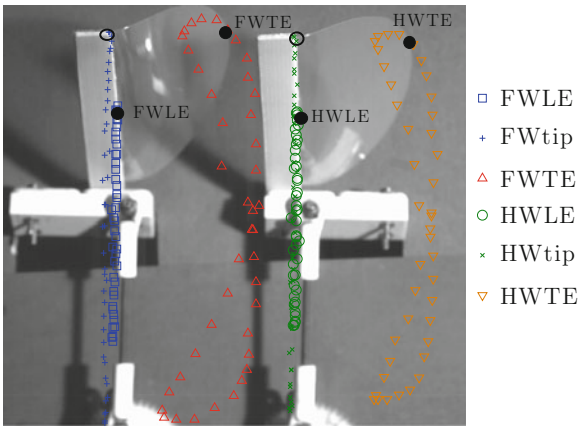

Fig. 6 Tracking the wing motion. Example of in-phase flapping at $f = 23$ Hz. *Black circles* are the points tracked on each wing for the leading and trailing edges (FWLE and FWTE, correspond to the forewing, while HWLE and HWTE correspond to the hindwing). The *open circles* are the positions of the win tips tracked

the right side wings and have a clearer view of the kinematics. The main feature that can be seen in these time series of snapshots is the large deformation of the wings during the flapping cycle. Indeed, the wings bend over a length scale that is of the same order of magnitude than the chord length. In addition to the kinematics of the compliant wings, which can be followed for each wing independently, Figs. 4 and 5 hint on the complex interaction that arises from the combination of the bending dynamics and the imposed forewing-hindwing phase lag. We will analyse this interaction in the following by tracking the motion of different points on each wing.

Figure 6 presents the tracking in time of the (x, y) positions of the leading and trailing edges of each wing at the point of maximum chord length (black circles, FWLE and FWTE denoting forewing leading and trailing edge, respectively, while HWLE and HWTE correspond to the equivalent points on the hindwing). Additionally, the tip of each wing is also tracked (empty circles). The latter is useful to minimize the measurement error in the leading edge amplitude of motion since it has a larger swept amplitude and the relative error is thus smaller. The time-series of the positions of these points are shown in Fig. 7a, b for two different values of φ. The main observation here is the trailing-edge-leading-edge phase lag γ for each wing, which has been reported in Ramananarivo et al. (2011) to be a crucial element of the propulsive performance of flexible flapping wings. The measured value of γ for several forewing-hindwing phase lags is shown in Fig. 7c. A slight decrease is observed for γ when φ decreases from 2π to 1.3π, i.e., when the systems go from in-phase flapping to a configuration with the hindwings leading by approximately a third of a period, but the effect is very weak.

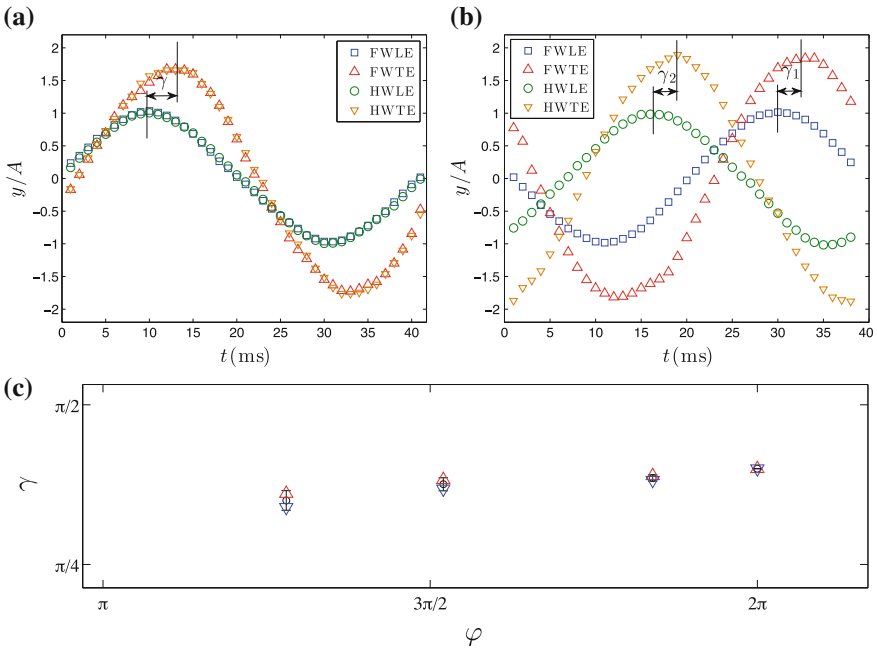

Fig. 7 Time series of the y-position of the leading and trailing edges of both wings for $f = 23\,\mathrm{Hz}$ and **a** $\varphi = 0$ and **b** 1.3π. The leading-edge-trailing-edge phase lag γ is shown schematically. In the $\varphi = 0$ case, $\gamma_1 = \gamma_2 \equiv \gamma$. The y-axis is rendered dimensionless using A, the peak-to-peak amplitude swept by the leading edge at mid-chord. **c** Trailing-edge-leading-edge phase lag γ for different forewing-hindwing phase lags. The two different markers correspond to the forewing γ_1 ($\triangle$) and hindwing γ_2 ($\triangledown$)

4 Discussion

Before discussing the effect of the forewing-hindwing phase lag we start with a comment on the role of the flapping frequency. The existence of an optimal flapping frequency for the present setup (as is evident in Fig. 3) is related to the effect of wing compliance on the propulsive performance of the flapping wings, a question that has been widely discussed in the literature (Shyy et al. 2010; Spagnolie et al. 2010; Masoud and Alexeev 2010; Thiria and Godoy-Diana 2010; Ramananarivo et al. 2011; Kang et al. 2011). For flexible wings flapping in air, where the mass ratio of the wing with respect to the surrounding fluid is high, the main bending motor is the wing inertia (Daniel and Combes 2002; Thiria and Godoy-Diana 2010). Increasing the flapping frequency leads to an increased deformation of the wing, which is useful in terms of propulsive performance up to a certain point where the effective lifting surface is diminished and thrust production drops (Ramananarivo et al. 2011). An interesting point is that the optimal frequency f_{opt} that can be estimated by inspection of Fig. 3 is different depending on whether one considers maximum cruising speed

($f_{opt} \sim 24$ Hz) or maximum efficiency ($f_{opt} \sim 21$ Hz). This can be explained by the fact that the consumed power, which enters the quotient defining efficiency Eq. (2) in the denominator, increases monotonically with increasing frequency. This will thus shift the location of the peak in the efficiency that corresponds to the aerodynamic power peak.

In order to focus on the effect of the forewing-hindwing phase lag, a fixed frequency can be chosen. In Fig. 2, for each of the two frequencies represented, the same trends are observed in the cruising speed and the consumed power and, as shown in the insets, the frequency dependence is well explained using the "elasto-inertial" dimensionless variables u and p defined above. Now, with respect to the phase lag φ, two main points appear clearly: on the one hand, the fastest flying performance is found around in-phase flapping (i.e. $\varphi = 0$), while around anti-phase flapping ($\varphi = \pi$) this cruising speed is the lowest. We may note that the curve is not symmetric with respect to $\varphi = 0$, since it diminishes only slightly (one could consider a plateau) between $\varphi = 0$ and $\pi/2$, whereas it drops more rapidly when the hindwing leads (i.e., when going from $\varphi = 0 = 2\pi$ towards $\varphi = 3\pi/2$). The consumed power curve on the contrary has two maxima (around $\varphi = 0$ and π) and two minima around ($\varphi = \pi/2$ and $3\pi/2$). In-phase and anti-phase flapping being the most expensive can be explained by a simple inertial argument since during these configurations the motor has to accommodate the acceleration/deceleration of both pairs of wings at the same time, contrary to the intermediate phase lags $\varphi = \pi/2$ and $3\pi/2$, where the deceleration of one pair of wings occurs while the other pair is accelerating, hence redistributing the load on the motor.

The shape of the cruising speed and consumed power curves determines the location of the maximum observed in the efficiency contours in Fig. 3 being around $\varphi = \pi/2$. A secondary maximum can be expected around $\varphi = 3\pi/2$ (a zone of the parameter space that was not fully explored in the present experiments). We can now compare the optimum phase-lags that lead to peaks of cruising speed and of efficiency and comment on their physical origin: while the maximum cruising speed is observed for phase-lags between zero and $\pi/4$, the optimum phase-lags in terms of efficiency are around $\pi/2$. The former are ruled solely by the aerodynamics, where the performance of different kinematic patterns will have to be analysed considering, for instance, the interaction between hindwing and the vortex structures shed by the forewing. A wake capture process of this sort has been proposed by Kolomenskiy et al. (2013) as a possible explanation for the large propulsive force found at 0.75π in their 2D numerical simulations.[1] Concerning the optimum phase lag in terms of efficiency requires, on the other hand, considering the power consumption, which is not only correlated to the aerodynamics, but has a large contribution determined by solid inertia, as we have mentioned in reference to the power plot in Fig. 2b.

The effect of the modulation of φ in terms of aerodynamics, as mentioned previously, will be intrinsically related to the roles of the distance d between the two wing pairs and the deformation kinematics. In this paper, we have fixed d and considered

[1] Note that in Kolomenskiy et al. (2013) the phase lag is defined with a negative sign with respect to φ as used here so that 0.75π here corresponds to their 1.25π.

a single flexibility in order to explore the possible roles of the wing deformation in the propulsive performance. Considering our previous studies on the effect of flexibility with a two wing flyer (Thiria and Godoy-Diana 2010; Ramananarivo et al. 2011), where the trailing-edge-leading-edge phase lag γ was shown to be a crucial parameter to determine performance, we attempted here to monitor modifications in γ as a function of φ (see the analysis of wing kinematics in Figs. 6 and 7). We picked a range of φ (decreasing from 2π to 1.3π) where a clear deterioration of the flying performance is observed in Fig. 2 as the hindwing starts leading the forewing. The observations on the trailing-edge-leading-edge phase lag γ are, however, not conclusive. A slight decrease of γ is indeed observed, while φ goes from 2π to 1.3π, which at these frequencies could explain a diminishing thrust performance, but the effect is too weak and the present results do not permit to give a thorough and quantitative confirmation of the effect if it exists.

5 Conclusions

We have shown that a four-winged flapping flyer in a cruising regime does present different optimal forewing-hindwing phase lags depending on whether one would want to tune the system for maximum cruising speed or minimum energy expenditure. These results are in accordance with previous studies in hovering configurations (Wang and Russell 2007; Usherwood and Lehmann 2008), hinting that the mechanisms described here should be robust elements to consider in any aerodynamic model: on the one hand, wing inertia is a major player in the power expenditure, while, on the other hand, the thrust production is ruled by the aerodynamics around the flexible wings.

A full flow field reconstruction around the wings is certainly desirable to compare different points in the parameter space with different performances and clearly identify the aerodynamic mechanisms at play. Experimentally this can be challenging, and numerical simulations such as a 3D version of the fluid-structure simulations of Kolomenskiy et al. (2013) can be an interesting option to define robust aerodynamic models.

Other issue that remains not fully understood is the effect of the forewing-hindwing separation d as a parameter independent of the forewing-hindwing phase lag which will have a different role depending on whether the system is hovering or cruising. This point will be of particular importance when going beyond the "steady" regimes of hovering or cruising and into the study of transient regimes. These bring indeed a vast set of open questions related to the unsteadiness—like for instance the multi-body dynamics of manoeuvring—and where the wings are to be analysed as part of a full system accelerating, performing sharp turns (Bergou et al. 2010) or taking off (Bimbard et al. 2013).

Acknowledgments We thank all people at the PMMH workshop for their help with the experimental setup, in particular D. Pradal, who conceived and built most of its parts. We thank also X. Benoit-Gonin, M. Vilmay and G. Lemoult for the LabView interfacing, and S. Ramananarivo, V. Raspa, D. Kolomenskiy and G. Spedding for useful discussions. This work was supported by the French National Research Agency through project No. ANR-08-BLAN-0099 and by EADS Foundation through project "Fluids and elasticity in biomimetic propulsion". M. C. acknowledges financial support from CONACyT and UNAM, México. P. J. acknowledges support from the Charpak Internship Program.

References

Alexander DE (1984) Unusual phase relationships between the forewings and hindwings in flying dragonflies. J Exp Biol 109(1):379–383

Alexander DE (1986) Wind tunnel studies of turns by flying dragonflies. J Exp Biol 122(1):81–98

Azuma A, Azuma S, Watanabe I, Furuta T (1985) Flight mechanics of a dragonfly. J Exp Biol 116(1):79–107

Azuma A, Watanabe T (1988) Flight performance of a dragonfly. J Exp Biol 137(1):221–252

Bergou AJ, Ristroph L, Guckenheimer J, Cohen I, Wang ZJ (2010) Fruit flies modulate passive wing pitching to generate in-flight turns. Phys Rev Lett 104(14):148101

Bimbard G, Kolomenskiy D, Bouteleux O, Casas J, Godoy-Diana R (2013) Force balance in the take-off of a pierid butterfly: relative importance and timing of leg impulsion and aerodynamic forces. J Exp Biol 216(18):3551–3563

Daniel TL, Combes SA (2002) Flexible wings and fins: bending by inertial or fluid-dynamic forces. Integr Comp Biol 42(5):1044

Kang CK, Aono H, Cesnik CES, Shyy W (2011) Effects of flexibility on the aerodynamic performance of flapping wings. J Fluid Mech 689(1):32–74

Kolomenskiy D, Engels T, Schneider K (2013) Numerical modelling of flexible heaving foils. J Aero Aqua Bio-mech 3(1):22–28

Masoud H, Alexeev A (2010) Resonance of flexible flapping wings at low Reynolds number. Phys Rev E 81(5):056304

Maybury WJ, Lehmann FO (2004) The fluid dynamics of flight control by kinematic phase lag variation between two robotic insect wings. J Exp Biol 207(26):4707–4726

Ramananarivo S, Godoy-Diana R, Thiria B (2011) Rather than resonance, flapping wing flyers may play on aerodynamics to improve performance. Proc Natl Acad Sci (USA) 108(15):5964–5969

Rival D, Schönweitz D, Tropea C (2011) Vortex interaction of tandem pitching and plunging plates: a two-dimensional model of hovering dragonfly-like flight. Bioinspir Biomim 6(1):016008

Rüppell G (1989) Kinematic analysis of symmetrical flight manoeuvres of Odonata. J Exp Biol 144(1):13–42

Shyy W, Aono H, Chimakurthi SK, Trizila P, Kang CK, Cesnik CES, Liu H (2010) Recent progress in flapping wing aerodynamics and aeroelasticity. Prog Aerosp Sci 46(7):284–327

Spagnolie SE, Moret L, Shelley MJ, Zhang J (2010) Surprising behaviors in flapping locomotion with passive pitching. Phys Fluids 22(4):041903

Thiria B, Godoy-Diana R (2010) How wing compliance drives the efficiency of self-propelled flapping flyers. Phys Rev E 82:015303(R)

Thomas ALR, Taylor GK, Srygley RB, Nudds RL, Bomphrey RJ (2004) Dragonfly flight: free-flight and tethered flow visualizations reveal a diverse array of unsteady lift-generating mechanisms, controlled primarily via angle of attack. J Exp Biol 207(24):4299–4323

Usherwood JR, Lehmann FO (2008) Phasing of dragonfly wings can improve aerodynamic efficiency by removing swirl. J R Soc Interface 5(28):1303–1307
Wakeling JM, Ellington CP (1997a) Dragonfly flight. II. Velocities, accelerations and kinematics of flapping flight. J Exp Biol 200(3):557–582
Wakeling JM, Ellington CP (1997b) Dragonfly flight. III. Lift and power requirements. J Exp Biol 200(3):583–600
Wang ZJ, Russell D (2007) Effect of forewing and hindwing interactions on aerodynamic forces and power in hovering dragonfly flight. Phys Rev Lett 99(14):148101

Flows from Bins: New Results

D.A. Serrano, A. Medina, G. Ruíz Chavarría and F. Sanchez Silva

Abstract Gravity granular flows of cohesionless materials emerging from bottom exits and from lateral exit holes, both in vertical bins, and from face walls in tilted bins were modeled and measured. The models are based on continuum mechanics, whereas friction and gravity are the main involved forces. Measurements of the granular mass flow rates were obtained from temporal measurements of weights by using force sensors. In vertical and tilted bins the face wall thicknesses were considered in the governing correlations. Measurements are in good agreement with the theoretical predictions.

1 Introduction

This article considers the granular counterpart of the Torricelli's theorem. Torricelli's theorem is a theorem in fluid dynamics relating the speed of fluid flowing, under the action of gravity, out of an opening to the height of fluid above the opening. Torricelli's law states that the speed of efflux, v, of a fluid through a sharp-edged hole at the bottom of a tank filled to a depth, h, is the same as the speed that a body (in this case a drop of water) would acquire if falling freely from a height h, i.e., $v = \sqrt{2gh}$, where g is the acceleration due to gravity (Fig. 1).

D.A. Serrano (✉) · F. Sanchez Silva
ESIME Zacatenco, Instituto Politécnico Nacional, 07738 México, D.F., México
e-mail: arman2390@hotmail.com

F. Sanchez Silva
e-mail: fsanchezs@ipn.mx

A. Medina
ESIME Azcapotzalco, Instituto Politécnico Nacional, 02250 México, D.F., México
e-mail: amedinao@ipn.mx

G. Ruíz Chavarría
Facultad de Ciencias UNAM, Ciudad Universitaria, 04510 México, D.F., México
e-mail: gruiz@unam.mx

J. Klapp et al. (eds.), *Selected Topics of Computational and Experimental Fluid Mechanics*, Environmental Science and Engineering,
DOI 10.1007/978-3-319-11487-3_9

Fig. 1 Frontispiece to "*Lezioni accademiche d'Evangelista Torricelli ...*", published in 1715 (http://www.photolib.noaa.gov/htmls/libr0366.htm)

This last expression comes from equating the kinetic energy gained by an element of mass m, $mv^2/2$, with the potential energy lost, mgh, and solving for v. The law was discovered (though not in this form) by the Italian scientist Evangelista Torricelli, in 1641. It was later shown to be a particular case of Bernoulli's principle.

Torricelli was Galileo's assistant and companion during the last two years of the elder scientist's life, and he succeeded Galileo in the post of grand ducal mathematician. In his *Opera Geometrica*, published at the expense of Grand-Duke Ferdinand II, Torricelli elucidated and diffused the difficult geometry of Cavalieri, thereby gaining himself widespread recognition throughout Europe. The first part, compiled around 1641, studies figures arising through rotation of a regular polygon inscribed in or circumscribed about a circle around one of its axes of symmetry. In the second section, *De moto gravium*, Torricelli continued Galileo's study of the parabolic motion of projectiles (Torricelli 1641). The treatise includes several significant contributions to mechanics, the calculus and ballistics. It also refers to the movement of water in a paragraph so important that Ernst Mach proclaimed Torricelli the founder of hydrodynamics.

Torricelli's law can be demonstrated in the spouting can experiment, which is designed to show that in a liquid with an open surface, pressure increases with depth. It consists of a tube with three separate holes and an open surface. The three holes are blocked, then the tube is filled with water. When it is full, the holes are unblocked. The jets become more powerful, the fluid exit's velocity is greater the further down the tube they are (Fig. 2a). Instead, in a bin filled with dry sand and having staggered holes of diameter D, the sand exit's velocity is the same and thus the shapes of the sand jets are similar between them (Fig. 2b).

In a container of vertical walls the pressure due to dry sand changes very slowly with height when the level of filling, respect to the bottom, overcomes a critical value, λ (Janssen 1895). This is the first hint that the sand jets must be very different respect

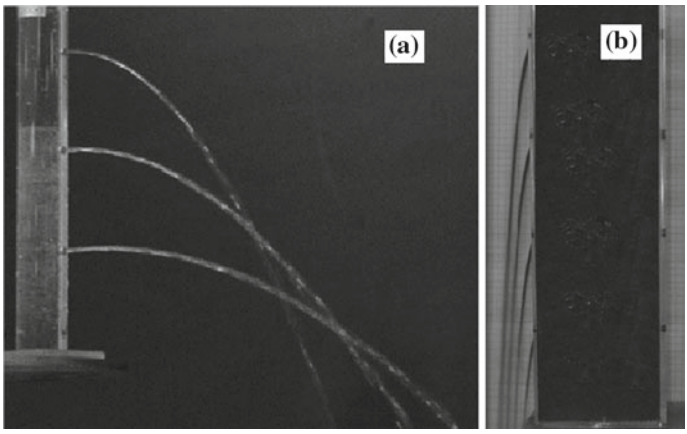

Fig. 2 Spouting can jets: **a** liquid and **b** non cohesive dry sand

to the liquid jets, another hint is that the wall thickness, w, affects a lot the intensity and shape of sand jets. In both cases the competition among the friction force and the gravity force will affect the pressure and the jet properties. This work is devoted to clarify the origin of these facts.

In order to reach our goal, the plan of the paper is as follows: in Sect. 2 we give a historical outline of the dry friction phenomenon, in a general context, and how it has been included in the theoretical treatments of confined granular material. In Sect. 3, we give a short review of the experimental studies of the gravity flows and mass flow rates when the orifices are made in lateral walls. We also describe some experiments where the influence of D, w and d, the grain diameter, are so important that they control the flow. In Sect. 4, we study tilted bins and we propose, on the basis of our experimental results, a correlation that embraces both changes in D and w and the tilt angle of the bins, β. In Sect. 5 we discuss some new results based on a modification to the Janssen law for the pressure in a bin and finally, in Sect. 6, we give the main conclusions of this work.

2 Dry Friction: A Historical Review

The late Egyptians were already occupied with the problem of friction. From historical traditions we know already that they wetted the sand on which they transported their stones. Today, we know that this reduces the friction coefficient.

The macroscopic friction laws, that we know, have been discovered during the last centuries, mainly by Leonardo da Vinci (1452–1519), Guillaume Amontons (1663–1705), Leonhard Euler (1707–1783) and Charles Augustin Coulomb (1736–1806).

Leonardo da Vinci (Fig. 3) postulated in the Codex Atlanticus (da Vinci 1480) that friction is proportional to load and independent of the area of the item being

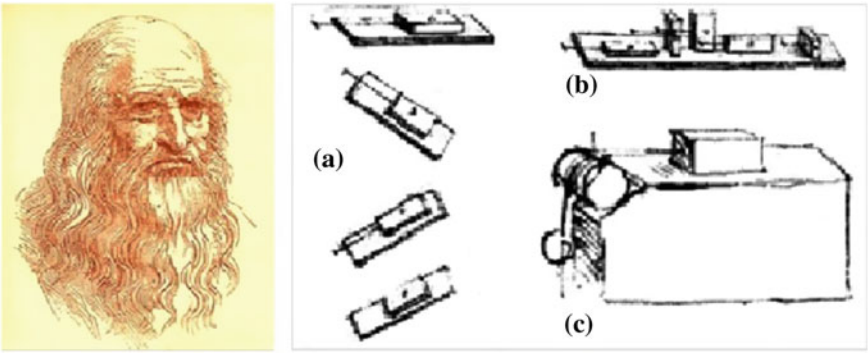

Fig. 3 *Left hand side* Leonardo's self-portrait. *Right hand side* sketches from da Vinci's notebook, ca. 1480 demonstrating some of his notable friction experiments (www.nano-world.org)

moved. Leonardo's experimental setup for macroscopic friction measurements was rather simple. He measured the angle of an inclined plane, where a body, put on the plane, started to slide and the weight needed to make a block on a table to move. With this method, he was only able to measure static friction and most probably he wasn't aware of the difference between static and kinetic friction. Leonardo found the following two laws of friction, in which we essentially recover friction laws 1 and 2:

Law 1. The friction made by the same weight will be of equal resistance at the beginning of its movement although the contact may be of different breadths and lengths.

Law 2. Friction produces twice the amount of effort if the weight be doubled.

Amontons (1699), a French physicist (Fig. 4), two centuries after Leonardo's discoveries, made experiments on a horizontal surface and measured the friction

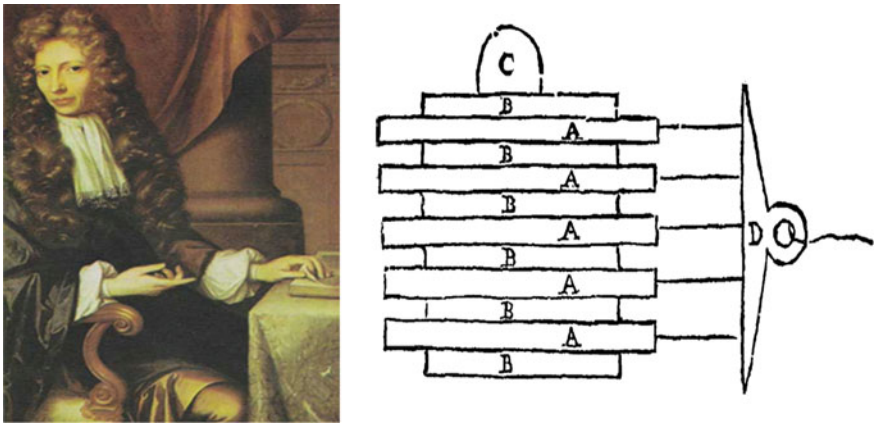

Fig. 4 *Left hand side* Guillaume Amontons. *Right hand side* Amontons' experiment on multiplied friction with overlapped *horizontal plates* (Amontons 1699)

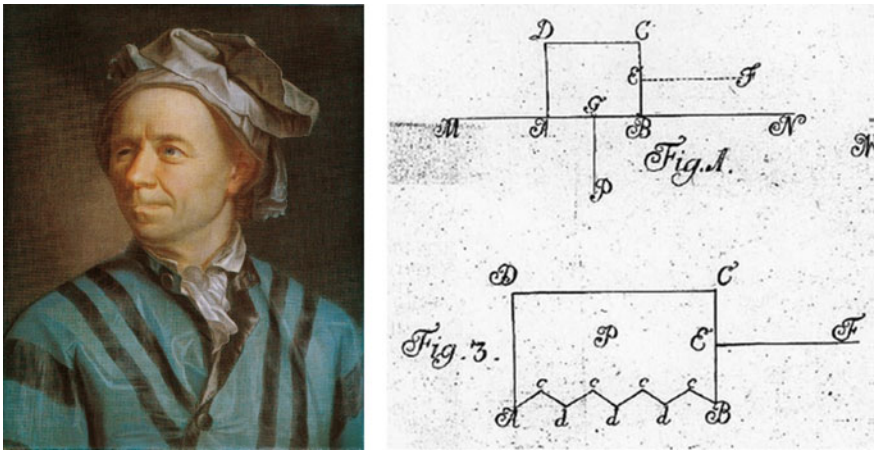

Fig. 5 *Left hand side* Leonhard Euler. *Right hand side* Euler's model of friction: a pair of hilly surfaces in a saw tooth pattern, which interlock perfectly. For one body to slide over the other, an oblique motion is required to surmount the asperities and a force F is needed. Figure taken from Euler (1748)

force with a spring. He found that friction is proportional to the normal force and independent on the area of contact. He called the proportional factor friction constant; erroneously, he believed in the existence of a universal friction coefficient. While Leonardo tested static friction, Amontons dealt with kinetic friction.

It was found by Leonhard Euler by 1748 (Fig. 5) that one has to distinguish between static and kinetic friction (Euler 1748). He studied theoretically the mechanism of the sliding motion of a block on an inclined plane. He adopted the model of rigid interlocking asperities as the cause of frictional resistance. He concluded that static friction is always larger than kinetic friction. With these assumptions he was able to describe analytically the motion of a block on an inclined plane.

In 1773, the third classic friction law came into being with Charles-Agustin Coulomb's research, which posited the theory that friction is independent of sliding speeds. Coulomb (Fig. 6) did the first attempts to develop some theories pertaining to design of foundations and other constructions. Coulomb formulated the theory of Earth pressure (Coulomb 1773). In this theory, Coulomb also introduced the concepts of frictional resistance and cohesive resistance for solid bodies, which he assumed to be applicable *to granular bodies*, including soils, which was intuitively used by Leonardo da Vinci three centuries before.

The macroscopic law of Leonardo appears to be a true paradox. Intuitively one would expect the friction force to be proportional to the area of contact. The paradox was resolved by Bowden and Tabor (1950), who gave a physical explanation for the laws of friction. They determined that the true area of contact is a very small percentage of the apparent contact area. The true contact area is formed by the asperities. As the normal force increases, more asperities come into contact and the average area of each asperity contact grows. The frictional force was shown to

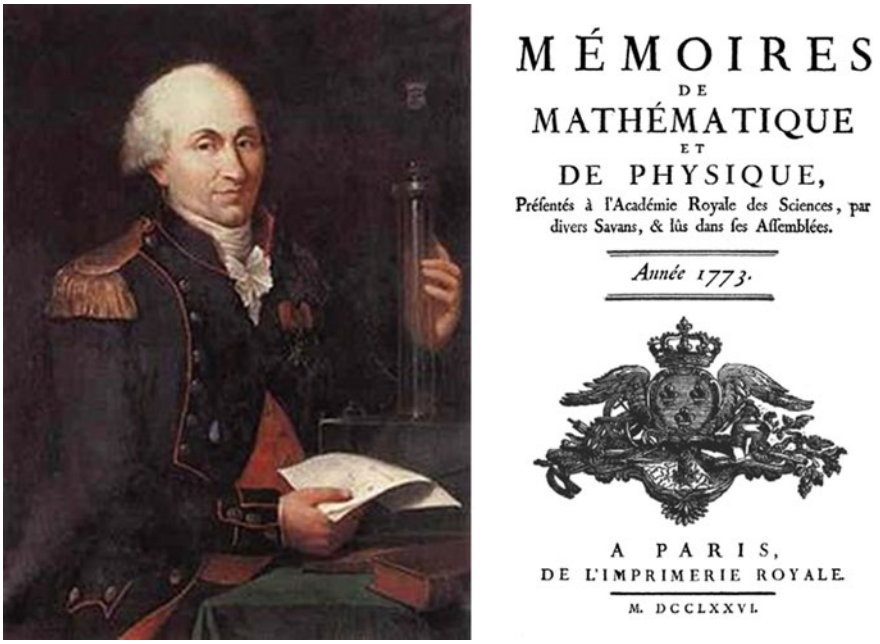

Fig. 6 *Left hand side* Charles-Agustin Coulomb. *Right hand side* Coulomb's publication by 1773

depend on the true contact area—a much more intuitively satisfying argument than what the Amontons-Coulomb law allows. Bowden and Tabor argued that within these asperities all of the dynamics of friction take place.

Despite the substantial advance of the inclusion of friction into granular material problems, the physics of friction processes still remains insufficiently clear because there still remain a lot of unsolved questions in problems such as wear and heating of materials in friction, the distribution of normal and tangential stresses in the contact region, plastic deformations, and the physical nature of frictional forces (molecular adhesion, hysteresis losses, losses in the case of surface layer failure, etc.) (See, for instance, Zhuravlev 2013).

3 The Mass Flow Rate Problem

The silo discharge through a bottom circular outlet, the granular analogous of the Torricelli's theorem, is one of the oldest and most widely studied problems in granular flow owing to the simple setup and geometry of the system (Brown and Richards 1970; Beverloo et al. 1961; Franklin and Johanson 1955; Hagen 1852; Wieghardt 1975). It has been extensively investigated both experimentally and computationally. Today, many granular, gravity flow theories use silo discharge as a benchmark for validation (Brown and Richards 1970). Conversely, the study of the mass flow rate

from orifices on side walls has been largely neglected and, to our knowledge, only a few works have been published (Bagrintsev and Koshkovskii 1977; Davies and Foye 1991; Davies and Desai 2008; Franklin and Johanson 1950; Sheldon and Durian 2010; Medina et al. 2013, 2014), perhaps due to the asymmetric flow profile which occurs close to the vertical wall. Despite it, the practical use of lateral outlets is also very frequent, for instance, in household silos.

In their seminal papers on the flow of granular solids through circular orifices at the bottom of silos, (Hagen 1852, see Fig. 7) and more than a century later, Beverloo et al. (1961) reported that the most suitable correlation to predict the mass flow rates, m_0', from bottom exits in open-top bins, silos and hoppers is the so called Hagen-Beverloo correlation, which has the form

$$m_0' = c\rho g^{1/2}(D - kd)^{5/2}, \tag{1}$$

where c is the dimensionless discharge coefficient, ρ is the bulk density of the granular material, g is the acceleration of gravity, k is a dimensionless constant with typical values $k \sim 1 - 2$ (Brown and Richards 1970; Beverloo et al. 1961; Wieghart 1975) and d is the mean grain diameter.

Equation (1) expresses that the mass flow rate, when grains are big, is reduced due to the effect of excluded volume. Conversely, when $D \gg d$ the term $(D - kd) \to D$ and thus the mass flow rate increases and does not involves the grain diameter.

On the other hand, despite the enormous utility of the granular flow on the side walls only a few studies have been conducted to test the validity of the Hagen-Beverloo correlation in such a configuration (Bagrintsev and Koshkovskii 1977; Davies and Foye 1991; Davies and Desai 2008; Franklin and Johanson 1950; Sheldon and Durian 2010).

Recently, in a couple of works (Medina et al. 2013, 2014), we derived a formula for the mass flow rate through orifices on side walls, m', that embraces the dependence on the orifice diameter D and the wall thickness w for granular solids in the limit

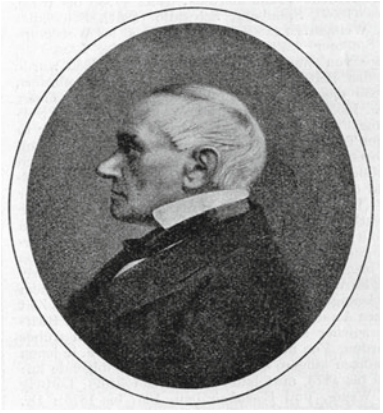

Fig. 7 G.H.L. Hagen (http://en.wikipedia.org/wiki/Gotthilf_Hagen)

where $D \gg d$. In this case, we performed experiments with sand and granulated sugar and we found that the mass flow rate m' obeys the relation

$$m' = c\rho g^{1/2} D^{5/2}[\arctan(D/w) - \theta_r] = c\rho g^{1/2} D^{5/2}[\alpha - \theta_r], \tag{2}$$

where now c is an effective dimensionless discharge coefficient for side wall flow, θ_r is the angle of repose of the granular material and $\alpha = \arctan(D/w)$ has been termed the *angle of wall* (Medina et al. 2013, 2014). Equation (2) implies that the wall thickness of the bin has an important influence on this gravity flow. Moreover, the frictional nature of the granular material is introduced through the angle of repose itself: in lateral outflows the flow will occurs if the orifice allows the existence of an angle of wall larger than the angle of repose (see Fig. 8).

By virtue of these facts it is clear that the wall thickness can be used to control the discharge rate and the granular flow can be eventually arrested if w exceeds a critical value which depends also on the angle of repose of the granular material. From Eq. (2) it is straightforward to estimate the critical value, w_c, for which the outflow will be arrested, i.e., there is no flow at all when $m' = 0$ or if $\alpha = \theta_r$. Thus, the critical value of w for the arrest, is

$$w_c = D/\tan\theta_r. \tag{3}$$

Experiments made with sand and granulated sugar (granular solids) confirm this result (Medina et al. 2013, 2014).

3.1 Mass Flow Rate for Large Grains Through Side Walls

Here we report experiments for non-cohesive granular materials made of grains with large diameters. Specifically, in the experiments we used mustard grains and tapioca pearls. Mustard has the following properties: mean diameter $d = 1.85\,\text{mm}$, bulk density $\rho = 0.72\,\text{gr/cm}^3$ and angle of repose $\theta_r = 22°$. Tapioca pearls have mean

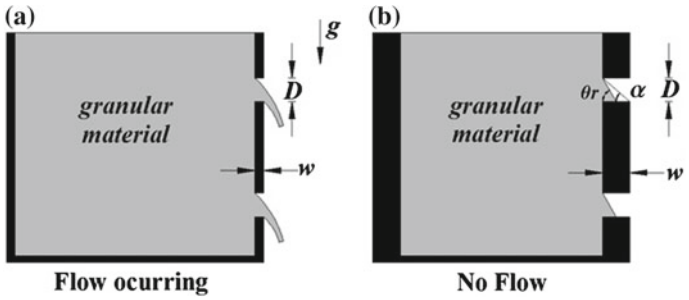

Fig. 8 Schematic view of the bin and holes in the side wall when granular material crosses it. In **a** the wall thickness, w, is small, consequently, $\alpha > \theta_r$ and the granular material will pass the orifice. In **b** the wall thickness produces the condition $\alpha < \theta_r$, whence there is no flow

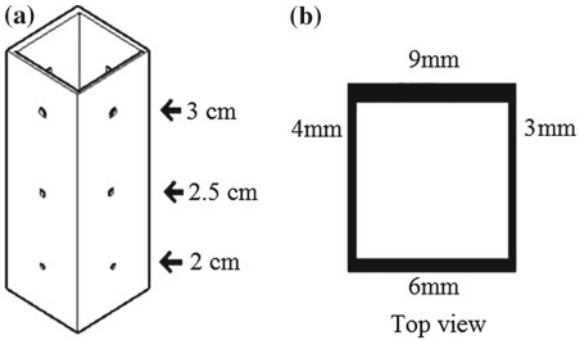

Fig. 9 **a** Scheme of a bin with staggered holes of different size D; **b** *Top view* of the bin showing the four different thicknesses of the face walls

diameter $d = 2.2\,\text{mm}$, bulk density $\rho = 0.57\,\text{gr/cm}^3$ and angle of repose $\theta_r = 27°$. Experiments were done in a temperature controlled room ($25 \pm 1\,°\text{C}$ and $45 \pm 10\,\%$ R.H.), upon a transparent, acrylic box, $10 \times 10\,\text{cm}$ inner cross-section and 50 cm height.

As it is sketched in Fig. 9, in the acrylic-made bin circular orifices of diameters $D = 2, 2.5$ and 3 cm were drilled. The wall thicknesses were $w = 0.3, 0.4, 0.6$ and 0.9 cm.

In Fig. 10 we show the corresponding particle size distributions which were determined by using a microscope software (Steindorff digital microscope) which allowed to find the surface area of each particle and its surface diameter. This method yields the average (median) particle sizes which were $d = 1.85\,\text{mm}$ for mustard and 2.2 mm for tapioca pearls.

Insets in each plot correspond to pictures of the respective granular materials.

In agreement with the experimental procedure established elsewhere (Medina et al. 2013, 2014) we need to measure the mass flow rate for exit holes at the bottom,

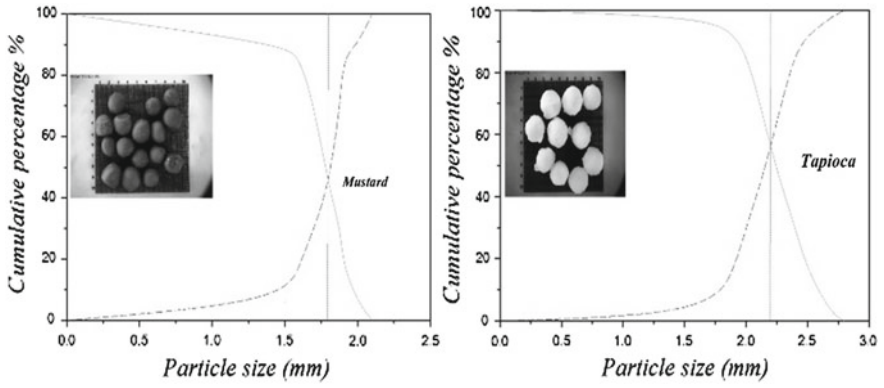

Fig. 10 Micrographs of the particle shapes of samples of mustard (*left-hand side*) and tapioca (*right-hand side*) used in our experiments

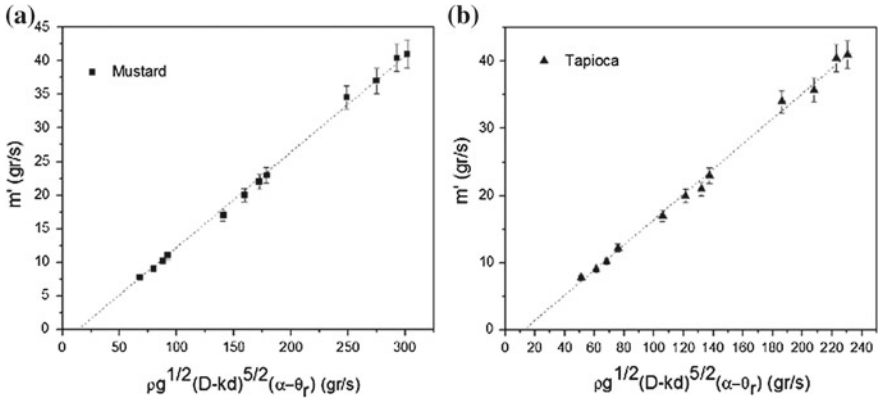

Fig. 11 Plot of the experimental mass flow rates through holes on side walls, m', as a function of $\rho g^{1/2}(D-kd)^{5/2}[\alpha-\theta_r]$. The linear fit given by Eq. (4) yields $c = 0.13$ for mustard and (a) $c = 0.15$ for tapioca (b). Error bars are of 4 %

m'_0. This procedure allows us to find that $m'_0 \sim \rho g^{1/2}(D-kd)^{5/2}$ for both types of grains. Moreover, we have found that $k = 1.5$ for mustard and $k = 1$ for tapioca.

Plots of the mass flow rates measured for holes on the side walls, m', as a function of $\rho g^{1/2}(D-kd)^{5/2}$, $[\arctan(D/w)-\theta_r]$ show that the experimental data for both granular materials were well fitted by straight lines (see Fig. 11). So, the best relation that fits the experimental data has the form

$$m' = c\rho g^{1/2}(D-kd)^{5/2}[\arctan(D/w)-\theta_r], \tag{4}$$

where the dimensionless discharge coefficient c has the value $c = 0.13$ for mustard and $c = 0.15$ for tapioca.

From these results, we can establish that Eq. (4) is a generalized Hagen-Beverloo law for the mass flow rate of holes on the side walls. Incidentally, by employing the several values of D used in the experiments with mustard and tapioca and using their respective angles of repose, we have verified that relation (4) predicts very accurately the thicknesses of the walls for which the outflow will be arrested.

4 Tilted Bins

4.1 The Problem

Here we report a series of experiments of the discharge for tilted bins. Bins with orifices in a side face of a rectangular acrylic-box were gradually inclined from the horizontal position up to the position where the granular flow is arrested in order to

quantify the dependence of the mass flow rate on β, the angle of tilt. To our knowledge, investigations of this character are very scarce. Franklin and Johanson (1950) studied systematically the effect of the inclination on the flow rate by taking into account the horizontal and vertical cases and two other intermediate angles. Later, Sheldon and Durian Sheldon and Durian (2010) reported similar studies where the Franklin and Johanson's correlation was maintained. Here, we consider the fact that the bin walls have a finite thickness, and as a consequence this will bias the determination of the mass flow rate at a given angle β.

In summary, we will contrast through experiments the new findings for the flow rate in tilted bins with those recently published by other authors (Sheldon and Durian 2010; Liu 2014). A general correlation valid for the angles of inclination will not be reached, but, instead solid arguments related to the flow occurrence will be featured.

4.2 The Franklin and Johanson Formula

Near 60 years ago, Franklin and Johanson (1950) established, by using a logical reasoning, that the mass flow rate from an inclined, circular orifice at an angle θ with the horizontal, is given by the relation

$$m'_\theta = m'_0 \left(\frac{\cos\theta_r + \cos\theta}{\cos\theta_r + 1} \right), \tag{5}$$

where θ is measured counterclockwise, θ_r is the angle of repose and m' is the flow rate through a horizontal orifice, which essentially is given by the Hagen's law

$$m'_0 = a\rho g^{1/2} D^{5/2}, \tag{6}$$

where a is the discharge coefficient.

From Eq. (5) it is clear that if $\theta = 0, m'_\theta = m'_0$, meanwhile if $\theta = \pi - \theta r$ then $m'_\theta = 0$. When $\theta = \pi/2$ Eq. (6) suggests that the flow rate for the vertical case is directly obtained from the flow rate in the horizontal case by simply using the multiplying factor $cos\theta_r/(cos\theta_r + 1)$. As mentioned above, this result is not correct because in the vertical case the wall thickness determines the existence of the flow, even for the ideal case where the wall thickness is zero (sharp-edge hole). As was mentioned previously, in our formula we have that $\alpha = \pi/2$ and consequently, $m' = m'_0(\pi/2 - \theta_r)$ which fit the experimental data very well. Thus, a correct correlation for the flow rate among the horizontal and the vertical cases must include information about the wall thickness.

In order to derive a correct formula valid for a wide range of tilt angles we have performed a set of experiments that also involve changes in D, w and θ_r. We describe such experiments in the next section (Fig. 12).

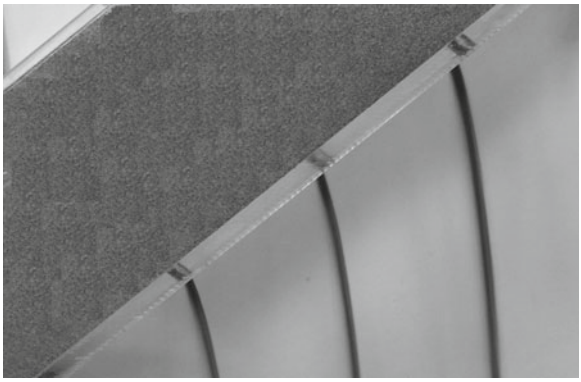

Fig. 12 Picture of sand jets emerging from a tilted bin

4.3 Experiments

In this work, the simultaneous effects of D, w, β and θ_r on the mass flow rate are examined. As in our previous studies (Medina et al. 2013, 2014) here we employ well characterized dry and non cohesive materials like sand beach (composed of irregular grains of mean diameter $d = 0.03$ cm, bulk density $\rho = 1.5 \pm 0.01$ gr/cm^3 and angle of repose $\theta_r = 33° \pm 0.5° = 0.57 \pm 0.008$ rad) and granulated sugar (mean diameter $d = 0.073$ cm, bulk density $\rho = 0.84 \pm 0.01$ g/cm^3 and angle of repose $\theta_r = 33.5° \pm 0.5° = 0.58 \pm 0.008$ rad). These materials are made to emerge from circular orifices of diameters $D = 0.9$, 1 and 2 cm made on the side faces of an acrylic-made box having walls with $w = 0.3$ and 0.9 cm. The experiments were carried out in a temperature controlled laboratory (25 ± 1 °C and 45 ± 10 % R.H.).

Experiments were performed using a transparent box, 10×10 cm^2 inner cross-section and 50 cm height. Four different face-wall-thicknesses were used: $w = 0.3$, 0.4, 0.6 and 0.9 cm. A schematic of the experimental setup is given in Fig. 13 where

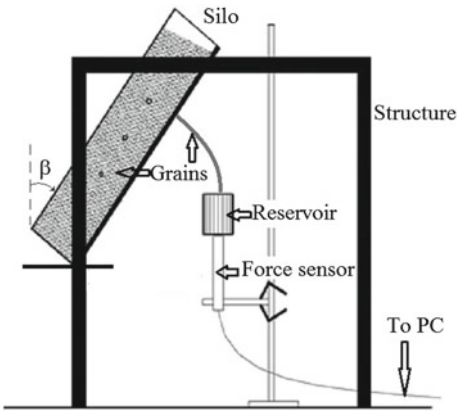

Fig. 13 Scheme of the experimental setup

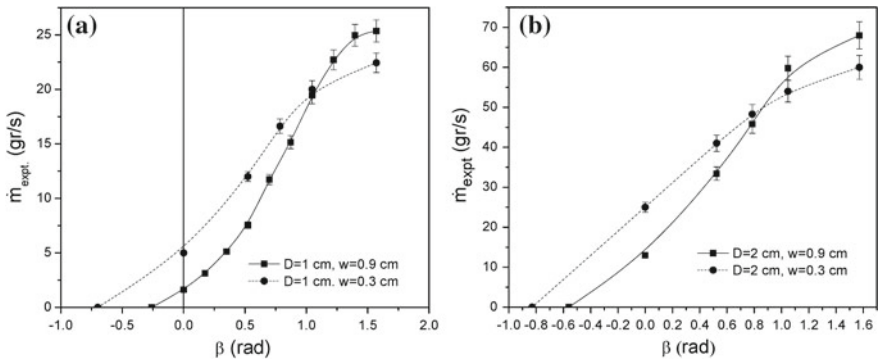

Fig. 14 Plot of the measured mass flow rates in tilted bins, $m'_{\beta expt}$, as a function of the tilt angle, β, through circular orifices. In **a** we use sand and orifices of diameter $D = 1\,\text{cm}$ and face walls of thicknesses $w = 0.3\,\text{cm}$ and $w = 0.9\,\text{cm}$ to notice the effect of w. In **b** granulated sugar were employed and in this case we used holes of diameter $D = 2\,\text{cm}$. Lines connecting the data were draw for visual facility, error bars are of 4 %

the bin is tilted up to the desired angle β with the vertical (measured clockwise), the granular jet emerging perpendicular to the face wall is gather into a reservoir fixed to a digital force sensor. Details of the measurement procedure of the discharge rates with a force sensor model Pasco CI-6537 are given elsewhere (Medina et al. 2014). In the current experiments we found that the wall friction coefficient among granulated sugar and acrylic was $\mu_w = 0.70 \pm 0.01$, while among sand beach and acrylic it was $\mu_w = 0.80 \pm 0.01$.

At a first stage, the mass flow rates for a given angle β were measured for face walls having wall thicknesses with values $w = 0.3$ and $0.9\,\text{cm}$. For each face wall several circular orifices were drilled. In Fig. 14 we show the experimental values of $m'_{\beta expt}$, as a function of β, for both materials which show a sine-like behavior. It is important to comment that the flows of sand and sugar were arrested at different critical inclination angles, β^*, for sand: $\beta^* = -0.26\,\text{rad}$ if $D = 1\,\text{cm}$ and $w = 0.9\,\text{cm}$, while $\beta^* = -0.76\,\text{rad}$ if $D = 1\,\text{cm}$ and $w = 0.3\,\text{cm}$. For sugar $\beta^* = -0.57\,\text{rad}$ if $D = 2\,\text{cm}$ and $w = 0.9\,\text{cm}$ and $\beta^* = -0.83$ if $D = 2\,\text{cm}$ and $w = 0.3\,\text{cm}$. Another important physical fact in this figure is that for the same orifice size but large tilt angles β the flow rate is stronger in the orifices of larger thickness!

4.4 The Formulation of a Correlation

The search of a general correlation that embraces the dependence of the flow rate m'_β on D, w and β deserves a careful analysis. At a first glance it is easy to conclude that if the vertical wall is considerably thick, there will be no efflux of granular material through the orifices. Thus, the influence of the wall thickness, w, must be present wherever the granular flow occurs. Here we introduce a correlation that is

valid for a wide range of values of β, including the cases $\beta = 0$ (vertical orifices) and $\beta = \beta^*$ (the critical negative inclination when the flow is arrested). Moreover, it must be valid for the vertical case and it will be a sine-like function to take into account the experimental behavior given in the previous section. Therefore, we propose that

$$m'_\beta = c\dot{m}_0 \left(\beta + \alpha - \theta_r\right) \frac{\sin\left(\beta + \alpha - \theta_r\right)}{\sin\left(\alpha - \theta_r\right)}, \tag{7}$$

which yields

$$m'_\beta = 0, \quad \text{if} \quad \beta = -(\alpha - \theta_r), \tag{8}$$

when the flow is arrested, and

$$m'_{\beta=0} = \mathrm{cm}'_0 \left(\alpha - \theta_r\right), \quad \text{if} \quad \beta = 0, \tag{9}$$

which is a general correlation valid for the vertical cases (Medina et al. 2013, 2014).

In order to show that Eq. (7) gives a correct correlation for circular orifices, we display in Fig. 14 the experimental flow rates, $m'_{\beta expt}$, versus the theoretically predicted, $m'_{\beta T}$, given by Eq. (7). From Fig. 14 we see that straight lines fit very well the experimental data obtained when the bin is gradually tilted.

In our experiments with sand we found that the value of c was $c = 0.070 \pm 0.002$ if $D = 0.9\,\mathrm{cm}$ and $w = 0.9\,\mathrm{cm}$, i.e., with a wall angle $\alpha = 0.57\,\mathrm{rad}$; if $D = 1\,\mathrm{cm}$ and $w = 0.9\,\mathrm{cm}$, then $\alpha = 0.83\,\mathrm{rad}$ and we have that $c = 0.083 \pm 0.002$. For sugar $c = 0.066 \pm 0.002$ if $D = 0.9\,\mathrm{cm}$ and $w = 0.9\,\mathrm{cm}$; if $D = 1\,\mathrm{cm}$ and $w = 0.9\,\mathrm{cm}$ we have that $c = 0.083 \pm 0.002$ and finally, $c = 0.127 \pm 0.002$ if $D = 2\,\mathrm{cm}$, $w = 0.9\,\mathrm{cm}$ and $\alpha = 1.15$.

Actually, we found that m'_β as given by Eq. (7) reaches a maximum value and then decreases. So, this theoretical formula is not valid in a region close to $\beta \to \pi/2$. To estimate such a value, we compute $dm'_\beta/d\beta$. It yields that

$$\beta + \alpha - \theta_r = -\tan\left[\beta + \alpha - \theta_r\right]. \tag{10}$$

Consequently, to get the maximum value β_m we need to solve the transcendental equation $x = -tanx$, where $x = \beta_m + \alpha - \theta_r$. Whence the general solution of Eq. (10) is

$$\beta_m = 2.028 - (\alpha - \theta_r), \tag{11}$$

where the value 2.028 is correct up to a numerical precision of 10^{-13}. Thus, for each couple of values (α, β) we get a value of β_m, where the maximum occurs. This criterion was used to build the plots in Fig. 15. Finally, we note that this formula is worst if α is large. Incidentally, we have plotted in Fig. 16 $m'_{\beta T}$, given by Eq. (7), as a function of β in order to show that this later plot is similar to the plots in Fig. 14.

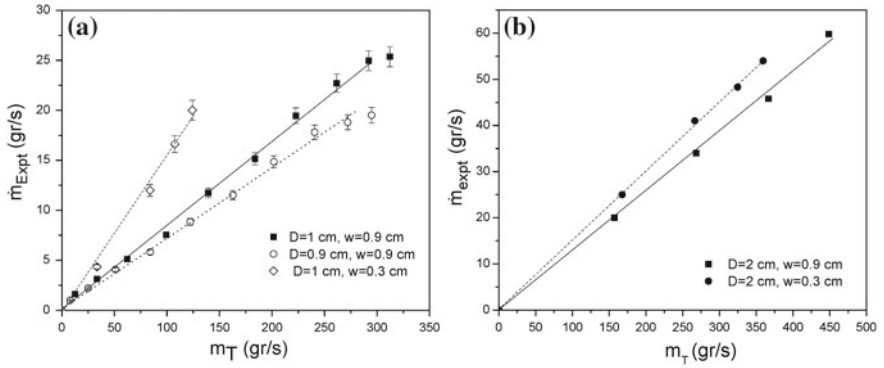

Fig. 15 Plots of the experimental mass flow rates: **a** for sand beach and **b** for granulated sugar

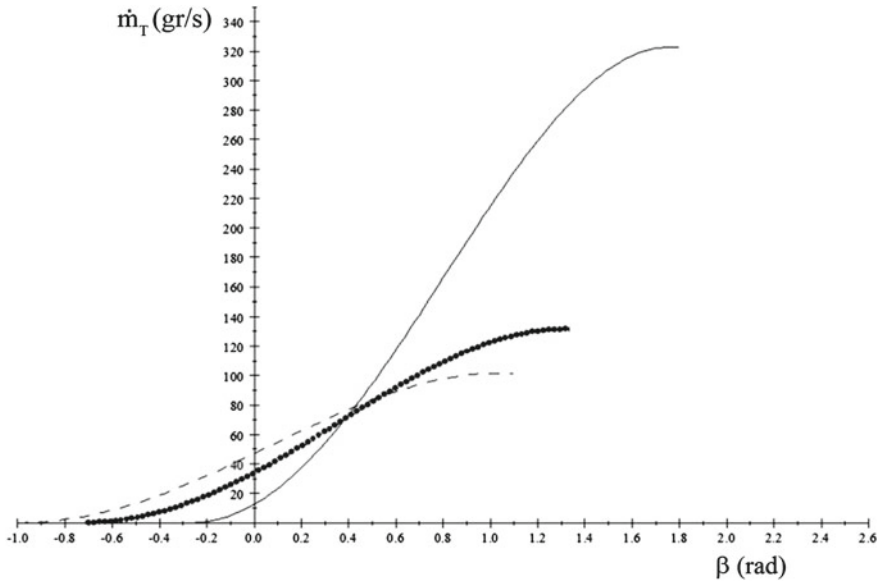

Fig. 16 Plot of Eq. (2) by using data from our experiments

5 Pressures in a Silo

As it was mentioned before, pressures in quiescent liquids (White 1994) and in non-cohesive granular materials at rest (Janssen 1895) are quite different among them. Consider a vertical cylindrical container filled with a granular material. The vertical pressure on a horizontal plane at a certain depth below the surface of the material does not increase linearly with depth, as it would be for a normal liquid. Instead, the Janssen's model predicts that this pressure tends to a constant value independently

of depth. The origin of this behavior is in the static friction between the grains and the walls of the container. Due to this friction, the container walls can support part of the weight of the material.

The validity and possible shortcomings of the simple theory underlying the original Janssen model have been extensively tested experimentally and numerically. Janssen himself carried out experiments to measure the pressure on the base of a silo, and apparently found good agreement with his theoretical results. However, careful laboratory observations have revealed serious difficulties in the measurements of this vertical pressure, with the results depending on the method of filling and even on the jamming of the displacement of the piston employed to measure the pressure. Precise and reproducible pressure profiles have been measured in some carefully designed experiments, and molecular dynamics simulations which rely on the notion that the grains have settled to a final state (Landry et al. 2003) have reproduced these measurements. A comparison shows that the predictions of Janssen model are reasonably good for most of the granular material but degrade in a region around the top of the column where the pressure varies nearly linearly with vertical distance. This discrepancy has led to modifications of Janssen's model. Among these, a two-parameter modification, which suppresses friction with the wall in an upper slice of the column, improves the agreement with the experimental and numerical vertical pressure profiles in that region.

Here we explore the main changes between the pressure distributions and traction forces due to the use of Janssen's model and the modified Janssen's model. In a recent work we have shown that the measurements of the traction force that the granular material exerts on the wall overcomes the difficulties often encountered in the direct measurements of the vertical pressure on a piston, which are due to jamming of the piston displacement induced by the compression force. Measurements of the traction force give further evidence of the existence of a region not predicted by the original Janssen model.

5.1 Calculation of the Pressure and Traction Force in the Silo

Consider a cylindrical vertical tube of radius r_0 filled with a dry granular material to a certain height H. Take a horizontal section of the tube at a depth z in the granular material. According to Janssen's model, the force exerted per unit area of this section by the material above it on the material below is a vertical pressure $p_z(z)$. This pressure is not equal to the horizontal pressure $p_r(z)$ of the material on the wall of the tube at the same depth, but the two pressures are linearly related by Janssen (1895)

$$p_r(z) = K p_z(z), \tag{12}$$

where K, called the Janssen parameter, is a dimensionless constant that characterizes the conversion of vertical stress into horizontal stress within the granulate.

The horizontal pressure acting on the wall of the tube causes a vertical friction stress τ between the wall and the granular material. A simple balance of the vertical forces acting on a slab of the granular material gives

$$\pi r_0^2 \frac{dp_z}{dz} = \pi r_0^2 \rho g - 2\pi r_0 \tau, \tag{13}$$

where ρ is the bulk density of the granular material, assumed to be independent of z. In the original Janssen's model, the vertical friction stress is assumed to be given by Coulomb's law, $\tau = \mu_w p_r$, with a constant static wall friction coefficient μ_w. The solution of Eq. (13) with the condition $p_z(0) = 0$ is then

$$p_z(z) = P_J(z), \tag{14}$$

with

$$P_J(z) = \rho g \lambda \left[1 - \exp\left(-\frac{z}{\lambda}\right)\right] \quad \text{and} \quad \lambda = \frac{r_0}{2\mu_w K}. \tag{15}$$

Equation (15) shows that the vertical pressure increases linearly with z, as $p_z(z) \approx \rho g z$, for $z/\lambda \ll 1$ and tends to the limiting value $\lambda \rho g$ for $z/\lambda \gg 1$. The length λ is the characteristic size of the region where the pressure undergoes this transition. In laboratory columns $\lambda \approx 0.1$ m, and so the wall of the container supports most of the weight of the grains when $H \gg 1$ m.

As it was modified above, the two-parameter model suppresses friction with the wall in a slice at the top of the column by making $\tau = 0$ for $z < a$ and $\tau = \mu_w p_r$ for $z > a$, where a, the thickness of the frictionless slice, is the second parameter of the model. The solution of Eq. (13) is then

$$p_z(z) = \begin{cases} \rho g z \text{ for } z < a \\ \rho g a + \left(1 - \frac{a}{\lambda}\right) P_J(z - a) \text{ for } z > a. \end{cases} \tag{16}$$

The vertical shear stress $\tau(z)$ causes an additional deformation of the wall of a tube filled with granular material. The maximum vertical force acting on the wall of a tube filled to a height H is

$$T(H) = 2\pi r_0 \int_0^H \tau(z) dz = T_J(H), \tag{17}$$

with

$$T_J(H) = \pi r_0^2 \rho g \left\{ H - \lambda \left[1 - \exp\left(-\frac{H}{\lambda}\right)\right]\right\}. \tag{18}$$

The experimental test of the previous equations will be left for future work.

6 Conclusions

In this work we have studied experimentally the problem of the mass flow rate of granular material through circular orifices on vertical side walls of bins as a small step toward understanding grains flowability. We have shown that friction (the angle of repose) plays an essential role in all these cases through the existence of a limit of flowability. In a first case, we have studied, simultaneously, the dependence of m' on the diameter of the orifice, the grain's diameter and the wall thickness by using, well characterized, round grains of mustard and tapioca. Experiments show that the excluded volume effect occurs for big grains through the term $(D - kd_g)^{5/2}$. Thus the estimation of the mass flow rate for holes on side walls satisfies, very accurately, the formula $m' = c\rho g^{1/2}(D - kd)^{5/2}[\arctan(D/w) - \theta_r]$, where in our experiments the dimensionless discharge coefficient has the value $c \sim 0.1$, when the cgs units are used. Thus, we believe that Eq. (4) is a general formula valid in a wide range of practical configurations.

In a second case we have studied experimentally the problem of the mass flow rate of granular material through circular orifices in tilted bins. Our new correlation Eq. (7) takes into account the wall thickness which other models consider as obvious (Franklin and Johanson 1955; Sheldon and Durian 2010; Liu 2014). Consequently, we have proposed a new correlation that predicts the value for which the flow is arrested $\beta^* = -(\alpha - \theta_r)$, and it reduces to Eq. (9) when $\beta = 0$. Moreover, the current model is correct up to a value close to $\pi/2$. The theory fits pretty well the experimental data for a wide range of cases. Finally, we hope the new predictions of our modified Janssen model of pressures and traction can be experimentally corroborated soon.

Acknowledgments Authors wish to thank the support by Facultad de Ciencias UNAM and by SIP IPN through the project 20141404.

References

Amontons G (1699) De la Résistance Causée Dans les Machines. Mem Acad Roy Sci 206–222

Bagrintsev II, Koshkovskii SS (1977) Investigation of the outflow of granular materials through openings in the wall of a vertical cylindrical tube. J Chem Pet Eng 6:503–505

Beverloo WA, Leniger HA, van de Velde J (1961) The flow of granular solids through orifices. Chem Eng Sci 15:260–269

Bowden FP, Tabor D (1950) The friction and lubrication of solids. Oxford University Press, Oxford

Brown RL, Richards JC (1970) Principles of powder mechanics. Pergamon, New York

Coulomb CA (1773) Memoires de Mathématiques et de Physique Présentés a l'Académie Royale des Sciences par Divers Sávants et lus dens les Assemble. L'Imprimerie Royale, Paris, pp 343–382

Davies CE, Foye J (1991) Flow of granular material through vertical slots. Trans Inst Chem Eng 69:369–373

Davies CE, Desai M (2008) Blockage in vertical slots: experimental measurement of minimum slot width for a variety of granular materials. Powder Technol 183:436–440

da Vinci L (1480) Circa Il codice Atlantico di Leonardo da Vinci nella Biblioteca Ambrosiana di Milano

Euler L (1748) Sur la Diminution de la Résistance du Frottement. Histoire de l'Académie Royale des Sciences et Belles-Lettres de Berlin 4:133–148
Franklin FC, Johanson LN (1955) Flow of granular material through a circular orifice. Chem Eng Sci 4:119–129
Hagen GH (1852) Aber den Druck und die Bewegung des trocknen Sandes. Bericht uber die zur Bekanntmachung geeigneten Verhandlungen der Koniglich Preussischen Akademie der Wissenschaften zu Berlin 35:35–42
Janssen HA (1895) Versuche über Getreidedruck in Silozellen [On the measurement of pressures in grain silos] Zeitschr. d. Vereines deutcher Ingenieure 39:1045–1049
Landry JW, Grest GS, Silbert LE, Plimpton SJ (2003) Confined granular packings: structure, stress, and force. Phys Rev E 67:041303-1–041303-9
Liu Y (2014) The theoretical calculation of the flow rate of granular matter from an inclined orifice. Granul Matter 16:133–139
Medina A, Serrano DA, Gutiérrez GJ, Kesava Rao K, Vargas CA (2013) On the mass flow rate in silos with lateral exit holes. Rev Mex Fis 59:287–291
Medina A, Cabrera D, López-Villa A, Pliego M (2014) Discharge rates of dry granular material from bins with lateral exit holes. Powder Technol 253:270–275
Sheldon HG, Durian DJ (2010) Granular discharge and clogging for tilted hoppers. Granul Matter 12:579–585
Torricelli E (1641) Opera Geometrica. Downloaded from https://archive.org/details/operageometrica00torrgoog
Wieghardt K (1975) Experiments in granular flow. Annu Rev Fluid Mech 7:89–114
White FM (1994) Fluid mechanics, 3rd edn. McGraw-Hill, New York
Zhuravlev VPh (2013) On the history of the dry friction law. Mech Solids 48:364–369

Some Aspects of Turbulence Role in Oceanic Currents

A. Ruiz Angulo

Abstract This manuscript is intended to review some of the methods used to estimate one of the most useful parameters in Ocean Modeling: the diapycnal diffusivity. Specifically it focus on simultaneous measurements carried out at two different locations in the deep ocean. The techniques reviewed here to estimate diapycnal mixing in the ocean interior are: tracer-release experiments, microstructure direct measurements and fine-structure estimates based on LADCP/CTD data. There are only few data sets in the world that have simultaneous measurements of the three techniques mentioned above. The importance of the lack of spatial and temporal estimates of the turbulent mixing parameters and the implication of those parameters on modeling the Global Circulation are also reviewed.

1 Introduction

The Global Ocean Circulation is a vastly studied topic and yet several aspects remain uncovered. The big picture of the General Ocean Circulation is captured by the relatively recent concept of Thermohaline Circulation or Conveyor Belt (Gordon 1986; Broecker 1987b; Rahmstorf 2003). From this point of view, the main oceanic currents follow large scale trajectories; however, those main streams derivate into a very large number of smaller circulation trajectories. Some of those small deviations from the big picture are completely unpredictable. Thus, despite the fact that the large picture of the Ocean Circulation can be captured on a closed and relatively stable system, to complete the picture it is necessary to include the small scales along with their turbulent nature.

The resolution of the General Circulation Models (GCM) does not, until now, resolve turbulent mixing (Baumert and Peters 2009); therefore, the governing equations used by the models need to parametrize the turbulence. This manuscript mainly

A. Ruiz Angulo (✉)
Centro de Ciencias de la Atmósfera, Universidad Nacional Autónoma de México, Mexico city, México
e-mail: angel@atmosfera.unam.mx

J. Klapp et al. (eds.), *Selected Topics of Computational and Experimental Fluid Mechanics*, Environmental Science and Engineering,
DOI 10.1007/978-3-319-11487-3_10

focuses on the vertical turbulent diffusivity parameter, which is often related with the diapycnal mixing. In the ocean the vertical stratification is much larger than the horizontal stratification. The diapycnal mixing is a mechanical process, which allows water parcels to cross an isopycnal surface (surface of same density) and mix with adjacent water masses. This parameter can be estimated either using direct measurements or by an estimation technique known as "fine-structure parametrization". Additionally, a third method, tracer release experiments, allows to estimate both horizontal and vertical diffusivities. In the following sections those techniques will be briefly described and compared in two simultaneous experiments that have been carried out with the participation of the author.

The first two methods provide only snapshots at single points (stations), which are not completely representative neither for the spatial nor for the temporal variability. This issue jeopardizes the observations as very long term time series covering large areas in the interior of the ocean are required and this is rather impossible. Therefore, there are big efforts on developing proper parametrizations of the small scale variables, which could be measured in situ, to be integrated into the GCM's. The third method, tracer release experiment, provides temporally and spatially integrated effects of turbulence, but the method is constrained to be within few density levels from the injection point, which does not represent the entire water column.

This manuscript points out the importance of the topography of the seafloor (e.g. sea mounts, submarine canyons, ridges, etc.), which in certain cases constitute "hotspots" for high values of diapycnal mixing. In order to close the global overturning circulation, numerically, there is a deficit of diapycnal mixing (missing mixing). Thus, to properly model the general circulation it is necessary to have larger datasets of those turbulent coefficients to be integrated into the models. Observational evidence suggests that the diapycnal mixing spans a range of average diapycnal diffusivity values from $0.1\,\mathrm{cm}^2\ \mathrm{s}^{-1}$ on the open-ocean with smooth abyssal plains to $10\,\mathrm{cm}^2\ \mathrm{s}^{-1}$ for the rough topography (Polzin et al. 1997; Thurnherr et al. 2005). The importance of proper diapycnal mixing parametrizations is not only global, which has evidently great importance on Climate modeling; regionally, modeling the dispersion of contaminants such as oil spills requires the access of those parameters for proper implementations.

1.1 Ocean General Circulation

The main concept of the Ocean Circulation was first published in the late 80's by Gordon (1986) and Broecker (1987b). Remarkably both authors came up to similar conclusions based on very different methods. The first sketches of this patterns are shown in Fig. 1. Although the thermohaline circulation, THC, has been modified from its first sketches, the main concept has not changed much. The THC is driven by density differences, the water density of the ocean is a function of temperature (T), salinity (S) and pressure (p) $\rho = \rho(S, T, p)$. The result is explained from the intense upper currents in the Atlantic "... when these waters reach the vicinity of Iceland,

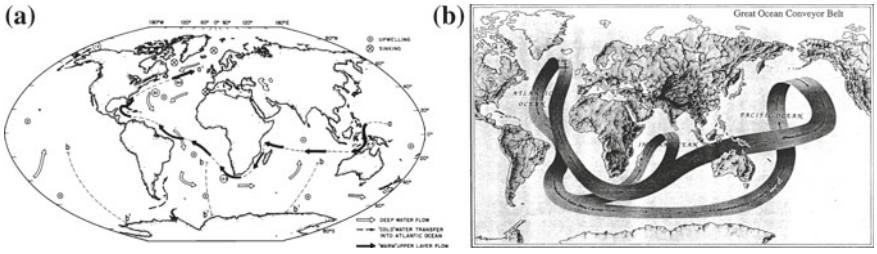

Fig. 1 The Ocean General Circulation as first depicted by Gordon (1986) (**a**) and Broecker (1987b) (**b**). Both figures show where the deep and cold water sink and the regions where those upwell

they are cooled by the cold winter air that streams off Canada and Greenland. These waters, which arrive at 12–13 °C, are cooled to 2–4 °C. The Atlantic is a particularly salty ocean, so this cooling increases the density of the surface waters to the point where they can sink all the way to the bottom. The majority of this water flows southward, and much of it rounds Africa, joining the Southern Ocean's circumpolar current" (Broecker 1991).

Based on those early studies, the big picture of the circulation was driven by the cooling at high latitudes. Recent studies have shown that the Southern Ocean is more relevant for the closure of the Meridional Circulation (Marshall and Speer 2012). Nevertheless, the small scale mixing is an important quantity that needs to be properly parametrized to be included in the General Circulation Models, as it has a huge impact on the Climate (Broecker 1987a; Rahmstorf 2003).

1.2 Turbulence in the Ocean

In general, turbulence is a concept which is rather hard to define. In this manuscript turbulence intensity is defined as the rate at which energy is being transferred from large scale features to smaller scales. From the classical fluid dynamics point of view, most of the processes in the ocean are turbulent (large Reynolds numbers). The turbulent parameters that are covered in this text are an effective diffusivity which includes the parametrization of turbulence and is used on the GCM's. There are several assumptions which will not be covered but one of the most important is that the diapycnal mixing is the same for density, temperature and salinity, i.e., $K_\rho = K_T = K_S$. The turbulent intensity is high enough to neglect the differential diffusivity (Ruiz-Angulo 2007). The turbulent diffusivity, K, in the interior of the ocean is of the order of $\sim 10^{-5}\,\mathrm{m}^2/\mathrm{s}$. This quantity is inferred from the dissipation rate of turbulent kinetic energy, ε, following the Osborn relationship (Osborn 1980): $K = \Gamma \frac{\varepsilon}{N^2}$, where Γ is the mixing efficiency and N^2 is the Brunt-Väisälä frequency, defined as:

$$N^2 = -\frac{g}{\rho_0}\frac{\partial \rho}{\partial z}, \tag{1}$$

where g is the acceleration due to gravity, ρ_0 is a reference density and $\frac{\partial \rho}{\partial z}$ is the vertical density gradient. In order to break a stable stratification or mix water masses, it is required to input some energy into the system. In the absence of statically unstable patches in the water column, the energy comes from the vertical shear of the horizontal velocity components as a shear instability mechanism as a source of turbulence. The total vertical shear is defined as:

$$S = \left[\left(\frac{\partial U}{\partial z}\right)^2 + \left(\frac{\partial V}{\partial z}\right)^2\right]^{1/2}. \tag{2}$$

The ratio of them is known as Richardson number, $Ri = \frac{N^2}{S^2}$, which is the ratio of the oscillation characteristic time of a water parcel and the vertical shear characteristic time. These two terms are constantly competing in the interior of the ocean; Ri defines the onset of instability, which locally leads to mixing. Theoretically, it could be shown that $Ri < 0.25$ is the necessary condition for the vertical shear characteristic time to overcome the Brunt-Väisälä oscillation characteristic time so that turbulent mixing is expected to occur. This onset could be reached by different ways. One of the mechanisms that has been proposed in later years is produced by the interaction of Internal Gravity Waves, which are ubiquitous in the oceans interior. The interaction between hydrodynamic processes (barotropic tides) and the ocean floor topographic features such as sea mounts, ridges, submarine canyons, etc., enhance turbulent mixing (Toole et al. 1997; Kunze et al. 2006). Internal wave driven by mixing is the basis of the parametrizations that will be discussed in this paper. In particular, "fine-structure parametrization" method is based on wave-wave interactions.

2 In-Situ Measurements

The diapycnal mixing estimates are obtained based on several measurements. This manuscript briefly explains "fine-structure", "microstructure" and tracer release experiments. All of them have shown that there is evidence of high mixing rates over rough topography (Ledwell et al. 2000; Kunze et al. 2006). The two regions presented in this manuscript are unique in the sense that they have experienced almost simultaneously all three methods. Figure 2 shows the regions where the measurements were taken.

The temporal and spatial scales for both projects are quite different. However, they were some of the first experiments used to compare and validate the existing techniques to estimate diapycnal mixing rates. The next section will discuss the different methods and the results of them will be addressed in the discussion.

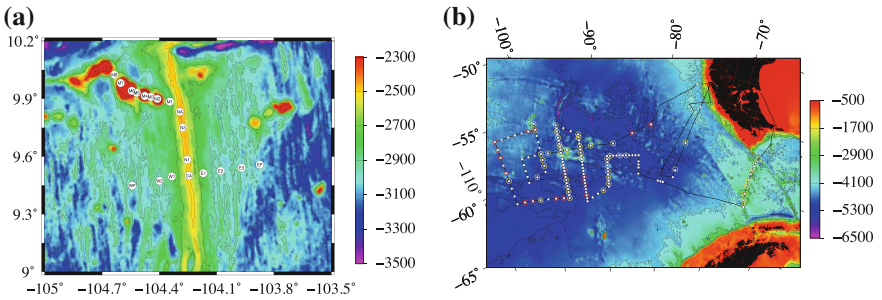

Fig. 2 Detailed maps of the survey regions for the two different projects: **a** LADDER, Larval dispersal on the deep east Pacific rise and **b** DIMES, Diapycnal and Isopycnal mixing experiment in the southern ocean

2.1 Fine-Structure Parameterization

The particular "fine-structure parametrization" described in this manuscript is used to estimate the vertical diffusivity parameters based on hydrographic profiles (temperature, salinity and pressure) and velocity profiles (zonal and meridional velocities). These variables are some of the most vastly measured quantities in the ocean using LADCP/CTD casts (Lowered Acoustic Doppler Current Profiler/Conductivity Depth Temperature). From those profiles, the internal wave field shear, V_Z, (Eq. 2) and strain, $\xi_z = \frac{N^2 - \bar{N}^2}{\bar{N}^2}$, can be estimated. This internal wave field undergoes non-linear interactions and departs from a wave field of reference commonly called "Garrett-Munk spectrum". The more it departs from this semi-empirical background spectrum the more/less turbulent mixing results. The scalings of turbulence in the ocean interior resulting from wave-wave interactions have been validated since 1989 (Gregg 1989). Those methods have been improved from the shear-based parametrization (Gregg 1989), to the strain-based parametrization with a prescribed shear/strain variance ratio (Polzin et al. 1995), and finally the combination of both: shear-and-strain-based parametrization (Gregg et al. 2003).

These "fine-structure" approaches have been used to estimate diffusivities as part of a very large ongoing project, CLIVAR (Climate Variability and Predictability), which among many other measurements performs LADCP/CTD measurements on routinely basis. Kunze et al. (2006) performed one of the most exhaustive estimates of diapycnal mixing using the databases from that particular experiment. He kindly provided the code used in Kunze et al. (2006) and after validating it, it was possible to observe for the LADDER project large values of dissipation near the seamount chain.

2.2 Microstructure Direct Measurements

The microstructure measurements are performed with an autonomous device, which contains several probes with high resolution: shear probes ($\partial u/\partial z$ and $\partial v/\partial z$),

temperature, conductivity, accelerometers and pressure. The probes on the instruments need to be in contact with unperturbed water, trying to be the least intrusive to the shear layers in the water column. To achieve these conditions the instruments are deployed and left in free-fall until they reach a terminal velocity. As they approach the pre-programed depth, they release the weights that make them sink and the instrument comes back to the surface. To analyze the data it is required to make several corrections to compensate the tilting and the rotation during the descent. From the shear measurements it is possible to estimate dissipation from the total shear. The buoyancy frequency is estimated from the measurements of temperature, conductivity (salinity) and pressure using the equation of state of seawater. This data sets are direct measurements, for shear, the dissipation and diffusivity variables are obtained from typical relations using the typical mixing efficiency values.

2.3 Tracer-Release Experiment

This experiment consists of releasing a tracer patch at a given depth. The tracers need to be inexistent in the environment they will be released. Thus, they tend to be gases that will dissolve in water at those high pressures. After the tracer injection, it spreads vertically and horizontally, depending on the spatial scales of the experiment, and the tracer is sampled over time scales of months or years. For example, the LADDER experiment had a relatively small spatial scale and the tracer was sampled for months after the injection. On the contrary, the DIMES experiment is quite large and it has taken over 5 years to sample the tracer. Together with sampling the tracer there have been a lot of other instruments and research teams, making of this experiment one of the largest in the world. For a detailed description on the estimation of the turbulent diffusivity from the tracer injection, we refer to the appendix in Watson et al. (2013).

3 Observations and Results

The oceanic expeditions presented in Fig. 2 highlighted the importance of rough topography as "hotspots" for high levels of mixing. This high levels are crucial to mix the deep waters. For the EPR case, the location of the sea mounts and the ridge for the EPR determine the spatial patterns of the turbulence (Fig. 3), which are of the order of $\sim 10^{-4}\,\mathrm{m}^2/\mathrm{s}^2$ in between the seamounts and below the crests of the ridge. That value is consistent with the tracer release experiment carried out a year before the fine-structure/microstructure cruise (Jackson et al. 2010). However, it is important to notice that $K \sim O(1/N^2)$, therefore the smaller is the stratification, N^2, the larger are the values of K. However, if the stratification is high (high strain values) the onset of instability, based on Richardson number and leading to turbulent mixing, requires higher shear levels.

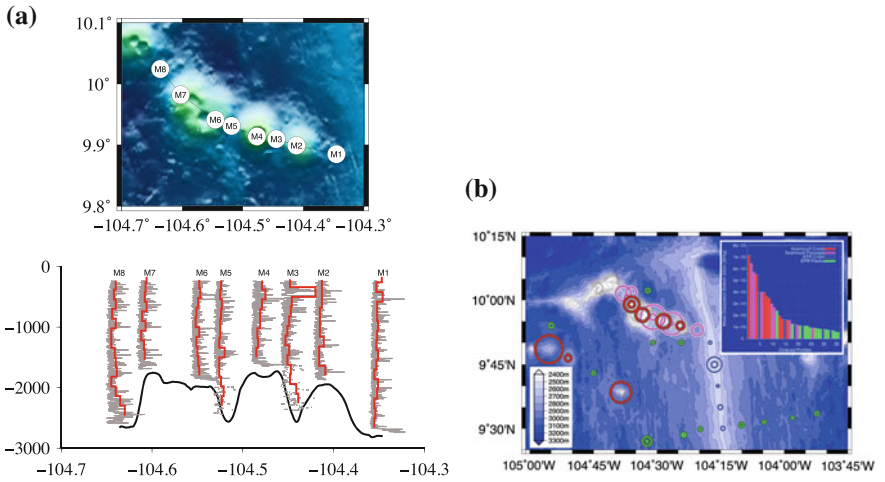

Fig. 3 **a** Section of the EPR seamount showing the microstructure dissipation rates, and **b** a map of the first 500 m above the seafloor integrated dissipation rates

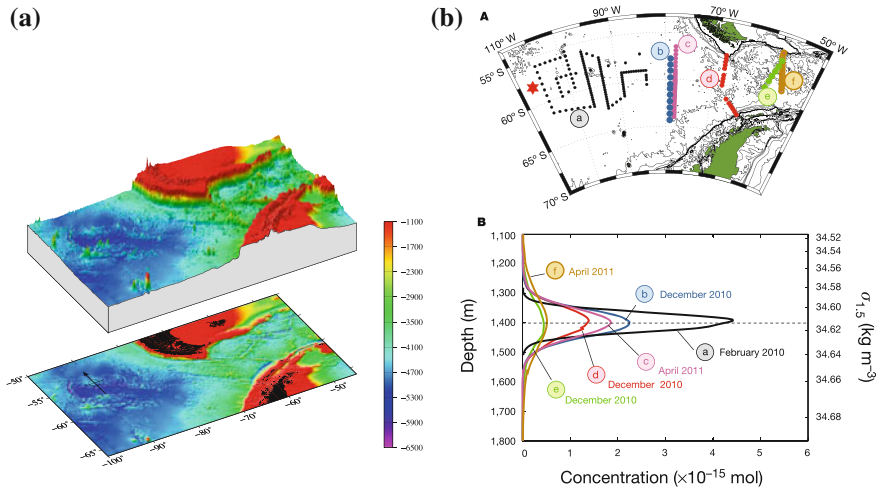

Fig. 4 **a** The Drake passage on a exaggerated 3D view has a rather rough topography compared to the west of Chile where DIMES US2 took place for most of the stations. **b** The tracer distribution shows a rather different distribution on the early stations of the Drake passage

The spatial variation on the diffusivity values associated with the changes on the ocean floor topography was also observed during the DIMES expedition US2. As shown in Fig. 4, the sampled area to the west of the Drake passage has a relatively smooth bathymetry. The corresponding diffusivity values derived from "fine-structure", microstructure and tracer release experiment were typical background values. Near the Drake passage, the abrupt change in bathymetry (Fig. 4) is correlated

to high mixing levels. The "fine-structure" estimates, the microstructure measurements and the tracer released experiment method showed high levels of diapycnal mixing (Ledwell et al. 2011; St. Laurent et al. 2012; Watson et al. 2013), i.e. about one order of magnitude higher than the background values.

4 Summary

The importance of mapping the hotspots regions for diapycnal mixing is an ongoing worldwide effort, which has shown evidence of regions with high turbulent diffusivity values. The DIMES experiment belongs to one of those efforts since encompass The Circumpolar Current, which plays an important role in modulating the world climate. The measurements presented in this paper show a relatively good agreement among them; however many more experiments to validate the methods are needed. Specifically on regions that are shear dominated, strain dominated or both. The "fine-structure" method is one of the cheapest and there are by far many more datasets spanning large areas of the ocean including sections that are visited continuously. For example, the currently ongoing project CLIVAR (Climate Variability and Predictability), which among many other measurements performs LADCP/CTD measurements on routinely basis. Kunze et al. (2006) performed one of the most exhaustive estimates of diapycnal mixing using some of those databases. The downside of this method is the low effective vertical resolution usually given by the LADCP $\sim$50 mm, in contrast with the microstructure profiler $\sim$1 mm. The tracer experiment provides a very accurate estimation with the downside that is only a small region above and below the injection point. However, one of the beauties of this method is the possibility of estimating the horizontal and vertical turbulent diffusivity. There is until now a continuous effort on improving the methods. Additionally, there are other methods that were not mentioned here, which complement enormously the effort of mapping the world turbulent diapycnal mixing. The methods mentioned above are usually good for the ocean interior leaving the coastal regions abandoned. The mixing processes around coastal regions is very important regionally and also needs a proper parametrization for the correct implementation of regional models.

Acknowledgments The author would like to thank Dr. Abraham Medina Ovando for the invitation to the Enzo Levi Symposium, also A.M. Thurnherr for great and fruitful discussions and sharing a lot of his knowledge on LADCP/CTD. The author would like to thank as well L. St Laurent and J. Toole for fruitful conversations during the cruises and outside. Special thanks go to the PIs Lauren Mullineaux and Jim Ledwell for their invitations to collaborate on LADDER and DIMES projects. Funding for the LADDER project and the microstructure add-on was provided by the National Science Foundation under grants OCE-0728766, OCE-0425361 and OCE-0424953. DIMES project was supported by the U.S. National Science Foundation and by the Natural Environment Research Council of the United Kingdom.

References

Baumert HZ, Peters H (2009) Turbulence closure: turbulence, waves and the wave-turbulence transition - part 1: Vanishing mean shear. Ocean Sci 5(1):47–58. doi:10.5194/os-5-47-2009

Broecker WS (1987) Unpleasant surprises in the greenhouse? Nature 328:123

Broecker WS (1987) The biggest chill. Nat Hist Mag pp 74–82

Broecker WS (1991) The great ocean conveyor. Oceanography 4(2)

Gordon AL (1986) Interocean exchange of thermocline water. J Geophys Res 91(C4):5037–5046

Gregg MC (1989) Scaling turbulent dissipation in the thermocline. J Geophys Res 94

Gregg MC, Sanford TB, Winkel DP (2003) Reduced mixing from the breaking of internal waves in equatorial waters. Nature 422(6931):513–515. doi:10.1038/nature01507

Jackson PR, Ledwell JR, Thurnherr AM (2010) Dispersion of a tracer on the east pacific rise (9 degrees n–10 degrees n), including the influence of hydrothermal plumes. Deep-sea research. Part I: oceanographic research papers, 57(1):37–52

Kunze E, Firing E, Hummon JM, Chereskin TK, Thurnherr AM (2006) Global abyssal mixing inferred from lowered ADCP shear and CTD strain profiles. J Phys Oceanogr 36(8):1553–1576. doi:10.1175/JPO2926.1

Ledwell JR, Montgomery ET, Polzin KL, St. Laurent LC, Schmitt RW, Toole JM (2000) Evidence for enhanced mixing over rough topography in the abyssal ocean. Nature 403(6766):179–182. doi:10.1038/35003164

Ledwell JR, St. Laurent LC, Girton JB, Toole JM (2011) Diapycnal mixing in the antarctic circumpolar current. J Phys Oceanogr, 41(1):241–246

Marshall J, Speer K (2012) Closure of the meridional overturning circulation through southern ocean upwelling. Nat Geosci 5(3):171–180. ISSN 1752-0894.10.1038/ngeo1391

Osborn TR (1980) Estimates of the local rate of vertical diffusion from dissipation measurements. J Phys Oceanogr 10:83–89

Polzin KL, Toole JM, Schmitt RW (1995) Finescale parameterizations of turbulent dissipation. J Phys Oceanogr 25(3):306–328

Polzin KL, Toole JM, Ledwell JR, Schmitt RW (1997) Spatial variability of turbulent mixing in the abyssal ocean. Science 276(5309):93–96. doi:10.1126/science.276.5309.93

Rahmstorf S (2003) The concept of the thermohaline circulation. Nature 421(6924):699

Ruiz-Angulo A (2007) Simultaneous differential diffusion under weak turbulence. Geophys Fluid Dyn (Program Notes)

St. Laurent L, Naveira Garabato AC, Ledwell JR, Thurnherr AM, Toole JM, Watson AJ (2012) Turbulence and diapycnal mixing in drake passage. J Phys Oceanogr, 42(12):2143–2152. doi:10.1175/jpo-d-12-027.1

Thurnherr AM, St. Laurent LC, Speer KG, Toole JM, Ledwell JR (2005) Mixing associated with sills in a canyon on the midocean ridge flank*. J Phys Oceanogr 35(8):1370–1381

Toole JM, Schmitt RW, Polzin KL, Kunze E (1997) Near-boundary mixing above the flanks of a midlatitude seamount. J Geophys Res 102(C1):947–959

Watson AJ, Ledwell JR, Messias M-J, King BA, Mackay N, Meredith MP, Mills B, Garabato ACN (2013) Rapid cross-density ocean mixing at mid-depths in the drake passage measured by tracer release. Nature 501(7467):408–411. doi:10.1038/nature12432

Alya Red CCM: HPC-Based Cardiac Computational Modelling

M. Vázquez, R. Arís, J. Aguado-Sierra, G. Houzeaux, A. Santiago, M. López, P. Córdoba, M. Rivero and J.C. Cajas

Abstract This paper describes Alya Red CCM, a cardiac computational modelling tool for supercomputers. It is based on Alya, a parallel simulation code for multiphysics and multiscale problems, which can deal with all the complexity of biological systems simulations. The final goal is to simulate the pumping action of the heart: the model includes the electrical propagation, the mechanical contraction and relaxation and the blood flow in the heart cavities and main vessels. All sub-problems are treated as fully transient and solved in a staggered fashion. Electrophysiology and mechanical deformation are solved on the same mesh, with no interpolation. Fluid flow is simulated on a moving mesh using an Arbitrary Lagrangian-Eulerian (ALE) strategy, being the mesh deformation computed through an anisotropic Laplacian equation. The parallel strategy is based on an automatic mesh partition using Metis and MPI tasks. When required and in order to take profit of multicore clusters, an additional OpenMP parallelization layer is added. The paper describes the tool and its different parts. Alya's flexibility allows to easily program a large variety of physiological models for each of the sub-problems, including the mutual coupling. This flexibility, added to the parallel efficiency to solve multiphysics problems in complex geometries render Alya Red CCM a well suited tool for cardiac biomedical research at either industrial or academic environments.

M. Vázquez (✉) · R. Arís · J. Aguado-Sierra · G. Houzeaux · A. Santiago · M. López · P. Córdoba · M. Rivero · J.C. Cajas
Barcelona Supercomputing Center, Ed. Nexus I, Campus Nord UPC, Barcelona, Spain
e-mail: mariano.vazquez@bsc.es

M. Vázquez
IIIA-CSIC, UAB Campus Bellaterra, Barcelona, Spain

J. Klapp et al. (eds.), *Selected Topics of Computational and Experimental Fluid Mechanics*, Environmental Science and Engineering,
DOI 10.1007/978-3-319-11487-3_11

1 Introduction

Under *Alya Red* we group all the biomedical research projects whose central simulation tool is (Alya System 2015), including some specifically developed software. The resulting software is then targetted to biomedical research and based on a general purpose simulation code for coupled multiphysics and programmed for parallel computers. This strategy allows a great flexibility to cover the wide range of problems found in biological systems, with all of them seen in the same way and as any other engineering problem: systems of differential equations coupled together (Fig. 1).

The final goal of its developers is to put in the hands of biomedical researchers a multiphysics cardiac simulation tool based on High Performance Computing (HPC) techniques, capable of efficiently running in thousands of cores. The simulation tool should be as comprehensive as possible, recreating with the highest detail the heart at organ level, focusing on the electro-mechanical behaviour as it pumps blood to and from the system (Fig. 2).

The proposed tool targets the following aspects:

- Large geometries: data coming from high definition acquisition and processed through clinical image treatment. High resolution at both geometrical and material levels, producing high resolution meshes in both electrical and mechanical problems.

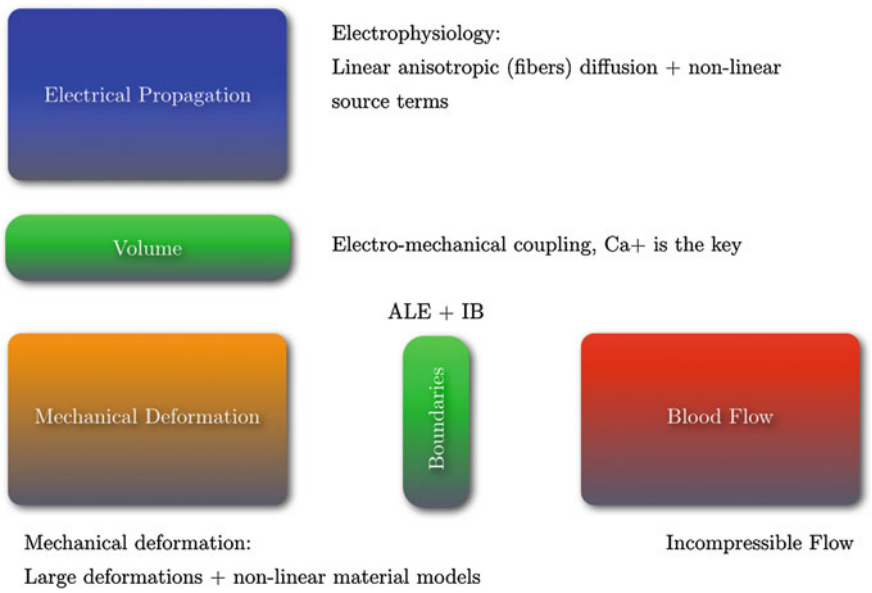

Fig. 1 The cardiac computational model CCM general scheme

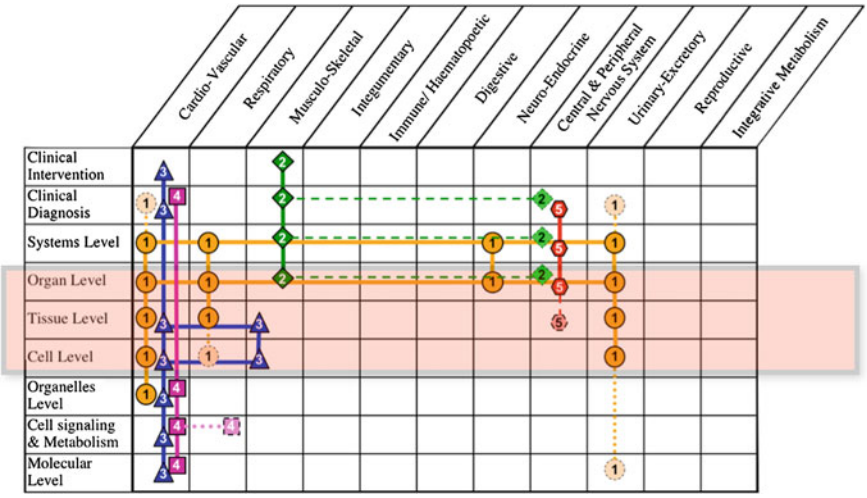

Fig. 2 Organ systems versus levels of organizations. Extracted from Thomas et al. (2008)

- Complex physiological models: electrophysiological, material and coupling models of high complexity, with thousands of degrees of freedom per node.
- Multi-physics problems: electrical activity, mechanical deformation and blood flow.

In this paper we focus in the electro-mechanical problem.

2 Alya, an HPC-Based Computational Mechanics Tool

2.1 General Description

Alya is an HPC-based simulation tool for coupled multi-physics problems (see for instance (Houzeaux et al. 2008, 2011). On general terms, it is a numerical solver for coupled systems of partial differential equations (PDE), discretized on unstructured meshes. It has a large database of element types, including low and higher order, up to Q3. Transient problems are solved with either explicit or implicit schemes, with time integration schemes of different order. Except for METIS (Metis 2015) and low level libraries (such as MPI), Alya has no dependency on third-party libraries, being all solvers developed in-house. It is written in a modular way, with a kernel that includes all the functionalities required to solve the physical problems including parallelization and a set of modules, where each module represent a different PDE.

At the organ level, the cardiac computational model requires the solution of the electrical component, which is a non-linear reaction-diffusion system; and the mechanical component, which produces the deformation and a coupling model to

link both problems together. In the next sections, we explain each model and how they are coupled.

2.1.1 Electrophysiological Models

The activation potential propagation is modelled using an excitable media model,

$$\frac{\partial \phi_\alpha}{\partial t} = \frac{\partial}{\partial x_i}\left(D_{ij}\frac{\partial \phi_\alpha}{\partial x_j}\right) + L(\phi_\alpha). \tag{1}$$

which consists of a diffusion equation with anisotropic diffusion tensor D_{ij} (Rubart and Zipes 2001; Coghlan et al. 2006) and local non-linear terms. The anisotropy comes from the fact that the cardiac tissue is made of muscular fibers with different diffusion along or transversal to the fibers. The non-linear term $L(\phi_\alpha)$ represents the ionic current I_{ion} cell model, ranging from simple phenomenological schemes (FitzHugh 1961) up to more complex and physiologically meaningful models (Tusscher et al. 2004). Then, the electrophysiology modelling equations are labelled with Greek subindices for the activation potentials involved. We focus here in the so-called monodomain models, where intra- and extra-cellular potentials are modelled with one single equation, so $\alpha = 1$. The electromechanical impulse, that is to say the electrical activation which drives muscular contraction starts at the junctions of the Purkinje network. In our model, synthetic networks are generated for each geometry (Sebastian et al. 2012).

2.1.2 Mechanical Models

The myocardium is modelled as a compressible solid, with three-dimensional elements. The material model is hyper-elastic, with anisotropic behaviour ruled again by the fiber structure. In this work, we use a transversally isotropic version of a Holzapfel-Ogden material (Holzapfel and Ogden 2009), already presented by Lafortune et al. (2012). We briefly describe it in this section.

In a total-Lagrangian formulation, the governing equations are written as:

$$\rho_o \frac{\partial^2 u_i}{\partial t^2} = \frac{\partial P_{iJ}}{\partial X_J} + \rho_o B_i. \tag{2}$$

The Cauchy stress $\boldsymbol{\sigma} = J^{-1}\boldsymbol{P}\boldsymbol{F}^T$, is defined through the Piola-Kirchoff P_{iJ}, the deformation gradient $F_{iJ} = \dfrac{\partial x_i}{\partial X_J}$ and its Jacobian J. Stress is a combination of active and passive parts:

$$\boldsymbol{\sigma} = \boldsymbol{\sigma}_{pas} + \sigma_{act}(\lambda, [Ca^{2+}])\boldsymbol{f} \otimes \boldsymbol{f} \tag{3}$$

Fig. 3 Purkinje network terminations on the ventricles endocardiac wall. Extracted from Arís (2014)

The passive part is governed by a transverse isotropic exponential strain energy function $W(b)$ that relates the Cauchy stress σ to the right Cauchy-Green deformation b. The passive stress is then

$$J\boldsymbol{\sigma}_{pas} = (a\, e^{b(I_1-3)} - a)\boldsymbol{b} + 2a_f(I_4-1)e^{b_f(I_4-1)^2}\boldsymbol{f}\otimes\boldsymbol{f} + K(J-1)\boldsymbol{I}. \quad (4)$$

The strain invariant I_1 represents the non-collagenous material while strain invariant I_4 represents the stiffness of the muscle fibers, and a, b, a_f, b_f are parameters to be determined experimentally. K sets the compressibility, while vector $\boldsymbol{f}$ defines the fiber direction (Fig. 3).

2.1.3 Electromechanical Coupling

The active part of the material model drives the electromechanical action. It depends on the ionic concentration in the tissue. The electrical component is initiated where the Purkinje system delivers the initial impulse and simulates the transmembrane potential propagation.

Cardiac mechanical deformation is the result of the active tension generated by the myocytes. The model includes passive and active properties of the myocardium. It assumes that the active stress is produced only in the direction of the fiber and depends on the calcium concentration of the cardiac cell, as described by Niederer et al. (2006):

$$\sigma_{act} = \gamma\, \frac{[Ca^{2+}]^n}{[Ca^{2+}]^n + C_{50}^n}\sigma_{max}(1+\beta(\lambda_f - 1)). \quad (5)$$

In this equation, C_{50}^n, σ_{max} and λ_f are model parameters. We have introduced a parameter $0 < \gamma < 1$ to calibrate the amount of active stress and measure its sensitivity.

2.1.4 Blood Flow

In this model, blood is considered as incompressible and Newtonian. The time discretization is a second order backward differentiation scheme. Linearization is done using the Picard method. The space discretization is based on the finite element method, combined with a variational multiscale method (VMS) described by Houzeaux and Principe (2008). At each time and linearization iteration, the following system is solved:

$$\begin{bmatrix} \mathbf{A}_{uu} & \mathbf{A}_{up} \\ \mathbf{A}_{pu} & \mathbf{A}_{pp} \end{bmatrix} \begin{bmatrix} \mathbf{u} \\ \mathbf{p} \end{bmatrix} = \begin{bmatrix} \mathbf{b}_u \\ \mathbf{b}_p \end{bmatrix} \tag{6}$$

where **u** and **p** are velocity and pressure nodal unknowns. Avoiding the use of complex preconditioners to account for the velocity-pressure coupling for the monolithic system, an algebraic fractional scheme is used (see Houzeaux et al. 2011). Through this scheme, we segregate velocity and pressure systems at the algebraic level, solving the pressure Schur complement using an iterative method (herein the Orthomin(1)). This strategy offers two main advantages. Therefore, one shot of the method involves the solution of the momentum equation and the solution of a symmetric system for the pressure (Laplacian) representing the continuity equation. The momentum equations usually converge very well, even with a simple diagonal preconditioner. On the contrary, the continuity equation is much stiffer, so it is solved with the Deflated Conjugate Gradient solver (DCG) (Löhner et al. 2011), together with a linelet preconditioner when anisotropic boundary layers (Soto et al. 2003) are present. Besides and with respect to classical fractional step methods, no fractional errors are introduced and the solution converges to the same as the monolithic one.

2.1.5 Arbitrary Lagrangian-Eulerian ALE Scheme for the Fluid Mesh Deformation

Coupling between the blood flow and the ventricles is done by the Arbitrary Lagrangian-Eulerian (ALE) method. While the blood transmits the force to the ventricle, the ventricle transmits a deformation to the mesh where the moving blood is simulated. This has a double effect. On one hand, as the Navier-Stokes equations are solved on a moving mesh, they include a correction term taking into account the relative velocity of the fluid and the mesh. On the other hand, the volume fluid mesh must be smoothly deformed following the surface mesh solidary to the ventricle wall (see Donea et al. (2004) for a comprehensive description of the ALE method). There are several methods to perform the volume mesh deformation. In this paper we follow the method proposed by Calderer and Masud (2010). This method has proven as extremely robust and specially well-suited for a parallel multi-physics code like

Alya, because mesh deformation is computed as an additional low-cost problem. The method consists of solving a Laplacian equation:

$$\frac{\partial}{\partial x_i}\left(D_{ij}\frac{\partial u_i}{\partial x_j}\right) = 0 \ \text{ in } \ \Omega_{\mathrm{t}} \tag{7}$$
$$u_i = g_i(x_j, t) \ \text{ on } \ \partial\Omega_{\mathrm{t}}^{\mathrm{m}}$$
$$u_i = 0 \ \text{ on } \ \partial\Omega^{\mathrm{f}}$$

where Ω_t is the time changing domain, $\partial\Omega_t^m$ is the moving boundary, $\partial\Omega^f$ is the fix boundary and

$$D_{ij} = (1 + \frac{1 - V_{min}/V_{max}}{V_e/V_{max}})\delta_{ij} \tag{8}$$

is the diffusion parameter which is a function of the local Volume element. The effect of this parameter is to progressively make stiffer the smaller elements, preserving boundary layers and refined zones, thus allowing for large deformations in larger elements.

2.1.6 Solution Scheme and Computational Aspects

A fully coupled problem comprises two material parts (tissue and blood) and four coupled simulation problems (electrophysiology and mechanical deformation on the tissue and mesh deformation and fluid mechanics on the blood). Two different instances of Alya deals with each of the parts, running linked together in a staggered fashion. At each time step, coupled problems can be solved either monolithically or by blocks, grouping the unknowns. We use here a by-block structure, being electrophysiology, mechanical, blood flow and mesh deformation separated problems solved in a staggered and paired way.

On one hand, one instance of Alya solves the governing equations of both the electrical and mechanical parts on a spatially discretized mesh of the heart volume using the finite element method, being the same mesh used for both problems, thus avoiding instabilities and interpolation errors. Given the always increasing resolution and accuracy of anatomical information obtained from clinical imaging, Alya Red is conceived from design to deal with large, high-definition unstructured meshes. On the other hand, a second instance of Alya solves the Navier-Stokes and the mesh deforming equations. In turn, each of the two coupled Alya instances run in parallel thanks to an automatic mesh partition of the unstructured meshes using Metis and MPI tasks. A careful grouping of each problem's respective MPI tasks allows an efficient communication thanks to MPI communicators. This strategy is reported by Cajas et al. (2014).

On the tissue part, both problems are solved explicitly using the same time step allowing for a straight synchronization. The time step is the smallest one computed for each of the two problems based on stability criteria. Solid mechanics time step is related to the approximate sound speed propagation (Belytschko et al. 2000). For the electrophysiology problem, we found that the most stringent criterion, no mat-

ter what cell model is chosen, comes from the conductivity in Eq. (1), computed as $\Delta t = h^2/2D$, where D is the largest component of the D_{ij}, which usually corresponds to the fiber direction. After many numerical experiments we have found that both time steps are approximately of the same order, being the solid mechanics time step usually the smallest one. We have observed that due to the small time steps, there is usually no need for subiterations. On the blood part, both fluid and mesh deformation are solved implicitly, with no time restriction due to stability issues. Papers describing the parallelization scheme are given by Vázquez et al. (2011), Lafortune et al. (2012) and Houzeaux et al. (2009).

For the tissue problem, the scheme proposed here has some specific features that have not been the standard in electromechanical cardiac coupling. Firstly, both electrophysiology and mechanical problems are solved in the same mesh, avoiding stability issues and interpolation errors but paying the price of a high computational cost for the mechanical problem. As we program and solve all problems in the same code, supported on the same mesh and with the same parallelization scheme, we find our approach very natural. Providing the high parallel efficiency of the code, it has proven both an efficient and accurate option. Consider also the increasingly higher resolution obtained from the clinical images, which results in high fidelity simulations. Secondly, the mechanical problem is dynamically solved so the transient effects are taken into account. Therefore, no quasi-static approximation is used. Considering the fully coupled problem, references are scarce. For instance, Hosoi et al. (2010) proposed an electro-mechanical-blood flow model. The main differences with our model is that they use a different electrical propagation model, a monolithic approach for the fluid-structure interaction and an homogeneization procedure for the tissue mechanical properties.

The two parts (tissue deformation and blood flow) of the fluid-structure interaction (FSI) scheme run in an overlapping manner, concurring when forces and displacements are interchanged for the wet surface. In turn, each part runs in parallel. To assure good load-balance each Alya instance creates its partition taking into account the relative weight of the four problems. Therefore, contrary to many other strategies for FSI, both fluid and solid sides are equally parallelized.

The wet surface is shared between the two instances. The boundary conditions are an important issue, with different aspects to be considered. Firstly, the nodes on both sides need not be coincident. Both fluxes and unknowns can be interpolated in a conservative way. However, to avoid the interpolation errors, we prefer coincident surface meshes. Secondly, to avoid so-called added mass effect when fluid and solid densities are similar, we use the method proposed by Wall et al. (2007), where an Aitken scheme relax the wet surface motion on the fluid side. This relaxation scheme is not always required, but it gives additional robustness.

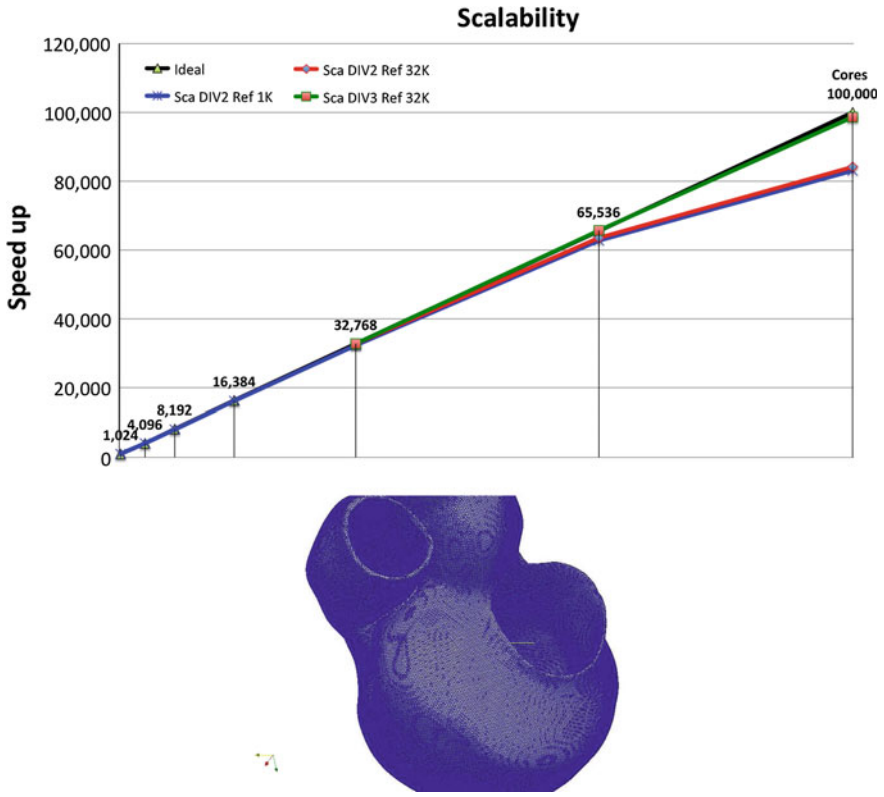

Fig. 4 Strong scalability for the coupled electro-mechanical problem as compared with the ideal linear scalability. The *vertical axis* shows the speedup, the *lower horizontal axis* is the number of cores and the *upper horizontal axis* is the elements-per-core average. Tests were carried out in NCSA's Blue Waters supercomputer. Reprinted from Vázquez et al. (2014)

3 Parallel Computational Aspects

3.1 Parallel Efficiency

In this paper we only present parallel efficiency results for the tissue part, i.e., the electro-mechanical coupling. The fully coupled problem scalability is still being assessed.

Strong scalability measures the Cardiac Computational Model (CCM) parallel efficiency for the coupled electro-mechanical problem. Alya has shown high parallel efficiency up to several thousands of cores for different physical problems, either coupled or single-physics (Houzeaux et al. 2008, 2009, 2011; Puzyrev et al. 2013). In Vázquez et al. (2014), the authors have performed a scalability test assessing Alya's parallel performance up to 100,000 cores in NCSA's Blue Waters supercomputer.

Among other coupled problems, a cardiac electro-mechanical simulation is run for a high-resolution bi-ventricular geometry. Figure 4 shows the geometry and the strong scalability plot. The test is performed in the following way. A 6M tetrahedral mesh is generated for the bi-ventricular geometry provided by Dr. A. Berruezo (Hospital Clinic de Barcelona) in collaboration with R. Sebastian (UVEG) and O. Camara (UPF). Following Houzeaux et al. (2013), the original mesh is progressively subdivided in smaller elements, creating a hierarchy of larger meshes. To perform the scalability test, two meshes coming from the subdivision cycle, 427M and 3.4B elements, are used. They are respectively labelled "DIV2" and "DIV3" in Fig. 4. Scalability is measured upon the time needed to solve one time step.

The smaller mesh "DIV2" shows linear scalability up to 65 K processors, being normalized with the 1,024 cores run. At 65 K "DIV2" has a mean of 6,500 tetrahedra per core. At this end, communications' time starts to be noticeable with respect to computing time. However, scalability figures for the larger mesh "DIV3" are linear up to the top: it is 8 times larger, with a mean of 52 K elements per core at 65 K cores.

It is worth mentioning that after several tests we have established a practical rule of thumb for the wall clock time of coupled electro-mechanical problems. With 5,000–10,000 elements per core for a rabbit size heart with millions of elements, a coupled problem for 1 s of real time runs in approximately 10–15 min wall clock time in BSC's Marenostrum III if no special optimization option is used and compiling the code with the Intel Fortran Compiler. Depending on the electrophysiology model used (FHN or TT) this time could vary around 20–30 %. We believe that after a heavy code optimization and cleaning, these figures should go down to 1 s of real time solved in 1 min of wall clock time.

4 Examples

Arís (2014) and Arís et al. (2014) have shown the potential of Alya Red CCM by performing a sensitivity analysis for several conditions. The goal is to investigate the effect of initial conditions in the resultant simulation, determining how a change in an input will affect the output. In particular, we study the influence of the electrical activation in the contraction of the tissue. The analysis is performed in a bi-ventricular geometry, where 14 different activation protocols are tested. In addition, two different fiber field orientations are interpolated in the geometry, and each activation protocol is combined with each fiber field description. For each case, simulations are evaluated by quantifying the variation of epicardial breakthrough, total activation time, ejection fraction and time of maximal contraction. Considering the complexity of cardiac models, the sensitivity analysis carried out by Arís (2014) and Arís et al. (2014) emphasizes the possibility to optimise the cardiac activation protocols by using the present method. The results presented show that the proposed CCM tool is capable of capturing variations to small input parameter changes.

In this paper we briefly present some of the results.

4.1 Electro-Mechanical Coupling in a Bi-Ventricular Geometry

The CCM tool is used to simulate a pumping heart, focusing on the electromechanical propagation through the tissue. It has been reported that the specific location where the stimuli enters the myocardium, along with the anatomical variations, determine the overall activation sequence of the heart and the epicardial breakthrough of the electrical wave (Durrer et al. 1970). Obtaining an accurate representation of the Purkinje system in the in-vivo heart is a huge challenge still unsolved, and the variability of the Purkinje fiber geometry across and within species is unknown. We aim to understand the effect of modelling various initial stimuli protocols and its resulting electromechanical response. A Purkinje system modeller has been developed by Sebastian et al. (2012) at the University of Valencia. Each initial stimuli protocol is composed of a set of locations and times determined by the Purkinje tree structure and its PMJs, where the electrical stimuli reach the right or left ventricular myocardium.

In Arís et al. (2014), a bi-ventricular geometry is employed to study the model's sensitivity to different settings of the heart structure. Fourteen initial activation protocols (Pk1, Pk2,…, Pk14) and two transmural fiber field interpolation models (ST1 and ST3) are tested. For each case the simulations are evaluated and analyzed to assess whether the variation of the inputs has an impact on the pumping motion of the muscle. Two different fiber fields are assessed, both coming from a rule-based synthetic fiber distribution: linear and cubic Streeter models (ST1 and ST3). When possible, a third one coming from experimental measurements (from Diffusion Ten-

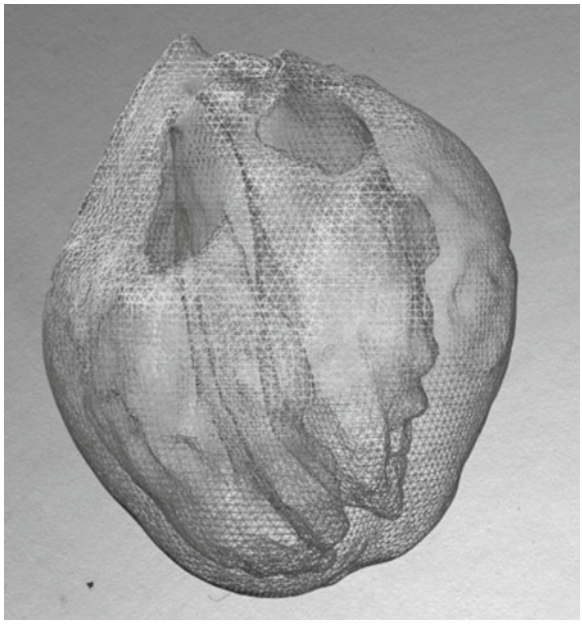

Fig. 5 Rabbit ventricular mesh containing 432,000 tetrahedra as generated from magnetic resonance images at the Oxford University. The figure shows the surface meshes

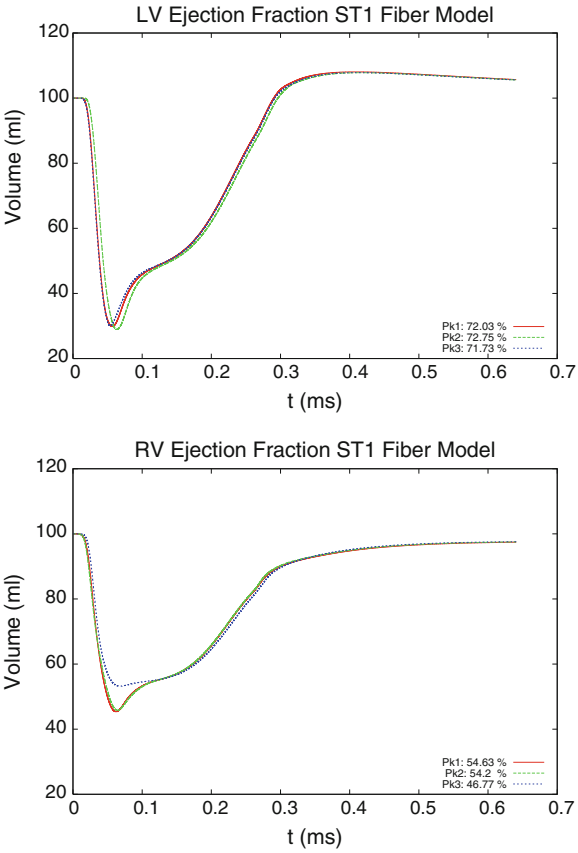

Fig. 6 Comparison of ejection fraction evolution for three different Purkinje models, with ST1

sor Imaging, DTI) is also used and compared with the synthetic ones. The different activation protocols (Pk1, Pk2,…, Pk14) are obtained by changing distributions of the Purkinje end points, including cases of impaired hearts.

To perform the simulations, the rabbit ventricular geometry developed by Bishop et al. (2010) the University of Oxford is used. The model represents the ventricles of the heart and does not include valves, great vessels, pericardium and organs around the heart. The geometry consists of 432,000 linear tetrahedra and 82,619 nodes with a resolution of 0.05 cm (see Fig. 5).

4.1.1 Results

The ejection fraction has been calculated for each combination of Purkinje system and fiber field and by sweeping the parameter γ in Eq. (5), which controls the active stress intensity. First, by fixing γ, the ejection fraction is measured for several configurations. An example of the results obtained is shown in Fig. 6. It is observed

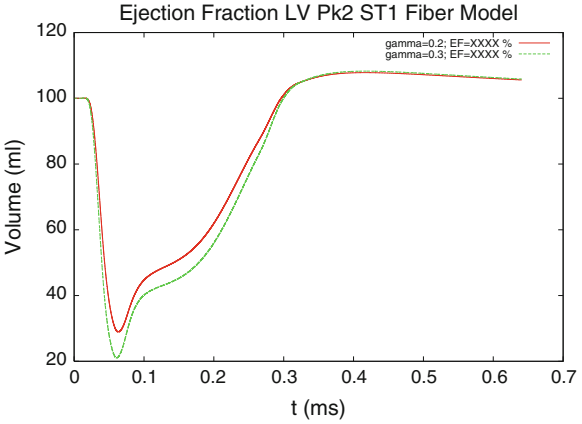

Fig. 7 Results in ejection fraction for two different values of the coupling parameter γ

Table 1 Anterior view of the ventricles

1	2	3	4	5	6	7
8	9	10	11	12	13	14

Simulation of the electrical and mechanical components of the EM wave propagating at t = 45 ms for each activation protocol. ST1 fiber field interpolated in the geometry. Red coloured areas in the first row correspond to the electrical component of the EM wave. In the second row, we present the bi-ventricular deformation of the tissue. Reprinted from Arís et al. (2014)

that the ejection fraction is not too sensitive to the kind of changes in the density and distribution of the Purkinje system we have applied.

In Fig. 7, we compare the ejection fraction curves for two different values of the parameter γ in Eq. (5). A remarkable fact is observed, that has been already noted by Arís et al. (2014): thanks to the complex helicoidal structure of the fiber field, large differences in γ produce small differences in the ejection rates. Varying this value from 0.3 to 0.2 reduces the muscular active stress by 30 %. However, the peak ejection fraction is only 8 % smaller.

The ejection fraction time evolution represents an integral parameter which shows great robustness to the selected varying input parameters, at least in the ranges we explore here. Another aspect we analyze concern the local variations. Although the impact in the integral parameters could be small, it is important to see how localized transient behaviour is affected. Table 1 shows a qualitative analysis of the wavefront at $t = 45$ ms measured from the initial activation. At these early times, the electromechanical wave has already reached the epicardium in all cases but the total activation of the ventricles is not completed yet. In Table 1, we can also observe that different initial stimuli leads to different activation sequences of the heart. For instance, the closest matching appears between the activation protocols which have the same number of nodes in the activation of the right ventricle (RV), activation protocols 5–12, 8–10 and 7–11. In the cases 10, 11 and 12, no sites are activated in the left ventricle (LV), and so the activation is produced purely by transmission from the RV and the contraction occurs later.

In Arís (2014) and Arís et al. (2014) we have analyzed in depth the influence of the fiber architecture and synthetically created Purkinje systems. We studied the propagation dynamics throughout the volume of the ventricles giving measures like ejection fraction and rotation around the long axis.

These results show that Purkinje system variations must be very large to really account for changes in the ventricles contractile action. On the other hand, the fiber model has a much greater influence in contraction than the initial activation through the Purkinje system. As a consequence, linear and cubic rule-based models predict different displacements, especially in areas such as the base or the apex. Additionally, thanks to the complex helicoidal fiber structure, heart contraction is very robust also against changes in active stress intensity. Indeed, the heart is the perfect pump, created after millions years of evolution.

4.2 Electro-Mechanical-Fluid Coupling in a Simplified Ventricular Geomety

The next example shows the fully-coupled scenario. Here we present some preliminary results using simplified geometries (Fig. 8).

Figure 9 shows a sequence of a bar of cardiac tissue submerged in blood as it contracts under electromechanical activation. The bar is fixed on the right, where the electrical activation starts. The fibers are oriented longitudinally to the bar. As the

electrical activation propagates, the bar contracts dragging the blood around it. This setup is very useful to calibrate the parameters of the material model.

Figure 10 shows a mid section of an ellipsoid as its walls contracts under the electromechanical action. The electrical impulse starts at the bottom of the ellipsoid. The fiber model is created from a linear Streeter rule-based model. This first preliminary test on the fully coupled scheme allows us to calibrate several material and electromechanical coupling parameters of the model. In this example, pressure in the outflow is fixed to the atmospheric one. Finally, it is worth to mention that calibration of the active stress generation is under way, so muscle contraction is still not realistic.

5 Conclusions and Future Lines

The final goal of the authors and collaborators is to put in the hands of biomedical researchers a multiphysics cardiac simulation tool based on HPC-techniques, capable of efficiently running in thousands of cores a fully-coupled electro-mechanical-fluid

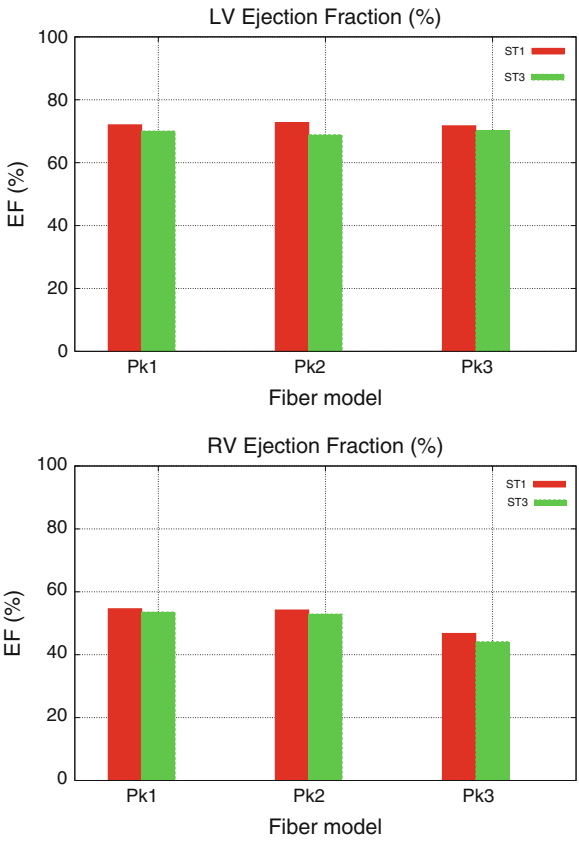

Fig. 8 Comparison of ejection fraction evolution for three different Purkinje models and the two different Streeter's rule-based fiber orientation models ST1 and ST2

cardiac model. The motivation is to create a simulation scenario as comprehensive as possible, recreating with the highest detail the heart, in line with both the dramatic improvement of data acquisition techniques and the steep ramp of computational power increase.

To be comprehensive enough, the model should include electrical activation, mechanical deformation, blood flow, perfusion, systemic contributions, cell models, etc., in a well-defined geometry with the best anatomical information available. In this paper we have presented results for two kinds of problems. First, the electro-mechanical simulation and the model's ability to measure the sensitivity of outputs to different inputs are shown. Second, we introduce some simple examples of the coupled electro-mechanical-fluid problem. We additionally show the scalability of the electro-mechanical problem up to 100 K cores of NCSA's Blue Waters supercomputer.

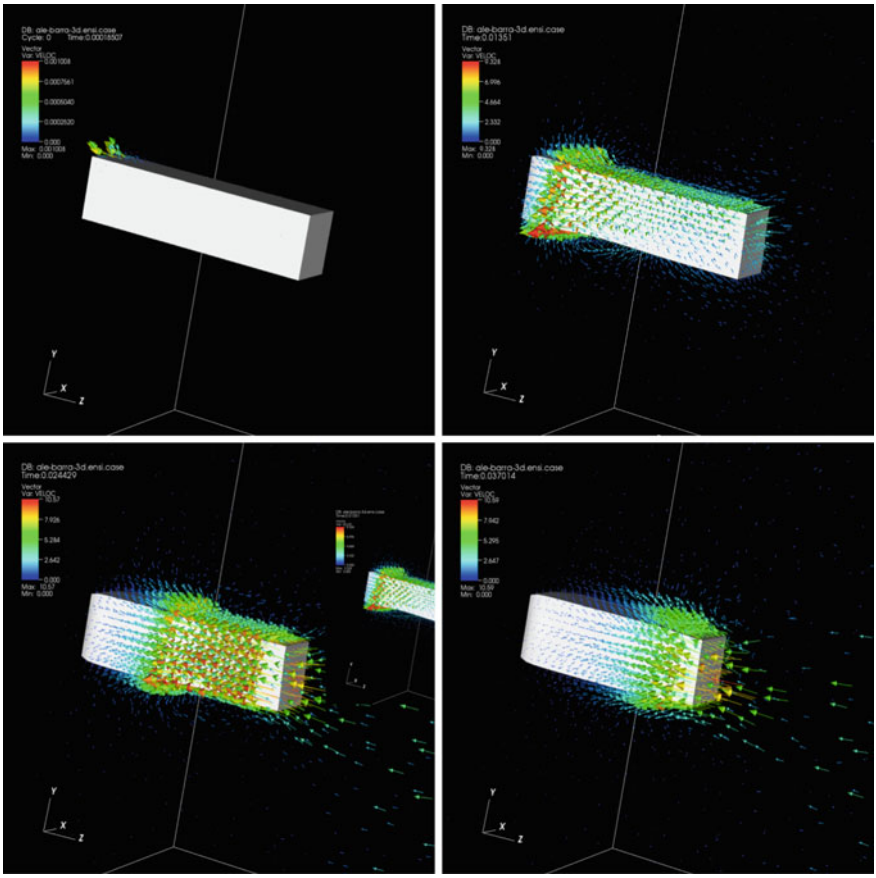

Fig. 9 Motion sequence of a tissue bar under electromechanical contraction, showing the velocity vectors of the blood as it moves around it

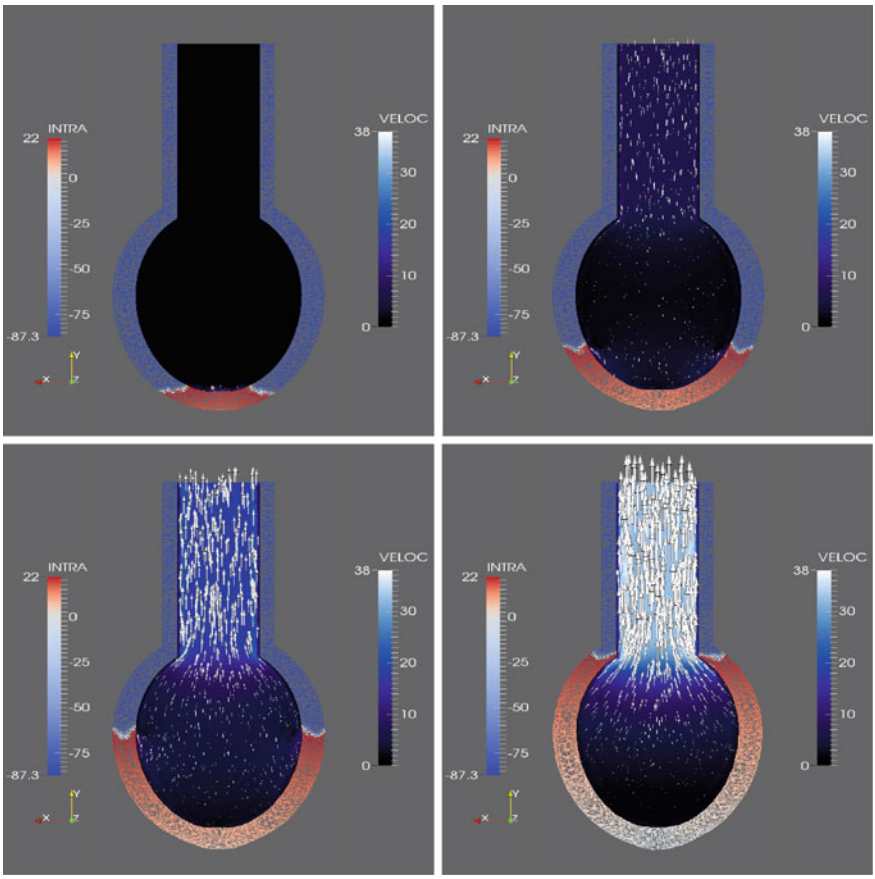

Fig. 10 Motion sequence of an ellipsoid under electromechanical contraction, showing the velocity vectors of the blood as it moves inside it (mid section)

The simulation platform is Alya. Electrical propagation and mechanical contraction is computed and solved in independent modules. The electro-mechanical coupling is performed along the fiber field, which comes either from images or semi-empirical models. Blood flow and mesh deformation are solved in a second instance of Alya. Both instances communicates through MPI.

The HPC tool that has been presented is a powerful platform to test sensitivities of the cardiac modelling scenario. We have shown that the proposed computational model can be useful to test exhaustively the sensitivity to various activation sequences, even for computationally expensive problems, thanks to the use of HPC programming techniques and resources. At this moment, the wall clock time is between about two and three orders of magnitude longer than the physical time for a rabbit size bi-ventricular geometry, with millions of elements and a resolution of

less than 0.1 mm for an EM simulation. Although, the so-called "real time" simulations are not among our goals, the use of the HPC techniques will allow to simulate complex problems for high definition geometries in human time scales.

Acknowledgments This work was partially supported by the Spanish projects TIN2009-13618, TIN2012-33116, CSD2007-00018. Also, it was partially supported with the grant SEV-2011-00067 of Severo Ochoa Program, awarded by the Spanish Government. Debora Gil has been supported by the Ramon y Cajal Program of the Spanish Ministry of Economy and Competitiveness.

References

Alya system (2015). http://www.bsc.es/computer-applications/alya-system

Arís R (2014) Electromechanical large scale computational models of the ventricular myocardium. PhD thesis, Universitat Politécnica de Catalunya, Spain

Arís R, Aguado-Sierra J, Houzeaux G, Gil D, Borràs A, Sebastian R, Vázquez M (2014) Sensitivity analysis to initial stimuli and fiber orientation of a biventricular electromechanical computational model of the heart. PLOS One (Submitted)

Belytschko T, Liu W, Moran B (2000) Nonlinear finite elements for continua and structures. Wiley, New York

Bishop MJ, Plank G, Burton RA, Schneider JE, Gavaghan DJ, Grau V, Kohl P (2010) Development of an anatomically detailed MRI-derived rabbit ventricular model and assessment of its impact on simulations of electrophysiological function. Am J Physiol - Heart Circ Physiol 699–718

Cajas J, Houzeaux G, Zavala M, Vázquez M, Uekermann B, Gatzhammer B, Mehl M, Fournier Y, Moulinec C (2014) Multi-physics multi-code coupling on supercomputers. In: 1st international workshop on software solutions for ICME (Aachen/Rolduc, 24–27 June 2014)

Calderer R, Masud A (2010) A multiscale stabilized ale formulation for incompressible flows with moving boundaries. Comput Mech 46:185–197

Coghlan H, Coghlan A, Buckberg G, Cox J (2006) The electrical spiral of the heart: its role in the helical continuum. The hypothesis of the anisotropic conducting matrix. Eur J Cardiothorac Surg 29:178–187

Donea J, Huerta A, Ponthot J-P, Rodríguez-Ferran A (2004) Arbitrary Lagrangian-Eulerian methods. In: Stein E, de Borst R, Hughes TJ (eds) Encyclopaedia of computational mechanics. Wiley, New York

Durrer D, van Dam RT, Freud GE, Janse MJ, Meijler FL, Arzbaecher RC (1970) Total excitation of the isolated human heart. Circulation 41:899–912

FitzHugh RA (1961) Impulses and physiological states in theoretical models of nerve membrane. Biophys J 1:445–466

Holzapfel GA, Ogden RW (2009) Constitutive modelling of passive myocardium: a structurally based framework for material characterization. Philos Trans R Soc A: Math Phys Eng Sci

Hosoi A, Washio T, Kadooka Y, Nakajima K, Hisada TA (2010) Multi-scale heart simulation on massively parallel computers. In: Proceedings of the ACM/IEEE SC2010 - international conference for high performance computing (New Orleans, Louisiana, USA, 13–19 November 2010)

Houzeaux G, Principe J (2008) A variational subgrid scale model for transient incompressible flows. Int J Comp Fluid Dyn 22(3):135–152

Houzeaux G, Aubry R, Vázquez M (2011) Extension of fractional step techniques for incompressible flows: the preconditioned orthomin(1) for the pressure schur complement. Comput Fluids 44:297–313

Houzeaux G, Vázquez M, Aubry R, Cela J (2009) A massively parallel fractional step solver for incompressible flows. J Comput Phys 228(17):6316–6332

Houzeaux G, de la Cruz R, Owen H, Vázquez M (2013) Parallel uniform mesh multiplication applied to a navier-stokes solver. Comput Fluids 80:142–151

Houzeaux G, Vázquez M, Saez X, Cela J (2008) Hybrid MPI-OpenMP performance in massively parallel computational fluid dynamics. Presented at PARCFD 2008 international conference on parallel computational fluid dynamics. Lyon, France

Lafortune P, Arís R, Vázquez M, Houzeaux G (2012) Coupled electromechanical model of the heart: parallel finite element formulation. Int J Numer Methods Biomed Eng 28:72–86

Löhner R, Mut F, Cebral J, Aubry R, Houzeaux G (2011) Deflated preconditioned conjugate gradient solvers for the pressure-poisson equation: extensions and improvements. Int J Numer Methods Eng 87:2–14

Metis (2015) Family of multilevel partitioning algorithms. http://glaros.dtc.umn.edu/gkhome/views/metis

Niederer SA, Hunter PJ, Smith NP (2006) A quantitative analysis of cardiac myocyte relaxation: a simulation study. Biophys J 90:1697–1722

Puzyrev V, Koldan J, de la Puente J, Houzeaux G, Vázquez M, Cela JM (2013) A parallel finite-element method for three-dimensional controlled-source electromagnetic forward modelling. J Int Geophys. doi:10.1093/gji/ggt027

Rubart M, Zipes D (2001) Genesis of cardiac arrhythmias: electrophysiological considerations. In: Braunwald E, Zipes D, Libby P (eds) Heart disease, vol 1. W.B. Saunders Company, Philadelphia

Sebastian R, Zimmerman V, Romero D, Sanchez-Quintana D (2012) Characterization and modeling of the peripheral cardiac conduction system. IEEE Trans Med Imaging

Soto O, Löhner R, Camelli F (2003) A linelet preconditioner for incompressible flow solvers. Int J Numer Methods Heat Fluid Flow 13(1):133–147

Ten Tusscher KHWJ, Noble D, Noble PJ, Panfilov AV (2004) A model for human ventricular tissue. Am J Physiol Heart Circ Physiol 286:1573–1589

Thomas SR et al (2008) VPH Exemplar project strategy document. Deliverable 9, VPH NoE

Vázquez M, Arís R, Houzeaux G, Aubry R, Villar P, Garcia-Barnós J, Gil D, Carreras F (2011) A massively parallel computational electrophysiology model of the heart. Int J Numer Methods Biomed Eng 27(12):1911–1929

Vázquez M, Houzeaux G, Koric S, Artigues A, Aguado-Sierra J, Aris R, Mira D, Calmet H, Cucchietti F, Owen H, Taha A, Cela JM (2014) Alya: towards exascale for engineering simulation codes. arxiv:1404.4881

Wall W, Genkinger S, Ramm E (2007) A strong coupling partitioned approach for fluid-structure interaction with free surfaces. Comput Fluids 36:169–183

Singularities in Surface Waves

G. Ruíz Chavarría and T. Rodriguez Luna

Abstract In this paper we investigate the evolution of surface waves produced by a parabolic wave maker. This system exhibits, among other, spatial focusing, wave breaking, the presence of caustics and points of full destructive interference (dislocations). The first approximation to describe this system is the ray theory (also known as geometrical optics). According to it, the wave amplitude becomes infinite along a caustic. However this does not happen because geometrical optics is only an approximation which does not take into account the wave behavior of the system. Otherwise, in ray theory the wave breaking does not hold and interference occurs only in regions delimited by caustics. A second step is the use of a diffraction integral. For linear waves this task has been made by Pearcey (1946) (Pearcey, Philos Mag 37 (1946) 311–317) for electromagnetic waves. However the system under study is non linear and some features have not counterpart in the linear theory. In the paper our attention is focused on three types of singularities: caustics, wave breaking and dislocations. The study we made is both experimental and numerical. The experiments were conducted with two different methods, namely, Schlieren synthetic for small amplitudes and Fourier Transform Profilometry. With respect the numerical simulations, the Navier-Stokes and continuity equations were solved in polar coordinates in the shallow water approximation.

1 Introduction

Waves are ubiquitous in nature. The light and the sound are two examples of them, but possibly the most classical picture is that of a wave on the surface of a liquid. They carry energy but not mass and exhibits a myriads of phenomena like reflection, refraction, interference and diffraction. The linear waves are by far the most studied due to the fact that its properties can be deduced analytically. Usually a wave is represented as having a sinusoidal shape, with constant amplitude and a defined

G. Ruíz Chavarría (✉) · T. Rodriguez Luna
Facultad de Ciencias, Universidad Nacional Autónoma de México, Ciudad Universitaria, 04510 Mexico, D.F., Mexico
e-mail: gruiz@unam.mx

J. Klapp et al. (eds.), *Selected Topics of Computational and Experimental Fluid Mechanics*, Environmental Science and Engineering,
DOI 10.1007/978-3-319-11487-3_12

wavelength, however this is just an idealized image. Most of times the wave field contains a continuum of wavelengths, so its shape takes a complicated form and often it evolves in time. This paper deals with waves on the surface of a liquid, which are governed by the Navier-Stokes and continuity equations. They share some features with linear waves, but some of its properties are the result of nonlinear interactions. An example is the waveform, which is no more symmetric as in a sinusoidal wave. On the other side, the amplitude of a surface wave cannot grow indefinitely, after a threshold the wave breaks. The energy carried is rapidly dissipated into turbulence, the formation of air bubbles and drops, etc. (Babanin 2011). This phenomenon is commonly observed along the coasts, when the waves approach the shore. Under these circumstances the wave amplitude grows essentially by a decrease in the sea depth, until the slope of surface becomes infinite. This is the bathymetric breaking, which has been studied extensively. In the open sea the wave breaking is also present, but the mechanisms involved in its production are quite different. Let us consider a continuous wave field and the fact that surface waves are dispersive. Then, components of different wavelengths moves with different phase velocity. The further evolution could produce a rise in the wave amplitude and eventually to the development of the breaking. Of course there are others mechanisms involved in the wave breaking, among them, the interaction between the wind and the waves and the occurrence of currents moving in opposite direction to the wave motion (Zemenzer 2009).

In the ocean there are three stages in the wave evolution (Babanin 2011). In the first one the wind blows and deforms the water-air interface, so an initially small amplitude wave is produced. During a time scale covering thousand of periods energy is injected to the wave, allowing to a slow growth of its amplitude. In this step the wave evolution can be described with a weak nonlinear theory. In the second stage, which covers only few periods, the wave becomes highly asymmetric either in the horizontal and vertical directions. The peaks become steeper and the troughs retract. At a certain time the free surface becomes multivaluated and breaking develops just in a fraction of a period. The breaking is the mechanism to dissipate energy, which is converted in heat, turbulence, bubble production, etc. The case we study has a different driving mechanism, namely the spatial focusing. The aim to make experiments with this kind of breaking is to study this phenomenon in laboratory, where waves cannot evolve over thousand of wavelengths, but in which underlying nonlinear interactions are still present. In addition the study of the wave field under spatial focusing reveals the existence of other singularities apart breaking, like caustics and dislocations, and phenomena as interference and diffraction.

As stated before a nonlinear wave is asymmetric. In order to quantify this asymmetry two quantities are introduced, the skewness and the asymmetry, defined as (Babanin 2011):

$$S = \frac{a_1}{a_2} - 1, \tag{1}$$

$$A_s = \frac{b_1}{b_2} - 1, \tag{2}$$

where a_1 is the amplitude of the peak, a_2 is the amplitude of the trough, b_1 is the distance from the peak to the next point of zero amplitude, and b_2 is the distance from the peak to the previous point of zero amplitude. For a linear wave both quantities vanish. In a nonlinear wave the first one is positive while the second one is negative.

Most of analytical results about surface waves have been obtained when the amplitude is small and consequently non linear terms are neglected in the governing equations. In addition, another hypothesis are made, namely, the velocity field is assumed irrotational and viscosity is neglected. Under all these assumptions, it is possible to derive a dispersion relation, which in the general case is given by the following equation (Elmore and Heald 1969):

$$\omega^2 = \left(gk + \frac{\sigma k^3}{\rho} \right) \tanh(kH), \tag{3}$$

where k is the wavenumber, σ the surface tension coefficient, ρ the fluid density and H is the liquid depth. In the limit of deep waters ($\lambda \ll H$) the term $\tanh(kH) \approx 1$. Then, waves are dispersive, that is, the phase velocity $c = \omega/k$ is dependent on the wavenumber k. The opposite limit is the shallow water case ($\lambda \gg H$) for which the phase velocity is $c = \sqrt{gH}$, irrespective the wavelength.

In Fig. 1 the phase velocity for waves in the deep water approximation is plotted as a function of the wavelength λ. The wavelength lies in the range 1–200 cm. In the figure it is clear that waves are dispersive and that phase velocity attains a minimal value for $\lambda = 2\pi\sqrt{\frac{\sigma}{\rho g}} = 1.70$ cm. It is important to note that the dependence of phase velocity on wavelength in deep waters is a key feature for the time focusing.

This paper is organized as follow. Section 2 is devoted to describe the wave field produced by a parabolic wave maker, the ray theory, the theories of Airy and Pearcey and the singularities in this wave field (caustics and dislocations). In Sect. 3 we describe the optical methods to study surface waves and the experimental setup. In

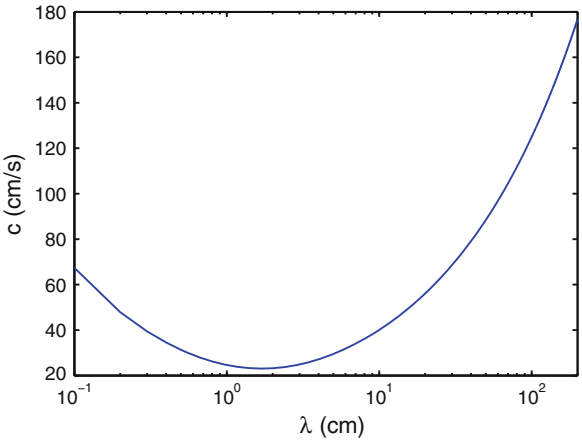

Fig. 1 Phase velocity (c) of surface wave versus wavelength (λ) in the deep water approximation ($\lambda \ll H$). The phase velocity depends upon the wavelength. In experiments and numerical simulations, the wavelength lies in the range $1 < \lambda < 10$ cm

Sect. 4 the numerical method, valid in shallow water approximation, is presented. The main results are presented in Sect. 5, in particular, the emergence of wave breaking, the behavior of the waves around caustics, the existence of dislocations and the recovery of a linear behavior far from the caustics. Finally in Sect. 6 the conclusion are drawn.

2 Spatial Focusing, Caustics and Dislocations

In order to give a picture of the spatial focusing let us consider that surface waves are produced by a parabolic wave maker. The equation of a parabola is:

$$y_0 = a x_0^2. \tag{4}$$

The first approximation in the study of this wave field is the use of geometrical optics, that is, it is assumed that rays start in the parabola and move perpendicular to it. The wave fronts—as shown in Fig. 2—are obtained by a knowledge of normal vector at each point of the parabola. As it can be seen, in the vicinity of the parabola the size of wavefronts decrease as the wave progresses, that implies a growth in the amplitude because energy must be conserved (the viscosity has been neglected). Locally the rays form a beam converging in the center of curvature of the parabola. For a point (x_0, y_0) lying in the parabola, the curvature is:

$$\kappa = \frac{2a}{\left(1 + 4a^2 x_0^2\right)^{3/2}}. \tag{5}$$

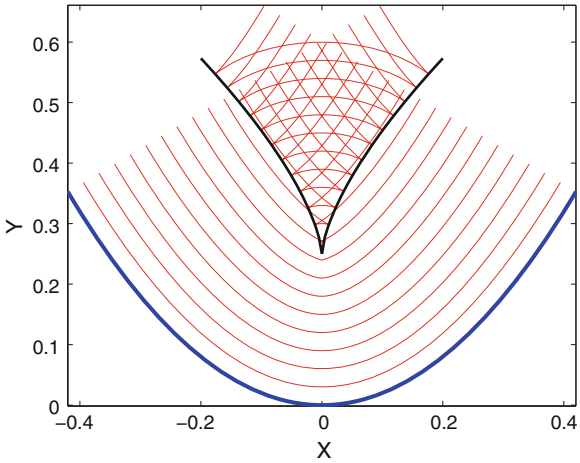

Fig. 2 Wave fronts produced by a parabolic wave maker. The *black lines* are caustics, which intersect in a point (Huygens cusp). The caustics can be considered as the locus where the wavefronts are folded and also as the *curves* where wave amplitude become infinite according to ray theory. Focusing is evident if we consider that size of wave fronts reduces before the Huygens cusp

The radius of curvature is the inverse of κ ($\rho_c = 1/\kappa$). The method of stationary phase allows us to obtain an expression for the wave amplitude in terms of the distance traveled (d) by the ray and ρ (Paris and Kaminsky 2001):

$$A = A_0 \sqrt{\frac{\rho_c}{\rho_c - d}}, \tag{6}$$

where A_0 is the initial amplitude. The last equation predicts that amplitude diverge for $d = \rho_c$. The curve (or the surface in 3D waves) where optical geometry predicts the divergence of wave amplitude is known as a caustic. In reality this does not happen because ray theory is only an approximation in which the wave properties are not considered. However, along a caustic we have a bright region (we use the terminology of optics). In our system, we deal with a pair of caustics intersecting in a point. This point is known as Huygens cusp and around it maximal wave amplitudes take place. The equation of the caustics is:

$$x = \pm \frac{4}{3} \sqrt{\frac{a}{3}} \left(y - \frac{1}{2a} \right)^{\frac{3}{2}}. \tag{7}$$

It is interesting to remark that other characteristics can be invoked for the definition of a caustic. Note that along the caustic the wave fronts folds. This means that caustic is the line (surface) separating illuminated from shaded regions. In this sense, a caustic is the envelope of a ray family. An alternative definition of caustic follows from Fig. 3, in which some rays originating in wave maker have been drawn. The caustic separates region I, where only an individual ray reaches each point, from region II, where three rays reach each point.

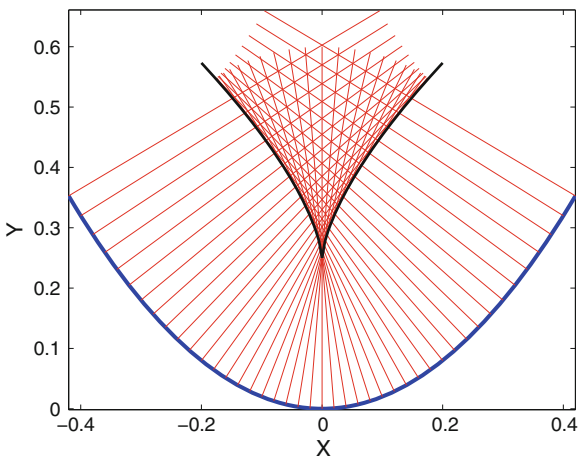

Fig. 3 Rays originating in the parabolic wavemaker. In region I only a ray passes through a point, while in region II three rays reach each point. The *curve* separating both regions is again the caustics

In region II occur some wave phenomena, noticeably, the interference. The presence of three rays give rise to the appearance of points where fully destructive interference happens. This points are called dislocations because of its similarity with dislocations in a crystal lattice. This kind of object is a true singularity, where the phase becomes undefined. It is important to stress that dislocations appear not only in the illuminated region, but a line of dislocations occur in the dark zone because of the diffraction.

As we have stated before, the geometrical optics fails to predict the behavior in the vicinity of a caustic. The divergence has been overcome for the first time with the formulation of a theory by Airy in 1838. In order to describe the wave field near a caustic Airy introduced a function called in his honor, which have some important properties related to the existence and the absence of rays in both sides of a caustic. This function is the solution of the differential equation:

$$\frac{d^2w}{dz^2} = zw. \tag{8}$$

The Airy function has a oscillating behavior for $z < 0$ and for $z > 0$ the function decays exponentially. It is important to mention that this theory is intended for simple caustic, that is, if only two rays reach each point in the illuminated region. The wave field produced by a parabolic wave maker differs from those studied by Airy because in the illuminated region, the wave is the result of the interference of three rays. The behavior of a linear wave in this configuration has been obtained by Pearcey (1946). The work of Pearcey is based in the use of a diffraction integral, which is an approximate solution of the wave equation. This integral is:

$$h(x, y) = \int_{-\infty}^{+\infty} \frac{dx_0}{cos(\theta(x_0))} \frac{exp(ikd(x_0, x, y))}{\sqrt{d(x_0, x, y)}}, \tag{9}$$

where $\theta(x_0)$ is the angle between the tangent of parabola at point x_0 and the x axis. This quantity usually is small, implying that $cos(\theta(x_0)) \approx 1$. Because interest is focused in the behavior around the Huygens cusp (its coordinates are $\left(0, \frac{1}{2a}\right)$ we perform a Taylor expansion of $d(x_0, x, y)$ to first order around this position. The final results is known as the Pearcey integral:

$$h(x, y) = \frac{k}{i2\pi} \frac{exp(ikR)}{\sqrt{R}} \left(\frac{2R}{ka^2}\right)^{1/4} \int_{-\infty}^{+\infty} exp\left(i\left[t^4 + Ut^2 + Vt\right]\right) dt, \tag{10}$$

where $R = \frac{1}{2a}$, $U = 2\left(\frac{k}{2R}\right)^{1/2}(R - y)$ and $V = -\frac{2}{\sqrt{a}}\left(\frac{k}{2R}\right)^{3/4} x$. If the wave maker has a finite size and wavelength is not small when compared with R, the integral must be carried over a finite domain.

3 Optical Methods to Study Surface Waves

In the last decade two optical methods have been developed to detect the deformation of the free surface in liquids. Both exploit the emergence of high definition digital cameras. The first one, known as synthetic Schlieren (Moisy et al. 2009), is based in the refraction of light and the second one, named Fourier transform profilometry (Cobelli et al. 2009; Maurel et al. 2009), is based in the reflection of light. In the two cases a full reconstruction of the free surface topography is realized, but they differ in the range of wave amplitudes they can measure. The underlying principle of synthetic Schlieren is the same used to detect density fluctuations inside a transparent fluid, that is, the change in the light trajectory due to variations in the refraction index. Consider a ray that starts at the bottom of a liquid layer and moves to the liquid-air interface. The trajectory followed by the ray satisfies the Snell law. If the surface is deformed, incidence angle is modified and consequently refraction angle is also modified. For the implementation of this method a set of dots randomly distributed is put at the bottom of the fluid. In a first step a snapshot of the dots pattern is recorded when free surface is flat, this is called the reference image. In a second step, an image is taken when the wave progresses. Due to the modification of the incidence angle, related to the deformation of the liquid-air interface, an apparent displacement of dots appear when we compare first and second images. If we assume that deformations are small (compared with wavelength) and if we remain in the paraxial approximation, the apparent displacement δr is proportional to the gradient of the free surface, namely (Moisy et al. 2009):

$$\nabla h = -\frac{\delta r}{h^*}, \tag{11}$$

where $\frac{1}{h^*} = \frac{1}{\alpha H} - \frac{1}{L}$, H is the depth layer, L is the distance to the camera to the bottom ow liquid layer and α is the related to the ratio of the refractive indices, that is $\alpha = 1 - \frac{n'}{n}$. The determination of δr is performed with a PIV software. To this end the digital image is divided in small cells, where a cross correlation is made between actual image and the reference one. The reconstruction of the topography of free surface is made through the integration of the gradient field. The number of equations is twice the number of unknowns, so the system is overdetermined. For this reason, solution is made with a technique of least square. This method works well for small deformations. This fact limits the use of the method for cases where non linearity are still weak, however it allows the investigation of phenomena like diffraction or the appearance of dislocations in the dark side of caustics. A method better suited for the study of non linear waves is the Fourier transform profilometry (PTF). This procedure is based on light reflection. If we are interested in the study of waves in a fluid, the liquid must remain opaque to produce diffuse reflection. In order to implement it a pattern of fringes is projected on the liquid surface with the aid of a high definition video projector. The size of images is $1{,}920 \times 1{,}080$ pixels, it has depth of 12 bits per color and its intensity is 2,000 lumens. Images of the fluid surface are recorded with a digital camera using a raw format to avoid lost of information

due to preprocessing. We have used a Fujifilm digital camera Finepix HS50 EXR, with a maximal resolution of 4,608 × 3,456 pixels, capable of recording images with 16 bits per color, which are after converted to a readable format. As in the synthetic Schlieren method, PFT require a comparison of digital images. In a first step, we take a snapshot of the fringe pattern when liquid surface is at rest. The second step consists in taking an image of the fringe pattern when the wave is present. Information of h is contained in the phase difference between two images. There are several possible configurations to arrange the camera and the video projector. In our experiments, axis of the camera and video projector are parallel. The relation between h and the phase difference $\Delta\phi$ is (Cobelli et al. 2009; Maurel et al. 2009):

$$h = \frac{\Delta\phi L}{\Delta\phi - \frac{2\pi}{p} D}, \tag{12}$$

where L is the distance of camera to liquid surface, D is the distance between lenses of camera and video projector and p is the wavelength of the fringe pattern. In an ideal case only two images are required to reconstruct the waveform. In reality we need to subtract undesirable factors, then corrections must be incorporated. Let us project on the liquid surface an image in which all pixels have the same intensity level. When this pattern is recorded with the digital camera, intensity is not constant. This is due, among other things, to the fact that when light reaches the liquid surface three phenomena take place, that is, reflection, transmission and absorption. The amount of energy carried by the reflected light is dependent on the incidence angle. In order to remove this source of undesirable effects we need also to record this kind of images and include them in the process for determining phase difference.

3.1 Experimental Setup

Experiments were carried out in a basin made in plexiglass whose dimensions are 120 cm × 50 cm × 15 cm. Waves were produced with a parabolic wave maker whose parameter a is 2 (see Eq. 4) and has 42 cm wide. The wave maker is connected to a mechanical vibrator which produces a sinusoidal motion of frequencies lying in the range 4–10 Hz, corresponding to wavelengths between 2.4 and 10 cm. The water level is set to 10 cm for both synthetic Schlieren and FTP experiments. The deep water approximation is well fulfilled because in all cases $\tanh(kH) > 0.999$. Images for synthetic Schlieren method cover an area of 20 cm × 11.2 cm, they were recorded with a full HD digital camera. In each realization a film of 50 frames/s was taken during 50 s. Each film includes frames for both unperturbed and wavy surfaces. Individual images are extracted from the film through the use of the free software ffmpeg. Digital processing was performed with DPIVsoft software (Meunier and Leweke 2003), which allows to obtain the free surface gradient. Finally the reconstruction

of the surface topography h(x, y) is made by a finite difference approximation for spatial derivatives of the surface gradient.

With respect the implementation of Fourier Transform Profilometry an opaque liquid surface is required. This is achieved by adding a concentrated white dye to the water. The fringe pattern projected on the free surface covers an area of 28 cm $\times$ 50 cm, which is sufficient to investigate wave field before and after the Huygens cusp. On the other hand, the distance from projector to liquid surface is L = 1.14 m, the distance D is 0.30 cm and wavelength of fringe pattern was p = 0.003 m (3 mm). In order to avoid the appearance of undesirable bright spot the image produced by the videoprojector was shifted with no deformation (a feature available in newer equipment) and additionally two crossed polarizers have been put on the lenses of camera and videoprojector. As stated before, we use a digital camera capable of recording in raw format. A further conversion of images to a standard format (tif images of 16 bits per color) was made and finally processing was made with routines written in matlab.

4 Numerical Method

The surface waves are governed by the Navier-Stokes and continuity equations. In recent decades many researches of surface waves were made through numerical codes, however there are some difficulties in its use, for instance, the domain of integration changes in time. In this work we present numerical results for surface waves in the shallow water approximation, that is, when liquid depth is much lower than the wavelength λ ($H \ll \lambda$). The choice of this approximation was made on the basis that the system remains 2D but at the same time non linearity is retained. The equations to solve are:

$$\frac{\partial u}{\partial t} + u\frac{\partial u}{\partial r} + \frac{v}{r}\frac{\partial u}{\partial \theta} - \frac{v^2}{r} = -g\frac{\partial h}{\partial r}, \tag{13}$$

$$\frac{\partial v}{\partial t} + u\frac{\partial v}{\partial r} + \frac{v}{r}\frac{\partial v}{\partial \theta} - \frac{uv}{r} = -\frac{g}{r}\frac{\partial h}{\partial \theta}, \tag{14}$$

$$\frac{\partial h}{\partial t} + \frac{1}{r}\left(\frac{\partial (rhu)}{\partial r} + \frac{\partial (hv)}{\partial \theta}\right) = -\frac{H}{r}\left(\frac{\partial (ru)}{\partial r} + \frac{\partial v}{\partial \theta}\right), \tag{15}$$

where u and v are the horizontal components of the velocity field, h is the free surface deformation and H is the depth of the liquid layer. In the deduction of these equations, the viscosity was neglected and the continuity equation and the kinematical condition have been used. The numerical method used for solving Eqs. (13)–(15) involves a centered second order finite differences for radial coordinate, a backward second order finite difference for time and a spectral code for θ coordinate. The numerical code cannot predict the wave breaking because this process implies that variable h

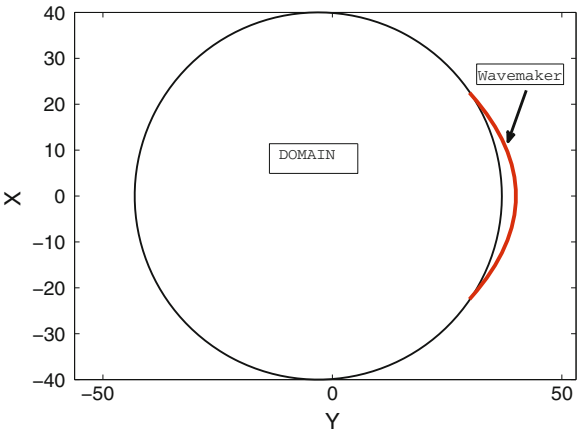

Fig. 4 Spatial domain used in the numerical solution. It is a annular ring ($r_1 < r < r_2$). The wave maker is outside this domain, it intersects the outer boundary in two points. The boundary conditions are set assuming that the wave front evolves according to the stationary phase method

become multivaluated. However it is possible to study the focusing and the emergence of nonlinearities appearing during the growth of waves. It is important to remark that when non linear terms are dropped from Eqs. (13)–(15) we recover the equations of a linear wave. The numerical solution is performed in a annular domain, for $r_1 < r < r_2$. The wave maker is outside this domain, it intersects the outer boundary in two points (see Fig. 4). We consider that initially the fluid is at rest, that is, surface is not deformed. For imposing the boundary conditions we approximate the values of surface deformation assuming that the wave evolve from wave maker to the outer boundary according to the stationary phase method. The numerical solution was carried out using a mesh of 400 points in radial direction and 256 modes in the angular variable θ. Otherwise the time step is set to $\delta t = 0.01$.

Numerical simulation was made under two conditions. In the first one the nonlinear terms are dropped, then solution correspond to a linear wave. In the second case nonlinear terms are retained. In both cases maximal amplitude is attained in the vicinity of Huygens cusp, along the symmetry axis. Otherwise, due to finite size of the wave maker we observe that interference in the region delimited by caustics occurs only in a section near the cusp.

5 Experimental and Numerical Results

As stated in Sect. 3 surface waves were produced with a parabolic wave maker. In order to characterize the initial wave front we recall that the equation of a parabola is $y_0 = ax_0^2$. In our experiments and in numerical simulations the value of parameter a is 2; thus the position of the Huygens cusp is $R = \frac{1}{2a} = 0.25\,\mathrm{m}$ away from the parabola vertex. Most of results presented here correspond to waves with a frequency $f = 7\,\mathrm{Hz}$ or equivalently $\lambda = 3.82\,\mathrm{cm}$. Experiments and numerical simulations were conducted to study three types of singularities: wave breaking, caustics and

dislocations. Attention is paid to the growth of wave amplitude in the vicinity of the Huygens cusp, because in this region these singularities occur. On one side a non linear wave cannot rise indefinitely, at certain time the wave breaking begins. On the other side diffraction is capable to produce dislocations on the dark side of caustics. Some comments will be addressed to the decay of wave field far from the Huygens cusp and the recovery of the linear behavior far from caustics. In most of experiments the topography of the free surface is recovered with the method of Fourier Transform Profilometry. The images recorded by the digital camera cover only a fraction of the fringe pattern, but in any case we consider regions around the Huygens cusp. On the other side, experiments with synthetic Schlieren method were conducted covering an area of 20 cm $\times$ 11.2 cm. Images were taken at 4 different positions in the range $10 < y < 50$. The area covered in a position of the camera overlap with the next one, so we have a complete set of data in a region of 20 cm $\times$ 40 cm. In some cases it is best the use of synthetic Schlieren method. For instance, in a previous work this method has been successfully used to prove that for small amplitude waves (Ruiz-Chavarria et al. 2014) ($h < 10^{-4}$ m) the nonlinearities are already relevant. Another case were synthetic Schlieren method is suitable deals with the study of divergent waves because amplitude decreases as they progress. This happens in our system after passing the cusp.

Figure 5 shows the wave field as measured by the FTP method for a driving frequency of 7 Hz in the area delimited by $-11 < x < 11$ cm and $7 < y < 32$ cm. As in all figures in this paper, wave progresses from right to left. The Huygens cusp is located inside this region. Otherwise, the focusing becomes evident by two facts: (a) the size of wave front decreases from right to left and (b) the wave amplitude (represented by colors) grows when approaching the cusp. At the left border of figure

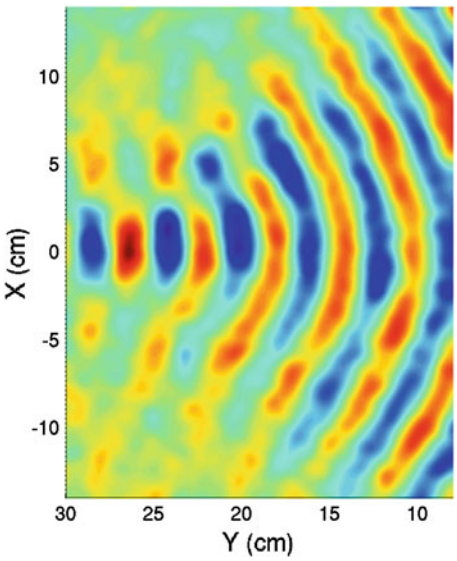

Fig. 5 Wave field of a monochromatic wave of f = 7 Hz produced by a parabolic wave maker. Wave progresses from *right* to *left*. In the figure the maximal amplitude occurs after passing the cusp

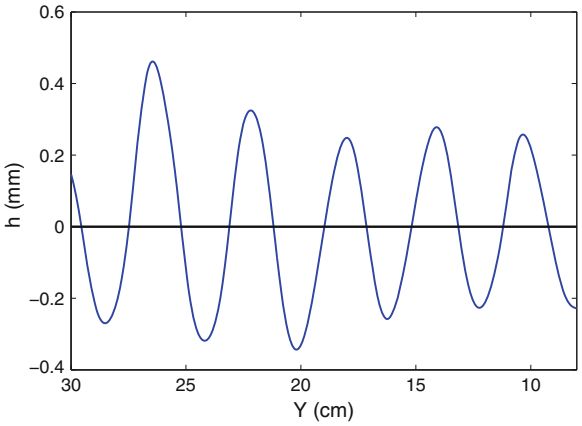

Fig. 6 Monochromatic wave of f = 7 Hz produced by a parabolic wave maker along the symmetry axis. Wave progresses from *right* to *left*. The asymmetry of the wave reveals that nonlinearities are important

there is a change of sign of the wavefront curvature, so waves become divergent. Consequently the further evolution leads to a decrease of the wave amplitude.

Taking into account that the maximal value of surface deformations occurs along x = 0, in Fig. 6 we show the curve h versus y along the symmetry axis. The maximal amplitude occurs at $y = 27$ cm, after passing the cusp, in agreement with results by Pearcey. A key feature of Fig. 6 is the asymmetry of the wave. This is a signature of a nonlinear behavior. For $y > 27$ cm the wave amplitude decreases because wave becomes divergent. In order to follow evolution of such divergent waves we have

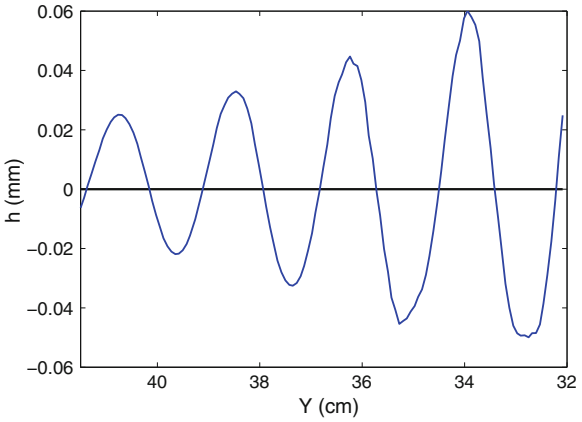

Fig. 7 Wave field of a monochromatic wave of f = 10 Hz produced by a parabolic wave maker. The topography of the free surface was obtained with the synthetic Schlieren method. Wave progresses from *right* to *left*. At y = 40 the values of skewness and asymmetry are respectively 0.06 and −0.02. At y = 34 cm these quantities take the following values $A_s = 0.16$ and $S = -0.04$

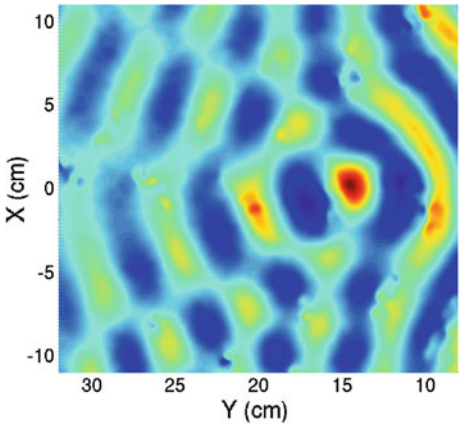

Fig. 8 Wave field in which breaking is developing. The wave frequency is 7 Hz. The amplitude increases monotonically before y = 15 cm. After this point the wave becomes divergent. During the wave breaking a fraction of the energy is dissipated

measured the free surface topography for $y > 30$ cm with the synthetic Shlieren method. The result presented in Fig. 7, corresponds to a wave of frequency f = 10 Hz ($\lambda = 2.4$ cm). An important feature is that, as wave progresses the amplitude decreases and nonlinear behavior weakens. In fact, skewness and asymmetry have the following values at y = 40 cm: $A_s = 0.06$ and $S = -0.02$, whereas the same quantities take the values $A_s = 0.16$ and $S = -0.04$ at y = 34 cm. This is a proof that far from the caustics the wave is well described by the linear theory.

In order to produce wave breaking, a higher amplitude is required. In Fig. 8 we show a snapshot of the wave field in which breaking develops. We remark two facts: (a) the nonlinear interactions lead to a greater ratio of maximal to initial amplitudes (the amplitude at the wave maker) when compared with results shown in Figs. 5, 6 and 7 and (b) the position of maximal wave amplitude is $y = 15$ cm, some wavelength before the Huygens cusp.The shape of the wave fronts is clearly modified by the breaking. First at all the wave appears as divergent for $y > 15$ cm. In addition, just before $y = 15$ cm the growth of wave develops rapidly over a distance comparable to a wavelength. In Fig. 9 the wave along the symmetry axis ($x = 0$) is shown. Before $y = 15$ cm the amplitude grows monotonically but after this point the wave exhibits important modifications. For instance the peaks located at $y = 26$ cm and $y = 30$ split in two local maxima. Finally it is important to say that the decrease of the amplitude during the breaking reveals that energy is dissipated.

Now we present some results of the numerical simulations. All the wave maker characteristics are retained and the driving frequency is again 7 Hz. In Fig. 10 we show snapshots of both linear (Fig. 10a) and nonlinear waves (Fig. 10b). For a linear wave the initial amplitude is irrelevant (only the ratio of the actual to initial amplitude is important), but the same does not apply for a nonlinear wave. In the simulations, initial amplitude is 2 % of the liquid depth. The overall trend of wave fronts is qualitatively the same in both cases. In Figs. 10a, b interference holds either inside

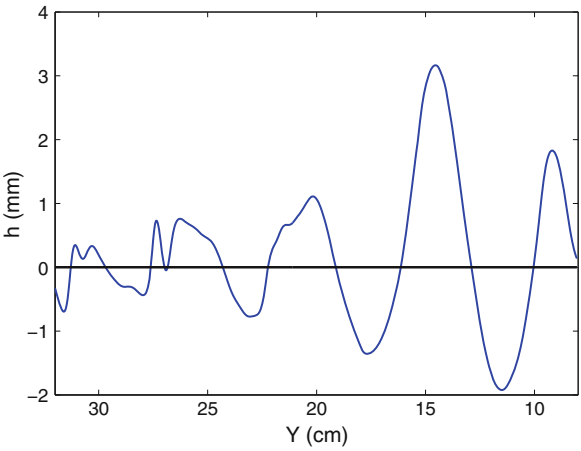

Fig. 9 Monochromatic wave of frequency f = 7 Hz along the symmetry axis. Before y = 15 cm the wave amplitude grows monotonically, but after this position there are important modification in wave, for instance around the peaks located approximately at y = 26 cm and y = 30 cm we found two local maxima

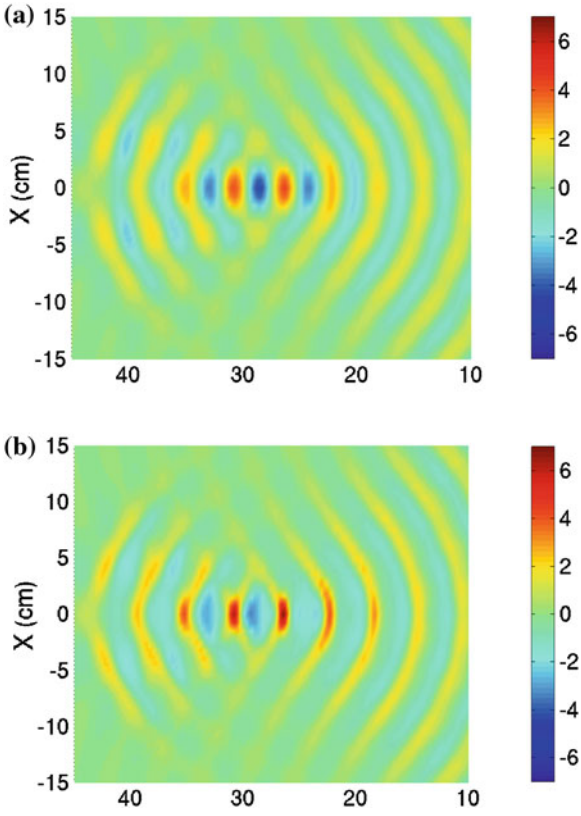

Fig. 10 Wave field of a monochromatic wave of f = 7 Hz produced by a parabolic wave maker. **a** Linear wave and **b** nonlinear wave with an initial amplitude of 2 % of the liquid depth. Wave progresses from *right* to *left*. In the figure the maximal amplitude occurs after passing the cusp. Maximal amplitude for non linear wave is greater with respect the linear wave

and outside the caustics. In the same manner, after passing the Huygens cusp, the amplitude decreases because wave becomes divergent. However some differences must be highlighted. A first thing to emphasize is that the peaks around the cusp

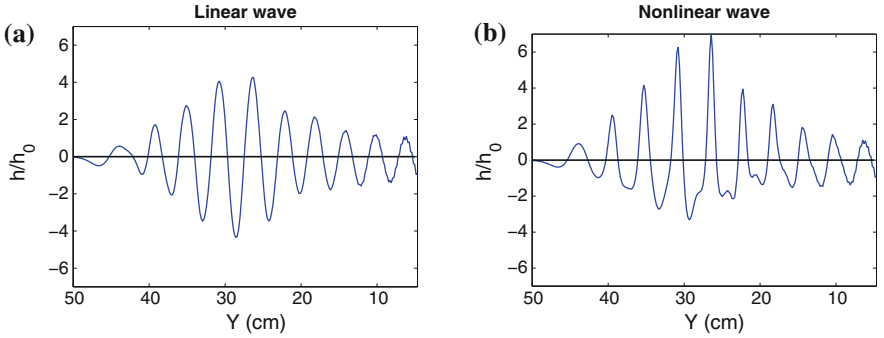

Fig. 11 Wave of frequency 7 Hz along the symmetry axis produced by a parabolic wave maker. Maximal amplitude attained by non linear wave is greater than those of the linear wave. In addition, peaks and troughs are clearly asymmetric. In the figure the maximal amplitude occurs after passing the cusp. **a** Linear wave. **b** Nonlinear wave

becomes narrower for the non linear wave if compared with the linear one. This is a proof that peaks became steeper as already seen in experiments.

A better way to see the focusing and the nonlinear behavior is to plot a wave along the symmetry axis. This is made in Fig. 11 for waves considered in Fig. 10. The first thing to remark that the linear wave is symmetric everywhere. Concerning the nonlinear wave, as already stated, we have a maximal amplitude higher than those attained in the linear case. In addition, the asymmetries between peaks and troughs are very clear. We are still far from wave breaking but nonlinear effects are already present. Instead of showing a particular wave profile, a way to see the overall behavior

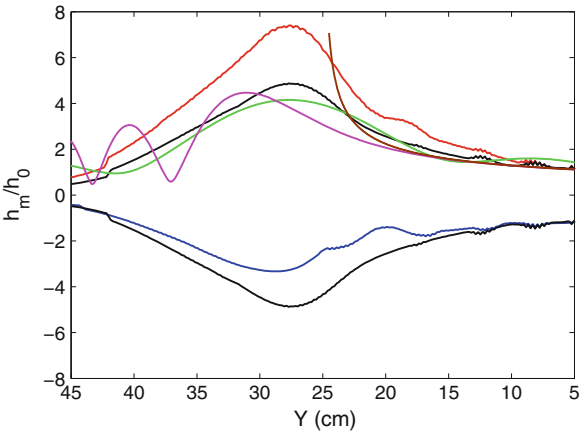

Fig. 12 Wave envelope calculated in different cases: (i) Linear wave (*black line*), (ii) nonlinear wave with initial amplitude 0.02H (*red* and *blue lines*), (iii) Pearcey integral for a finite wave maker (*green line*), (iv) Pearcey integral for an infinite wave maker (*magenta line*) and (v) envelope obtained with the stationary phase method (*brown line*). In the nonlinear case, positive and negative branches are clearly different

is to plot the wave envelope along the symmetry axis. In Fig. 12, we plot envelopes in the following cases: (i) linear wave, (ii) non linear wave with initial amplitude 0.02H., (iii) Pearcey prediction for a finite size wave maker, (iv) Pearcey prediction for an infinite wave maker, (v) envelope predicted by the stationary phase method. In all cases amplitudes are normalized with initial amplitude (h_0). It is important to point out that interference in the region inside the caustics leads to oscillations of the envelope. These oscillation are predicted by the Pearcey results. However, in a wave field produced by a finite wave maker these oscillations are less important because the zone where three rays reach a point is only a fraction of the area limited by the caustics. Far from the cusp, and according to ray theory, only a ray reaches each point. In this figure the asymmetries related with nonlinearities are evident. First, the negative branch of linear wave envelope is exactly the reflection of the positive one (black lines). The same does not apply for the non linear wave and only far from the cusp both branches becomes symmetric.

Caustics are fictitious singularities appearing in the ray theory. On the other side, dislocations are a kind of singularity which remains beyond the geometrical optics. They are points of full destructive interference and can be recognized by two facts: the wave amplitude is always zero and the phase is undetermined. According to the last feature, in a dislocation the contours of constant phase cross. The Fig. 13 shows both a diagram of the wave amplitude and curves of constant phase, calculated with the Pearcey integral. The ray theory predicts that dislocations occurs only inside the caustics, but due to diffraction two dislocations outside the caustics appear. The numerical solution of wave equation (linear and nonlinear) predicts also the existence of dislocations outside the caustics as we can see in Fig. 14, where wave amplitude as a function of (x, y) is shown. Dislocations are located in the blue regions of each

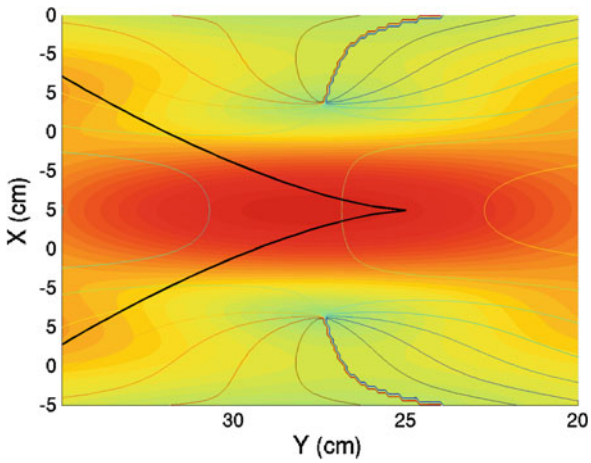

Fig. 13 Graph of wave amplitude and *curves* of constant phase obtained from the Pearcey integral, assuming a finite wave maker. The phase is undetermined in the points of full destructive interference. Then the *curves* of constant phase cross in such points. These singularities are known as dislocations

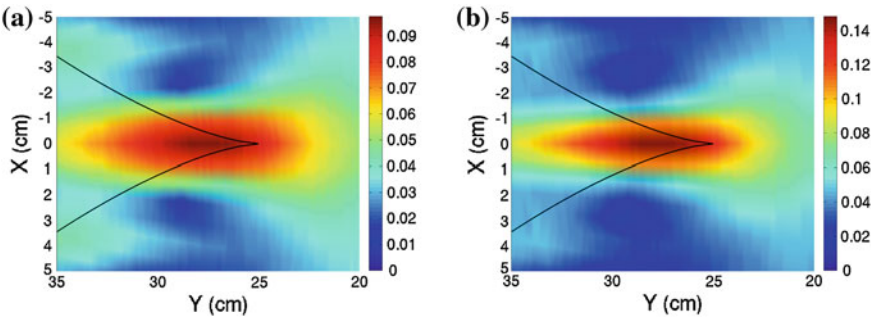

Fig. 14 Graph of the wave amplitude obtained from numerical simulation. **a** Linear case and **b** non linear case. Two dislocations appear outside the caustics both in linear and in nonlinear waves. They are located inside the *blue region* of each figure

figure, they are symmetrically situated around x = 0. The dislocations are located at (−2.3, 28.9) and at (2.3, 28.9) for the linear wave. For the nonlinear wave the dislocations are located at (−3, 29.5) and at (3, 29.5).

6 Conclusions

In this paper we have performed an experimental and numerical study of the wave field having three types of singularities: caustics, wave breaking and dislocations. The first one is a fictitious singularity appearing in the ray theory. It disappears when wave properties are taken into account, but its position reveals bright regions. The second kind of singularity (wave breaking) is produced by non linear interactions. In our experiments the breaking is produced through spatial focusing over a distance of some wavelengths. The wave breaking modify the shape of wave fronts and produces a dissipation of the energy. Finally, the third kind of singularities are the dislocations, which are defined as points of complete destructive interference. The singularity deals with the fact that in a dislocation phase is undefined. The experiments and numerical simulations were conducted to enhance the nonlinear effects. This research is in the first stage. A more complete research of singularities requires, among others, a detailed study of conditions of wave breaking, the determination of the amount of energy dissipated and the study of dislocations both inside and outside the caustics.

Acknowledgments G. Ruíz Chavarría acknowledges DGAPA-UNAM by support for a sabbatical period at IRPHE between September 2010 and August 2011. Additionally the authors acknowledge support by DGAPA-UNAM under project 116312, Vorticidad y ondas no lineales en fluidos. Authors acknowledge also Eric Falcon from University Paris Diderot for his assistance in the implementation of the Fourier Transform Profilometry.

References

Babanin A (2011) Breaking and dissipation of the ocean surface waves. Cambridge University Press, Cambridge

Cobelli PJ, Maurel A, Pagneux V, Petitjeans P (2009) Global measurement of water waves by Fourier transform profilometry. Exp Fluids 46:1037–1047

Elmore WC, Heald MA (1969) Phys waves. McGraw Hill, New York

Maurel A, Cobelli PJ, Pagneux V, Petitjeans P (2009) Experimental and theoretical inspection of the phase to height relation in Fourier transform profilometry. Appl Opt 48:380–392

Meunier P, Leweke T (2003) Analysis and minimization of errors due to high gradients in particle image velocimetry. Exp Fluids 35:408–421. https://www.irphe.fr/meunier/PIV

Moisy F, Rabaud M, Salsac K (2009) A synthetic Schlieren method for the measurement of the topography of a liquid surface. Exp Fluids 46:1021–1036

Paris RB, Kaminsky D (2001) Asymptotic Mellin-Barnes integrals. Cambridge University Press, Cambridge

Pearcey I (1946) The structure of an electromagnetic field in the neighborhood of a cusp of a caustic. Philos Mag 37:311–317

Ruiz-Chavarria G, Le Bars M, Le Gal P (2014) Focusing of surface waves in experimental and computational fluid mechanics. 315–325. ISSN 1431-2492

Zemenzer S (2011) Etude experimentale du deferlement des vagues en eau profonde par focalisation spatiale; Rapport de stage, Universite de la Mediterranee

Part II
Multiphase Flow and Granular Media

Isotherms of Natural and Forced Convection Around a Heated Horizontal Cylinder Embedded in a Porous Medium

M. Sánchez, A. Torres, F. Aragón, I. Carvajal and A. Medina

Abstract This work presents an experimental analysis of free and forced convection due to a heated cylinder in a fluid-saturated porous medium. The resulting features of the temperature distribution under the action of a continuous and uniform air stream were investigated through the use of four different configurations: first, by inducing an air stream from below the heated cylinder; second, by placing an air stream on the left-hand side of the heat source; third by an air stream acting from the top of the heat source, and fourth by varying the injection angle. The consequences on the free and forced convection when all phenomena reach the steady state were analyzed by using an infrared camera. Close agreement is found through the conformed plumes with the theoretical solutions proposed by Kurdyumov and Liñán (2001).

M. Sánchez (✉) · A. Medina
Instituto Politécnico Nacional, Escuela Superior de Ingeniería Mecánica y Eléctrica, Unidad Profesional Azcapotzalco, Av. de Las Granjas 682, Santa Catarina, Azcapotzalco, 02250 Mexico, D.F., Mexico
e-mail: foxandkirvi@hotmail.com

A. Medina
e-mail: abraham_medina_ovando@hotmail.com

A. Torres
Coordinación del Posgrado, Instituto Mexicano del Petróleo, Eje Central Lázaro Cárdenas 152, Del. Gustavo A. Madero, 07730 Mexico, D.F., Mexico
e-mail: higherintellect@hotmail.com

F. Aragón · I. Carvajal
Instituto Politécnico Nacional, Sección de Estudios de Posgrado e Investigación, Escuela Superior de Ingeniería Mecánica y Eléctrica, Unidad Profesional Adolfo López Mateos, Av. Instituto Polit écnico Nacional S/N Col. Lindavista, Del. Gustavo A. Madero, 07738 Mexico, D.F., Mexico
e-mail: micme2003@yahoo.com

J. Klapp et al. (eds.), *Selected Topics of Computational and Experimental Fluid Mechanics*, Environmental Science and Engineering,
DOI 10.1007/978-3-319-11487-3_13

1 Introduction

This work is based on the theoretical work developed by Kurdyumov and Liñán (2001) who studied the effects of the forced convection acting on a heated horizontal cylinder that is buried in a fluid-saturated porous medium. Problems that involve both free and forced convection due to a heat source, q, in a porous medium have been studied theoretically by several authors (Wesseling 1974; Bejan 1978; Poulikakos 1984; Pop and Ingham 2001).

On the other hand, to our knowledge, there are few experimental studies aimed to reproduce and observe the development of the laminar thermal plumes due to the action of free and forced convection. In this work we use thermography techniques (Astarita and Carlomagno 2013) to experimentally study several configurations; an infrared camera allows us to see the isotherms due to the convection process along a transverse face of the porous medium. Detailed properties of the buoyant plumes will be discussed after the theoretical elucidation of the problem and the description of the experimental setup.

2 Theoretical Model

Consider an horizontal long and infinitesimal heated cylinder embedded in an unbounded and fluid-saturated porous medium with permeability K and porosity ϕ. The heated cylinder yields a constant heat flow of intensity q to the homogeneous unconfined porous medium, and a laminar air stream of velocity V_∞ can be induced, pointing towards the heat source, as it can be seen in Fig. 1.

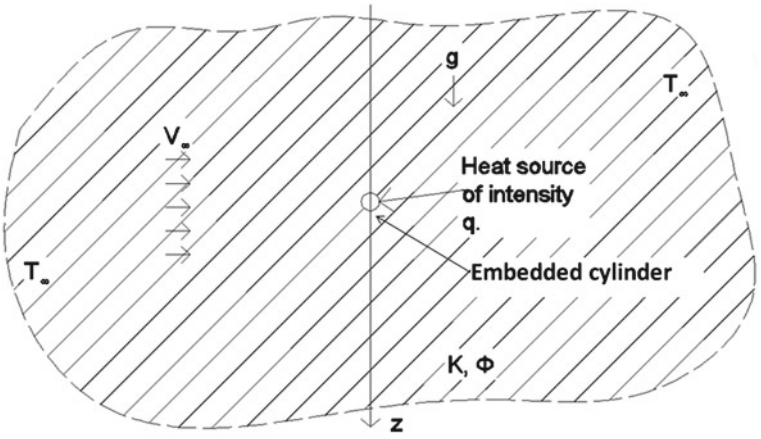

Fig. 1 Schematic transversal view of an *horizontal* heated cylinder embedded in a fluid saturated porous medium. The temperature far from the cylinder is $\boldsymbol{T}_\infty$. A uniform stream comes to the cylinder at velocity $\boldsymbol{V}_\infty$

If there is no laminar stream, then a free convection occurs. On the contrary, a forced convective regime is established in the porous medium by the action of the continuous injection of air stream. The stream orientation is modified in the zones close to the punctual heated source. Consequently, the temperature distribution will be changed resulting in a new plume configuration. The model studied by Kurdyumov and Liñán (2001) predicts the behavior of the two-dimensional velocity field of an air stream around the heated source, as well as its relationship with the temperature gradients that conform the buoyant plumes under the action of free and forced convection.

In the first stage of this work, the pure free convection case is reproduced experimentally, analyzed and compared to the theoretical solutions obtained by Kurdyumov and Liñán (2001), and in a second part the effects of the forced convection are studied, and the buoyant plumes are obtained by varying the direction of the induced streams.

3 Experimental Setup

Despite the fact that the theory was made for an infinite medium, in the present experiments we have used a cardboard box (parallelepiped) of 0.28 m height, 0.20 m length and 0.1 m depth, which was filled with Ottawa sand (ASTM C778), building a non consolidated homogeneous porous matrix. At the middle of the box a cylindrical resistance of 0.00959 m diameter was embedded. To supply a continuous air rate, a compressor 1.2 MPa was used together with flow aligners to induce a uniform air stream. In order to sense the resistance temperature a type T thermocouple was placed at the rear end of it and was connected to a WEST (6100+) process indicator for the temperature control. For all the tests, the resistance reaches 353.15 K.

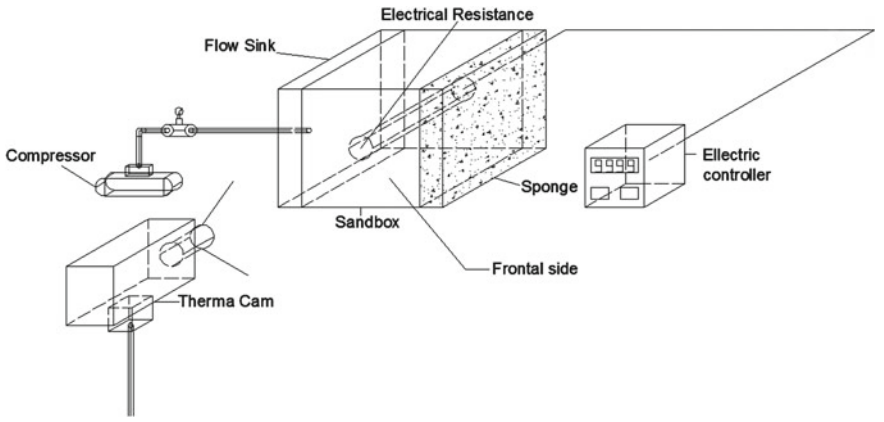

Fig. 2 Scheme of the experimental array

To capture accurately the development of the buoyant plumes, an infrared camera FLIR (ThermaCAM SC660) was employed. The infrared camera works at a range of temperatures from 233.15 to 1773.15 K and records images of size 640 × 480 pixels (VGA quality). In the experiments the infrared camera was placed approximately at a distance of 1 m, pointing towards the center of the frontal side of the sand box. All experimental measurements were made at a room temperature of 295.15 K and at atmospheric pressure. The experimental setup is show in the sketch of Fig. 2.

4 Isotherms Around the Source

The experiments presented here were designed to be allow direct comparison with the theoretical work of Kurdyumov and Liñán (2001) and are divided in two parts, where the first one is devoted to show the effects of the natural convection around a buried heat cylinder in an air-saturated porous medium, while in the second part, the experiments show the effects of the forced convection, as a result of the change in position of the air stream that acts on the air saturated porous medium.

The Rayleigh number (Ra) and the Nusselt number (Nu) are defined as follows: $Ra = K\rho_f \beta g(T_w - T_\infty)a/\alpha\mu_f$ and $Nu = q/2\pi\lambda(T_w - T_\infty)$, and all parameters used in the experiments are listed in Table 1. A characteristic length and a non-dimensional formula for the temperature were defined by Kurdyumov and Liñán (2001) as: $l_h = \alpha\mu_f\lambda/K\rho_f g\beta q$ and $\theta = (T - T_\infty)/(T_w - T_\infty)$, respectively. All experiments were carried out at a Rayleigh number $Ra \sim 3.41 \times 10^{-2}$ and a Nusselt Number $Nu \sim 0.1590$.

Table 1 General parameters used in the experiments

Property	Value
Permeability (K)	6.0E-11 m^2
Fluid density (Air at 293.15° K) (ρ_f)	1.2 kg/m^3
Fluid viscosity (Air at 293.15° K) (μ_f)	1.71E-05 Pa·s
Gravity acceleration (g)	9.81 m/s^2
Temperature of the heated cylinder (T_w)	353.15 K
Room temperature (T_∞)	295.15 K
Radius of the heated cylinder (a)	0.004795 m
Coefficient of expansion of Air at 293 K (β)	0.003388 K^{-1}
Sand effective thermal diffusivity (α)	2.45E-08 m^2/s
Effective conductivity (λ)	0.039 W/mK

5 Isotherms Under Free Convection

At this stage of the experiments, the effects of the free convection are shown. It is important to say that close to the heated cylinder the conduction dominates and the resulting plumes get a concentrically circular shape, but if we turn away of the heated cylinder, the convection begins to dominate the phenomenon and the plumes begin to deform acquiring an ovoidal shape in its upper part. Figure 3 shows the evolution of the plumes due the free convection. The time between successive images in the sequence is 5 min. Figure 4 shows the dependence of the dimensionless temperature θ

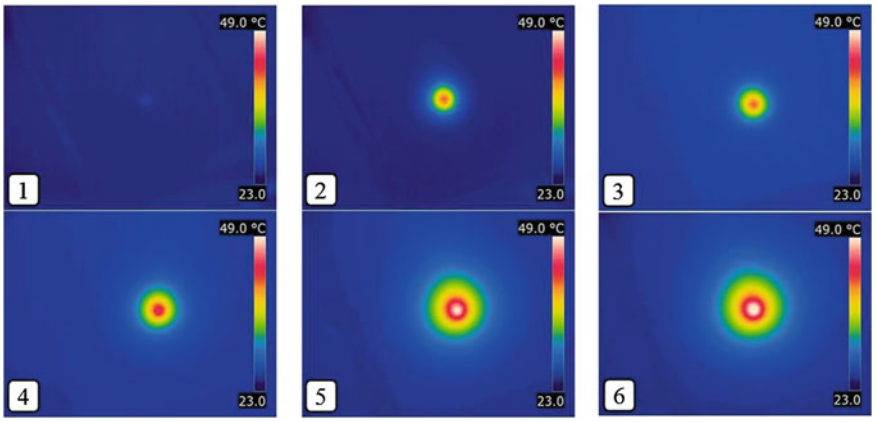

Fig. 3 Sequence of infrared snapshots showing the evolution of the plumes under pure free convection until a stationary state is reached. The time between consecutive snapshots is $\Delta t = 5$ min

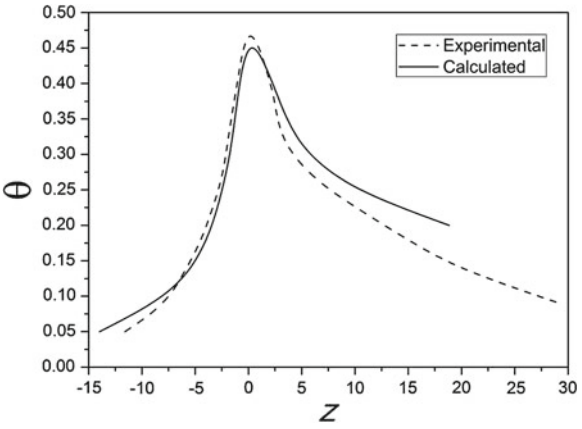

Fig. 4 Dependence of the numerically obtained dimensionless temperature θ distribution (*continuous line*) as a function of the dimensionless distance z (length taken with reference to the *vertical* axis passing through the heat source), as compared with distribution obtained experimentally (*dashed line*) for the free convection case. The experimental *curve* was build up from the isotherms of snapshot 6 in Fig. 3

on the dimensionless vertical coordinate z. The distribution obtained experimentally (dashed line) is compared with the numerically obtained solution of Kurdyumov and Liñán (2001) (solid line). The experimental curve corresponds to the case depicted in the snapshot 6 of Fig. 3.

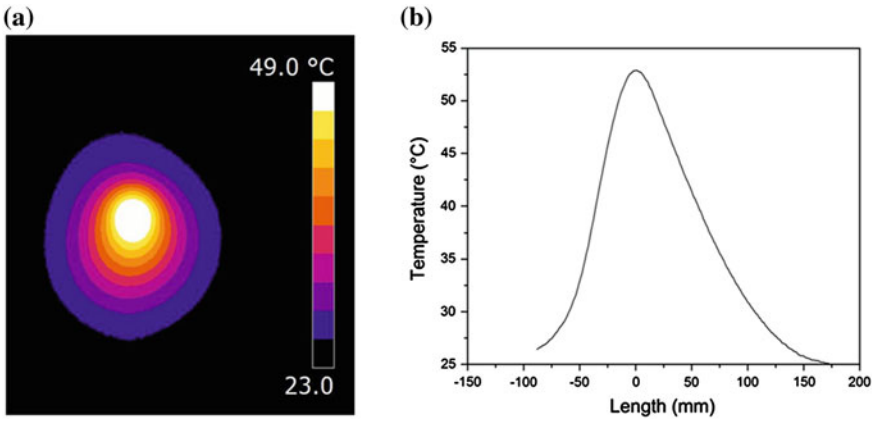

Fig. 5 **a** Infrared image showing the plume shape due to forced convection induced from the *upper part* of the saturated porous medium. **b** Plot showing the temperature distribution as a function of the distance (length taken with reference to the *vertical z*-axis passing through the heat source)

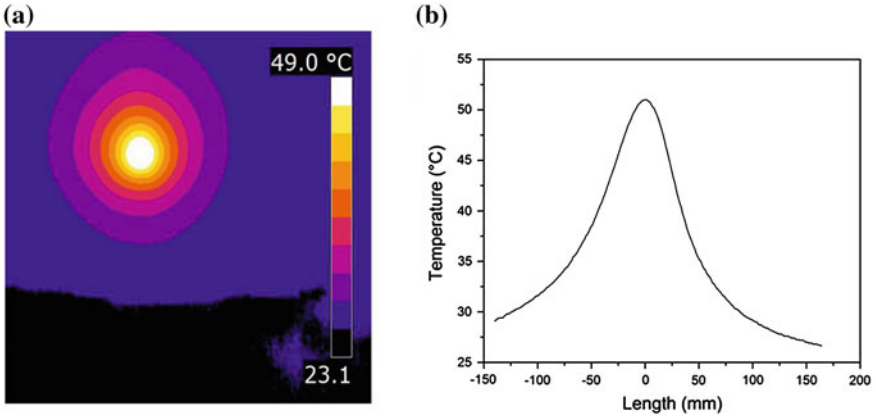

Fig. 6 **a** Infrared picture showing the plume formed due to forced convection induced from the *lower part* of the saturated porous medium. **b** Plot showing the temperature distribution as a function of the distance (length taken with reference to the *vertical z*-axis passing through at the heat source)

5.1 Isotherms for a Horizontal Line Source of Heat Under a Uniform Stream

The second part of the experiment consists of obtaining the isotherms by inducing a continuous stream of air at different configurations. It is important to say that the constant stream of air was injected at three different pressures (49 kPa, 73.5 kPa, 98 kPa) and the increase of the injection pressure is seen to delay the time for which the buoyant plumes reach the steady state. The final form of the buoyant plume was not modified as time elapses. In Fig. 5 the final shape of the plume, as a result of the induced free stream of air in the upper part of the porous medium can be seen. It is clear that under this new condition the convection dominates over the conduction even in the zones close to the source of heat. The plumes for this cases take elliptic shapes which are more strongly change toward the direction of the induced stream.

In a further experiment, the air stream was injected at the lower part of the porous medium. The resulting plume can be seen in Fig. 6. It is evident that the final

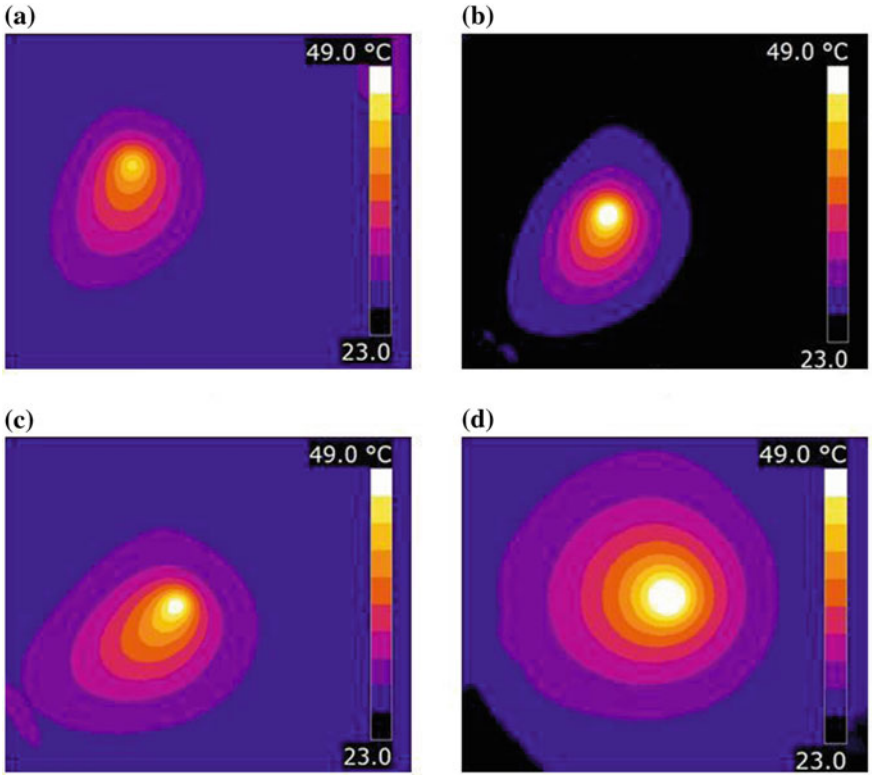

Fig. 7 Infrared images of the isotherms around the heated cylinder due to forced convection induced from different air injection angles (measured with respect to the *vertical* axis): **a** 30°, **b** 45°, **c** 60°, **d** 70°

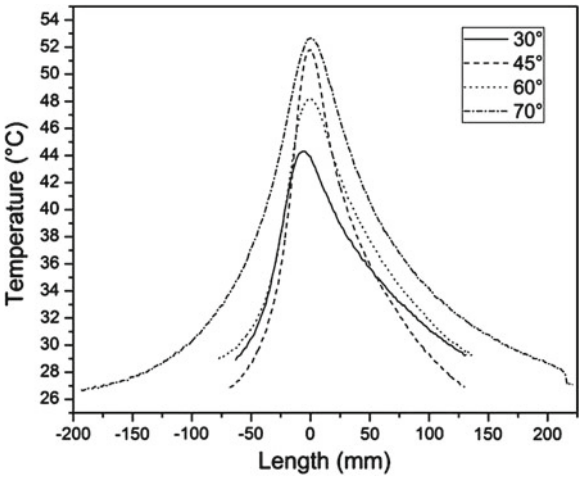

Fig. 8 Plot showing the resulting temperature distributions for different angles of injection as a function of length (length taken with reference to the *vertical* z-axis passing through at the heat source)

deformation attained in this later case was larger than that observed in Fig. 5. This may be due to the induced air stream going to the same direction as the buoyant forces.

In the last part of the experiments different plumes were obtained by inducing the air stream at different angles, as referred to the positive vertical z-axis and measured clockwise, and by placing the origin at the center of the heat source. The steady configuration adopted by the plumes is shown in Fig. 7. The shape of these plumes is strongly influenced by the direction of the induced stream. In Fig. 8, the corresponding values of temperature for each of these later cases were plotted as a function of length.

6 Conclusions

The resulting buoyant plumes or isotherms around a heated source, due to free and forced convection acting on a heated cylinder buried in an air-saturated porous medium, have been experimentally studied by using infrared thermography. Infrared thermography allowed to observe the overall evolution of the buoyant plumes, since the phenomenon was governed by conduction from zones close to the heated source to zones where the convection effects dominate. As we have seen by comparing the effect of a continuous stream with the pure convection case, the shapes adopted by the buoyant plumes, are were strongly affected by the action of the continuous air flow. We do not find any important correlation with the rate of air injected. The final shape of the plumes indicates that the stream lines of the flow change their trajectory in zones nearby the heat source. Finally, the actual study agrees with the main theoretical predictions, of Kurdyumov and Liñán (2001), for the isotherms during free and forced convection. Incidentally, this kind of studies can be useful, for instance,

in problems related to the oil industry, specifically in the Steam Assisted Gravity Drainage (SAGD) process where it is important to redirect the oil flow towards a recovery well through a saturated porous medium. We believe that this process can be improved by manipulating the temperature gradients in the oil reservoir through a suitable collocation of the heat sources.

Acknowledgments A. Torres wishes to thank the Instituto Mexicano del Petróleo for the unconditional support given to this project. M. Sánchez and A. Medina thank partial support of Instituto Politécnico Nacional, through the SIP Project No. 20141404. Finally, we acknowledge Professor Amable Liñán from E.T.S. Ingenieros Aeronáuticos, Universidad Politécnica de Madrid, who suggested us this experimental study.

References

Astarita T, Carlomagno GM (2013) Infrared thermography for thermo-fluid. Springer, Berlin

Bejan A (1978) Natural convection in an infinite porous medium with a concentrated heat source. J Fluid Mech 89:97–107

Kurdyumov VN, Liñán A (2001) Free and forced convection around line sources of heat and heated cylinders in porous media. J Fluid Mech 427:389–409

Pop I, Ingham DB (2001) Convective heat transfer: mathematical and computational modeling of viscous fluids and porous media. Elsevier, Oxford

Poulikakos DA (1984) On buoyancy induced heat and mass transfer from a concentrated source in an infinite porous medium. Int J Heat Mass Transf 28:621–629

Wesseling P (1974) An asymptotic solution for slightly buoyant plumes. J Fluid Mech 70:81–87

Parameter Estimation in a Model for Tracer Transport in One-Dimensional Fractals

E.C. Herrera-Hernández and M. Coronado

Abstract The problem of parameter estimation in a model for one-dimensional fractals is analysed and solved. The model describes advection and dispersion of a tracer pulse in a one-dimensional fractal continuum with uniform flow. It involves three parameters: fractal dimension of length, connectivity index associated to dispersion and dispersion coefficient. By using synthetic tracer breakthrough data the effect of data noise level, amount of data points and number of fitting parameters on the results have been analysed. It has been found that the developed estimation methodology is in general robust to the standard data noise level, and to the amount of data points between the typical cases of around 10 and 40. It has been also found that the curve fitting procedure is consistently more sensitive to the fractal dimension of length than to the other two parameters: the connectivity and the dispersion coefficient.

1 Introduction

Parameter estimation is a relevant stage in the dynamic characterization of aquifers, oil fields and geothermal reservoirs. It is a process that looks for the determination of reservoir properties like porosity, thickness of the production layer, fluids saturation, dispersion coefficient, fault orientation, etc. It allows the understanding of the way fluids move inside porous media, thus providing important elements in the design of efficient oil recovering strategies in mature and partially depleted reservoirs (Illiassov and Datta-Gupta 2002; Ramírez-Sabag et al. 2005; Coronado et al. 2011).
Of particular interest are models related to anomalous dispersion since they provide new insights into the physics of the transport phenomenon. Anomalous behaviour in heterogeneous systems is observed in field and laboratory scales (see for example,

E.C. Herrera-Hernández (✉)
Centro de Ingeniería y Desarrollo Industrial, Querétaro, Qro., Mexico
e-mail: erik.herrera@cidesi.mx

M. Coronado
Instituto Mexicano del Petróleo (IMP), México, D.F., Mexico
e-mail: mcoronad@imp.mx

J. Klapp et al. (eds.), *Selected Topics of Computational and Experimental Fluid Mechanics*, Environmental Science and Engineering,
DOI 10.1007/978-3-319-11487-3_14

Bogatkov and Babadagli 2010 and Fourar and Radilla 2009). This behaviour is characterized by an early tracer breakthrough and long-decaying tails. It has been found that classical advection-dispersion equations do not properly describe the tracer breakthrough behaviour at long times as other approaches do, particularly fractional advection-dispersion models. Therefore, parameter estimation based on anomalous transport models becomes very relevant (Suzuki et al. 2012; Chakraborty et al. 2009). Among other approaches for studying anomalous transport, that do not have the high computational costs involved in evaluating fractional time derivatives, are the fractal continuum models (Herrera-Hernández et al. 2013). In this paper, we present a methodology for parameter estimation for one of the models described in this previously mentioned work. It is a one-dimensional advective-dispersive model in which the space is a fractal continuum (Tarasov 2005) and dispersion follows a power-law dependence with the length scale (Sahimi 1993).

The paper is planned as follows: In Sect. 2 the mathematical model and its solution are presented. The procedure for parameter estimation is described in Sect. 3. Further, in Sect. 4 the generation of synthetic tracer breakthrough data is discussed, and in Sect. 5 the robustness of the estimation method is examined. Finally, the results are analysed in Sect. 6 and conclusions are given in Sect. 7.

2 The Model

2.1 The Fractal Continuum Model

The system we consider consist of an underground fractured porous formation where uniform flow takes place. Fluid and tracer are injected in a plate (located at $x = x_w$) and extracted at another plate (at $x = L$) as illustrated in Fig. 1, where the planes are perpendicular to the paper sheet. This reproduces common assumptions made in Euclidean inter-well one-dimensional flow models (Bear 1972; Chaberneau 2000). We consider a porous medium that is Euclidean in the y–z plane and fractal in x direction. Here a Cartesian coordinate system with the x-axes perpendicular to the plates is employed. The fractality is introduced as a fractal continuum and a geometric mapping of the fractal space into the Euclidean space is proposed. The fractal element of volume is written in terms of fractal and Euclidean elements as in Balankin 2012; Hernandez-Coronado et al. 2012; Herrera-Hernández et al. 2013

$$dV_\alpha = d\ell_\alpha dS_2, \tag{1}$$

where dS_2 is the Euclidean cross-section element and $d\ell_\alpha$ is the fractal length element, whose definition according to Ostoja-Starzewski (2009) is

$$d\ell_\alpha = c_1(x;\ \alpha, x_0)dx, \qquad c_1(x;\ \alpha, x_0) = \frac{\phi}{\Gamma(\alpha)}|x - x_0|^{\alpha-1}, \tag{2}$$

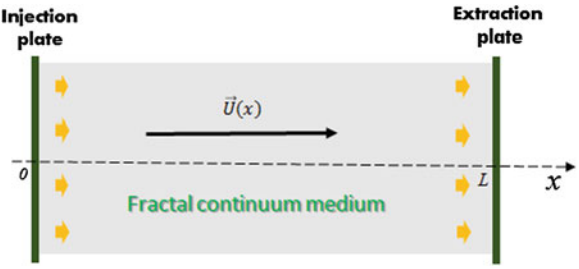

Fig. 1 Physical description of the fractal system with uniform fluid flow

where ϕ is the porosity (added here to the Ostaja-Starzewski model) and α is the fractal dimension of length along the x-direction with $0 < \alpha \leq 1$. It is worth to mention that the fluid can flow in the x-direction even if $\alpha < 1$ since we have a 3D system, where the basic flowing units (fracture planes) can connect outside the x-line. If we consider stationary fluid injection and a fluid velocity pointing in the x-direction, whose magnitude depends on x only, i.e. $\mathbf{u} = u(x)\hat{x}$, the corresponding fluid conservation equation is

$$\frac{1}{c_1}\nabla \cdot (\phi\rho\mathbf{u}) = S_F. \tag{3}$$

The tracer is introduced in the injection plate and extracted in the extraction plate. An expression for the velocity can be derived by integrating it over a volume that contains the fluid source and a part of fractal continuum. It results that

$$u_x(x) = \frac{\dot{M}_F}{A_{cs}\phi\rho(x)}, \tag{4}$$

where $\dot{M}_F$ is the amount of fluid mass injected into the fractal porous medium per unit of time, A_{cs} is a cross section perpendicular to the x-direction in which the fluid is injected, ϕ is the porosity and $\rho(x)$ is the fluid density. Note that for constant fluid density the velocity is constant.

2.2 The Tracer Advection-Dispersion Equation

The tracer pulse dynamics is obtained from the conservation equation

$$\frac{\partial C}{\partial t} + \nabla \cdot \mathbf{J} = S_T. \tag{5}$$

Here the tracer flux contains the advective part due to the process carrying fluid and the dispersive part. This is $\mathbf{J} = \mathbf{U}C - D\nabla C$. According to percolation theory (Gefen et al. 1983; Orbach 1986; Sahimi 1993), we introduce the dispersion coefficient as a

power law of the length travelled, i.e.,

$$D(x) = D_L \left(\frac{x}{L}\right)^{-\theta}. \tag{6}$$

In the above equation D_L is the dispersion coefficient at the extraction length ($x = L$) and θ is the connectivity index associated to the hydrodynamic dispersion.

There are several parameters involved in the model, specifically in Eqs. (4) and (6) appear ϕ, A_{cs}, D_L and θ. The tracer flux for constant fluid density is given by

$$J(x,t) = \frac{\dot{M}_F}{A_{cs}\phi\rho_0} C(x,t) - D_L L^{\theta} x^{-\theta} \frac{\partial C(x,t)}{\partial x}, \tag{7}$$

where the first term describes advection, and the second one depicts dispersion. Accordingly, the tracer conservation equation for uniform flow is (Herrera-Hernández et al. 2013)

$$\frac{\partial C(x,t)}{\partial t} + \frac{\Gamma(\alpha)}{x^{\alpha-1}} \frac{\partial J(x,t)}{\partial x} = S_T. \tag{8}$$

After substituting Eq. (7) into Eq. (8), using dimensionless variables, $x_D = x/L$, $C_D = C/C_{Max}$ and $t_D = t/\Delta t$, and assuming that no source is present, we obtain

$$\frac{\partial C_D}{\partial t_D} + \frac{\Gamma(\alpha)}{L^{\alpha}} \frac{\dot{M}_F \Delta t}{A_{cs}\phi\rho_0} x_D^{1-\alpha} \frac{\partial C_D}{\partial x_D} - \frac{\Gamma(\alpha)}{L^{\alpha-1}} \frac{D_L \Delta t}{L^2} x_D^{1-\alpha} \frac{\partial}{\partial x_D}\left(x_D^{-\theta} \frac{\partial C_D}{\partial x_D}\right) = 0. \tag{9}$$

Δt is an arbitrary reference time and C_{Max} is a reference tracer concentration. The mathematical model given by Eq. (9) contains various parameters that can be grouped as

$$U_{ad} = \frac{\Gamma(\alpha)}{L^{\alpha}} \frac{\dot{M}_F \Delta t}{A_{cs}\phi\rho_0}, \tag{10}$$

$$D_{ad} = \frac{\Gamma(\alpha)}{L^{\alpha-1}} \frac{D_L \Delta t}{L^2}. \tag{11}$$

Rewriting Eq. (9) in terms of these parameters, it becomes

$$\frac{\partial C_D}{\partial t_D} + U_{ad}\, x_D^{1-\alpha} \frac{\partial C_D}{\partial x_D} - D_{ad}\, x_D^{1-\alpha} \frac{\partial}{\partial x_D}\left(x_D^{-\theta} \frac{\partial C_D}{\partial x_D}\right) = 0. \tag{12}$$

2.3 Boundary and Initial Conditions

2.3.1 Boundary Conditions

As mentioned in Sect. 2.1, the tracer and fluid are injected at $x = x_w$ (wellbore radius) and extracted at $x = L$. Those points (plates) constitute the boundaries of the system where particular conditions are imposed. At the injection plate ($x = x_w$) a zero-flux condition is imposed, this is

$$\frac{\partial C_D}{\partial x_D}\Big|_{x_D=\frac{x_w}{L}} = \frac{\dot{M}_F L}{A_{cs}\rho_0\phi D_0}\left(\frac{x_w}{L}\right)^{\theta} C_D, \tag{13}$$

and at the extraction plate ($x = L$) zero dispersive flux is set since beyond this point no more porous medium is present (Danckwerts 1953)

$$\frac{\partial C_D}{\partial x_D}\Big|_{x_D=1} = 0. \tag{14}$$

2.3.2 Initial Condition

The initial condition establishes that no tracer is present inside the fractal medium, except for a small truncated Gaussian pulse located between $x_{D_{min}}$ and $x_{D_{max}}$ and centred at x_D^* in a zone close to the injection plate, this is

$$C_D(x_D, t_D = 0) = \begin{cases} \dfrac{B\exp\left[-L^2\frac{(x_D - x_D^*)^2}{2\sigma^2}\right]}{\sqrt{2\pi\sigma^2}} & \text{if } x_{D_{min}} \le x \le x_{D_{max}} \\ 0 & \text{elsewhere,} \end{cases} \tag{15}$$

where B is related to the amount of tracer injected to the system, σ is the initial width of the pulse and x_D is the dimensionless length as defined in Sect. 2.2.

2.4 Numerical Solution of the Advection-Dispersion Equation

We solve Eq. (12) numerically, and for this purpose we write it as

$$\frac{\partial C_D}{\partial t_D} = f_1(x_D)\frac{\partial C_D}{\partial x_D} + f_2(x_D)\frac{\partial^2 C_D}{\partial x_D^2}, \tag{16}$$

whose coefficients are

$$f_1(x_D) = U_{ad}\, x_D^{1-\alpha} - \theta D_{ad}\, x_D^{-\alpha-\theta} \tag{17}$$

$$f_2(x_D) = D_{ad}\, x_D^{1-\alpha-\theta}. \tag{18}$$

Equation (16) is discretized by using a time-averaged finite-difference method (Crank-Nicolson) for the time and backward and symmetric finite differences for the first and second order spatial partial derivatives, respectively. This is

$$\frac{C_j^{n+1} - C_j^n}{\delta t_D} = \frac{f_{1_j}}{2\delta x_D}\left(C_j^n - C_{j-1}^n + C_j^{n+1} - C_{j-1}^{n+1}\right) = \frac{f_{2_j}}{2(\delta x_D)^2}\left(C_{j-1}^n - 2C_j^n + C_{j+1}^n + C_{j-1}^{n+1} - 2C_j^{n+1} + C_{j+1}^{n+1}\right), \tag{19}$$

which after grouping terms and doing some algebra is

$$\begin{aligned}\left(\gamma_j - \beta_j\right) C_{j-1}^{n+1} + \left(1 - \gamma_j + 2\beta_j\right) C_j^{n+1} - \beta_j C_{j+1}^{n+1} = \\ \left(\beta_j - \gamma_j\right) C_{j-1}^n + \left(1 + \gamma_j - 2\beta_j\right) C_j^n + \beta_j C_{j+1}^n\end{aligned} \tag{20}$$

where $\gamma_j = \frac{\delta t_D f_{1_j}}{2\delta x_D}$ and $\beta_j = \frac{\delta t_D f_{2_j}}{2(\delta x_D)^2}$.

The last equation allows matrix representation so that the solution to the direct problem (Eq. 16) can be expressed as

$$\mathbf{C}^{n+1} = \mathbf{A}^{-1}\mathbf{b}\mathbf{C}^n, \tag{21}$$

where **A** and **b** are tridiagonal spatial-dependent matrices.

3 Parameter Estimation Procedure

The methodology for determining the fitting parameters has been derived by (a) defining adequate dimensionless variables and fitting parameters, (b) specifying proper validity ranges for the parameter values, (c) providing an objective function and a suitable optimization method, and (d) performing a robustness analysis of the whole procedure. These issues will be described below. The use of synthetically generated tracer breakthrough data is essential in the robustness analysis, since it provides control on the procedure and allows the quantification of the fitting goodness.

3.1 Fitting Parameters

As can be seen in Eq. (12), there are four fitting parameters: U_{ad}, D_{ad}, α, and θ. However, as will be seen below, one of them, U_{ad}, depends on the other parameters, and thus only three parameters are actually present. The fitting parameters are:

- *Fractal length dimension*, α. It is the effective fractal dimension of length along the flow direction. As shown in Eqs. (10) and (11), it affects both the tracer velocity and its dispersion. The Euclidean limit is $\alpha = 1$.
- *Connectivity index*, θ. It is a dynamical parameter related to the tracer dispersion in the fractal structure. In the Euclidean limit, $\theta = 0$, the dispersion coefficient remains constant, whereas for $\theta > 0$ it decreases with the travelled distance.
- *Dimensionless dispersion coefficient*, D_{ad}. It is a dimensionless parameter associated to the dispersion phenomenon in the fractal media at the inter-well scale.
- *Dimensionless velocity*, U_{ad}. It is a dimensionless effective tracer velocity in the fractal porous medium. This velocity can be expressed in terms of the other parameters by considering the time the tracer pulse requires to sweep (fill) the whole fractal volume between $x = x_w$ and $x = L$. Further, if we choose the reference time (Δt) as this total sweep time, it follows that

$$U_{ad} = \frac{1}{\alpha}. \tag{22}$$

This relationship reduces the amount of fitting parameters to three: α, θ, and D_{ad}.

3.2 The Inverse Problem

The objective function (OF) is written in terms of the synthetic data $\{C_{D_i}, t_{D_i}\}$ and the model prediction $\{C(t_{D_i};\ \alpha, D_{ad}, \theta)\}$ in the least square sense as

$$OF(\alpha, D_{ad}, \theta) = \sum_{i=1}^{N} \left[C_{D_i} - C(t_{D_i};\ \alpha, D_{ad}, \theta)\right]^2, \tag{23}$$

where the parameters are constrained according to the model formulation: $0 < \alpha \leq 1$, $0 < D_{ad} \leq 0.1$ and $0 \leq \theta \leq 0.5$. The last equation describes a hyper-surface in the parameter space. The inverse problem consists in finding the optimal values of the parameters that minimizes the OF (Eq. (23)) on the hyper-surface. In doing so, a constrained optimization algorithm is needed.

3.3 Optimization Algorithm

There exist diverse optimization algorithms that can be used to minimize functions like Eq. (23). However, the particularities of our case, i.e., noisy data and solutions that are found numerically, make gradient-free optimization algorithms more appropriate even though the gradient-based methods are more efficient. The reason is that the numerical evaluation of the Jacobian and the Hessian matrices from noisy data increases the uncertainty. The gradient-free algorithm used in the optimization process is a modified Nelder-Mead method, which requires neither Jacobian nor Hessian matrix evaluation and allows constraints in parameter values. This method evaluates the OF at the vertices of a n-dimensional simplex ($n = 3$ in this work and the simplex is a tetrahedron) so that the search moves away from the poorest value and the minimum is enclosed in a simplex which continuously changes in size. The final simplex is reached when the OF or the parameters fulfill some prescribed stopping criterion.

4 Synthetic Data Generation

To generate the synthetic data, (i) we first choose a set of model parameter values, (ii) then we numerically solve the advection-dispersion equation for a given distance to the production well and a selected set of tracer breakthrough times, and finally (iii) we add uniformly distributed noise to the concentration values obtained. Two levels of noise are taken into account: 5 and 10 % with respect to the maximum tracer concentration and three levels of the amount of data points: 10, 20 and 40. The time data are sampled in a non-uniform way in order to construct the breakthrough curve in a prescribed time range. The data will consist in a series of pair values: time and concentration $\{t_i, C_i\}$. In this specific case, the synthetic data were generated by setting: $\alpha = 0.75$, $D_{ad} = 0.0133$ and $\theta = 0.05$ and the following fixed parameters: $\Delta t = 10$ days, $L = 400$ m and $x_w = 0.1$ m. As mentioned above several sets of tracer concentration versus time were constructed from the model. For each noise level (5 and 10 %) three different amount of data points were generated (approximately 10, 20 and 40). The amount of points is not constant since negative concentration values are eliminated. Therefore, we will work with six data sets. By using them we analyse the effect of the amount of data, the noise level and the amount of fitting parameters. To measure the fitting quality, the percentage of relative error (PRE) and the OF value are used.

In the optimization process a random search was used to get the starting parameters. Ten trials per parameter are tossed so that 1,000 function evaluations are performed. The parameter set with the lowest FO value is chosen. By this way, the starting point will presumably be close to the global minimum of the OF.

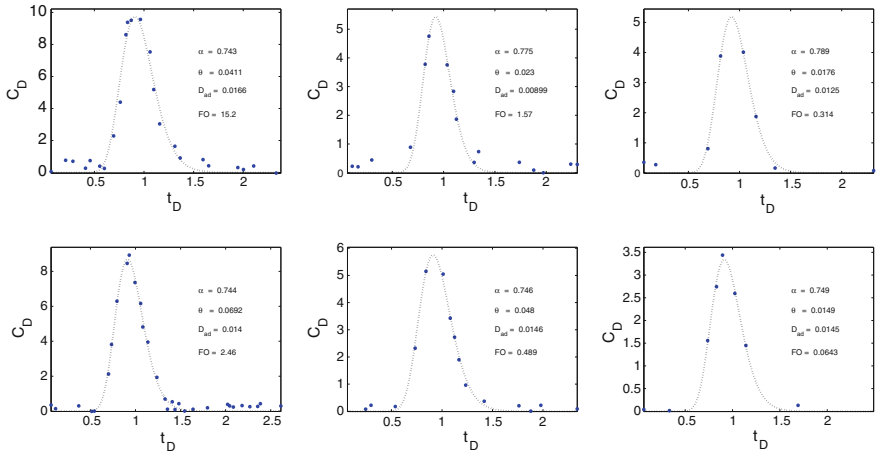

Fig. 2 Qualitative comparison between the synthetic data (*blue points*) and the model predictions (*dashed black line*). From *left* to *right*, in each column, the amount of data varies from approximately 40, 20 to 10. The first and second rows correspond to 10 and 5 % of noise, respectively. The parameters are $\alpha = 0.75$, $D_{ad} = 0.0133$ and $\theta = 0.05$

5 Robustness of the Method

As mentioned before, the robustness analysis of the developed methodology considers a sensitivity analysis of the effect of the (a) noise level, (b) amount of data, and (c) amount of parameters on the fitting. For this purpose the six synthetic data set generated are used.

5.1 Sensitivity to the Level of Data Noise

The results regarding the fitting sensitivity to data noise level are presented in Fig. 2. In this figure the fitted breakthrough curve and the original data are displayed. The top three plots correspond to 10 % noise and the three bottom plots to 5 % noise. The two vertical plots at the left correspond to approximately 40 data points, the two vertical plots at the center to near 20 data points and the two plots at the right to around 10 data points. The effect of the noise level can not be inferred from the qualitative comparison in Fig. 2 and a look to the quantitative results in Tables 1 and 2 is necessary. As shown in Table 1 the OF increases if the amount of noise increases (keeping the same amount of data points). On the other hand, the percentage of relative error (PRE) does not follow the same behaviour; an increment in noise level does not necessarily imply an increment in its value. Conversely, as can be observed from Table 2, for 40 and 10 data, an increment in the noise level means an unexpected reduction of the PRE value. The PRE value for each parameter reveals how far they

Table 1 Comparison between original and estimated fractal parameters for different amount of data and noise levels

		40 Data		20 Data		10 Data	
Parameter	Original	5 %	10 %	5 %	10 %	5 %	10 %
α	0.75	0.744	0.743	0.746	0.775	0.749	0.789
θ	0.05	0.069	0.041	0.048	0.023	0.015	0.018
D_{ad}	0.0133	0.0140	0.0166	0.0146	0.0090	0.0145	0.0125
OF		2.46	15.2	0.489	1.57	0.0643	0.314

Table 2 Percentage of relative error in the estimated fractal parameters for different amount of data and levels of noise

	40 Data		20 Data		10 Data	
Parameter	5 %	10 %	5 %	10 %	5 %	10 %
α	0.80	0.93	0.53	3.33	0.13	5.20
θ	38.00	18.00	4.00	54.00	70.00	64.00
D_{ad}	5.00	24.00	9.77	32.33	9.02	6.02
PRE	43.80	42.93	14.30	89.66	79.15	75.22

are from the original value. In this sense α and D_{ad} are better estimated than θ. The PRE values for α and D_{ad} scarcely exceed the 5 and 30 %, respectively, whereas for θ this value achieves 60 %. Estimation of α slightly depends on the level of noise compared to the other parameters. From these results it is possible to infer the sensitivity of the model to the parameters which is in the following order: α, D_{ad}, θ. The estimation depends on the level of noise.

5.2 Sensitivity to the Amount of Data

The effect of the amount of data on the fitting can be seen in Figs. 1 and 2 by fixing the row and changing columns. The quantitative description is deployed in Tables 1 and 2. From Table 1 we see that a decrement in the amount of data implies a decrement in the OF. This is a meaningless result since the OF is proportional to the amount of data. The PRE values in Table 2 do not have a well-defined trend, although it suggests that the estimation is sensitive to the amount of data. As expected, the estimation of D_{ad} and θ in general improves with the amount of data.

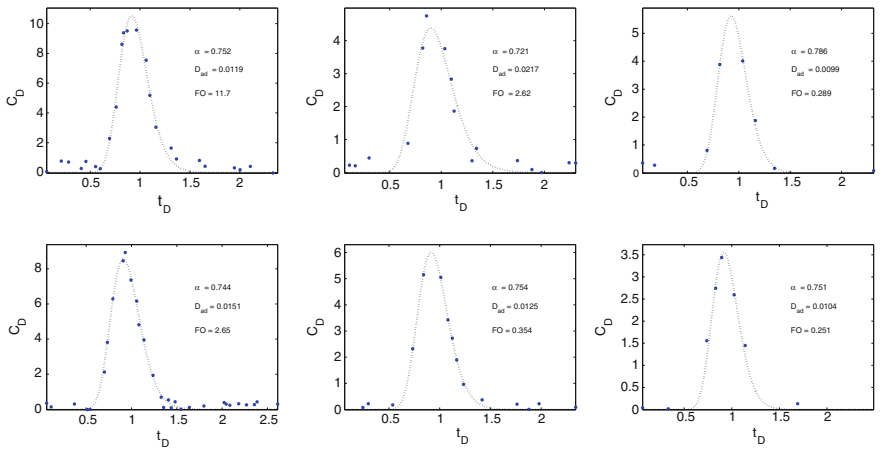

Fig. 3 Qualitative comparison between the synthetic data and the model predictions for the case where α and D_{ad} are the fitting parameters. Description is the same as in Fig. 2. The original parameters are $\alpha = 0.75$, $D_{ad} = 0.0133$ and $\theta = 0.05$

Table 3 Comparison between original and estimated fractal parameters for different amount of data and noise levels

		40 Data		20 Data		10 Data	
Parameter	Original	5 %	10 %	5 %	10 %	5 %	10 %
α	0.75	0.744	0.752	0.754	0.721	0.751	0.786
D_{ad}	0.0133	0.0151	0.0119	0.0125	0.0217	0.0104	0.0099
OF		2.65	11.7	0.334	2.62	0.25	0.29

Here α and D_{ad} are the fitting parameters

5.3 Sensitivity to the Amount of Fitting Parameters

To analyse the effect of the amount of fitting parameters on the results, two additional cases are included: one where the fitting parameters are α and D_{ad}, (see Fig. 3), and the other where only α is considered as fitting parameter, (see Fig. 4). The fixed parameters are set according to the original values. Regarding to the case where three parameters were estimated, in the first case a general improvement in the estimation of α is observed whereas the estimation of D_{ad} worsened. This can be seen in Tables 3 and 4. When only one fitting parameter is considered the PRE does not exceed the 5 % regardless the amount of data or the amount of noise. It is very similar to the values obtained where two or three fitting parameters are considered. Therefore, estimation strongly depends on the amount of fitting parameters, as expected. It improves as the number of parameters is reduced, especially if the model is sensitive to the selected fitting parameters.

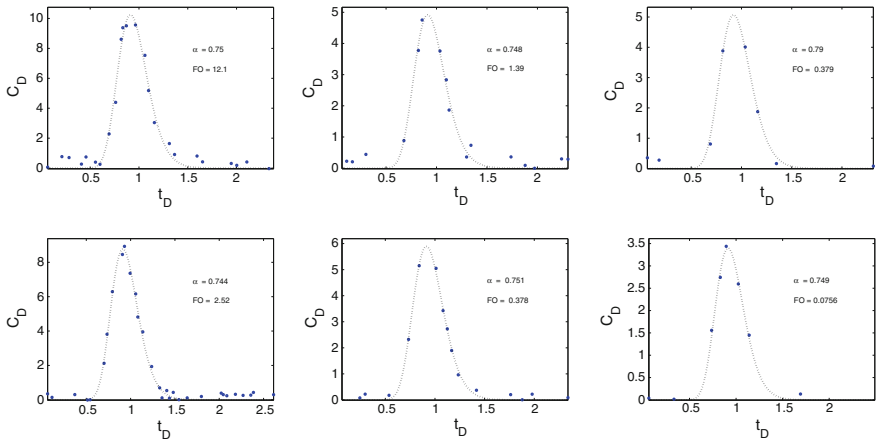

Fig. 4 Qualitative comparison between the synthetic data and the model predictions when only α is the fitting parameter. Description is the same as in Fig. 2. The original parameters are $\alpha = 0.75$, $D_{ad} = 0.0133$ and $\theta = 0.05$

Table 4 Percentage of relative error in the estimated fractal parameters for different amount of data and noise levels

	40 Data		20 Data		10 Data	
Parameter	5 %	10 %	5 %	10 %	5 %	10 %
α	0.80	0.27	0.53	3.87	0.13	4.80
D_{ad}	13.53	10.53	6.02	63.16	21.81	25.56
PRE	14.33	10.80	6.55	89.66	21.94	30.36

Here α and D_{ad} are the fitting parameters

6 Discussion of Results

The parameter estimation methodology developed for the fractal continuum model works adequately. In the analysis the level of data noise, the amount of data points, and other characteristics of the model such as the number of fitting parameters were considered. The level of noise increases the level of uncertainty in the obtained tracer transport parameter values. It holds in general that the higher the noise level, the more complex the parameter estimation becomes. The percentage of relative error (PRE) is a good estimator of the quality of fitting since the smallest values matches the best estimation. This does not mean that all parameters have lower values of PRE compared to others, but the total sum is smaller. Regarding the fitting parameters, the level of noise affects the estimation of each parameter differently. The estimation of α is slightly affected by the noise level because it is mainly associated to the pulse position and its peak height. On the other hand, D_{ad} and θ values strongly depend on the noise level, since both are linked to tracer dispersion. As can be observed in Figs. 2, 3 and 4, the noise level creates major uncertainty on

dispersion than on tracer velocity. As expected, increasing the amount of data points improves the parameters estimation as it is shown in the 40 data case (first column in Figs. 2, 3 and 4). This improvement is directly related to the fact that larger amount of information is provided. It is important to point out the relevance of the quality of the information because if the data are not sampled properly, as it may happen even in synthetic data, the results can be influenced or biased by external factors that are inconsistent with the estimation methodology.

The number of fitting parameters has important effects on the parameter estimation. This can be seen in the data from Figs. 2, 3 and 4. Clearly, fitting three parameters is more complicated than fitting only one and therefore the result improves significantly. The estimation of α, D_{ad} and θ at the same time shows that the last parameter almost does not affect the transport model and it can be explained in function of the involved phenomena. As mentioned before D_{ad} and θ are related to the tracer dispersion, but the first has a strong effect, as it depends on other physical properties like fluid density, fractal length dimension, etc., whereas the second is an isolated parameter relevant only at small values of length. If this parameter is fixed and the others are fitting parameters, the estimation of α slightly improves but the estimation of D_{ad} significantly worsens, as shown in Table 4. This is a consequence of a rescaling process in the model sensitivity due to the presence of only two fitting parameters. When only α is a fitting parameter, the estimation does not changes significantly with respect to the previous case. This may suggest that one-parameter optimizations provide robust results,regardless the noise or the amount of data.

7 Conclusions

A methodology for parameter estimation in a given fractal model for tracer transport is presented. The effect of the data noise level, the amount of data and the amount of fitting parameters on the parameter estimation for tracer pulse injection has been analysed.

Even though the parameter estimation is sensitive to the level of data noise, to the amount of data, and to the amount of fitting parameters, in general the proposed methodology is robust, particularly in estimating α and D_{ad}. Estimation of each parameter not only depends on such properties, but mainly on the model sensitivity to the specific parameter. In this sense the model is more sensitive to α than to D_{ad} and θ. The estimation of θ has more uncertainty than it has with the other parameters. Moreover the contribution to the percentage of relative error (PRE) of α is smaller than that associated to D_{ad} and θ. Finally, care must be taken in the following issues when working with synthetic data and numerical solutions:

- Estimation depends on the discretization parameters used in the numerical solution.
- A sensitivity analysis must be performed before the parameter estimation.
- The results may change if data noise is generated using other distribution functions different from the uniform one used here.

- Synthetic data must be properly-sampled in order to avoid bias in the parameter estimation.

Acknowledgments This work has been suported by Sener-Conacyt-Hidrocarburos Fund through the project No. 143935. ECHH acknowledges financial support from Conacyt for the postdoctoral fellowship at the Instituto Mexicano del Petróleo and the Cátedra Conacyt at CIDESI.

References

Balankin AS, Elizarraraz EB (2012) Map of fluid flow in fractal porous medium into fractal continuum flow. Phys Rev E 85:056314

Bear J (1972) Dynamics of fluid in porous media. Dover Publications, New York

Bogatkov D, Babadagli T (2010) Fracture network modelling conditioned to pressure transient and tracer test dynamic data. JPSE 75:154

Chaberneau RJ (2000) Groundwater hydraulics and pollutant transport. Prentice Hall, New Jersey

Chakraborty P, Meerschaert MM, Lim CY (2009) Parameter estimation for fractional transport: a particle-tracking approach. Water Resour Res 45:W10415

Coronado M, Ramírez-Sabag J, Valdiviezo-Mijangos O (2011) Double-porosity model for tracer transport in reservoirs having open conductive geological faults: determination of the fault orientation. JPSE 78:65

Danckwerts PV (1953) Continuous flow systems: distribution of resident times. Chem Eng Sci 2:3857

Fourar M, Radilla G (2009) Non-Fickian description of tracer transport through heterogeneous porous media. Transp Porous Media 80:561

Gefen Y, Aharony A, Alexander S (1983) Anomalous diffusion on percolating clusters. Phys Rev Lett 50:77

Hernandez-Coronado H, Coronado M, Herrera-Hernández EC (2012) Transport in fractal media: an effective conformal group approach. Phys Rev E 85:066316

Herrera-Hernández EC, Coronado M, Hernández-Coronado H (2013) Fractal continuum model for tracer transport in a porous medium. Phys Rev E 88:063004

Illiassov PA, Datta-Gupta A (2002) Field-scale characterization of permeability and saturation distribution using partitioning tracer tests: the ranger field. Texas, SPE, Annual Technical Conference and Exhibition, New Orleans, 71320

Orbach R (1986) Dynamics of fractal networks. Science 231:814

Ostoja-Starzewski O (2009) Continuum mechanics models of fractal porous media: integral relations and extremum principles. J Mech Mater Struct 4:901

Ramírez-Sabag J, Valdiviezo-Mijangos, Coronado M (2005) Inter-well tracer test in oil reservoir using different optimization methods: a field case Geofís Int 44

Sahimi M (1993) Fractal and superdiffusive transport and hydrodynamic dispersion in heterogeneous porous media. Transp Porous Media 13:3

Suzuki A, Makita H, Niibori Y, Fomin SA, Chugunov VA, Hashida T (2012) Characterization of tracer response using fractional derivative-based mathematical model and its application to prediction of mass transport in fractured reservoirs. GRC Trans 36:1391

Tarasov VE (2005) Fractional hydrodynamic equations for fractal media. Ann Phys 318:286

Mixed Convection in a Rectangular Enclosure with Temperature-Dependent Viscosity and Viscous Dissipation

A. Gómez López, B. Estela García Rojas, R.O. Vargas Aguilar and L.A. Martínez-Suástegui

Abstract The problem of laminar opposing mixed convection inside a two-dimensional rectangular enclosure with asymmetrical heating is studied numerically using the vorticity-stream function formulation of the Navier-Stokes and energy equations. The model considers viscous dissipation and viscosity is assumed to vary with temperature according to an exponential relation, while other fluid properties are considered constant. Numerical experiments have been performed for fixed values of the geometrical parameters, Reynolds number of $Re = 20$, Prandtl number of $Pr = 3{,}060$, a range of Richardson numbers from 0 to 10, and Brinkman numbers ranging between 0 to 40. Streamlines, temperature contours, maximum fluid temperature and average Nusselt number at both walls are obtained. The results show that combined viscous dissipation and variable fluid viscosity can be important in the overall flow and heat transfer characteristics.

1 Introduction

Mixed convection studies in rectangular enclosures are important in many industrial applications for the design of compact heat exchangers, solar collectors, cooling of electronic equipment and other thermal devices. A comprehensive review of this subject can be found in Aung (1987). However, most efforts have focused on studying the effect of combined forced and free convection for different channel geometries, boundary and operating conditions based on the hypothesis that the effect of viscous

A. Gómez López · R.O. Vargas Aguilar · L.A. Martínez-Suástegui (✉)
ESIME Azcapotzalco, Instituto Politécnico Nacional, Avenida de las Granjas No. 682, Colonia Santa Catarina, Delegación Azcapotzalco, 02250 México, D.F., Mexico
e-mail: lamartinezs@ipn.mx

R.O. Vargas Aguilar
e-mail: reneosvargas@yahoo.com.mx

B. Estela García Rojas
Departamento de Ingeniería y Ciencias Químicas, Universidad Iberoamericana, Prolongación Paseo de la Reforma 880, 01219 México, D.F., Mexico

J. Klapp et al. (eds.), *Selected Topics of Computational and Experimental Fluid Mechanics*, Environmental Science and Engineering,
DOI 10.1007/978-3-319-11487-3_15

dissipation in the fluid is negligible and assuming constant thermophysical properties (Hartnett and Kostic 1989; Peterson and Ortega 1990), while only relatively few studies that assess the effect of variable properties and viscous dissipation are available. Barletta (1998) studied analytically the laminar mixed convection with viscous dissipation in a vertical channel and showed that the latter enhances the buoyancy forces. Barletta and Nield (2009) studied numerically the mixed convection in a lid-driven square enclosure by taking into account the effects of viscous dissipation and pressure work and showed that their effects are not negligible. Costa (2006) pointed out that erroneous conclusions about flow and temperature fields and heat transfer results are obtained in convection heat transfer problems if viscous dissipation effects are neglected with respect to the First Law of Thermodynamics. Zamora and Hernández (1997) studied numerically the influence of variable property effects on natural convection flows in asymmetrically heated vertical channels and found that variable property effects have a strong influence on the Nusselt number. Hernández and Zamora (2005) assessed the effects of variable properties and non-uniform heating on natural convection flows in vertical channels and pointed out that variable property effects are significant and cannot be neglected.

The above literature review reveals that there are relatively few studies that deal with the investigation of temperature dependent viscosity effects and viscous dissipation during mixed convection heat transfer. The aim of the present study is to perform a numerical investigation for opposing laminar mixed convection in a rectangular enclosure subjected to isothermal side walls that are kept at different temperatures, while the top and bottom walls are assumed to be adiabatic. Emphasis on the effect of the Richardson and Brinkman numbers on the overall flow and heat transfer is presented.

2 Problem Formulation

A schematic diagram of the enclosure configuration studied is shown in Fig. 1. The height and width of the enclosure are L and W, respectively, with $W = 1.5\,L$.

The top and bottom walls are assumed to be adiabatic, while the left (hot) and right (cold) walls have uniform surface temperatures T_{H} and T_{C}, respectively. The flow enters through the upper left inlet with uniform velocity u_0 and temperature $T_0 = (T_{\mathrm{H}} + T_{\mathrm{C}})/2$. The density variations in the buoyancy term are treated according

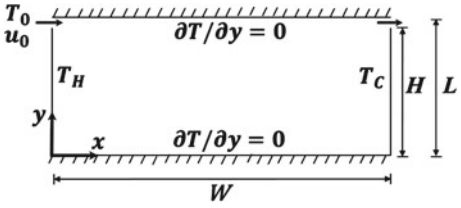

Fig. 1 Schematic diagram of the flow and heat transfer problem

to the Boussineq approximation for an incompressible viscous fluid. The viscous dissipation in the energy equation is considered, and the widely used exponential or Arrhenius type relation (Kakaç 1987) is employed to represent the temperature dependence of the viscosity $\mu(T) = \mu_0\, exp[-B_0(T - Tc)]$, where μ_0 is the viscosity and B_0 is an empirical constant, both at the reference temperature T_0. Using the vorticity ($\Omega = \partial V/\partial X - \partial U/\partial Y$) and stream function formulation ($U = \partial\psi/\partial Y$, $V = -\partial\psi/\partial X$), the flow is described by the following dimensionless equations:

$$\frac{\partial^2\psi}{\partial X^2} + \frac{\partial^2\psi}{\partial Y^2} = -\Omega, \tag{1}$$

$$\begin{aligned}
&\frac{\partial\psi}{\partial Y}\frac{\partial\Omega}{\partial X} - \frac{\partial\psi}{\partial X}\frac{\partial\Omega}{\partial Y} = \frac{\exp(-B\theta)}{\mathrm{Re}}\left(\frac{\partial^2\Omega}{\partial X^2} + \frac{\partial^2\Omega}{\partial Y^2}\right)\\
&+ \frac{4B^2\exp(-B\theta)}{\mathrm{Re}}\left(\frac{\partial^2\psi}{\partial X\partial Y}\frac{\partial^2\theta}{\partial X\partial Y} - \frac{\partial\theta}{\partial X}\frac{\partial\theta}{\partial Y}\frac{\partial^2\psi}{\partial X\partial Y}\right)\\
&- \frac{2B\exp(-B\theta)}{\mathrm{Re}}\left(\frac{\partial\theta}{\partial X}\frac{\partial\Omega}{\partial X} + \frac{\partial\theta}{\partial Y}\frac{\partial\Omega}{\partial Y}\right)\\
&+ \frac{B^2\exp(-B\theta)}{\mathrm{Re}}\left(\frac{\partial^2\psi}{\partial Y^2} - \frac{\partial^2\psi}{\partial X^2}\right)\left[\left(\frac{\partial\theta}{\partial X}\right)^2 - \left(\frac{\partial\theta}{\partial Y}\right)^2\right]\\
&+ \frac{B\exp(-B\theta)}{\mathrm{Re}}\left(\frac{\partial^2\psi}{\partial Y^2} - \frac{\partial^2\psi}{\partial X^2}\right)\left(\frac{\partial^2\theta}{\partial X^2} + \frac{\partial^2\theta}{\partial Y^2}\right)\\
&+ Ri\frac{\partial\theta}{\partial X},
\end{aligned} \tag{2}$$

$$\begin{aligned}
&\frac{\partial\psi}{\partial Y}\frac{\partial\theta}{\partial X} - \frac{\partial\psi}{\partial X}\frac{\partial\theta}{\partial Y} = \frac{1}{Pe}\left(\frac{\partial^2\theta}{\partial X^2} + \frac{\partial^2\theta}{\partial Y^2}\right)\\
&+ \frac{Br\exp(-B\theta)}{Pe}\left(\frac{\partial^2\psi}{\partial Y^2} - \frac{\partial^2\psi}{\partial X^2}\right).
\end{aligned} \tag{3}$$

where $\boldsymbol{V} = (U, V)$ is the dimensionless velocity vector and θ is the dimensionless temperature. In the above equations, all velocity components (U in the X direction and V in the Y direction) are scaled with the inflow velocity u_0, $U = u/u_0$ and $V = v/u_0$; the longitudinal and transverse coordinates are scaled with the height of the enclosure L, $X = x/L$ and $Y = y/L$; the temperature is normalized as $\theta = (T - T_C)/(T_H - T_C)$; the pressure is scaled with ρu_0^2, and the temperature dependent viscosity is scaled with $B = B_0(T_H - T_C)$. The nondimensional parameters are the Reynolds number, $Re = u_0L/\nu$, the Peclet number, $Pe = u_0L/\alpha$, the Richardson number, $Ri = g\beta(T_H - T_0)L/{u_0}^2$, the Brinkman number, $Br = \mu u_0^2/k(T_H - T_0)$, and the dimensionless viscosity $\mu/\mu_0 = \exp(-B\theta)$, where $B = -\ln(\mu/\mu_0)$. Here, g is the acceleration due

to gravity and β is the thermal expansion coefficient. Equations (1)–(3) have to be solved with the following boundary conditions. Uniform flow at the channel entrance, with ψ varying from 0 to 1 and $\Omega = 0$ for $H \leq Y \leq L$; no slip at the walls with $\psi = 0$ at the left, bottom and right walls and $\psi = 1$ at the top wall; and relaxed parallel flow conditions at the outlet: $\partial\psi/\partial X = \partial^2\psi/\partial X\partial Y = 0$. Wall vorticities are evaluated using Thom's classical formula, $\Omega_W = 2(\psi_{W+1} - \psi_W)/\Delta n^2$, where Δn^2 is the grid space normal to the wall (Thom 1933). The boundary conditions for the temperature are the following: fixed temperature, $\theta = 1, 0$ at the left and right walls, respectively; fixed fluid inlet temperature, $\theta = 0.5$; adiabatic top and bottom walls, $\partial\theta/\partial Y = 0$; the condition at the exit is the normally assumed relaxed condition $\partial\theta/\partial X = 0$. The local Nusselt numbers at the left and right isothermal walls are computed as $Nu(Y) = \pm\partial\theta/\partial X|_{X=0,1.5}$. The space averaged Nusselt number is then computed by integrating the local Nusselt number along each wall, $\overline{Nu} = (1/H)\int_0^H Nu(Y)dY$.

3 Numerical Results and Model Validation

The equations were discretized using a second-order central difference formulation for all the spatial derivatives and solved using the ADI scheme. The system of nonlinear equations (1)–(3) along with their corresponding boundary conditions are solved numerically using a uniform grid of 60×60 that yielded independent results in terms of the average Nusselt number and the maximum value of the stream function. A nondimensional time step $\Delta\tau = u_0\Delta t/L = 1 \times 10^{-3}$ has been used for all computations for fixed $Pr = 3{,}060$. A tolerance value of 1×10^{-7} was used to measure the convergence of the dependent variables. The code has been validated by comparing the results of the simulations against those of Singh and Sharif (2003) for mixed convective cooling of a rectangular cavity with inlet and exit opening. The computed results for the average Nusselt number at the left wall for different values of the Richardson number are shown in Table 1. Clearly, good agreement between the present predictions is found with a maximum discrepancy of 2.37 %, justifying the numerical method used in this study.

Table 1 Comparison of variation of the average Nusselt number at the left wall

	Average Nusselt number at $Re = 50$ with $Pr = 0.71$				
Ri	0.001	0.01	0.1	1	10
Singh and Sharif (2003)	9.2	9	8.8	10.5	13.98
Present work	9.1432	9.2136	8.6343	10.7212	13.7654

4 Results

Figure 2 shows the predicted overall Nusselt number at both walls for $Re = 20$, $Pr = 3{,}060$ and $B = 1$ for several values of the Brinkman and Richardson numbers.

We note that due of the imposed boundary conditions, small values of the mean Nusselt number are obtained at the left wall, while enhanced heat transfer occurs at the right wall. In the absence of buoyancy ($Ri = 0$), the overall heat transfer at the left wall reduces when the Brinkman number increases, while the opposite is observed at the right wall. This behavior is explained by the increase of the energy generated by viscous dissipation, which in turn yields a higher fluid temperature. A similar trend is observed for all values of the buoyancy parameter at the left and right walls, respectively.

For a Richardson number of $Ri = 2$ and for all the computed values of the Brinkman number, heat transfer at the left wall is enhanced because of an increase in the size of the recirculation zone that appears at the lower left corner of the enclosure. In addition, a recirculation bubble at the lower right corner with twice the size of the left vortex increases the temperature close to the right wall, while reducing its corresponding Nusselt number. This effect occurs because of the internal forcing that the system undergoes due to viscous dissipation and variable viscosity effects. For a

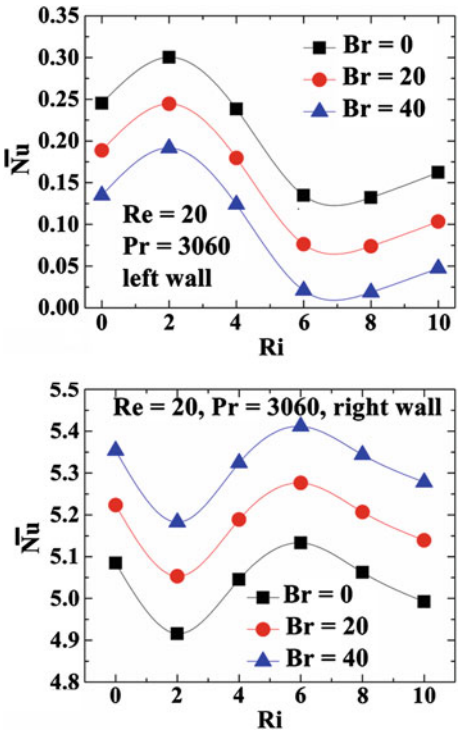

Fig. 2 Overall Nusselt number at the *left* and *right wall* for $Re = 20$, $Pr = 3{,}060$ and $B = 1$ for several values of the Br and Ri, respectively

Richardson number of $Ri = 6$, as the induced kinetic energy raises, the shear induced heating increases the temperature within the fluid. As a result, the overall Nusselt number at the left and right walls decreases and increases, respectively. For a Richardson number of $Ri = 10$, the variable viscosity enhances the fluid velocity close to the walls and widens the flow reversal regions, while the overall Nusselt numbers at the left and right walls slightly increase and decrease, respectively. Figure 3 shows temperature contours with superimposed streamlines at various Ri and Br. The color scales below each column map the temperature distributions. Clearly, for all the Brinkman number values considered, the size of the recirculation zones—appearing at the bottom corners of the enclosure—increase as the Richardson number values step up. We note that for a given Richardson number, higher values of the nondimensional temperature occur for increasing values of the Brinkman number, which implies an increase in the shear-induced heating because of the presence of higher

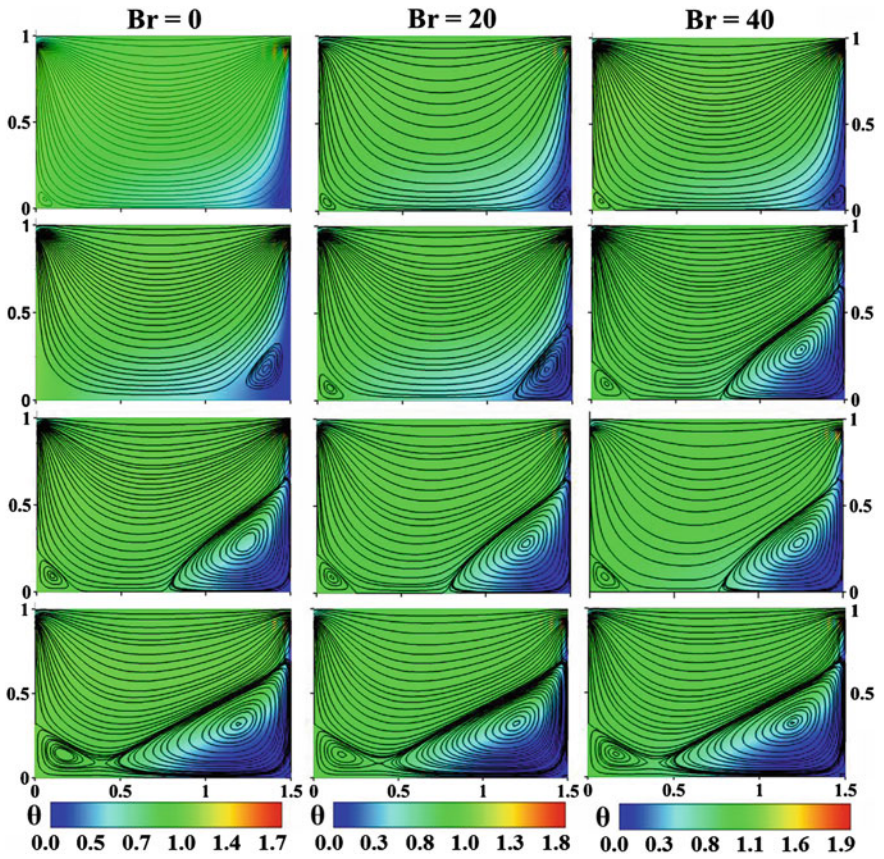

Fig. 3 Temperature contours with superimposed streamlines for $Re = 20$, $Pr = 3{,}060$ and $B = 1$ for several values of Br and Ri. The images from *top* to *bottom* display the final flow solution for $Ri = 0$, 2, 6 and 10, respectively

forced kinetic energy. The images shown exemplify the importance of viscous heating effects and temperature dependent viscosity on the dimensionless velocity and temperature profiles.

5 Conclusions

The problem of laminar mixed convection in a rectangular enclosure has been studied numerically by taking into account the effect of viscous dissipation and temperature-dependent viscosity. Uniform wall temperatures with asymmetric heating have been considered. The problem depends on several non-dimensional parameters, such as the Reynolds number, the Prandtl number, the Richardson number (buoyancy parameter), the Brinkman number, the temperature-dependent viscosity and the geometrical parameters of the enclosure. It has been shown that the effect of viscous dissipation can be important on the heat and fluid flow phenomena in fluids with high Prandtl number, with regions within the enclosure reaching fluid temperatures above the hot wall temperature.

Acknowledgments This work has been supported by the Consejo Nacional de la Ciencia y Tecnología (CONACyT), Grant No. 167474 and SIP-IPN 20131675.

References

Aung W (1987) Handbook of single-phase convective heat transfer. Wiley, New York

Barletta A (1998) Laminar mixed convection with viscous dissipation in a vertical channel. Int J Heat Mass Transf 41:3501–3513

Barletta A, Nield DA (2009) Mixed convection with viscous dissipation and pressure work in a lid-driven square enclosure. Int J Heat Mass Transf 52:4244–4253

Costa VAF (2006) Thermodynamics of natural convection in enclosures with viscous dissipation. Int J Heat Mass Transf 49:2215–2226

Hartnett J, Kostic M (1989) Heat transfer to Newtonian and non-Newtonian fluids in rectangular ducts, vol 10. Academic Press Inc

Hernández J, Zamora B (2005) Effects of variable properties and non-uniform heating on natural convection flows in vertical channels. Int Commun Heat Mass Transf 48:793–897

Kakaç S (1987) The effect of temperature-dependent fluid properties on convective heat transfer. In: Kakaç S, Shah RK, Aung W (eds) Handbook of single-phase convective heat transfer. Wiley, New York

Peterson G, Ortega A (1990) Thermal control of electronic equipment and devices, vol 20. Academic Press Inc

Singh S, Sharif MAR (2003) Mixed convective cooling of a rectangular cavity with inlet and exit openings on differentially heated side walls. Numer Heat Tr A-Appl 44:233–253

Thom A (1933) The flow past circular cylinders at low speeds. Proc R Soc A 141:651–666

Zamora B, Hernández J (1997) Influence of variable property effects on natural convection flows in asymmetrically-heated vertical channels. Int Commun Heat Mass Transf 8:1153–1162

Characterization of a Bubble Curtain for PIV Measurements

R.G. Ramírez de la Torre, D.C. Vargas-Ortega, M.S. Centeno-Sierra, R. Méndez-Fragoso and C. Stern Forgach

Abstract In this contribution we present the characterization of a bubble curtain produced with compressed air. The final goal is to implement a PIV system, with bubbles as tracers, that will help to understand drag and propulsion of a swimmer during a dolphin kick. The system will be used directly in a swimming pool. The first trials were made in a controlled water channel.

1 Introduction

The use of scientific results to improve the performance and efficiency of athletes in all sports is constantly increasing. In particular, swimming techniques have changed over the years, not only the biomechanical gestures of the swimmers, but also the design of the gear they use and the procedures to measure their performance. Its direct consequence is the continuous reduction in time of the world records (FINA 2013, 2014).

This paper describes the development and validation of a non-intrusive method to determine the velocity field around a swimmer. It provides a quantitative tool to analyze the flow and gives information needed to modify swimming techniques and improve performance.

R.G. Ramírez de la Torre · D.C. Vargas-Ortega · M.S. Centeno-Sierra
R. Méndez-Fragoso · C. Stern Forgach (✉)
Departamento de Física, Facultad de Ciencias, Universidad Nacional Autónoma de México, México, México
e-mail: reynapez@ciencias.unam.mx

D.C. Vargas-Ortega
e-mail: Karolz_27@yahoo.com.mx

M.S. Centeno-Sierra
e-mail: starpolarismx@gmail.com

R. Méndez-Fragoso
e-mail: rich@ciencias.unam.mx

C. Stern Forgach
e-mail: catalina@ciencias.unam.mx

J. Klapp et al. (eds.), *Selected Topics of Computational and Experimental Fluid Mechanics*, Environmental Science and Engineering,
DOI 10.1007/978-3-319-11487-3_16

1.1 Theoretical Framework

The most common nondimensional parameter used to characterize fluid motion is the Reynolds number, defined as,

$$Re = \frac{DV}{\nu}, \tag{1}$$

where D is a characteristic length, V is a characteristic velocity and ν is the kinematic viscosity (Crowe et al. 2009).

Due to the viscosity of the fluid, when it comes in contact with any solid boundary, the speed is diminished near the surface. This zone is known as boundary layer, and is characterized by low velocity and high speed gradients. The latter are responsible for generating vorticity $\overrightarrow{\omega}$ which is defined mathematically as,

$$\overrightarrow{\omega} = \nabla \times \overrightarrow{V}, \tag{2}$$

where $\overrightarrow{V}$ represents the velocity field.

When the surface is curved, pressure gradients appear in the streamwise direction. If the pressure gradient is adverse, flow reversal can occur and the boundary layer separates creating a wake with well-defined vortical structures, as shown in Fig. 1.

As the flow velocity increases, the vortices formed due to flow reversal, start to shed at a frequency proportional to the velocity. The pattern thus formed is known as the von Kármán street and is shown in Fig. 2a. The effect of von Kármán's street on drag has been largely studied for different geometric forms, in particular behind cylinders (2D) and spheres (3D). There are active and passive forms of manipulation of the wake vortices that can diminish the drag, or even create propulsion. For example, vortices are manipulated by animals, with the motion of their wings or fins, to form a modified pattern as shown in Fig. 2b, (Triantafyllou et al. 2012). This pattern, that increases propulsion, is known as the reversed von Kármán street.

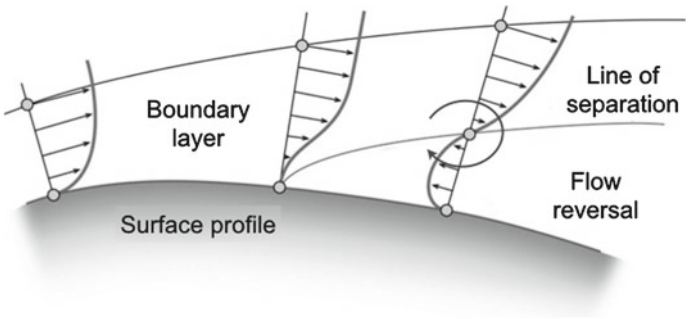

Fig. 1 Velocity profile in the surface of a curved body immersed in a fluid. In the region where the pressure gradient is adverse, flow reversal occurs and vortices are generated

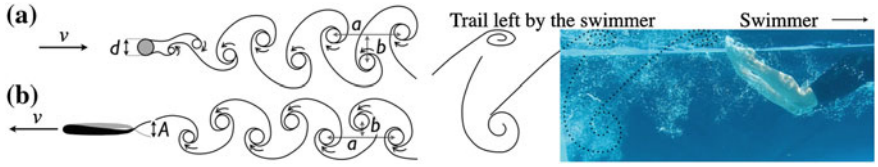

Fig. 2 On the *left*, a comparison of the wakes behind (**a**) a sphere (von Karman's Street) and (**b**) a fish (reversed von Kármán street). On the *right*, vortices *left* by a swimmer during a dolphin kick, which affect the propulsion and efficiency of a swimmer

Swimmers use the kick and the arm stroke for propulsion, imitating animal motion (Biewener 2003). In particular, the dolphin kick generates vortex pairs similar to those produced by fish as shown in Fig. 2 (Arellano et al. 2002).

2 Background

Studies on swimming have shown that in a competition, over 40 % of the time the swimmer is completely submerged (Costa et al. 2010). For this reason, it was decided to implement a 2D PIV technique, commonly used for flow analysis. In this type of analysis, tracer particles are required to follow the flow. In the laboratory, a laser sheet of light is displayed, and the motion of the particles in that plane is recorded with a high speed camera. It is very difficult to introduce tracers in a swimming pool, because they are difficult to control and mostly, because they pollute the water. Thus, it was decided to use bubbles as tracers.

To produce the bubbles a PVC tube with a row of holes, connected to a tank of compressed air was built. The first tests were conducted in the Olympic Pool at the main UNAM campus in order to check if the bubbles could follow the flow generated by the passage of the swimmer.

Figure 3 shows the experimental arrangement used and an image with the preliminary results. A vortical structure is observed. From these preliminary results it became clear that greater control over the size of the generated bubbles to obtain

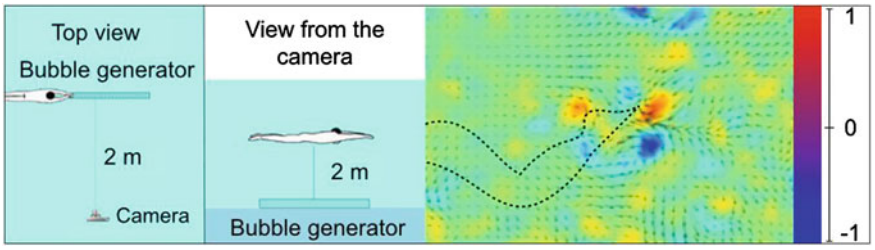

Fig. 3 On the *left* the experimental setup used at the Olympic Pool is shown. The image on the *right* shows the results obtained after analysis of PIV

better resolution was needed. Also, because the motion of the bubbles is not strictly vertical, a more detailed characterization of the curtain was required.

3 Methodology

A new device that allowed control of the size and number of the generated bubbles was developed. Very small, equally sized holes were made on a tube using a laser cutting machine. One end of the tube was sealed, and the other was connected to a continuous supply of air. To create an almost uniform flow inside the bubble generator, an inner tube was introduced as shown in Fig. 4.

The characterization of the bubble curtain was conducted in the wave flume at the "Coast and Ports Laboratory" at the Engineering Institute of the UNAM, where the environment is controlled. A video camera with a speed of 120 frames per second was used. To ensure a constant flow of air, the pressure is monitored with a mercury manometer connected between the air pump and the bubble generator as shown in Fig. 5.

The study was divided into three stages. First, the behavior of bubbles generated by one hole was analyzed. Bubbles have a spiral trajectory as they travel upwards.

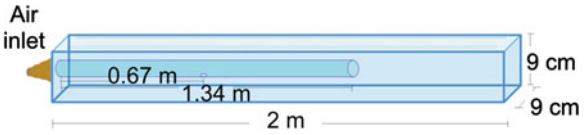

Fig. 4 Diagram of the bubble generator

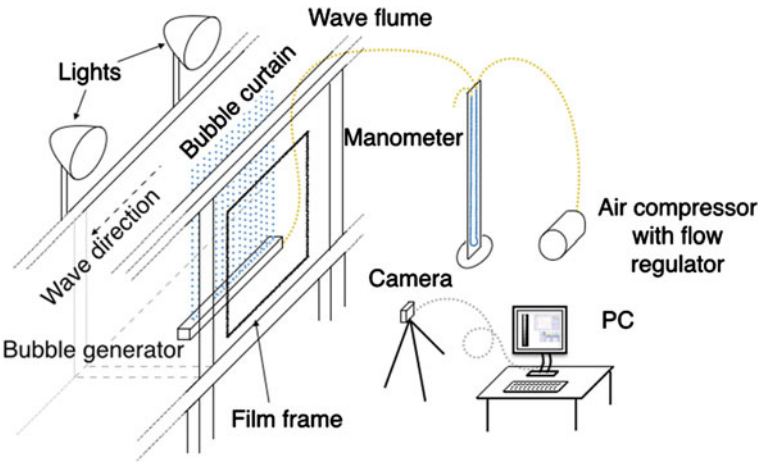

Fig. 5 Experimental setup to characterize the behavior of the bubbles

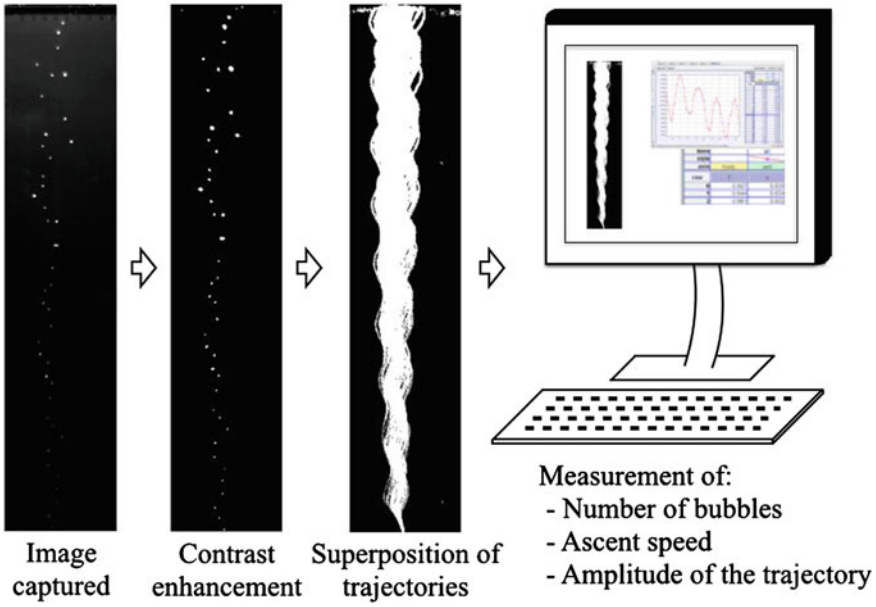

Fig. 6 Scheme of the image and data processing with the Tracker Program and other software developed in MATLAB

The amplitude of the spiral increases with altitude. It was necessary to determine the velocity, the amplitude and the period of the spiral in order to determine a range of pressures and a measuring area appropriate for the final experiment.

On the second stage, the behavior of the bubbles generated by three holes was analyzed and compared to stage one. On the third stage, waves with different frequencies were generated, and the whole curtain was used to recover the fluid particle behavior in a wave.

The images were manipulated with software developed in MATLAB. A tracker program was used to obtain the velocities from the images. In Fig. 6, a diagram of the data processing sequence is shown.

4 Results and Discussion

4.1 Results for One Column of Bubbles

The upper left image in Fig. 7 shows the ascending velocities obtained for different pressures and water depths. It is important to note that for manometric pressures higher than 14.5 cm Hg the velocities tend to cluster in a range of two centimeters. This measurement helps eliminate background noise in PIV.

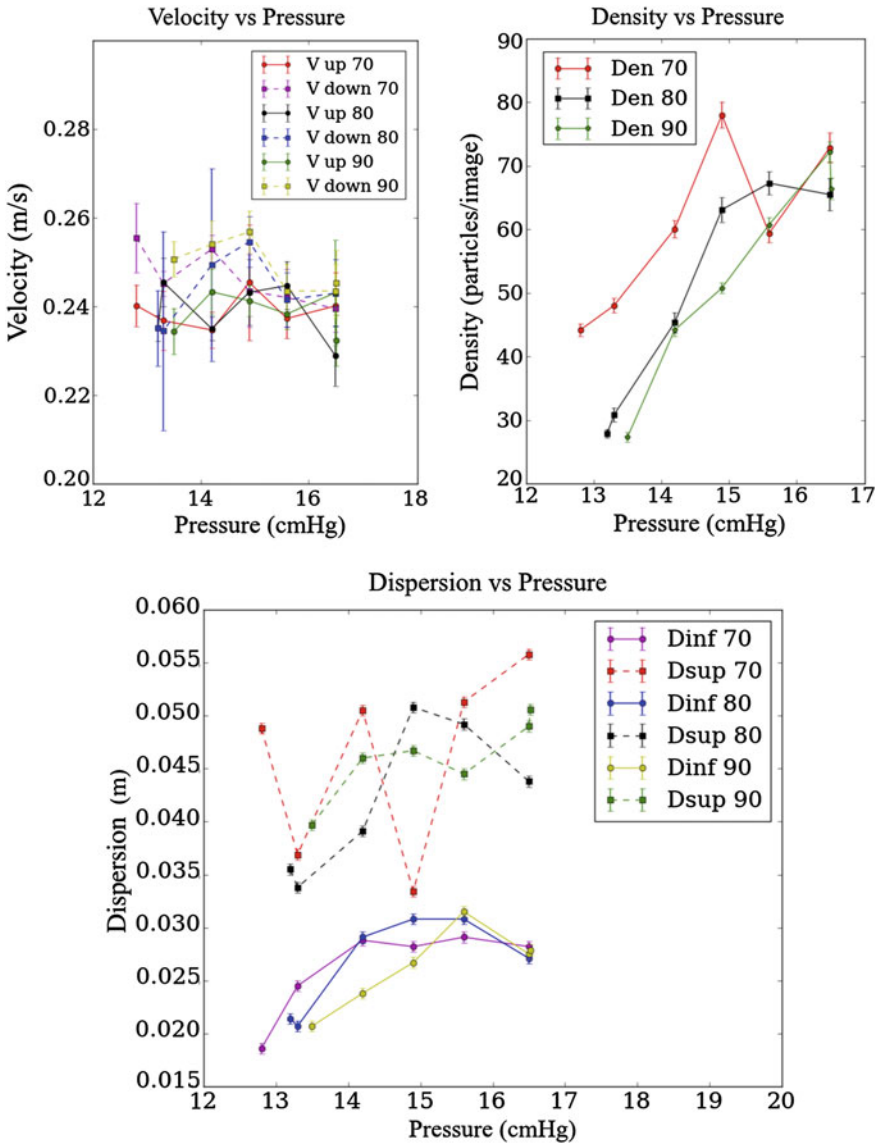

Fig. 7 *Upper left* Average upward speed of bubbles versus pressure. *Upper right* Particle density image versus pressure. *Bottom* Bubble dispersion at a height of 11 cm ('Dinf' on the graph) and a height of 48 cm ('Dsup' on the graph) as a function pressure

Two reference points are taken into account to analyze the amplitude of oscillation of the rising bubbles, the first at 11 cm and the second at 48 cm from the bubble generator. The bottom image of Fig. 7 shows that for pressures greater than 14.5 cm Hg

the values of the amplitude are very close and independent of the height. The same thing happens with the velocity values.

The bubble density per unit area changes as the pressure is increased. In Fig. 7 (upper right) the average density of particles per image is shown. Data obtained for pressures greater than 14.5 cm Hg are clustered, consistent with the Fig. 7 (upper left and bottom).

The analysis of the graphs above determined that the optimal pressure must be greater than 14.5 cm Hg regardless of height. In this area the speeds, densities and dispersions stay in a similar range. The average displacement on the horizontal axis is zero. Therefore, it is only relevant to note that there are periods of oscillation within the range of 0.16–0.25 s for the bubbles. This oscillation will be taken into account in the final analysis, and will not affect considerably the measurements.

4.2 Results for Three Bubbles

Measurements of the speeds of bubbles from three nearby holes are used to determine whether the interactions between the bubbles affect their behavior. These measurements were compared with those obtained for bubbles produced by one hole only. The left side of Fig. 8 shows that the bubbles have speeds close to 25 cm/s, which means that the increase in the number of bubbles does not induce any change in its upward velocity. The device was maintained at pressures higher than 14.5 cm Hg.

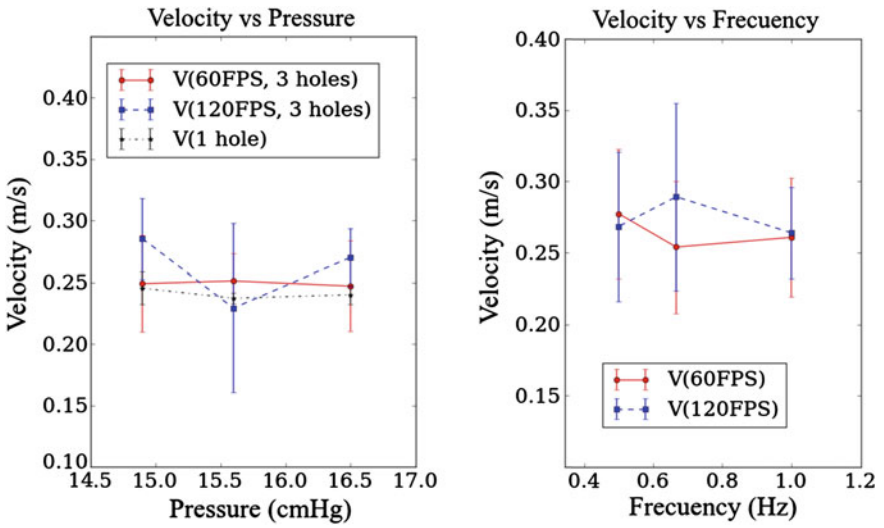

Fig. 8 *Left* speeds in the upward direction for three holes compared to one hole. *Right* upward speeds of bubbles when waves were produced in the flume

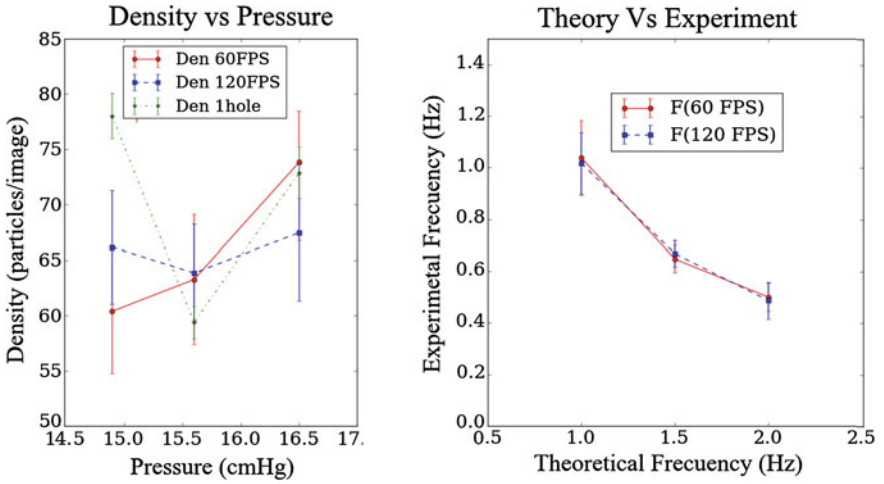

Fig. 9 *Left* bubble density against pressure for three holes, compared with the results of one hole. *Right* oscillation frequency of the waves compared with the frequency of the bubbles

4.3 Results Obtained When Waves Were Introduced

The right side of Fig. 8 shows speeds of bubbles in the upward direction at a pressure of 15.6 cm Hg, when controlled waves with different frequencies were introduced in the flume. The speed remains close to 25 cm/s, which indicates that the average ascending velocity of the bubbles is maintained.

The air pressure is controlled and the flow is steady. The left panel of Fig. 9 shows that the particle density generated by each hole is retained even with all holes uncovered.

The periods of the waves produced were compared with the periods measured from the bubbles. The results are depicted in the right panel of Fig. 9. It can be seen that the frequency of the bubbles matches the frequency of the waves.

5 Conclusions

The results show that bubbles are able to trace the flow behavior. Their horizontal variation has a well defined period. The amplitude of oscillation increases as the bubble rises. Measurements can be made in an area where both phenomena are small and can be easily taken into account. The upward velocity of the bubbles was not affected when waves with frequencies above 0.5 Hz were created. However, for waves of longer period the slower motion between peaks and valleys provide almost a 10 % difference.

The study has provided an optimum operating range of the air pressure and of the illuminated area. The next step is to introduce the device in the swimming pool, and observe the flow around a swimmer.

References

Arellano R, Pardillo S, Gavilán A (2002) Underwater undulatory swimming: kinematic characteristics, vortex generation and application during the start, turn and swimming strokes. Universidad de Granada

Biewener A (2003) Animal locomotion. Oxford University Press, Oxford

Crowe C, Elger D, Williams R, Roberson J (2009) Engineering fluid mechanics. Wiley, New York

Costa L, Ribeiro J, Figueiredo P, Fernandes RJ, Marinho D, Silva AJ4, Rouboa A4, Vilas-Boas JP1, Machado L (2010) Hydrodynamic characterization of the first and second glide positions of the underwater stroke technique in breaststroke. In: Biomechanics and medicine in swimming xi. proceedings of the international symposium for biomechanics and medicine in swimming, Per-Ludvik Kjendlie, Robert Keig Stallman and Jan Cabri (Eds), Published by the Norwegian School of Sport Science, Oslo

FINA (Fédération Internationale de Natation) (2013) Swimming. Medallists and statistics at olympic games. http://www.fina.org/H2O/docs/histofina/swimming_og.pdf

FINA (Fédération Internationale de Natation) (2014) Swimming world rankings. http://www.fina.org/H2O/index.php?option=com_wrapper&view=wrapper&Itemid=805

Triantafyllou MS, Triantafyllou GS, Yue DKP (2012) Hydrodynamics of fishlike swimming. Annu Rev Fluid Dyn 32(1):33–53

Numerical Simulation of a Gas-Stirred Ladle

H. Zambrano, A. Bencomo, L. Trujillo and L. Di G. Sigalotti

Abstract In this paper we present three-dimensional, numerical simulations of the turbulent recirculatory flow in a gas-stirred vessel. The physical model consists of air injected in a water cylindrical vessel, corresponding to a one-seventh scale model of an industrial 35 tons steel-making ladle. Plume development and recirculation is investigated for air blowing through an eccentric porous plug placed at the bottom of the vessel. The experimentally observed plume behaviour and the mixing process due to recirculatory water motion within the ladle is qualitatively well reproduced by the numerical simulations. When the airflow rate is increased, the intensity of agitation and turbulence increases, thereby enhancing the mixing in the ladle.

H. Zambrano
Facultad de Ingeniería, Universidad Central de Venezuela, UCV,
(Doctorado Individualizado), Apartado Postal 47750,
Caracas 1041, Venezuela
e-mail: hectorj.zambranom@gmail.com

A. Bencomo
Escuela de Ingeniería Metalúrgica y Ciencia de los Materiales,
Facultad de Ingeniería, Universidad Central de Venezuela, UCV,
Apartado Postal 47750, Caracas 1041, Venezuela
e-mail: alfonso.bencomo@gmail.com

L. Trujillo
Centro de Física, Instituto Venezolano de Investigaciones Científicas, IVIC,
Apartado Postal 20632, Caracas 1020, Venezuela
e-mail: leonardo.trujillo@gmail.com

L. Di G. Sigalotti
Instituto Venezolano de Investigaciones Científicas, IVIC,
Apartado Postal 20632, Caracas 1020, Venezuela

L. Di G. Sigalotti (✉)
Departamento de Ciencias Básicas,
Universidad Autónoma Metropolitana-Azcapotzalco, Av. San Pablo 180,
02200 Mexico, D.F., Mexico
e-mail: leonardo.sigalotti@gmail.com

J. Klapp et al. (eds.), *Selected Topics of Computational and Experimental Fluid Mechanics*, Environmental Science and Engineering,
DOI 10.1007/978-3-319-11487-3_17

1 Introduction

In the metallurgical industry the liquid steel is stirred to promote homogenization by percolating argon gas through a single refractory stir plug arrangement in the bottom of the ladle. For example, gas injection is used to enhance the speed of chemical reactions, eliminate thermal and/or composition gradients, and remove inclusions among other tasks (Bird et al. 1960). Submerged gas injection also plays an important role in copper and aluminium refining processes. However, experimental observations of the dynamics of liquid metal processing operations are very limited due to the high temperatures, visual opacity, and large sizes of the processing units. Consequently, most studies of the hydrodynamics of gas stirred ladles have been restricted to numerical and experimental models of simple gas injection configurations, i.e., injection of air into a cylindrical water vessel, where the vessel is some scaled model of an industrial steel-making ladle.

The mathematical models describing fluid motion in gas-stirred ladle systems can be classified into two main groups: (a) the quasi-single phase models based on the continuum approach (Grevet et al. 1982; Sahai and Guthrie 1982; Woo et al. 1990; Balaji and Mazumdar 1991; Sheng and Irons 1992; Goldschmit and Coppola Owen 2001; Taniguchi et al. 2002), where the combined gas-liquid fluid is treated as a mixture and so the form of the mass and momentum conservation equations reduce to those of a homogeneous fluid in terms of the mixture density and velocity, and (b) the two-phase fluid models (Schwarz and Turner 1988; Xia et al. 1999, 2002; Ramírez-Argáez 2007; De Felice et al. 2012), where there is a separate solution field for each phase and inter-phase transfer terms are employed to simulate the interaction between the two phases. In essence, the two-fluid models are based on the concept of unequal phase velocities. However, they will show a tendency to equalize because of the inter-phase interaction forces. For instance, the main interaction between phases is provided by the drag forces, which act in the direction opposite to the relative motion. Other forces may also influence the flow as the lift force, the virtual mass force, and the turbulent dispersion force. While most early two-fluid scaled models of gas-stirred ladles are two-dimensional models with axial symmetry, full three-dimensional (3-D) calculations have also started to appear (Pan et al. 1997; Zhang 2000; Aoki et al. 2004; Olsen and Cloete 2009; Cloete et al. 2009), with some of them reporting model calculations of full-scale gas-stirred ladles (Aoki et al. 2004; Cloete et al. 2009).

In this paper, we report further two-fluid model calculations of a gas-stirred ladle in three-space dimensions to study the characteristics of fluid flow and the influence of the wall on plume development. The numerical results are compared with visualization experiments on water models in the literature to get an insight into the plume behaviour and the mixing process. The physical model consists of an off-centred, submerged air injection in water to simulate argon and molten steel in a cylindrical vessel, corresponding to a 1:7 scale model of an industrial 35 tons steel-making ladle. We solve the two-phase transport equations in Eulerian form using the commercial code *FLUENT 6.3*. Turbulent effects are accounted for using a

Re-Normalization-Group (RNG) k-ε model for the governing equations of turbulence (Yakhot et al. 1992; Yakhot and Smith 1992).

2 Two-Phase Fluid Flow Model

The gas-stirred ladle is essentially a bubble-driven recirculation flow system. When the air is released from the porous plug, the flow is governed by the inertial force of the injected gas and large bubbles are formed at a small height from the nozzle exit (*primary or momentum region*). As the gas loses its kinetic energy, the large bubbles disintegrate into small ones (*transition region*) and owing to the density difference between air and water, they will float to the top until reaching the water surface (*bubble region*). When air bubbles float, they induce the water to flow and form a recirculation region outside the plume-shaped, two-phase region. In the upper part of the recirculation region the water flows towards the vessel walls. It then flows down along them and finally gets the ladle bottom. Therefore, the system can be divided into two zones: the plume zone, where air bubbles (dispersed phase) and water (continuous phase) coexist, and the water zone, where recirculation takes place.

If we assume isothermal conditions, the equations governing this two-phase flow in Eulerian form are: the mass conservation equation

$$\frac{\partial\left(\phi_\alpha \rho_\alpha\right)}{\partial t} + \nabla \cdot \left(\phi_\alpha \rho_\alpha \mathbf{v}_\alpha\right) = 0, \tag{1}$$

and the momentum conservation equation

$$\begin{aligned}\frac{\partial\left(\phi_\alpha \rho_\alpha \mathbf{v}_\alpha\right)}{\partial t} + \nabla \cdot \left(\phi_\alpha \rho_\alpha \mathbf{v}_\alpha \mathbf{v}_\alpha\right) = &- \phi_\alpha \nabla p + \nabla \cdot \mathbf{T}_\alpha + \phi_\alpha \rho_\alpha \mathbf{g} \\ &- \nabla \cdot \left(\phi_\alpha \rho_\alpha \langle \delta \mathbf{v}_\alpha \delta \mathbf{v}_\alpha \rangle\right) + \mathbf{F}_\alpha,\end{aligned} \tag{2}$$

for each phase α, where $\alpha = w$ and b for the water and bubbly phase, respectively, and where the phase pressures have been taken to be equal, i.e., $p_\alpha = p$. This assumption is considered to be valid except in the case of expanding bubbles (Drew 1983). Each phase has its own intrinsic mass density ρ_α, velocity $\mathbf{v}_\alpha$, volume fraction ϕ_α, and viscous stress tensor

$$\mathbf{T}_\alpha = \phi_\alpha \mu_\alpha \left(\nabla \mathbf{v}_\alpha + \nabla \mathbf{v}_\alpha^{\mathrm{T}}\right) - \frac{2}{3} \phi_\alpha \mu_\alpha \left(\nabla \cdot \mathbf{v}_\alpha\right) \mathbf{I}, \tag{3}$$

where μ_α is the dynamic viscosity of phase α, $\mathbf{I}$ is the identity tensor, and the superscript $^{\mathrm{T}}$ means transposition. In addition to Eqs. (1) and (2) we have the following constraints

$$\sum_\alpha \phi_\alpha = 1, \quad \rho = \sum_\alpha \phi_\alpha \rho_\alpha, \tag{4}$$

for the volume fractions and the density of the mixture.

The third term on the right-hand side of Eq. (2) is the gravitational acceleration force directed along the negative z-axis, while the fourth and fifth terms are the Reynolds stress (accounting for turbulent effects, where $\delta \mathbf{v}_\alpha = \mathbf{v}_{l,\alpha} - \mathbf{v}_\alpha$ is the fluctuating component of the velocity and $\mathbf{v}_{l,\alpha}$ is the local instant velocity of phase α) and a force per unit volume due to phase interactions which cause the transfer of momentum between relatively moving phases. Here this term is given by the sum of three additional forces: the drag force, which represents the force on a bubble due to its velocity relative to the water, the lift force, which accounts for the effects of velocity gradients in the water flow field on the bubbles, and the virtual mass force due to the inertia of the water mass on the accelerating bubbles. We assume a steady-state drag on the bubbles so that there is no acceleration of the relative velocity between the bubbles and the conveying fluid. This force is given by (Mazumdar and Guthrie 1995; Crowe et al. 1998)

$$\mathbf{F}_{D,w} = -\mathbf{F}_{D,b} = -\frac{3}{4}\sum_{k=1}^{N} \frac{C_D \mu_w}{D_{b,k}^2} \mathrm{Re}_k \left(\mathbf{v}_w - \mathbf{v}_{b,k}\right) \phi_{b,k}, \tag{5}$$

where $C_D (= 0.44$ for $\mathrm{Re} > 1{,}000)$ is the drag coefficient, $D_{b,k} = 6\,\mathrm{mm}$ is the mean diameter of the spherical bubbles, Re_k is the disperse phase relative Reynolds number

$$\mathrm{Re}_k = \frac{\rho_w D_{b,k}}{\mu_w} |\mathbf{v}_w - \mathbf{v}_{b,k}|, \tag{6}$$

and the sum is taken over the total number N of bubbles contained in a unit cell (or control volume). The lift force is given by (Drew and Lahey 1987)

$$\mathbf{F}_{L,w} = -\mathbf{F}_{L,b} = -0.5 \phi_b \rho_w \left(\mathbf{v}_w - \mathbf{v}_b\right) \times \left(\nabla \times \mathbf{v}_w\right), \tag{7}$$

while the virtual mass effects of the bath on the bubble column are given by (Drew and Lahey 1987)

$$\mathbf{F}_{V,w} = -\mathbf{F}_{V,b} = 0.5 \phi_b \rho_w \left(\frac{d\mathbf{v}_w}{dt} - \frac{d\mathbf{v}_b}{dt}\right), \tag{8}$$

where d/dt denotes the phase material time derivative. We note that these forces act as sinks for the continuous (water) phase and as sources for the dispersed (bubbles) phase.

Turbulence is modelled using the Re-Normalization Group (RNG) k-ε model (Yakhot et al. 1992; Yakhot and Smith 1992). This method differs from the standard k-ε model in that it accounts for smaller scales of turbulence by means of a renormalization of the Navier-Stokes equations, thereby allowing for turbulence at high Reynolds numbers. The Reynolds stresses in Eq. (2) are defined using Boussinesq's assumption

$$-\rho_\alpha \langle \delta \mathbf{v}_\alpha \delta \mathbf{v}_\alpha \rangle = \mu_{\alpha,t} \left(\nabla \mathbf{v}_\alpha + \nabla \mathbf{v}_\alpha^{\mathrm{T}}\right) - \frac{2}{3} \rho_\alpha k_\alpha \mathbf{I}, \tag{9}$$

where k_α is the turbulent kinetic energy density for phase α and

$$\mu_{\alpha,t} = \frac{C_{\mu\alpha}\rho_\alpha k_\alpha^2}{\varepsilon_\alpha}, \tag{10}$$

is the coefficient of the turbulent eddy viscosity, where ε_α is the dissipation rate of turbulence for phase α and $C_{\mu\alpha}$ is a parameter that depends on the phase volume fraction. In the actual simulations the turbulent eddy viscosity in relation (9) is replaced by an effective dynamic viscosity, which is a sum of the dynamic and eddy viscosities, i.e., $\mu_{\alpha,\text{eff}} = \mu_\alpha + \mu_{\alpha,t}$. Note that for the dispersed phase $\alpha = b, k$ in relation (9) and a sum is taken, as in expression (5), over all bubbles contained in a unit cell. The transport equations for the turbulent kinetic energy k_α and its dissipation rate ε_α as well as the values of all constants, including $C_{\mu\alpha}$, are taken as those derived explicitly in the RNG procedure for a single phase (Yakhot and Smith 1992; Pope 2000).

The transport equations are solved using the *FLUENT 6.3* code for a cylindrical water vessel of diameter 27.5 cm and height 40 cm, with its axis of symmetry aligned along the z-axis. An eccentric nozzle exit of 6 cm diameter is placed at the bottom of the vessel at one-third of its radius away from the wall, through which air is allowed to flow at a constant velocity. At the beginning of the calculations, the water volume fraction $\phi_w = 1$, while the air volume fraction ϕ_b is set to zero. No-slip boundary conditions for the fluid velocities apply along the wall of the vessel and the water free surface is assumed to remain flat. However, air bubbles reaching the free surface are allowed to flow out. To do so a sink term is added to Eq. (1) for the dispersed phase for those control volumes at the free surface. A tetrahedral mesh covering the full cylindrical domain was created with the help of the commercial software *Gambit 2.0* and trial calculations were conducted to determine convergence of the solutions. True convergence is guaranteed using a tetrahedral mesh with 333,465 elements.

3 Results and Discussion

Most industrial gas-stirred ladles have their porous plugs located off-centre because it is believed that this configuration produces a better stirring effect than when the porous plug is placed at the centre. Therefore, we simulate the injection of air into a water vessel when the plug position is one-third of the vessel radius away from the wall for two different constant airflow rates (i.e., $Q = 9.01 \times 10^{-6}$ and 1.03×10^{-5} $\text{m}^3\ \text{s}^{-1}$) in order to investigate the effects on the flow field. In the present model, the bubbles are assumed to be spherical with a uniform size distribution and released from the nozzle exit with constant frequency.

For $Q = 9.01 \times 10^{-6}\ \text{m}^3\ \text{s}^{-1}$ ($\approx 0.009\,1\ \text{s}^{-1}$), Fig. 1 shows the resulting stable flow pattern. The central axis of the plume is evidenced by the nearly vertical red pathlines, while the yellow ones closely coincide with its lateral borders. In the upper portion of the ladle, just above the plume region, there is no recirculation and the flow pathlines

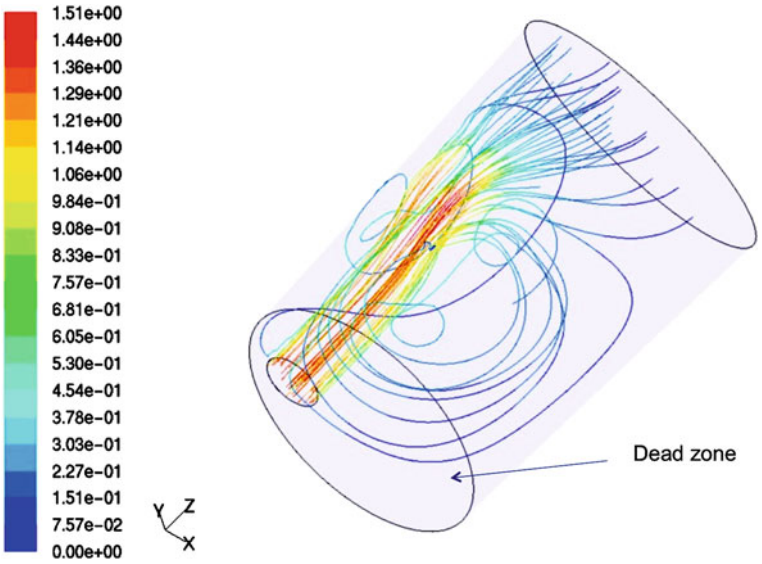

Fig. 1 Pathline velocity curves describing the flow within the ladle for a volumetric airflow rate of 9.01×10^{-6} m^3 s^{-1}. The *colour-scale bar* and numbers on the *left* border indicate the magnitude of the velocity in units of m s^{-1}

reach the flat water surface almost perpendicularly. Strong recirculation in the water phase is observed away from the vessel wall on one side of the plume, which occupies most of the ladle volume as shown by the green and blue pathlines. In the upper parts of the recirculation region, the water flows towards the walls with velocities that are nearly half the maximum velocities at the plume centre. In the proximity of the wall, the pathlines bend and the water flows down along the wall with progressively decreasing velocities. A further bending of the pathlines is produced when the flow reaches the bottom of the ladle, converging to the lower parts of the plume region. A small dead volume is formed below the recirculation region at the bottom of the ladle as indicated by the arrow in Fig. 1.

A striking aspect of the present calculations is the formation of an open eye in close contact with the wall, as is shown in Fig. 1 just behind the plume where a blue pathline is observed to follow a spiral-like trajectory in a clockwise sense. This interesting feature has been observed in air-water experiments with two eccentric porous plugs (Méndez et al. 2002). The open eye forms at a height where the plume is closest to the wall (its upper part) because part of the kinetic energy that would be transferred to the water is lost by viscous friction and so the flow velocities involved there are close to zero.

The predicted air volume fraction is depicted in Fig. 2, where a systematic attraction of the plume by the wall is seen towards its upper part. This behaviour was observed in model experiments of eccentric air injection in a square-section water channel for small and moderate flow rates and predicted by two-phase flow,

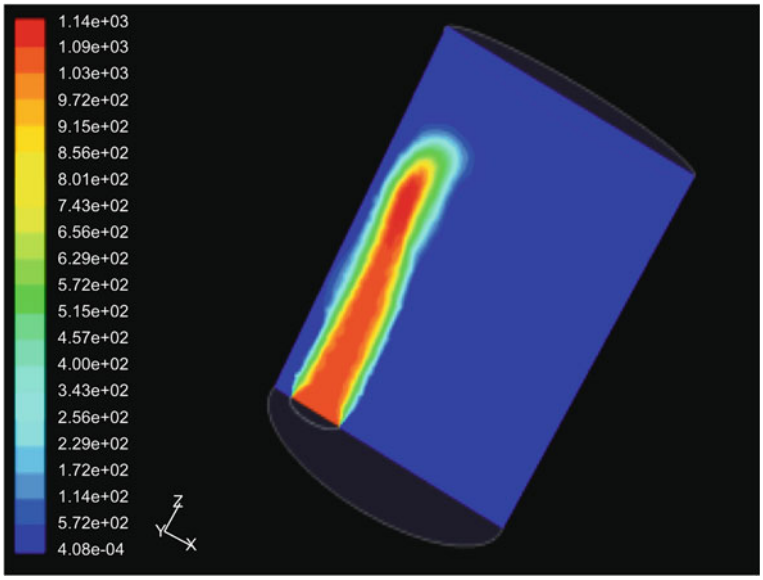

Fig. 2 Contours of the dynamic gas pressure showing the plume structure for the same model of Fig. 1. The *colour-scale bar* and numbers on the left border indicate the pressure values in units of Pa

steady-state simulations (Domgin et al. 1999). Figure 3 shows gas velocity contours on a cut section of the plume through its axis. We see that the bubble rising velocity is almost constant in most of the inner parts of the plume with an average value of $\approx$1.2 m s^{-1}. This value is in close agreement with the experimentally measured value of about 1 m s^{-1} for the flow velocity of molten metals in a ladle model at centric gas blowing (Xie and Oeters 1992).

A view of the cross-sectional area of the plume is shown in Fig. 4 at three different heights. Close to the nozzle exit, the plume exhibits a fairly circular cross-section, which then contracts and deforms as the swarm of bubbles rises due to the density difference with the water. This implies that the gas volume fraction is larger near the bottom half of the reactor and then becomes smaller near the free surface due to gas dispersion. Finally, Fig. 5 shows the distribution of the kinetic energy within the entire system. The lowest values of the kinetic energy occur at the bottom of the ladle, where the flow is inactive, and the largest values are concentrated in the upper part of the plume and close to the free surface where most of the bubbly gas is being dispersed.

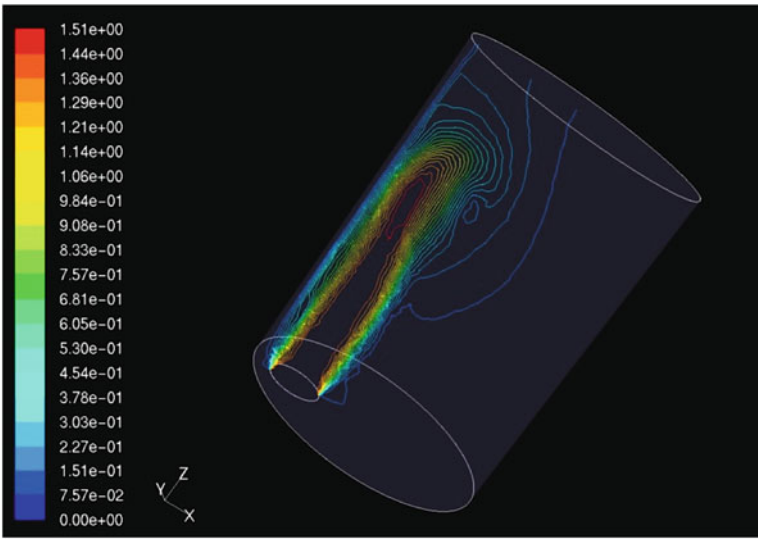

Fig. 3 Isocontour of the gas velocity in a section plane of the plume through its axis for the same model of previous figures. The *colour-scale bar* and numbers on the left border indicate the magnitude of the velocity in units of m s^{-1}

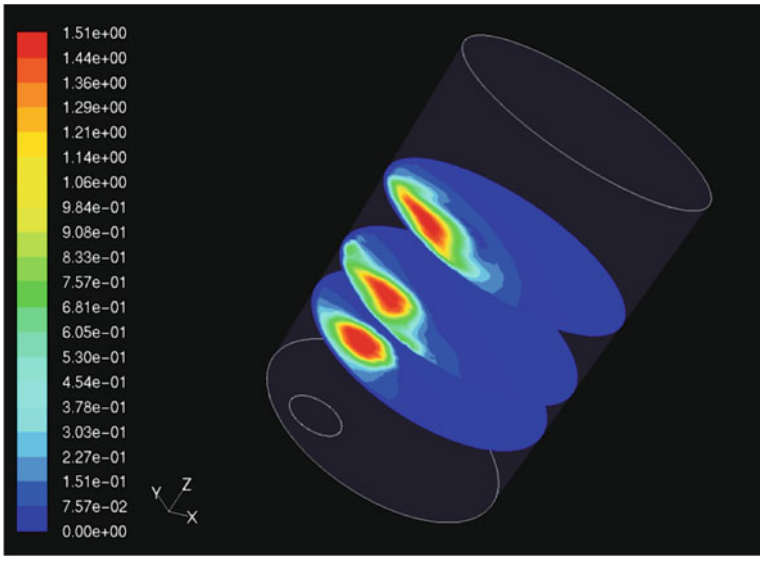

Fig. 4 Contours of the gas velocity showing the cross-sectional structure of the plume at three different heights for the same model of previous figures. The *colour-scale bar* and numbers on the left border indicate the magnitude of the velocity in units of m s^{-1}

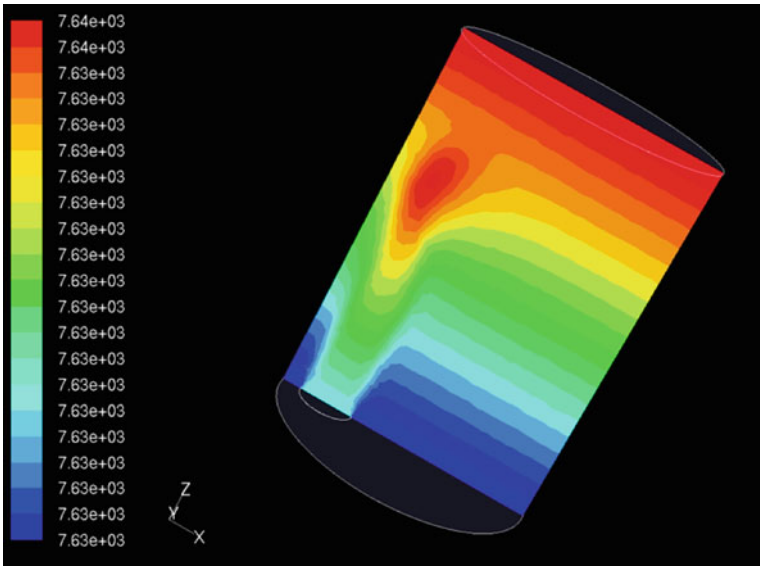

Fig. 5 Distribution of the kinetic energy in the entire ladle system for the same model of previous figures. The *colour-scale bar* and numbers on the left border indicate the values of the kinetic energy in units of g m^2 s^{-2}

4 Conclusions

In this paper, we have presented numerical simulations of two-phase flows in a scaled air-water model of an industrial gas-stirred ladle using the *FLUENT 6.3* code. We find that the intensity of agitation and turbulence in the ladle increases by increasing the gas flow rate at the nozzle exit. As expected, an eccentric gas blowing improves the mixing as it enforces the reduction of inactive flow regions, or dead zones, just below the recirculating liquid flow at the bottom of the ladle. In addition, changing the diameter of the porous plug hardly affects the flow pattern as the rising of the gas bubbles is dominated by inertial forces near the nozzle exit and by gravitational forces at higher heights. The results are in excellent agreement with experimental observations of eccentric gas injection models as well as observations and numerical calculations of plume development and behaviour.

References

Aoki J, Thomas BG, Peter J, Peaslee KD (2004) Experimental and theoretical investigation of mixing in a bottom gas-stirred ladle. In: Proceedings of the association for iron and steel technology (AISTech 2004), vol I, pp 1045–1056

Balaji D, Mazumdar D (1991) Numerical computation of flow phenomena in gas-stirred ladle systems. Steel Res 62(1):16–23

Bird RB, Stewart WE, Lightfoot EN (1960) Transport phenomena. Wiley, New York
Cloete SWP, Eksteen JJ, Bradshaw SM (2009) A mathematical modelling study of fluid flow and mixing in full-scale gas-stirred ladles. Prog Comput Fluid Dyn 9(6/7):345–356
Crowe C, Sommerfeld M, Tsuji Y (1998) Multiphase flows with droplets and particles. CRC Press, Boca Raton
De Felice V, Daoud ILA, Dussoubs B, Jardy A, Bellot J-P (2012) Numerical modelling of inclusion behaviour in a gas-stirred ladle. ISIJ Int 52(7):1273–1280
Domgin JF, Gardin P, Brunet M (1999) Experimental and numerical investigation of gas stirred ladles. In: Proceedings of the second international conference on CFD in the minerals and process industries, CSIRO, Melbourne, 6–8 December 1999, pp 181–186
Drew DA (1983) Mathematical modelling of two-phase flow. Annu Rev Fluid Mech 15:261–291
Drew DA, Lahey RT (1987) The virtual mass and lift force on a sphere in rotating and straining inviscid flow. Int J Multiph Flow 13(1):113–121
Goldschmit MB, Coppola Owen AH (2001) Numerical modelling of gas stirred ladles. Ironmak Steelmak 28(4):337–341
Grevet JH, Szekely J, El-Kaddah N (1982) An experimental and theoretical study of gas bubble driven circulation systems. Int J Heat Mass Transf 25(4):487–497
Mazumdar D, Guthrie RIL (1995) The physical and mathematical modelling of gas stirred ladle systems. ISIJ Int 35(1):1–20
Méndez CG, Nigro N, Cardona A, Begnis SS, Chiapparoli WP (2002) Physical and numerical modelling of a gas stirred ladle. In: Idelshon SR, Sonzogni VE, Cardona A (eds) Mecánica computacional, vol XXI. Santa Fe-Paraná, Argentina, pp 2646–2654
Olsen JE, Cloete S (2009) Coupled DPM and VOF model for analyses of gas stirred ladles at higher gas rates. In: Proceedings of the seventh international conference on CFD in the minerals and process industries, CSIRO, Melbourne, 9–11 December 2009, pp 1–6
Pan S-M, Ho Y-H, Hwang W-S (1997) Three-dimensional fluid flow model of gas-stirred ladles. J Mater Eng Perform 6(3):311–318
Pope SB (2000) Turbulent flows. Cambridge University Press, Cambridge
Ramírez-Argáez MA (2007) Numerical simulation of fluid flow and mixing in gas-stirred ladles. Mater Manuf Process 23(1):59–68
Sahai Y, Guthrie RIL (1982) Hydrodynamics of gas stirred melts: part I. Gas/liquid coupling. Metall Trans B 13B:193–202
Schwarz MP, Turner WJ (1988) Applicability of the standard k-ε turbulence model to gas-stirred baths. Appl Math Model 12(3):273–279
Sheng YY, Irons GA (1992) Measurement and modeling of turbulence in the gas/liquid two-phase zone during gas injection. Metall Trans B 24B:695–705
Taniguchi S, Kawaguchi S, Kikuchi A (2002) Fluid flow and gas-liquid mass transfer in gas-injected vessels. Appl Math Model 26(2):249–262
Woo JS, Szekely J, Castillejos AH, Brimacombe JK (1990) A study on the mathematical modelling of turbulent recirculating flows in gas-stirred ladles. Metall Trans B 21B:269–277
Xia JL, Ahokainen T, Holappa L (1999) Modelling of flows in a ladle with gas stirred liquid Wood's metal. In: Proceedings of the second international conference on CFD in the minerals and process industries, CSIRO, Melbourne, 6–8 December 1999, pp 187–192
Xia JL, Ahokainen T, Holappa L (2002) Analysis of flows in a ladle with gas-stirred melt. Scand J Metall 30(2):69–76
Xie Y, Oeters F (1992) Experimental studies on the flow velocity of molten metals in a ladle model at centric gas blowing. Steel Res 63:93–104
Yakhot V, Orszag SA, Thangam S, Gatski TB, Spaziale CG (1992) Development of turbulence models for shear flows by a double expansion technique. Phys Fluids A 4(7):1510–1520
Yakhot V, Smith LM (1992) The renormalization group, the ε-expansion, and derivation of turbulence models. J Sci Comput 7:35–51
Zhang L (2000) Mathematical simulation of fluid flow in gas-stirred liquid systems. Model Simul Mater Sci Eng 8:463–476

Folding of the Apolipoprotein A1 Driven by the Salt Concentration as a Possible Mechanism to Improve Cholesterol Trapping

M.A. Balderas Altamirano, A. Gama Goicochea and E. Pérez

Abstract The folding of the cholesterol—trapping apolipoprotein A1 in aqueous solution at increasing ionic strength—is studied using atomically detailed molecular dynamics simulations. We calculate various structural properties to characterize the conformation of the protein, such as the radius of gyration, the radial distribution function and the end-to-end distance. Additionally we report information using tools specifically tailored for the characterization of proteins, such as the mean smallest distance matrix and the Ramachandran plot. We find that two qualitatively different configurations of this protein are preferred: one where the protein is extended, and one where it forms loops or closed structures. It is argued that the latter promote the association of the protein with cholesterol and other fatty acids.

1 Introduction

The apolipoprotein A1 (APOA1) is the main component of high-density lipoproteins and has an important role in lipid metabolism. APOA1 is found in the human blood stream and promotes fatty acid efflux, including cholesterol, from tissues to the liver for excretion. Its study is important because of its protective effect against atherosclerosis (Breslow 1996) and its function as a cholesterol transport from white blood cells within artery walls (Glomset 1968). APOA1 contains a single polypeptide chain of 243 amino acid residues (Brewer et al. 1978) with 11 or 22 regularly repeating residues in the sequence (McLachlan 1977). These multiple repeating units were proposed to form amphipathic helices with distinct hydrophilic and hydrophobic faces (Segrest et al. 1974). The fat transport is then expected to be modulated by the hydrophilic and hydrophobic residues along APOA1, but also by physiological conditions like pH and ionic strength in the blood or physiological fluid.

M.A. Balderas Altamirano (✉) · A. Gama Goicochea · E. Pérez
Instituto de Física, Universidad Autónoma de San Luis Potosí,
Álvaro Obregón 64, Luis Potosí, 78000 Mexico, San Luis Potosí, Mexico
e-mail: miguelangel.balderas@gmail.com

J. Klapp et al. (eds.), *Selected Topics of Computational and Experimental Fluid Mechanics*, Environmental Science and Engineering,
DOI 10.1007/978-3-319-11487-3_18

Computer simulations have come to play an increasingly important role in the understanding of protein folding, protein–protein interactions and the surface activity of proteins, to name but a few. Some of the advantages of atomistic simulations are the complete control over the physicochemical variables of the problem and the essentially exact solution of the equations of motion that govern the nature of the system, not to mention the vivid representations of the spatial conformations of molecules and their evolution with time. In this work we focus mainly on predicting how APOA1 folds as the salt content is increased, using atomistically detailed computer simulations. In particular, we study the contraction followed by re-expansion of some residues of APOA1 induced by the increasing concentration of monovalent salt ions. This phenomenon has been found to occur in other polyelectrolytes in aqueous solution using a variety of methods (Hsiao and Luijten 2006; Feng et al. 2009; Alarcón et al. 2013; Pollard et al. 2013; Frank and Marcel 2000). In this context, APOA1 is a much more complex system because there are positive, negative and neutral sequences along its structure, as well as hydrophilic and hydrophobic residues. We expect that the spatial conformation is a crucial factor in determining the ability of APOA1 to capture cholesterol and other fatty acids, which is the functionality we would like to optimize so that a mechanism can be proposed to help design drugs and treatments that improve the quality of life.

2 Model and Methodology

We start by taking the fragment of APOA1 known as 1GW3 from the Protein Data Bank (PDB, http://www.rcsb.org; Wang et al. 1997), which has 142–187 aminoacid residues from the complete APOA1. It is computationally very demanding to model the entire protein, while only a fraction of its residues is responsible for the folding we are interested in. We take into account only a 20 % of the original protein. Therefore, we work only with the above mentioned fragment and set up molecular dynamics simulations with it and varying NaCl concentrations, ranging from 0.01 M up to 2.0 M. For the interatomic interactions we used the Lennard–Jones model (Allen and Tildesley 1987), while for the electrostatic interactions we used the so called Particle Mesh Ewald (PME) method (Darden et al. 1993). To conserve the bonds between the atoms that make up the protein we used LINCS (Linear Constraint Solver, Hess et al. 1997). The force field parameters for the protein were taken from OPLS (Optimized Potential for Liquid Simulations) (Jorgensen and Tirado-Rives 1988), and the water model used was SPCE (Berendsen et al. 1987). Then all interactions are solved using GROMACS 4.6.4 (Spoel et al. 2005), where the interactions are calculated at every time step using the Verlet scheme (Pall and Hess 2013) with a grid scheme for GPU's, which allow us to perform large simulations. The cut off distance for the Lennard–Jones and electrostatic interactions was equal to 1.0 nm. A leapfrog algorithm (Snyman 2000) was used for the calculation of the atoms positions and velocities. The energy minimization was performed using the steepest descends method (Chaichian and Demichev 2001).

The simulations were carried out under the thermodynamic conditions known as the canonical ensemble, where the number of particles, volume of the simulation box, and temperature (*NVT*) are constant; the latter was fixed at 300 K using the V-rescale method (Buss et al. 2007). To bring the system to equilibrium we ran the simulations for up to 200 ps, after which we switched to the *NPT* ensemble (where the pressure is held constant, in addition to the number of particles and the temperature) to fix the pressure at 1 bar, using the Parrinello–Rahman method (Parrinello and Rahman 1981), again for 200 ps. Once the pressure of the system is equilibrated under these conditions, we ran the simulations for an additional 5 ns for the equilibrium phase and another 5 ns for the production phase, during which we performed the calculation of the properties of interest. The time step for the integration of the equation of motion was equal to 2 fs. We worked on a cubic simulation box with lateral size equal to 10 nm.

3 Results and Discussion

Since we are interested in determining how APOA1 folds, we performed simulations to calculate its radius of gyration (R_g) at each of the salt concentrations we modeled. R_g is calculated from the center of mass of the molecule, as is done in polymer science (Grosberg and Khokhlov 1994). Figure 1 shows the values of R_g for every

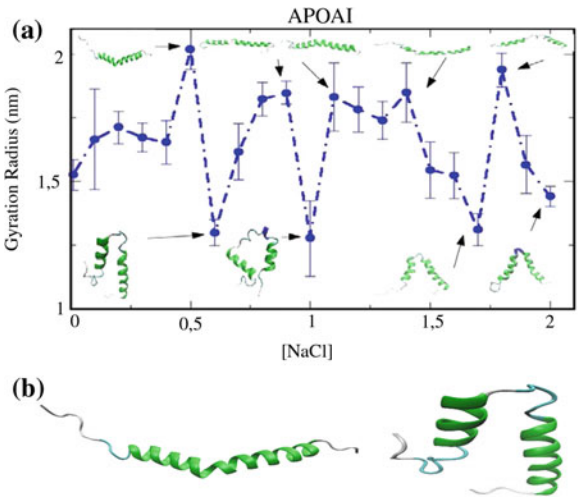

Fig. 1 **a** Gyration radius of APOA1 as a function of NaCl concentrations. The *error bars* represent the standard deviation of the data point averaged over 5 ns. The snapshots shown at the *top* and *bottom* of the data correspond to the open and close conformation of APOA1, respectively. The arrows identify each conformation with its salt concentration. The *line* is only a guide for the eye. **b** Typical APOA1 open (0.5 M) and closed (0.6 M) conformations.

NaCl concentration; we have also included snapshots of the spatial configuration of the protein at certain salt concentration where the folding changes intermittently from loops (or "closed" conformations) to an extended (or "open") conformation. At the top part of Fig. 1 we include snapshots of the open conformations and in the bottom part the close conformations. The arrows at the top of Fig. 1 indicate the 0.5, 0.9, 1.1, 1.4 and 1.8 M concentrations, where the open conformations take place.

The arrows shown at the bottom of Fig. 1 represent the concentrations 0.6, 1.0, 1.7 and 2.0 M, which correspond to close conformations. A behavior qualitatively similar to this has been obtained by Alarcón and coworkers (Alarcón et al. 2013) on biopolymers, by Hsiao (Hsiao and Luijten (2006)) for polyelectrolytes of multivalent ions, and in experiments (Kozer et al. 2007; Dawson et al. 1997; Käs et al. 1996). The formation of closed configurations is the result of the electrostatic charge inversion mechanism (Nguyen et al. 2000), while the open configurations are attributed to electrostatic repulsion between adjacent monomers (Wong and Pollack 2010). Trapping of cholesterol and other fatty acids becomes favorable when closed configurations are formed because these molecules are closer to APOA1, therefore the formation of hydrogen bonds between them is promoted. Under these circumstances this protein would have an increased functionality. To test the stability of the open and close configurations seen in Fig. 1, we have monitored their evolution in time, which we show in Fig. 2. The curves seen on the top of the figure correspond to open structures, while those at the bottom correspond to closed conformations.

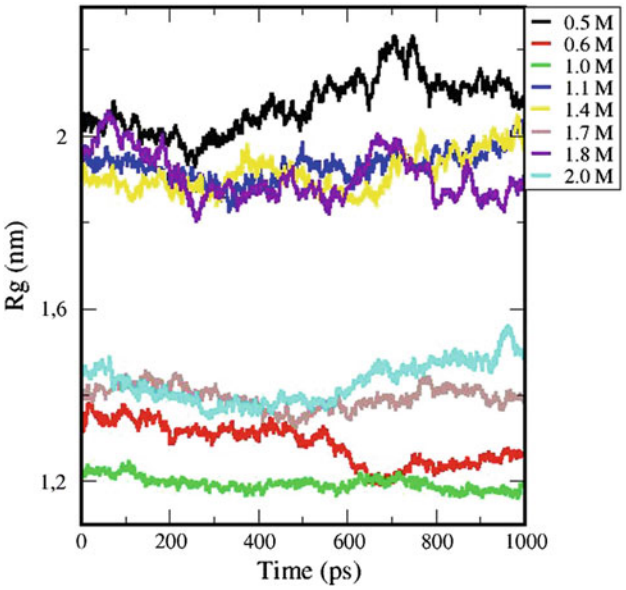

Fig. 2 Time evolution of the radius of gyration (R_g) of APOA1 at various NaCl concentrations, as specified in the inset on the right border of the figure. The *top curves* correspond to the so-called open structures; those at the *bottom* correspond to closed configurations

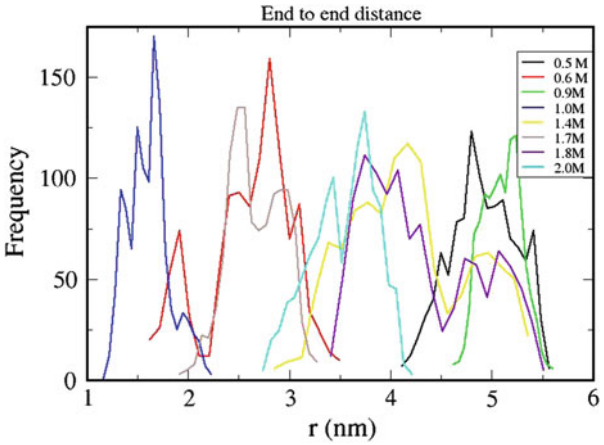

Fig. 3 Histograms of the distance between one end and the other of APOA1, for various concentrations of salt ions. Open conformations correspond to salt concentrations of 0.5, 0.9, 1.4 and 1.8 M, while the rest belongs to closed configurations

An inspection of Fig. 2 shows that most conformations are stable throughout the production phase of the simulation, which indicates that they correspond to situations of thermodynamic equilibrium of the system at those salt concentrations. Although in some cases one observes an increase (as in, for example, the cyan and black curves) or a decrease (red and purple curves) of R_g with time, the fluctuations are to no more than a few percent change of the averaged R_g.

It should be stressed that both open and closed configurations have a distribution of values of the radius of gyration rather than a single value. To prove this fact we calculate the end-to-end distance distribution and depict it in Fig. 3. The end-to-end distance is the distance from the first to the last residues in the protein. The curves seen in Fig. 3 represent histograms of the distribution of end-to-end distances found at various salt concentrations. The so-called open configurations have larger end-to-end distances, as expected, corresponding to the concentrations 0.5 M (black line), 0.9 M (green), 1.4 M (yellow) and 1.8 M (purple). The closed conformations have smaller end-to-end distances, as given by the lines for 0.6 M (red line in Fig. 3), 1.0 M (blue), 1.7 M (gray), and 2.0 M (cyan). Most of this information was known at this point, particularly from the analysis of Figs. 1 and 2. However, the added value of Fig. 3 is that it provides a quantitative estimate of the average distance between the ends of APOA1, where we find open (the largest being ∼5.3 nm) and closed configurations as well (the smallest being 1.6 nm).

The structural characteristics of APOA1 are further analyzed through the so-called "mean smallest distance matrix" (msdm), which is obtained from the averaged distance between each residue and all other residues in the protein. In Fig. 4, the x and y axes indicate the index that identifies each residue of the protein, and each data point in Fig. 4 register the distance between each pair of residues. Such distance is

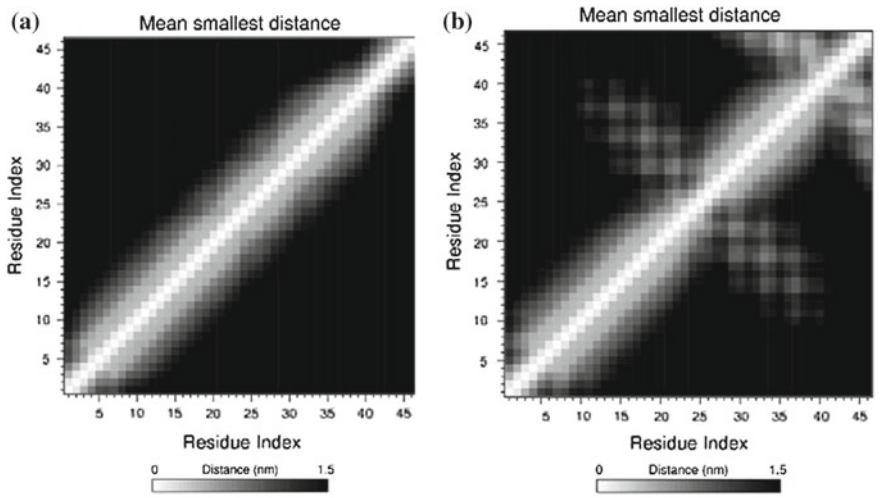

Fig. 4 The mean smallest distance matrix for 0.5 M (**a**) and 0.6 M (**b**) concentrations of NaCl. The axes represent the residues that conform APOA1. The maximum distance considered to be part of the protein is 1.5 nm

represented in a gray scale, with the maximum distance being 1.5 nm; if a distance between residues is larger than this value a black dot is added to this figure.

The principal diagonal line in Fig. 4 (white colored) represents a relative distance equal to zero, because it is the distance of a residue with itself. Therefore, a protein leaves a fingerprint of itself in a msdm graph. This is a useful tool to compare between open and closed structures because it shows how the protein modifies its conformations from open to closed as it evolves in time and which residues are moving the most. In Fig. 4 we show two graphs, with the left corresponding to an open APOA1 structure at a salt concentration equal to 0.5 M, and the right for the closed configuration at 0.6 M. The left graph (Fig. 4a) shows the msdm between the aminoacid residues that make up APOA1, where a diagonal line across the graph means that there are similar distances between the residues, which corresponds to the extended protein conformation (open). In Fig. 4b, one observes a qualitatively different behavior from that found for the open conformation (left panel in Fig. 4). In the center of the graph on the right of Fig. 4, there is a gray area representing relative distances between residues that are smaller than 1.5 nm, meaning that the structure of the protein is of the closed conformation and it also identifies the residues that are closer to each other because of this folding. We selected the residues 21–26 from the right panel of Fig. 4 because they are in the zone where the closed conformation is formed. These residues are H (Hystidine), L (Leucine), A (Alanine), P (Proline), Y (Tyrosine) and S (Serine). The sequence of APOA1 studied here is therefore called HLAPYS. In the upper right corner of the right panel in Fig. 4, we find another zone where residues are closer than 1.5 nm; these residues correspond to the end of the protein.

To determine which aminoacid residues are the responsible for the open and closed conformations discussed previously, we obtained the Ramachandran plot (Mathews et al. 2002), which maps out the conformations of the alpha carbon in a protein (or visualize backbone dihedral angles ψ versus φ of aminoacid residues in protein structure). In a Ramachandran plot we display the zone where the alpha carbon conformations are stable through time and also the zones where there are alpha helices and beta sheets. In Fig. 5, we show two graphs where the top (a) represents the open conformation (at 0.5 M of NaCl), and the bottom (b) corresponds to a closed structure, at 0.6 M. Black dots represent the configurations (over all the simulation time) of all the aminoacids in APOA1, while the different colors belong to specific aminoacid residues (HLAPYS) throughout the entire simulation time. In Fig. 5a, one sees that the HLAPYS aminoacids are preferentially found in a relatively narrow zone of angular values: this is the region of the alpha helix zone. By contrast, in Fig. 5b we see that the HLAPYS residues move to the beta sheet area (top left quadrant in each graph), although this does not mean that they are forming beta sheets, instead it

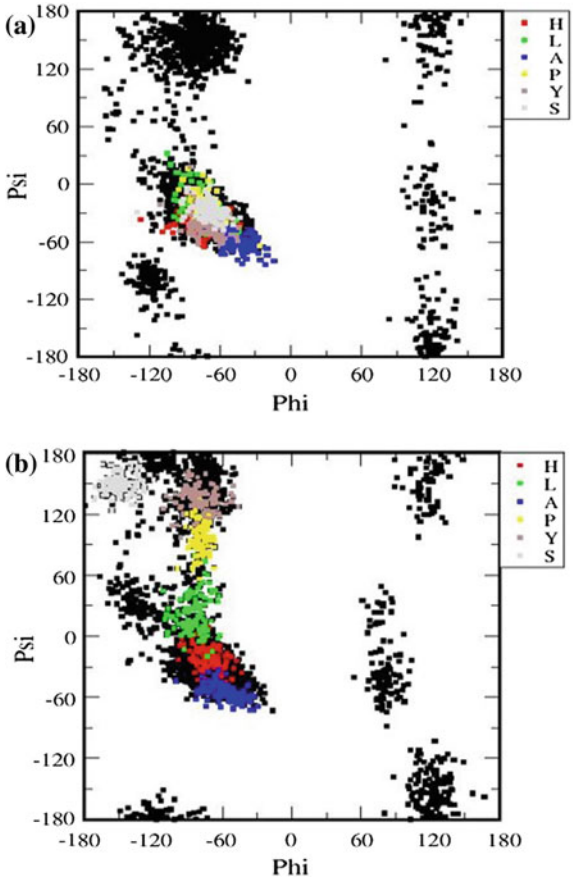

Fig. 5 Ramachandran plot for **a** the open configuration at 0.5 M, and **b** for the closed one at 0.6 M of NaCl. The axes represent the angles that the α–C atom form with its bonding neighbors. The *colors* and *symbols* on the right borders represent the H, L, A, P, Y and S residues of the APOA1. The different data points for a given residue represent its time evolution

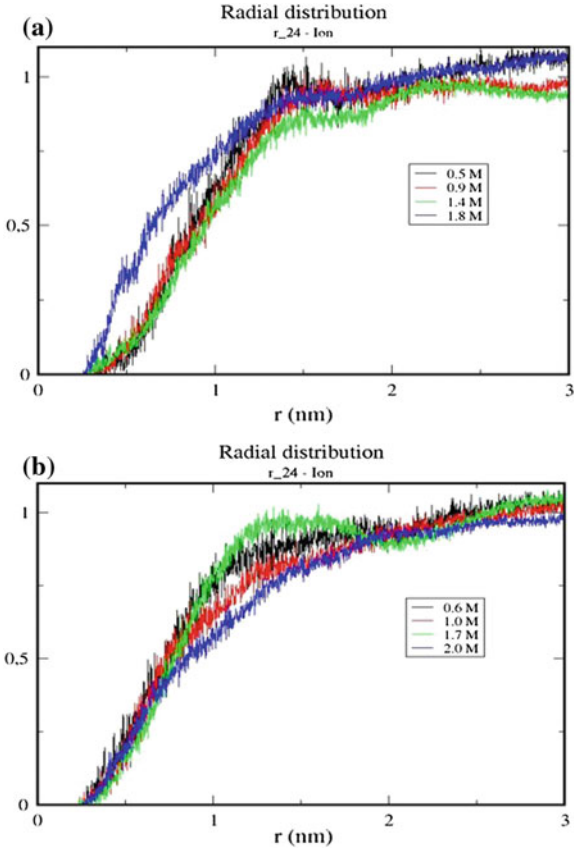

Fig. 6 Averaged radial distribution function of the P residue with the both salt ions, at different NaCl concentrations **a** Open conformation; **b** closed conformation. The residue index 24 in the sequence of APOA1 is Proline (P)

just means that the aminoacids have values of their angles which are similar to those found in the beta sheets. We can also see that the aminoacids having moving angles with time are PYS, while the other ones are (H, L, A). Therefore, the Ramachandran plot helps us identify specifically the residues that are responsible for the folding of the protein driven by the addition of ions. Up to this point we have studied the residues that drive APOA1 to form closed conformations.

Next, we must understand the influence of the salt ions and water. With that purpose in mind we calculated the radial distribution function (rdf) of these residues and their interaction with water and ions. The rdf is obtained from the relative distance between a chosen particle in a fluid and all other particles that surround it; therefore it quantifies how the local density in a fluid varies (Allen and Tildesley 1987). In the case of water, we did not see any significant difference between the rdf's of the water—open configuration, and those between the water—closed conformation, and so we do not show them here. Instead, we focused on calculating the rdf's between the ions and the residues. In Fig. 6 we show the rdf of the P—residue with the ions (namely, with the sum of Na and Cl ions).

In Fig. 6a we show the rdf of the P—residue and the ions (Na + Cl), at different concentrations for the case of an open conformation of APOA1. One feature that stands out is the relatively large number of ions in close proximity to the P residue at 1.8 M (blue line). Although P is a non-polar residue, it is highly movable, which implies that the ions can easily surround it and cause it to have a solvation radius larger than its own radius, which in turn would compel the neighboring residues to stay at relatively larger distances from P. This fact, in turn, leads to an open configuration. In Fig. 6b there is a uniform distribution of relative distances between the P—residue and the salt ions at all concentrations; for example, at all salt concentrations in Fig. 6b there is approximately the same probability to have ions and the P—residue a distance $r \sim 0.7$ nm apart. The fact that all rdf's in this case follow the same trend at small relative distances means that these rdf's correspond to configurations where there is no more room available for the ions to get closer to P. This must be the case when APOA1 is in a closed conformation, as in Fig. 6b.

4 Conclusions

We have shown in this work how atomistically detailed molecular dynamics computer simulations can help us understand the folding process in proteins under controlled physicochemical conditions as, for example, the ionic strength. For this case study we have chosen APOA1 because of its key role in producing the efflux of fatty acids in the human blood stream. It was found that, under increasing salt concentration, the protein undergoes alternatively folding and unfolding. The simulations suggest that it is driven by the formation of solvation spheres around the most mobile aminoacids in the APOA1 sequence, competing with the electrostatic interactions. The structural properties of the protein were characterized through powerful tools such as the radius of gyration, the end-to-end distance, the mean-square distance matrix, the Ramachandran plot, and the radial distribution function. In particular, we found that the P, Y and S residues are moving the most when going from an open to a close conformation. This work helps elucidate the effect of the charge in APOA1, where the important sequence turns out to be HLAPYS. The role of the closed configurations should not be underestimated either, for those are precisely the ones thought to be responsible for the trapping of fatty acids such as cholesterol. Work is presently under way to determine the association of APOA1 with cholesterol under varying ionic strength, but it is mandatory to gain first a basic understanding of this protein's folding at increasing salt content before attempting the study its complexation with other molecules.

Acknowledgments This project was financed by CONACYT, grant 132056. We would like to acknowledge many educational conversations on this topic with A. López–Vallejo López. The authors thank also J. Limón (IFUASLP) for technical support with GPU installation. MABA and AGG thank the UASLP for its hospitality.

References

Alarcón F, Pérez-Hernández G, Pérez E (2013) Coarse-grained simulations of the salt dependence of the radius of gyration of polyelectrolytes as models for biomolecules in aqueous solution. Eur Biophys J 42:661

Allen MP, Tildesley DJ (1987) Computer simulation of liquids. Clarendon Press, Oxford

Berendsen HJC, Grigera JR, Straatsma JP (1987) The missing term in effective pair potentials. J Phys Chem 91:6269

Breslow JL (1996) Mouse model of atherosclerosis. Science 272:685

Brewer HB Jr, Fairwell T, LaRue A, Ronan R, Houser A, Bronzert TJ (1978) The aminoacid sequencing of human APOA1, an apolipoprotein isolate from high density lipoproteins. Biochem Biophys Res Commun 80:623

Buss G, Donadio D, Parrinello M (2007) Canonical sampling through velocity rescaling. J Chem Phys 126:014101

Chaichian M, Demichev A (2001) Path integrals in physics, volume 1: stochastic process and quantum mechanics. Taylor and Francis, London (ISBN 075030801X)

Darden T, York D, Perera L (1993) Particle mesh Ewald: an Nlog (N) method to Ewald sums in large systems. J Chem Phys 98:10089

Dawson KA, Gorelov AV, Timoshenko EG, Kuznetsov YA, DuChesne A (1997) Formation of mesoglobules from phase separation in dilute polymer solutions: a study in experiment, theory and applications. Phys A: Stat Mech 244:68

Feng J, Wong K-Y, Lynch GC, Gao X, Pettitt BM (2009) Salt effects on surface-tethered peptides in solution. J Phys Chem B 113:9472

Frank PG, Marcel YL (2000) Apolipoprotein A-1: structure function relationships. J Lipid Res 41:853

Glomset JA (1968) The plasma lecithin: cholesterol acyltransferase reaction. J Lipid Res 9:155

Grosberg AY, Khokhlov AR (1994) Statistical physics of macromolecules. AIP Press, New York (ISBN 1563960710)

Hess B, Berker H, Berendsen HJC, Fraaije JGEM (1997) LINCS: a linear constraint solver for molecular simulations. J Comput Chem 18:1463

Hsiao P-Y, Luijten E (2006) Salt-induced collapse and re expansion of highly charged flexible polyelectrolytes. Phys Rev Lett 97:148301

Jorgensen WL, Tirado-Rives J (1988) The OPLS force field for proteins: energy minimizations for crystals of cyclic peptides and crambin. J Am Chem Soc 110:1657

Käs J, Strey H, Tang JX, Finger D, Ezzell R, Sackmann E, Janmey PA (1996) F-actin, a model polymer for semiflexible chains in dilute, semi dilute and liquid crystalline solutions. Biophys J 70:609

Kozer M, Kuttner YY, Haran G, Schreiber G (2007) Protein - protein association: from dilute to semi dilute to concentrated. Biophys J 92:2139

Mathews CK, van Holde KE, Ahern KG (2002) Biochemistry, 3rd edn. printed in Spain

McLachlan AD (1977) Repeated helical pattern in apolipoprotein A. Nature 267:465

Nguyen TT, Rouzina I, Shklovskii BI (2000) Reentrant condensation of DNA induced by multivalent counterions. J Chem Phys 112:2562

Pall S, Hess B (2013) A flexible algorithm for calculating pair interaction on SIMD architectures. Comput Phys Commun 184:2641

Parrinello M, Rahman A (1981) Polymorphic transition in single crystals: a new molecular dynamics method. J Appl Phys 52:7182

Pollard RD, Fulp B, Samuel MP, Sorci-Thomas M-G, Thomas MJ (2013) The conformation of lipid free human apolipoprotein A1 in solution. Biochemistry 52:9470

Segrest JP, Jackson RL, Morrisett JD, Gotto AM (1974) A molecular theory of lipid protein interaction in the plasma lipoprotein. FEBS Lett 38:247

Snyman JA (2000) The LFOPC leap frog algorithm for constrained optimization. Comput Math Appl 40:1085

van der Spoel D, Lindahl E, Hess B, Groenhoef GM, Mark EA, Berendsen HJC (2005) Gromacs: fast, flexible and free. J Comput Chem 26:1701

Wang G, Sparrow JT, Cushley RJ, (1997)The helix-hinge-helix structural motif in human apolipoprotein a-i determined by NMR spectroscopy. Biochemistry 36:13657

Wong GCL, Pollack L (2010) Electrostatics of strongly charged biological polymers: ion mediated interactions and self-organization in nucleic acids and proteins. Annu Rev Phys Chem 61:171

Graphical Analysis of Fluid Flow Through Polymeric Complex Structures Using Multi-scale Simulations

Estela Mayoral-Villa, Mario A. Rodríguez-Meza, Jaime Klapp, Eduardo de la Cruz-Sánchez, César Ruiz-Ferrel and Aaron Gómez-Villanueva

Abstract Efficient and detailed visualization of fluid flow simulations through complex meso-porous structures are fundamental for many applications in different areas such as medicine, biotechnology, oil recovery procedures, industry applications, environmental science and design of new intelligent and efficient meso-porous materials. Here we present the visual results of polymeric fluid flow through different complex porous media using multi-scale simulations performed over graphical processors (GPU's). A Lagrangian numerical model known as Smoothed Particle Hydrodynamics (SPH) was used in order to simulate the flow through complex structures taken from real images or from other simulations which represents different porous media. Performance of the model and its visualization were analyzed for a regular and also for an irregular three-dimensional array of solid spheres that represents a porous media with different polymeric fluids. The comprehensive examination of different sections in the system help us to analyze in an improved way the dynamical behavior of fluids through sophisticated structures. Micro-channels built via mesoscopic Dissipative Particle Dynamics (DPD) simulations were also introduced

Winner poster in the gallery of fluids of the XIX Congress of the Fluid Dynamic Division of the Mexican Physical Society.

E. Mayoral-Villa (✉) · M.A. Rodríguez-Meza · J. Klapp · E. de la Cruz-Sanchez
Instituto Nacional de Investigaciones Nucleares, Carretera México-Toluca S/N,
La Marquesa, 52750 Estado de Mexico, Ocoyoacac, Mexico
e-mail: estela.mayoral@inin.gob.mx

J. Klapp
Departamento de Matemáticas, Cinvestav del I.P.N., 07360 Mexico, D.F., Mexico
e-mail: jaime.klapp@inin.gob.mx

C. Ruiz-Ferrel
Universidad Tecnológica del Valle de Toluca, Carretera del Departamento del D.F.
km 7.5, Santa María Atarasquillo, Lerma, Mexico

A. Gómez-Villanueva
Instituto Tecnolgico de Toluca, Avenida Tecnolgico S/N Fraccionamiento la Virgen,
Estado de Mexico, 52149 Metepec, CP, Mexico

J. Klapp et al. (eds.), *Selected Topics of Computational and Experimental Fluid Mechanics*, Environmental Science and Engineering,
DOI 10.1007/978-3-319-11487-3_19

with great detail and the flow through these micro-porous structures was analyzed in order to understand microvascular turbulent fluid flow. Detailed visualization in real time could be used not only to help in the study of different systems but also to obtain amazing images that would be impossible to achieve by other techniques, here we present some of this beautiful pictures.

1 Introduction

Today, scientific and information visualization is a fundamental research area with applications in the industry, medicine, design of new materials an environmental analysis. Advances in this area involve new branches of computer graphics and the use and development of interfaces designed in such a way to permit, in an efficient and attractive way, the analysis of the results obtained in different numerical calculations. The aim is to improve the presentation and facilitate the analysis in a perceptible manner. As a good example we can mention the medical imaging which offers a broad field for scientific visualization, where it is important to enhance imaging results graphically in real time. Also, programs capable to present interactive molecular models with applications in biology, chemistry and physics are fundamental in the new era of applied science. Simulations of fluid flow through porous, meso-porous media and micro-channels also require extensive computational resources and visualization in order to get good performance. The numerical simulation of this kind of processes must be able to model in a satisfactory way sophisticated information, concerning the porous medium structure as, for example, complex structures in real solid materials, existence of fractures, mobile interphases or unstable boundaries as found in geo and biochemical processes. In this work, we present some pictures obtained during the visual study of polymeric fluid flow simulations through different porous media using multi-scale simulation via the Smoothed Particle Hydrodynamics (SPH) and the Dissipative Particle Dynamics (DPD) methodologies.

2 Smoothed Particle Hydrodynamics and Dissipative Particle Dynamics

2.1 Smoothed Particle Hydrodynamics

The numerical method that we employ to solve the hydrodynamic equations is the Smoothed Particle Hydrodynamics (SPH) method, which is a Lagrangian method used for solving the equations governing fluid motion. It is based on an interpolation scheme (Monaghan 1982, 1992, 2005; Benz 1990; Liu and Liu 2003). A fieldfunction $A(\mathbf{r}, t)$ is approximated by $A(\mathbf{r}, t) \approx \sum_{i=1}^{N} A(\mathbf{r}_i, t) W(\mathbf{r} - \mathbf{r}_i) \Delta V_i$,

where the computational space is subdivided into a finite number of cells of volume ΔV. These volume elements, which have thermodynamical and dynamical properties, are defined as "particles". For numerical work, $A(\mathbf{r}, t)$ is approximated by the interpolant summation over the field at particle positions:

$$A(\mathbf{r}) = \sum_j \frac{m_j}{\rho_j} A_j W(|\mathbf{r} - \mathbf{r}_j|, h)\,, \tag{1}$$

where m_j, ρ_j, and A_j are the mass, density, and field function, respectively, at the position of particle j. The quantity m_j/ρ_j is the inverse of the number density at particle j and is effectively the fluid volume associated with particle j. The summation is over all particles within the region of compact support of the kernel function. In the following we will write, for simplicity, W_{ij} instead of $W(|\mathbf{r}_i - \mathbf{r}_j|, h)$.

The kernel function monotonically decreases with distance and behaves as a delta function as the smoothing length, h, tends to zero. We refer the reader to Benz (1990), Monaghan (1992) and Liu and Liu (2003) for a detailed discussion on the kernel functions. Usually, numerical codes employ different kernel functions (Gesteira et al. 2010). The Gaussian kernel is one of the most widely used (Monaghan 1992). Other commonly used functions are the cubic, the quartic, and the quintic polynomials (see Gesteira et al. (2010) for their mathematical expressions and details). The tensile correction is automatically activated when using kernel functions with first derivatives that go to zero with decreasing inter-particle spacing (Monaghan 2000).

We now write down the SPH equations. The momentum conservation equation for a continuum field is written in SPH form as

$$\frac{d\mathbf{v}_i}{dt} = -\sum_j m_j \left(\frac{P_j}{\rho_j^2} + \frac{P_i}{\rho_i^2} + \Pi_{ij} \right) \nabla_i W_{ij} + \mathbf{g}\,, \tag{2}$$

where P_k and ρ_k denote the pressure and density evaluated at the position of particle k, respectively. The viscosity term, Π_{ij}, is given by

$$\Pi_{ij} = \begin{cases} -\frac{\alpha \overline{c_{ij}} \mu_{ij}}{\rho_{ij}} & ; \mathbf{v}_{ij} \cdot \mathbf{r}_{ij} < 0 \\ 0 & ; \mathbf{v}_{ij} \cdot \mathbf{r}_{ij} > 0 \end{cases} \tag{3}$$

where $\mu_{ij} = h\mathbf{v}_{ij} \cdot \mathbf{r}_{ij}/(\mathbf{r}_{ij}^2 + \eta^2)$, $\mathbf{r}_{ij} = \mathbf{r}_i - \mathbf{r}_j$, $\mathbf{v}_{ij} = \mathbf{v}_i - \mathbf{v}_j$, with $\mathbf{r}_k$ and $\mathbf{v}_k$ being the position and velocity of particle k, $\overline{c_{ij}} = (c_i + c_j)/2$, $\eta^2 = 0.01h^2$, and α is a free parameter that can be changed according to the problem under consideration.

The particles' positions are evolved using the equation (Monaghan 1989)

$$\frac{d\mathbf{r}_i}{dt} = \mathbf{v}_i + \varepsilon \sum_j \frac{m_j}{\overline{\rho_{ij}}} \mathbf{v}_{ij} W_{ij}\,, \tag{4}$$

where $\varepsilon = 0.5$ and $\overline{\rho_{ij}} = (\rho_i + \rho_j)/2$. Thus, each SPH particle moves with a velocity that is close to the average velocity in its neighborhood.

Finally, we need an equation of state, relating P and ρ. The fluid in SPH is treated as weakly compressible. The compressibility is adjusted to reduce the speed of sound so that the time step takes reasonable values. In SPH a Courant condition based on the speed of sound is used. The compressibility is limited by the fact that the sound speed should be about ten times faster than the maximum fluid velocity in order to keep variations of density to within less than one percent. Therefore, we use Monaghan and Kos (1999) relationship which is given by

$$P = B\left[\left(\frac{\rho}{\rho_0}\right)^{\gamma} - 1\right], \tag{5}$$

where $\gamma = 7$ and $B = c_0^2\rho_0/\gamma$, with the reference density $\rho_0 = 1{,}000\,\mathrm{Kg/m^3}$ and the sound speed at this density $c_0 = c(\rho_0)\sqrt{(\partial P/\partial\rho)|_{\rho_0}}$.

For more details on the SPH method and its numerical implementation we refer the reader to the papers by Liu and Liu (2003) and Gesteira et al. (2010).

2.2 Dissipative Particle Dynamics

Normally, complex fluids consist of different solvents and macromolecules such as polymers, surfactants, ions, and solid structures interacting among one another. All these molecules have very different sizes and many of the interesting phenomena occur at different time scales. By their nature, microscopic molecular dynamic simulations demand a great amount of computational resources and one option to alleviate this problem is to use *coarse graining* simulations such as *dissipative particle dynamics* simulations (DPD) (Hoogerbrugge and Koelman 1992). The DPD method as was originally introduced by Hoogerbrugge and Koelman (2010) consists of grouping numerous molecules or fraction of molecules, in a representative way into soft mesoscopic beads. In a similar way as in ordinary molecular dynamics simulations, in DPD one has to integrate the equations of motion to get the particles' velocities and positions, but in this case three contributions to the total force are present: *conservative*, *dissipative* and *random*. Not all these forces are independent because the random force compensates the energy dissipated to keep the temperature T constant, and so they act as a regulating thermostat. This fact leads to the *fluctuation-dissipation* theorem which gives: $\gamma = \frac{\sigma^2}{2k_BT}$ where k_B is the Boltzmann's constant.

Dissipative forces account for the local viscosity of the medium, and are of the form

$$\mathbf{F_{ij}^D} = -\boldsymbol{\gamma}\,\boldsymbol{\omega}^{\mathbf{D}}(\mathbf{r_{ij}})\,\left[\hat{\mathbf{e}}_{\mathbf{ij}}\cdot\mathbf{v_{ij}}\right]\hat{\mathbf{e}}_{\mathbf{ij}} \tag{6}$$

where γ is the dissipation constant, $\mathbf{v_{ij}} = \mathbf{v_i} - \mathbf{v_j}$ is the relative velocity, and $\omega^D(r_{ij})$ is a dimensionless weight function. The random force disperses the heat originated by the dissipative force and converts it into Brownian motion by keeping the local temperature T constant. It is expressed as:

$$\mathbf{F_{ij}^R} = -\sigma\, \boldsymbol{\omega}^{\mathbf{R}}(\mathbf{r_{ij}})\, \boldsymbol{\xi}_{\mathbf{ij}}\, \hat{\mathbf{e}}_{\mathbf{ij}} \tag{7}$$

with $\xi_{ij} = \theta_{ij}\,(1/\sqrt{\delta_t})$, where θ_{ij} is a random Gaussian number with zero mean and unit variance and δ_t is the integration time-step. As it has been pointed out before these two forces are related as $\omega^D(r_{ij}) = \left[\omega^R(r_{ij})\right]^2$.

Finally, conservative forces account for local hydrostatic pressure and are of the form

$$\mathbf{F}_{ij}^c = \begin{cases} a_{ij}\, \omega^c(r_{ij})\, \hat{\mathbf{e}}_{ij}, & (r_{ij} < r_c) \\ 0, & (r_{ij} \geq r_c). \end{cases} \tag{8}$$

In this equation, a_{ij} is a very important parameter because it represents the maximum repulsion between particles i and j and a good parametrization of this is essential to obtain a realistic representation of our systems. In addition, $\mathbf{r_{ij}} = \mathbf{r_i} - \mathbf{r_j}$, $r_{ij} = |\mathbf{r_{ij}}|$, and $\hat{\mathbf{e}}_{ij} = \mathbf{r_{ij}}/\mathbf{r_{ij}}$, where $\mathbf{r_i}$ is the position of particle i and the weight function is given by $\omega^c(r_{ij}) = 1 - r_{ij}/r_c$. If an adequate parametrization of the a_{ij} value is stabilized it is possible to obtain a very good representation of the structure of many complex fluids.

3 Simulations and Visualization

In this section, we present some pictures obtained by the visual study of polymeric and non-polymeric fluid flow simulations through different porous media using the Smoothed Particle Hydrodynamics (SPH) and the Dissipative Particle Dynamics (DPD) methodologies. A complete description of the pictures is given in their corresponding figure captions. (see Figs. 1, 2, 3, 4)

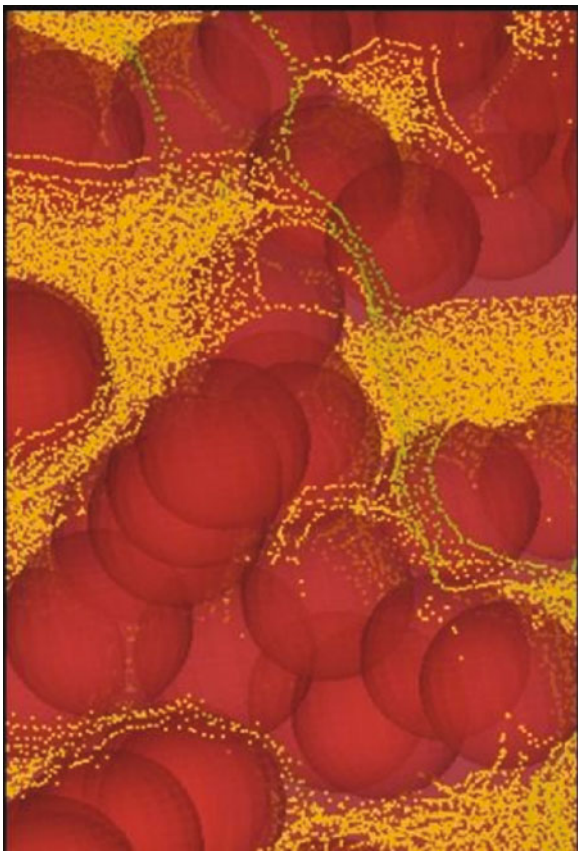

Fig. 1 Analysis of permeability of polymeric complex structures using multi-scale simulations. This study was developed for the adequate design of contention barriers made of polymeric porous materials, which involves the calculation of structural parameters such as porosity and intrinsic permeability. The calculations were done to analyze the fluid discharge velocities at different body forces through the porous structure. These studies are relevant in different areas, not only in the control of soil contamination and the design of effective remediation procedures, but also to improve the analysis of enhanced oil recovery and the design of intelligent materials for energy storage applications

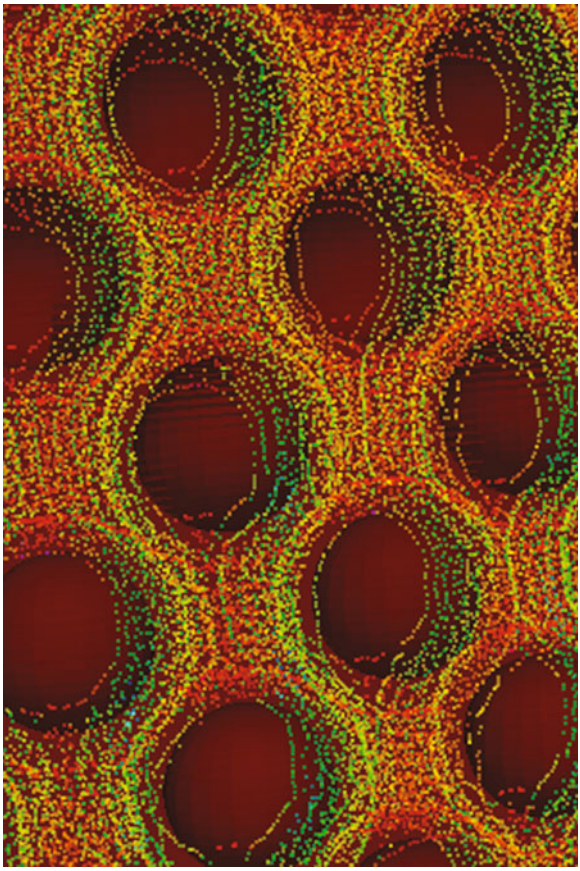

Fig. 2 Fluid flow through a regular structure as obtained using Smoothed Particle Hydrodynamic simulations. This picture corresponds to validation test results for polymeric fluid flow in saturated and non-saturated hexagonal regular porous media. For the saturated case the Darcy's law is obtained and the hydraulic conductivity k is calculated for all geometries. The examination and validation of these parameters could help us to predict the dynamical behavior of fluids through more sophisticated structures

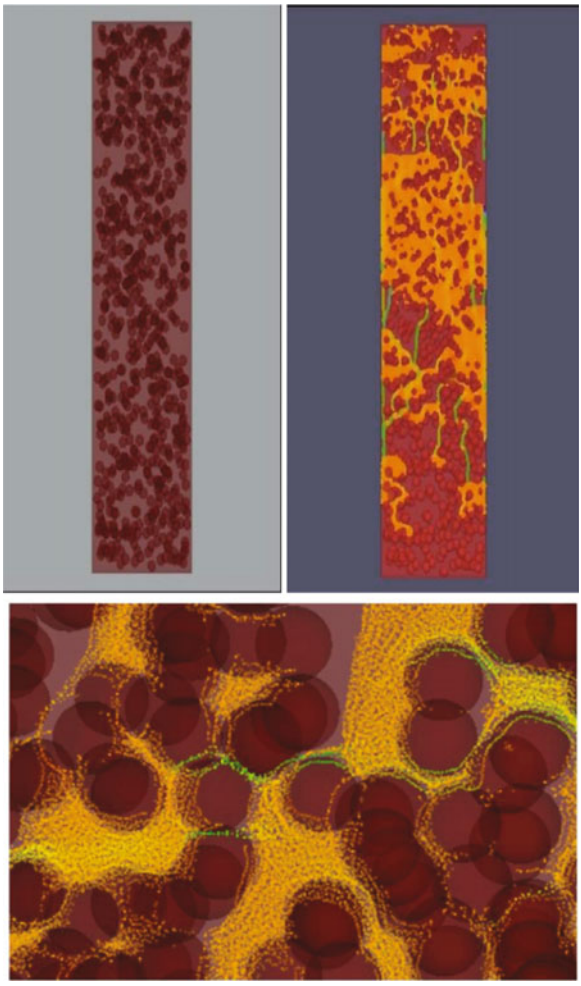

Fig. 3 Flow of polymeric fluids with different viscosities and densities. The predicted performance of the polymeric resin flow through the unsaturated porous media is qualitatively correct and makes possible the analysis of industrial processes, such as mould filling in the resin transfer moulding process, drying processes, oil-industry applications, where polymers are injected in order to enhance oil recovery, and techniques to control soil pollution by industrial polymeric products, among many others. The SPH simulations have shown to be very efficient and present some advantages over the macroscopic scale models to analyze this kind of systems where mobile interfaces are involved

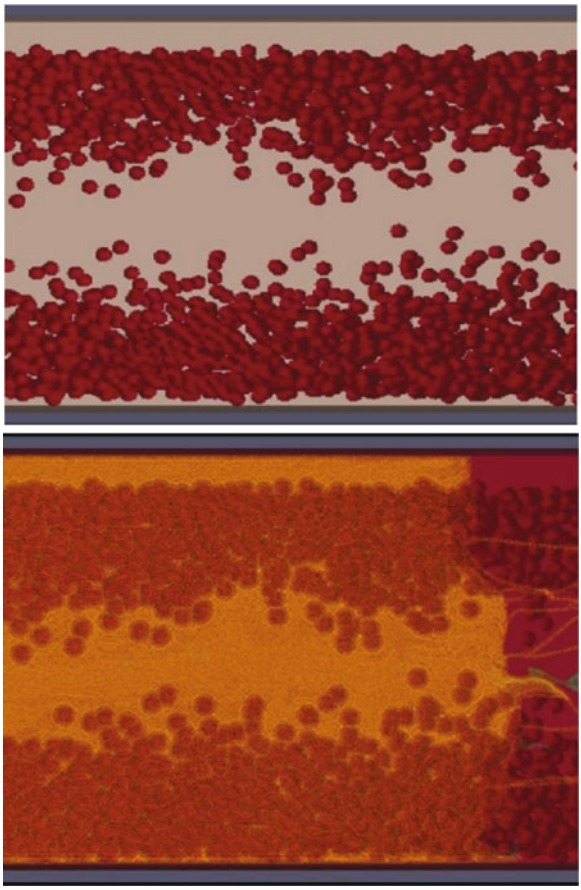

Fig. 4 Micro-channels built via mesoscopic Dissipative Particle Dynamics (DPD) simulations. The flow through these micro-porous structures was analyzed in order to understand microvascular turbulent fluid flow. Stable structures involving adsorption of polymeric components to form brushes were obtained by DPD dynamics simulations at different temperatures

4 Conclusions

The use of simulation methods, such as DPD and SPH, at different scales makes the study of fluid flow through complex meso-porous structures more effective. On the other hand, computational techniques help us to build more reliable and adequate interfaces for improving the visualization of this kind of geometries, thus facilitating the structural analysis of complex systems.

Acknowledgments This work has been partially supported by the Consejo Nacional de Ciencia y Tecnología of Mexico (CONACyT) under the project CONACyT-EDOMEX-2011-C01-165873.

References

Benz W (1990) Smoothed particle hydrodynamics. In: Butchler JR (ed) The numerical modeling of nonlinear stellar pulsations: problems and prospects. Kluwer Academic Publishers, New York, p 269

Gesteira MG, Rogers BD, Dalrymple RA, Crespo AJC, Narayanaswamy M (2010) User guide for the SPHysics code

Hoogerbrugge PJ, Koelman JMVA (1992) Simulating microscopic hydrodynamic phenomena with dissipative particle. Europhys Lett 19:155

Liu GR, Liu MB (2003) Smoothed particle hydrodynamics: a mess free particle method. World Scientific Publishing Co., Pte. Ltd, London

Monaghan JJ (1982) SIAM J Sci Stat Comput 3:422

Monaghan JJ (1989) On the problem of penetration in particle methods. J Comput Phys 82:1–15

Monaghan JJ, Kos A (1999) J Waterw Port, Coast Ocean Eng 125:145

Monaghan JJ (1992) Smoothed particle hydrodynamics. Annu Rev Astron Appl 30:543–574

Monaghan JJ (2000) J Comput Phys 159:290

Monaghan JJ (2005) Rep Prog Phys 68:1703

Mass Flow Rate of Granular Material from an L-Valve Without Aeration

D.A. Serrano, G. Ruíz Chavarría, S. Álvarez and A. Medina

Abstract In this work we introduce a correlation to estimate the mass flow rate from an L-valve, without aeration, but under gravity flow, of a non-cohesive granular material. This criterion is based on the mass flow rate formula for vertical pipes and the comparison among, the here termed L-valve angle, and the angle of repose of the material. Experiments support this criterion.

1 Introduction

Solid flow control devices are necessary and important components in industrial applications that handle solids transport. Non-mechanical devices (such as seal pots, loop seals, J-valves, L-valves and V-valves) are used for solid flow control. Among all the non-mechanical valves, an L-valve has been one of the most widely employed types. Not only because it is suitable for operation at elevated temperatures and pressures, but also because of its simple design and cost effectiveness with minimum maintenance.

D.A. Serrano (✉) · S. Álvarez
ESIME Zacatenco, Instituto Politécnico Nacional, Avenida Luis Enrique Erro S/N,
Zacatenco, 07738 Mexico, D.F., Mexico
e-mail: arman2390@hotmail.com

G. Ruíz Chavarría
Facultad de Ciencias UNAM, Av. Universidad, Ciudad Universitaria, Coyoacán,
04510 Mexico, D.F., Mexico
e-mail: gruiz@unam.mx

A. Medina
ESIME Azcapotzalco, Instituto Politécnico Nacional, Av. De las Granjas 682,
02250 Santa Catarina, Mexico, D.F., Mexico
e-mail: amedinao@ipn.mx

J. Klapp et al. (eds.), *Selected Topics of Computational and Experimental Fluid Mechanics*, Environmental Science and Engineering,
DOI 10.1007/978-3-319-11487-3_20

Flow dynamics around the L-valve have been investigated and reported extensively in previous studies (Chan et al. 2009; Chovichien et al. 2013; Knowlton and Hirsan 1978; Woodcock and Mason 1987; Yazdanpanah et al. 2012). Different models have been proposed to describe the hydrodynamic behaviors of the valve.

Almost all models are found to be derived from L-valve operations under ambient environment, while actual practical applications involve high temperature and/or high pressure conditions. Furthermore, validation of these models to describe L-valve behaviours at elevated temperature or pressure has not been tested so far. The limitation might be caused by the difficulties in terms of solids and materials handling at high temperature or pressure.

In Fig. 1 we depict an L-valve. It consists of an horizontal pipe joined to an upper standpipe through an elbow, meanwhile the other edge of the horizontal pipe is joined to a lower standpipe. The height of the standpipe is H whereas the height of the lower one is not important. The slope of the dashed line defines the L-valve angle, α. Such slope is defined as $tan(\alpha) \equiv tan(D/w)$, where D s the pipe's diameter and w is the distance among the adjacent, exterior face walls of pipes. Notice that if $\alpha > \theta_r$ (Fig. 1a) a gravity flow there occurs, whilst, if $\alpha \leq \theta_r$ (Fig. 1b) the gravity flow will be arrested.

Currently, in many practical applications the granular column in the standpipe will be mobilized through the application of aeration at a rate Q. Depending on the intensity of the injected gas flow several types of solid flow can be developed (Chan et al. 2009; Chovichien et al. 2013; Knowlton and Hirsan 1978; Yazdanpanah et al. 2012, see Fig. 2). Despite it, the particles flow in the dense phase mode due to the gravity force and this phase is very important to establish the pressure drops and the relative solid–gas velocity across the solid bed.

The aim of this work is to quantify the intensity of the gravity flow in an L-valve, when the geometrical parameters of the valve allow it.

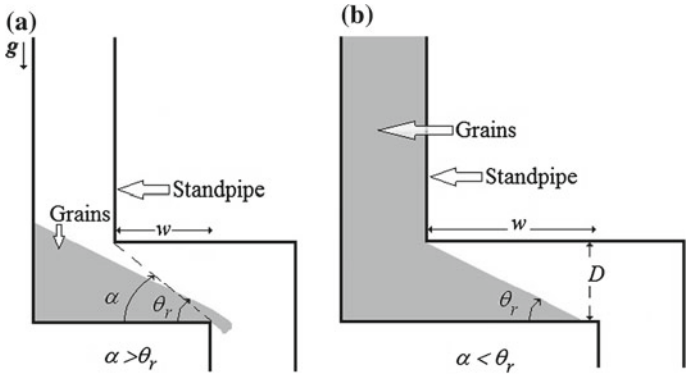

Fig. 1 Depicts of the transversal sections (at the *middle part*) of an L-valve: **a** the L-valve angle, α, overcomes the angle of repose of the granular material, θ_r and a granular gravity flow occurs. The slope of the *dashed line* defines the L-valve angle, α, see text. **b** Here the angle of repose is larger than α

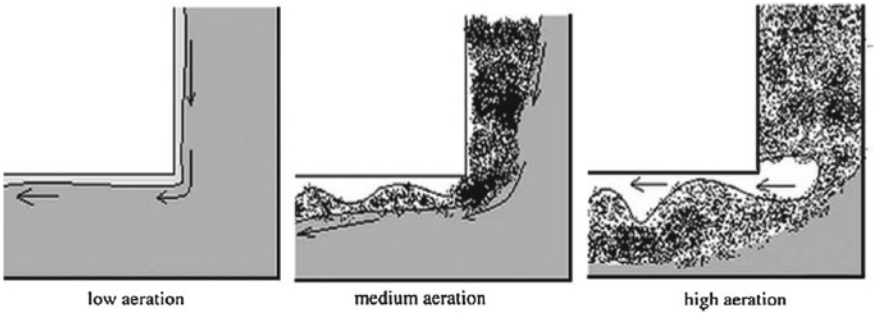

Fig. 2 Some flow regimes, during operation, in an L-valve. These regimes depend on the intensity of aeration

2 Gravity Flow: A Simple Model

As can be seen in Fig. 1a the L-valve has itself an angle. If, it as was noticed by Knowlton and Hirsan (1978) and Woodcock and Mason (1987), that a gravity granular flow there occurs. It is illustrated in Fig. 3 where three snapshots permit conclude that a granular column (picture on the left-hand side) cannot be maintained when the angle of the valve is smaller than θ_r. In this case $D = 1.90\,\text{cm}$, $w = 1.25\,\text{cm}$ and, consequently, $\alpha = 56.65° = 0.98\,\text{rad}$ and $\theta_r = 33° = 0.57\,\text{rad}$.

We have estimated, from data of the snapshots in Fig. 3, that the granular column is reduced at a rate $v = 0.47\,\text{cm/s}$; See Fig. 4.

Conversely, if $\alpha \leq \theta_r$ a gravity flow does not occurs and the granular column must be maintained. See Fig. 4.

In recent works on the estimation of the mass flow rate from circular holes in face walls of bins with thick walls we have shown (Medina et al. 2013, 2014) that the intensity of the flow must be proportional to $(\alpha - \theta_r)$. As both problems are very

Fig. 3 Snapshots of an L-valve with $\alpha = 0.98$ rad and $\theta_r = 0.57$ rad. This valve does not maintain the granular column

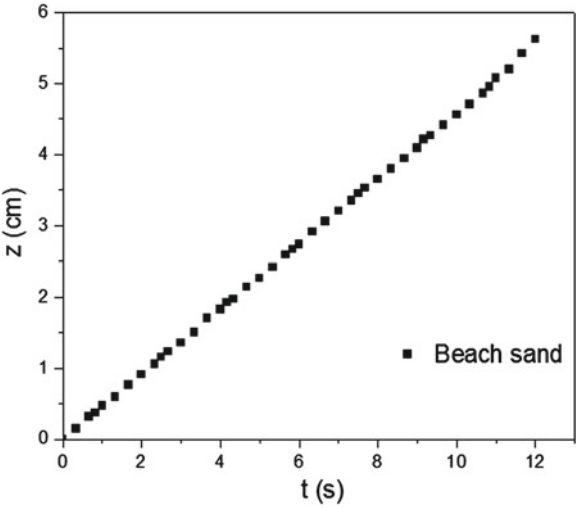

Fig. 4 Plot of height as a time function. We assumed that the initial level of the column is at $z = 0$ cm. From these data we estimate that the granular column it is reduced at a mean velocity $v = 0.47$ cm/s

similar, we use the same criterion to estimate the mass flow rate in the L-valve, so the mass flow rate m'_{LV} in an L-valve with gravity flow, must be

$$m'_{LV} = a m'_{sp}(\alpha - \theta_r) = a\, m'_{sp}\left(\arctan\left[\frac{D}{w}\right] - \theta_r\right), \tag{1}$$

where a is the discharge coefficient, m'_{sp} is the mass flow rate from a standpipe, only due to the gravity action, which obeys the relation

$$m'_{sp} = c\rho_b g^{1/2} D^{5/2}. \tag{2}$$

In Eq. (2), c is other discharge parameter (related only to the standpipe), ρb is the bulk density and θ_r is the angle of repose of the granular material. The relation (2) was regarded as valid by Kesava and Nott (2008) to estimate the flow rate from vertical, circular pipes and it is known as the Hagen's law (Medina et al. 2013).

In the next section we performed experiments to show that Eqs. (1) and (2) are correct.

3 Experiments

Initially, we did experiments to measure m'_{sp}, the mass flow rate from vertical pipes, in order to check if Eq. (2) is valid. We performed experiments by using beach sand (composed of irregular grains of mean diameter $d = 0.03$ cm, bulk density $\rho_b = 1.5 \pm 0.01$ g/cm^3 and angle of repose $\theta r = 33° \pm 0.5° = 0.57 \pm 0.008$ rad (other properties of this material were reported elsewhere: Medina et al. 2014).

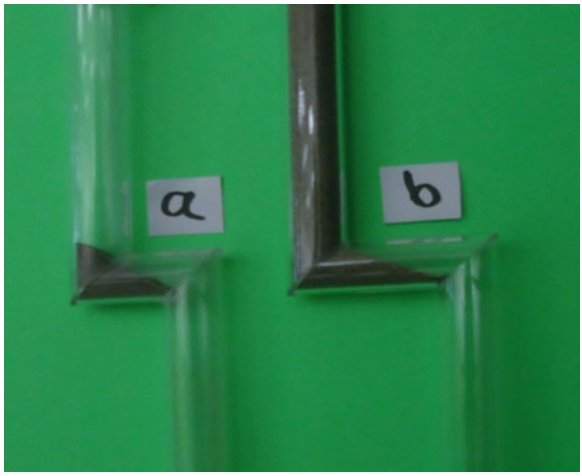

Fig. 5 In the pipe on the *left hand side* a granular column in the standpipe does not is maintained because $\alpha > \theta_r$, whilst in the pipe on the *right hand side* $\alpha < \theta_r$ ($\alpha = 0.49$ rad and $\theta_r = 0.57$ rad).

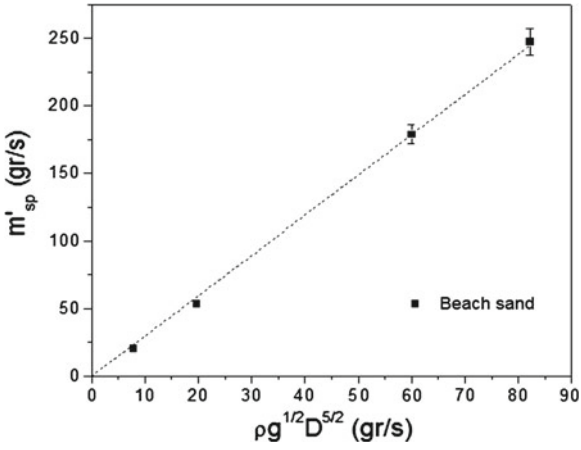

Fig. 6 Plot of the measured mass flow rate of beach sand from standpipes for several diameters as a function of $\rho_b g^{1/2} D^{5/2}$. Error bars are of 4 %

In experiments we used acrylic pipes 50 cm lengths and inner diameters $D = 0.49$, 0.70, 1.10, 1.34 and 1.94 cm, respectively. The mass flow rates were measured by using a force sensor model Pasco CI-6537 with a resolution of 0.03 N. Details of the measurement procedure are given elsewhere (Medina et al. 2014) (Fig. 5).

In Fig. 6 we show the plot of m'_{sp}, the experimentally measured mass flow rate from vertical pipes of several diameters, as a function of $\rho_b g^{1/2} D^{5/2}$, and it yields a linear fit for all filling heights. It means that the formula (2) is a good correlation to describe the mass flow rate from pipes. The best fit produces a dimensionless discharge parameter $c = 2.97$.

Finally, we measured the mass flow rate from L-valves, m'_{LV}, by using beach sand. In Fig. 7 we plot m'_{LV} versus $\rho_b g^{1/2}\ D^{5/2}(\alpha - \theta_r)$ to prove if Eq. (1) is fulfilled. We made two L-Valves that allowed the gravity flow: one was made with a pipe 1.94 cm

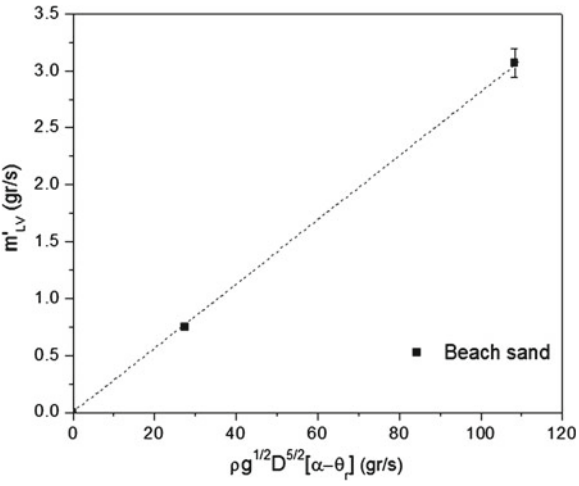

Fig. 7 Plot of the mass flow rate of beach sand emerging from the lower standpipe versus the theoretical correlation $\rho_b g^{\frac{1}{2}} D^{\frac{5}{2}} (\alpha - \theta r)$. This flow comes from the upper standpipe and crosses the elbow zone

diameter and $w = 1.2$ cm. In this case the L-valve angle was $\alpha = 1.01$ rad and the term $(\alpha - \theta_r) = 0.44$. In another case the L-valve had has $D = 1.34$ mA, $w = 1.2$ cm. Therefore $\alpha = 0.85$ rad and thus $(\alpha - \theta_r) = 0.28$. The linear fit in such a plot shows that Eq. (1) is correct. In this case $a = 0.0283$.

In conclusion an L-Valve without aeration can be useful to reduce drastically the mass flow rate, moreover, it maintains the mass flow rate constant as is deduced from Figs. 4 and 7.

4 Conclusions

In this work we did experiments to estimate the granular mass flow rate from L-valves. We found that the flow rate from an L-valve obeys Eq. (1) very well. To our knowledge this type of studies are the first in the specialized literature for this specific regime.

Acknowledgments This work was made under the partial support of Project SIP20141404.

References

Chan ChW, Seville J, Fan X, Baeyens J (2009) Particle motion in L-valve as observed by positron emission particle tracking. Powder Technol 193:137–149

Chovichien N, Pipatmanomai S, Chungpaibulpatana S (2013) Estimate of solids circulation rate through an L-valve in a CFB operating at elevated temperature. Powder Technol 235:886–900

Kesava RK, Nott PR (2008) An introduction to granular flow. Cambridge University Press, New York

Knowlton TM, Hirsan I (1978) L-valves characterised for solids flow. Hydrocarb Process 57: 149–156

Medina A, Serrano DA, Gutiérrez GJ, Vargas CA (2013) On the mass flow rate in silos with lateral exit holes. Rev Mex Fis 59:287–291

Medina A, Cabrera D, López-Villa A, Pliego M (2014) Discharge rates of dry granular material from bins with lateral exit holes. Powder Technol 253:270–275

Woodcock CR, Mason JS (1987) Bulk solids handling: an introduction to practice and technology. Blackie and Son Ltd, London

Yazdanpanah MM, Forret A, Gauthier T, Delebarre A (2012) An experimental investigation of L-valve operation in an interconnected circulating fluidized bed system. Powder Technol 221:236–244

Part III
Convection and Diffusion

Heat Transfer in Biological Tissues

M.E. Bravo, P. De Jesús Sánchez, R.O. Vargas Aguilar and A.E. Chávez

Abstract The heat transfer process in biological tissues is studied through the Pennes bioheat equation, in dimensionless form, taking into account the temperature gradient delay by the Maxwell-Cattaneo model. Stochastic perturbations from the environment applied on the surface of the tissue and different external energy sources are considered. Comparison of temperature distributions with constant biological parameters are presented, from the skin surface and through the tissue transfer processes and to contribute to a better understanding on how nature works, it is essential to include biological, physical and biochemical.

1 Introduction

The complexity of the mass, energy and amount of motion transfer processes that take place in biological tissues has drawn the attention to the need for multidisciplinary research, in which fundamental concepts of engineering and physics are integrated with biological sciences. In order to develop mathematical models that adequately represent biological factors into the actual phenomenological models that describe different transfer processes found in living tissues. In addition, the analysis of the transport mechanisms will serve to innovate and optimize diagnostic and therapeutic

M.E. Bravo · A.E. Chávez
Departamento de Ingeniería Química, Facultad de Química, Universidad Nacional Autónoma de México (UNAM), Ciudad Universitaria,
04510 México, D.F., Mexico
e-mail: mbgtz16@gmail.com

A.E. Chávez
e-mail: angelenc@unam.mx

P. De Jesús Sánchez · R.O. Vargas Aguilar (✉)
ESIME Azcapotzalco, Instituto Politécnico Nacional, Avenida de las Granjas No. 682, Colonia Santa Catarina, Delegación Azcapotzalco, 02250 México, D.F., Mexico
e-mail: reneosvargas@yahoo.com.mx

P. De Jesús Sánchez
e-mail: peterdjss@gmail.com

J. Klapp et al. (eds.), *Selected Topics of Computational and Experimental Fluid Mechanics*, Environmental Science and Engineering,
DOI 10.1007/978-3-319-11487-3_21

interventions. Given the importance of the issue, several authors have studied various methods for describing the energy transfer process in tissues. However, the main contribution was made in 1948 by Harry H. Pennes, who published a study on the temperature distribution in the human body Pennes (1948). This model uses one of the most successful equations in continuum physics, the traditional Fourier's law of heat conduction to describe the energy flux. One of the main shortcomings of Fourier's law is that it leads to a parabolic equation for the temperature field. This means that any initial disturbance is felt instantly throughout the entire medium. This behavior is said to contradict the principle of causality. To correct this unrealistic feature, which is known as the "paradox of the heat conduction", various modifications of Fourier's law have been proposed over the years Jordan et al. (2008). Of these, the best known is the Maxwell-Cattaneo model Joseph and Preziosi (1989, 1990), Chandrasekharaiah (1998), Ostoja-Starzewski (2007).

This study uses a modified expression of the Pennes model and focuses on the phenomena that occur when there is a perturbation in the environment that modifies the surface temperature of the tissue. This happens when the tissue is exposed to a stream of ambient air and to temperatures with stochastic values Fiala et al. (1999), Deng and Liu (2002, 2004). The analysis focuses on the response of the tissue when it is subjected to a temperature gradient due to the variation of the thermal environment.

2 Model Description

Energy transfer in biological systems was firstly described through the biological energy equation developed by Pennes in 1948. His work involved theoretical and experimental investigation of the temperature distribution in the forearm of a group of people Pennes (1948). The derived mathematical model consists on an energy balance in the tissue that incorporates the effects of metabolism and blood perfusion. The biological heat transfer equation in expanded form (2D) is given by Eq. (1).

$$\rho_m C_{p_m} \frac{\partial T}{\partial t} = k \left\{ \frac{\partial^2 T}{\partial x^2} + \frac{\partial^2 T}{\partial y^2} \right\} + w_b \rho_b C_{p_b} (T_a - T) + Q_m + Q_r \tag{1}$$

where $\boldsymbol{x}$ and $\boldsymbol{y}$ are spatial variables, $\boldsymbol{t}$ is the temporal variable, $\boldsymbol{T}$ the temperature of the tissue, $\boldsymbol{k}$ thermal conductivity, $\boldsymbol{C}_{pm}$ the specific heat of tissue, $\boldsymbol{\rho_m}$ the tissue's density, $\boldsymbol{Q_m}$ the energy that generates within the tissue as a result of the metabolic activity, $\boldsymbol{\rho_b}$ is the blood density, $\boldsymbol{C}_{p_b}$ the specific heat of blood, $\boldsymbol{W_b}$ the volumetric flow of blood perfusion, $\boldsymbol{Q_r}$ is an external heat source and $\boldsymbol{T_a}$ the temperature of the blood in the arteries.

The definition of the system of study is based on a portion of epithelial tissue. To ensure that the internal temperature remains constant and that the temperature distributions in the tissue are symmetrical, the depth of the section should not be greater than 3 cm. Given the maximum temperature that a normal tissue can stand before degrading, the highest temperature allowed will be 42 °C. It will be considered

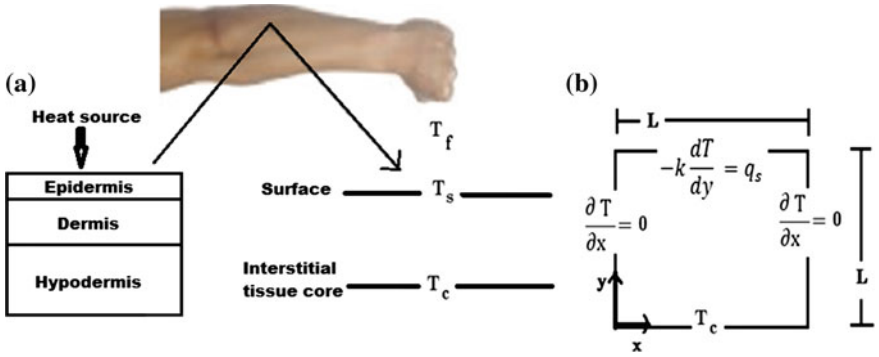

Fig. 1 **a** Representation of the system of study and **b** heat transfer problem

that blood and tissue properties are not altered by time or position, and also, blood perfusion will remain constant. It will be assumed a thermal equilibrium between the arterial blood temperature and the interstitial tissue core, as it remains constant, $\boldsymbol{T_a} = \boldsymbol{T_c}$. The surface temperature $\boldsymbol{T_s}$ will be determined by the transfer processes within the tissue and the thermal exchange with the environment, as shown in Fig. 1. For transient processes or very small scales, it will be necessary to take into account the delay between the temperature gradient and the energy flux. Accordingly, the classical Fourier equation is modified by the Maxwell-Cattaneo Joseph and Preziosi (1989, 1990), Chandrasekharaiah (1998), Ostoja-Starzewski (2007) model given by:

$$q(x, t + \lambda) = q(x, t) + \lambda \frac{\partial q(x, t)}{\partial t} = -k\nabla T(x, t), \tag{2}$$

where $\boldsymbol{\lambda} = \boldsymbol{\alpha}/\boldsymbol{C}^2$ denotes the relaxation time of the tissue, $\boldsymbol{\alpha}$ the thermal diffusivity, $\boldsymbol{C}$ the thermal velocity of propagation in the medium, $\boldsymbol{k}$ is the thermal conductivity and $\boldsymbol{q}$ is the heat flux. The relaxation time represents the time lag required to establish steady heat conduction in a volume element once a temperature gradient has been imposed across it Chandrasekharaiah (1998). The partial time derivative added by Cattaneo in the constitutive relationship between the heat flux and the temperature succeeded in resolving the main shortcoming of the Fourier model, rendering the heat-conduction equation to a damped hyperbolic equation.

2.1 Dimensionless Equation

A dimensionless form of the heat transfer model (Eq. 1) can be obtained by using the following dimensionless variables: $\boldsymbol{\theta} = \frac{T}{T_C}$ for temperature; $\boldsymbol{\xi} = \frac{x}{L}$ and $\boldsymbol{\eta} = \frac{y}{L}$ for position, which are bounded in a range from 0 to 1; and $\boldsymbol{\tau} = \frac{\alpha}{L^2}t$ for time, defined as the Fourier number which compares the conduction energy with the storage in

transient processes. The perfusion term can be written in a dimensionless form when compared with a diffusive time as follows $\boldsymbol{\sigma = (L^2 W_b)/\alpha}$, just as $\boldsymbol{\phi = (L^2 Q)/(kT_c)}$ is the diffusive flux of energy, and $\boldsymbol{\theta_a = T_a/T_c}$ the dimensionless blood temperature. A thermal Deborah number is defined to characterize the fluidity of materials under specific flow conditions, $\boldsymbol{De_T = \alpha\lambda/L^2}$; based on the premise that given enough time even a solid-like material will flow. Flow characteristics are not inherent properties of the material itself, but relative properties which depend on two fundamental different characteristic times. By substituting the above mentioned terms, the following dimensionless differential equation for temperature distributions is obtained.

$$\mathrm{De_T}\frac{\partial^2\theta}{\partial\tau^2} + \frac{\partial\theta}{\partial\tau} = \left\{\frac{\partial^2\theta}{\partial\varepsilon^2} + \frac{\partial^2\theta}{\theta\eta^2}\right\} + \sigma[\theta_a - \theta] = \{\emptyset_m + \emptyset_r\} \tag{3}$$

The proposed dimensionless solution for the Eq. (3) is given by

$$\theta(\xi, \eta, \tau) = \theta_0(\xi, \eta) + \theta_\mathrm{t}(\xi, \eta, \tau)e^{-\sigma\tau} \tag{4}$$

where $\boldsymbol{\theta_0(\xi, \eta)}$ is the steady state temperature and $\boldsymbol{\theta_t(\xi, \eta, \tau)}$ the transient temperature. By using the Eq. (4) in Eq. (3), a differential equation with relaxation is obtained:

$$\mathrm{De}_t\frac{\partial^2\theta_\tau}{\partial\tau^2} + [1 - 2\sigma\mathrm{De}_t]\frac{\partial\theta_\tau}{\partial\tau} + \sigma^2\mathrm{De}_t = \frac{\partial^2\theta}{\partial\varepsilon^2} + \frac{\partial^2\theta_\tau}{\partial\eta^2} + \emptyset_r e^{\sigma\tau}\}, \tag{5}$$

where $\boldsymbol{\theta_t = \theta_0(\varepsilon, \eta, \tau)}$ and $\boldsymbol{\emptyset_r = \emptyset_r(\varepsilon, \eta, \tau)}$.

The corresponding dimensionless boundary conditions for $\boldsymbol{\tau > 0}$ are:

$$\mathrm{B.C.1} : \eta = 1; -\frac{\mathrm{d}\theta_t(\xi, 1, \tau)}{\mathrm{d}\eta} = \{\phi_\mathrm{s} + \mathrm{Bi}_0[\theta_f - \theta_{0_s}]\}\mathrm{e}^{\sigma\tau}, \tag{5a}$$

$$\mathrm{B.C.2} : \eta = 0; \theta_\mathrm{t}(\eta, 0, \tau) = 0, \tag{5b}$$

$$\mathrm{B.C.3} : \xi = 0; \frac{\mathrm{d}\theta_\tau}{\mathrm{d}\xi} = 0, \tag{5c}$$

$$\mathrm{B.C.4} : \xi = 1; \frac{\mathrm{d}\theta_\tau}{\mathrm{d}\xi} = 0. \tag{5d}$$

Where $\boldsymbol{Bi_0}$ is the Biot number in steady state, which compares the internal resistance of the energy transfer with the resistance at the border, in this case, with the surface of the tissue; $\boldsymbol{\theta_0}$ is the steady state temperature, $\boldsymbol{\theta_\tau}$ the transient temperature, $\boldsymbol{\theta_{0_\varepsilon} = \theta_0(\xi = 0)}$ the surface temperature, and $\boldsymbol{\theta_f}$ the dimensionless air temperature. The last parameter of Eq. (5a) may be altered by a sudden change or a small perturbation in the atmosphere, which occurs when the surface of the tissue is subjected to an air stream, creating a stochastic value. Equation (6) may be used to determine this perturbation:

$$\theta f = \theta_{0_s} + \in(t); \textit{where } \in(t) = \lambda_T(0.5 - \sigma_i), \tag{6}$$

where $\in (t)$ is the discrete stochastic variation. λ_T is a constant temperature, since this study is based on the average normal human body temperature of 37 °C and considering that thermal damage occurs around the 42 °C Torvi and Dale (1994), this constant must not exceed from 5 °C. Finally σ_i is the stochastic parameter which takes values of $0 < \sigma_i < 1$. As the temperature only depends on time, the set of equations generated can be numerically integrated by using the following initial condition:

$$\tau = 0, \quad \theta_t(\xi, \eta) = 0, \tag{7}$$

3 Results and Discussion

The solution of the model was discretized using a second-order central difference formulation for all the spatial derivatives, with an explicit method and uniform grid of 100×100. The numerical simulations were generated by a code developed in the programming language Fortran, Ripley (1987).

3.1 Steady State Temperature

The first case is used to verify the numerical code and as reference model. It considers a uniform heat source, which represents the conditions when the tissue is in thermal equilibrium with the surroundings. Factors affecting this state are due to the metabolic activities and to the energy exchange with the environment, this justifies using the Biot number as reference. The temperature distribution is shown in Fig. 2, alongside with

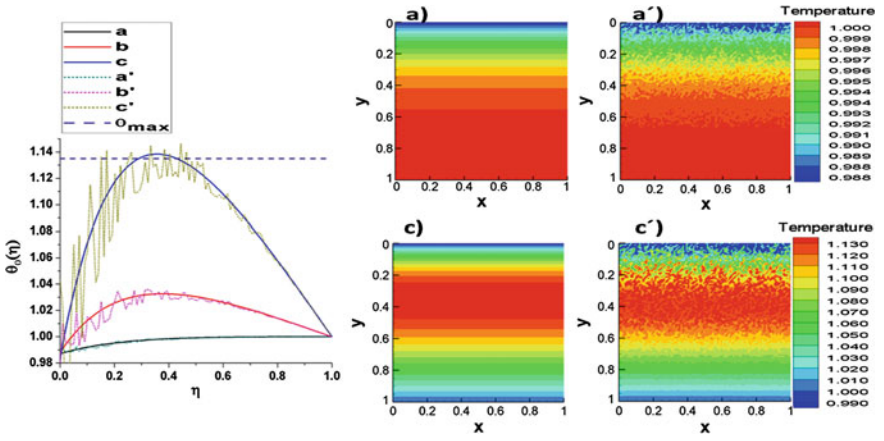

Fig. 2 Temperature distributions in steady state with different Biot numbers and forms of metabolic heat. **a** Bio = 0.2, $\emptyset_m = 0.038$, **b** Bio = 1.3, $\emptyset_m = 1.4554$, **c** Bio = 1.3, $\emptyset_m = 5.2903$

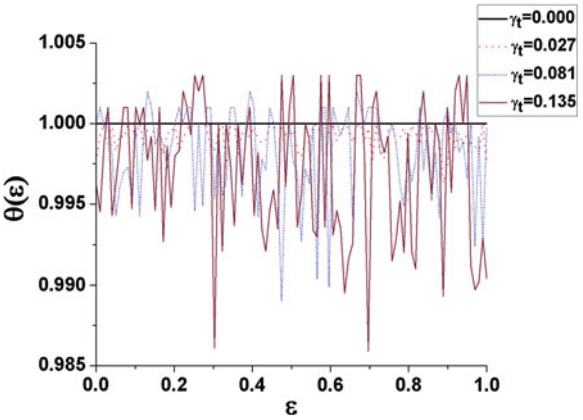

Fig. 3 Dimensionless skin surface temperature for different perturbations

the temperature profiles developed. Curve **A** indicates that the effect of the metabolic heat on the temperature is very small, hence, this value will be taken as reference for the results reported. Curve **B** does not exceed the maximum temperature, however a Bi $>$ 0.4347 indicates some pathology such as cancer. In curve **C**, the trajectory exceeds the maximum temperature causing thermal damage. Curves A′, B′ and C′ include the perturbation to θ_f by placing a stochastic parameter; this has a damping effect along the curve due to the perfused tissue. Figure 3 shows the effect of the perturbation on the skin surface temperature. It is worth mentioning that when the value of λ increases, the surface presents higher variations and this effect is damped inside the tissue by the blood perfusion, according to Fig. 2. In order to facilitate the profile comparison, the seed used to generate the perturbation in this case was the same. Lastly, the temperature distributions using a constant surface flux are depicted in Fig. 4. This situation occurs when the tissue is burned by a point contact with an object. Case (1). The classical Fourier equation is compared ($De_T = 0$) with the relaxation equation for different values of De_T and for a time $\tau = 0.2$. The results show that with the increase of De_T the relaxation effects are more likely to reach a steady state. However, for short times and small scales an opposite effect is produced, the tissue begins to raise its internal energy in a more controlled manner. Namely, the temperature increases more slowly than the classical Fourier Case (2).

A comparison with Case (1) is exposed, including the stochastic effect in θ_f; which results in a variation of the temperature distribution that increases as τ does. For values of $De_T > 0.0013$, it can be seen that the temperature ranges between $[0.02 - 0.25]$ through the whole curve, as compared with the relaxation curves.

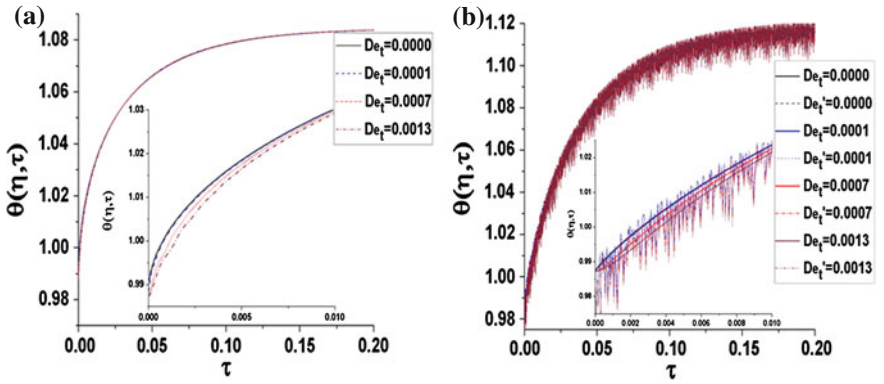

Fig. 4 Temperature as a function time for different thermal Deborah numbers, **a** unperturbed **b** perturbed De_T, with $\xi = 0$, $\boldsymbol{\emptyset_r = 0}$, $\boldsymbol{\emptyset_s = 0.3405}$

4 Conclusions

The heat transfer process in biological tissues is studied numerically through a modified Pennes bioheat equation. This study showed that for very large times the temperature distributions within the tissue can be well described by the classical Fourier law. Nonetheless, the effects that occur on short time scales may not be equally predictable with these theories. The Maxwell-Cattaneo model considers a relaxation time which represents the time lag required to establish steady heat conduction, which is the time that takes to transmit the signal from the stimulus to the whole structure of the tissue. The energy transfer process in a biological tissue involves the interaction of multiple internal mechanisms (i.e. metabolic activity and blood flow) and their response to external stimulus. When blood perfusion increases, the energy transfer process occurs faster and easily, until the system achieves thermal equilibrium. When the air temperature is perturbed, the temperature profiles are constantly modified near the upper boundary of the tissue, however they recover a linear trend along the system; in addition to the timely behavior that presents a monotonous growth until it reaches a steady state.

Acknowledgments This project was supported by the research grants SIP-IPN 20141466.

References

Chandrasekharaiah DS (1998) Hyperbolic thermoelasticity: a review of recent literature. Appl Mech Rev 51:705–729

Deng Z-S, Liu J (2002) Analytical study on bioheat transfer problems with spatial or transient heating on skin surface or inside biological bodies. J Biomech Eng 124:638–649

Deng Z, Liu J (2004) Mathematical modelling of temperature over skin surface and its implementation in thermal disease diagnostics. Comput Biol Med 34:495–521
Fiala D, Lomas KJ, Stohrer M (1999) A computer model of the human thermoregulation for the wide range of environmental conditions: the passive system. J Appl Physiol 87:1957–1972
Jordan PM, Dai W, Mickens RE (2008) A note on the delayed heat equation: instability with respect to initial data. Mech Res Commun 35:414–420
Joseph DD, Preziosi L (1989) Heat waves. Rev Mod Phys 61:41–73
Joseph DD, Preziosi L (1990) Adendum to the paper heat waves. Rev Mod Phys 21:375–391
Ostoja-Starzewski M (2007) A derivation of the Maxwell-Cattaneo equation from the free energy and dissipation potentials. Int J Eng Sci 47:807–810
Pennes HH (1948) Analysis of tissue and arterial blood temperature in the resting human forearm. J Appl Physiol 1:93–122
Ripley B (1987) Stochastic simulation. Wiley, New York
Torvi DA, Dale JD (1994) A finite element model of skin subjected to a flash fire. ASME 116:250–255

Simulation of In-situ Combustion in a Matrix-Fracture System at Laboratory Scale

O. Cazarez-Candia and C.G. Aguilar-Madera

Abstract In this work, a mathematical model for in-situ combustion (ISC) was numerically solved for one heterogeneous system composed by a porous-matrix adjacent to a fracture. The main aim was to investigate the effect of fractures on the ISC behaviour. Three mobile-phases were considered: non-volatile single-component oil, incondensable gas, and water. The combustion process was modeled with a kinetic model and two chemical reactions: cracking reaction (coke production), and combustion reaction (coke consumption). A benchmark case was established by comparison of suited numerical results against experimental data from a homogeneous combustion tube experiment reported from the literature. It was found an acceptable agreement between theoretical and experimental data for the temperature field and other variables of interest. The validated mathematical model was extended for one system including adjacent fractures, and their effects over the ISC were investigated. It was observed gas breakthrough because it moves preferably through fractures. It was found that around the combustion front, significant amount of oxygen penetrates from the fracture to the porous matrix, as here the coke combustion takes relevance. In addition, an important amount of oil is expelled from the matrix to the fracture.

1 Introduction

ISC is an enhanced oil recovery technique for mature or non-conventional reservoirs. Its main objective is to enhance oil mobility by reduction of viscosity occurring when temperature increases in the reservoir. Before the implementation to a commercial scale, previous field- and lab-scale assessments are required in order to evaluate

O. Cazarez-Candia (✉) · C.G. Aguilar-Madera
Instituto Mexicano del Petróleo, Eje Central Lázaro Cárdenas 152,
Del. Gustavo A. Madero, 07730 Mexico, D.F., Mexico
e-mail: ocazarez@imp.mx

C.G. Aguilar-Madera
Present Address Facultad de Ciencias de la Tierra, Universidad Autónoma de Nuevo León,
Ex–Hacienda de Guadalupe, 67700 Linares, N.L., México
e-mail: carlos.aguilar@fct.uanl.mx

J. Klapp et al. (eds.), *Selected Topics of Computational and Experimental Fluid Mechanics*, Environmental Science and Engineering,
DOI 10.1007/978-3-319-11487-3_22

the possibility of success. To study the phenomenon at core-scale, combustion tubes and simulators are used to investigate the formation and propagation of a combustion front.

In ISC experiments there are several phenomena with engineering interests. One of them concerns the oxygen transport into the reservoir in order to reach zones with fuel for further reaction and heat releasing. Using in-situ combustion tubes, experimental efforts have been done to understand the main mechanisms and phenomena controlling the ISC. To quote some examples, Moore and coworkers have developed extensive investigations at lab-scale and simulations for various types of operations, geometrical configurations and oils (Alamatsaz et al. 2011; Montes et al. 2010).

In reservoirs with heterogeneous characteristics such as fractured systems, the transport of phases and components is different in comparison with homogeneous media. Due to phases move preferably by fractures, fluids breakthrough appears and oxygen transport from fractures to the porous matrix plays a crucial role for the propagation of the combustion front. To broaden the understanding of ISC in fractured systems, some theoretical (Fatemi and Kharrat 2008; Schulte and Vries 1985) and experimental (Awoleke et al. 2010; Greaves et al. 1991) efforts have been made. Nevertheless, the complex nature of ISC involving simultaneous heat, mass and momentum transfer between phases, thermodynamic restrictions and chemical reactions, suggests further investigations for the sake of gaining more knowledge applicable to actual field-scale reservoir conditions.

Based on published works so far, it seems that fractures in ISC processes hinder the propagation of the combustion front and eventually the burning process is extinguished. The oxygen availability in the burning zone may play a crucial role, and such a feature is highly influenced by the contrast of fluids mobility between the porous matrix and fracture. Thus, in this work we focus on the numerical investigation of the effect that one fracture adjacent to one porous matrix has over an ISC process. The study is carried out at 2D lab-scale (combustion tube), and profiles of most relevant variables are presented and discussed.

2 Theoretical Model

In this study a three-phase, six-component ISC model was implemented. Table 1 shows components and phases taken into account in the model.

The mathematical model comprises the mass balance for oil- (o), gas- (g) and water-phases (w) as follows,

$$\frac{\partial\left(\phi\rho_\alpha s_\alpha\right)}{\partial t}+\nabla\cdot\left(\rho_\alpha\mathbf{u}_\alpha\right)=q_\alpha,\quad \alpha=o,g,w, \tag{1}$$

where ϕ is porosity, and ρ and s are density and saturation, respectively. q is the mass source/sink due to exchange between phases or chemical reactions. The phase velocity $\mathbf{u}$ is computed according to Darcy's Law,

Table 1 Phases and components

Component	Phase			
	Water	Oil	Gas	Solid
Oxygen, O_2			X	
Inert gas, IG			X	
Rock				X
Coke				X
Oil		X		
Water, H_2O	X		X	

$$\mathbf{u}_\alpha = -\frac{K k_{r\alpha}}{\mu_\alpha} \left(\nabla p_\alpha - \rho_\alpha \mathbf{g}\right), \alpha = o, w, g, \tag{2}$$

with K being permeability, k_r, μ and p are relative permeability, viscosity and pressure, respectively, whilst $\mathbf{g}$ is the gravity acceleration.

The energy balance assuming local thermal equilibrium is

$$\begin{aligned}\left(\rho c_p\right)_{eq} \frac{\partial T}{\partial t} + \nabla \cdot \left[\phi \left(s_o \rho_o c_{p,o} \mathbf{u}_o + s_g \rho_g c_{p,g} \mathbf{u}_g + s_w \rho_w c_{p,w} \mathbf{u}_w\right) T\right] \\ = \nabla \cdot \left(\mathbf{k}^*_{eff} \cdot \nabla T\right) + q_o^T + q_g^T + q_w^T + q_s^T - \Psi\end{aligned} \tag{3}$$

where

$$\begin{aligned}\Psi = \phi T \Big\{ \left[\rho_o c_{p,o} - \rho_g \left(c_{p,g} - c_g R/\bar{M}_g\right)\right] \frac{\partial s_o}{\partial t} \\ \left[\rho_w c_{p,w} - \rho_g \left(c_{p,g} - c_g R/\bar{M}_g\right)\right] \frac{\partial s_w}{\partial t} + \left(c_{p,g} - c_g R\right) s_g \frac{\partial \rho_g}{\partial t} \Big\}\end{aligned} \tag{4}$$

$$\begin{aligned}\left(\rho c_p\right)_{eq} = \phi \left[s_o \rho_o c_{p,o} + s_g \rho_g \left(c_{p,g} - c_g R/\bar{M}_g\right)\right. \\ \left. + s_w \rho_w c_{p,w} + \left(1/\phi - 1\right) \rho_s c_{p,s}\right]\end{aligned} \tag{5}$$

with $\mathbf{k}^*_{eff}$ being the total thermal dispersion tensor, q^T the thermal source/sink, T the temperature, $\bar{M}_g$ the average gas molecular weight, c_p the heat capacity, c_g the gas compressibility, and R the ideal gas constant.

The oxygen balance is given by,

$$\frac{\partial \left(\phi s_g \omega_{gO_2} \rho_g\right)}{\partial t} + \nabla \cdot \left(\phi s_g \omega_{gO_2} \rho_g \mathbf{u}_g\right) = \nabla \cdot \left(\phi s_g \rho_g \mathbf{D}^*_{gO_2} \cdot \nabla \omega_{gO_2}\right) + R_{O_2} \tag{6}$$

And for coke we have that,

$$\left(1 - \phi\right) \frac{\partial \left(\rho_s \omega_{sCoke}\right)}{\partial t} = R_{Coke} \tag{7}$$

where ω_{sCoke} is the coke mass fraction in the solid, ω_{gO_2} is the oxygen mass fraction in the gas, $\mathbf{D}^*_{gO_2}$ is the oxygen total mass dispersion tensor, and R_{O_2} and R_{Coke} are the oxygen and coke mass sink/source due to chemical reactions. Moreover, phase properties, the restriction $s_o + s_w + s_g = 1$, and relations between phase pressures (capillary pressures) were utilized. Additionally, two chemical reactions (cracking and combustion) were considered as follows,

$$Oil \rightarrow \eta_{Coke/Oil} Coke \tag{8}$$

$$Coke + \eta_{O_2/Coke} O_2 \rightarrow \eta_{IG/Coke} IG + \eta_{H_2O/Coke} H_2O \tag{9}$$

where $\eta_{i/j}$ is the stoichiometric factor between the i and j chemical species. In Eq. (9) the chemical species IG (inert gas) represents an hypothetical mixture of CO_x and N_2. To compute chemical reactions, Arrhenius-like expressions were used.

In order to set up completely the mass, momentum and energy transport problem, initial and boundary conditions are needed. These are the corresponding ones for injection boundaries:

$$\mathbf{n} \cdot \boldsymbol{\psi} = \boldsymbol{\psi}^{inj} \tag{10}$$

isolation boundaries:

$$\mathbf{n} \cdot \boldsymbol{\psi} = 0 \tag{11}$$

production boundaries

$$\mathbf{n} \cdot \nabla \boldsymbol{\psi} = 0 \tag{12}$$

$$\boldsymbol{\psi} = \boldsymbol{\psi}^{p} \tag{13}$$

and continuity conditions at the matrix-fracture boundary:

$$\mathbf{n} \cdot \boldsymbol{\psi}^{m} = \mathbf{n} \cdot \boldsymbol{\psi}^{f} \tag{14}$$

Here the subscripts inj, p, m and f refer to the injection, production, matrix and fracture boundaries (generally known values), respectively, and $\mathbf{n}$ is a unit vector perpendicular to the boundary and pointing outside. For brevity, the generic variable $\boldsymbol{\psi}$ refers to any primary (scalar or vector) variable; for instance, for energy transport $\boldsymbol{\psi} = T\mathbf{I}$ ($\mathbf{I}$ being the identity tensor) or the total (convective plus conductive) heat flux, if applicable. The same formulation applies for the each mass balance, and can be applied also for initial conditions, i.e. $\boldsymbol{\psi} = \boldsymbol{\psi}^0$.

3 The Base Case

The benchmark case performed to validate the numerical results was carried out by comparison of relevant results with those reported by Mamora (1993). The main

Table 2 Main characteristics of Mamora's experiment

Hamaca crude oil (Venezuela)	
Tube length (m)	0.9906
Internal radius (m)	0.0376936
Total mixture weight (kg)	7.739
Oil (%w/w)	4.6
Water (%w/w)	4.1
Sand (%w/w)	86.8
Clay (%w/w)	4.6
Oil saturation	0.29
Water saturation	0.27
Gas saturation	0.44
Porosity	0.31
Oil gravity (°API)	10.2
Oil viscosity (cP)	14,000
Initial temperature (°C)	50
Production pressure (psig)	100

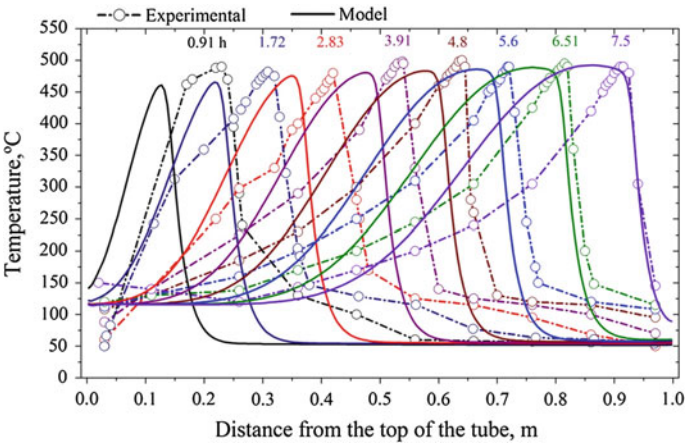

Fig. 1 Comparison of temperature profiles from numerical results and data from Mamora (1993)

characteristics of experiments are reported in Table 2. Characteristics of Mamora's experiments correspond for a 1D homogeneous combustion tube.

Figure 1 shows theoretical and experimental temperature fields in the combustion tube. At early times, the theoretical front advance slower than the experimental one, but eventually both profiles match for further times. Nevertheless, the combustion front width increases with time, meanwhile the experimental front preserves its thickness, leading to substantial errors for long times. In a general sense, the numerical

results fairly follow the tendency of experimental data in spite of simplifications assumed in the mathematical model. Other comparisons of relevant variables such as: oil, water and oxygen production, combustion front location and produced oil gravity were carried out with good agreement. However, such comparisons were omitted here for the sake of brevity.

4 The Matrix-Fracture Case

Comparison of temperature profiles for the benchmark case, and that one where 1 mm adjacent fracture is added, are plotted in Fig. 2. As one *small* fracture is considered, heat transport is not strongly affected by the channelization phenomenon as effective thermal properties, as heat capacity and thermal conductivity, do not vary significantly in the matrix and fracture. However, effective transport properties, as mass dispersion and permeability, are very contrast. This leads to one marked effect of fracture over phase flows and oxygen availability, as shown later.

Figure 3 shows the oxygen and oil fluxes at the porous-fracture boundary as function of time, when a fracture is adjacent to the porous matrix (the heterogeneous case). Larger values indicate that coke combustion is taking place at that position. As convention, a positive flux indicates that there is mass transport from the matrix to the fracture, and the opposite is true. At the vicinity of combustion front, there is high oxygen consumption, because of the coke combustion, and more oxygen must be feed from the fracture, where there is more oxygen available than in the matrix (see Fig. 4).

At surroundings of the combustion front, significant oxygen concentration gradients take place and, as this is the driving force for diffusive mechanisms, then the matrix microstructure (tortuosity and porosity) plays a crucial role to facilitate y the

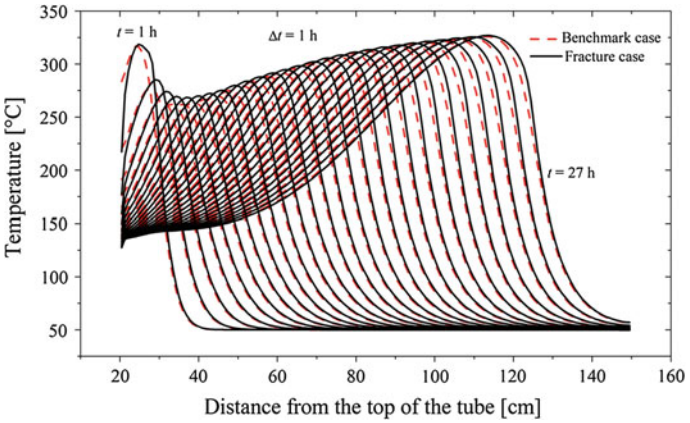

Fig. 2 Comparison of temperature profiles between the benchmark case and the fracture case

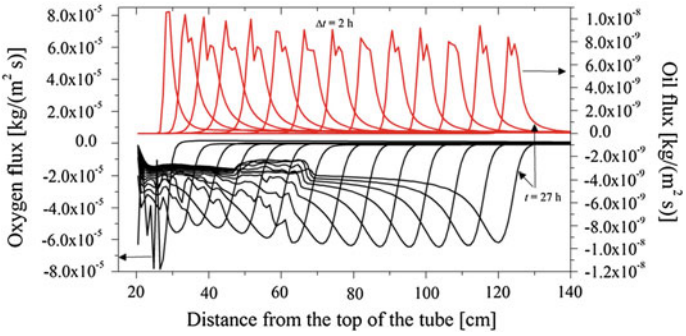

Fig. 3 Oxygen and oil fluxes at the matrix-fracture boundary

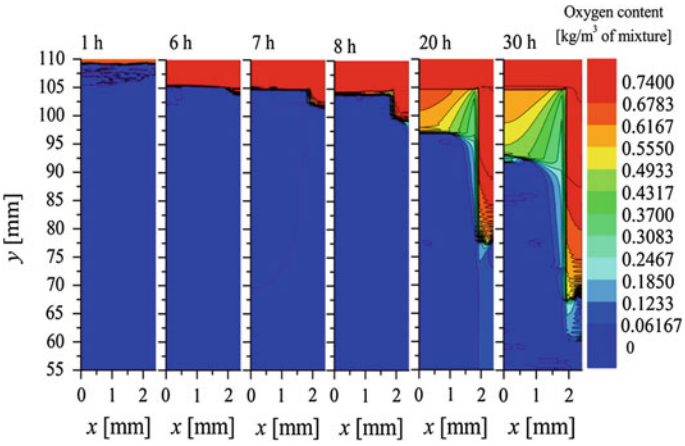

Fig. 4 Evolution of oxygen content

oxygen transport inside the matrix. It is obvious that a poorly permeable matrix could not favour oxygen transport with further combustion front extinction.

Along the tube, the high temperatures decrease the oil viscosity, and then due to a pressure gradient between matrix and fracture, a significant amount of oil is expelled from the matrix to the fracture region close to the combustion front (see Fig. 3).

5 Concluding Remarks

A mathematical model, for ISC at lab-scale, was numerically solved for a matrix-fracture system. The model was based on a benchmark case for a homogeneous system, which was validated with experimental data, obtaining good agreement. The matrix-fracture system presents fluids breakthrough due to the phases and

components move easier through the fracture. The oxygen penetrates from fracture to the matrix and plays a crucial role to the propagation of the combustion front. A significant oil expulsion from the matrix to the fracture also was observed, which is a consequence of the enhanced oil mobility by the high temperatures and permeability of fracture. We found that: (1) temperature is not strongly affected by the fracture, (2) oxygen concentration gradients is the driving force for diffusive mechanisms, then the matrix microstructure plays a crucial role to facilitate the oxygen transport inside the matrix, (3) a poorly permeable matrix could not favour oxygen transport with further combustion front extinction, and (4) along the tube, the high temperatures lead to a decrease the oil viscosity, and then due to a pressure gradient between matrix and fracture, a significant amount of oil is expelled from the matrix to the fracture region close to the combustion front.

References

Alamatsaz RG, Moore RG, Mehta SA, Ursenbach MG (2011) Experimental investigation of in situ combustion at low air fluxes. In: SPE Western North American regional meeting, Anchorage

Awoleke OG, Castanier LM, Kovscek AR (2010) An experimental investigation of in situ combustion in heterogeneous media. In: Canadian unconventional resources and international petroleum conference, Calgary, Canada

Fatemi SM, Kharrat R (2008) Feasibility study of top-down in-situ combustion in fractured carbonate systems. Braz J Pet Gas 2:96–105

Greaves M, Javanmardi G, Field RW (1991) In situ combustion (ISC) in fractured heavy oil reservoirs. In: 6th European IOR-symposium. Stavanger, Norway

Mamora DD (1993) Kinetics of in situ combustion. PhD thesis, Stanford University. Ann Arbor

Montes AR, Gutiérrez D, Moore RG, Mehta SA, Ursenbach MG (2010) Is high-pressure air injection (HPAI) simply a flue-gas flood? J Can Pet Technol 49:56–63

Schulte WM, de Vries AS (1985) In-situ combustion in naturally fractured heavy oil reservoirs. SPE J 25:67–77

Numerical Simulation of In-situ Combustion in a Fracture-Porous Medium System

O. Cazarez-Candia, P.V. Verazaluce-Barragán and J.R. Hernández-Pérez

Abstract In this work, the numerical simulation of in-situ combustion in a fracture-porous medium system at laboratory scale, was done. The simulations were developed in a commercial reservoir simulator designed to evaluate oil recovery by thermal methods. The simulator involves the mass, momentum (Darcy law) and energy balance equations for multiphase and multicomponent flows. The main aim of this work was to study the effect of the airflow rate and oil saturation on the in-situ combustion behaviour. In the first stage of this study, the in-situ combustion was simulated in a homogeneous porous medium and the simulation was validated using experimental data. In a second stage, such simulation was modified in order to incorporate fractures in the porous medium. It was found that the oxygen diffusion from fractures to porous medium controls the in-situ combustion in fractured systems. Moreover, it is necessary to restrict the injected air flow rate due to the breakthrough phenomenon and because the oil recovery is not substantially increased for larger flow rates.

1 Introduction

In-situ combustion (ISC) is a thermal oil recovery technique used in the petroleum industry. Mainly, this method has been applied in heavy-oil fields. In order to evaluate if a given oil reservoir is a candidate for an ISC project, it is common to study the propagation of the combustion front in small multiphase systems known as in-situ combustion tubes.

O. Cazarez-Candia (✉) · P.V. Verazaluce-Barragán · J.R. Hernández-Pérez
Instituto Mexicano del Petróleo, Eje Central Lázaro Cárdenas 152,
Del. Gustavo A. Madero, 07730 Mexico, D.F., Mexico
e-mail: ocazarez@imp.mx

P.V. Verazaluce-Barragán
e-mail: pvverazaluce@hotmail.com

J.R. Hernández-Pérez
e-mail: rhperez@imp.mx

J. Klapp et al. (eds.), *Selected Topics of Computational and Experimental Fluid Mechanics*, Environmental Science and Engineering,
DOI 10.1007/978-3-319-11487-3_23

Currently, a large amount of petroleum is in naturally fractured reservoirs. This has leaded to develop theoretical and experimental works for gaining knowledge about the effects that fractures have on the thermal and hydrodynamic performance of the ISC (Awoleke et al. 2010; Greaves et al. 1991; Schulte and de Vries 1985). Most of these works agree that the oxygen transport is one of the main phenomena to sustain and propagate the combustion front. Thus, oxygen dispersion from fracture to matrix plays a crucial role for the ISC inside the porous medium. Despite the theoretical and experimental research that has been done, the ISC behavior in fracture systems is no clear nowadays.

In this work, we simulated one experiment of the ISC process in a combustion tube filled with a homogeneous system (Kumar 1987) obtaining an excelent fitting. Later, the simulation model was modified in order to include fractures. This model was compared against the conducted simulation by Tabasinejad et al. (2006) obtaining also excellent fitting. The last model was used to evaluate the effect of air flow rate and the oxygen diffusion from fractures to porous medium.

2 Governing Equations, Boundary and Initial Conditions

The general model, for multicomponent multiphase flow (gas, oil and water) in porous media used in this work, is presented below:

Mass conservation equation

$$(1-\sigma)\frac{\partial \sum_{\alpha=g,o,w} \phi S_a \rho_\alpha \omega_{i\alpha}}{\partial t} = -\nabla \cdot \left(\sum_{\alpha=g,o,w} \rho_\alpha D_{\alpha i} \nabla \omega_{i\alpha} \right) - \nabla \cdot (\rho_i \omega_{i\alpha} \mathbf{u}_\alpha) + \sum_{\alpha=g,o,w} r_{i\alpha} + \sum_{\alpha=g,o,w} \omega_{i\alpha} q_\alpha \quad i = 1, \ldots, n_c. \tag{1}$$

Energy equation

$$\frac{\partial}{\partial t}\left(\sum_{\alpha=g,o,w} \phi S_a \rho_\alpha U_\alpha + (1-\phi)\rho_s C_s T \right) + \nabla \cdot \sum_{\alpha=g,o,w} \rho_\alpha \mathbf{u}_\alpha H_\alpha - \nabla \cdot (k_T \nabla T) = q_c - q_L \tag{2}$$

where

$$\mathbf{u}_\alpha = -\frac{k k_{r\alpha}}{\mu_\alpha} (\nabla p_\alpha - \rho_\alpha \mathbf{g}) \tag{3}$$

$$\sum_{i=1}^{n_c} A_i \omega_i = \sum_{i=1}^{n_c} B_i \omega_i \tag{4}$$

$$\sum_{\alpha=g,o,w} S_\alpha = 1 \tag{5}$$

$$\sum_{i=1}^{n_c} \omega_{i\alpha} = 1, \quad \alpha = g, o, w \tag{6}$$

$$p_{cow}(S_w) = p_o - p_w, \quad p_{cgo}(S_g) = p_g - p_o \tag{7}$$

$$\omega_{i\alpha} = K_{i\alpha\beta}\,(p, T)\,\omega_{i\beta}; \quad i = 1, \ldots, N_c, \quad \alpha, \beta = g, o, w \tag{8}$$

Initial and boundary conditions

$$\begin{aligned} \omega_{i\alpha}(\mathbf{x}, 0) &= \omega_{i\alpha}(\mathbf{x}), \quad i = 1, \ldots, n_c - 1, \quad \alpha = o, w \\ S_w(\mathbf{x}, 0) &= S_{w0}(\mathbf{x}) \\ S_g(\mathbf{x}, 0) &= S_{g0}(\mathbf{x}) \\ \mathrm{p}_o(\mathbf{x}, 0) &= p_{o0}(\mathbf{x}) \\ T(\mathbf{x}, 0) &= T_0(\mathbf{x}) \\ \mathbf{u}_\alpha(\mathbf{x}, t) &= 0, \quad \mathbf{x} \in \partial\Omega \\ \nabla T(\mathbf{x}, t) &= 0, \quad \mathbf{x} \in \partial\Omega \end{aligned} \tag{9}$$

In Eqs. (1)–(9) A_i represents the reactants stoichiometric coefficients, B_i the products stoichiometric coefficients, C_s the solid mass heat capacity, $D_{i\alpha}$ the diffusion coefficient of component i in phase α, $\mathbf{g}$ is the gravity vector, H is the enthalpy, k_T is the total thermal conductivity of the porous media, k is absolute permeability, k_r is the relative permeability, $K_{i\alpha\beta}$ is the equilibrium K-value of component i between phases α and β, n_c is the number of components, p is pressure, p_{cow} is the oil-water capillary pressure, p_{cog} is the oil-gas capillary pressure, q is the source volumetric rate, q_c is heat source rate, q_L is heat loss rate, $r_{i\alpha}$ is the rate of production of component i by reactions, S is saturation, T is temperature, U is internal energy, $\mathbf{u}$ is velocity, $\mathbf{x}$ is position vector, ϕ is porosity, ρ_α is phase density, ρ_s is solid density, μ_α is phase dynamic viscosity, $\omega_{i\alpha}$ is the mass fraction of component i in phase α, and σ is the solid volume fraction. The subscript $\alpha(= g, o, w)$ represents phase evaluated as gas, oil or water.

For more information about the mathematical model, we refer to the reader to the STARS user's guide (see references list).

3 Homogeneous System Simulation

The model simulation was validated using experimental data from a combustion tube reported in the work from Kumar (1987). In the experiment, a sand pack (mixture of oil, water and sand) was put in the tube. An electrical igniter was used at the top of the tube in order to generate a combustion front that propagates along the tube. For more information, we refer the reader to the work of Kumar (1987).

The experiment was simulated using the commercial software known as STARS, which is the software most used around the world to simulated thermal oil recovery process (in-situ combustion, steam injection and hot-water injection).

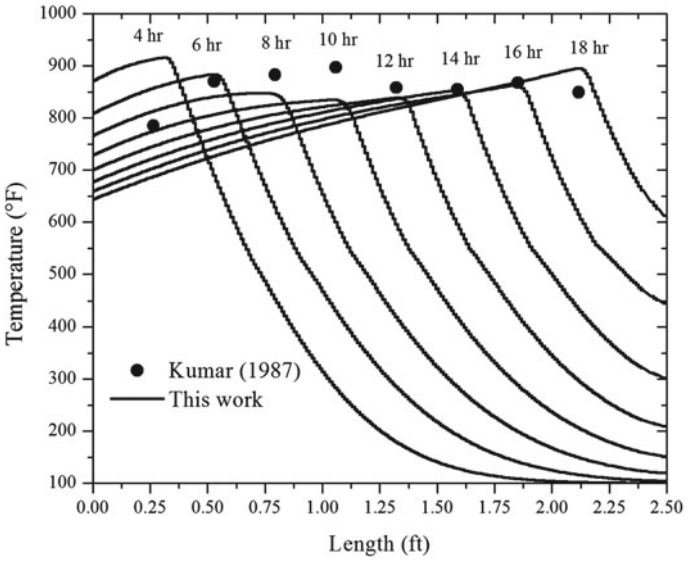

Fig. 1 Temperature profiles along the tube

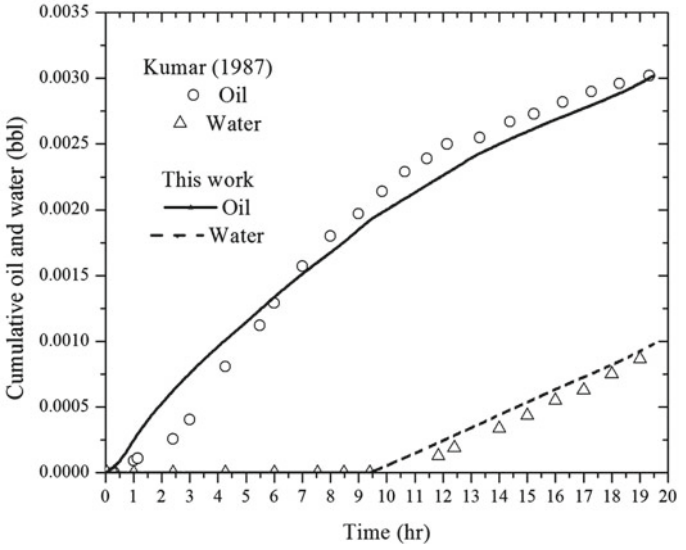

Fig. 2 Oil and water recovery

The reaction model used is the same one from the work of Fadaei et al. (2009). Such model involves the cracking reaction and the HO, LO and coke combustion reactions. Figure 1 shows that combustion front temperature has a good fitting against experimental data from Kumar (1987). The differences at top of the tube are attributed to the boundary effects due to the experimental procedure.

Figure 2 shows oil and water recovery. The very good agreement between predictions and experimental data allows to conclude that the fluids mass balance was well simulated.

4 Fracture-Porous Medium System Simulation

The validated model, used to simulate a homogeneous system (Sect. 3), was modified in order to involve a fracture formed by the porous medium and the tube wall. Table 1 shows the data used for the simulation (Tabasinejad et al. 2006).

Figure 3 shows that temperature profiles along the tube have a very good fitting against the predictions from the work of Tabasinejad et al. (2006). The oil recovery also shows a good agreement (Fig. 4), then the simulation model obtained represents a tool to study in-situ combustion in fracture-porous medium systems.

The simulation model, obtained in this section, was the benchmark case to study the effect of air flow rate on: (1) the oil recovery factor, and (2) the behavior of oxygen from the fracture to the porous medium. The effect of oil saturation on the oil recovery factor was also studied.

Figure 5 shows that the larger the air flow rate the larger the oil recovery factor, however if the air flow rate is very large oxygen breakthrough could occur, then there is an optimum flow rate to obtain the largest oil recovery without or with a little oxygen breakthrough. Due to this, the oxygen behavior was also studied.

Figure 6 shows the oxygen mole fraction for 0.277, 0.554, and 1.108 ft^3/h. The larger the flow rate the larger the Peclet number (for gas and oil) and Reynolds

Table 1 Parameters used in the simulation

Parameter	Value
Matrix permeability (md)	1.27×10^4
Fracture permeability (md)	1.27×10^6
Matrix porosity (%)	39.7
Fracture porosity (%)	100
Oxygen molecular diffusion (ft^2/s)	1.1×10^{-5}
Pressure (psi)	2,000
Temperature (°F)	100
Water saturation (%)	17.8
Oil saturation (%)	65.4
Gas saturation (%)	16.8
Air flow rate (ft^3/h @ s.c.)	0.277, 0.55, 1.108

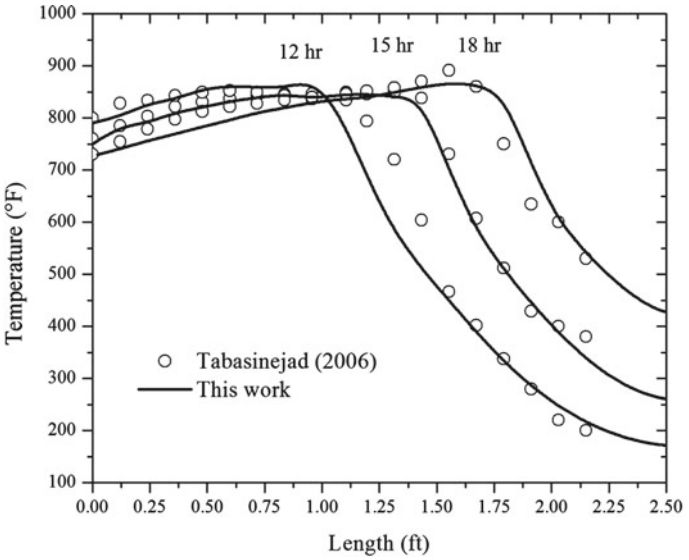

Fig. 3 Temperature profiles along the tube for a fracture system

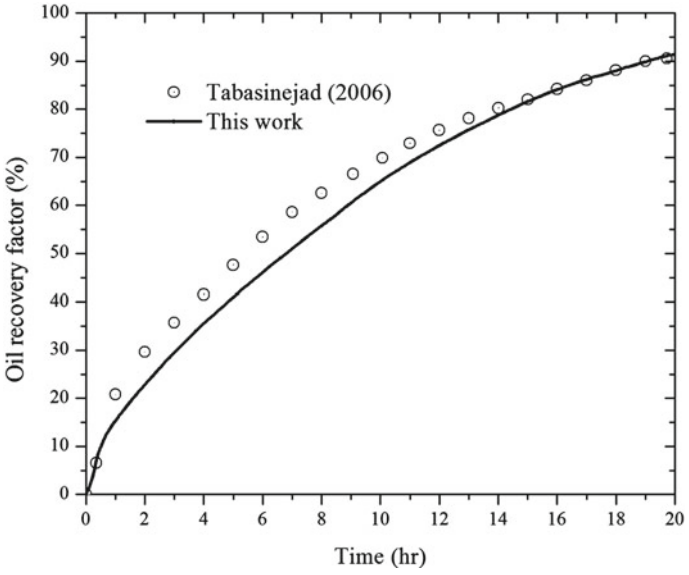

Fig. 4 Oil recovery from a fracture system

number in the porous medium. This indicates that more oxygen penetrates from the fracture to the porous medium by convection, and more oil is pushed from the porous medium to the fracture. However, it must take care because the larger flow rate the larger amount of oxygen produced. For the air flow rates used in this work

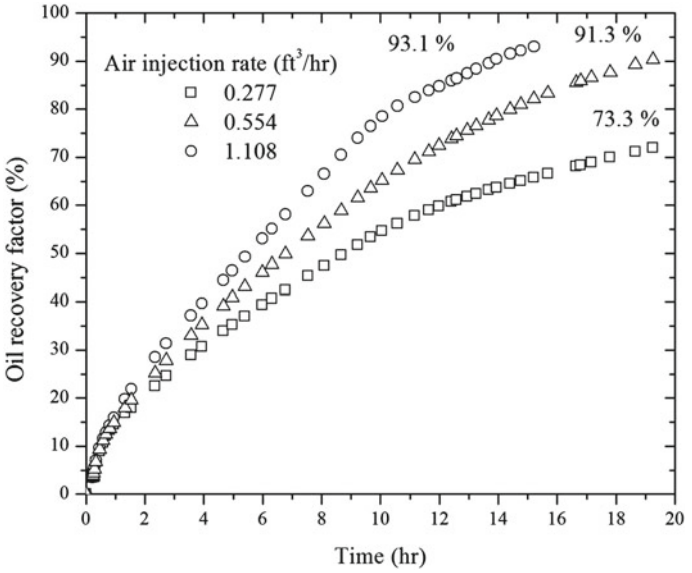

Fig. 5 Oil recovery for different airflow rates

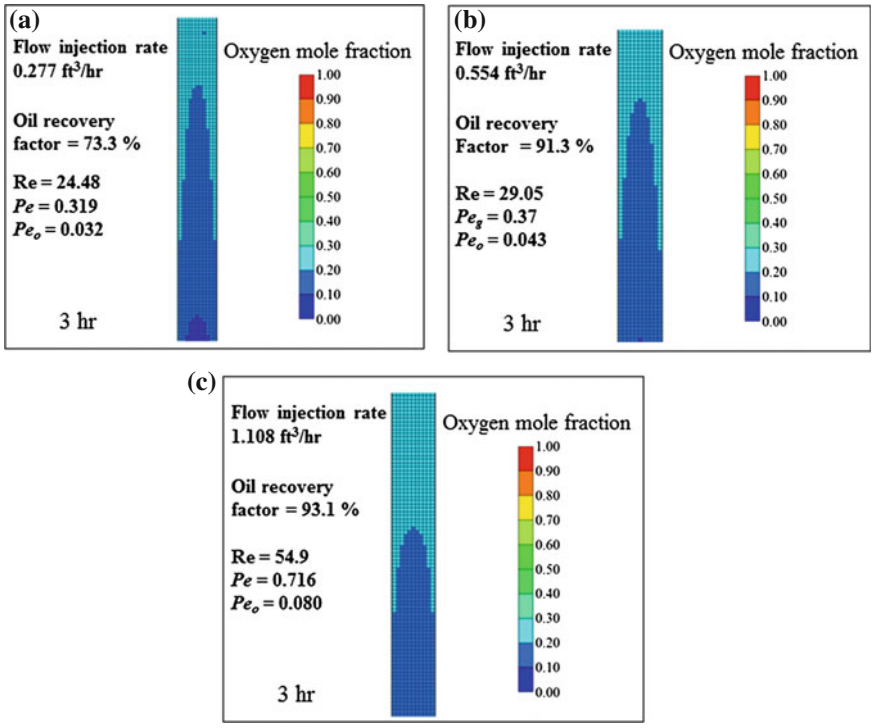

Fig. 6 Oxygen mole fraction for an air flow injection rate of: **a** 0.277 ft^3/hr, **b** 0.554 ft^3/hr, and **c** 1.108 ft^3/hr

0.554 ft^3/h was the best value because it allows recover 91.3 % of oil and a small amount of oxygen is produced (less than 10 %).

Figure 7 shows that the larger the oil saturation the larger the oil recovery factor, however for oil saturations larger than 40 %, the total oil recovery factor is little

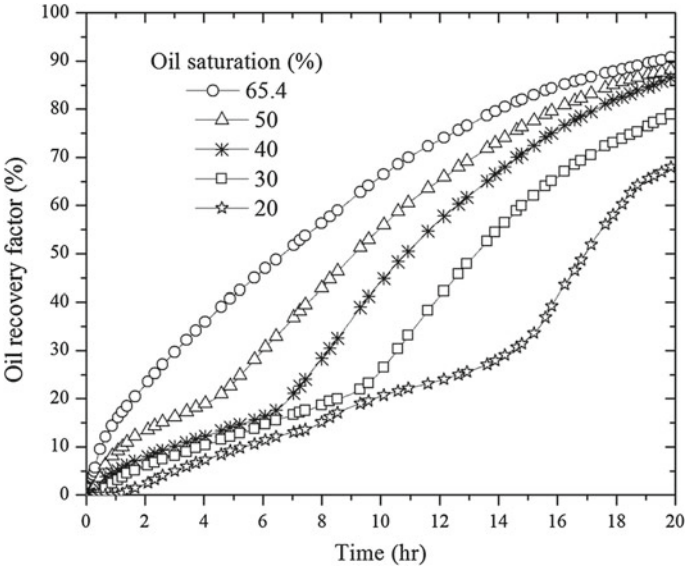

Fig. 7 Oil recovery for different oil saturations

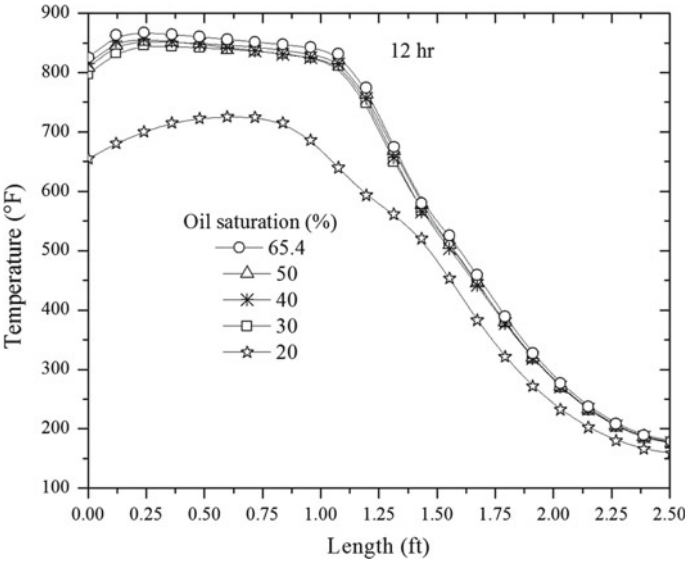

Fig. 8 Temperature for different oil saturations

affected. This means that the amount of produced coke is almost the same for oil saturation values of 40, 50 and 65.4. Then, the amount of energy release from the coke combustion is similar. Thus, temperature profiles should be similar, as shown in Fig. 8 (at 12 h).

Note that although the total oil recovery factor is similar for oil saturation values of 40, 50 and 65.4, its behavior is different along the time. For large oil saturations, the most oil is produced at short times. For instance, at 12 h. we have an oil recovery factor of 75 % of a total of 92 % for an oil saturation of 65.4, but we have only an oil recovery factor of 23 % of a total of 68 % for an oil saturation of 20.

5 Conclusions

In this work the numerical simulation of in-situ combustion in a fracture-porous medium system at laboratory scale, was done. It was found that in a fractured system, the oil recovery factor increases when air flow rate increases, however exist an optimum flow rate value for which: (1) the oil recovery is high, and (2) the oxygen transport from the fracture to the porous zone is high without oxygen breakthrough.

The results of this work show that the oxygen diffusion from fractures to porous medium controls the in-situ combustion in fractured systems. This because the extinction of the combustion front occurs when a small amount of oxygen comes into the matrix, and oxygen breakthrough occurs when a large amount of oxygen is injected.

On the other hand, as the initial oil saturation is larger, the oil recovery factor is larger; however, for oil saturations larger than 40 %, the total oil recovery factor is little affected.

References

Awoleke OG, Castanier LM, Kovscek AR (2010) An experimental investigation of in-situ combustion in heterogeneous media. In: Canadian unconventional resources and international petroleum conference. No. 137608-MS. Canadian society for unconventional gas/society of petroleum engineers, Calgary, Alberta, Canada, pp 19–21

Computer Modelling Group (2008) STARS user's guide. Advanced process and thermal reservoir simulator, version

Fadaei H, Castanier L, Kamp AM, Debenest G, Quintard M, Renar G (2009) Experimetal and numerical analysis of in-situ combustion in a fracture core. SPE J 1411117:358–373

Greaves M, Javanmardi G, Field RW (1991) In situ combustion (isc) in fractured heavy oil reservoirs. In: 6th European IOR-symposium. Stavanger, Norway, 21–23 May 1991

Kumar M (1987) Simulation of laboratory in-situ combustion data and effect of process variations. Paper SPE 16027-MS presented at the SPE Symposium on reservoir simulation, San Antonio, Texas, USA, 1–4 February. doi:10.2118/16027-MS

Schulte WM, de Vries AS (1985) In-situ combustion in naturally fractured heavy oil reservoirs. Soc Pet Eng J 25(1):67–77

Tabasinejad F, Karrat R, Vossoughi S (2006) Feasibility study of in-situ combustion in naturally fractured heavy oil reservoirs. In: Paper SPE 103969 presented at the first international oil conference and exhibition in Mexico, Cancun, Mexico, 31 August–2 September. doi:10.2118/103969-MS

Mathematical Modeling of Steam Injection in Vertical Wells

F. Aguilar-Gastelum and O. Cazarez-Candia

Abstract In this work, a steady-state hydrodynamic model for steam injection vertical wells and a transient thermal model (2D energy diffusion equation) for the heat losses from a well towards the porous medium are presented. The hydrodynamic model is formed by mass, momentum and energy conservation equations (drift-flux model) for a steam-water two-phase flow. The steady-state drift-flux model was resolved using the finite differences method and the explicit Godunov scheme, while the thermal model solution was found with an implicit Godunov scheme. Models allow predicting the next parameters: pressure, temperature, steam quality, heat losses and flow patterns along the well. The parameter predictions presented good agreement against field data and simulations reported in literature. For the conditions simulated, it was found that: (1) the thermal model reaches its steady state at 500 h, (2) due to few steam condensation, pressure drop due to gravity is smaller than the friction and acceleration contributions, and (3) temperature gradients are large at the beginning of steam injection, but they diminish along time.

1 Introduction

Direct Steam injection through vertical wells is a promising technique to improve oil recovery from reservoirs where natural energy or a primary/secondary recovery method is not enough to still producing. Some researchers (Ramey 1962; Pacheco and Ali 1972; Ali 1981; Fontanilla and Aziz 1982; Durrant and Thambynayagam 1986; Hasan and Kabir 1994) have made important investigations into this area, however, they were not able to get a completely understanding. In order to simulate steam injection through vertical wells, Bahonar et al. (2009) proposed a not-

F. Aguilar-Gastelum · O. Cazarez-Candia (✉)
Instituto Mexicano del Petróleo (IMP), Eje Central Lázaro Cárdenas 152,
Del. Gustavo A. Madero, 07730 Mexico, D.F., Mexico
e-mail: ocazarez@imp.mx

F. Aguilar-Gastelum
e-mail: pedro_00001@hotmail.com

J. Klapp et al. (eds.), *Selected Topics of Computational and Experimental Fluid Mechanics*, Environmental Science and Engineering,
DOI 10.1007/978-3-319-11487-3_24

isothermal mathematical model that was resolved using the finite difference method and a Godunov discretization scheme. The model solution was divided in three steps: (1) the hydrodynamic modeling of two-phase flow through the well using a drift-flux model proposed by Hasan et al. (2007), (2) the heat losses from the wall well toward the formation using a global heat transfer coefficient, and (3) the heat diffusion in the formation. The heat diffusion was modeled by the transient cylindrical 2D heat equation. Their results showed good agreement against field data. On the other hand, Mozaffari et al. (2011) solved numerically a mixture model for steam injection, following the same approach as Bahonar et al. (2009). Their predictions of pressure, temperature and steam quality showed good agreement against field data.

Previous studies have shown that the drift-flux model coupled to a transient 2D heat diffusion equation, allow to analyze the steam injection process in vertical wells. The aim of this work is to study the behavior (pressure, temperature, steam quality, and heat loss) of a vertical steam injection well using a drift-flux model.

2 Model Formulation

2.1 Physical Model

Figure 1 shows the physical model of a system formed by a steam injection vertical well and a surrounding porous medium. The system is divided in three main parts: (1) the well tubing, (2) insulation, annulus (filled with air), casing and cementing, and (3) the porous medium, which is considered as a continuum media. The system is fed with a water-steam mixture at constant pressure and steam quality.

2.2 Mathematical Model

To simulate the steam injection system showed in Fig. 1, the semi-unsteady-state model proposed by Bahonar et al. (2009) is used. Such model involves: (1) a steady-state drift-flux model to simulate the hydrodynamic behavior of a steam-water downward flow into the injection well, (2) an overall heat transfer coefficient to evaluate the total heat loss from the well to the porous medium, and (3) a thermic model, which consists of a 2D transient heat diffusion equation to evaluate the heat transfer through the porous medium.

The hydrodynamic model consists of mass, momentum and energy conservation equations as follows.

Mass balance equation

$$-\frac{\partial}{\partial z}\left(\rho_g v_{sg} + \rho_l v_{sl}\right) = 0 \tag{1}$$

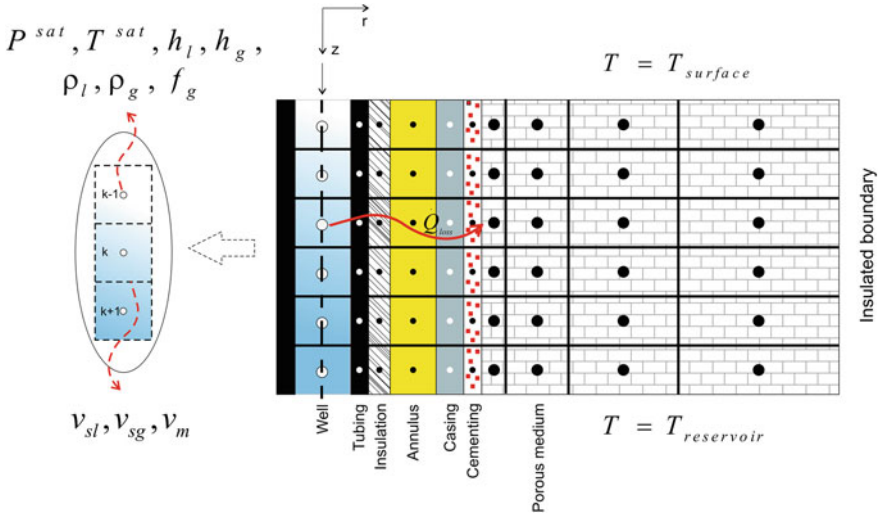

Fig. 1 Physical model and schematic representation of the well and porous medium discretization

Momentum balance equation

$$-\frac{dP}{dz} = -\frac{\rho_m g \cos\theta}{g_c} + \frac{f_m v_m^2 \rho_m}{2 d_{ti} g_c} + \frac{\rho_m v_m}{g_c}\frac{dv_m}{dz} \tag{2}$$

Energy balance equation

$$\begin{aligned} &\frac{\dot{Q}_{loss}}{3600 x A_{ti}} + \frac{\partial}{\partial t}\left\{\sum_p \left[f_p \rho_p \left(u_p + \frac{v_p^2}{2 g_c J_c}\right)\right]\right\} \\ &= -\frac{\partial}{\partial z}\left\{\sum_p \left[\rho_p v_{sp}\left(h_p + \frac{v_p^2}{2 g_c J_c}\right)\right]\right\} + \sum_p \frac{\rho_p v_{sp} g \cos\theta}{g_c J_c} \end{aligned} \tag{3}$$

where the subscripts g, l and m represent gas, liquid and mixture, respectively, P is pressure (which is the saturation pressure P_{sat}), ρ is density, v_s is superficial velocity, g is the gravity acceleration, θ is the local angle between the well and the vertical direction, g_c is the gravitational conversion constant, d_{ti} is the inner diameter of the tubing, f_m is friction factor, v is velocity, $\dot{Q}_{loss}$ is the fluid heat loss, A_{ti} is the inner tubing area, p is the phase index (liquid or gas), h is enthalpy, u is internal energy, f is the gas volume fraction, J_c is the mechanical equivalent of heat (788 ft-lbf/Btu), and 3,600 converts hours to seconds.

The heat losses, from the water-steam mixture to the porous medium, are diminished by thermal resistances due to the wall well, insulation, annulus, casing and the cementing wall (see Fig. 1), then we have that

$$\dot{Q}_{loss} = 2\pi r_{to} U_{to} (T_f - T_{wb}) \tag{4}$$

where, r_{to} is the outer tubing radius, U_{to} is the overall heat transfer coefficient based on r_{to}, T_f is the fluid temperature (saturation temperature, T_{sat}) inside the injection well and T_{wb} is the temperature in the well-porous medium boundary. The overall heat transfer coefficient is given by

$$\frac{1}{U_{to}} = \frac{r_{to}}{r_{ti} h_t} + \frac{r_{to} \ln (r_{to}/r_{ti})}{k_t} + \frac{r_{to} \ln (r_{ins}/r_{to})}{k_{ins}} + \frac{r_{to}}{r_{ins}(h_c + h_r)} + \frac{r_{to} \ln (r_{co}/r_{ci})}{k_c} + \frac{r_{to} \ln (r_{wb}/r_{co})}{k_{cem}} \tag{5}$$

where k_t, k_{ins}, k_c and k_{cem} are the thermal conductivity of the tubing, insulation, casing and cementing, respectively. r_{ins} and r_{co} are the insulation and casing external radius, r_{ci} is the casing internal radius and r_{wb} is the cementing-porous medium interface radius. h_t is the convective heat transfer coefficient for the water-steam mixture, h_c and h_r are the convective and radiation heat transfer coefficients in the annulus.

The thermic model involves a 2D transient heat diffusion equation in cylindrical coordinates

$$\frac{1}{r}\frac{\partial}{\partial r}\left(k_{er} r \frac{\partial T_e}{\partial r}\right) + \frac{\partial}{\partial z}\left(k_{ez}\frac{\partial T_e}{\partial z}\right) = \rho_e C_{pe} \frac{\partial T_e}{\partial t} \tag{6}$$

where, T_e is the porous medium temperature, k_{er} is the conduction coefficient in the radial direction, k_{ez} is the conduction coefficient in the vertical direction z, ρ_e is the porous medium density, C_{pe} is the porous medium heat capacity and r is the radius. One initial condition and four boundary conditions are necessary to solve Eq. (6). The geothermal gradient was used as initial condition

$$T_{ei} = T_{ei_{wh}} + g_T z \cos\theta \tag{7}$$

where, T_{ei} is the initial porous medium temperature and $T_{ei_{wh}}$ is the initial wellhead temperature. The boundary conditions are given by;

$$T_e = T_{surface} \quad \rightarrow \quad z = 0,\ r \geq r_{wb} \tag{8}$$

$$T_e = T_{reservoir} \quad \rightarrow \quad z = L,\ r \geq r_{wb} \tag{9}$$

$$\frac{\partial T_e}{\partial r} = 0 \quad \rightarrow \quad 0 \leq z \leq L,\ r \rightarrow \infty \tag{10}$$

$$\dot{Q}_{loss} = -2\pi r k_e \frac{\partial T_e}{\partial r} \quad \rightarrow \quad 0 \leq z \leq L,\ r = r_{wb} \tag{11}$$

The mathematical model solution allows knowing the pressure, temperature, steam quality, and flow patterns of the water-steam mixture, as well as the thermal energy that is dissipated to the surroundings. Although a steady-state drift-flux was used, such solution is on semi-unsteady-state due to the accumulation term in the 2D heat diffusion equation allows us to evaluate temperature changes in the porous medium as time elapses.

On the other hand, to get a closed system, some auxiliary equations were used to evaluate: (1) the gas volume fraction, (2) the drift velocity, (3) flow patterns transitions and (4) fluids properties. Peng-Robinson and Valderrama-Patel-Teja state equations were also implemented to evaluate steam and air density.

3 Numerical Implementation

Finite difference method was used to resolve the steam injection mathematical model. A staggered mesh (see Fig. 1) was implemented for the hydrodynamic model, so most of variables were evaluated at the center of each cell, but superficial and mixture velocities were evaluated at the boundary of the cells. The transient 2D heat diffusion equation was discretized with an implicit scheme, with an irregular grid in r direction and regular spacing in z direction (see Fig. 1). Spatial derivatives were discretized applying the standard Godunov first-order upwinding scheme, while for the time derivative in the heat diffusion equation we used a forward first-order scheme. A computational algorithm was built in the FORTRAN language to solve the discretized system of equations. We refer to the reader to the work of Bahonar et al. (2009) for detail about the flowchart that shows the steps of the numerical algorithm that has been used in this work. The following steps proposed by Bahonar et al. (2009) yield a more detailed description of the numerical solution procedure:

1. At first grid block, P_{sat} and $\dot{w}$ are known, so the properties x, ρ_l, ρ_g, v_{sl}, v_{sg}, h_l and h_g can be calculated using correlations or an state equation.
2. For the first iteration, the properties of the previous grid block are used at the current grid block. However, from second iteration the values of the previous iteration are used at the current grid block.
3. Knowing P_{sat}; T_{sat}, h_l, h_g, ρ_l and ρ_g are calculated.
4. The overall heat transfer coefficient is calculated as a function of depth using an iterative scheme. For the first iteration, U_{to} is calculated based on both, the initial temperature distribution along the well and the boundary formation. For other iterations, U_{to} takes the value from the previous iteration. Knowing U_{to}, we can calculate T_{to} and T_{ci}, and then know a new value for U_{to}. If there is difference between them (old and new value for U_{to}), the iterative process has to continue until convergence is achieved.
5. For the first iteration a superficial gas velocity, v_{sg_k}, is assumed and it is approximated to $v_{sg_{k+1/2}}$. Then the superficial liquid velocity $v_{sl_{k+1/2}}$ is calculated using

the mass balance equation (Eq. 1). Also, water and steam densities at $k + 1/2$, are approximated as $\rho_{l_{k+1/2}} = \rho_{l_k}$ and $\rho_{g_{k+1/2}} = \rho_{g_k}$.

6. In-situ volume fraction, f_g, is calculated using correlations for downward two phase flow for different flow patterns.
7. v_{sg} is recalculated using the momentum balance equation (Eq. 2), and the fluid properties are reevaluated.
8. Heat loss is calculated using Eq. (4).
9. v_{sg} is calculated from the energy balance equation using an iterative Newton-Raphson scheme. The v_{sg} calculated is compared against the v_{sg} assumed, and if they are different, step 5 is repeated; otherwise, the pressure convergence at current grid block is reviewed. If P_{sat} calculated in step 7 is different than P_{sat} assumed, then step 2 is repeated; otherwise, steps 1–9 must be done for the next grid block until all the grid blocks are visited.
10. Equation (6) is solved and the results are saved in a text file. If the simulation time has been reached, the solution process will stop, otherwise; steps 1–9 must be repeated for a next time step.

4 Results and Discussions

In order to validate the computational code, predictions were compared against numerical/field data reported in literature. Table 1 shows the field data parameters of the Martha Big Pond well (Bahonar et al. 2009), which were used to get predictions.

Figure 2 shows a comparison of predictions (flow pattern, pressure, temperature, steam quality, and heat loss) against numerical/field data. Pressure and temperature profiles have good agreement and small differences (smaller than 2 %) were gotten for steam quality and heat loss. Figure 2d shows that there is not a large steam condensation, then: (1) the hydrostatic pressure drop is small and pressure diminishes along the well (Fig. 2a), (2) there is annular flow along the whole well.

Table 1 Field data parameters of Martha Big Pond well (Bahonar et al. 2009)

r_{ti}	0.08850 ft	k_{cem}	0.2 BTU/h ft °F
r_{to}	0.104167 ft	ε_{to}	0.9
r_{ins}	No insulation	ε_{ci}	0.9
r_{ci}	0.166667 ft	W	4850 lbm/h
r_{co}	0.187500 ft	X	0.8
r_{wb}	0.600000 ft	P	250 psia
k_e	1 BTU/h ft °F	T_{wh}	50 °F
α_e	0.0286 ft^2/h	Depth	1600 ft
g_T	0.0283 °F/ft	Annulus pressure	14.7 psia

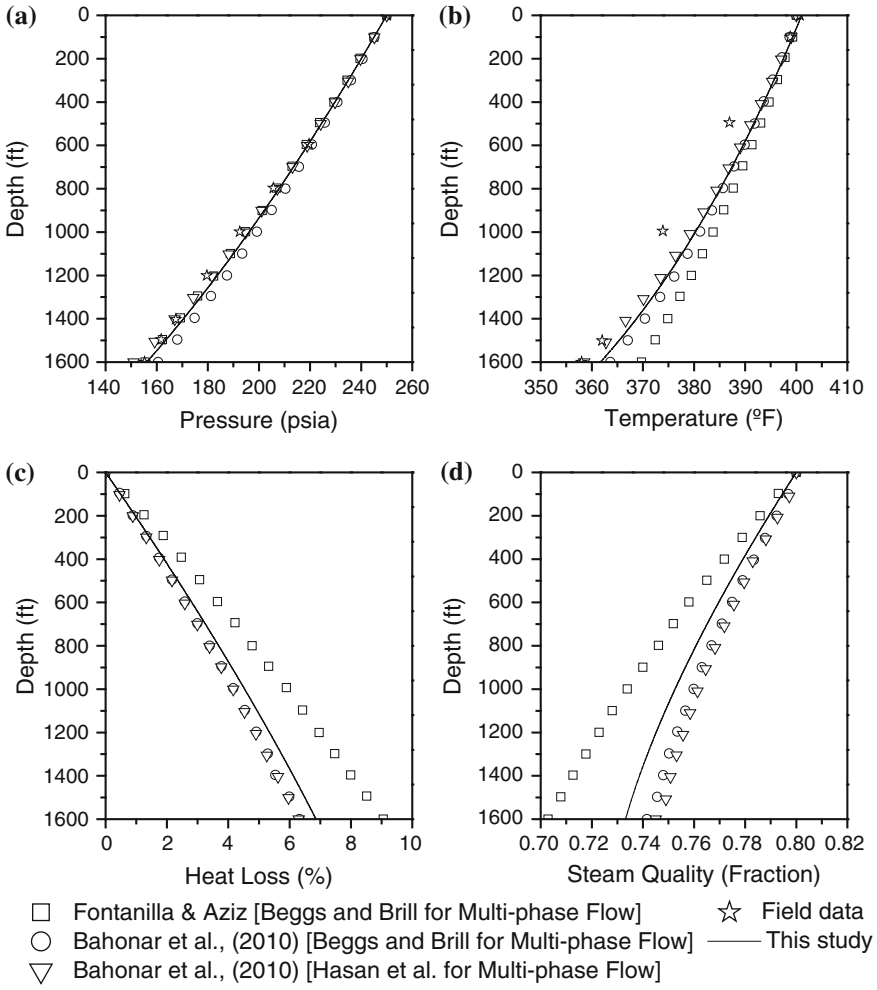

Fig. 2 Predictions at 71 h: **a** pressure (annular flow), **b** temperature (at 117 h), **c** heat loss, **d** steam quality

Figure 3 shows temperature in the cementing-porous medium interface. Temperature profile changes significantly for small steam injection times, however, as the steam injection period is higher temperature profiles are closer to each other. The system gets its steady state at 500 h, this means that the temperature difference between the well wall and the interface is almost constant. Therefore, the energy dissipation through the porous medium does not changes significantly when steam injection time is increased, this because the accumulation term in the energy diffusion equation (Eq. 6) is negligible.

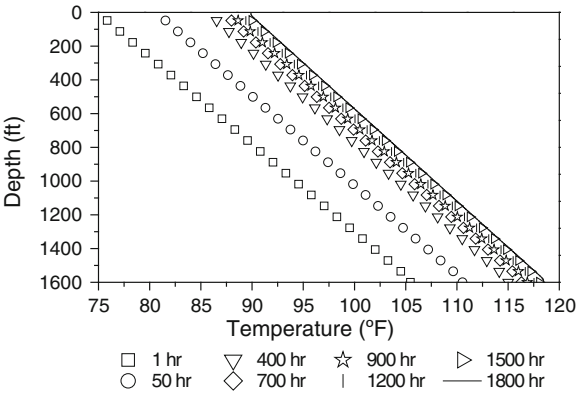

Fig. 3 Temperature prediction in the cementing-porous medium interface

5 Conclusions

The numerical results have good agreement against field data and predictions reported in literature.

For the conditions simulated, it was found that: (1) the thermal model reaches its steady state at 500 h, (2) due to few steam condensation, pressure drop due to gravity is smaller than the friction and acceleration contributions, and (3) temperature gradients are large at the beginning of steam injection, but they diminish along time.

References

Ali SMF (1981) A comprehensive wellbore stream/water flow model for steam injection and geothermal applications. SPE J Pet Technol 21(5):527–534. SPE-7966-PA. doi:10.7910.2118/7966-PA

Bahonar M, Azaiez J, Chen Z (2009) A semi-unsteady-state wellbore steam/water flow model for prediction of sandface conditions in steam injection wells. J Can Pet Technol 49(9):13–21

Durrant AJ, Thambynayagam RKM (1986) Wellbore heat transmission and pressure drop for steam/water injection and geothermal production: a simple solution technique. SPE, BP Petroleum Dev. Co

Fontanilla JP, Aziz K (1982) Prediction of bottom-hole conditions for wet steam injection wells. J Can Pet Technol 21(2):82–88

Hasan AR, Kabir CS (1994) Aspects of wellbore heat transfer during two-phase flow. Society of petroleum engineers

Hasan AR, Kabir CS, Sayarpour M (2007) A basic approach to wellbore two-phase flow modeling. In: Paper SPE 109868 presented at the SPE annual technical conference and exhibition, Anaheim, 11–14 November. doi:10.2118/109868-MS

Mozaffari S, Ehsani MR, Nikookar M, Sahranavard L (2011) Heat and mass transfer modeling in wellbore during steam injection process. Can J Chem Eng Technol 2(1):74–104

Pacheco EF, Ali SMF (1972) Wellbore heat losses and pressure drop in steam injection. SPE J Pet Technol 24(2):139–144. SPE-3428-PA. doi:10.3410.2118/3428-PA

Ramey HJ (1962) Wellbore heat transmission. SPE J Pet Technol 14(4):427–435. SPE-496-PA. doi:10.410.2118/2196-PA

Oxygen Transport Under Combustion Conditions in a Fracture-Porous Medium System

O. Cazarez-Candia, G. Rojas Altamirano and C.G. Aguilar-Madera

Abstract In this work the oxygen transport was modeled numerically, at pore scale, in a matrix-fracture system saturated by nitrogen. This system appears when the in-situ combustion (ISC) method is applied for oil recovery in fractured reservoirs. The main aim was to study the effect of oxygen flow rate and the fracture width on the oxygen transport from the fracture to the porous matrix due to this controls the combustion front propagation. The porous matrix microstructure was modeled as a medium composed by circular particles in a periodic arrangement. In order to simulate the combustion reaction that occurs in an in-situ combustion process, the coke-oxygen reaction was taken into account on the particles surface. The gas, coke and oxygen mass balances as well as the gas momentum balance were resolved using a software that involves the finite element technique. The oxygen distribution was studied in the matrix-fracture system as a function of: (1) the oxygen flow rate, and (2) the fracture width. It was found that increasing such parameters stimulate the coke consumption. Moreover, they increase the oxygen transport from the fracture to the matrix.

O. Cazarez-Candia (✉) · C.G. Aguilar-Madera
Instituto Mexicano del Petróleo, Eje Central Lázaro Cárdenas 152,
Del. Gustavo A. Madero, 07730 Mexico, D.F., Mexico
e-mail: ocazarez@imp.mx

G. Rojas Altamirano
Departamento de Metalmecánica, Instituto Tecnológico de Zacatepec,
Calzada Tecnológico No. 27, C.P. 62780 Zacatepec de Hidalgo, MOR, Mexico
e-mail: gullermo_rojas@live.com

C.G. Aguilar-Madera
Present Address Facultad de Ciencias de la Tierra, Universidad Autónoma de Nuevo León,
Ex–Hacienda de Guadalupe, C.P. 67700 Linares, N.L., Mexico
e-mail: carlos.aguilar@fct.uanl.mx

J. Klapp et al. (eds.), *Selected Topics of Computational and Experimental Fluid Mechanics*, Environmental Science and Engineering,
DOI 10.1007/978-3-319-11487-3_25

1 Introduction

The in-situ combustion (ISC) is one enhanced oil recovery method. It is applied mainly in heavy-oil reservoirs. In the ISC method, standard or oxygen enriched air are injected into the reservoir to promote the oil ignition and propagation of a combustion front from the injections wells to the producer wells. Thus, the high temperatures taking place inside the reservoir improve the oil mobility due to the reduction of its viscosity and fluid (steam, combustion gases, water) flooding. In ISC there are several complex mechanisms driving the momentum, energy and mass transport. The modelling of such mechanisms plays a crucial role for understanding the physics behind the process parameters.

Currently, a large amount of petroleum is in naturally fractured reservoirs. This has leaded to develop theoretical and experimental works for gaining knowledge about the effects that fractures have over the thermal and hydrodynamic performance of the ISC (Awoleke et al. 2010; Greaves et al. 1991; Schulte and de Vries 1985). The most of these works agree that the oxygen transport is one of the main features to sustain and propagate the combustion front. Thus, the oxygen dispersion from the fracture to the matrix plays a crucial role for the ISC inside the porous medium.

In an ISC process, the availability of oxygen is a key factor because several chemical reactions involve it with further heat releasing. The oxygen might react directly with some oil components, or with coke, which is produced by a pyrolysis reaction.

In this work, we focus specifically on the oxygen transport from fractures to porous medium at pore-scale, and eventually the influence of the fracture width, Peclet number and oxygen-coke reaction rate were studied. With these aims, we avoid the real complexity of an ISC process and we consider a two-phase (rock and gas), three-component (N_2, O_2 and coke), isothermal system. The porous medium has an idealized 2D microstructure, which is initially saturated with nitrogen.

2 Physical and Mathematical Models

An ISC process involves several phenomena interacting simultaneously in a multiphase mixture. For instance, we can quote: (1) the existence of several chemical reactions, (2) multicomponent and multiphase equilibrium, (3) multiphase flow, (4) thermal expansion, etc. In order to study such phenomena at lab-scale, combustion tube experiments are carried out, where air is injected to promote and propagate a combustion front (Mamora 1993; Cazarez-Candia et al. 2010).

The predominance of some phenomena over others yields characteristic zones in an ISC as: the burned, combustion, coking, condensing steam, water, oil and undisturbed zones (starting from the injection to the production well). A detailed explanation of each zone can be found in the work of Sarathi (1999). In Fig. 1 a simplified scheme of the coke and surrounding zones are depicted. There, the picture corresponds to a hypothetical combustion tube where the porous core is surrounded by an annular space representing the fracture. In our study we are interested only

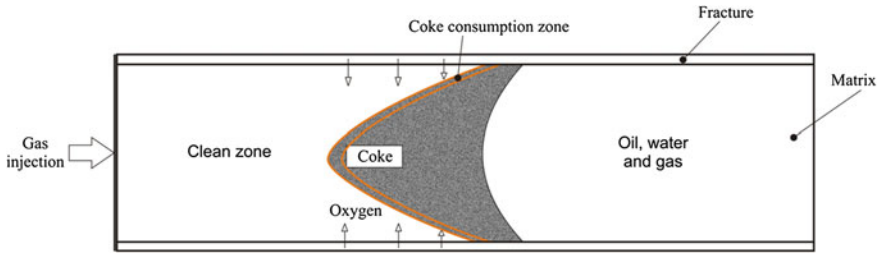

Fig. 1 Scheme of combustion and coke zones in a combustion tube

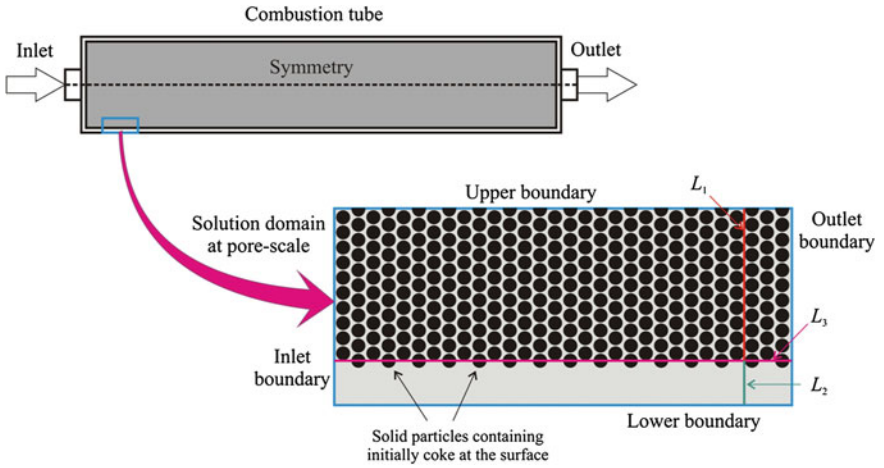

Fig. 2 Scheme of combustion tube and pore-scale domain for simulation

in the movement of oxygen through the clean zone until the coke zone be reached. With this aim, the production of combustion gases are ignored as these travel mainly ahead the coke consumption zone. Under the same premise, within the clean zone we consider only nitrogen and oxygen.

In order to carry out simulations at the pore-scale we need to reduce the solution domain to decrease the computing costs. With this aim, as depicted in Fig. 2, from the combustion tube containing a core surrounded by an annular fracture we take a small region encompassing some few solid particles. For the sake of simplicity, we adopt some assumptions and we focus only in the oxygen transport and its interaction with the coke through a combustion reaction. It is assumed that this reaction does not release heat neither produce other gases, i.e., the combustion reaction is used only to simulate the oxygen and coke consumption over the particles surface. The assumptions are summarized as follows:

(1) There is only gas in the system, avoiding the existence of oil and water. This is an idealized system, which can be found behind a combustion front (see Fig. 1).
(2) Initially there is coke homogeneously distributed over the entire particles surface.

(3) The porous matrix is idealized consisting in a periodic array of infinitely long, rounded solid rods, allowing to reduce the dimensionality to 2D (see Fig. 2).
(4) A first-order combustion reaction is assumed.
(5) The combustion reaction is isothermal, avoiding the solution of the energy balance.

The last issue indicates that the conditions for simulations are close to those encountered at the vicinity of the combustion front, where the combustion reaction takes relevance.

The existence of only gas in the system and an initial coke distribution is supported on the idea that these conditions are mainly met behind the combustion front. Indeed, as seen in Fig. 1, the assumptions mentioned above mean that our simulations correspond for the clean zone, where only there are sand and gas, and the coke zone represents the vicinity of the combustion front where simultaneously there are generation and consumption of coke.

2.1 Governing Equations, Initial and Boundary Conditions

The mathematical model includes the oxygen mass balance in the gas-phase

$$\frac{\partial C_{O_2}}{\partial t} + \mathbf{u} \cdot \nabla C_{O_2} = D_{O_2} \nabla^2 C_{O_2} \tag{1}$$

where C_{O_2} is the oxygen molar concentration and $D_{O_2}$is the oxygen diffusion coefficient inside the gas-phase. The field velocity $\mathbf{u}$ is computed through the solution of the gas momentum balance:

$$\rho \frac{\partial \mathbf{u}}{\partial t} + \rho \left(\mathbf{u} \cdot \nabla\right) \mathbf{u} = -\nabla \cdot (p\mathbf{I}) + \nabla \cdot \left\{ \mu \left[\nabla \mathbf{u} + (\nabla \mathbf{u})^T \right] - \frac{2}{3} \mu \left(\nabla \cdot \mathbf{u}\right) \mathbf{I} \right\} \tag{2}$$

Here ρ is the mixture density, p is pressure and μ viscosity. In addition, the gas-phase continuity equation is required,

$$\frac{\partial \rho}{\partial t} + \nabla \cdot (\rho \mathbf{u}) = 0 \tag{3}$$

Equations (2) and (3) are enforced to satisfy the following initial and boundary conditions (see Fig. 2 to identify each boundary):

$$\text{At} \qquad t = 0, \quad C_{O_2} = 0, \quad \mathbf{u} = 0, \quad p = p_{atm} \tag{4}$$

At the inlet boundary:

$$C_{O_2} = C_{O_2}^{inj}, \quad \mathbf{u} = -\frac{F^{inj}}{\rho} \mathbf{n} \tag{5}$$

At the upper boundary:

$$-\mathbf{n}\cdot\mathbf{N}_{O_2}=0,\quad \mathbf{u}\cdot\mathbf{n}=0,\left[\nabla\mathbf{u}+(\nabla\mathbf{u})^T\right]\mathbf{n}-\left\{\left[\nabla\mathbf{u}+(\nabla\mathbf{u})^T\right]\mathbf{n}\cdot\mathbf{n}\right\}\mathbf{n}=0 \tag{6}$$

At the lower boundary:

$$-\mathbf{n}\cdot\mathbf{N}_{O_2}=0,\quad \mathbf{u}=0 \tag{7}$$

At the outlet boundary

$$-\mathbf{n}\cdot\left(\nabla C_{O_2}\right)=0,\ p=p_{atm},\left[\nabla\mathbf{u}+(\nabla\mathbf{u})^T-\frac{2}{3}(\nabla\cdot\mathbf{u})\mathbf{I}\right]\mathbf{n}=0 \tag{8}$$

At the particle surface:

$$-\mathbf{n}\cdot\mathbf{N}_{O_2}=-K_r C_{O_2} C_{coke},\ \mathbf{u}=0 \tag{9}$$

In Eqs. (4)–(9) p_{atm} is the atmospheric pressure, $\mathbf{I}$ is the identity tensor, $C_{O_2}^{inj}$ is the oxygen concentration in the injected gas, F^{inj} is the mass flux of the injected gas, $\mathbf{n}$ is the unit normal vector pointing outside the boundary, K_r is the reaction rate constant, C_{coke} is the coke surface molar concentration at the particle surface, and $\mathbf{N}_{O_2}$ represents the oxygen total molar flux expressed in the next form

$$\mathbf{N}_{O_2}=-D_{O_2}\nabla C_{O_2}+\mathbf{u}C_{O_2} \tag{10}$$

The units of C_{O_2} and C_{coke} are mole/m^3 and mole/m^2, respectively. As initially the oxygen concentration is 0, then the gas is only composed by nitrogen with a molar concentration depending on temperature and pressure.

In turn, the coke concentration at the particle surface is computed through the solution of the following differential equation

$$\frac{\partial C_{coke}}{\partial t}=-\eta K_r C_{O_2} C_{coke} \tag{11}$$

where η is the stoichiometric coefficient between oxygen and coke. This equation has the next initial condition

$$\text{At}\qquad t=0,\ C_{coke}=C_{coke}^{o} \tag{12}$$

where C_{coke}^{o} is the initial coke concentration.

On the other hand, the density (ρ) was calculated using the real gas equation, the reaction rate constant (K_r) was obtained using an Arrhenius-type expression, and the gas viscosity was calculated with the Wilke approach (Wilke 1950) for binary mixtures at low pressures. The oxygen diffusivity was obtained from the work of Bird et al. (2010).

3 Results and Discussions

For solving Eqs. (1)–(3), along its initial and boundary conditions, we used a finite element solver ensuring mesh-independent results. For model validation purposes the experimental concentration profile of a tracer (Rolle et al. 2012), that is injected in a system of porous medium saturated with water, was simulated. An excellent fitting was obtained. For more details we refer the reader to the work of Rolle et al. (2012).

In all simulations, we used 300 particles with 0.3 mm diameter, and arranged in a simple periodic array. Such particle diameters are according to those encountered in combustion tube experiments (Cazarez-Candia et al. 2010). In our study, the matrix porosity was 0.4. The total length of the domain is 10.49 mm and the height only including the porous medium is 3.5137 mm, see Table 1.

3.1 Effect of the Fracture Peclet Number

The effect of the fracture Peclet number (Pe_f) over the non-dimensional oxygen and coke concentration profiles is illustrated in Fig. 3, for t = 25 and 145 s. The plotted results correspond for diffusive ($Pe_f = 0{:}01$), competitive ($Pe_f = 1$) and convective ($Pe_f = 10$) regimes in the fracture. Indeed, a given value of Pe_f does not necessarily mean that such Pe_f also stands inside the porous medium. However, we use Pe_f, as our priority is to investigate the influence that fractures have over the ISC inside the porous matrix. In our simulations, the manipulation of Pe_f was made by increasing or decreasing the injected flow F_{inj}.

As F_{inj} increases, coke is faster consumed mainly by the increasing oxygen availability that takes place by two reasons:

Table 1 Values of some parameters used in the simulations

Parameter	Value	Reference/comments
μ_{O_2}	1.76×10^{-5} kg/(m s^2) at 293.15 K	White (2001), Table A.4
μ_{N_2}	2.00×10^{-5} kg/(m s^2) at 293.15 K	White (2001), Table A.4
D_{O_2}	0.181 cm^2/s at 273.2 K	Bird et al. (2010), Table 17.1-1
η	1/1.18	Fadaei (2009), Table 3.4
Oil API	26	
M_{coke}	13.1 g/mole	Fadaei (2009), Table 3.3
M_{oil}	290 g/mole	Fadaei (2009), Table 3.3
C^0_{coke}	6,745 mol/(a_v m^3)	Based on the assumption that 10 % of oil is converted to coke (Schulte and de Vries 1985). a_v is the particle specific surface area

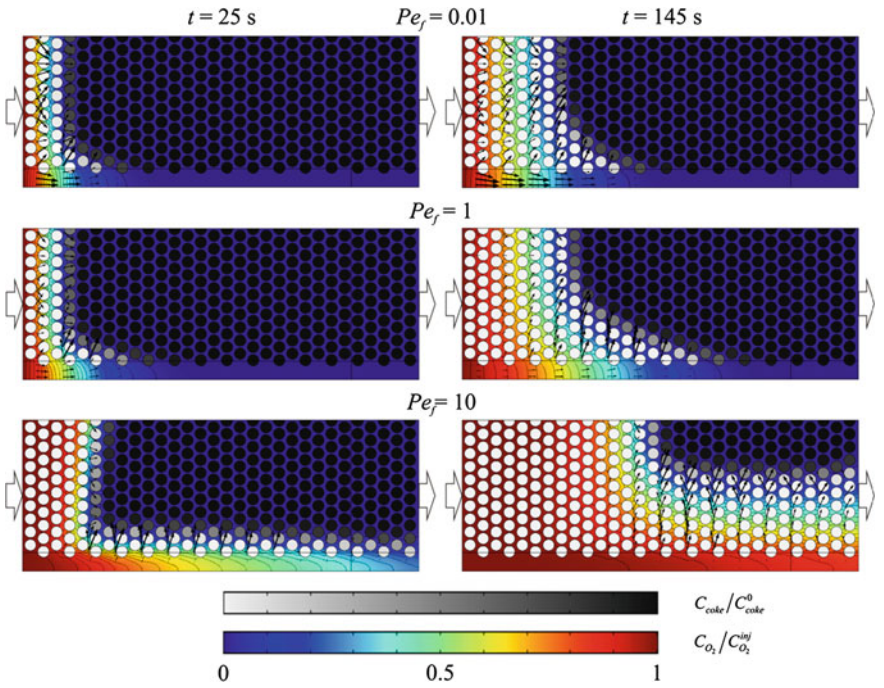

Fig. 3 Oxygen and coke concentration profiles as function of time and fracture Peclet number ($W_f = 1.67d_p$)

3.2 Effect of the Fracture Width

As the fracture width increases the amount of oxygen being transported through the fracture is augmented. As the oxygen storage in the fracture is increased, the oxygen flow from the fracture to the matrix is enhanced. This issue is shown in Fig. 4 where oxygen concentration profiles are presented for t = 55 and 255 s, and $W_f = 1.67$, 3.34 and $6.67d_p$. The arrows direction show that oxygen is transported from the fracture and, in this way, the coke is faster consumed as W_f increases.

4 Conclusions

The oxygen transport, in a matrix-fracture system saturated by nitrogen, was modeled numerically, at pore scale. In an in-situ combustion process, a coke-oxygen reaction occurs and it was taken into account. The oxygen distribution was studied in the matrix-fracture system as a function of: (1) the oxygen flow rate, and (2) the fracture width. It was found that increasing such parameters stimulate: (1) the coke

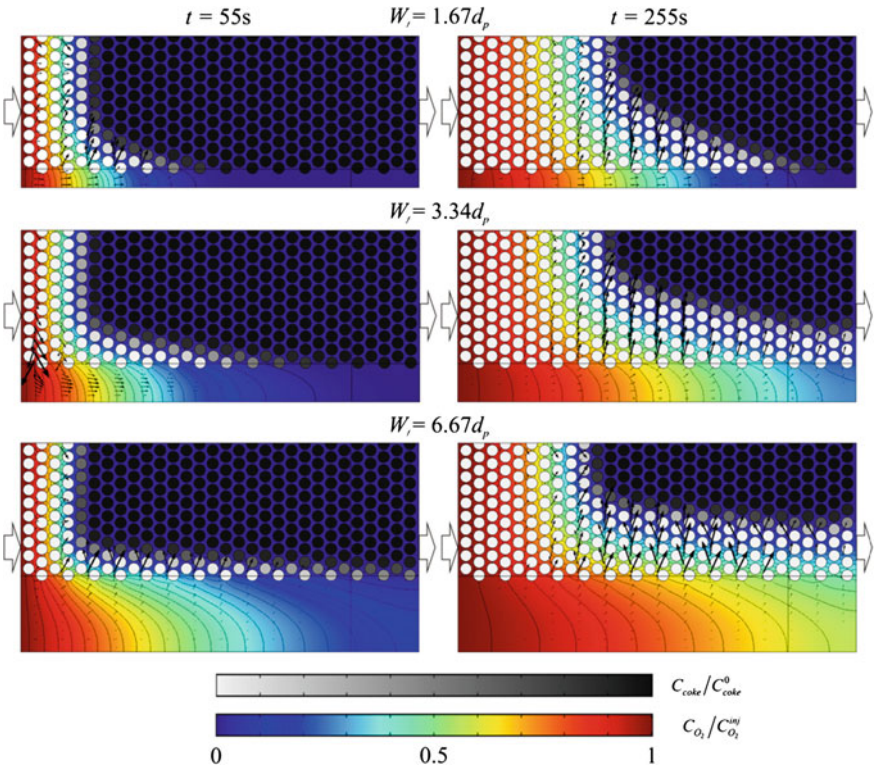

Fig. 4 Oxygen and coke concentration profiles as function of time and fracture width ($Pe_f = 1$)

consumption and (2) the oxygen transport from the fracture to the porous zone. These conclusions are explained below.

As oxygen flow rate increases, coke is faster consumed mainly by the increasing oxygen availability that takes place by two reasons: (1) the amount of oxygen, entering to the porous zone through the inlet boundary, is increased and, (2) the amount of oxygen, entering from the fracture to the matrix, is considerably augmented. On the other hand, as the fracture width increases, the amount of oxygen being transported through the fracture is augmented. Then, as the oxygen storage in the fracture is increased, the oxygen flow from the fracture to the matrix is enhanced.

References

Awoleke OG, Castanier LM, Kovscek AR (2010) An experimental investigation of in-situ combustion in heterogeneous media. In: Canadian unconventional resources and international petroleum conference. No. 137608-MS. Canadian Society for Unconventional Gas/Society of Petroleum Engineers, Calgary, Alberta, Canada, 19–21 October 2010

Bird RB, Stewart WE, Lightfoot EN (2010) Fenomenos de transporte. Limusa Wiley, Mexico DF
Cazarez-Candia O, Cruz-Hernandez J, Islas-Juarez R, Marquez-Ramirez E (2010) A theoretical and experimental study of combustion tubes. Pet Sci Technol 28:1186–1196
Fadaei H (2009) Etude de la récupération de bruts lourds en réservoir carbonaté fracturé par le procédé de combustion in situ. Doctoral dissertation, Université de Toulouse
Greaves M, Javanmardi G, Field RW (1991) In situ combustion (isc) in fractured heavy oil reservoirs. In: 6th European IOR-symposium. Stavanger, Norway, 21–23 May 1991
Mamora DD (1993) Kinetics of in situ combustion. Doctoral dissertation, Stanford University
Rolle M, Hochstetler D, Chiogna G, Kitanidis PK (2012) Experimental investigation and pore-scale modeling interpretation of compound-specific transverse dispersion in porous media. Transp Porous Media 93:347–362
Sarathi P (1999) In-situ combustion handbook- principles and practices. Technical Report DOE/PC/91008-0374, OSTI ID 3174, National Petroleum Technology Office, Tulsa, USA
Schulte WM, de Vries AS (1985) In-situ combustion in naturally fractured heavy oil reservoirs. Soc Pet Eng J 25(1):67–77
White FM (2001) Fluid mechanics. McGraw-Hill, Boston USA
Wilke CR (1950) A viscosity equation for gas mixtures. J Chem Phys 18:517

Numerical Simulation of the Flow in an Open Cavity with Heat and Mass Transfer

G.E. Ovando Chacon, S.L. Ovando Chacon, J.C. Prince Avelino, A. Servin Martínez and J.A. Hernández Zarate

Abstract In the present work, we analyze the laminar steady-state fluid dynamics, heat and mass transfer in a two-dimensional open cavity for the decomposition of a substance. The numerical study is carried out for Reynolds numbers of 10, 25 and 50 with a Schmidt number of 425. A hot plate is provided at the bottom of the cavity which generates the thermal decomposition of the substance. In order to investigate the effect of the length of the plate two different plate sizes are considered. The governing equations of continuity, momentum, mass transport and energy for incompressible flow are solved by the finite element method combined with an operator-splitting scheme. We calculate the temperature field, the streamlines, the velocity and the concentration field and analyze the velocity, concentration and temperature profiles as a function of the transversal position. We find that the Reynolds number plays a major role in the mass transport and the thermal behavior of the flow inside the cavity.

G.E. Ovando Chacon (✉) · J.C. Prince Avelino · A. Servin Martínez
J.A. Hernández Zarate
Depto. de Metal Mecánica y Mecatrónica, Instituto Tecnológico de Veracruz,
Calzada Miguel A. de Quevedo 2779, 91860 Veracruz, Col. Formando Hogar, Mexico
e-mail: geoc@itver.edu.mx

J.C. Prince Avelino
e-mail: jcpa@itver.edu.mx

A. Servin Martínez
e-mail: alservinm@gmail.com

J.A. Hernández Zarate
e-mail: jorgeahz67@yahoo.com.mx

S.L. Ovando Chacon
Depto. de Química y Bioquímica, Instituto Tecnológico de Tuxtla Gutiérrez,
Carretera Panamericana Km. 1080, Tuxtla Gutiérrez, Chiapas, Mexico
e-mail: ovansandy@hotmail.com

J. Klapp et al. (eds.), *Selected Topics of Computational and Experimental Fluid Mechanics*, Environmental Science and Engineering,
DOI 10.1007/978-3-319-11487-3_26

1 Introduction

The fluid flow in an open cavity with heat and mass transfer is an important issue in many technological processes. Deng et al. (2004) investigated the fluid, heat and contaminant transport structures of mixed convection in a two-dimensional ventilated room with heat and contaminant sources while Beya and Lili (2007) analyzed the unsteady heat and mass transfer by mixed convection in a two-dimensional ventilated enclosure, obtaining the streamlines, heatlines and masslines for different cases. More recently, Serrano-Arellano and Gijon-Rivera (2014) studied the heat and mass transfer in a two dimensional differentially heated closed square cavity, where the working fluid is initially at rest and with a uniform temperature. Kuznetsov and Sheremet (2009) reported a numerical study on the conjugate heat transfer in a rectangular enclosure under the assumption of internal mass transfer and in the presence of local heat and contaminant sources. The double-diffusive mixed convection in a lid-driven triangular cavity filled with air has been examined by Hasanuzzaman et al. (2012). The bottom and inclined walls of the triangle had constant high temperature and low temperature, respectively. On the other hand Shehata et al. (1999) both studied both experimentally and numerically the mass transfer to the bottom wall of a cavity in the presence of an external unsteady flow, while Jeng et al. (2009) reported an experimental and numerical study of the flow structure and mass transfer on inclined, low aspect ratio enclosures. The present study addresses the effect of the heater length and Reynolds number on the heat and mass transfer in an open cavity.

2 Problem Formulation

Consider an open cavity with a hot plate at the bottom which generates the thermal decomposition of a substance, as shown in Fig. 1. The flow is assumed to be laminar, steady and two-dimensional. The Reynolds numbers ($Re = U_m h/\nu$), based on the velocity of the inlet flow U_m and the height h of the entrance of the cavity, studied in this investigation were $Re = 10, 25$ and 50 for a Schmidt number of $\mathrm{Sc} = 425$

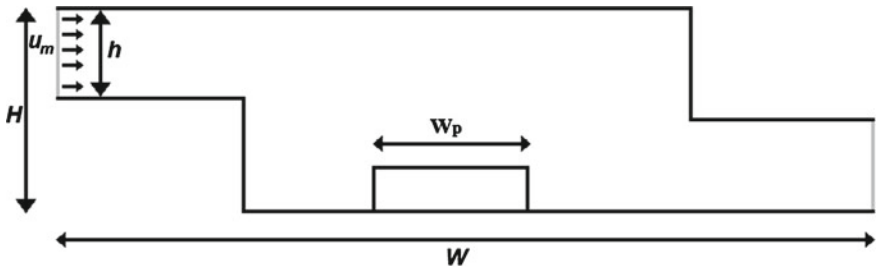

Fig. 1 Geometry of the open cavity with heat and mass transfer

and a Prandtl number of $Pr = 6.0$. The entrance and exit of the cavity was fixed to $h = 0.4\,H$, where H is the height of the cavity with a length of $W = 4H$. Two different lengths of the heater plate $W_p = W/5$ and $W_p = W/3.33$ were analyzed. The horizontal and vertical dimensions of the cavity are $W = 0.2\,\text{m}$ and $H = 0.05\,\text{m}$, respectively.

The governing equations for a non-isothermal incompressible steady-state flow in a two-dimensional domain Ω are given by:

$$-\frac{1}{\text{Re}}\Delta\mathbf{u} + \mathbf{u}\cdot\nabla\mathbf{u} = -\nabla p, \tag{1}$$

$$\nabla\cdot\mathbf{u} = 0, \tag{2}$$

$$-\frac{1}{\text{Re}\,\text{Pr}}\Delta T + \mathbf{u}\cdot\nabla T = Q. \tag{3}$$

The mass transfer by thermal decomposition inside the cavity depends on both the fluid flow and the temperature distribution, and is given as:

$$-\frac{1}{\text{Re}\,Sc}\Delta C_A + \mathbf{u}\cdot\nabla C_A = R, \tag{4}$$

In the above equations $\mathbf{u} = (u_1, u_2)$ is the velocity vector, being u_1 y u_2 the horizontal and vertical velocity components, respectively; p is the pressure, T is the temperature, and C_A is the concentration. Q and R are the source term in the energy and mass transport equations, respectively, defined as follows:

$$Q = \frac{r\Phi h}{\rho C_p U_m\,(T_H - T_C)}, \tag{5}$$

and

$$R = \frac{-rh}{U_m C_{Ac}}, \tag{6}$$

where Φ is the heat of reaction, ρ is the density, Cp is the specific heat capacity at constant pressure and C_{Ac} is the concentration of reference. In addition r is the reaction rate defined as:

$$r = kC_A, \tag{7}$$

where k is the rate constant:

$$k = Ae^{-E/R_g T}. \tag{8}$$

Here A is the frequency factor, E is the activation energy and R_g is the fluid constant.

3 Numerical Solution and Validation of the Results

Numerical simulations were conducted for the laminar flow inside a horizontal open cavity for Reynolds numbers ranging between 10 and 50. A 2D geometry was used (see Fig. 1) and several types of meshes were included in order to obtain independent results from the numerical parameters. The governing equations were solved with the finite element method combined with the operator splitting scheme Glowinski (2003). This approach was implemented in a numerical code, developed by the authors and written in Fortran 90. The convergence analysis was done for three different meshes consisting of 4,850, 14,900 and 18,250 elements. An analysis of the temperature profiles on the middle horizontal and vertical lines indicates that the largest difference of the results between the meshes of 4,850 and 14,900 was 8.5 %, while the maximum difference of the results between the meshes of 14,900 and 18,250 was 1.0 %. The analysis was also done for the velocity components, in which cases the worst relative error between the meshes of 14,900 and 18,250 was less than 1.0 %. The simulations presented in this paper were performed for a cavity with a mesh of 18,250 elements. The validation of the computer code has been carried out for the double-diffusive mixed convection in a ventilated cavity by Deng et al. (2004). The average Nusselt number obtained with this code for $Gr = 18{,}207$ and $Re = 500$ was 1.59 which coincides with the value of (1.61) reported by Deng et al. (2004).

4 Results and Discussions

The results are given in terms of streamlines, isotherms, Nusselt numbers and velocity profiles, temperature and concentration. Figure 2 shows streamlines for the case of $W_p = W/5$. The top panel shows the behavior of the fluid inside the cavity for $Re = 10$, where three vortices can be observed, the first one is a big, strong and

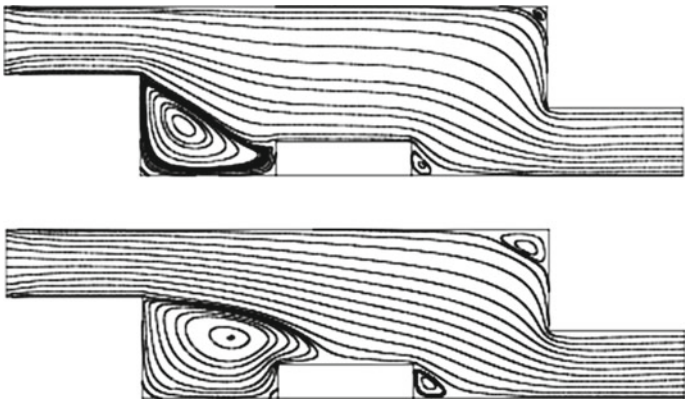

Fig. 2 Streamlines for $W_p = W/5$. *Top* $Re = 10$. *Bottom* $Re = 50$

clockwise vortex located after the step of the cavity; the second vortex appears after the heater of the cavity with a clockwise rotation. These two vortices are formed as a result of the boundary layer detachment from the surface driven by the fluid motion that crosses the cavity. At the superior right corner, a third weak, anti-clockwise vortex emerges from the impingement of the fluid with the corner. Furthermore, for $Re = 50$ the same vortex distribution can be observed (see bottom panel). However, the size of the vortices is increased. The main vortex extends over the heater affecting the energy and mass transport inside the cavity. The jet emerges horizontally from the flow inlet of the cavity, but as it moves ahead of its horizontal component decreases and the vertical component increases due to the change of the transversal area of the cavity.

Figure 3 shows the isotherms for $W_p = W/5$. The top panel shows the thermal behavior of the fluid inside the cavity for $Re = 10$, while the bottom panel is for $Re = 50$. It can be seen that the temperature contours are clustered around the heater, and a hot temperature region grows toward the middle of the cavity due to the thermal plume that heats the fluid in the neighborhood of the heater. However, beyond this region the contours tend to elongate from the heater toward the exit of the cavity and they also spread toward the interior part of the cavity with smaller values since the fluid is cooled as a result of the flow motion that crosses the cavity. Increasing the Reynolds number, a stronger disturbance of the contours can be appreciated behind the heater. Furthermore, for a higher Reynolds number the thermal plume does not completely ascend up to the top part of the cavity, instead it is dispersed towards the exit of the cavity.

For $Re = 50$, the fluid behind the heater is hotter than the fluid in front of it, hence, the left region of the heater can have a higher heat generation rate. For $Re = 10$, the fluid in front of the heater is hotter than the fluid behind the heater, and hence, the right region of the heater can have a higher heat generation rate. However, we note that in both cases the temperature decreases away from the heater, and the maximum temperature occurs in the layer of fluid adjacent to the heater. For the low Reynolds number stratification can be observed in the isothermal; and the lower the

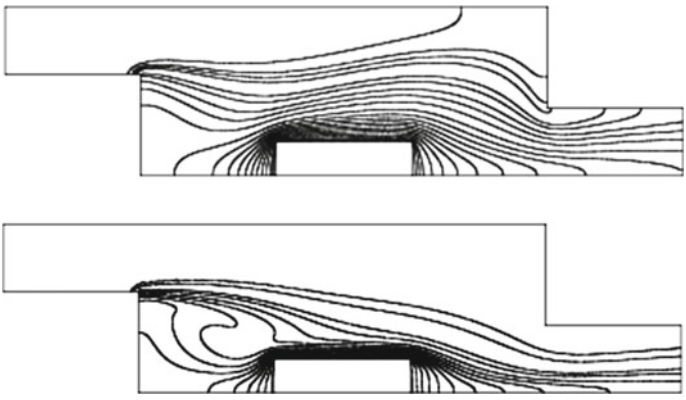

Fig. 3 Isotherms for $W_p = W/5$. *Top* $Re = 10$. *Bottom* $Re = 50$

flow velocity the hotter is the cavity. As expected, on the right side of the heater the contours are distorted and follow the main stream direction toward the outlet of the cavity. The two vortices associated to the heater transport hot fluid heating the main stream of fluid. The interaction of the solid heater with the flow generates a thermal boundary layer separation which is recirculated there by increasing the heat transfer from the heater to the fluid.

Figure 4 shows the concentration contours for $W_p = W/5$. The top panel shows the behavior of the concentration inside the cavity for $Re = 10$, where gradual reduction of the concentration can be observed along the fluid motion path due to the heating decomposition of the substance. At the entrance the concentration is $C_A = 1$. However, at the neighborhood of the heater it is zero as a consequence of the effect of the temperature. On the top right corner the concentration also tends to zero as a result of the heating of the fluid in this region, which is associated with the rise of the thermal plume. At the exit of the cavity the concentration is practically zero, meaning that the substance has been completely decomposed. The bottom panel shows the behavior of the concentration inside the cavity for $Re = 50$. For this case, incomplete decomposition is observed and the concentration is reduced to only about 50 % because the flow velocity increases and the main stream of fluid remains cool. For $Re = 10$, the outlet flow concentration was 0.08, while for $Re = 50$, the outlet flow concentration was 0.5.

Figure 5 shows the axial velocity profile (left panel), and the temperature profile (right panel) on the middle vertical line for $W_p = W/5$ and three different Reynolds numbers. From the axial velocity profile, we may observe that this velocity component increases as the Reynolds number is increased. On the heater the axial velocity is zero and increases up to a maximum value to finally decrease to zero on the upper wall of the cavity. From the temperature profile, it can be appreciated that the temperature is 1 on the heater and starts to reduce as the transversal coordinate increases and becomes zero at $y/H = 0.5$. Furthermore, the temperature is reduced more rapidly as the Reynolds number is increased.

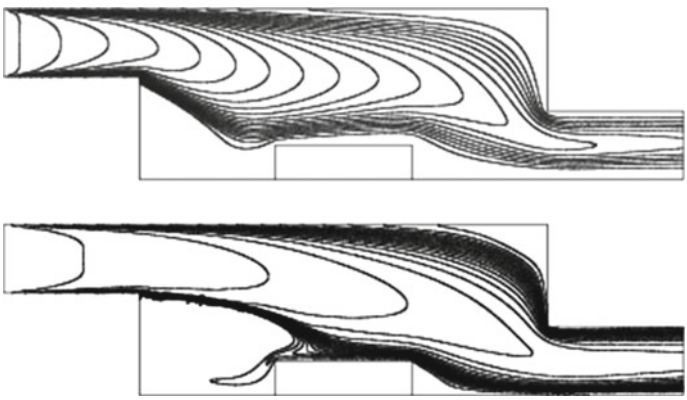

Fig. 4 Concentration for $W_p = W/5$. *Top* $Re = 10$. *Bottom* $Re = 50$

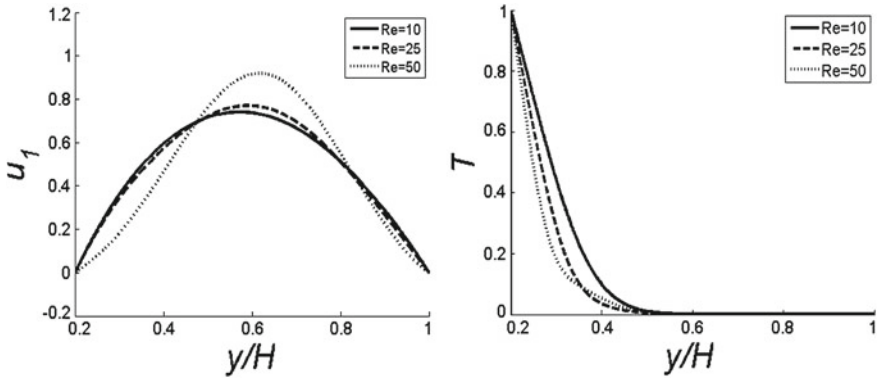

Fig. 5 Axial velocity profile (*left*) and temperature profile (*right*) at $x/H = 2.0$ for $W_p = W/5$ with three different Reynolds numbers

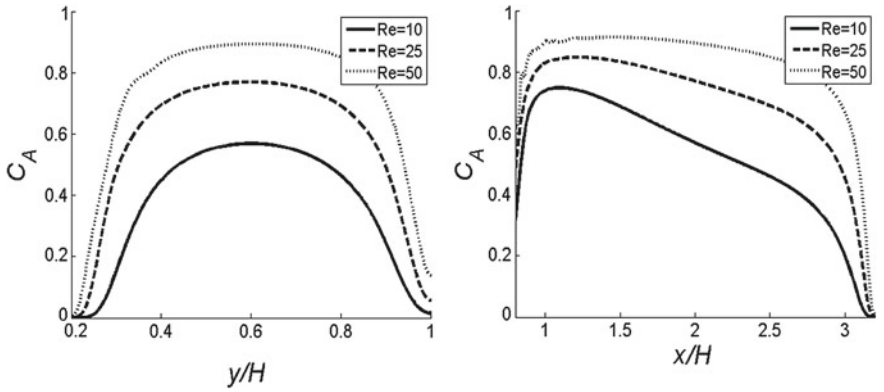

Fig. 6 *Left* Transversal concentration profiles at $x/H = 2.0$. *Right* Axial concentration profiles at $y/H = 0.6$ for $W_p = W/5$

Figure 6 shows the concentration profiles for $W_p = W/5$. The left profile is the transversal concentration on the middle vertical line, indicating that the concentration starts to increase, reaches a maximum value about $y/H = 0.6$ and then decreases. The larger the Reynolds number the greater the concentration values are. The right profile is the axial concentration at $y/H = 0.6$, which indicates that the concentration tends to reduce as the fluid passes through the heater. The initial reduction of the concentration can be explained by the heating of the fluid at the region where the vortices recirculate hot fluid. It is also observed that as the Reynolds number is increased the variations in the concentration of the substance are lower due to less heating of the fluid.

Figure 7 shows the effect of the heater length on the temperature profile at the middle vertical line and the Nusselt number as a function of the Reynolds number. From the left panel of the figure, it can be observed that increasing the length of the

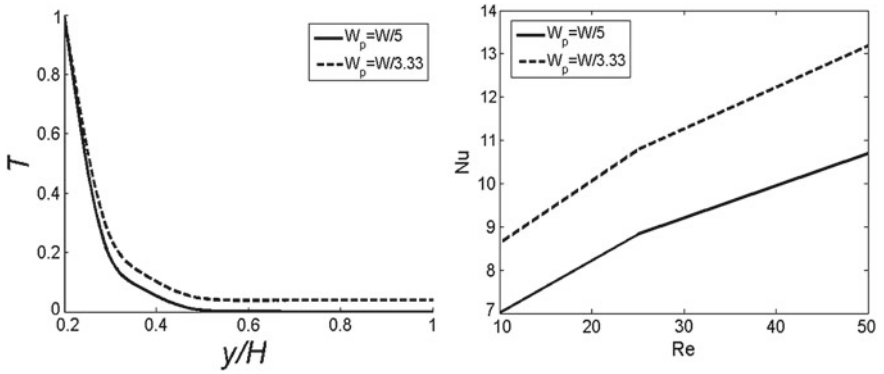

Fig. 7 Effect of the heater length on the temperature profile at $x/H = 2.0$ and Nusselt number for various Reynolds number

heater the fluid temperature does not decay to zero, since more energy is injected by the heater to the fluid. The right panel of the figure indicates that for a specific Reynolds number, increasing the length of the heater leads to an increase of the heat transfer rate. By further increasing the Reynolds number for a given length of the heater, the heat transfer rate to the fluid is also increased, so more energy can be transported by the fluid, which therefore causes it to release more heat from the cavity.

5 Conclusions

The fluid dynamics, heat and mass transfer in an open cavity for the de composition of a substance is investigated in this work. The analysis is carried out for the laminar flow and the governing equations were solved with the finite element method. The simulations revealed several interesting features concerning the flow structure, thermal and mass transport inside the open cavity as function of the length of the heater and the Reynolds number. For $Re = 10$, the concentration at the exit of the cavity is practically zero and the substance has been completely decomposed. However, for $Re = 50$ incomplete consumption of the substance is observed and the outlet concentration is reduced to only about 50 % due to higher inlet velocity keeping the main stream of the flow at lower temperature. On the other hand, if the length of the heater increases, the temperature inside the cavity is increased due to energy injection from the plate to the fluid being improved. As a result the decomposition of the substance inside the cavity is more efficient.

References

Beya BB, Lili T (2007) Oscillatory double-diffusive mixed convection in a two-dimensional ventilated enclosure. Int J Heat Mass Transf 50:4540–4553

Deng Q, Zhou J, Mei C, Shen Y (2004) Fluid, heat and contaminant transport structures of laminar double-diffusive mixed convection in a two-dimensional ventilated enclosure. Int J Heat Mass Transf 47:5257–5269

Glowinski R (2003) Numerical methods for fluids. Part 3. In: Garlet PG, Lions JL (eds) Handbook of numerical analysis, vol IX. North-Holland, Amsterdam

Hasanuzzaman M, Rahman MM, Oztop HF, Rahim NA, Sidur R (2012) Effects of Lewis number on heat and mass transfer in a triangular cavity. Int Commun Heat Mass Transf 39:1213–1219

Jeng DZ, Yang CS, Gau C (2009) Experimental and numerical study of transient natural convection due to mass transfer in inclined enclosures. Int J Heat Mass Transf 52:181–192

Kuznetsov GV, Sheremet MA (2009) Conjugated heat transfer in an enclosure under the condition of internal mass transfer and in the presence of the local heat source. Int J Heat Mass Transf 52:1–8

Serrano-Arellano J, Gijon-Rivera M (2014) Conjugated heat and mass transfer by natural convection in a square cavity filled with a mixture of air-CO_2. Int J Heat Mass Transf 70:103–113

Shehata AK, Yang JD, West AC, Modi V (1999) Effect of an unsteady external flow on mass transfer to cavities. Int J Heat Mass Transf 42:673–683

3D Numerical Simulation of Rayleigh-Bénard Convection in a Cylindrical Container

N.Y. Sánchez Torres, E.J. López Sánchez, S. Hernández Zapata and G. Ruiz Chavarría

Abstract The heat transport by natural convection is a central mechanism in the explanation of many natural phenomena. Despite many existing work on the Rayleigh-Bénard convection, often the phenomenon is studied by making a two-dimensional approach or using a rectangular container. In this work, we solve numerically the Navier-Stokes, continuity and energy equations in cylindrical coordinates. To this end a finite difference scheme is used for the time and spatial coordinates r and z, whereas a Fourier spectral method is used for the angular coordinate. The advantage of this procedure is that it can be easily parallelized. The numerical results include the formation of concentric rolls and other patterns, which are compared with experimental results reported in the literature.

1 Introduction

An important problem in Fluid Mechanics is the study of convection. In this paper we focus our attention on a liquid layer heated from below and initially at rest. Depending on a dimensionless parameter, that is, the Rayleigh number (R_a), the final state can be a pattern of cells or even the transition to a turbulent state. The stability theory, the experiments and numerical simulations agree in that the critical Rayleigh number is 1708 (Chandrasekhar 1961; Rayleigh 1916; Guyon et al. 2001; Bodenschatz et al. 2000). Below this value the fluid remains at rest. Analytical results on this problem have been obtained within the framework of hydrodynamic stability, which provides information about critical values of dimensionless parameters and the wavenumber of the most unstable perturbation. Often the stability analysis is performed assuming small two-dimensional disturbances so that nonlinear terms are neglected (Drazin and Reid 1981; Chandrasekhar 1961). The factors influencing the growth of instabilities are viscosity, bouyancy and the surface tension if the upper boundary is a free surface.

N.Y. Sánchez Torres · E.J. López Sánchez (✉) · S. Hernández Zapata · G. Ruiz Chavarría
Facultad de Ciencias, Universidad Nacional Autónoma de México,
Ciudad Universitaria, 04510 Mexico, D.F., Mexico
e-mail: lsej@ciencias.unam.mx

J. Klapp et al. (eds.), *Selected Topics of Computational and Experimental Fluid Mechanics*, Environmental Science and Engineering,
DOI 10.1007/978-3-319-11487-3_27

When Bénard began to study this problem, he decided to keep free the upper surface. He observed the formation of hexagonal cells [Bénard-Marangoni problem, (Bénard 1900; Guyon et al. 2001; Bodenschatz et al. 2000)]. When Rayleigh studied this problem, he assumed that all boundaries of the fluid layer are solid walls. He observed the formation of rolls instead of hexagonal cells [Rayleigh-Bénard problem, hereafter referred to as the R-B problem (Chandrasekhar 1961; Rayleigh 1916; Guyon et al. 2001; Bodenschatz et al. 2000)].

In this work we solve numerically the equations governing the R-B convection in a cylindrical container (3D). This problem has been studied previously (Getling and Brausch 2003). In most cases the geometry was a rectangular box (Valencia 2005; Ternik et al. 2013), or cylindrical one (Tagawa et al. 2003; Li et al. 2012; Paul et al. 2003). The numerical simulation was done by using a Fourier spectral method (Boyd 2000; Peyret 2002) for the angular coordinate and finite differences for the radial and vertical coordinates. In addition, we use a semi-implicit Adams-Bashforth second order scheme. The choice of a Fourier spectral method was made on the basis that it is easy to run the code in parallel provided the Adams-Bashforth scheme is used. Under this condition we have for each Fourier mode a system of equation decoupled from other modes. Finally the Navier-Stokes equations are solved with the projection method.

This paper is organized as follows. In Sect. 2, we expose the methodology used in the numerical study, including the differential equations for the R-B convection. In Sect. 3, we show some numerical results and a comparison with cases reported in the literature. In the last section, we draw some conclusions.

2 Methodology

For the study of convection of a liquid heated from below we need to solve the three components of the Navier-Stokes equations along with the continuity and the energy equations. In order to compare with other results, we need to write down the equations in dimensionless form. To this end we use κ/d as a representative velocity, the characteristic length is the height of the container d and the characteristic time is d^2/κ, where κ is the thermal diffusivity coefficient. In addition, we assume that the density depends on temperature. We use the Boussinesq hypothesis according to which the density is left constant except in the bouyancy term. The equations to solve are:

$$\nabla^* \cdot \mathbf{u}^* = 0$$

$$\frac{\partial \mathbf{u}^*}{\partial t^*} + (\mathbf{u}^* \cdot \nabla^*)\mathbf{u}^* = -[g^* - R_a P_r (T^* - T_0^*)]\hat{k} - \nabla^* P^* + P_r \nabla^{*^2} \mathbf{u}^*$$

$$\frac{\partial T^*}{\partial t^*} + \mathbf{u}^* \cdot \nabla^* T^* = \nabla^{*^2} T^*,$$

where the asterisk means dimensionless variables and operators. The dimensionless parameters are Prandtl $P_r = \nu/\kappa$ and Rayleigh $R_a = g\alpha\beta d^4/(\kappa\nu)$ numbers. The unknowns are the velocity field (with components u_r, u_θ, and u_z), the temperature T and the pressure P. In cylindrical coordinates, the above equations become:

$$\frac{\partial u_r}{\partial r} + \frac{u_r}{r} + \frac{1}{r}\frac{\partial u_\theta}{\partial \theta} + \frac{\partial u_z}{\partial z} = 0, \qquad \text{(continuity eq.)}$$

$$\frac{\partial u_r}{\partial t} + u_r\frac{\partial u_r}{\partial r} + \frac{u_\theta}{r}\frac{\partial u_r}{\partial \theta} + u_z\frac{\partial u_r}{\partial z} - \frac{u_\theta^2}{r} = -\frac{\partial p}{\partial r} + P_r\left(\frac{\partial^2 u_r}{\partial r^2} + \frac{1}{r}\frac{\partial u_r}{\partial r} + \frac{1}{r^2}\frac{\partial^2 u_r}{\partial \theta^2} - \frac{2}{r^2}\frac{\partial u_\theta}{\partial \theta} - \frac{u_r}{r^2} + \frac{\partial^2 u_r}{\partial z^2}\right), \qquad \text{(radial eq.)}$$

$$\frac{\partial u_\theta}{\partial t} + \frac{u_\theta u_r}{r} + u_r\frac{\partial u_\theta}{\partial r} + \frac{u_\theta}{r}\frac{\partial u_\theta}{\partial \theta} + u_z\frac{\partial u_\theta}{\partial z} = -\frac{1}{r}\frac{\partial p}{\partial \theta} + P_r\left(\frac{\partial^2 u_\theta}{\partial r^2} + \frac{1}{r}\frac{\partial u_\theta}{\partial r} + \frac{1}{r^2}\frac{\partial^2 u_\theta}{\partial \theta^2} + \frac{2}{r^2}\frac{\partial u_r}{\partial \theta} - \frac{u_\theta}{r^2} + \frac{\partial^2 u_\theta}{\partial z^2}\right), \qquad \text{(angular eq.)}$$

$$\frac{\partial u_z}{\partial t} + u_r\frac{\partial u_z}{\partial r} + \frac{u_\theta}{r}\frac{\partial u_z}{\partial \theta} + u_z\frac{\partial u_z}{\partial z} = -\left[g\frac{d^3}{\kappa^2} - R_a P_r(T - T_0)\right] - \frac{\partial p}{\partial z} + P_r\left(\frac{\partial^2 u_z}{\partial r^2} + \frac{1}{r}\frac{\partial u_z}{\partial r} + \frac{1}{r^2}\frac{\partial^2 u_z}{\partial \theta^2} + \frac{\partial^2 u_z}{\partial z^2}\right), \qquad \text{(vertical eq.)}$$

$$\frac{\partial T}{\partial t} + u_r\frac{\partial T}{\partial r} + \frac{u_\theta}{r}\frac{\partial T}{\partial \theta} + u_z\frac{\partial T}{\partial z} = \frac{\partial^2 T}{\partial r^2} + \frac{1}{r}\frac{\partial T}{\partial r} + \frac{1}{r^2}\frac{\partial^2 T}{\partial \theta^2} + \frac{\partial^2 T}{\partial z^2}. \qquad \text{(Energy eq.)} \qquad (1)$$

In order to solve these equations we use the projection method (Fuentes and Carbajal 2005), which consists in the introduction of a fictitious velocity which is the solution of the Navier-Stokes equation for a constant pressure. For this fictitious velocity the condition $\nabla \cdot \mathbf{u} = 0$ is not fulfilled. In a second step, the pressure is calculated by solving an equation resulting from taking the divergence of the Navier-Stokes equations and imposing the condition of zero divergence to the velocity field. Finally, a real velocity is obtained from the Navier-Stokes equations by including the pressure calculated in the previous step.

2.1 Fourier Series Approximation

Since the angular coordinate is 2π-periodic, we can approximate the velocity, the temperature and the pressure (represented by ϕ) as a Fourier complex series:

$$\phi(r,\theta,z,t) \approx \sum_{k=1}^{m} \hat{\phi}_k(r,z,t)e^{ik\theta}. \tag{2}$$

So, the first and second derivatives with respect to θ are:

$$\frac{\partial\phi(r,\theta,z,t)}{\partial\theta} \approx \sum_{k=0}^{m} ik\hat{\phi}_k(r,z,t)e^{ik\theta}, \tag{3}$$

$$\frac{\partial^2\phi(r,\theta,z,t)}{\partial\theta^2} \approx -\sum_{k=0}^{m} k^2\hat{\phi}_k(r,z,t)e^{ik\theta}, \tag{4}$$

Then, the unknowns are the Fourier coefficients $\hat{\phi}_k(r,z,t)$.

2.2 Projection Method

The method is called "projection" because the velocity field is calculated in two steps. The first step consists in the calculation of the Navier-Stokes equations by assuming a constant pressure. In a second step, this velocity field is projected onto a space of zero divergence and satisfying the appropriate boundary conditions (Fuentes and Carbajal 2005).

We assume a uniform pressure field and we approximate the time derivative with a backward finite difference formula. This leads to the following equation

$$\frac{3\mathbf{u}^* - 4\mathbf{u}^n + \mathbf{u}^{n-1}}{2\Delta t} + \aleph(\mathbf{u}_r^{n,n-1}) + \left[g\frac{d^3}{\kappa^2} - R_a P_r(T - T_0)\right]\hat{k} + P_r\nabla^2\mathbf{u}^* = 0, \tag{5}$$

where $\mathbf{u}^*$ is the fictitious velocity field and $\aleph(\mathbf{u}_r^{n,n-1})$ is the estimate of the nonlinear term according to the Adams-Bashforth scheme. The term $\aleph(\mathbf{u}_r^{n,n-1})$ requires knowledge of the velocity field at the two previous times n and $n-1$ ($n+1$ represents the actual time). On the other hand, the equation for the true velocity field is:

$$\frac{3\mathbf{u}^{n+1} - 4\mathbf{u}^n + \mathbf{u}^{n-1}}{2\Delta t} + \aleph(\mathbf{u}_r^{n,n-1}) + \left[g\frac{d^3}{\kappa^2} - R_a P_r(T - T_0)\right]\hat{k} + \nabla p^{n+1} + P_r\nabla^2\mathbf{u}^{n+1} = 0. \tag{6}$$

Subtracting Eq. (6) from (5) we obtain:

$$\mathbf{u}^{n+1} = \mathbf{u}^* - \frac{2\Delta t}{3}\left[\nabla p^{n+1} + P_r \nabla^2(\mathbf{u}^* - \mathbf{u}^{n+1})\right]. \tag{7}$$

Taking the divergence of Eq. (7) and using the fact that $\nabla \cdot \mathbf{u}^{n+1} = 0$ we obtain the equation for the pressure:

$$\nabla^2 p^{n+1} = \frac{3}{2\Delta t}\nabla \cdot \mathbf{u}^* - P_r \nabla^2(\nabla \cdot \mathbf{u}^*). \tag{8}$$

2.3 Initial and Boundary Conditions

As the initial conditions we consider a temperature distribution with a constant gradient $\Delta T/d$, so that the pressure is hydrostatic and the fluid at rest. For the boundary conditions we impose a non-slip condition at the solid walls for the velocity field, whereas the temperature is set to a constant (in agreement with the imposed temperature gradient) in both the lower and upper walls. For the remaining boundaries (this includes velocity at $r = 0$) Neumann and/or Dirichlet boundary conditions are imposed. The Neumann conditions mean that the normal derivative of ϕ vanishes at $r = 0$, and the Dirichlet condition implies that $\phi(r = 0) = 0$.

3 Results

The numerical simulations were carried out with a constant Prandtl number ($P_r = 0.7$), which correspond to air and other gases, and some Rayleigh number above the critical one $Ra = 1{,}708$. To what concerns the geometry, we use either a cylindrical container ($0 < r < r_{ext}$) or an annular domain ($r_{int} < r < r_{ext}$).

Figure 1 shows the vertical component of the velocity in the container midplane. Each red region corresponds to positive vertical velocity, while the blue regions correspond to negative velocities. So, we can empirically establish that the number of rolls is twice the number of red regions (or blue regions). Figure 1a corresponds to the steady state for $R_a = 2{,}000$ and $r_{ext} = 10$. We can see eight concentric circular rolls. This figure is similar to the experimental result reported by Charru (2007). Figure 1b corresponds to the steady state for $R_a = 2{,}500$ and the annular domain, with $r_{int} = 1$ and $r_{ext} = 5$. We can count fourteen convective rolls, but they are not concentric.

Figure 2 shows the results of our simulations for $R_a = 2{,}500$ and a cylindrical container with $r_{ext} = 10$ at different times. At the beginning the pattern is always concentric but after a while (see Fig. 2a at $t = 13.8$), the concentric rolls begin to deform. We can see how the concentric circular pattern starts to ripple. In Fig. 2b,

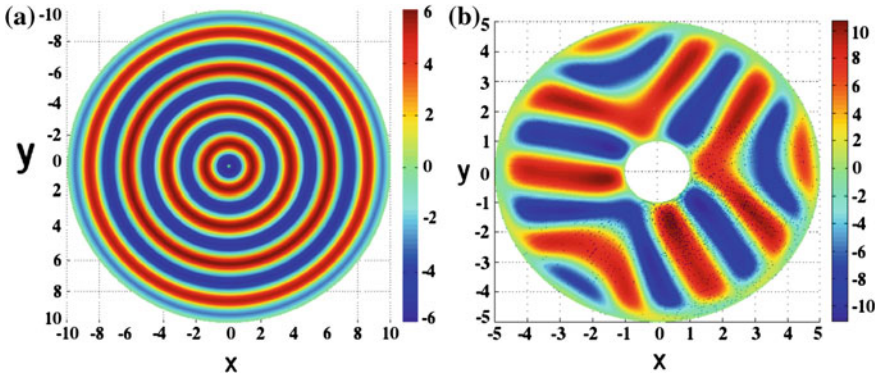

Fig. 1 **a** Steady state for $R_a = 2{,}000$. The rolls are *concentric circles*. **b** Steady state for the annular case for $R_a = 2{,}500$

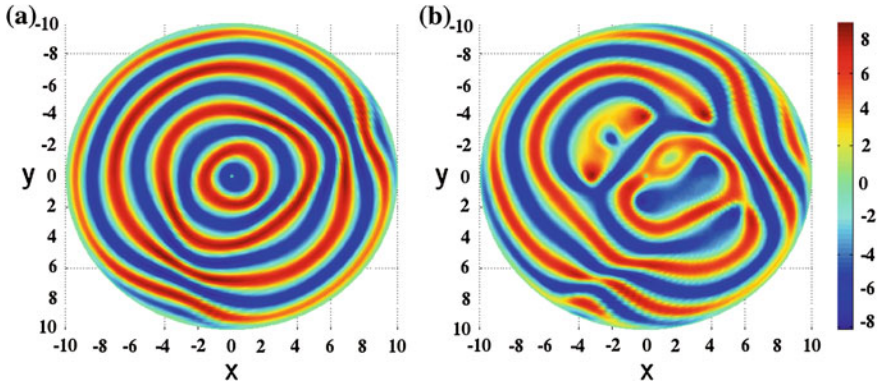

Fig. 2 Case $R_a = 2{,}500$. **a** At the beginning, the *concentric circles* pattern appears and after a while these circles begin to ripple. **b** The *concentric circles* pattern is totally destroyed

corresponding to $t = 28$, the initial pattern is lost completely. It is a different shape with respect to the case shown in the Fig. 1b. it is important to note that Fig. 2b has a similar trend with respect to the experimental results reported by Chandrasekhar (1961).

Figure 3 shows the vertical velocity in the midplane of the container for $R_a = 5{,}000$ at (a) $t = 3.8$ and (b) $t = 4.2$. We can see that the pattern changes rapidly and no steady state is reached in this time interval.

The dependence of the growth rate with the Rayleigh number has been well studied (Charru 2007). When the Rayleigh number coincides with the critical value $Ra_c = 1{,}708$ the growth rate is zero (this is the neutral stability state). It becomes positive when the Rayleigh number is above Ra_c. This is a very important criterion to test our simulations. We have performed two calculations, one is the time for the beginning of the pattern formation and the second is the time elapsed to attain the

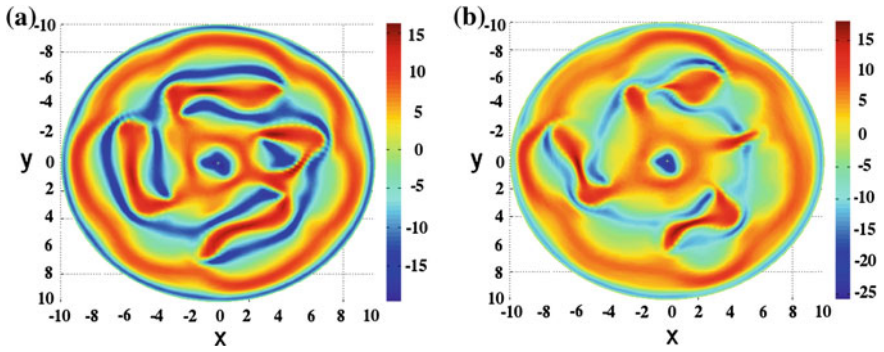

Fig. 3 Case $R_a = 5{,}000$. It begins forming a *concentric circles* pattern. **a** Time is $t = 3.8$. **b** Time is $t = 4.2$

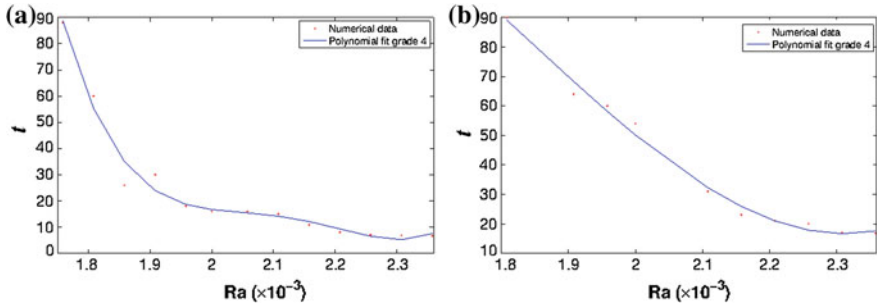

Fig. 4 **a** The time that it takes to the perturbation to overcome a certain threshold versus Rayleigh number. **b** The time that it takes to the system to attain a stationary state versus Rayleigh number

steady state. Both quantities must be decreasing functions of the Rayleigh number. Our simulation satisfies this criterion as we can see from Fig. 4. The calculation of the first quantity consists of obtaining the time for which the velocity at a certain point is no longer zero (in a numerical sense, see Fig. 4a). For the second time we determine the time elapsed until the velocity variations at a certain point are less than a value ϵ (see Fig. 4b). In both figures, we observe that the time is a decreasing function of the Rayleigh number.

4 Conclusions

The numerical simulations reproduce some of the patterns observed in experiments other than the annular cells. If the Rayleigh number is not much bigger than the critical value, the steady state consists of a collection of concentric rolls. As the Rayleigh number increases, the time to reach the steady state decreases, and the rolls pattern becomes unstable, as we showed for $R_a = 2{,}500$ case. For the $R_a = 5{,}000$

case our simulation does not exhibit a stationary state during the time of integration. We have shown a result in an annular domain. In this case the steady state does not consist of a pattern of concentric circles. The results of the numerical simulations can be compared qualitatively with experimental results and those reported in the literature.

The method we used is easy to run in parallel, taking advantage of the features of the Fourier spectral method.

Acknowledgments Authors acknowledge DGAPA-UNAM by support under project IN116312, "Vorticidad y ondas no lineales en fluidos".

References

Bénard H (1900) Les tourbillons cellulaires dans une nappe liquide. Revue Gén Sci Pur Appl 11:1261–1271 and 1309–1328

Bodenschatz E, Pesch W, Ahlers G (2000) Recent developments in Rayleigh-Benard convection. Annu Rev Fluid Mech 32:709–778

Boyd JP (2000) Chebyshev and Fourier spectral methods. Dover, New York

Chandrasekhar S (1961) Hydrodynamic and Hydromagnetic Stability. Oxford University Press, New York, Dover

Charru F (2007) Instabilités Hydrodynamiques. EDP Sciences CNRS Éditions, Paris

Drazin PG, Reid WH (1981) Hydrodynamic stability. Cambridge University Press, Cambridge

Fuentes R, Carvajal LF (2005) Método de diferencias finitas en mallas irregulares con soluciones analíticas parciales aplicado al flujo hidrodinámico. Rev Int Met Num Calc Dis Ing 21(3):263–272

Getling AV, Brausch O (2003) Cellular flow patterns and their evolutionary scenarios in three-dimensional Rayleigh-Bénard convection. Phys Rev E 67:046313

Guyon E, Hulin J-P, Petit L (2001) Hydrodynamique physique, Savoirs Actuels. EDP Sciences/CNRS Éditions, Paris

Li YR, Ouyang YQ, Peng L, Wu SY (2012) Direct numerical simulation of Rayleigh-Bénard convection in a cylindrical container of aspect ratio 1 for moderate Prandtl number fluid. Phys Fluids 24:074103. doi:10.1063/1.4731296

Paul MR, Chiam K-H, Cross MC, Fischer PF, Greenside HS (2003) Pattern formation and dynamics in Rayleigh-Bénard convection: numerical simulations of experimentally realistic geometries. Phys D 184:114–126

Peyret R (2002) Spectral methods for incompressible viscous flow. Springer, New York

Rayleigh L (1916) On convection currents in a horizontal layer of fluid, when the higher temperature in on the under side. Philos Mag 6(32):529–546

Tagawa T, Ujihara A, Ozoe H (2003) Numerical computation for Rayleigh-Bénard convection of water in a magnetic field. Int J Heat Mass Transf 46:4097–4104

Ternik P, Rudolf R, Zunic Z (2013) Numerical study of Rayleigh-Bénard natural-convection heat-transfer characteristics of water-based au nanofluids. Mater Technol 47(2):211–215

Valencia ML (2005) Estudio Numérico y Experimental de Flujo Rayleigh-Bénard en Cavidades Cúbicas para Régimen Transitorio y Turbulento. PhD Thesis. Universitat Rovira I Virgili. pp 1482–2006. ISBN: 978-84-690-8297-3/D.L: T

Solidification in the Presence of Natural Convection in a Hele-Shaw Cell

G. Ramírez, J.E. Cisneros, G. Hernández Cruz and E. Ramos

Abstract The solidification of water with particles in a suspension that fills the gap in a Hele-Shaw cell has been experimentally studied by visualization and using particle image velocimetry (PIV). The upper wall of the cell is kept at a temperature lower than 0 °C, while the lower wall is exposed to ambient temperature. Water starts solidifying near the upper wall of the cell, and a solidification front moves in the downward direction. Since the temperature gradient established is unstable in the gravity acceleration field, the liquid acquires a natural convective motion, and the solidification and convection interact with each other. The growth of the solidification region in the Hele-Shaw cell modifies the volume available to the liquid and in this way determines the convection pattern. In turn, the convective flow of the liquid is an efficient heat pump at the liquid-solid boundary, and determines the velocity and geometry of the solidification front. We present quantitative data of the velocity and shape of the solidification front and the velocity field in the liquid region as functions of time. We have found that the convective motion stops when the aspect ratio (height/width) of the liquid region is approximately 0.45 and from this time on, the motion of the solidification front follows Stefan's law.

G. Ramírez (✉) · J.E. Cisneros · G. Hernández-Cruz · E. Ramos
Renewable Energy Institute, Universidad Nacional Autónoma de México,
62580 Temixco, Mor, Mexico
e-mail: guraz@ier.unam.mx

J.E. Cisneros
e-mail: jcx2514@gmail.com

G. Hernández-Cruz
e-mail: ghc@ier.unam.mx

E. Ramos
e-mail: erm@ier.unam.mx

J. Klapp et al. (eds.), *Selected Topics of Computational and Experimental Fluid Mechanics*, Environmental Science and Engineering,
DOI 10.1007/978-3-319-11487-3_28

1 Introduction

The phenomenon of solidification is of great importance in many industrial processes like casting, refrigeration, crystal growth and others. Frequently, in these processes, the large temperature gradients and the unavoidable presence of gravity results in a convective motion that interacts with the change of phase. In turn, the geometry modification of the volume occupied by the fluid is decisive for the dynamic characteristics of the convective motion making this a two-way coupled phenomenon. The systematic study of heat transfer during solidification started in the nineteenth century with the analysis of the displacement of a solidification front by J. Stefan in the context of ice formation in the polar seas. In the classical Stefan problem, the growth of the solid takes place in absence of fluid motion, and it considers a one dimensional system composed of the liquid and solid regions and the interface, whose position is determined by the heat exchange between the two phases. An important result of this theory indicates that the displacement of the solidification front is proportional to the square root of time. Many refinements and generalizations of this model that consider more realistic physical situations are now available in the literature. See, for instance, Langlois (1985). Specifically, a two dimensional model of the solidification front indicates that a straight front is unstable and develops a wavy shape whose crests evolve to form cusps that are interpreted as the precursors of fingers and dendrites (Davis 1990). Presently, it is recognized that the solidification process is extremely complex, and many studies have focused in the description of the microstructure of the newly formed solid. A topic that has received much attention is the formation of a semisolid region that forms between the solid and the liquid regions which has been named the "mushy layer" and that has its own complex dynamics. For instance, the solidification of an aqueous ammonium chloride solution confined in a Hele-Shaw was studied by Chen (1995) to clarify the role played by the local convection in the formation of channels devoid of solid or "chimneys" in the solidified material. An approximate estimation of the convective velocity near the solidification front is given, but no attempt is made to describe the velocity distribution or its time dependence. In the presence of a body force, the thermal gradients that take place due to the latent heat released at the solidification front induce buoyancy-driven convection that greatly affects the interfacial patterns, i.e. the solidification microstructures that are present in the solidified material (Rosenberger 1979; Worster 1997). The emphasis of the present study is not on the analysis of the solid structure or in the liquid-solid transition layer but in the fluid motion. This phenomenon is strongly dependent on the geometry of the container, and thus our observations refer to a quasi two-dimensional motion in the direction parallel to the Hele-Shaw plates.

2 Experimental Device and Visualization Methods

The experimental device where observations were made consists of a Hele-Shaw cell formed by two 1 mm thick glass plates with an area of 2.0 cm × 2.0 cm. The plates were separated 1 mm by Nylamid pieces placed along the vertical walls of the cell which provide mechanical support and thermal insulation. The upper horizontal wall of the cell is a piece of copper that is physically in contact with the cold side of a square thermoelectric device. The hot side of the thermoelectric is in contact with a heat sink which is constituted by a container filled with pellets of solid CO_2 and designed such that a mini fan blows the cold gaseous CO_2 product of the sublimation to the upper wall of the Hele-Shaw cell. The illumination of the fluid inside the cell is made through the lower horizontal wall which is made of a plexiglas piece that acts as a light guide for three white light emitting diodes. The cell arrangement is shown in the left panel of Fig. 1. Small holes at the lower part of the vertical walls connected to atmospheric pressure allow for the expansion of the working fluid as it is cooled. The cell is fixed on a breadboard and aligned to a Microsoft, 960 × 540 pixels video camera that captures images at 15 fps (see the right panel of Fig. 1). The resulting spatial resolution is 23 pixels per mm. Special care was required to prevent water condensation from the ambient on the external walls of the cell since this reduces the quality of the images, and may modify the boundary conditions on the faces of the cell.

The working fluid is water with small (10 μm in diameter) neutrally buoyant hollowed glass particles in suspension. The temperature of the fluid inside the cell is monitored with two thermocouples located near the top and bottom horizontal walls as shown in Fig. 2. The flow pattern and the position of the solidification front are captured with the video camera and analyzed with the PIVLab software and image processing tools. The maximum velocity observed is 0.8 mm/s and the interrogation

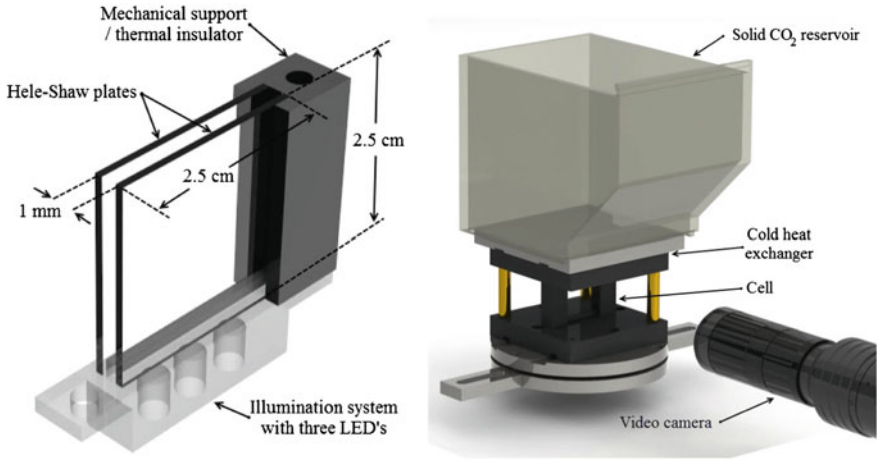

Fig. 1 *Left* Geometry and components of the Hele-Shaw cell. *Right* Experimental setup showing the heat sink (solid CO_2 reservoir), and the position of the video camera

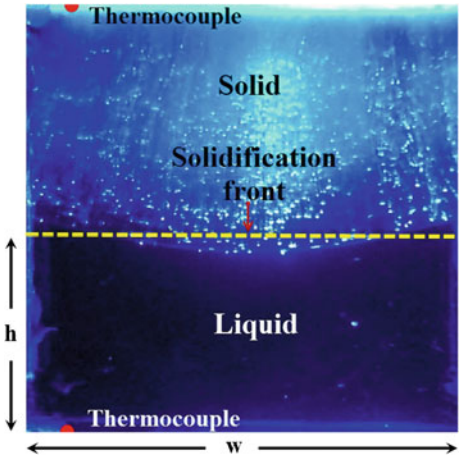

Fig. 2 Sample image of the cell and the solidification front. The positions of the upper and lower thermocouples are indicated by *red dots*. The *horizontal broken line* is the average vertical position of the solidification front. h is the (time dependent) vertical magnitude of the volume occupied by the liquid and w is the width of the cell

area is 12 × 6 pixels with an overlap of 50 %. The flow is mostly two dimensional and the color contrast between the solid and the liquid produced by the illumination coming from the lower wall of the cell provides images of excellent quality as can be seen in Fig. 2.

3 Results

As heat is pumped from the fluid and from the lower boundary by the upper, colder boundary, the temperature inside the cell drops and the thermodynamic conditions inside the cell correspond to solidification. As will be described in more detail below, the present design and operation of the cooling system leads to time-dependent upper and lower temperature boundary conditions. Although this feature makes it difficult to generalize the results presented in this report, it is expected that the qualitative observations will be similar to those obtained by keeping constant temperature boundary conditions. The total observation time is of the order of 40 min when the solidification front touches the lower wall of the cell. The temperature of the thermocouples inside the cell are shown in Fig. 3. As it can be seen, the temperature of the upper wall (T_C) is a monotonously decreasing function of time with an initial value of 0 °C and a final reading of approximately −30 °C. The temperature of the lower wall (T_H) is 22.5 °C at the onset of the observations and reduces to 10 °C at the end of the experiment. The temperature gradient between the upper and lower walls ($T_H - T_C$) is initially 20 °C but settles to 40 °C after approximately 14 min from the beginning of the experimental observations. Ambient temperature (T_{amb}) is 22 °C throughout the experiment. The vertical broken lines in the figure indicate the earliest time where the solidification front can be identified ($t_o = 2.7$ min) and the time when the motion of the fluid stops ($t_s = 15.7$ min).

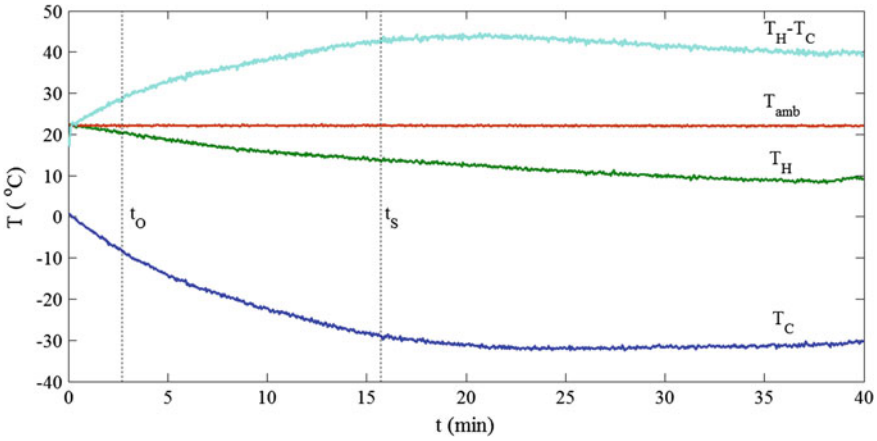

Fig. 3 Temperatures as functions of time. T_C denotes the temperature at the upper wall, T_H is temperature at the lower wall, T_{amb} is ambient temperature and $T_H - T_C$ is the temperature difference between the lower and upper horizontal walls. t_o and t_s indicate respectively the onset of solidification and the time when the liquid in the system becomes stagnant

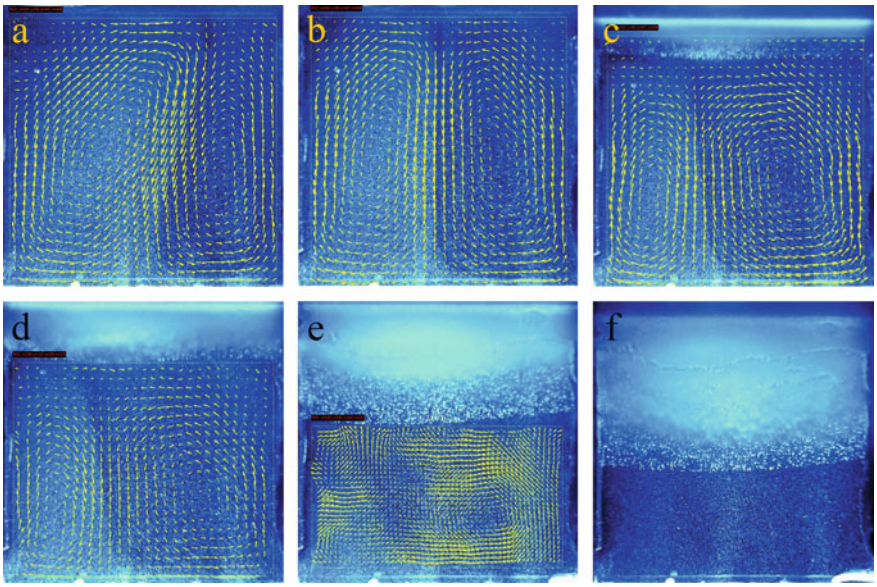

Fig. 4 Velocity field in the liquid region of the cell and advancing solidification front for six snapshots. The *white zone* on the upper part of the images is ice. **a** t = 2 min, Ra = 10^5; **b** t = 3.5 min, Ra = 6.9×10^4; **c** t = 6 min, Ra = 3.6×10^4; **d** t = 8 min, Ra = 1.9×10^4; **e** t = 10.5 min, Ra = 9×10^3; **f** t = 17.1 min, Ra = 3.2×10^3

A sequence of six representative snapshots that illustrate the dynamic behavior of the convective flow observed inside the cell is shown in Fig. 4. The velocity field obtained with the PIV technique is superposed to the liquid region to give quantitative information on the convective pattern. The most important feature of the flow is that the motion of the solidification front has the effect of modifying the aspect ratio of the volume where the fluid moves and therefore it has a definite influence on the dynamics and convective pattern. The dynamics of the convective flow is conveniently described in terms of the Rayleigh number (Ra) defined as

$$Ra = \frac{g\beta\Delta T \mathrm{h}^3}{\alpha\nu}, \tag{1}$$

where g is the acceleration of gravity, β, α and ν are respectively the coefficient of thermal expansion, the thermal diffusivity and the kinematic viscosity of the liquid. Since the thermal properties are functions of temperature, we have considered average values. The temperature difference between the upper and lowermost regions of the fluid, which in our case coincide with the solidification front, and the lower wall of the cell is ΔT. As shown in Fig. 2, the distance between the upper and lower boundaries of the liquid region in the cell is denoted by h. Notice that this distance reduces in time as the solidification front advances and, as was mentioned in the first paragraph of this section, ΔT is also time dependent and therefore the Rayleigh number is modified as the solidification progresses.

At the onset of the experiment, when the aspect ratio $A = \mathrm{h/w} = 1$, a single convective cell moving counterclockwise is observed. The average velocity is 0.66 mm/s, the Rayleigh number is $Ra = 10^5$ and the energy per unit mass of the system is $4.4 \times 10^{-7}\,\mathrm{m^2/s^2}$. Then, the single cell evolves into two symmetric cells with fluid descending in the central region and ascending near the vertical walls of the cell as shown in Fig. 4b, at t = 3.5 min and $A = 1$ since no advance of the solidification front can be noticed, $Ra = 6.9 \times 10^4$. The average velocity is 0.73 mm/s and the energy is $5.3 \times 10^{-7}\,\mathrm{m^2/s^2}$. In later stages, the two cell configuration persists (see Fig. 4c, d), and then the patterns of convective motion in the cell becomes highly irregular and undergo time dependent motions with time scales of the order of seconds when the aspect ratio is in the range $0.6 < A < 0.5$, as illustrated in Fig. 4e. At approximately 15.7 min after the onset of the observation when the aspect ratio $A \sim 0.45$, the liquid motion stops and the solidification proceeds in a stagnant fluid for the rest of the observation. The critical Rayleigh number when the convective motion stops is $Ra^c = 3.2 \times 10^3$.

The shape of the solidification front at different times is shown in Fig. 5. The front grows slightly faster near the center but its curvature is small. This effect is attributed to imperfect thermal insulation at the vertical walls of the cell. Observe that this feature is consistent with the rotation direction of the double cells displayed in Fig. 4b where the relatively hot fluid ascends near the vertical walls. It was found that at the scale of the cell, the geometry of the front is stable in the sense that no preferential growth positions along the solid front were detected; the whole front moves approximately at the same speed toward the lower wall.

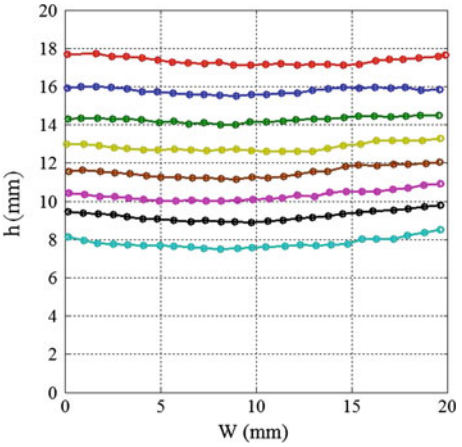

Fig. 5 Profiles of the solidification front as a function of time. Starting at the uppermost profile downwards, the position of the solidification fronts are captured at t = 6.1, 7.6, 9.2, 10.7, 12.3, 13.8, 15.4, 17.7 min

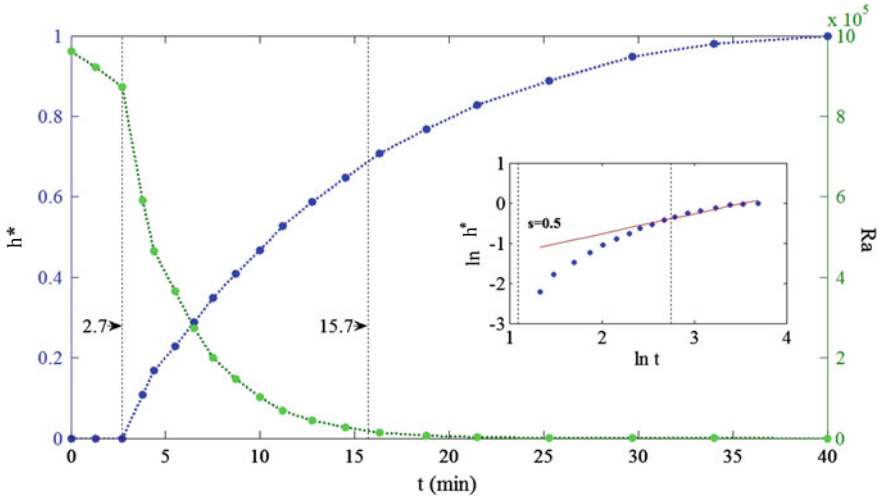

Fig. 6 Normalized position of the solidification front h^* and Rayleigh number based on the height of the liquid region as functions of time. In the inset, the log-log plot of the solidification front position as a function of time is given to establish the $h^* \sim t^{1/2}$ relation for t > 15.7 min. The *vertical lines* in the inset indicate the times corresponding to 3 and 15.7 min respectively

The time evolution of the position of the (normalized) solidification front $h^* = 1 - h/h(t = 0)$ and the Rayleigh number *Ra* are shown in Fig. 6. The front starts moving at $t = 2.7$ min (indicated in the graph with a vertical line) and reaches its maximum value at $t = 40$ min. The Rayleigh number is a monotonously decreasing function of time, but before the formation of the solidification front, the slope is

smaller since ΔT is decreasing but the aspect ratio remains constant. Then, two effects contribute to the reduction of the Rayleigh number, the characteristic distance h gets smaller as time progresses and the temperature gradient is also smaller. The critical Rayleigh number when the motion of the liquid stops is indicated with the second vertical line. Although the solidification front is not a horizontal line as would be required by a one-dimensional model, a simple one dimensional heat transfer balance at the position where phase change takes place can be proposed, considering also that the liquid is motionless. Upon assuming that the heat released at the solidification front is conducted away by the solid phase, the velocity of the front is proportional to the temperature difference at the front position and the temperature at the boundary condition in the ice divided by the distance that separates them. i.e.

$$-k\frac{T_f - T_C}{y} = \mathcal{L}v_f = -\mathcal{L}\frac{dy}{dt} \tag{2}$$

where k is the heat conductivity of ice, T_f is the temperature at the solidification front, the $\mathcal{L}$ is the enthalpy of phase change and y is the position of the front which is a function of time. The previous expression can be integrated considering that $y = 0$ at $t = 0$. The result indicates that the position of the front is given by:

$$y(t) = \mathcal{C}t^{1/2} \qquad \text{where} \qquad \mathcal{C} = \frac{\mathcal{L}}{k(T_f - T_C)} \tag{3}$$

Even though the front is not a horizontal line but has a small curvature, the simple model indicates the correct value of the exponent of time as compared with the observation once the velocity of the liquid has become small enough at time $t >$ 15.7 min. This feature is illustrated in the inset in Fig. 6. Although the motion of the solidification front has a major influence on the dynamics of the convective motion, under our experimental conditions, the motion of the fluid does not greatly modify the shape of the liquid-solid interface.

The intensity of the motion of the liquid is obtained by calculating the L^2 norm of the flow defined by:

$$\mathrm{L}^2 = \frac{1}{V_o}\int_{V_o}(u^2 + v^2)dV_o, \tag{4}$$

where $V_o(t)$ is the volume occupied by the liquid and is a function of time. The velocity components in the x and y directions are u and v respectively. Under the approximation of constant density, L^2 corresponds to twice the kinetic energy of the system. As can be observed from Fig. 7, the convective motion starts when the unstable temperature gradient is established in the cell and the velocity increases at t = 3 min due to the increase in the temperature gradient and the concurrent condition of constant aspect ratio of the liquid volume (see Fig. 3). At approximately t = 3 min, the solidification front starts moving downwards shortening the volume available to the liquid and the kinetic energy of the system reduces monotonically until the fluid

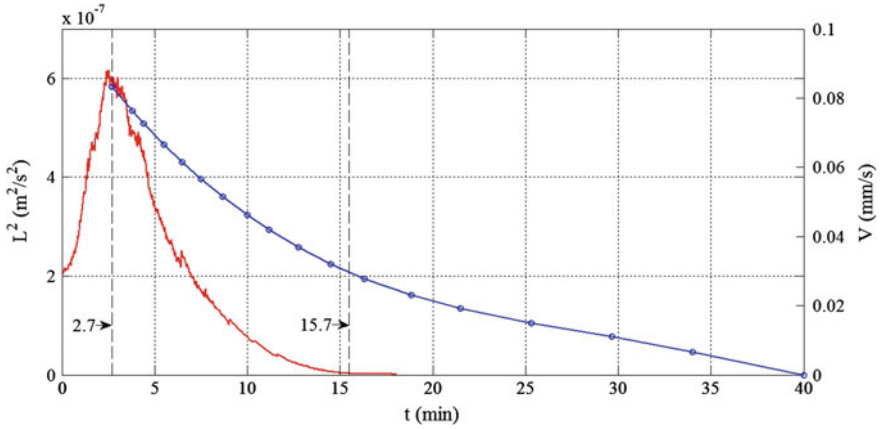

Fig. 7 *Red trace* Kinetic energy of the flow L^2 as a function of time. *Blue trace* Velocity of the solidification front

becomes stagnant at t = 15.7 min. The velocity of the solidification front is also shown in Fig. 7 to emphasize the different time scales of liquid and solid motions.

4 Discussion and Conclusions

Solidification in the presence of natural convection has been observed in a quasi two dimensional system composed by water with spherical particles in suspension confined to a Hele-Shaw cell. The experimental arrangement permits a full visualization of the process both in the solid and the liquid regions. In the present experimental set up, the temperature boundary conditions on the upper and lower horizontal walls are time dependent, but it is expected that the qualitative features of the results observed are similar to those obtained in the time independent case. Our observations indicate that the reduction of the region occupied by the liquid impacts greatly on the convective pattern, but the shape of the solidification front is not much affected by the convective motion. The presence of particle tracers may arguably modify the dynamics of the solidification as compared with the a pure liquid (Peppin et al. 2007); however, it is likely that this effect has its largest impact at a microscopic level and not on the macroscopic scale which is the main objective of the present report.

Acknowledgments Guillermo Ramírez acknowledges support from CONACYT-Mexico through MSc. and PhD. grants. Mr. Agustín Barrera built an early version of the convective cell.

References

Chen CF (1995) Experimental study of convection in a mushy layer during directional solidification. J Fluid Mech 293:81–98
Davis SH (1990) Hydrodynamic interactions in directional solidification. J Fluid Mech 212:241–262
Langlois WE (1985) Buoyancy-driven flows in crystal growth melts. Annu Rev Fluid Mech 17:191–215
Peppin SSL, Worster MG, Wettlaufer JS (2007) Morphological instability in freezing colloidal suspensions. Proc R Soc A 463:723–733
Rosenberger F (1979) Fundamentals of crystal growth I. Springer, Berlin
Worster MG (1997) Convection in mushy layers. Annu Rev Fluid Mech 29:91–122

Confinement and Interaction Effects on the Diffusion of Passive Particles

A. Gonzalez, E. Diaz Herrera, M. Sandoval, M.A. Chavez Rojo and J.A. Moreno Razo

Abstract We use Molecular Dynamics simulations to study the effect of interactions and confinement (walls) on particle diffusion. We extend previous studies by analyzing the mean squared displacement (MSD) of an interacting fluid constrained to a circular, square and triangular cavity of nanometric size. The interactions among particles and walls are modeled by means of three classic potentials namely, Lenard-Jones (CLJ), soft Lenard-Jones (SLJ) and hard Lenard-Jones (HLJ) potentials. For hard spheres, for all cavities, and for very diluted densities, diffusion is shown to be less favorable in comparison with particles interacting with a CLJ. It is also observed that HLJ particles do not show difference in their MSD with SLJ particles at these densities. Confinement effects also appear at these densities and it is shown that diffusion decreases in the following cavity shape order: triangular, square and circular. For moderated densities, the combination of confinement and interactions shows a non-trivial effect. It is observed that particles inside a triangular cavity interacting by means of HLJ, reduce their MSD in comparison with CLJ or SLJ particles, since for this cavity shape, hard collisions reduce the particles' speed. For higher densities, another non-trivial effect appears. Once again, the combination of interactions and confinement gives rise to order in the system that clearly reduces the system MSD. It is also shown that order appears for SLJ particles but it is absent for CLJ or HLJ particles.

A. Gonzalez · E. Diaz Herrera · M. Sandoval · J.A. Moreno Razo (✉)
Department of Physics, Universidad Autonoma Metropolitana-Iztapalapa,
09340 Mexico, D.F., Mexico
e-mail: jamr@xanum.uam.mx

M.A. Chavez Rojo
Facultad de Ciencias Quimicas, Universidad Autonoma de Chihuahua,
Nuevo Campus Universitario, Circuito Universitario, 31125 Chihuahua, Mexico

J. Klapp et al. (eds.), *Selected Topics of Computational and Experimental Fluid Mechanics*, Environmental Science and Engineering,
DOI 10.1007/978-3-319-11487-3_29

1 Introduction

Diffusion processes of molecules and particles are very common in nature. Breathing, human metabolism, motion of viruses and bacteria, medical drug delivery, are only some examples. The fundamental mechanism behind these processes was elucidated for the first time in 1905 when a theoretical framework for difussion was proposed by Einstein (1905). Since then, classical work concerning diffusion of non-interacting particles includes the study of isotropic particles in the absence (Einstein 1905; Chandrasekhar 1943; Batchelor 1977) and presence of external fields (Ferrari 1990; Zagorodny and Holod 2000; Foister and Ven 1980; Jimenez-Aquino et al. 2008). Additionally, anisotropic particles diffusing in the absence (Han et al. 2006; Hinch and Leal 1972) and presence of external fields (Grima and Yaliraki 2007) have also been considered. More recently, and based on the previous works, the impact of thermal agitation on non-interacting active particles (driven by an assumed internal mechanism) has received attention. For example, steadily-swimming self-propelled bodies of simple shape, one sphere (Howse et al. 2007; Hagen et al. 2011; Sandoval et al. 2014), multiple spheres (Lobaskin et al. 2008), or ellipsoids (Hagen et al. 2011) have been studied.

Another interesting aspect about diffusive processes is the effect of confinement on particle displacement. In nature and in many technological applications, particles (ions, molecules, photons) generally move under the presence of boundaries, like through ionic channels (Alberts et al. 2007), membranes (Hille 2001), artificial nanopores (Siwy et al. 2005; Healy et al. 2007) porus media (Daniel and Astruc 2004) and carbon nanotubes (Berezhkovskii and Hummer 2002). As it can be seen, confinement is mainly due to physical walls (although hydrodynamic confinement is also possible (Alar Ainla and Jesorka 2012)) hence the need of including wall effects on particle diffusion. A theoretical framework that includes wall effects on particle diffusion was achieved by Zwanzig (1992). Based on the idea that physical walls can be seen as entropic potentials,and that effective diffusion coefficients depend on position, he derived for the first time, a Smoluchowski equation for a confined particle. By solving this equation, an effective analytical diffusion coefficient that includes the influence of the walls can then be obtained. Recent work concerning confined, non-interacting particles is given by Reguera and Rubi (2001), Reguera et al. (2006), Kalinay and Percus (2005, 2008). Confined active non-interacting particles have also been computationally studied (Ghosh et al. 2013). A theoretical analysis of active non-interacting confined particles has just recently been developed (Sandoval and Dagdug 2014).

The latter works do not consider particle-particle interactions, hence in this research we study confined particles where interactions among elements of the system (particle-particle and wall-particle) are allowed. These interactions in their own provide to the system richer thermodynamic properties (like phase transitions). Moreover, the effect of confinement on the physical properties of geometrically constrained fluids is not yet well understood. It has been shown that confinement deviates a traditional bulk fluid phase transition (Evans 1990; Klein and Kumacheva 1998;

Heffelfinger et al. 1987), thus providing novel properties to that system. It also creates layers near the walls hence affecting crystallization on the system (Alba-Simionesco et al. 2006). Confinement also induces a non-uniform distribution of the particles' density (Magda et al. 1985). As one can see, confinement may provide new characteristics to constrained interacting systems, hence the necessity of studying them. Recent theoretical and computational works studying the influence of confinement on interacting fluids are given by Karbowniczek and Chrzanowska (2013), Das and Singh (2013), Hartkamp et al. (2012).

In this research we use Molecular Dynamics simulations to study the effect of interactions and confinement (walls) on particles diffusion. We extend previous studies by analyzing the mean squared displacement of an interacting fluid constrained to a circular, square and triangular cavity. The interactions among particles and walls are modeled by means of three classic interaction potentials namely, Lenard-Jones (CLJ), soft Lenard-Jones (SLJ) and hard Lenard-Jones (HLJ) potentials, and whose differences in the interaction they produce are also analyzed. This work is organized as follows. In Sect. 2 we set up the problem and detailed information on the simulations is given. Section 3 presents the obtained results, and finally we offer our conclusions in Sect. 4.

2 Model

Consider a fluid made up of spherical interacting particles of mass m, diameter σ, and confined in a two-dimensional closed cavity of three prototypical shapes (circular, square and triangular, as shown in Fig. 1). Particle-particle and particle-wall interactions are modeled via the Lennard-Jones potential. Thus we formally solve for a set of coupled first order differential equations for the position $\mathbf{r}_i$ and momentum $\mathbf{p}_i$ of the i-particle

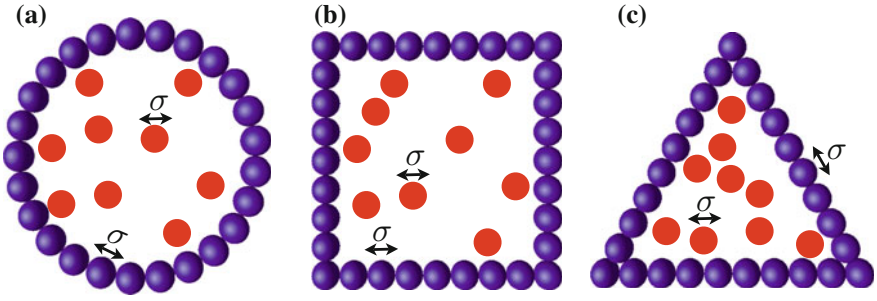

Fig. 1 (Color online) Schematics of the three cavities studied. Note that the spherical particles forming the walls and the fluid particles, have the same diameter σ for all cavities. **a** *circular* cavity; **b** *square* cavity; **c** *triangular* cavity

$$\dot{\mathbf{r}}_i = \frac{\partial H}{\partial \mathbf{p}_i} = \frac{\mathbf{p}_i}{m}, \tag{1}$$

$$\dot{\mathbf{p}}_i = -\frac{\partial H}{\partial \mathbf{r}_i} = -\nabla U_{ij} = \mathbf{F}_i, \tag{2}$$

where the Hamiltonian of the system is given by $H = (1/2m)\sum \mathbf{p}_i \cdot \mathbf{p}_i + U_{ij}$, and $\mathbf{F}_i = -\nabla\left(\sum_{j\neq i}^{N} U_{ij}\right)$ is the force acting on particle i due to intermolecular interactions, ∇ is the gradient operator, and the dot represents time derivative. Here U_{ij} is the interaction potential defined as

$$U_{ij}(r_{ij}) = 4\varepsilon\left[\left(\frac{\sigma}{r_{ij}}\right)^{2n} - \beta\left(\frac{\sigma}{r_{ij}}\right)^{n}\right], \tag{3}$$

where r_{ij} represents the nearest separation between particle i and wall particle/particle j, σ is the diameter for both, the fluid particles and particles conforming the wall, ε is the potential depth, n is a positive integer, and $\beta = \{0, 1\}$. To study the interaction effects on particles diffusion, we consider three different potentials (see Fig. 2), (a) the classic Lenard-Jones potential (CLJ), $n = 6$ and $\beta = 1$; (b) a soft Lennard-Jones potential (SLJ), $n = 6$ and $\beta = 0$; and (c) a hard repulsive potential (HLJ), $n = 36$ and $\beta = 0$. Note that to speed up the code, we consider $U_{ij} = 0$ for $r_{ij} > r_c$ where r_c is a cut-off distance defined as $r_c = 3\sigma$.

We confine the fluid with a wall made up of spherical particles fixed in space (see Fig. 1) and interacting with the fluid particles by means of the interaction potential

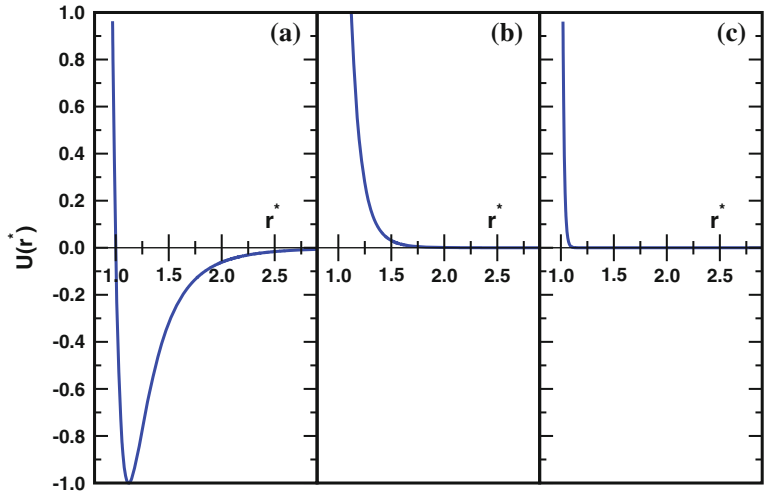

Fig. 2 (Color online) Schematics of the three potentials studied. **a** The classic Lenard-Jones potential (CLJ), $n = 6$ and $\beta = 1$; **b** a soft Lennard-Jones potential (SLJ), $n = 6$ and $\beta = 0$; and **c** a hard repulsive potential (HLJ), $n = 36$ and $\beta = 0$. Here $r^* = r/\sigma$ is a reduced variable

Table 1 Geometrical properties of the three cavities studied

Confinement	Number of particles at the wall	Relevant parameter (σ units)
Circle	200	Radius = 31.83
Square	228	Side = 57
Triangle	258	Side = 86

Table 2 Number of particles (density) inside the three cavities studied

ρ^*	Circular	Square	Triangular
0.1	318	324	320
0.25	795	812	800
0.5	1,521	1,624	1,601
0.75	2,387	2,436	2,401

U_{ij}. Confinement is built with a fixed number of spherical particles in such a way that the order of magnitude for the cavities is around nanometers. Table 1 shows detailed geometrical properties of the three cavities studied in this work.

In our simulations we vary the number of particles inside the cavities (density ρ), while keeping a reduced temperature $T^* = kT/\varepsilon = 1$, here k is the Boltzmann constant. The reduced density $\rho^* = \rho\sigma^3$ was varied from 0.1 to 0.75 at intervals of 0.25. A detailed description of the number of particles for each studied density is shown in Table 2.

For the integration of the governing equations (Eqs. 1 and 2) we use a Velocity-Verlet scheme with a step size of $\Delta t = 0.003$ (20 ns in the Argon scale). To start the simulations, particles are randomly distributed. For high densities, overlapped particles were relocated using a Monte Carlo algorithm. The simulations were performed in a canonical ensemble using 3×10^6 integration steps and 6×10^6 steps for the reported averages that characterize diffusion. To maintain thermodynamic equilibrium a classic (Berendsen et al. 1984) thermostat was used. To speed up the code a force decomposition MPI formalism plus neighbor list was used.

3 Results

In this section, we study the effect of confinement and interaction on particle diffusion based on Molecular Dynamics simulations. By focusing on three prototypical cavities (triangular, square and circular) we simulate four scenarios (varying ρ^* from 0.1 to 0.75 at intervals of 0.25) for each cavity, and for the three mentioned interaction potentials. Figure 3 shows three representative density scenarios (0.1, 0.5 and 0.75) and we plot in each column, the mean-square displacement as a function of cavity shape for the three analyzed potentials (CLJ, SLJ and HLJ). At low densities ($\rho^* =$

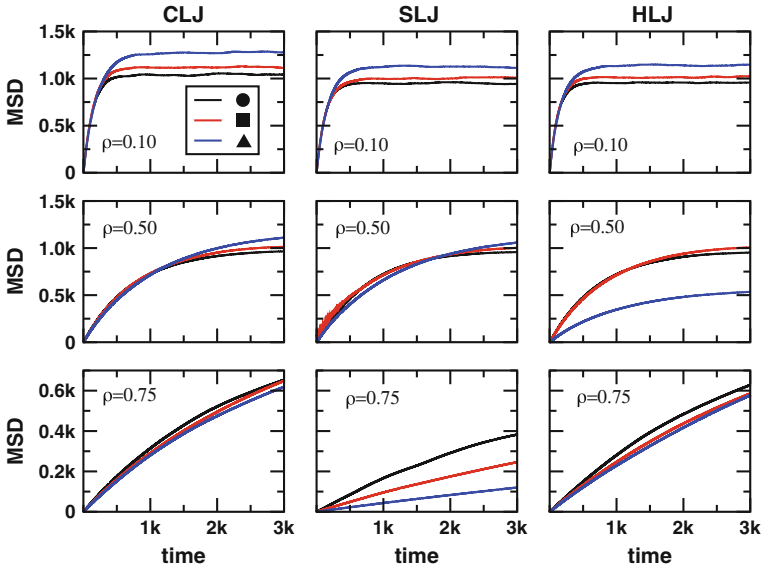

Fig. 3 (Color online) Confinement effect on the mean-square displacement (MSD). *Rows* shows three representative densities ($\rho^* = 0.1, 0.5$ and 0.75). *Columns* show the studied interaction potentials, classic Lenard-Jones (CLJ), soft Lenard-Jones (SLJ) and hard repulsive potential (HLJ)

0.1, first row) and for long times, the MSD tend to a constant value since particles have visited all the cavity area, therefore this plateau is a confinement effect. There is also a small effect of the cavity shape on the MSD for all the interaction potentials. We see that the magnitude of the MSD decreases in the following cavity shape sequence: triangular, square and circular. This trend can be easily understood since the maximum traveling distance (from the center of the cavity to its walls) occurs inside a triangle, followed by a square and finally by a circle (see Table 1 showing the relevant parameters of the cavities).

For $\rho^* = 0.5$, we can see a similar behavior between particles interacting with a CLJ and a SLJ, however, we observe that particles interacting with a HLJ and confined in a triangular cavity, reduce their MSD. This case can be explained as follows. HLJ originates hard collisions among particles, which reduce the speed of the spheres, resulting in more free space inside the cavity and smaller MSD compared with the SLJ. In the SLJ, collisions will not be so hard thus allowing to keep the speed of the spheres high, resulting in less free space and higher MSD. This situation is visually shown in Fig. 4 where particles inside a triangular shape and colliding by means of a HLJ, produce more free space (see Fig. 4b) compared with particles interacting by means of SLJ (see Fig. 4a). Note that for this density, the MSD has not yet reached a constant value (see Fig. 3, second row).

For $\rho^* = 0.75$ we observe in general a reduction of the system diffusion compared with the lower density cases due to a decrease of free space. The case $\rho^* = 0.75$

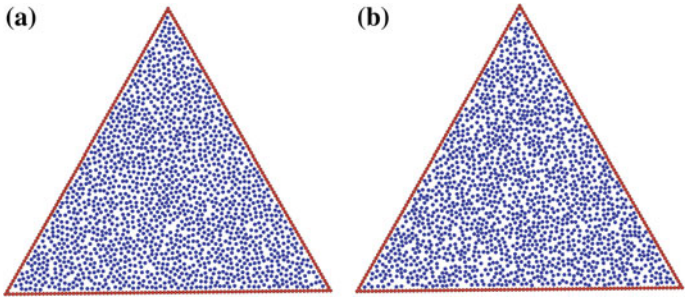

Fig. 4 (Color online) Particles inside a triangular cavity ($\rho^* = 0.5$) interacting by means of different potentials. **a** Particles interacting by means of a SLJ potential; **b** Particles interacting by means of a HLJ potential. Note that HLJ particles produce more free space, see (**b**), compared with particles interacting by means of a SLJ, see (**a**)

also shows an interesting effect due to an interplay among confinement and particle interaction. We notice that order appears for particles interacting with a SLJ and for all the three cavity shapes. This order reduces the MSD compared with the MSD of systems at the same density but subject to CLJ or HLJ (see Fig. 3, third row, second column). Figure 3 also shows that order appears as the strength of the interaction potential grows, however this order slowly disappears as the strength of U_{ij} is still growing (that is, if we make $2n = 36, 40$ and so on). Note for example that the HLJ potential at this density does not show order, hence its MSD increases again. The appearance of order is visually shown in Fig. 5 where one can see that order has emerged in the left triangular cavity interacting by means of a SLJ (see Fig. 5a). In contrast, the right triangular cavity does not show order thus allowing the particles to have more freedom and hence a higher MSD.

Figure 6 shows once again three representative density scenarios (0.1, 0.5 and 0.75). This time, each column shows the mean-square displacement for the same

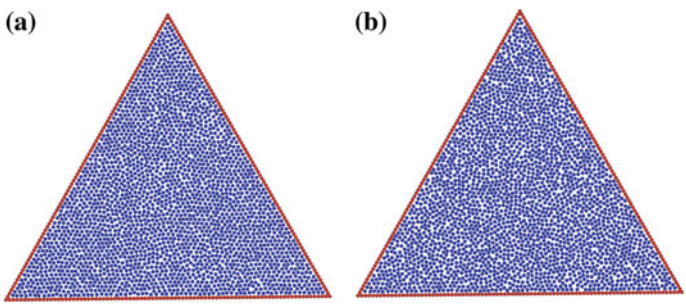

Fig. 5 (Color online) Particles inside a triangular cavity ($\rho^* = 0.75$) interacting by means of different potentials. **a** Particles interacting by means of a SLJ potential; **b** Particles interacting by means of a HLJ potential. Order has emerged in the *left* triangular cavity interacting by means of a SLJ, see (**a**)

cavity shape but for the three analyzed potentials (CLJ, SLJ and HLJ). As already discussed, the triangular cavity has the longest available distance, that for a very diluted system generates the highest MSD for all the interaction potentials studied (see Fig. 6, first row). For $\rho^* = 0.75$ we see that the MSD for CLJ particles is slightly higher than the MSD for HLJ particles for all cavities. A system made of hard spheres has also repulsion at the walls, so that the particles stay away from the walls and migrate to the center, with their impacts generating a high pressure that reduce diffusion. In contrast, CLJ has attraction and therefore particles attach to the walls originating free space at the center of the cavity and hence increasing diffusion.

The case of SLJ with a MSD even smaller than CLJ and HLJ (Fig. 6, third row, for all shapes) can be understood easily since for this case the system presents order thus decreasing its MSD. When order appears the argument of hard collisions decreasing the speed of spheres (case $\rho^* = 0.5$) is not longer valid since the system is not liquid-like, but rather crystal-like and hence entropy plays an important role. The effect of confinement for an ordered system, as in the case of particles interacting by means of a SLJ potential, can be seen in the third row of Fig. 6. Here, as one moves to the right, the MSD decreases in the following shape sequence: circular, square and triangular. This is a plausible result since geometrically and for high densities, the triangular cavity constrains more the particles. Note that for a diluted system the cavity shape effect on the MSD has the opposite sequence, that is, the MSD decreases in the following shape sequence: triangular, square and circular, since the longest

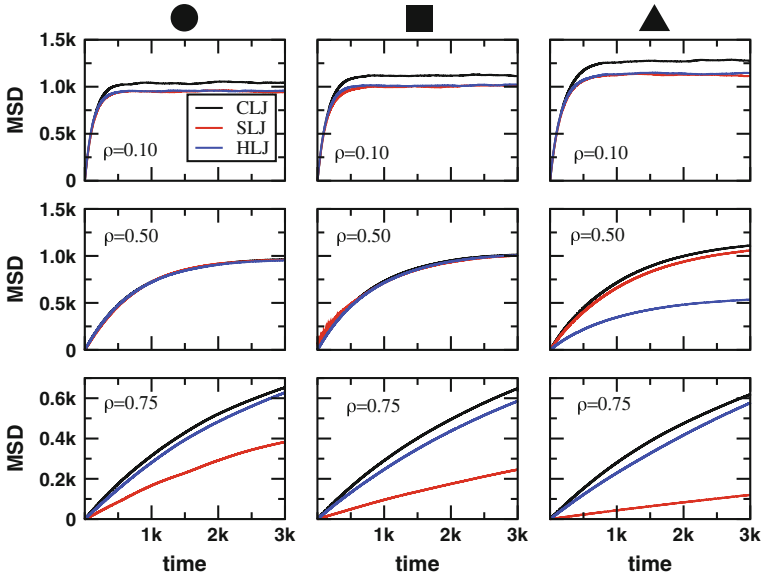

Fig. 6 (Color online) Interaction effects on the mean-square displacement (MSD). *Rows* shows three representative densities ($\rho^* = 0.1, 0.5$ and 0.75). *Columns* show the studied cavity shapes

available distance (from the center of the cavity to its walls) for particles, is in the triangular cavity.

4 Conclusions

In this work we have studied the behavior of confined particles (inside circular, square and triangular cavities) interacting by means of three different potentials namely, Lenard-Jones (CLJ), soft Lenard-Jones (SLJ) and hard Lenard-Jones (HLJ) potentials. We showed that diffusion is strongly affected when particles are confined inside nanometric cavities. In this work, we varied the number of particles inside the cavity (density) while keeping a reduced temperature $T^* = 1$, and studied particle displacement by using Molecular dynamics simulations in a canonical ensemble. We showed that for low densities ($\rho^* = 0.1$) diffusion for all fluids is similar, and that the highest MSD occurs for a triangular cavity since the longest available distance (from the center of the cavity to its boundaries) occurs in the triangular cavity. It is also found that the highest MSD occurs for particles with attractive interactions (CLJ). The first relevant result in this work occurs for moderated densities ($\rho^* = 0.5$). Here, HLJ particles confined in a triangular cavity, strongly reduce their MSD due to the absence of spatial order, resulting in a low particle speed. This effect should be investigated in detail in a future work. We also observe that fluids with attractive interactions (CLJ) and with week repulsion (SLJ) possess similar diffusivities inside all the cavities. Finally, the second relevant result is obtained at high densities ($\rho^* = 0.75$) where fluids with week repulsion (SLJ) and for all the cavity shapes, show the lowest MSD. This is a surprising result that can be explained due to the appearance of spatial order that particles show inside all the cavities. We conclude by pointing out that the appearance of order in our system shows how the interplay of confinement and interaction may produce non-trivial behavior in geometrically constrained fluids.

Acknowledgments We thank CONACYT-Mexico (Project No. 178963) for Financial support. Computational resources for this work were provided by the LSVP at UAM-I and also in part by Xiuhcoatl-CINVESTAV.

References

Alar Ainla GJ, Jesorka A (2012) Hydrodynamically confined flow devices, hydrodynamics—theory and model. InTech, Shangai

Alba-Simionesco C, Coasne B, Dosseh G, Dudziak G, Gubbins KE, Radhakrishnan R, Sliwinska-Bartkowiak M (2006) J Phys Condens Matter 18:R15

Alberts B, Johnson A, Lewis J, Raff M, Roberts K, Walter P (2007) Molecular biology of the cell. Garland Science, New York

Batchelor GK (1977) J Fluid Mech 83:97

Berendsen HJC, Postma JPM, van Gunsteren WF, DiNola A, Haak JR (1984) J Chem Phys 81:3684

Berezhkovskii AM, Hummer G (2002) Phys Rev Lett 89:064503

Chandrasekhar S (1943) Rev Mod Phys 15:813
Daniel MC, Astruc D (2004) Chem Rev 104:293
Das CK, Singh JK (2013) Theor Chem Acc 132:1351
Einstein A (1905) Ann Phys 17:549
Evans R (1990) J Phys Condens Matter 2:8989
Ferrari L (1990) Phys A 163:596
Foister RT, van de Ven TGM (1980) J Fluid Mech 96:105
Ghosh PK, Misko VR, Marchesoni F, Nori F (2013) Phys Rev Lett 110:268301
Grima R, Yaliraki SN (2007) J Chem Phys 127:084511
ten Hagen B, van Teeffelen S, Lowen H (2011) J Phys Condens Matter 23:194119
Han Y, Alsayed A, Nobili M, Zhang J, Lubensky TC, Yodh AG (2006) Science 314:626
Hartkamp R, Ghosh A, Weinhart T, Luding S (2012) J Chem Phys 137:044711
Healy K, Schiedt B, Morrison AP (2007) Nanomedicine 2:875
Heffelfinger G, van Swol F, Gubbins K (1987) Mol Phys 61:1381
Hille B (2001) Ion channels of excitable membranes. Sinauer, Sunderland
Hinch EJ, Leal LG (1972) J Fluid Mech 52:683
Howse JR, Jones RAL, Ryan AJ, Gough T, Vafabakhsh R, Golestanian R (2007) Phys Rev Lett 99:048102
Jimenez-Aquino JI, Velasco RM, Uribe FJ (2008) Phys Rev E 77:051105
Kalinay P, Percus JK (2005) J Chem Phys 122:204701
Kalinay P, Percus JK (2008) Phys Rev E 78:021103
Karbowniczek P, Chrzanowska A (2013) Acta Phys Pol B 44:1209
Klein J, Kumacheva E (1998) J Chem Phys 108:6996
Lobaskin V, Lobaskin D, Kulic I (2008) Eur Phys J Spec Top 157:149
Magda J, Tirrell M, Davis H (1985) J Chem Phys 83:1888
Reguera D, Rubi JM (2001) Phys Rev E 64:061106
Reguera D, Schmid G, Burada PS, Rubi JM, Reimann P, Hanggi P (2006) Phys Rev Lett 96:130603
Sandoval M, Dagdug L (2014) Effective diffusion of confined active Brownian swimmers. Phys Rev E 90(6):062711
Sandoval M, Marath NK, Subramanian G, Lauga E (2014) J Fluid Mech 742:50
Siwy Z, Kosinska ID, Fulinski A, Martin CR (2005) Phys Rev Lett 94:048102
Zagorodny A, Holod I (2000) Condens Matter Phys 3:295
Zwanzig R (1992) J Chem Phys 96:3926

Thermal Convection in a Cylindrical Enclosure with Wavy Sidewall

F.A. Sánchez Cruz, S. Martínez Martínez, H.G. Ramírez Hernández and S. Méndez Díaz

Abstract An axisymmetric convection flow within a vertical cylindrical enclosure with adiabatic wavy sidewall was studied. Two important cases of thermal convection were considered, heating from below and heating from the top, while the wavy sidewall is adiabatic. An analytical coordinate transformation was used to obtain a coordinate frame for computation in which the irregular domain fits into a square. Non-dimensional parameters which include the cavity aspect ratio, dimensionless wavelength, dimensionless amplitude, constant Prandtl number equal to 7, and Rayleigh numbers between 10^3 and 10^6, were used to characterize the convection heat transfer through the cavity. Computational solutions showed that the wavy wall promotes thermal stratification and low velocity multiple cells patterns. The effect of the wavy wall was found to restrict the convection fluid flow which yields low heat transfer through the cavity.

1 Introduction

Thermal convection heat transfer in enclosures has received considerable attention due to the relevance of the phenomena occurring in many engineering applications such as cooling of electronic equipment, solidification processes, buildings design, solar collectors and cooling chambers. Moreover, heat and mass transfer in enclosures are natural common processes found in science fields as geophysics and metallurgy. Many real cavities are irregular shaped and the fluid flow and heat transfer show complicated behaviors, nevertheless, typical analysis are focused on characterizing enclosures with regular shapes; hexahedral, cylindrical and spherical cavities being the most studied geometries. Roughness and waviness of walls are parameters scarcely considered when studying transport phenomena in enclosures. Since the shear stress and heat flux on the walls define the hydrodynamics and heat trans-

F.A. Sánchez Cruz (✉) · S. Martínez Martínez · H.G. Ramírez Hernández · S. Méndez Díaz
Facultad de Ingeniería Mecánica y Eléctrica, Universidad Autónoma de Nuevo León,
Av. Universidad s/n, Cd. Universitaria, San Nicolás de los Garza, NL, México
e-mail: fausto.sanchezcr@uanl.edu.mx

J. Klapp et al. (eds.), *Selected Topics of Computational and Experimental Fluid Mechanics*, Environmental Science and Engineering,
DOI 10.1007/978-3-319-11487-3_30

fer in enclosures, the inclusion of waviness parameters of walls, as amplitude and wavelength, could become important to model realistic conditions.

In recent years, studies of external natural convection from wavy walls have been investigated to analyze waviness parameters on heat transfer and fluid flow. Ashjaee et al. (2007) studied the natural convection heat transfer from a constant temperature wavy wall and computed local heat transfer coefficients using the Mach-Zehner interferometer. Experimental measurements were carried out for amplitude-wavelength ratios of 0.05, 0.1 and 0.2, and Rayleigh numbers from 2.9×10^5 to 5.8×10^5. Numerical results from a finite-volume based code were successfully compared with experimental measurements. The average heat transfer coefficient decreases as the amplitude-wavelength ratio increases. Additionally, experimental data were fitted to a single equation which gives the local Nusselt number along the wavy surface as function of the amplitude-wavelength ratio and the Rayleigh number. A thermal convection from a more complex wavy surface is found when a combination of two sinusoidal functions occurs, a fundamental wave and its first harmonic (Molla et al. 2007). Using transformed coordinates on the boundary layer equations yields a mapped regular and stationary computational domain to evaluate the wavy wall effect. The additional harmonic alters the flow field and temperature distribution near the vertical wavy surface. Prescribed heat flux along wavy surfaces have been investigated solving the boundary layer equations for unconfined flows (Tashtoush and Abu-Irshaid 2001). According to the specific amplitude and wave length a point of separation appears restricting the solution. Additionally, the wavelength of the local Nusselt number and surface temperature variation were found to be equal to those of the wavy surface. On the other hand, the wavelength of the average Nusselt number was a half of that on the wavy surface.

Wavy surfaces are also frequently involved with mass transfer. Effects of combined buoyancy forces due to concentration and thermal gradients from a vertical wavy surface have been analyzed for unconfined flows focusing on the evolution of the surface shear stress, the heat transfer, and surface concentration gradient (Hossain and Rees 1999). Wide ranges of the governing parameters have been considered such as Schmidt numbers ranging from 7 to 1,500, amplitude of the waviness from 0 to 0.4, and the buoyancy parameter ranging from 0 to 1. The wavy wall reduces the heat transfer, concentration gradient and shear stress. The effect of the inclination angle has been studied for laminar thermal convection from a constant temperature wavy wall in a square cavity (Dalal and Das 2004). For the case of a square cavity differentially heated through a hot wavy wall, the mean Nusselt is lower than that corresponding to the flat wall square cavity (Adjlout 2001). Turbulence improves the convection heat transfer on the wavy wall surface compared to the case of a square cavity with high Rayleigh numbers, and different from laminar flow, the presence of the wavy wall increases the local Nusselt number (Aounallah et al. 2006). Previous analysis regarding transport phenomena from wavy walls include the steady flow and solute uptake in a wavy-walled channel (Woollard et al. 2008) and the effect of variable viscosity and variable thermal conductivity on the magneto-hydrodynamics and the resulting local skin friction, and local Nusselt and Sherwood numbers

(Elgazery and Abd 2009). Frequently, natural processes involve transport phenomena from wavy walls through porous media in both, confined and unconfined flows.

For combined heat and mass transfer processes by natural convection along a vertical wavy surface in a fluid saturated porous enclosure, thermal and mass stratifications diminish the Nusselt and Sherwood numbers. Rathish-Kumar and Murthy (2010) analyzed the Soret and Dufour effects to estimate the combined heat and mass transfer processes by natural convection from a wavy vertical surface in a fluid-saturated semi-infinite porous medium. Numerical solutions have been developed to study natural convection inside an inclined wavy cavity filled with a porous medium (Misirlioglu et al. 1999). The fluid flow and thermal structures were found to be highly dependent on the surface waviness when the inclination angle is lower than 45°, specially for high Rayleigh numbers. Rostami (1999) studied the two-dimensional transient heat transfer and fluid flow in a laterally heated enclosure with vertical wavy walls, while the horizontal ones were flat and adiabatic. Dalal and Das (2006) studied the natural convection inside a two-dimensional cavity with a wavy vertical wall. The enclosure was heated through the bottom wall by varying the temperature spatially, while the other three walls were kept at constant temperature. Local and average Nusselt numbers were computed for both conduction- and convection-dominated regimes.

Transport phenomena in cylindrical enclosures result of practical interest. Nevertheless, the effect of a wavy-side wall on thermal convection is not reported in literature. The present study considers an axisymmetric flow inside a vertical cylindrical enclosure with adiabatic wavy sidewall. Two important cases are studied, heating from below and heating from the top. Under such conditions the adiabatic wavy sidewall affects the transport phenomena giving rise to different convection patterns which modify the heat transfer rate even for conditions where convection dominates.

2 Problem Statement

Consider the thermal convection within the cylindrical enclosure shown in Fig. 1a. The top and bottom walls are kept at constant temperature T_1 and T_2, respectively, while the wavy sidewall is thermally insulated. The cylinder has an average radius R and height L, the wavy wall generatrix curve is a sinusoidal function with wavelength λ and amplitude a, see the Fig. 1b. The enclosure is filled with a Newtonian fluid and the properties are assumed to be constant except the density for which the Boussinesq approximation is applied. The temperature difference between the bottom and top walls, $T_2 - T_1$, is either positive or negative and the gravity acts parallel to the cylindrical axis.

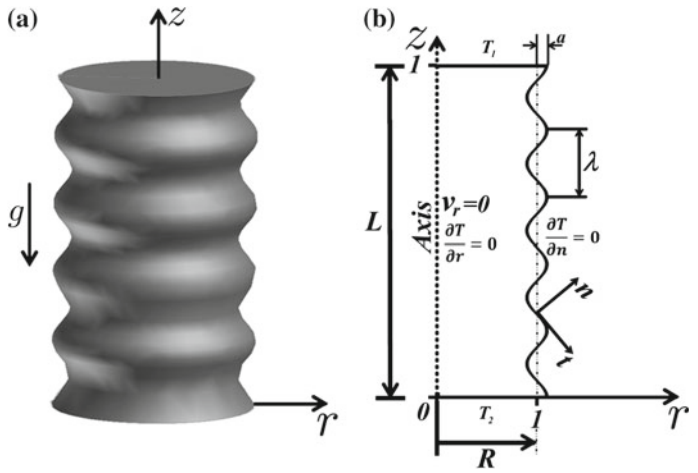

Fig. 1 **a** Physical model, **b** coordinates and boundary conditions

3 Mathematical Formulation

The problem can be solved as an axisymmetric flow using cylindrical coordinates. The axial direction z^* coincides with the axis of the cylinder and the wavy sidewall is located at $r^* = R + a\cos(2\pi z^*/\lambda)$. The continuity and steady-state momentum and energy equations are respectively:

$$\frac{\partial v_r^*}{\partial r^*} + \frac{v_r^*}{r^*} + \frac{\partial v_z^*}{\partial z^*} = 0 \tag{1}$$

$$v_r^* \frac{\partial v_r^*}{\partial r^*} + v_z^* \frac{\partial v_r^*}{\partial z^*} = -\frac{1}{\rho}\frac{\partial P^*}{\partial r^*} + \nu\left(\frac{\partial^2 v_r^*}{\partial r^{*2}} + \frac{1}{r^*}\frac{\partial v_r^*}{\partial r^*} - \frac{v_r^*}{r^{*2}} + \frac{\partial^2 v_r^*}{\partial z^{*2}}\right) \tag{2}$$

$$v_r^* \frac{\partial v_z^*}{\partial r^*} + v_z^* \frac{\partial v_z^*}{\partial z^*} = -\frac{1}{\rho}\frac{\partial P^*}{\partial z^*} + \nu\left(\frac{\partial^2 v_z^*}{\partial r^{*2}} + \frac{1}{r^*}\frac{\partial v_z^*}{\partial r^*} + \frac{\partial^2 v_z^*}{\partial z^{*2}}\right) + g\beta\,(T - T_m) \tag{3}$$

$$v_r^* \frac{\partial T^*}{\partial r^*} + v_z^* \frac{\partial T^*}{\partial z^*} = \alpha\left[\frac{1}{r^*}\frac{\partial}{\partial r^*}\left(r^*\frac{\partial T^*}{\partial r^*}\right) + \frac{\partial^2 T^*}{\partial z^{2*}}\right], \tag{4}$$

subject to the following boundary conditions:

$$v_r^* = v_z^* = 0, T = T_2 \; at \; z^* = 0, 0 \le r^* \le R + a, \tag{5}$$

$$v_r^* = v_z^* = 0, T = T_1 \; at \; z^* = L, 0 \le r^* \le R + a, \tag{6}$$

$$v_r^* = \frac{\partial v_z^*}{\partial r^*} = \frac{\partial T}{\partial r^*} = 0 \; at \; r^* = 0, 0 \le z^* \le L, \tag{7}$$

$$v_n^* = v_t^* = \frac{\partial T}{\partial n^*} = 0 \; at \; r^* = R + a\cos(2\pi z^*/\lambda), 0 \le z^* \le L, \tag{8}$$

where $*$ indicates dimensional variables, r and z are the radial and axial coordinates, v_r and v_z are the radial and axial components of velocity, respectively, ρ is the density, P is the modified pressure accounting for the hydrostatic effect, ν is viscosity, g is the acceleration of gravity, β is the thermal expansion coefficient, α is the thermal diffusivity, $T_m = (T_1 + T_2)/2$ is the mean temperature, v_n and v_t are the normal and tangential velocity components to the wavy sidewall, i.e. $v_n = \overline{v} \cdot \overline{n}$ and $v_t = \overline{v} \cdot \overline{t}$, where $\overline{n}$ and $\overline{t}$ are normal and tangential unit vectors to the wavy wall.

A scale analysis suggests the following dimensionless variables:

$$\begin{aligned} z = z^*/L; r = r^*/R; v_z = R^2 v_z^*/\nu L; v_r = R v_r^*/\nu; \\ \varepsilon = R/L; \Lambda = \lambda/L; \theta = (T^* - T_m)/(T_H - T_m); \end{aligned} \tag{9}$$

where ε is the aspect ratio, Λ is the dimensionless wavelength, θ is the dimensionless temperature, and T_H is the higher temperature between T_1 and T_2.

The explicit dependence of momentum equations on pressure is dropped and the dimensionless stream function $\psi(r, z) = \psi^*/\mu L$ is introduced as

$$\frac{\partial \psi}{\partial r} = r v_z, \tag{10}$$

$$\frac{\partial \psi}{\partial z} = -r v_r. \tag{11}$$

The resulting motion equation is

$$\begin{aligned} &\mathbb{A}\frac{\partial^4 \psi}{\partial r^4} + \mathbb{B}\frac{\partial^3 \psi}{\partial r^3} + \mathbb{C}\frac{\partial^2 \psi}{\partial r^2} + \mathbb{D}\frac{\partial \psi}{\partial r} + \mathbb{E}\frac{\partial^4 \psi}{\partial r^2 \partial z^2} + \mathbb{F}\frac{\partial^3 \psi}{\partial r \partial z^2} \\ &+ \mathbb{G}\frac{\partial^3 \psi}{\partial r^2 \partial z} + \mathbb{H}\frac{\partial^2 \psi}{\partial r \partial z} + \mathbb{I}\frac{^2\psi}{\partial z^2} + \mathbb{J}\frac{\partial^3 \psi}{\partial z^3} + \mathbb{K}\frac{\partial^4 \psi}{\partial z^4} = \mathbb{L}\frac{\partial \theta}{\partial r}, \end{aligned} \tag{12}$$

and the energy equation is as follows

$$\mathbb{N}\frac{\partial \theta}{\partial z} + \mathbb{O}\frac{\partial \theta}{\partial r} + \mathbb{P}\frac{\partial^2 \theta}{\partial r^2} + \mathbb{Q}\frac{\partial^2 \theta}{\partial z^2} = 0, \tag{13}$$

where coefficients $\mathbb{A}$–$\mathbb{Q}$ are given in Table 1 of the Appendix. The Rayleigh and Prandtl numbers are defined as $Ra = g\beta(T_H - T_m)L^3/\nu\alpha$ and $Pr = \nu/\alpha$, respectively.

An analytical coordinate transformation was used to obtain a coordinate frame for computation in which the irregular domain fits into a square. The new dependent and

independent variables were analytically introduced to transform the mathematical representation of the conservation principles before the equations were discretized.

The suitable transformation states

$$\xi = z, \tag{14}$$

$$\eta = \frac{r}{1 + \Gamma \cos\left(\frac{2\pi\xi}{\Lambda}\right)}, \tag{15}$$

where $\Gamma = a/R$ is the dimensionless wave amplitude. Once the coordinate transformation was applied, Eqs. 12 and 13 become

$$b\frac{\partial^2\psi}{\partial\xi^2} + c\frac{\partial^3\psi}{\partial\xi^2} + d\frac{\partial^4\psi}{\partial\xi^4} + e\frac{\partial^2\psi}{\partial\xi\partial\eta} + f\frac{\partial^3\psi}{\partial\xi^2\partial\eta} + g\frac{\partial^4\psi}{\partial\xi^3} + h\frac{\partial^3\psi}{\partial\xi\partial\eta^2} + i\frac{\partial^4\psi}{\partial\eta^3\partial\xi} + j\frac{\partial^4\psi}{\partial\eta^2\partial\xi^2} + k\frac{\partial\psi}{\partial\eta} + l\frac{\partial^2\psi}{\partial\eta^2} + m\frac{\partial^3\psi}{\partial\eta^3} + n\frac{\partial^4\psi}{\partial\eta^4} = 0, \tag{16}$$

$$o\frac{\partial\theta}{\partial\xi} + p\frac{\partial^2\theta}{\partial\xi^2} + q\frac{\partial^2\theta}{\partial\xi\partial\eta} + s\frac{\partial\theta}{\partial\eta} + t\frac{\partial^2\theta}{\partial\eta^2} = 0, \tag{17}$$

subject to the following boundary conditions

$$\psi = \frac{\partial\psi}{\partial\xi} = 0, \theta = \theta_2 \; at \; \xi = 0, 0 \le \eta \le 1; \tag{18}$$

$$\psi = \frac{\partial\psi}{\partial\xi} = 0, \theta = \theta_1 \; at \; \xi = 1, 0 \le \eta \le 1; \tag{19}$$

$$\psi = \frac{\partial\psi}{\partial\eta} = \frac{\partial\theta}{\partial\eta} = 0 \; at \; \eta = 0, 0 \le \xi \le 1; \tag{20}$$

$$\psi = A''\frac{\partial\psi}{\partial\eta} + B''\frac{\partial\psi}{\partial\xi} = \frac{\partial\theta}{\partial n} = 0 \; at \; \eta = 1, 0 \le \xi \le 1; \tag{21}$$

again, coefficients *b–t* are given in Table 2 of the Appendix, while the coefficients A and B are given in Table 3. Equations 16 and 17 were discretized using finite differences. The resulting square domain was meshed with 110 × 110 nodes. A computational code was programmed using the Fortran 95 language to solve the algebraic equations applying the *LU* inversion matrix algorithm. Since the motion equation is a fourth order non-linear differential equation an iterative scheme was employed. The motion equation was found to need around ten iterations to generate a total residual of order 10^{-9}, which was the selected criterion to consider the numerical solution convergence. The stream function solution was then applied to the energy equation to compute the temperature distribution. Five iterations were done between the energy and motion equations to generate a grand total residual of order 10^{-9}.

The total heat transfer through the horizontal walls is

$$q_w = -2\pi k \int_0^{R+a} r^* \left[\frac{\partial T}{\partial z^*}\right]_{z^*=0,L} dr^*. \tag{22}$$

If h_{av} is the average convection heat transfer coefficient on the horizontal walls, then the average Nusselt number, $Nu_{av} = h_{av}L/k$, is computed as

$$Nu_{av} = -2 \int_0^1 \eta \left[\frac{\partial \theta}{\partial \xi}\right]_{\xi=0,1} d\eta. \tag{23}$$

4 Results and Discussion

There are two possible cases for the natural convection here studied, the cylindrical enclosure heated from below, and the case where the cavity is heated from the top. For both cases the wavy wall is assumed to be adiabatic. The dimensionless parameters were varied in order to evaluate their effect on the thermal convection. The studied parameters were, for the aspect ratio $\varepsilon = 0.1, 0.3, 0.5$; dimensionless wavelength $\Lambda = 1/10, 1/5, 1/3$; dimensionless amplitude $\Gamma = 0.05, 0.1, 0.3$; Rayleigh number from 10^3 to 10^6, and constant Prandtl number, $Pr = 7$.

4.1 Enclosure Heated from Below

Figure 2 shows the dimensionless temperature and stream function for Rayleigh numbers from 10^3 to 10^6. The dimensionless temperature $\theta = 0$ corresponds to the average temperature T_m. When the Rayleigh number is of order 10^3, the stream function shows multiple convection cells near the wavy wall. Moreover, the cavity presents a stratified temperature distribution which yields low velocity convection cells. When the Rayleigh number is $Ra = 10^4$, the fluid flow is little intensified according to the stream function values, which increase around one order of magnitude, nevertheless, the velocity is relatively low and the thermal stratification persists. For a Rayleigh number of 10^5 the flow presents two convection cells, the lower cell with a clockwise rotation. Such a flow removes thermal stratification, increasing the temperature gradient near the upper and lower walls. For a Rayleigh number of 10^6 the flow shows two convection cells, the upper one flowing faster than the lower one, as shown by the streamlines in Fig. 2d. Moreover, the temperature distribution for $Ra = 10^6$ presents intense temperature gradients near the upper and lower walls.

The dimensionless wavelength of the wavy wall modifies considerably the convection flow and the heat transfer process, particularly for high Rayleigh numbers. Figure 3 shows that there is an almost stagnant thermally stratified core and multiple convection cells near the wavy wall when the dimensionless wavelength is small. On the other hand, there are two convection cells with no thermal stratification when

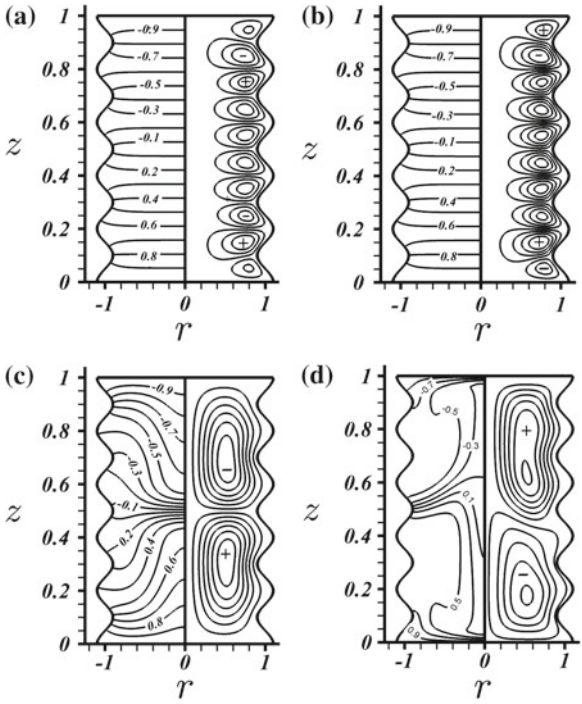

Fig. 2 Isotherms and stream function for the enclosure heated from *below* and $\varepsilon = 0.3$, $\Gamma = 0.1$ and $\Lambda = 1/5$. **a** $Ra = 10^3$, $\Delta\psi = 2.8 \times 10^{-6}$. **b** $Ra = 10^4$, $\Delta\psi = 8.6 \times 10^{-6}$. **c** $Ra = 10^5$, $\Delta\psi = 9.1 \times 10^{-3}$. **d** $Ra = 10^6$, $\Delta\psi = 8.5 \times 10^{-2}$

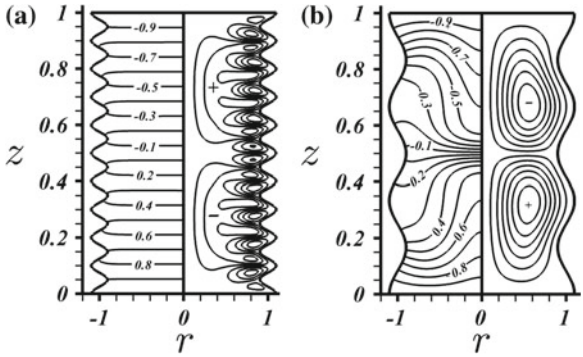

Fig. 3 Isotherms and stream function for the enclosure heated from *below*, $Ra = 10^5$, $\Gamma = 0.1$ and $\varepsilon = 0.3$. **a** $\Lambda = 1/10$, $\Delta\psi = 7.4 \times 10^{-6}$. **b** $\Lambda = 1/3$, $\Delta\psi = 1.1 \times 10^{-2}$

the dimensionless wavelength is large. The effect of Λ on the flow velocity may be estimated by the increments of the stream function values, $\Delta\psi$, corresponding to each figure. The heat transfer through the cavity is also strongly dependent on the dimensionless wavelength for high Rayleigh numbers. Figure 4 presents the average Nusselt number on the heating surface as a function of the Rayleigh number for $\Lambda = 1/10, 1/5, 1/3$, aspect ratio $\varepsilon = 0.3$, and dimensionless wave amplitude $\Gamma = 0.1$. For Rayleigh numbers lower than 10^4, the heat transfer is mainly due to conduction and the average Nusselt number is 1.74. Above $Ra = 10^4$ the average

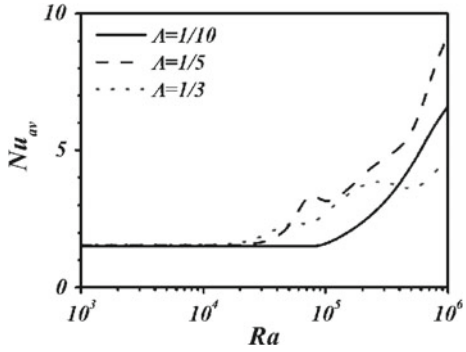

Fig. 4 Average Nusselt number for the enclosure heated from *below*, $\Gamma = 0.1$ and $\varepsilon = 0.3$

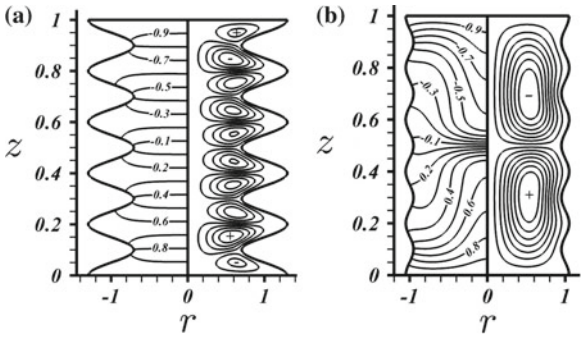

Fig. 5 Isotherms and stream function for the enclosure heated from *below*, $Ra = 10^5$, $\Lambda = 1/5$ and $\varepsilon = 0.3$. **a** $\Gamma = 0.3$, $\Delta\psi = 8.7 \times 10^{-5}$. **b** $\Gamma = 0.05$, $\Delta\psi = 9.2 \times 10^{-3}$

Nusselt number increases with Λ, and when Ra is of order 10^5 the heat transfer changes considerably, as shown in Fig. 4.

The dimensionless wave amplitude also defines the features of the convection cells and temperature distribution (see Fig. 5). Large wave amplitude causes the multiple cells pattern to induce slow motion in the whole cavity. Such a multiple cell convection pattern is associated to thermal stratification. On the other hand, when the wave amplitude is small there are two large convection cells and no thermal stratification exists. When the wave amplitude increases the average Nusselt number diminishes because of the thermal stratification and the resulting slow flow (Fig. 5a). For small wave amplitude the heat transfer increases due to the transport by two large convection cells (see Fig. 5b). Even for small Rayleigh numbers the effect of the wave amplitude on the average Nusselt number is notable, as can be seen in Fig. 6. The wave amplitude effect on heat transfer becomes more important as the Rayleigh number increases because convection dominates and the wall geometry defines the shape and velocity of the convection cells.

The cavity aspect ratio is a primary parameter for the convection patterns as shown in Fig. 7. If the cavity is tall, i.e. ε is small, a multiple convection cell pattern and a stratified temperature distribution hold along the whole cavity. If the cavity is short, two convection cells and no thermal stratification are present. Moreover, there exist thermal boundary layers near the upper and lower walls, while the fluid flow close

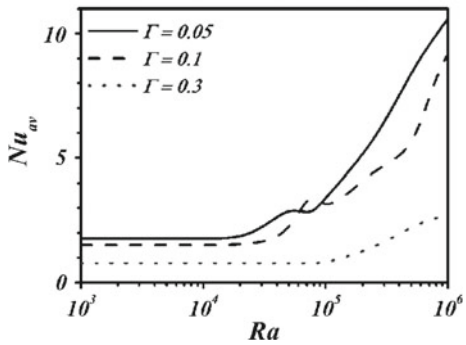

Fig. 6 Average Nusselt number for the enclosure heated from *below*, $\Lambda = 1/5$ and $\varepsilon = 0.3$

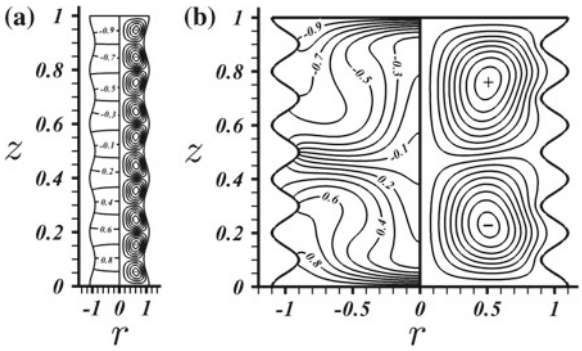

Fig. 7 Isotherms and stream function for the enclosure heated from *below*, $Ra = 10^5$, $\Lambda = 1/5$ and $\Gamma = 0.1$. **a** $\varepsilon = 0.1$ and $\Delta\psi = 4 \times 10^{-6}$. **b** $\varepsilon = 0.5$ and $\Delta\psi = 3.3 \times 10^{-2}$

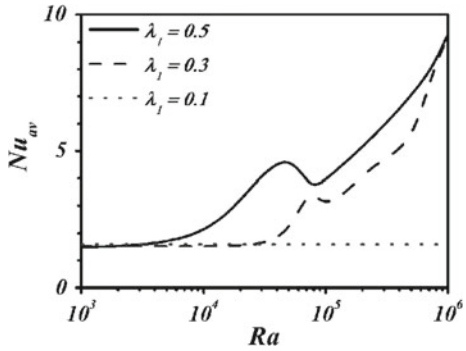

Fig. 8 Average Nusselt number for the enclosure heated from *below* and different values of ε. For this case $\Lambda = 1/5$ and $\Gamma = 0.1$

to the wavy wall is negligible. The increment of the stream function values $\Delta\psi$ in Fig. 7b shows a very low velocity for the multiple convection cells pattern. This last observation is also verified in Fig. 8, where the Nusselt number remains constant for $10^3 \leq Ra \leq 10^6$ and $\varepsilon = 0.1$, revealing the diffusion transport dominates the heat transfer process. As ε augments the heat transport increases considerable even for Rayleigh numbers of order 10^3. However, such a notable effect diminishes for large Rayleigh numbers, i.e. when convection dominates heat transfer.

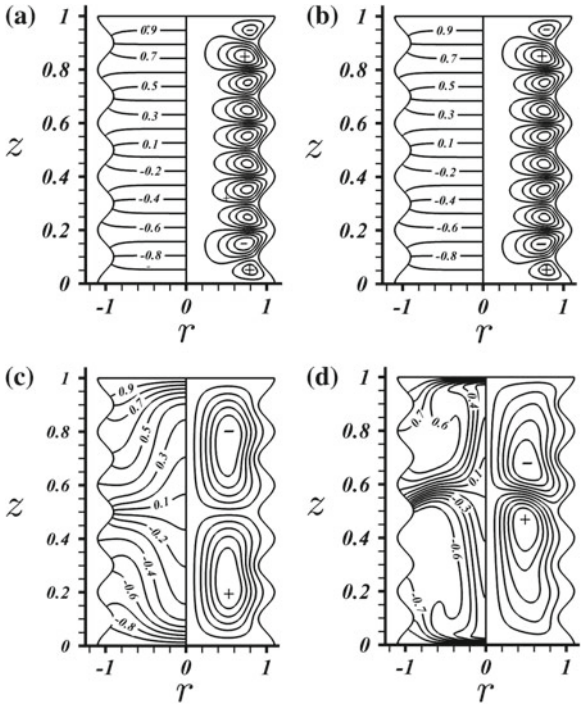

Fig. 9 Isotherms and stream function for the enclosure heated from the *top* and $\varepsilon = 0.3$, $\Gamma = 0.1$ and $\Lambda = 1/5$. **a** $Ra = 10^3$, $\Delta\psi = 8.8 \times 10^{-7}$. **b** $Ra = 10^4$, $\Delta\psi = 8.6 \times 10^{-6}$. **c** $Ra = 10^5$, $\Delta\psi = 1.1 \times 10^{-2}$. **d** $Ra = 10^6$, $\Delta\psi = 7.3 \times 10^{-2}$

4.2 Enclosure Heated from the Top

The second case studied considers that the cavity is heated from the top, cooled from below, while the lateral wavy wall is adiabatic. Dimensionless temperature and stream function distributions for Rayleigh numbers between 10^3 and 10^6 are shown in Fig. 9. The stream function shows multiple convection cells near the wavy wall when the Rayleigh number is of order 10^3. The cavity presents a stratified temperature distribution due to a weak convective transport. When the Rayleigh number increases around 10^4, the thermal stratification persists, while the fluid flow intensifies, according to the stream function values which increase at least one order of magnitude. For $Ra = 10^5$ the flow presents two convection cells, the lower cell with a clockwise rotation, and thermal distribution with notable temperature gradients near the upper and lower walls. Those temperature gradients become even more intensive for $Ra = 10^6$, when heat transfer is dominated by the two convection cells.

Figure 10 shows that the convection flow and the heat transfer are notably affected by the dimensionless wavelength, Λ, particularly for high Rayleigh numbers. When Λ is small there exists an almost stagnant thermally stratified core with multiple low velocity convection cells near the wavy wall. On the other hand, if Λ is large, there are two convection cells with no thermal stratification. Convection cells and ther-

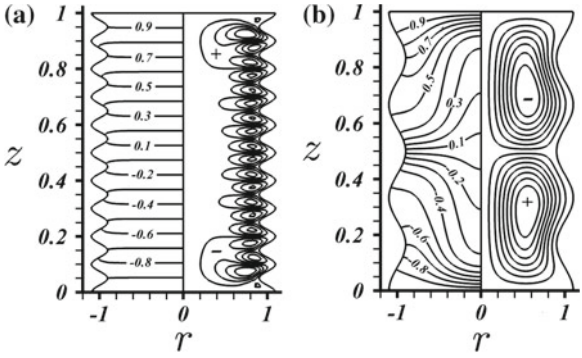

Fig. 10 Isotherms and stream function for the enclosure heated from the *top*, $Ra = 10^5$, $\Gamma = 0.1$ and $\varepsilon = 0.3$. **a** $\Lambda = 1/10$, $\Delta\psi = 7.1 \times 10^{-6}$. **b** $\Lambda = 1/3$, $\Delta\psi = 9.2 \times 10^{-3}$

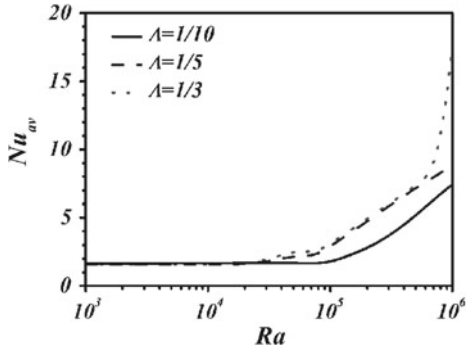

Fig. 11 Average Nusselt number for the enclosure heated from the *top*, $\Gamma = 0.1$ and $\varepsilon = 0.3$

mal distribution become sensitive to the wall geometry, specially for high Rayleigh numbers. Figure 11 presents the average Nusselt number as function of Ra when $\varepsilon = 0.3$, $\Gamma = 0.1$ and $\Lambda = 1/10, 1/5, 1/3$. When the Rayleigh number is lower than 10^4 the heat transfer is dominated by conduction and the average Nusselt number is approximately 1 (see Fig. 11). Above $Ra = 10^4$ the average Nusselt number increases with Λ, particularly when Ra is over 10^5. Additionally, when Λ is large its specific value does not change the convection heat transfer because large Λ yields a two cell flow pattern.

A comparison between Fig. 12a, b reveals that the increment of the wave amplitude causes a decrement of the convection velocity, according to the values of $\Delta\psi$ corresponding to each condition. Therefore, if the wave amplitude increases the average Nusselt number diminishes because of the thermal stratification and the resulting slow flow. On the other hand, for small wave amplitude the heat transfer increases due to the transport by two large convection cells (see Fig. 13). Even for small Rayleigh numbers the effect of the wave amplitude on the average Nusselt number is notable and becomes even more important as the Rayleigh number increases. Indeed, the wave amplitude restricts the convection heat transfer.

Figure 14 shows a multiple convection cell pattern which is thermally stratified and stands along the whole cavity when the cavity is tall. Contrarily, when the cavity is short there are two convection cells with negligible fluid flow near the wavy wall and

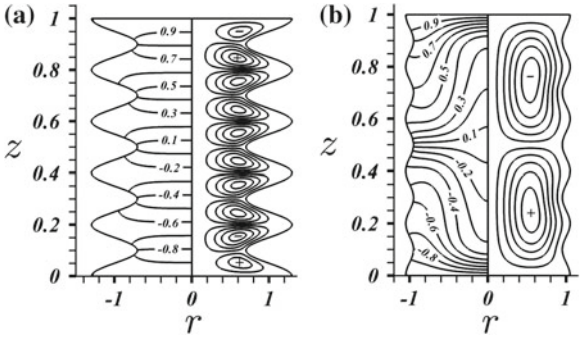

Fig. 12 Isotherms and stream function for the enclosure heated from the *top*, $Ra = 10^5$, $\Lambda = 1/5$ and $\varepsilon = 0.3$. **a** $\Gamma = 0.3$, $\Delta\psi = 8.1 \times 10^{-5}$. **b** $\Gamma = 0.05$, $\Delta\psi = 1.5 \times 10^{-2}$

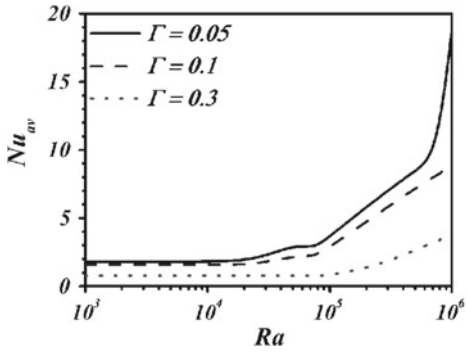

Fig. 13 Average Nusselt number for the enclosure heated from the *top*, $\Lambda = 1/5$ and $\varepsilon = 0.3$

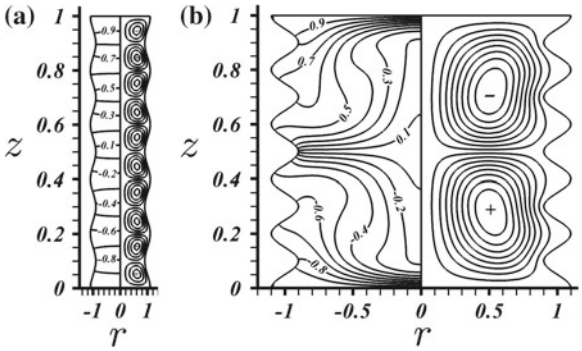

Fig. 14 Isotherms and stream function for the enclosure heated from the *top*, $Ra = 10^5$, $\Lambda = 1/5$ and $\Gamma = 0.1$. **a** $\varepsilon = 0.1$ and $\Delta\psi = 5.1 \times 10^{-6}$. **b** $\varepsilon = 0.5$ and $\Delta\psi = 3.3 \times 10^{-2}$

no thermal stratification is present, instead, there exist thermal boundary layers near the upper and lower walls. Comparing the values of $\Delta\psi$ in Fig. 14a, b it is clear that the multiple convection cells pattern flows very slowly. The remarkable difference between the heat transfer capabilities of those flows shown in Fig. 14 is also corroborated in Fig. 15, where the Nusselt number remains constant for $10^3 \leq Ra \leq 10^6$ and $\varepsilon = 0.1$, i.e. the diffusion transport dominates the heat transfer process. As ε augments the heat transfer increases considerable even for Rayleigh numbers of order 10^3, however, the effect of ε losses relevance for large Rayleigh numbers.

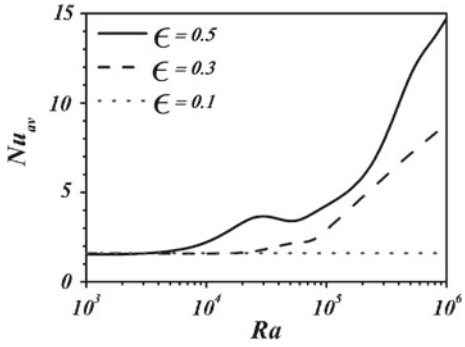

Fig. 15 Average Nusselt number for the enclosure heated from the *top* and different values of ε. For this case $A = 1/5$ and $\Gamma = 0.1$

5 Conclusions

An axisymmetric convection flow occurring within a vertical cylindrical enclosure with adiabatic wavy sidewall was studied. Thermal convection of two important cases were considered, heating from below and heating from the top, while the wavy sidewall is adiabatic. Different convection patterns arise which modify the heat transfer rate even for conditions where diffusion dominates. An analytical coordinate transformation was used to solve the axisymmetric problem which allowed to obtain a coordinate frame for computation in which the irregular domain fits into a square. Thermally stratified flow with multiple convection cells near the wavy wall arise when the Rayleigh number is of order 10^3. If the Rayleigh number increases the thermal stratification remains while the fluid flow intensifies. When the Rayleigh number increases even more, the flow presents two convection cells with notable temperature gradients near the upper and lower walls. For low values of the dimensionless wavelength there exists an almost stagnant thermally stratified core with multiple convection cells near the wavy wall. On the other hand, if the dimensionless wavelength is large, there are two convection cells with no thermal stratification, which resembles the well-known convection patterns corresponding to vertical cylindrical enclosures (Martynenko and Khramtsov 2005). Foregoing results demonstrate that the wave amplitude restricts the convection heat transfer. Tall cavities are related to thermal stratification with low heat transfer and there exists a remarkable difference between the heat transfer capabilities corresponding to short and tall cavities. The remarkable finding is that the wavy wall promotes thermal stratification and multiple cells patterns of low velocity, restricting the convection fluid flow which yields low heat transfer through the cavity.

Acknowledgments Authors would like to thank financial support from PAICyT-UANL through the Project IT 647-11.

Appendix: Coefficients and Parameters

Table 1 Coefficients of Eqs. 12 and 13

Name	Coefficient	Name	Coefficient
$\mathbb{A}$	$-\frac{1}{r}$	$\mathbb{I}$	$\frac{2\varepsilon^2}{r^3}\frac{\partial\psi}{\partial z}$
$\mathbb{B}$	$\frac{2}{r^2}-\frac{1}{r^2}\frac{\partial\psi}{\partial z}$	$\mathbb{J}$	$\frac{\varepsilon^2}{r^2}\frac{\partial\psi}{\partial r}$
$\mathbb{C}$	$\frac{3}{r^3}\frac{\partial\psi}{\partial z}-\frac{3}{r^3}$	$\mathbb{K}$	$-\frac{\varepsilon^4}{r}$
$\mathbb{D}$	$-\frac{3}{r^4}\frac{\partial\psi}{\partial z}+\frac{3}{r^4}$	$\mathbb{L}$	$\frac{Ra\varepsilon^4}{Pr}$
$\mathbb{E}$	$-\frac{2\varepsilon^2}{r}$	$\mathbb{N}$	$\frac{Pr}{r}\frac{\partial\psi}{\partial r}$
$\mathbb{F}$	$-\frac{\varepsilon^2}{r^2}\frac{\partial\psi}{\partial z}+\frac{2\varepsilon^2}{r^2}$	$\mathbb{O}$	$-\frac{1}{r}\left(Pr\frac{\partial\psi}{\partial z}+1\right)$
$\mathbb{G}$	$\frac{1}{r^2}\frac{\partial\psi}{\partial r}$	$\mathbb{P}$	-1
$\mathbb{H}$	$-\frac{1}{r^3}\frac{\partial\psi}{\partial r}$	$\mathbb{Q}$	$-\varepsilon^2$

Table 2 Coefficients of Eqs. 16 and 17

Name	Coefficient
b	$\mathbb{I}$
c	$\mathbb{J}$
d	$\mathbb{K}$
e	$\mathbb{F}\frac{2\Omega\Gamma\sin(\Omega\xi)}{\gamma^2}+\frac{\mathbb{H}}{\gamma}+\mathbb{I}\frac{2\eta\Gamma\Omega\sin(\Omega\xi)}{\gamma}+\mathbb{J}\left[\frac{3\eta\Gamma\Omega^2\cos(\Omega\xi)}{\gamma}+\frac{6\eta\Gamma^2\Omega^2\sin^2(\Omega\xi)}{\gamma^2}\right]+\mathbb{K}\left[\frac{-4\eta\Gamma\Omega^3\sin(\Omega\xi)}{\gamma}+\frac{24\eta\Gamma^2\Omega^3\cos(\Omega\xi)\sin(\Omega\xi)}{\gamma^2}+\frac{24\eta\Gamma^3\Omega^3\sin^3(\Omega\xi)}{\gamma^3}\right]$
f	$\frac{\mathbb{F}}{\gamma}+\mathbb{J}\frac{3\eta\Gamma\Omega\sin(\Omega\xi)}{\gamma}+\mathbb{K}\left[\frac{6\eta\Gamma\Omega^2\cos(\Omega\xi)}{\gamma}+\frac{12\eta\Gamma^2\Omega^2\sin^2(\Omega\xi)}{\gamma^2}\right]$
g	$\mathbb{K}\frac{4\eta\Gamma\Omega\sin(\Omega\xi)}{\gamma}$
h	$\mathbb{E}\frac{4\Gamma\Omega\sin(\Omega\xi)}{\gamma^3}+\mathbb{F}\frac{2\eta\Gamma\Omega\sin(\Omega\xi)}{\gamma^2}+\frac{\mathbb{G}}{\gamma^2}+\mathbb{J}\frac{3\eta^2\Gamma^2\Omega^2\sin^2(\Omega\xi)}{\gamma^2}+\mathbb{K}\left[\frac{12\eta^2\Gamma^2\Omega^3\sin(\Omega\xi)\cos(\Omega\xi)}{\gamma^2}+\frac{24\eta^2\Gamma^3\Omega^3\sin^3(\Omega\xi)}{\gamma^3}\right]$
i	$\mathbb{E}\frac{2\eta\Gamma\Omega\sin(\Omega\xi)}{\gamma^3}+\mathbb{K}\frac{4\eta^3\Gamma^3\Omega^3\sin^3(\Omega\xi)}{\gamma^3}$
j	$\frac{\mathbb{E}}{\gamma^2}+\mathbb{K}\frac{6\eta^2\Gamma^2\Omega^2\sin^2(\Omega\xi)}{\gamma^2}$
k	$\frac{\mathbb{D}}{\gamma}+\mathbb{F}\left[\frac{\Gamma\Omega^2\cos(\Omega\xi)}{\gamma^2}+\frac{2\Gamma^2\Omega^2\sin^2(\Omega\xi)}{\gamma^3}\right]+\mathbb{H}\frac{\Gamma\Omega\sin(\Omega\xi)}{\gamma^2}+\mathbb{I}\left[\frac{\eta\Gamma\Omega^2\cos(\Omega\xi)}{\gamma}+\frac{2\eta\Gamma^2\Omega^2\sin^2(\Omega\xi)}{\gamma^2}\right]+\mathbb{J}\left[\frac{-\eta\Gamma\Omega^3\sin(\Omega\xi)}{\gamma}+\frac{6\eta\Gamma^3\Omega^3\sin^3(\Omega\xi)}{\gamma^3}+\frac{6\eta\Gamma^2\Omega^3\cos(\Omega\xi)\sin(\Omega\xi)}{\gamma^2}\right]+\mathbb{K}\left[\frac{-\eta\Gamma\Omega^4\cos(\Omega\xi)}{\gamma}-\frac{8\eta\Gamma^2\Omega^4\sin^2(\Omega\xi)}{\gamma^2}+\frac{36\eta\Gamma^3\Omega^4\sin^2(\Omega\xi)\cos(\Omega\xi)}{\gamma^3}\right]+\mathbb{K}\left[\frac{24\eta\Gamma^4\Omega^4\sin^4(\Omega\xi)}{\gamma^4}+\frac{6\eta\Gamma^2\Omega^4\cos^2(\Omega\xi)}{\gamma^2}\right]$

(continued)

Table 2 (continued)

Name	Coefficient
l	$\frac{\mathbb{C}}{\gamma^2}+\mathbb{E}\left[\frac{6\Gamma^2\Omega^2\sin^2(\Omega\xi)}{\gamma^4}+\frac{2\Gamma\Omega^2\cos(\Omega\xi)}{\gamma^3}\right]+\mathbb{F}\left[\frac{\eta\Gamma\Omega^2\cos(\Omega\xi)}{\gamma^2}+\frac{4\eta\Gamma^2\Omega^2\sin^2(\Omega\xi)}{\gamma^3}\right]+\mathbb{G}\frac{2\Omega\Gamma\sin(\Omega\xi)}{\gamma^3}+\mathbb{H}\frac{\eta\Gamma\Omega\sin(\Omega\xi)}{\gamma^2}+\mathbb{I}\frac{\eta^2\Gamma^2\Omega^2\sin^2(\Omega\xi)}{\gamma^2}+\mathbb{J}\left[\frac{6\eta^2\Gamma^3\Omega^3\sin^3(\Omega\xi)}{\gamma^3}+\frac{3\eta^2\Gamma^2\Omega^3\sin(\Omega\xi)\cos(\Omega\xi)}{\gamma^2}\right]+\mathbb{K}\left[\frac{3\eta^2\Gamma^2\Omega^4\cos^2(\Omega\xi)}{\gamma^2}-\frac{4\eta^2\Gamma^2\Omega^4\sin^2(\Omega\xi)}{\gamma^2}\right]+\mathbb{K}\left[\frac{36\eta^2\Gamma^3\Omega^4\sin^2(\Omega\xi)\cos(\Omega\xi)}{\gamma^3}+\frac{36\eta^2\Gamma^4\Omega^4\sin^4(\Omega\xi)}{\gamma^4}\right]$
m	$\frac{\mathbb{B}}{\gamma^3}+\mathbb{E}\left[\frac{\eta\Gamma\Omega^2\cos(\Omega\xi)}{\gamma^3}+\frac{6\eta\Gamma^2\Omega^2\sin^2(\Omega\xi)}{\gamma^4}\right]+\mathbb{F}\frac{\eta^2\Gamma^2\Omega^2\sin^2(\Omega\xi)}{\gamma^3}+\mathbb{G}\frac{\eta\Gamma\Omega\sin(\Omega\xi)}{\gamma^3}+\mathbb{J}\frac{\eta^3\Gamma^3\Omega^3\sin^3(\Omega\xi)}{\gamma^3}+\mathbb{K}\left[\frac{6\eta^3\Gamma^3\Omega^4\sin^2(\Omega\xi)\cos(\Omega\xi)}{\gamma^3}+\frac{12\eta^3\Gamma^4\Omega^4\sin^4(\Omega\xi)}{\gamma^4}\right]$
n	$\frac{\mathbb{A}}{\gamma^4}+\mathbb{E}\frac{\eta^2\Gamma^2\Omega^2\sin^2(\Omega\xi)}{\gamma^4}+\mathbb{K}\frac{\eta^4\Gamma^4\Omega^4\sin^4(\Omega\xi)}{\gamma^4}$
o	$\mathbb{N}$
p	$\mathbb{Q}$
q	$\mathbb{Q}\frac{2\eta\Gamma\Omega\sin(\Omega\xi)}{\gamma}$
p	$\mathbb{N}\frac{\eta\Omega\Gamma\sin(\Omega\xi)}{\gamma}+\frac{\mathbb{O}}{\gamma}+\mathbb{Q}\left[\frac{\eta\Gamma\Omega^2\cos(\Omega\xi)}{\gamma}+\frac{2\eta\Gamma^2\Omega^2\sin^2(\Omega\xi)}{\gamma^2}\right]$

Table 3 Coefficients of the boundary condition in Eq. 21

Name	Coefficient
A''	$\frac{\eta\Gamma^2\varepsilon^2\Omega^2\sin^2(\Omega\xi)+1}{\gamma}$
B''	$\Gamma\varepsilon^2\,\Omega\sin(\Omega\xi)$

where

$$\Omega = 2\pi/\Lambda \text{ and } \gamma = 1+\Gamma\cos(\Omega\xi)\,.$$

References

Adjlout L, Imine O, Azzi A, Belkadi M (2001) Laminar natural convection in an inclined cavity with a wavy wall. Int J Heat Mass Transf 45:2141–2152

Aounallah M, Addad Y, Benhamadouche S, Imine O, Adjlout L, Laurence D (2006) Numerical investigation of turbulent natural convection in an inclined square cavity with a hot wavy wall. Int J Heat Mass Transf 50:1683–1693

Ashjaee M, Amiri M, Rostami J (2007) A correlation for free convection heat transfer from vertical wavy surfaces. Heat Mass Transf 44:101–111

Dalal A, Das MK (2004) Laminar natural convection in an inclined complicated cavity with spatially variable wall temperature. Int J Heat Mass Transf 48:3833–3854

Dalal A, Das MK (2006) Natural convection in a cavity with a wavy wall heated from below and uniformly cooled from the top and both sides. J Heat Transf 128:717–725
Elgazery NS, Abd NY (2009) The effects of variable properties on MHD unsteady natural convection heat and mass transfer over a vertical wavy surface. Mecanica 44:573–586
Hossain MA, Rees DAS (1999) Combined heat and mass transfer in natural convection flow from a vertical wavy surface. Acta Mech 136:133–141
Martynenko OG, Khramtsov PP (2005) Free-convective heat transfer. Springer, The Netherlands
Misirlioglu A, Baytas AC, Pop I (1999) Natural convection inside an inclined wavy enclosure filled with a porous media. Trans Porous Media 64:229–246
Molla M, Hossain A, Yao LS (2007) Natural-convection flow along a vertical complex wavy surface with uniform heat flux. J Heat Transf 129:1403–1407
Rathish Kumar BV, Murthy K (2010) Soret and Dufour effects on double-diffusive free convection from a corrugated vertical surface in a non-darcy porous medium. Transp Porous Media 85:117–130
Rostami J (1999) Unsteady natural convection in an enclosure with vertical wavy walls. Heat Mass Transf 44:1079–1087
Tashtoush B, Abu-Irshaid E (2001) Heat and fluid flow from a wavy surface subjected to a variable heat flux. Acta Mech 152:1–8
Woollard HF, Billingham J, Jensen OE, Lian G (2008) A multi-scale model for solute transport in a wavy-walled channel. J Eng Math 64:25–48

Part IV
Vortex, Oceanography and Meteorology

Numerical Simulation of the Flow Past a Pair of Magnetic Obstacles

J. Román, A. Beltrán and S. Cuevas

Abstract We present a quasi-two-dimensional numerical simulation of the flow of a thin layer of electrolyte past a pair of localized Lorentz forces, named *magnetic obstacles*, placed side by side. Opposing Lorentz forces are produced by the interaction of the magnetic field created by a pair of small permanent magnets and a D.C. current applied tranversally to the main flow. By varying the separation between the magnets and the intensity of the applied current, different flow regimes are analyzed. The attention is focused on the interference of the wakes created by the magnetic obstacles.

1 Introduction

The flow past solid obstacles is certainly one of the most widely studied problems in fluid dynamics and constitutes in itself a classic subject of research (Zdravkovich 1997). Its importance stems from countless applications where determining the behavior of flows past bluff bodies is of practical interest. From the point of view of dynamical system, the understanding of the spatio-temporal behavior of the wakes formed in flows past solid obstacles presents interesting challenges. When more than one obstacle is present, investigating the interference of wakes becomes a relevant issue (Gal et al. 1996). In fact, the behavior of coupled wakes created by a pair of cylinders placed side by side in a uniform flow has been studied experimentally and theoretically by several authors and different flow regimes have been identified according to the separation between the cylinders (Zdravkovich 1985; Le Gal et al. 1990; Peschard and Gal 1996; Sumner et al. 1999). But, wakes are not only

J. Román · S. Cuevas (✉)
Instituto de Energías Renovables, Universidad Nacional Autónoma de México,
A.P. 34, Temixco, 62580 Morelos, México
e-mail: scg@ier.unam.mx

A. Beltrán
Instituto de Investigaciones en Materiales, Unidad Morelia,
Universidad Nacional Autónoma de México, Antigua Carretera a Pátzcuaro No. 8701,
Col. Ex Hacienda de San José de la Huerta, 58190 Morelia, MICH, Mexico

J. Klapp et al. (eds.), *Selected Topics of Computational and Experimental Fluid Mechanics*, Environmental Science and Engineering,
DOI 10.1007/978-3-319-11487-3_31

produced by solid obstacles. It has been shown that localized magnetic forces in flows of electrically conducting fluids act as obstacles for the flow. When the conducting fluid is a liquid metal, the relative motion of the fluid and a localized magnetic field induces electric currents that interact with the same field to produce a Lorentz force braking the liquid (Cuevas et al. 2006; Votyakov et al. 2007). In the case of an electrolyte, due to the low conductivity of the fluid, induced currents are negligible but an opposing Lorentz force can still be created if an electric current is externally applied (Honji 1991; Honji and Haraguchi 1995; Afanasyev and Korabel 2006). In both cases, experimental and theoretical studies have shown the appearance of different flow regimes such as steady vortices, vortex shedding, and even turbulent wakes (Honji and Haraguchi 1995; Afanasyev and Korabel 2006; Votyakov et al. 2008; Kenjeres et al. 2011). In fact, the term *magnetic obstacle* was coined (Cuevas et al. 2006) to emphasize that localized Lorentz forces produce flow behaviors that in some aspects resemble flows past solid obstacles, although very important differences exist.

So far, investigations of flows past magnetic obstacles have mainly addressed the problem of a single obstacle in liquid metal flows (see, for instance, Votyakov et al. 2008; Kenjeres et al. 2011; Tympel et al. 2013). Recently, the flow in an array of three magnetic obstacles has been simulated numerically (Kenjeres 2012), a situation that may have relevance for heat transfer applications (Zhang and Huang 2013). Flows of electrolytes past magnetic obstacles have been less explored. Honji (1991) and Honji and Haraguchi (1995) performed experiments in a shallow layer of salt water contained in a long tank, where a D.C. current was applied transversally to the tank's long axis, while a permanent magnet located externally was dragged at a constant velocity along the center line of the water tank. Similarly, more extensive experiments were performed by Afanasyev and Korabel (2006). These authors considered flows produced by a single magnet as well as by two magnets with opposite orientations, aligned with the direction of motion and separated by a short distance. However, to the best of our knowledge, the electrolytic flow created by a pair of magnetic obstacles side by side has not been previously considered. This problem is interesting, since the analogous flow with solid obstacles has been investigated extensively so that flow regimes are well characterized (Zdravkovich 1985; Peschard and Gal 1996; Sumner et al. 1999). In the present paper, we explore numerically the flow past a pair of magnetic obstacles side by side and compare the flow regimes with those corresponding to the flow past solid cylinders.

2 Formulation of the Problem

We consider the flow of a shallow layer of an electrolyte in a rectangular container affected by localized Lorentz forces, i.e. magnetic obstacles. The forces are produced by the interaction of magnetic fields generated by two permanent magnets and a D.C. electrical current applied transversally to the main flow through electrodes located in the lateral walls and connected to a power source. Square magnets whose side length

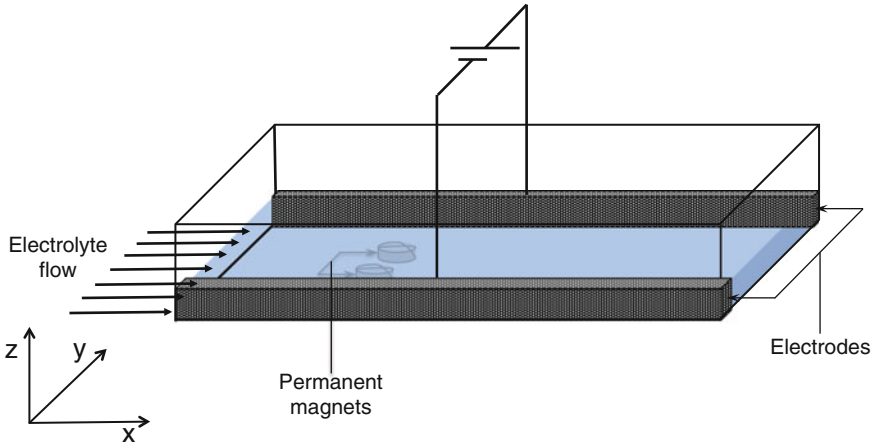

Fig. 1 Sketch of the electrolytic flow past a pair of magnetic obstacles side by side. See details in the text

L is much smaller than the distance between lateral walls, are placed beneath the bottom wall of the container with an orientation such that resulting Lorentz forces oppose the oncoming flow and generate vorticity. Figure 1 shows a sketch of the problem under consideration. Since the thickness of the fluid layer is assumed to be small compared with horizontal dimensions, we use a quasi-two-dimensional (Q2D) numerical model that only considers the component of the applied magnetic field normal to the plane of motion. This component can be expressed as

$$B_z^0(x, y, z) = B(x, y)g(z), \tag{1}$$

where $B(x, y)$ reproduces the variation of the magnetic field in the x–y plane and is modeled by a dipolar field distribution created by a square magnetized surface uniformly polarized in the normal direction, for which an explicit analytical expression is available (McCaig 1977; Cuevas et al. 2006). In fact, the shape of the magnets is irrelevant provided the plane of flow is separated from the surface of the magnet, so that border effects are smoothed out (Figueroa et al. 2009). In turn, $g(z) = \exp(-\gamma z)$ models the decay of the magnetic field in the normal direction z (normalized by the layer thickness h), where $\gamma = 0.51$ is an empirical constant obtained from fitting the decay of the magnetic field in the vertical direction (Beltrán 2010) with experimental data from a permanent magnet (Honji 1991). In addition, the Q2D model assumes that the momentum transfer through the thin electrolytic layer is mainly diffusive so that the velocity field can be expressed as

$$\mathbf{u}(x, y, z, t) = [\overline{u}(x, y, t)f(x, y, z), \overline{v}(x, y, t)f(x, y, z), 0], \tag{2}$$

where $\overline{u}$ and $\overline{v}$ are the mean velocity components in the x–y plane, while $f(x, y, z)$ reproduces the velocity profile in the layer thickness (Beltrán 2010). Since the electrical conductivity of the electrolyte is low compared with that of liquid metals, and the magnetic field intensity of permanent magnets is weak, induced currents in the fluid are negligible. Therefore, it becomes unnecessary to solve the induction equation to determine the induced magnetic field. Only the applied current is relevant for calculating the Lorentz forces (Figueroa et al. 2009).

Substituting Eqs. (1) and (2) in the three-dimensional equations of motion and averaging along the height of the fluid layer, we obtain the Q2D equations. A detailed description of the averaging procedure can be found in (Beltrán 2010; Figueroa et al. 2009). In dimensionless terms, the equations of motion in the Q2D approximation take the form

$$\frac{\partial u}{\partial x} + \frac{\partial v}{\partial y} = 0, \tag{3}$$

$$\frac{\partial u}{\partial t} + \left(u\frac{\partial u}{\partial x} + v\frac{\partial u}{\partial y} \right) = -\frac{\partial P}{\partial x} + \frac{1}{Re}\nabla_{\perp}^2 u + \frac{u}{\tau} - Q B_z^0, \tag{4}$$

$$\frac{\partial v}{\partial t} + \left(u\frac{\partial v}{\partial x} + v\frac{\partial v}{\partial y} \right) = -\frac{\partial P}{\partial y} + \frac{1}{Re}\nabla_{\perp}^2 v + \frac{v}{\tau}, \tag{5}$$

where the overline in the velocity components was dropped and subindex $\perp$ denotes the projection of the ∇ operator on the x–y plane. The velocity components, u and v, the pressure, P, the applied current density, j, and the applied magnetic field, B_z^0, are normalized by U, ρU^2, J_0 and B_{max}, respectively. Here, U is the uniform entrance velocity, ρ is the mass density, B_{max} is the maximum intensity of the magnetic field, and J_0 is the magnitude of the applied current density. Dimensionless coordinates x and y are normalized by L, while time, t, is normalized by L/U. Dimensionless parameters Re and Q stand for the Reynolds number $Re = UL/\nu$, where ν is the kinematic viscosity, and the Lorentz force parameter $Q = J_0 B_{max} L/\rho U^2$ which is the ratio of a magnetic pressure drop caused by the applied Lorentz force and the free-stream dynamic pressure. Essentially, Q characterizes the strength of the Lorentz forces. The third term on the right-hand-side of Eqs. (4) and (5) represents the Rayleigh friction between the fluid and the bottom wall. It involves a characteristic dimensionless timescale, τ, for the decay of vorticity due to dissipation in the viscous layers and is given by (Beltrán 2010)

$$\tau^{-1} = \frac{\gamma(1 - \mathrm{e}^{-\gamma})}{\frac{1}{\gamma}(1 - \mathrm{e}^{-\gamma}) + \frac{\gamma}{2}\mathrm{e}^{-\gamma} - 1}. \tag{6}$$

The considered boundary conditions are the following. At the entrance, a uniform flow is imposed in the x-direction, therefore

$$u = 1, \qquad v = 0, \qquad \text{at } x = 0, \quad 0 \le y \le H. \tag{7}$$

At the outlet, Neumann boundary conditions are used, that is,

$$\frac{\partial u}{\partial x} = \frac{\partial v}{\partial x} = 0, \qquad \text{at } x = X_L, \qquad 0 \le y \le H. \tag{8}$$

At the side walls, we use no-slip conditions:

$$u = 0, \qquad v = 0, \qquad \text{at } \; y = 0, H, \qquad 0 \le x \le X_L. \tag{9}$$

Here, H is the separation between lateral boundaries which determines the solid blockage of the confined flow, characterized by the blockage parameter $\beta = 1/H$. In turn, X_L is the total length of the channel. The magnetic obstacles are located at distances X_u from the entrance and X_d from the outlet. All the lengths are measured in dimensionless units. The centers of the magnets are separated by a dimensionless distance $D = d/L$, where d is the dimensional separation. Figure 2 shows a sketch of the flow conditions considered for the numerical solution.

A finite volume method implemented with a SIMPLEC algorithm is used to solve the governing equations (3)–(6) with boundary conditions (7)–(9). The diffusive and convective terms are discretized using a central difference scheme. Accurate temporal resolution is provided by choosing a small enough time step and employing a second order scheme for the time integration. The numerical solution was obtained in a rectangular domain with a length of $X_L = 35$ dimensionless units in the streamwise direction and $H = 7$ units in the cross-stream direction using an equidistant orthogonal grid of 212×202 nodes. It was determined that an upstream distance $X_u = 10$ and a downstream distance $X_d = 25$ guarantee results that are nearly independent of the location of the obstacles.

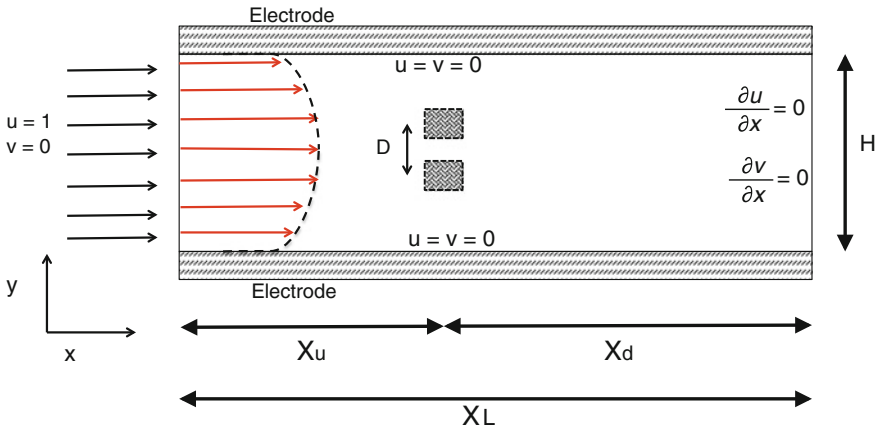

Fig. 2 Sketch of the geometry and boundary conditions considered for the analyzed flow

3 Numerical Results

In a similar way as when the obstacles are solid cylinders, flows past a pair of magnetic obstacles side by side present different regimes according to the flow conditions. While hydrodynamic regimes are governed only by the Reynolds number and the dimensionless separation distance D (provided three-dimensional effects are neglected), in the present case flow regimes are controlled by Q, in addition to Re and D. The variation of these parameters leads to steady or time-dependent regimes, as occurs in flows with a single magnetic obstacle (Honji and Haraguchi 1995; Afanasyev and Korabel 2006). We present numerical results for a pair of magnetic obstacles side by side with a fixed Reynolds number, $Re = 1{,}000$, and investigate the variation of Q and D on the flow dynamics. We consider flow conditions where vortex shedding is present and explore the effect of separation distance D on the coupling of the wakes behind the obstacles. The parameter Q is varied in the range $1.5 \leq Q \leq 10$, and for a given D, the value of Q corresponds to the minimum value where vortex shedding appears. In turn, four different values of D are explored, namely, 1, 1.5, 2, and 3, which are of interest since results for the hydrodynamic flow past a pair of solid obstacles are available in the literature for these cases (Peschard and Gal 1996; Zdravkovich 1985).

In hydrodynamic flows, it has been reported that for large distances between the cylinders, the pair of wakes presents a weak coupling where in phase and out of phase vortex shedding can appear. In turn, for shorter distances a strong coupling arises and only in phase shedding is observed which produces a unique von Kármán street (Peschard and Gal 1996; Zdravkovich 1985). At intermediate range of coupling, a bistable regime can emerge which is characterized by a biased flow that gives two possible values for the vortex shedding frequency. The biased flow is an intermittent flow between two asymmetric states. That is, through the gap the biased flow divides asymmetric states with narrow and wide wakes which can intermittently interchange between the two cylinders (Zdravkovich 1985), apparently driven by a random process (Peschard and Gal 1996). We now show that similar regimes are observed in the wakes created by a pair of magnetic obstacles side by side.

Figure 3 shows the Lagrangian tracking of flows obtained numerically for different values of D, with the corresponding minimum value of Q where vortex shedding appears. For the smallest separation distance, $D = 1$ (see Fig. 3a), the magnets are in contact and act as a larger magnetic obstacle that gives rise to a single wake similar to the von Kármán street. If the gap between the obstacles is increased to $D = 1.5$, we find a bistable regime where the flow pattern is rather complex, as is observed in Fig. 3b. A further increase to $D = 2$ (see Fig. 3c) leads to a more structured flow pattern with two interlaced wakes in phase. For the larger gap explored, namely $D = 3$, the separation between the wakes is neatly defined and the in phase behavior still persists, as observed in Fig. 3d.

To improve the understanding of the flow behavior and the coupling of the wakes behind the magnetic obstacles, the velocity component in the x-direction is shown in Fig. 4 as a function of time at two distinct points located on the central line of each

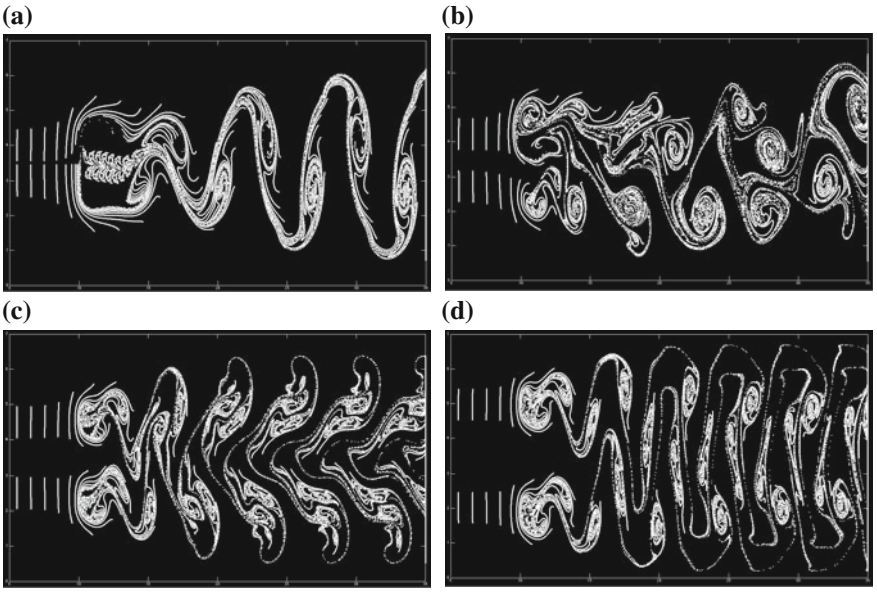

Fig. 3 Lagrangian tracking of the numerically calculated flow past a pair of magnetic obstacles side by side at different separation distances. $Re = 1{,}000$. **a** D = 1, $Q = 2.7$. **b** D = 1.5, $Q = 2.9$. **c** D = 2, $Q = 2.4$. **d** D = 3, $Q = 2.3$

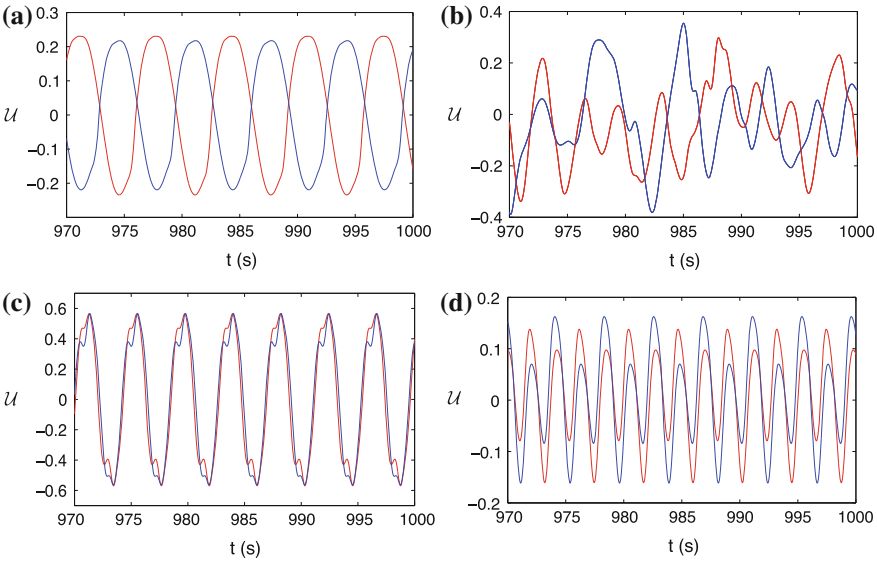

Fig. 4 Velocity component in the x-direction as a function of time at two different points. *Blue* (*red*) line corresponds to the point located at the central line of the *upper* (*lower*) obstacle five dimensionless units downstream. $Re = 1{,}000$. **a** $D = 1$, $Q = 2.7$. **b** $D = 1.5$, $Q = 2.9$. **c** $D = 2$, $Q = 2.4$. **d** $D = 3$, $Q = 2.3$

obstacle, five dimensionless units downstream. For $D = 1$ (Fig. 4a), corresponding to the single wake of a large magnetic obstacle, the velocity signals oscillate in antiphase. This is consistent with the fact that a large oscillating vortex structure is formed behind the obstacle so that in the symmetrically located points where the signals are registered, the velocity in the x-direction takes opposite values. For $D = 1.5$ which corresponds to the bistable flow, velocity oscillations do not present a defined structure. This seems to be a characteristic feature of this regime as it has been reported in the literature for the case of circular cylinders (Zdravkovich 1985; Peschard and Gal 1996). Figure 4c clearly shows in phase oscillations of the velocity signals when $D = 2$ where even the amplitude of the oscillations coincides. Finally, when $D = 3$ (Fig. 4d), although velocity oscillations are in phase, amplitudes do not coincide which indicate a weaker coupling of the wakes.

Important information can also be obtained from the Fourier analysis of the temporal behavior of the velocity signals, particularly for determining the dominant dimensionless frequency of the flow, that is, the Strouhal number. It is precisely at this frequency at which the greatest amount of energy in the flow is transported. Figure 5 shows the power spectrum obtained through the fast Fourier transform of the corresponding velocity signals presented in Fig. 4 for different values of D. Only the spectrum at one point is shown since it coincides with the one at the other point. In Fig. 5a ($D = 1$), a clear dominant characteristic frequency of 0.152 and its corresponding harmonics are shown. This frequency is close to the ones obtained

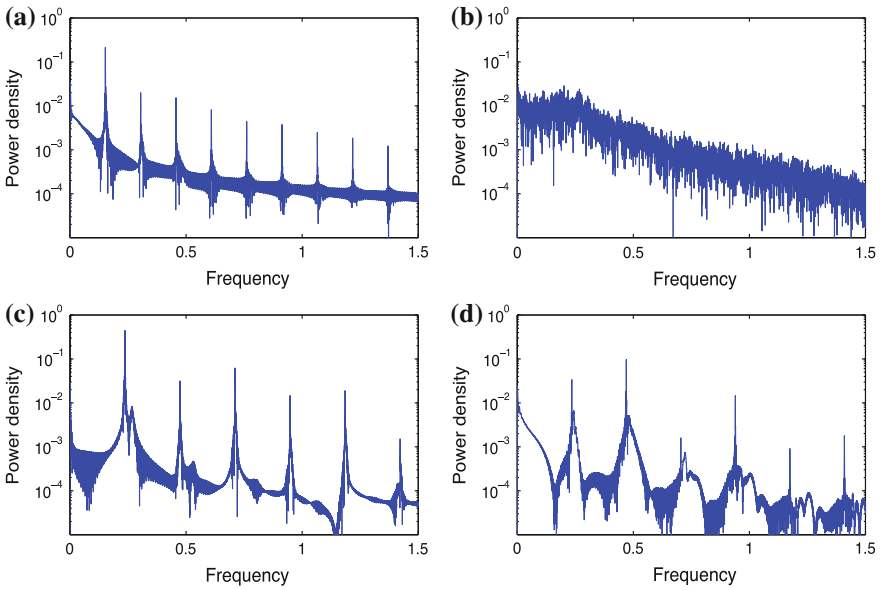

Fig. 5 Power spectrum calculated by the Fast Fourier Transform of the velocity signals presented in Fig. 4. $Re = 1{,}000$. **a** $D = 1$, $Q = 2.7$. **b** $D = 1.5$, $Q = 2.9$. **c** $D = 2$, $Q = 2.4$. **d** $D = 3$, $Q = 2.3$

experimentally by Honji and Haraguchi (1995) for the flow past a single magnetic obstacle. Further, it almost coincides with the value of 0.150 corresponding to the flow past a solid cylinder (Zdravkovich 1997). For the bistable flow at $D = 1.5$ (Fig. 5b), it does not exist a clear dominant frequency since this local analysis does not capture the global behavior of the biased flow that may present two distinct characteristic frequencies for the vortex shedding. Finally, Fig. 5c,d display very similar Strouhal numbers of 0.235 and 0.237 for $D = 2$ and $D = 3$, respectively. It could be expected that for a large enough separation distance, the dominant frequency of each wake should be close to that of a single magnetic obstacle ($\approx$0.152). The difference with the latter case for $D = 2$ and $D = 3$ manifests that the coupling of the wakes is still present at these separation distances. In fact, for the flow past a pair of solid cylinders side by side, the uncoupling of the wakes is observed at $D \approx 5.5$ (Le Gal et al. 1990).

A characteristic feature of the bistable regime is the tendency of the flow in the gap between the obstacles to tilt towards one obstacle at a given time and towards the other obstacle at a later time. This deflection breaks the symmetry of the flow pattern (Le Gal et al. 1990). Figure 6 illustrates this phenomenon through the instantaneous velocity fields at two different times for the bistable regime observed when $D = 1.5$.

Although in previous results only time-dependent flows were considered, at lower values of Q steady flow patterns displaying a vortex pair are found (Román 2013). With the aim of describing the studied flow in a more complete way, Fig. 7 presents a map that shows the regions of steady and time-dependent behavior in terms of the analyzed values of Q and D, for $Re = 1{,}000$. The transition zone between steady and unsteady flows is presented with a gray strip since it is not possible to determine an exact value for this transition. This map is built based on the time behavior of the velocity signals. It is observed that for a fixed D, vortex shedding disappears as Q decreases.

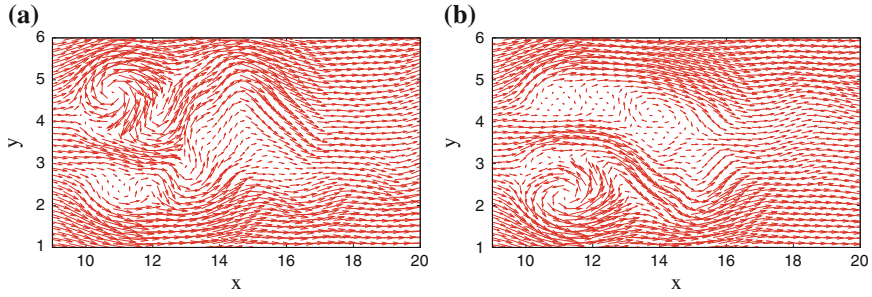

Fig. 6 Instantaneous velocity fields for the bistable regime. $Re = 1{,}000$, $Q = 2.9$ and $D = 1.5$. **a** $t = 1975$, **b** $t = 1992$

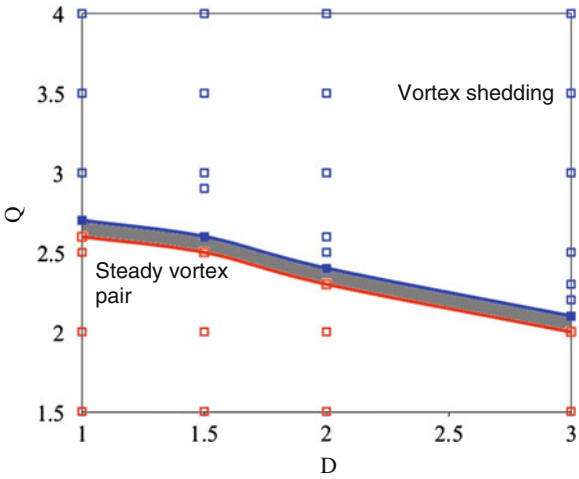

Fig. 7 Stability map of the flow past a pair of magnetic obstacles side by side. The *gray* strip displays the transition zone between steady and time-dependent flow. $Re = 1{,}000$

4 Concluding Remarks

In this work, we have investigated numerically using a Q2D model the flow past a pair of magnetic obstacles side by side at a fixed Reynolds number, $Re = 1{,}000$. We analyzed the coupling of the wakes behind the magnetic obstacles under vortex shedding conditions for different values of the dimensionless separation distance, namely, $D = 1$, 1.5, 2, and 3. From the numerical velocity field, Lagrangian trajectories were obtained which allow to visualize different flow structures. A strong coupling was found for $D = 1$ where the pair of obstacles act as a large magnetic obstacle that produces a single wake whose dominant frequency is close to the one found experimentally (Honji and Haraguchi 1995) and almost coincide with that of the flow past a solid cylinder. A more complex pattern was found for $D = 1.5$ where an intermediate coupling leads to a bistable regime, characterized by a biased flow with asymmetric flow structures. Finally, a weaker coupling of the wakes was found for $D = 2$ and $D = 3$, where well defined in phase wakes are observed. In general terms, it can be stated that the flow past a pair of magnetic obstacles side by side presents similar regimes as those observed in the wakes created by a pair of solid cylinders.

Acknowledgments This work has been supported by CONACyT, Mexico, under project 131399. J. Román also acknowledges a grant from CONACyT. The authors are grateful to Saul Piedra for providing the subroutine for the particle tracking that we present in this article.

References

Afanasyev YD, Korabel VN (2006) J Fluid Mech 553:119–141
Beltrán A (2010) Flow dynamics in magnetic obstacles. PhD thesis, National Autonomous University of Mexico
Cuevas S, Smolentsev S, Abdou MA (2006) J Fluid Mech 553:227–252
Figueroa A, Demiaux F, Cuevas S, Ramos E (2009) J Fluid Mech 641:245–261
Honji H (1991) J Phys Soc Jpn 60(4):1161–1164
Honji H, Haraguchi Y (1995) J Phys Soc Jpn 64(7):2274–2277
Kenjeres S (2012) Phys Fluids 24:115111
Kenjeres S, ten Cate S, Voesenek CJ (2011) Int J Heat Fluid Flow 32:510–528
Le Gal P, Chauve MP, Lima R, Rezende J (1990) Phys Rev A 41:4566–4569
Le Gal P, Peschard I, Chauve MP, Takedaa Y (1996) Phys Fluids 8(8):2097–2106
McCaig M (1977) Permanent magnets in theory and practice. Wiley, New York
Peschard I, Le Gal P (1996) Phys Rev Lett 77:3122–3125
Román J (2013) Numerical study of the heat transfer in flows past arrays of magnetic obstacles. MSc thesis, National Autonomous University of Mexico (In Spanish)
Sumner D, Wong SST, Price SJ, Paidoussis MP (1999) J Fluids Struct 13:309–338
Tympel S, Boeck T, Schumacher J (2013) J Fluid Mech 735:553–586
Votyakov EV, Kolesnikov Yu, Andreev O, Zienicke E, Thess A (2007) Phys Rev 98:144504
Votyakov EV, Zienicke E, Kolesnikov Yu (2008) J Fluid Mech 610:131–156
Zdravkovich MM (1985) J Sound Vib 101:511–521
Zdravkovich MM (1997) Flow around circular cylinders, vol I. Oxford University Press, New York
Zhang X, Huang H (2013) ASME J Heat Transf 135:021702

Steady and Unsteady Vortex Flow Generated by Electromagnetic Forcing

C.G. Lara, A. Figueroa and S. Cuevas

Abstract In this paper, we present a numerical and experimental study of the laminar flow that results from the interaction of vortices driven electromagnetically in a thin layer of an electrolyte. The fluid motion is generated by a Lorentz force due to a uniform D.C. current and a non-uniform magnetic field produced by different symmetric arrays of small permanent magnets placed on the perimeter of a circle. Depending on the number of magnets and the intensity of the electric current, we find that steady or unsteady vortex flow patterns may arise. We developed a quasi-two-dimensional numerical model that accounts for the effect of the boundary layer adhered to the bottom wall. Once the velocity field is obtained, we perform a Lagrangian tracking that shows a good qualitative comparison with the experimental flow visualization. From numerical and experimental results, a map of stability that defines regions of steady and unsteady flow, according to the electric current intensity and magnet arrays, is built. We find that the larger the number of magnets, the less intense the applied current required to transit from steady to unsteady flow patterns.

1 Introduction

Vortex dynamics is a topic of great importance in many natural and technological phenomena. In particular, the study of laminar vortices may improve the comprehension of the fundamental mechanisms involved in mixing processes at low Reynolds numbers (Ottino 1990). Usually, the interaction of vortices gives rise to very interesting behaviors and flow patterns as occurs, for instance, when a pair of corotating vortices merge into a single structure (Meunier and Leweke 2005). To a large degree,

C.G. Lara · S. Cuevas (✉)
Instituto de Energías Renovables, Universidad Nacional Autónoma de México,
A.P. 34, 62580 Temixco, Morelos, Mexico
e-mail: scg@ier.unam.mx

A. Figueroa
Facultad de Ciencias, Universidad Autónoma del Estado de Morelos,
62209 Cuernavaca, Morelos, Mexico

J. Klapp et al. (eds.), *Selected Topics of Computational and Experimental Fluid Mechanics*, Environmental Science and Engineering,
DOI 10.1007/978-3-319-11487-3_32

nonlinear effects determine the flow field that results from vortex interaction. One of the classical problems of fluid dynamics consists in finding the motion of a set of point vortices, and particularly to determine the conditions under which a certain configuration of point vortices is stable. Since the pioneering work of Helmholtz (1858) and Kelvin (1867), many important contributions have been published on this problem, see for example Aref (2007, 2009). The main issue is to establish the relative equilibrium of identical point vortices that rotate uniformly without change in shape or size. The term relative equilibrium is used to distinguish it from absolute equilibrium of the system at rest. In these systems, some points in the fluid named co-rotating points, are in equilibrium with respect to the pattern of vortices. A compilation of different flow patterns that show relative equilibrium between co-rotating points and ideal point vortices has been presented by Dirksen (2012).

From the experimental side, to produce flow patterns that behave closely as a configuration of ideal point vortices is not an easy task. However, we can explore in a simple way the interaction of vortices created by electromagnetic forces in a thin layer of electrolyte. This is a common non-intrusive method that has been successfully applied to investigate the vortex dynamics and transport processes in quasi-two-dimensional systems (Figueroa et al. 2009, 2011, 2014; Durán-Matute et al. 2010; Rossi and Lardeau 2011). This paper aims to study the stability and spatio-temporal behavior of electromagnetically driven sets of vortices in a thin electrolytic layer. Lorentz forces are generated by the interaction of a uniform D.C. current with localized magnetic fields produced by arrays of three to ten permanent magnets placed equidistantly on the perimeter of a circle whose diameter is much larger than the diameter of the magnets. When a single magnet is considered, the Lorentz force originates a dipolar vortex. If we place more than one magnet at a close enough distance, dipolar vortices produced by each magnet interact with each other and lead to more complex flow patterns. Therefore, the question is whether the resulting flow is stable or unstable and presents a steady or time-dependent behavior. Evidently, the resulting flow not only depends on the number and separation of the magnets but also on the intensity of the applied current. In addition to the experimental flow visualization, we obtain numerically the velocity fields in different magnet configurations which are used to perform a Lagrangian tracking.

2 Experimental Setup and Flow Visualization

The experimental setup consists of an open rectangular frame with interior dimensions of 28 cm $\times$ 36 cm $\times$ 1.3 cm; three sides are made of Plexiglas and one is made of glass. The container is filled up with an electrolyte solution of sodium bicarbonate ($NaHCO_3$) at 8.6% in weight. The depth of the electrolyte layer is 0.4 cm with a total volumen of 400 cm^3. The mass density, kinematic viscosity, and electrical conductivity of the electrolyte to ambient temperature are, respectively, $\rho = 1,086\,kg/m^3$, $\nu = 10^{-6}\,m^2/s$, and $\sigma = 6.36\,S/m$. Cooper electrodes are placed along the farther sides of the cell connected to an adjustable D.C. voltage power supply so that a uni-

form current within the range of 3–200 mA circulates in the fluid. The magnetic field is produced by Neodymium permanent dipolar magnets of cylindrical shape with a diameter of 0.92 cm and 0.63 cm of height, axially magnetized with a maximun magnetic strength on their surface of 0.33 T. Magnets are located below the bottom wall of the container in arrays of three to ten magnets placed equidistantly on the perimeter of a circle with diameter of 7.5 cm, so that for each array, the magnets rest on the vertices of a regular polygon.

Figure 1a, b shows schematically the top and lateral views of the experimental setup, respectively. For illustration, only two magnets with opposite orientations are shown, the normal component of the magnetic field being perpendicular to the bottom wall. The interaction of the current and the non-uniform magnetic field originates Lorentz forces in the fluid that are perpendicular to both the current direction and the normal component of the magnetic field. Evidently, the direction of the force depends on the orientation of the magnets and the polarity of the electrodes. We now show different arrays of magnets that give rise to flow patterns with varying degrees of complexity. Figure 2a shows schematically an array of four magnets with alternated orientation, north orientation being represented by blue solid circles and south orientation by red solid circles. Dipolar vortices generated by electromagnetic forcing are represented by curved lines with the arrows indicating the direction of rotation. Figure 2b shows the experimental visualization with dye of the steady flow obtained for this configuration with a current of 10 mA. Note that exterior vortices remain mainly unaffected while interior vortices interact strongly. Figure 3a shows the experimental visualization of the steady flow pattern obtained by applying an electric current of 3 mA to an array of three magnets with north orientation placed at the vertices of a equilateral triangle inscribed in the circle whose center is denoted by a cross. Since the separation between magnets is large and the electric current rather small, dipolar vortices created by each magnet persist mainly independently without

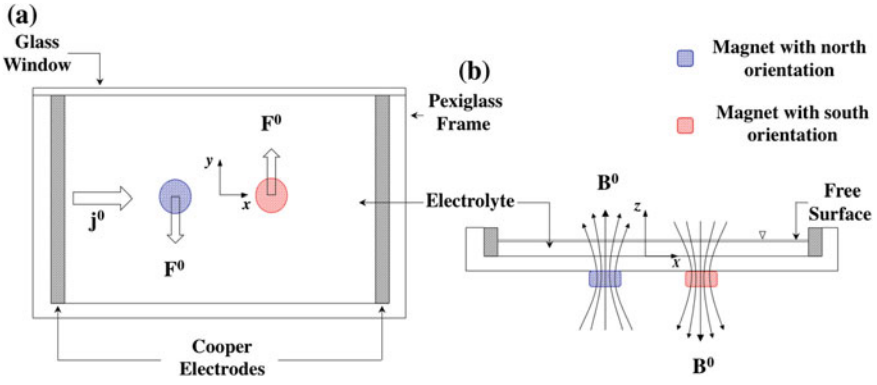

Fig. 1 Sketch of the experimental device used to investigate the interaction of vortices driven by a D.C. uniform current and localized magnetic fields produced by different distributions of permanent magnets. **a** Top view. **b** Lateral view

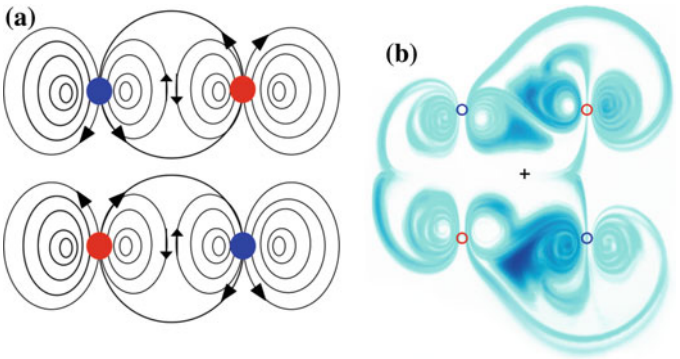

Fig. 2 **a** Sketch of an array of four magnets with alternating orientation. *Curved lines* represent dipolar vortices driven by electromagnetic forces and *arrows* indicate the direction of rotation. **b** Experimental visualization with dye of the steady flow pattern obtained for an array of four alternating magnets with an applied current of $I = 10\,\mathrm{mA}$

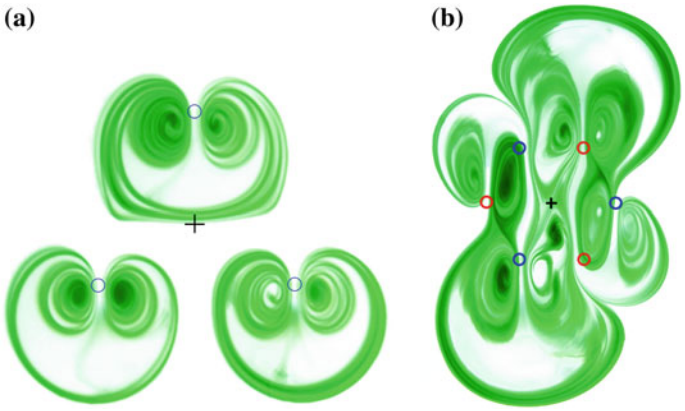

Fig. 3 Experimental flow visualization in different configurations: **a** array of three magnets with north orientation and applied current of $I = 3\,\mathrm{mA}$; **b** array of six magnets with alternating orientation and applied current of $I = 100\,\mathrm{mA}$

interaction. On the other hand, Fig. 3b shows the steady flow generated by an electric current of 100 mA and a magnetic field produced by six alternating magnets placed at the vertices of a regular hexagon. Since the distance between magnets is smaller and the current much larger than in the case of three magnets, vortex interactions are stronger. We observe that the interaction of counter-rotating dipolar vortices cause the merging or coalescence of vortices forming larger and elongated structures. In fact, vortex interactions originate a complex flow pattern although clear symmetry features can be observed.

3 Quasi-Two-Dimensional Numerical Model

Quasi-two-dimensional (Q2D) models for thin liquid layers have been successfully applied in both hydrodynamic (Satijn et al. 2001; Clercx and Heijst 2003) and magnetohydrodynamic flows (Sommeria 1988; Figueroa et al. 2009, 2014). In these models, the governing equations are integrated in the vertical direction or along the magnetic field lines in such a way that effects due to the boundary layer at the bottom of the container are considered by means of a linear friction term. Since induced currents are negligible in low-conductivity electrolytes, the Lorentz force is fully known and the dimensionless governing equations of motion are

$$\nabla \cdot \mathbf{u} = 0, \tag{1}$$

$$\frac{\partial \mathbf{u}}{\partial t} + (\mathbf{u} \cdot \nabla)\mathbf{u} = -\nabla p + \nabla^2 \mathbf{u} + Re^* \mathbf{j} \times \mathbf{B}, \tag{2}$$

where the velocity, $\mathbf{u}$, and pressure, p, are normalized by U_0 and ρU_0^2, respectively. The characteristic velocity $U_0 = j_0 B_{max} L^2/\rho\nu$ comes from a balance between viscous and Lorentz forces, where the characteristic length L is the magnet side length, j_0 the applied current density, B_{max} the maximum magnetic field strength, ρ the mass density and ν the kinematic fluid viscosity. In turn, the current density and the magnetic field are normalized by j_0 and B_{max}. For numerical purposes the Reynolds number in Eq. (2) is defined as $Re^* = U_0 L/\nu$, hence it depends on the applied current. Due to the small layer thickness, the dominant magnetic field component along the normal z-direction is the only one considered. For a single permanent magnet, we assume that this component can be expressed as (Figueroa et al. 2009)

$$B_z^0(x, y, z) = B_z(x, y) g(z), \tag{3}$$

where $B_z(x, y)$ reproduces the variation of the magnetic field in the x–y plane given by the superposition of two magnetized square surfaces, separated by a distance c, uniformly polarized in the normal direction (McCaig 1977). The term $g(z) = \exp(-\gamma\varepsilon z)$ models the variation of the magnetic field in the normal direction, where z is normalized by the depth of the liquid layer h. In turn, the constant $\gamma = 2.05$ was obtained by fitting the experimental data of the magnetic field decay (Figueroa et al. 2009), and $\varepsilon = h/L$ is the aspect ratio. It has been shown that Eq. (3) accurately reproduces the experimental magnetic field within the fluid layer (Figueroa et al. 2009). An array of magnets is modeled as the superposition of the field generated by each magnet. In the Q2D approximation, we assume that the momentum in the boundary layer at the bottom of the container is mainly transported by diffusion in the normal direction to the wall. Therefore, the velocity components are expressed in the form

$$\mathbf{u}(x, y, z, t) = [\overline{u}(x, y, t) f(x, y, z), \overline{v}(x, y, t) f(x, y, z), 0], \tag{4}$$

where $\overline{u}$ and $\overline{v}$ are the mean velocity components in the x–y plane, while $f(x, y, z)$ reproduces the velocity profile in the layer thickness (Lara 2013). Substituting Eq. (4) in Eqs. (1)–(2) and averaging along the height of the fluid layer, the governing equations in the Q2D approximation are found to be (Figueroa et al. 2009; Lara 2013)

$$\frac{\partial u}{\partial x} + \frac{\partial v}{\partial y} = 0, \tag{5}$$

$$\frac{\partial u}{\partial t} + u\frac{\partial u}{\partial x} + v\frac{\partial u}{\partial y} = -\frac{\partial p}{\partial x} + \nabla^2 u + \frac{u}{\tau}, \tag{6}$$

$$\frac{\partial v}{\partial t} + u\frac{\partial v}{\partial x} + v\frac{\partial v}{\partial y} = -\frac{\partial p}{\partial y} + \nabla^2 v + \frac{v}{\tau} - \alpha Re^* B_z^0, \tag{7}$$

where, for simplicity, the overline in the velocity components was dropped. The factor $\alpha = \frac{1}{\gamma\varepsilon}(1 - e^{-\gamma\varepsilon^2})$ in Eq. (7) represents the attenuation of the magnetic field in the normal direction while the linear terms that appear in both Eqs. (6) and (7) account for the friction at the bottom of the container. The dimensionless time scale τ for the decay of vorticity due to viscous effects is given by

$$\tau^{-1} = \frac{\gamma(1 - e^{-\gamma\varepsilon^2})}{\frac{1}{\gamma}(1 - e^{-\gamma\varepsilon^2}) + \frac{\gamma\varepsilon^4}{2}e^{-\gamma\varepsilon^2} - \varepsilon^2}. \tag{8}$$

The governing equations (5)–(7) were solved using a Finite Volume Method and the SIMPLEC algorithm (Versteeg and Malalasekera 1995), with no-slip boundary conditions at the walls of the rectangular frame and a motionless fluid as initial condition. Once the velocity field is calculated, the advection equations (Figueroa et al. 2014) are solved to perform the Lagrangian tracking.

4 Comparison Between Numerical and Experimental Results

Let us now compare the numerical calculations with experimental visualizations. For each array of magnets, different applied current intensities are explored and the associated Reynolds number is calculated from the maximum velocity reached by the numerical solution, $Re = U_{max}L/\nu$. Figure 4 shows the experimental and numerical results for the steady flow produced with an array of four magnets with alternating orientation and a current of 50 mA, five times larger than the one used in Fig. 2b. The corresponding Reynolds number is $Re = 69$. The experimental visualization is shown in Fig. 4a while Fig. 4b, c correspond to the streamlines and Lagrangian tracking obtained from the numerical solution, respectively. The comparison of Eulerian and Lagrangian results is very illustrative. While the streamlines capture the symmetry of the flow field, they do not show the characteristic features of the advec-

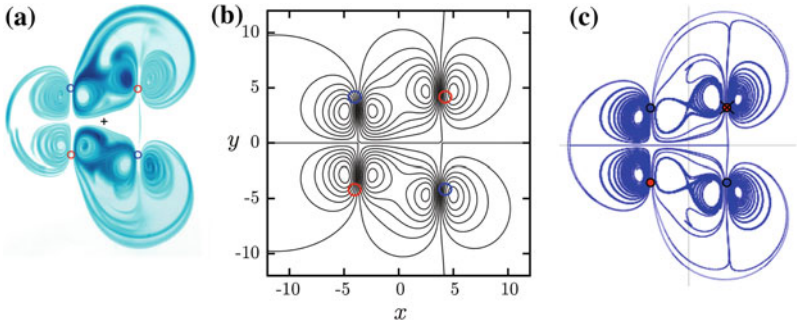

Fig. 4 Steady flow produced by an array of fourth magnets with alternating orientation and applied current of 50 mA that corresponds to a Reynolds number $Re = 69$. **a** Experimental flow visualization with dye. **b** Streamlines calculated numerically. **c** Lagrangian pathlines obtained by integration of the advective equations using the numerical flow field

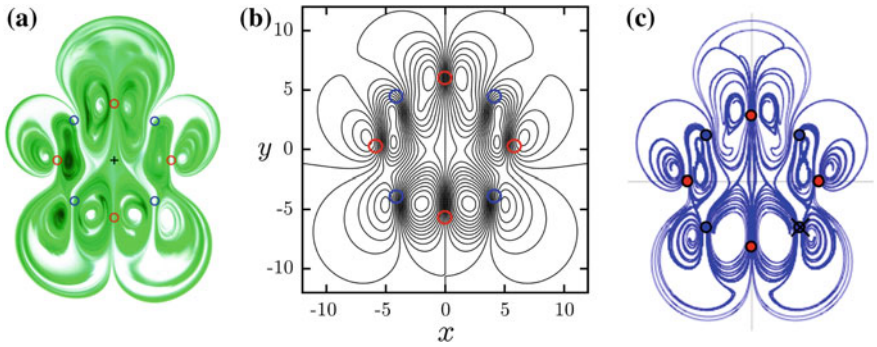

Fig. 5 Steady flow produced with an array of eight magnets with alternating orientation and applied current of 50 mA ($Re = 77$). **a** Experimental flow visualization. **b** Numerical streamlines. **c** Lagrangian trajectories obtained by integration of the advective equations from the numerical flow field

tive scalar transport, which are neatly reproduced through the Lagrangian tracking. Even the hyperbolic points created by the interaction of central vortices are clearly observed. The lack of diffusion in the Lagrangian simulation is the main difference with the experimental visualization. In fact, diffusion can be incorporated using the Diffusion Strip Method (Figueroa et al. 2014). Figure 5 shows experimental and numerical results for the steady flow obtained with an array of eight magnets with alternating orientation and applied current of 50 mA that corresponds to $Re = 77$. As in the previous case, the experimental visualization, numerical streamlines and Lagrangian trajectories are presented in Fig. 5a–c, respectively. Due to the shorter distance between magnets, in this case vortex interactions are stronger but still the Lagrangian numerical simulation reproduces the main qualitative features of the flow.

For any array of magnets, if the intensity of the current is sufficiently high the resulting flow presents a time-dependent behavior. For instance, with an array of eight

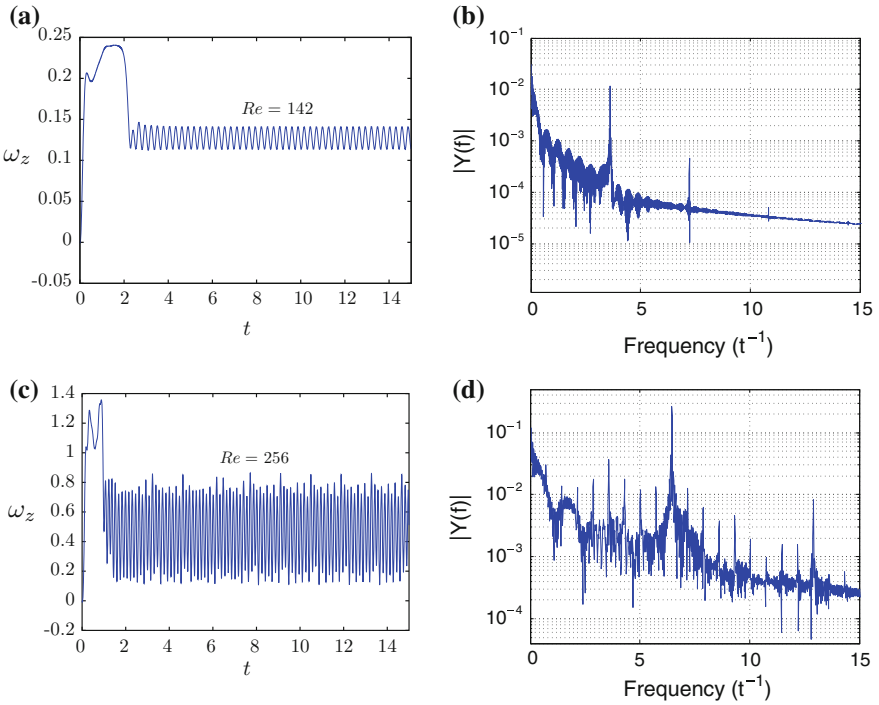

Fig. 6 Panels **a**, **c** show vorticity as a function of time for an array of eight magnets (see Fig. 5b). **b**, **d** Power spectrum of the vorticity signal calculated by the Fast Fourier Transform. The first row corresponds to $I = 120$ mA ($Re = 142$) and the second row to $I = 250$ mA ($Re = 256$)

alternating magnets we found experimentally and numerically that the transition from steady to time-dependent flow occurs in the range $100 < I < 120$ mA, corresponding to $132 < Re < 142$. For a current of 120 mA, the flow develops a time-dependent behavior characterized by the oscillatory motion of the vortices, as shown in Fig. 6a where the vorticity as a function of time at a certain point in the central flow region shows a completely periodic behavior. Figure 6b shows the corresponding power spectrum obtained from the Fast Fourier Transform (FFT) of the vorticity signal which yields a (dimensionless) characteristic frequency of $f_c = 3.72$. If the applied current increases to 250 mA that corresponds to $Re = 256$, the amplitude of the vorticity oscillation is not constant (see Fig. 6c) and the characteristic frequency becomes $f_c = 6.25$. The power spectrum (see Fig. 6d) also shows some harmonics and seems to indicate the beginning of a distinct physical behavior than a purely periodic flow.

Figure 7a, b show, respectively, the experimental flow visualization and Lagrangian numerical trajectories at a given instant of the time-dependent flow produced by an array of eight magnets with alternating orientation and an applied current of 200 mA ($Re = 212$). We observe that the experimental visualization is reasonably reproduced by the numerical simulation. At initial steps, the flow pattern presents a symmetry with respect to the y axis (as observed in Fig. 5a) but vortex interaction

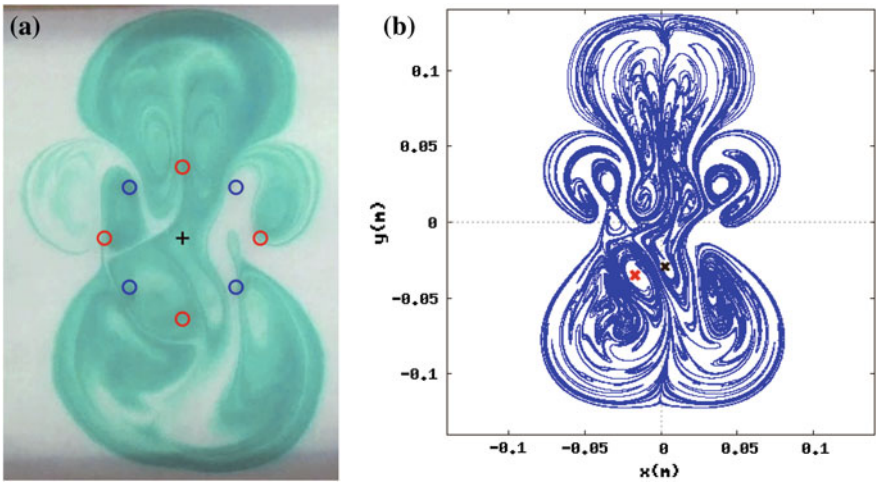

Fig. 7 Time-dependent flow produced by an array of eight magnets with alternating orientation at $t = 143$. **a** Experimental visualization. **b** Lagrangian trajectories calculated from the numerical simulation. $I = 200\,\text{mA}$ ($Re = 212$)

lead to symmetry breaking. In general, symmetry breaking can appear due to non-symmetric magnetic field distribution or non-linear effects. In fact, through experimental flow visualization and animation of the numerical results, we observed that some vortices in the central flow region rotate counterclockwise and cause vortex shedding in the y-direction.

As in the previous case, the time-dependent behaviour of the flow was explored by varying the applied current for the arrays of three, four, six, eight and ten magnets. For each configuration, the current intensity at which the flow transits from steady to unsteady state was determined. Although aparently unsteady flows show turbulent-like behaviour (Rossi et al. 2006) (see, for instance, Fig. 7), the Reynolds number is low ($Re = 220$), thus the unsteady flow patterns remain in the laminar regime. The applied electric current is not high enough to generate a turbulent flow. Figure 8 shows the stability map that condenses the information of the temporal behavior of the flows from all the available numerical and experimental results. In the map, solid black points show the numerically determined value of the current where the transition from steady to unsteady flow occurs for each array of magnets. Due to practical reasons, most of the results were obtained from numerical simulations, however, note that for the available experimental results the numerical prediction agrees with the experimental observation. From the stability map, it is clear that increasing the number of magnets in the array, the transition from steady to unsteady flow occurs at lower intensities of the applied current. Evidently, by increasing the number of magnets the number of vortices also increases while the distance between them decreases. This causes stronger interactions of vortices that lead to less stable configurations prone to develop a time-dependent behavior. In fact, this behavior favors a better fluid mixing (Figueroa et al. 2014).

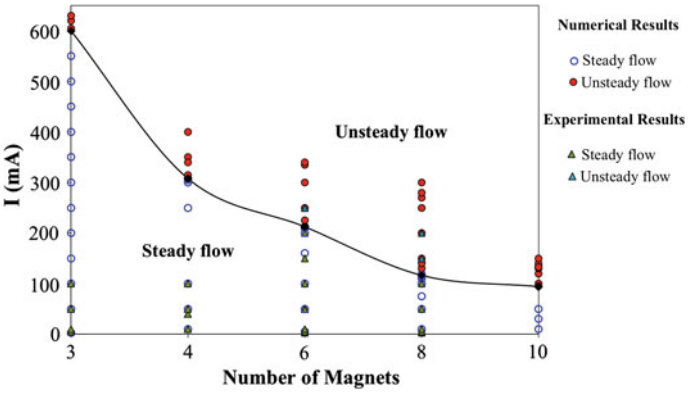

Fig. 8 Stability map of electrically driven flows with the different arrays of permanent magnets placed on the perimeter of a *circle*. The interpolated *solid line* divides the regions of steady and unsteady flow

5 Conclusions

In this work, we performed an experimental and numerical study of the spatio-temporal behavior of laminar flows generated in a thin electrolyte layer through the interaction of a D.C. current and a magnetic field produced by different arrays of magnets placed on the perimeter of a circle. Flows were experimentally visualized using dye and recorded for comparison with numerical simulations. We used a Q2D numerical model that includes both the detailed Lorentz driving force produced by the electromagnetic interaction and the friction effects of boundary layers at the bottom of the container. The comparison of numerical simulations with available experiments show a satisfactory agreement for both steady and unsteady flows. In fact, Lagrangian trajectories calculated numerically suitably capture the motion and elongation of the vortical structures caused by the Lorentz force. For steady flows, well-defined spatial symmetries that depend on the magnet arrays can be identified. For all the explored arrays of magnets, we found either experimentally or numerically the applied current for which the flow transits from steady to unsteady state. With this information, we built a stability map that collects all the available experimental and numerical results. It was found that the larger the number of magnets, the lower the intensity of the applied current required to transit from steady to unsteady state which could favour the fluid mixing. The characterization of time-dependent flows and the possible appearance of a chaotic behavior remains as a future topic of study.

Acknowledgments Financial support from CONACYT, Mexico, through Project 131399 is gratefully acknowledged. C.G. Lara and A. Figueroa thank, respectively, a grant and a posdoctoral fellowship from CONACYT.

References

Aref H (2007) J Math Phys 48:065401
Aref H (2009) Phys Fluids 21:094101
Clercx HJH, Van Heijst GJF, Zoeteweij (2003) Phys Rev E 67:066303
Dirksen T (2012) Masters thesis, Technical University of Denmark
Durán-Matute M, Kamp LPJ, Clercx HJH, van Heijst GJF (2010) Phys Rev E 82:026314
Figueroa A, Cuevas S, Ramos E (2011) Phys Fluids 23:013601
Figueroa A, Demiaux F, Cuevas S, Ramos E (2009) J Fluid Mech 641:245–261
Figueroa A, Meunier P, Cuevas S, Villermaux E, Ramos E (2014) Phys Fluids 26:013601
Helmholtz HV (1858) J für die reine und angewandte Mathematik 55:25–55
Kelvin L (1867) Proc R Soc Edinb VI:94–105
Lara CG (2013) Theoretical and experimental study of electromagnetic stirring in shallow fluid flows. MSc Thesis, National Autonomous University of Mexico (in Spanish)
McCaig M (1977) Wiley
Meunier P, Leweke T (2005) J Fluid Mech 533:125–159
Ottino JM (1990) Annu Rev Fluid Mech 22:207–253
Rossi L, Lardeau S (2011) J Turbul 12:1–31
Rossi L, Vassilicos JC, Hardalupas Y (2006) Phys Rev Lett 97(14):144501
Satijn MP, Cense AW, Verzicco R, Clercx HJH, Van Heijist GJF (2001) Phys Fluids 13(7):1932–1945
Sommeria J (1988) J Fluid Mech 189:553–569
Versteeg HK, Malalasekera W (1995) Longman Scientific & Technical

Numerical Simulation of a Spanwise Vortex in a Periodic Forced Flow

E.J. López-Sánchez and G. Ruíz Chavarría

Abstract In geophysical flows, vortices are present at very different scales. Examples of them are the meddies, formed at the outlet of the Mediterranean Sea or the vorticity dipoles, occurring when water flushes from a channel into the open sea. In this paper we investigate the formation and the evolution of a spanwise vortex in the latter system, when a periodic forcing is imposed. To this end the Navier-Stokes and continuity equations are solved with a finite volume code (OpenFOAM 2008). The numerical solution has been obtained for a Reynolds number $Re = 1{,}000$ and a Strouhal number $S = 0.02$. For comparison, we carried a simulation in a flow produced by a single pulse. We have found that the spanwise vortex appears in front of the dipole. It detaches from the bottom and moves away. When flow is produced by a pulse, this vortex has a horseshoe shape, while for a periodic forcing flow, the shape of the spanwise vortex evolves in time.

1 Introduction

When a fluid leaves a channel and flushes into an open domain the vorticity produced into the channel leads to the formation of two counter rotating eddies. This pair of vortices is a coherent structure, known as dipole, which moves away due to its self induced velocity. The properties of the dipole depend on parameters as the Reynolds number, the aspect ratio (the quotient of fluid layer depth to the dipole size) and the Strouhal number. This kind of structures has been the aim of previous works. For instance, Chaplygin (2007) has modeled a 2D dipole in a different way than considering just two point vortices. The velocity field of the Lamb-Chaplygin dipole is such that vorticity is different from zero only inside a circle of radius R. Earlier on, Wells and Heijst (2003) modeled in two dimension the evolution of a dipole under

E.J. López-Sánchez · G. Ruíz Chavarría (✉)
Facultad de Ciencias, Universidad Nacional Autónoma de Mexico,
Ciudad Universitaria, 04510 Mexico, D.F., Mexico
e-mail: gruiz@unam.mx

E.J. López Sánchez
e-mail: lsej@ciencias.unam.mx

J. Klapp et al. (eds.), *Selected Topics of Computational and Experimental Fluid Mechanics*, Environmental Science and Engineering,
DOI 10.1007/978-3-319-11487-3_33

periodic forcing. To this end the flow is assumed to be the sum of two point vortex and a linear sink whose intensity is time dependent. They found that the dipole escapes or returns to the channel outlet depending on the value of the Strouhal number. With respect to experimental works, the properties and the evolution of the dipole have been investigated in two cases: (a) a dipole produced by an impulsively jet (Sous et al. 2004; Lacaze et al. 2010) and (b) a dipole produced under periodic forcing (Nicolau del Roure et al. 2009). Finally, a numerical study of a periodic forced flow has been performed by López-Sánchez and Ruiz-Chavarría (2013). They found that lifetime of vortices extends over more than a driving period. In this case interaction between two dipoles can occur, leading under certain circumstances to vortex coalescence.

In shallow-water, apart from the two counter-rotating vortices, a third vortex has been reported, which is perpendicular to the dipole (Albagnac 2010). In this respect, Lacaze et al. (2010) have experimentally studied the properties of the spanwise vortex produced by an impulsively jet. They found that all three vortices have comparable intensities. On the other hand, Duran-Matute et al. (2010) made a numerical simulation to study this structure in a thin horizontal layer. They assumed that initially the velocity field is like a Lamb-Chaplygin vortex in the horizontal plane and in the vertical plane the velocity field follows a Poiseuille profile. They found that, under certain conditions, the 2D approach is no longer sufficient to describe this flow because 3D effects are present. The three dimensional nature of the flow depends on a single parameter $K = \delta^2 Re$, where δ is the aspect ratio (the fluid depth to the size R of the dipole) and Re is the Reynolds number. If $K < 6$ the flow is dominated by the viscosity, so the vertical motion can be neglected. In the range $6 < K < 15$, the dipole properties are modified by the vertical motion and a spanwise vortex appears in front of the dipole. Finally, for $K > 15$ the intensity of the spanwise vortex becomes comparable with those of the counter-rotating vortices. In the present work we make a study of the spanwise vortex under periodic forcing. For comparison we also present some results for a impulsively forcing. For this purpose we solve numerically the Navier-Stokes and continuity equations with a finite volume method, using the free software OpenFOAM. The originality lies in the fact that the flow rate is periodic. The study of this spanwise vortex is important in coastal systems (where periodic forcing is induced by tides) because it influences the lift, transport and deposition of particles located at the bottom or inside the fluid.

This paper is organized as follow. Section 2 is devoted to describe the system under study and the numerical method. In Sect. 3 we present some numerical results of both impulsively and periodic forcing. Section 4 deals with the convergence of the numerical code and in Sect. 5 the conclusions are drawn.

2 Description of the System and Numerical Simulation

The flow we study occurs in a channel and an open domain. In order to use OpenFOAM the overall domain is decomposed in four parallelepiped, as shown in Fig. 1.

The equations to be solved are the Navier-Stokes (1) and the continuity (2) equations for an incompressible flow. In dimensionless form, these equation are:

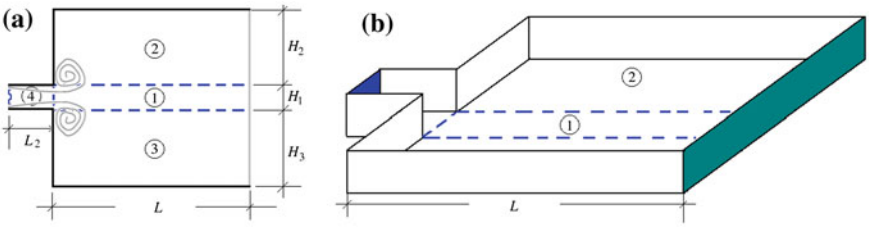

Fig. 1 Integration domain to solve Navier-Stokes and continuity equations. This domain is decomposed in four parallelepipeds. **a** *Upper* view **b** view in *perspective*

$$\frac{D\mathbf{u}}{Dt} = -\frac{1}{\rho}\nabla P + \frac{1}{Re}\nabla^2\mathbf{u} \tag{1}$$

$$\nabla \cdot \mathbf{u} = 0. \tag{2}$$

Here, $D/Dt \equiv \partial/\partial t + (\mathbf{u} \cdot \nabla)$ is the material derivative.

The forcing is introduced through a sinusoidal flow rate:

$$Q(t) = Q_0 \sin(2\pi S t) \tag{3}$$

The dimensionless parameters appearing in Eqs. 1 and 3 are the Reynolds (Re) and the Strouhal (S) numbers. The first one is defined ad $Re = UH/\nu$ while the last one is defined as $S = H/UT$, where H is the channel width, U the maximal velocity in the channel, ν is the kinematic viscosity and T is the forcing period. The Strouhal number can be see like a dimensionless frequency (López-Sánchez and Ruiz-Chavarría 2013; López-Sánchez 2013).

Equations 1–2 are supplemented with boundary conditions. The bottom, the lateral wall in the channel and some lateral walls in the open domain are solid, then velocity must vanish there. In the free surface we assume that both vertical velocity and tangential stress vanish. Finally, along the channel input (wavy line in Fig. 1a) and along the far boundary in front of the channel (dark side in Fig. 1b) the flow rate given by Eq. 3 must be fulfilled.

Open Field Operation And Manipulation (OpenFOAM 2008) is a collection of solvers for partial differential equations. This program is structured in modules written in C++. It incorporates pre and post-processing utilities to generate meshes and present the results of simulations (The open source 2004).

In order to test the spatial convergence, we carried simulations with different numbers of points in the grid. We start with 108,000 points and we finish with 2,100,000. The criterion to stop a further increase is that the difference of velocity values in two subsequent meshes becomes less than a threshold $\varepsilon = 10^{-6}$. On the other hand, to guarantee time convergence we introduce the Courant number (Co), defined as follow:

$$Co = \frac{U_q \Delta t}{\Delta q}, \tag{4}$$

where U_q is the velocity component in the direction q and Δq is the spatial step in the q-direction. The Courant number can be interpreted as the ratio of the distance traveled by a particle during a time step Δt and the size of a volume element. To guarantee time convergence the Courant number must be less than 1.

3 Results

Numerical simulations were carried out for two cases: a pulse and a periodic flow with $S = 0.02$. For the pulsing flow we have chosen a channel width of 2 cm, a layer depth of 2 cm and a maximal flow rate $Q_0 = 2 \times 10^{-5}$. On the other hand, for the periodic forcing flow we have chosen a channel width of 4 cm, a layer depth of 2 cm and the same maximal flow rate $Q_0 = 2 \times 10^{-5}$. In order to have $S = 0.02$ the forcing period must be T = 80 s. In both cases the Reynolds number is $Re = 1{,}000$.

3.1 The Pulse

A pulse was applied for 4 s in the following manner (see Fig. 2): during 0.5 s the flow rate grows from zero to the maximal value $Q_0 = 2 \times 10^{-5}$. After, the flow rate remains constant for 3 s. Finally Q decreases from Q_0 to zero during 0.5 s.

In Fig. 3 we plot the velocity field in the symmetry plane (y = 0) and the vorticity distribution in a region in front of the channel at t = 20 s. Figure 3a, b, c show how the spanwise vortex detaches from the bottom as it moves. At t = 10 s (Fig. 3a) the spanwise vortex is already present, its center is located at (x, z) = (7 cm, 0.5 cm), whereas at t = 20 s the vortex has moved to position (x, z) = (13 cm, 1.2 cm) (Fig. 3c). To see the shape of the spanwise vortex we include Fig. 3d, in which dipole's isovorticity surfaces are shown. The top of the surface with value $|\omega| = 0.5/\text{s}$ was removed in order to see the inner surface corresponding to the spanwise vortex (value $\omega_x = -1/\text{s}$ in blue). We can observe that the spanwise vortex has a horseshoe shape and that it

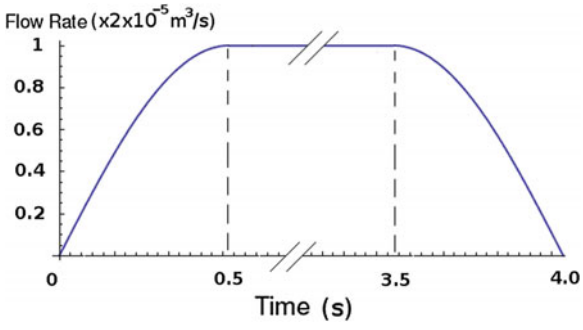

Fig. 2 Pulse applied to generate the flow through the channel

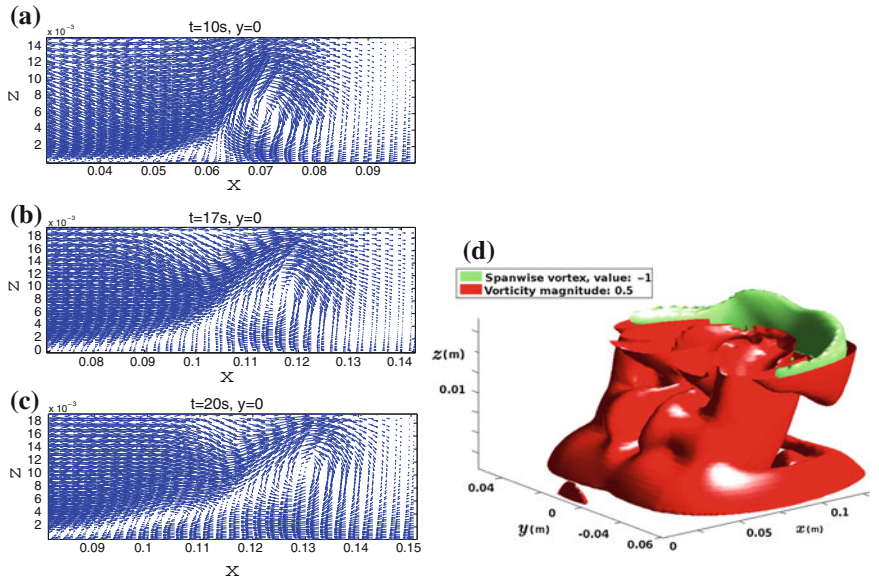

Fig. 3 **a**–**c** Velocity field in the vertical symmetry plane. **d** Isovorticity surfaces of the dipole structure. The *top* was removed to see the spanwise vortex

is away from the bottom. It is important to remark that this vortex is located in front of the dipole (the dipole is roughly delimited by the red surface).

3.2 Periodic Forced Flow, S = 0.02

The other case we studied is the flow under a periodic forcing. The values of Strouhal and Reynolds numbers are respectively $S = 0.02$ and $Re = 1{,}000$. Figure 4 shows the isovorticity surface of the spanwise vortex for three different times (15, 20 and 40 s). The data we show correspond to times in the interval $0 < t < 0.5\,T$, that is, over a half period. Otherwise we include only positive values of y to better visualize the structure of the vorticity field. The spanwise vortex appears approximately at $t = 10$ s. As in the previous case, the vortex detaches from the bottom as it moves. However it moves slowly. At $t = 15$ s (Fig. 4a), the vortex is located at $x = 4$ cm, whereas at $t = 20$ (Fig. 4b) the vortex has moved to $x = 8$ cm. As we can see in the figure this spanwise vortex has never a horseshoe shape as in the pulsating flow. Finally at $t = 40$ s (Fig. 4a), the shape of the spanwise vortex has been completely modified if we compare with the shape at $t = 15$ s and at $t = 20$ s.

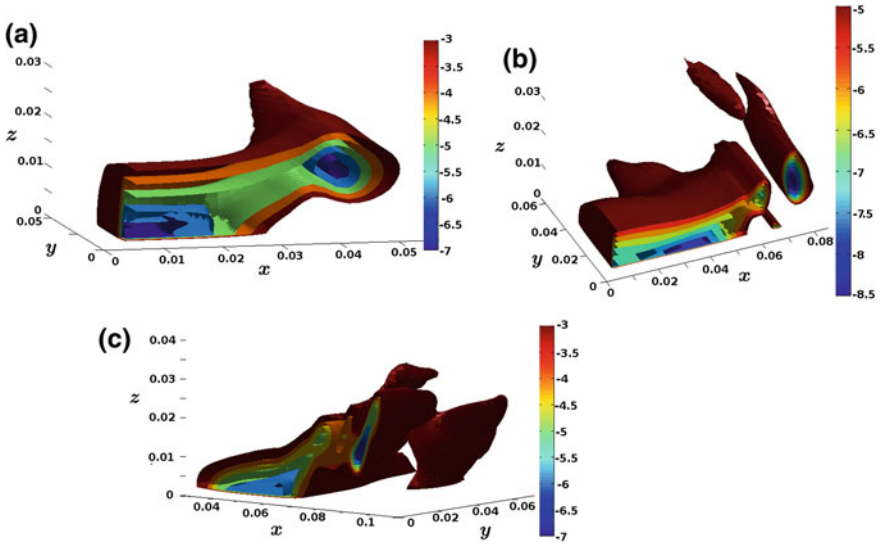

Fig. 4 Isovorticity surfaces of the spanwise vortex in a periodically forced flow at **a** $t = 15\,\mathrm{s}$ **b** $t = 20\,\mathrm{s}$ and **c** $t = 40\,\mathrm{s}$

4 Time Convergence

Figure 5 shows the maximal Courant number (maximal over all the mesh) as a function of time for the cases studied here. Figure 5a exhibits the maximal Courant number in the pulsating flow. The curve never exceeds the value of 0.3, then the time convergence is always guaranteed over all time integration. For the periodic forcing flow ($S = 0.02$) the curve has a maximal value of approximately 0.7 (see Fig. 5b). Again, the maximal Courant number is less than 1, that is, time convergence is guaranteed for the periodic forcing flow.

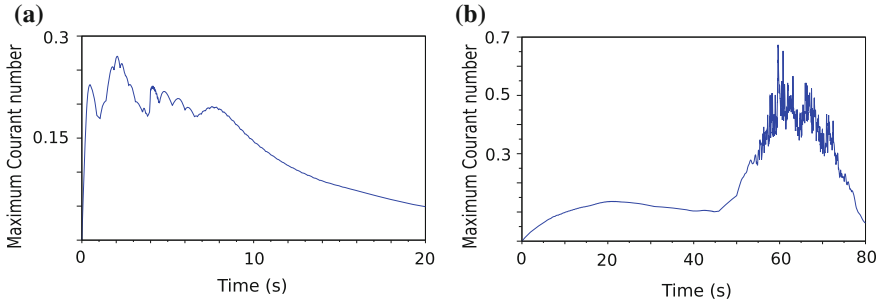

Fig. 5 Courant number in some of three coordinates. **a** The pulse case. **b** The periodic flow rate case

Figure 5a shows that the maximum values appear when the pulse is generated. However, these values do not exceed 0.3, and therefore the simulation converges to the true solution over all integration time.

In the pulse case, after the half period ended, the maximum Courant number value is approximately 0.7 (see Fig. 5b), and so convergence is also ensured.

5 Conclusions

In this paper we have presented numerical results of a flow in a channel connected to an open domain. We studied some characteristics of the flow for two cases, namely, flow generated by a pulse and a periodic driving flow with a Strouhal number $S = 0.02$. In both cases we observe the formation of a spanwise vortex in front of the dipole. The horseshoe shape occurs only for the pulse case. In the periodic forcing case, the shape of the spanwise vortex is modified along time. The spanwise vortex appears near the bottom and after a while it detaches and moves away. This structure has an influence on the lift and the transport of solid particles like sand.

Acknowledgments Authors acknowledge DGAPA-UNAM by support under project IN116312, "Vorticidad y ondas no lineales en fluidos".

References

Albagnac J (2010) Dynamique tridimensionnelle de dipoles tourbillonnaires en eau peu profonde. Thèse de doctorat, Université Paul Sabatier Toulouse III Institut de Mcanique des Fluides de Toulouse. France

Chaplygin SA (2007) One case of vortex motion in fluid. Reg Chaotic Dyn 2(12):219–232

Duran-Matute M, Albagnac J, Kamp LPJ, van Heijst GJF (2010) Dynamics and structure of decaying shallow dipolar vortices. Phys Fluids 22:116606

Lacaze L, Brancher P, Eiff O, Labat L (2010) Experimental characterization of the 3D dynamics of a laminar shallow vortex dipole. Exp Fluids 48:225–231

López-Sánchez, E. J. (2013) Vorticidad y transporte de partículas en un flujo periódico a la salida de un canal. Doctoral thesis, Universidad Nacional Autónoma de México, México

López-Sánchez EJ, Ruiz-Chavarría G (2013) Vorticity and particle transport in periodic flow leaving a channel. Eur J Mech B/Fluids 42:92103

Nicolau del Roure F, Sokolofsky SA, Chang K (2009) Structure and evolution of tidal starting jet vortices at idealized barotropic inlets. J Geophys Res 114:C05024

OpenFOAM (2008). The Open Source CFD Toolbox. Programmers Guide. Version 1:5

Sous D, Bonneton N, Sommeria J (2004) Turbulent vortex dipoles in a shallow water layer. Phys Fluids 16:2886–2898

The open source CFD toolbox (2004). http://www.opencfd.co.uk/openfoam Consulted: April 2, 2013

Wells MG, Van Heijst G-JF (2003) A model of tidal flushing of an estuary by dipole formation. Dyn Atmos Oceans Elsevier 37:223–244

Erosion and Deposition of Particles in a Periodic Forced Flow

P. Villamil Sapien, I. Sánchez Calvo González, E.J. López-Sánchez and G. Ruíz Chavarría

Abstract In this paper we present an experimental study of the erosion and accumulation of particles produced by a periodic forced flow in two domains connected by a channel. For this purpose a thin layer of sand is deposited on the bottom of the channel and one of these domains. Then, a periodic flow rate is produced with the aid of a block partially submerged in the fluid and subject to a sinusoidal vertical motion. The evolution of the system was observed for thousands of periods. The aim of this study is to model the particle transport in a tidal induced flow between an estuary and the open sea. The erosion and accumulation zones observed in our study are compared with results obtained in numerical simulations and observational works.

1 Introduction

Along the shore, the drag and deposition of sand or other particles are phenomena that influence human activities. For instance, sand banks formed by turbulent currents affect the near coast navigation. On the contrary, the same sand banks, if appropriately situated, can mitigate the impact of a tsunami. Due to its importance, the particle transport in shallow waters has been studied in the last decades. First, if we focus our attention on fundamental studies, it is necessary to mention a work by Maxey and Riley (1983). They deduced from first principles an equation of motion for spherical particles inside a fluid, in which forces apart from drag and bouyancy are incorporated. From an experimental approach, Mordant et al. (2001) developed a method, based on Doppler effect, for measuring the position and velocity of particles in a turbulent flow. A monochromatic wave is scattered by the target particles, and then a set of detectors record the scattered sound. The signal contains information about the velocity and position of the particles. The particle transport has been investigated when vortices are present (as in the flow we investigate). For instance, Angilella

P. Villamil Sapien · I. Sánchez Calvo González · E.J. López-Sánchez · G. Ruíz Chavarría (✉)
Facultad de Ciencias, Universidad Nacional Autónoma de México,
Ciudad Universitaria, 04510 Mexico, D.F., Mexico
e-mail: gruiz@unam.mx

J. Klapp et al. (eds.), *Selected Topics of Computational and Experimental Fluid Mechanics*, Environmental Science and Engineering,
DOI 10.1007/978-3-319-11487-3_34

(2010) studied the transport of dust by two identical point vortices rotating around a common center. They found that the centrifugal and Coriolis forces enhance the dispersion of particles and that if the drag force is dominant, the particle trajectories exhibit chaotic behavior, leading to an increase of mixing. Finally, some numerical simulations of the system considered in this paper show that a pair of counter rotating vortices (a dipole) detaches from the channel in each period (López-Sánchez and Ruiz-Chavarría 2013a). The existence of this dipole enhances the mass transport, because the velocity is considerably greater in the region between the vortices. Particles are sucked into that region and expelled forward. Some particles are deposited in the region where dipole passes and others are pushed away from the symmetry axis. According to the numerical and experimental evidence (Lacaze et al. 2010), in shallow waters, apart from the two eddies in this flow, there is a spanwise vortex moving in front of the dipole. The transverse vortex produces lift and enables the motion of particles located at the bottom. It has been shown that particles accumulate in certain regions (López-Sánchez and Ruiz-Chavarría 2013a) or follow chaotic trajectories (López-Sánchez and Ruiz-Chavarría 2012). In this system two dimensionless parameter are relevant, the first one is the Reynolds number ($Re = UH/\nu$), and the second is the Strouhal number, defined as $S = H/UT$, where U is a representative velocity, H is the channel width, T is the driving period and ν is the kinematic viscosity. The Strouhal number is a dimensionless frequency.

This paper is organized as follows. In Sect. 2 we describe the experimental setup. In Sect. 3 we show some results and we made a comparison with data reported in the literature. In the last section we draw conclusions.

2 Experimental Setup

The experiments were performed in a container composed of two basins connected by a channel, as shown in Fig. 1. The dimensions of the smaller basin are 45 cm × 60 cm × 15 cm, whereas the dimensions of the larger one are 120 cm × 120 cm ×

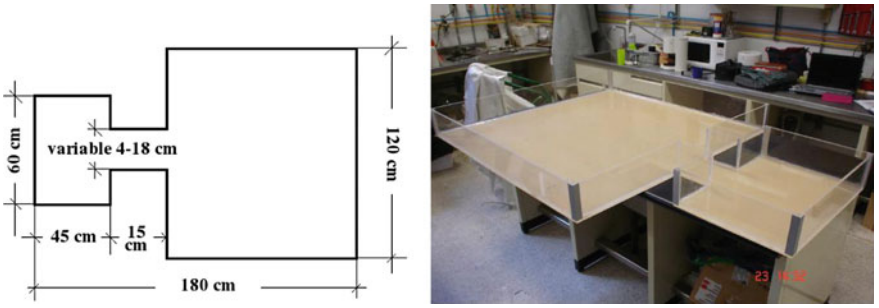

Fig. 1 *Left* Dimensions of the container used to model the transport of particles. *Right* Snapshot of the container

15 cm. Both basins are connected by a channel 15 cm long and variable width (the channel width lies in the interval 4–18 cm.). In order to produce a variable flow rate we use a block connected to a stepper motor through a crankshaft mechanism. The block, made in styrofoam and plexiglas, is partially submerged in the liquid layer and develops a periodically vertical motion. The experiments were made under the following conditions: the depth of the liquid layer was 4 cm and the amplitude of vertical motion of the block was set to 3 cm. We have chosen two different driving frequencies, namely, 0.05 and 0.08 Hz and three different channel widths are considered: 2.5, 3 and 5 cm. In the experiments we cover the bottom of the channel and a fraction of the large domain with a thin layer of sand. The sizes of these particles are in all cases less than 1 mm. To follow the evolution of the system we use a high definition video camera, so that the images have a resolution of 1920×1080 pixels. One image is recorded every second for a time interval greater than 12 h. During this interval we observe the appearance of regions where particles are expelled or accumulated.

To estimate the flow rate and other parameters, we proceed as follows. When the block is submerged into the fluid, a certain amount of liquid is displaced. The volume displaced is equal to the volume of the block into the fluid:

$$V(t) = l \times a \times h(t), \tag{1}$$

where l is the block length, a is the block width, and $h(t) = h_m + h_0 \sin(2\pi \nu t)$ is the distance from the free surface to the bottom block (h_m is the mean value of $h(t)$). In our experiments $l = 57.5$ cm and we have used two different blocks, one with $a = 8$ cm and the other with $a = 2.5$ cm. The flow rate is the time derivative of $V(t)$:

$$Q = \frac{d\,V(t)}{d\,t} = 2\pi \nu l \times a \times h_0 \cos(2\pi \nu t). \tag{2}$$

The maximum flow rate Q_0 is:

$$Q_0 = 2\pi \nu l \times a \times h_0. \tag{3}$$

The representative velocity is the quotient of Q_0 and the cross section of the liquid layer in the channel (A):

$$U_0 = \frac{Q_{max}}{A}. \tag{4}$$

In this last equation, $A = H \times P$, where H is the width of the channel and P is the depth of the liquid layer. In all experiments the depth of liquid is $P = 4$ cm.

3 Results

3.1 Channel Width of 2.5 Centimeters

The experiments were conducted to detect the accumulation of particles after thousand of periods. For this case, the channel width is 2.5 cm and the driving frequency is 0.08 Hz. The experiment lasted for 15 h, which corresponds approximately to 4,000 periods. In a tidally induced flow 4,000 periods are approximately 6 years. According to Eqs. 3 and 4 the values of maximal flow rate and the representative velocity are respectively: $Q_0 = 3.47 \times 10^{-4}$ m^3/s and $U = 0.3468$ m/s. So the flow has a Reynolds number $Re = 8{,}700$ and a Strouhal number $S = 0.006$.

In Fig. 2 we present a snapshot of the final distribution of particles. In this figure we see how the flow lifts the particles and moves them away from their original positions. As we stated, we start with particles uniformly distributed on the bottom. After several periods, a fraction of the particles have been completely removed from their initial position in the channel and near the channel outlet. After thousands of periods the particles initially located in front of the channel have been removed. The region for which particles are expelled extends a little more than 20 cm (8 H) along the axis of symmetry and has a width of approximately 8 cm (3.2 H).

Under these conditions the particle distribution remains symmetric. Particles concentrate inside the channel and a trough is formed in front of it, in the open domain. This last structure has been observed in coastal system by Amoroso and Gagliardini (2010). The concentration of particles inside the channel has been reported in a numerical simulation but only over 15 periods (López-Sánchez and Ruiz-Chavarría 2013a).

Fig. 2 Distribution of sand in the system after 15 h of forcing. The channel width is 2.5 cm and the driving period is 12.5 s. Particles concentrate inside the channel and a trough appears in front of the channel

3.2 Channel Width of 3 Centimeters

Another experiment was made under the following conditions: the channel width is $H = 3\,\text{cm}$ and the driving frequency is 0.05 Hz. Then, the maximal flow rate and the representative velocity are: $Q_0 = 6.77 \times 10^{-5}\text{m}^3/\text{s}$ and $U = 0.056\,\text{m/s}$. The Reynolds and Strouhal numbers are respectively $Re = 1{,}400$ and $S = 0.035$.

In Fig. 3 we show the final distribution of particles in the channel and in a section of the larger domain. This distribution has a similar shape to those obtained in numerical simulations reported by López-Sánchez and Ruiz-Chavarría (2013b). The sand accumulates into the channel, near to its mouth and again a trough is formed in front of it. The trough extends about four times the channel width. However, there are some differences. That is, the length of the zone without particles in the numerical simulation is twice the corresponding region in this experiment.

3.3 Channel Width of 5 Centimeters

We made a third experiment with a 5 cm channel width and a driving frequency of 0.08 Hz. The experiment lasted for 18 h. The values of maximal flow rate and representative velocity are: $Q_0 = 3.47 \times 10^{-4}\,\text{m}^3/\text{s}$ and $U = 0.173\,\text{m/s}$. So the flow has a Reynolds number $Re = 8{,}700$ and a Strouhal number $S = 0.023$. The experiment extends over 5,200 periods. In a tidal induced flow this corresponds to a seven year. The final particle distribution is shown in Fig. 4. The particle distribution is not similar to the previous cases, since the white spots indicating the absence of particles are not symmetrical. The size of the trough is approximately twice the channel width. On the other hand, it is important to remark the appearance of two regions where particles (see Fig. 5) deposit. This regions are outside the area where particles were initially collocated. Such regions are situated to both sides of the symmetry axis and extend until the position where the dipole dissipates. In this sense we can state that the presence of the vortices enhances the particle transport.

Fig. 3 Final distribution of particles in a experiment with the following conditions: H = 3 cm, f = 0.05, Re = 1,400, S = 0.035

Fig. 4 Distribution of sand in the system after 18 h of forcing. The channel width is 5 cm and the driving period is 12.5 s. The trough in front of the channel has a approximately a length two times H

Fig. 5 Accumulation of particles after over 5,200 forcing periods. The channel width is 5 cm. There are two regions around the symmetry axis where particles deposit

4 Conclusions

In this paper we have shown some experimental results on the motion of particles in a periodic forced flow. We observe the formation of a trough in front of the channel, in agreement with data reported in previous papers. On the other hand, the particles inside and near the channel are subject to larger velocity gradients although the overall displacement is small. The final result is that these particles do not move away and

form a sand bank into the channel. With respect to the relation between the motion of particles and vortices we can assert the following: the dipole and the spanwise vortices are structures that enhance the particle transport. Particles are sucked in the region between vortices and are expelled forward. It is important to note that the accumulation of particles coincides with the region where the dipole moves. Finally, the experimental observations are consistent with numerical (López-Sánchez and Ruiz-Chavarría 2013a) and observational (Amoroso and Gagliardini 2010; de Swart and Zimmerman 2009) results reported in the literature.

Acknowledgments Authors acknowledge DGAPA-UNAM by support under project IN116312, "Vorticidad y ondas no lineales en fluidos".

References

Amoroso RO, Gagliardini DA (2010) Inferring complex hydrographic processes using remote-sensed images: turbulent fluxes in the Patagonian Gulfs and implications for scallop metapopulation dynamics. J Coast Res 26(2):320–332

Angilella J-R (2010) Dust trapping in vortex pairs. Phys D 239:1789–1797

de Swart HE, Zimmerman JTF (2009) Morphodynamics of tidal inlet systems. Annu Rev Fluid Mech 41:203–229

Lacaze L, Brancher P, Eiff O, Labat L (2010) Experimental characterization of the 3D dynamics of a laminar shallow vortex dipole. Exp Fluids 48:225–231

López-Sánchez EJ, Ruiz-Chavarría G (2012) Numerical study of water flow in a channel output with periodic forcing. Experimental and theoretical advances in fluid dynamics. Springer, Berlin ISSN 1863–5520

López-Sánchez EJ, Ruiz-Chavarría G (2013a) Transport of particles in a periodically forced flow. Experimental and computational fluid mechanics. Springer, Heildelberg ISSN 1431–2492

López-Sánchez EJ, Ruiz-Chavarría G (2013b) Vorticity and particle transport in periodic flow leaving a channel. Eur J Mech B/Fluids 42:92–103

Maxey MR, Riley JJ (1983) Equation of motion for a small rigid sphere in a nonuniform flow. Phys Fluids 26:883–889

Mordant N, Metz P, Michel O, Pinton JF (2001) Measurement of Lagrangian velocity in fully developed turbulence. Phys Rev Lett 87:214–501

Part V
General Fluid Dynamics and Applications

Numerical and Simplified Analytical Solutions for Typical Spillways

F. Rojano, A. Rojano, W. Ojeda, R. Mercado, M. Iniguez and T. Espinosa

Abstract The present work compares the numerical solution and the simplified analytical solution to describe behavior of spillways. Specifically, the study focuses on the identification of the water fall profile formed at crossing a spillway. Both, the numerical and simplified analytical solutions are derived from the Navier-Stokes equations. The numerical solution can take into account information regarding the velocities, pressure and sources distributed in space within the regime of turbulence. However, numerical solutions provide detailed information that usually demand a significant amount of time and computational resources. Alternatively, the simplified analytical solution can be reduced to the most important variables such as the head of water arrival and the slope of the facing. Such simplification can incorporate additional information obtained from numerical solutions to improve the accuracy of the predictions. The objective of this study is to show how the simplified analytical solutions can better describe the water fall profiles due to a modification that takes into account a limited number of numerical solutions. This modified analytical solution uses the Reynolds number (Re) and the coefficient (a) associated to the turbulent regime.

F. Rojano (✉)
EPHOR Lab. Agrocampus Ouest. 2, Rue André le Notre, 49045 Angers, France
e-mail: rojanoag@agrocampus-ouest.fr

A. Rojano · T. Espinosa
Universidad Autónoma Chapingo, Km 38.5 Carretera México-Texcoco,
56230 Chapingo, CP, Mexico
e-mail: abrojano@hotmail.com

T. Espinosa
e-mail: t.espinosa.s@gmail.com

W. Ojeda · R. Mercado · M. Iniguez
Coordinación de Riego y Drenaje. Instituto Mexicano de Tecnología del Agua.,
Paseo Cuahnáhuac 8532, Col. Progreso, 62550 Jiutepec, Morelos. CP, Mexico
e-mail: wojeda@tlaloc.imta.mx

R. Mercado
e-mail: rmercado@tlaloc.imta.mx

M. Iniguez
e-mail: mic@tlaloc.imta.mx

J. Klapp et al. (eds.), *Selected Topics of Computational and Experimental Fluid Mechanics*, Environmental Science and Engineering,
DOI 10.1007/978-3-319-11487-3_35

1 Introduction

The representation of water flow in spillways is widely studied due to the outnumbered scenarios that their design and operation bring. The necessity to analyze simultaneously the water properties, the operating conditions and the design of interest can demand a significant amount of time and computational resources in order to obtain successful solutions. Particular projects of high impact justify the detailed investigation to improve the design and efficient operation of spillways. However, in many other cases, a quick calculation through simplified equations can give an acceptable and meaningful outcome in advance.

The aim of this work is to improve the suggested equation presented by Arreguin (2000) and analyzed by Mercado et al. (2013) that describes the water fall profile of a spillway. Mercado et al. (2013) points out that the simplified analytical equation is adequately determined and considers the more significant variables: head of water arrival and the slope of the facing. The same equation has also been studied in Iniguez-Covarrubias et al. (2012) by summarizing various investigations. Both studies (Iniguez-Covarrubias et al. 2012; Mercado et al. 2013) bring the interest to further comparisons of the simplified analytical equation with results of a set of numerical solutions.

Furthermore, a proposal for a modification of the simplified analytical solution presented by Arreguin (2000) and originally introduced by the USBR (US Bureau of Reclamation) is presented. The modification suggested takes into account the results obtained in a series of numerical solutions using Computational Fluid Dynamics (CFD) through Fluent (2013). An exemplary set of two spillways that were previously studied in Mercado et al. (2013) is provided. CFD results served as a demonstration of the benefits in a suitable modification of the simplified analytical solution.

2 Problem Formulation

The water crossing a spillway forms a crest that has been studied using different techniques. For instance, the Navier-Stokes equations covering the inertial, viscous and external forces are capable to reproduce the water dynamics in a spillway including the turbulence phenomena. Nonetheless, difficulties related to the free boundary layer (Hirt et al. 1970), between the two phases: air and water, require the use of Volume of Fluid (VOF) approach to get the numerical solution. This kind of simulations in large domains may imply intensive use of computational resources; consequently, simplified analytical solutions have been used for prediction of the water fall profile avoiding the turbulence phenomena. In this prospect, the present work finds a relation between the numerical and simplified analytical solutions to enhance the prediction.

The simplified analytical solution (Eq. 1) deals with coefficients such as the head of arrival and the slope of the facing to determine the water fall profile; and values can be found in Arreguin (2000)

$$y = k \times x^n. \tag{1}$$

Mercado et al. (2013) proved that Eq. 1 was properly derived from the Navier-Stokes equations after a series of assumptions and simplifications. The deduced Eq. 1 takes care only of inertial forces; however, spillways operate under turbulent conditions, which mean that viscous and inertial forces determine the flow behavior. Furthermore, phenomena occurring at the spillway water discharge can certainly change the water dynamics significantly, such as the conversion of kinetic to potential energy at the moment of the spillway discharge; the air entrainment at the boundary layer between air and water; the surface ondulation; free surface instabilities and others. Thus, Eq. 1 can be improved by considering the Reynolds number (Re) and the coefficient (a) that incorporate the phenomena that occur in the water fall profile within turbulence regime.

The proposal in this work suggests a methodology that allows the improvement in the prediction of Eq. 1 after a limited number of numerical solutions in two spillways with similar design but different dimensions. Then, the term k in Eq. 1 can be replaced by a/Re in Eq. 2 in order to increase the accuracy of those calculations.

$$y = \left(\frac{a}{Re}\right) \times x^n. \tag{2}$$

This investigation evaluates two types of spillways as study cases (A and B) but similar characteristics in the design. The numerical solution of each case was found through Fluent (2013). The dimensions in each case are specified in Table 1 and indicated in Fig. 1. Six simulations in total were performed in steady state conditions. Five simulations were used to identify the coefficient (a) in Eq. 2 and the results of

Table 1 Spillway specifications

	Symbol	Cases		Units
		A	B	
Width	L	35.8	86.4	m
Head	H_o	var	var	m
Height of domain	H_1	$2(H_o+P)$	$2(H_o+P)$	m
Length of upstream spillway	W_1	$1.5(H_o+P)$	$1.5(H_o+P)$	m
Length of downstream spillway	W_2	$5(H_o+P)$	$5(H_o+P)$	m
Height of dam	P	3.5	34.2	m
Discharge	Q	var	var	$m^3 s^{-1}$
Hydraulic ratio	h_r	var	var	m

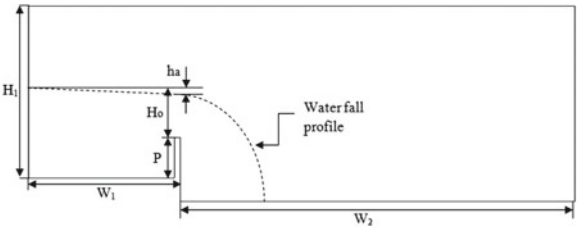

Fig. 1 Dimensions of the spillway

Table 2 Study cases

Spillway	Flow ($m^3\,s^{-1}$)	Reynolds ($\times 10^5$)
A1	5,000	2,088
A2	6,500	2,714
A3	8,000	3,341
B1	16,655	3,222
B2	18,155	3,512
B3	19,655	3,808

one simulation were used to validate Eq. 2. The operating conditions given for each of the six cases are indicated in Table 2.

Three scenarios for each case (A and B) were simulated. The two types of spillways were taken with the same specifications as the ones mentioned in Mercado et al. (2013) with the same operating conditions that were included as case A2 and B2.

A RANS (Reynolds Averaged Navier-Stokes) model was used (Eq. 3).

$$\frac{\partial u_j\,\phi}{\partial x_j} = \frac{\partial}{\partial x_j}\left(\Gamma_\phi \frac{\partial\,\phi}{\partial x_j}\right) + S_\phi \tag{3}$$

where ϕ is the variable of interest (velocity in the j direction, turbulent kinetic energy and dissipation kinetic energy). Γ_ϕ is the diffusion coefficient and S_ϕ is the source term. Through the two-equation approach ($\kappa - \varepsilon$), the turbulence effects were included. The model $\kappa - \varepsilon$ realizable was used and additional parameters were defined based on Eq. 4 (Fluent 2013).

$$\kappa = \frac{3}{2}(uI)^2;\ \epsilon = {c_\mu}^{0.75}\kappa^{1.5}{l_t}^{-1};\ I = 0.16Re^{-1/8} \text{ and } l_t = 0.07L \tag{4}$$

where Re is the Reynolds number, I is the turbulence intensity, in percent (%). l_t is the turbulence length scale in m. κ and ϵ are the turbulent kinetic and dissipation energy, respectively, in m^2s^{-2}. c_u is equal to 0.09. L is the characteristic length of the spillway, in m. Additional parameters for the same model were defined as $C_{1-\epsilon} = 1.44$ and $C_{2-\epsilon} = 1.92$.

This problem demands a free water surface simulation between the two phases (air and water) under the presence of instabilities during the spillway water fall. The model used the VOF approach in order to represent simultaneously in the same domain the interaction of air and water phases. The VOF method is followed since it has been successfully utilized in previous investigations (Ferrari 2010; Chakib 2013; Mohammadpour et al. 2013).

3 Results and Discussion

A series of grids with different number of cells were created. Each grid was evaluated in order to verify stability of the results. The process to obtain a convenient grid consisted of incrementing the number of cells uniformly at the whole domain with

a rate of 1.65. An evaluation of each one of the grids has been performed with Fluent (2013) by implementing the momentum equation until the water velocity at the spillway had stable results and it was found a variation of less than 5 % between the previous and current grid. The settings followed during the test of each grid correspond to the cases A2 and B2, for the spillway type A and B, respectively. The grid chosen was made of structured tetrahedral cells with a maximum ratio between cells of 22, y+ values to be less than 300 and skewness less than 0.9 as recommended by Fluent (2013). The grids evaluated and chosen were for the cases A and B with 540,000 and 740,000 cells, respectively.

In both cases the water velocity inlet was assumed to be a constant. No slip conditions were fixed at any wall with a roughness coefficient of 0.5. The turbulence model was also defined in Fluent (2013) according to Eqs. 3 and 4. The SIMPLE method (Semi Implicit Pressure Linked Equation) linking pressure and velocity was used in conjunction with the second order upwind scheme for the discretization of Eq. 3. The solution was found when the residuals were less than 10^{-5}. This condition was imposed to the x and y velocity, kinetic energy, turbulence energy dissipation, air phase and continuity.

The numerical results were found for each of the six cases indicated in Table 2. For instance, Fig. 2 indicates the numerical solution of the water fall profile indicating the water velocity and additionally how the spillway water discharge creates water recirculation at the downstream zone of the spillway. This water recirculation modifies the water fall profile based on the spillway operating conditions.

For all the operating conditions shown in Table 2 the water fall profile was obtained. Then, coefficient (a) of Eq. 2 was found using n equal to 1.84 and considering all the cases but not the case A2. The water fall profile predicted by Eq. 2 was adjusted by means of the coefficient (a) until it was similar for at least 90 % of the water fall profile found in the numerical solution. The summary of the five cases were plotted in Fig. 3 where it was easy to identify a correlation between the coefficient (a) and (Re).

The linear regression from five numerical solutions and indicated in Fig. 2 was then used to estimate the corresponding value of the coefficient (a) for the case A2 by means of the Reynolds number. The prediction obtained of Eq. 2 in the case A2

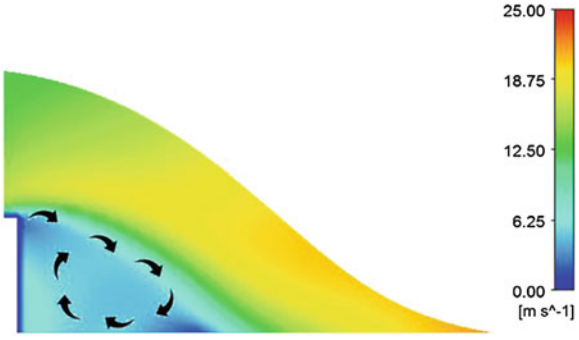

Fig. 2 Velocity gradient of the water fall profile of spillway B2

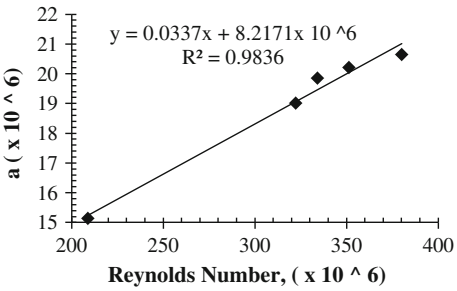

Fig. 3 Identification of coefficient (a)

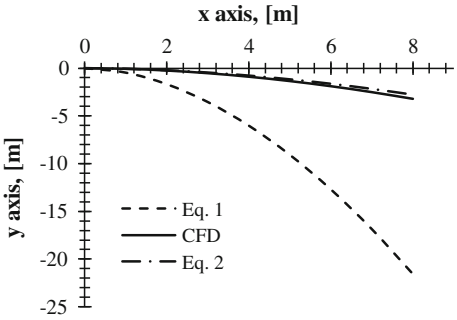

Fig. 4 Evaluation of coefficient (a) for the case A2 indicated in Table 2

was compared with Eq. 1 and the numerical solution, presenting the results in Fig. 4. The comparison shows that Eq. 2 significantly enhances the prediction and proves that an additional coefficient reduces the effort demanded in an evaluation of several scenarios through numerical solutions for a spillway with the same characteristics in the design.

Investigations related to the implementation of Eq. 2 for a set of numerical solutions with spillways of different characteristics in the design requires further analysis. For instance differences in a set of spillways with a marked difference in the slope of the wall at the upstream or downstream side of the spillway may affect the water flow behavior significantly.

4 Conclusions

This work presents a proposal to evaluate the predicted water fall profile for a spillway with no slope at any of the two faces. The modification in a simplified analytical equation consists only in the addition of the (Re) and an associated coefficient (a) as parameters that can include all the phenomena happening in a spillway water fall under turbulent conditions. The coefficient (a) will be reliable within a regime of operation of the spillway previously evaluated through numerical solutions. The inclusion of the coefficient (a) does not increase the difficulty in quick calcula-

tions; rather, Eq. 2 can be more reliable for prediction purposes. Also, five numerical solutions that include different operating conditions in two spillways with similar design but different dimensions can be enough to improve the accuracy of a spillway water fall profile.

References

Arreguin F (2000) Obras de Excedencia. IMTA Editorial, México, p 267

Chakib B (2013) Numerical computation of inception point location for flat-sloped stepped spillway. Int J Hydraul Eng 2(3):47–52

Ferrari A (2010) SPH simulation of free surface flow over a sharp-crested weir. Adv Water Resour 33:270–276

Fluent (2013) Fluent user's guide. ANSYS Inc, Canonsburg

Hirt CW, Cook JL, Butler TD (1970) A Lagrangian method for calculating the dynamics of an incompressible fluid with free surface. J Compt Phys 5:103–124

Iniguez-Covarrubias M, Ojeda W, Mercado R (2012) Vertedores de Caida Libre en Presas y las Estructuras de Control de Nivel en Canales. XXII Congreso Nacional de Hidraulica. Acapulco, Guerrero, México. Nov, 5th–9th

Mercado JR, Guido P, Ojeda W, Sánchez-Sesma J (2013) Water profile over an Ogee-shaped crest and the Reynolds fractional equations. J Math Syst Sci 1:1–6

Mohammadpour R, Ghani AA, Azamathulla HM (2013) Numerical modeling of 3-D flow on porous broad crested weirs. Appl Math Model 37:9324–9337

Modeling and Simulation of a Biopolymer Processing in a Single Screw Extruder

U. Romero Ortiz, A. López Villa and R.O. Vargas Aguilar

Abstract Modeling and numerical simulation of a biopolymer processing in a single screw extruder is developed. Polylactic acid (PLA) is one of the natural polymers proposed as a substitute for synthetic polymers because of the similarity in physical properties as well as processing conditions. The PLA behaves as a shear thinning fluid, in order to involve this feature the Power Law model is used as a constitutive equation and the temperature dependent viscosity is also considered. The model is validated comparing typical flow curves of a Newtonian fluid generated by the model with results previously reported in the literature. Finally, the drag flows and pressure flows are analyzed, the effect of the power index and the flow curves for Newtonian and non-Newtonian fluids are compared.

1 Introduction

Polymer extrusion is a process that offers advantages over most plastic transformation processes and with an economic cost with respect to any other. The single screw extruder is the most common equipment in the polymer industry. It can be part of an injection molding unit and found in numerous other extrusion processes, including blow molding, film blowing, and wire coating (Bird et al. 1960).

Environmental concerns have led over the past years to growing over new solution for plastics, "green plastics" have been motivated by two specific goals: reducing dependence of plastic production on petroleum supplies and developing solutions to plastic waste accumulation. The development of biodegradable polymers

U. Romero Ortiz · A. López Villa · R.O. Vargas Aguilar (✉)
ESIME Azcapotzalco, Instituto Politécnico Nacional, Avenida de Las Granjas No. 682, Colonia Santa Catarina, Delegación Azcapotzalco, 02550 México, D.F., Mexico
e-mail: reneosvargas@yahoo.com.mx

U. Romero Ortiz
e-mail: uvaortizz@gmail.com

A. López Villa
e-mail: abelvilla77@hotmail.com

J. Klapp et al. (eds.), *Selected Topics of Computational and Experimental Fluid Mechanics*, Environmental Science and Engineering,
DOI 10.1007/978-3-319-11487-3_36

is an option to use renewable resources and to reduce waste. Thermoplastic starch (TPS), polyhydroxyalkanoates (PHAs), polylactides and their blends are promising candidates for such replacement and are subject to many researches. Polylactic acid (PLA) has been intensively investigated in past years. This biodegradable polyester, which can be used in many applications from packaging to biocompatible materials, has a thermoplastic behavior combined with high mechanical performance, good appearance and low toxicity (Jamshidian et al. 2010). Due to its similar characteristics to other polymers such as polyethylene terephthalate (PET), high impact polystyrene (HIPS), and polyvinylchloride (PVC), the PLA is proposed as a substitute for these synthetic polymers.

This work presents the modeling and the simulation of the PLA processing in a single screw extruder. The model is based on the momentum equation coupled with the energy equation through physical parameters considering the rheological behavior of the PLA reported by Jacobsen et al. (2000) and Mehta et al. (2005).

2 Development

A single screw extruder consists of one screw rotating in a closely fitting barrel; the transport mechanism is based on friction between the polymer and the walls of the channel as shown in Fig. 1. The material enters through the feed throat (feed hopper) and comes into contact with the screw and in the final part of the barrel there is a die which gives the final product its profile.

The governing equations describing this problem, with the assumption of constant density, are the continuity equation:

$$\nabla \cdot \underline{v} = 0, \tag{1}$$

the momentum equation:

$$\rho \frac{D\underline{v}}{Dt} = -\nabla p + \nabla \cdot \underline{\underline{\sigma}} + \underline{f}, \tag{2}$$

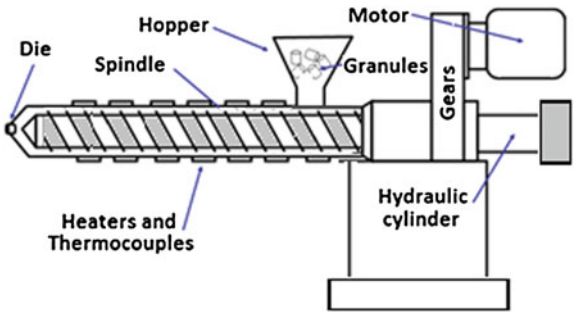

Fig. 1 Single screw extruder

and the energy equation:

$$\frac{DT}{Dt} = \nabla \cdot K \nabla T + \underline{\underline{\sigma}} : \nabla \underline{v}, \tag{3}$$

where $\underline{v}$, p, K, ρ and $\underline{\underline{\sigma}}$ denotes the velocity, pressure, thermal conductivity, density and the stress tensor, respectively.

As a first step in addressing the problem we assume that the screw is stationary and the barrel is rotatory, it is also assumed that the screw can be unrolled.

- The flow is time independent, fully developed and only occurs in a longitudinal direction (z axis).
- An incompressible fluid with constant thermal conductivity (k = constant) and non-Newtonian (power law model) is considered.
- Constant pressure gradient along the channel.
- The viscosity depends on the shear rate and on the temperate.

Because the PLA is a polymer in which their behavior is shear rate dependent (non-Newtonian), the power law model is used as a constitutive model coupled with the energy equation.

$$\eta(\dot{\gamma}) = m(T)\dot{\gamma}^{n-1}, \tag{4}$$

where

$$m(T) = m_0 e^{-a(T-T_0)}, \tag{5}$$

$a =$ is a constant with units $\left[\frac{1}{T}\right]$.

It is preferable to work in dimensionless terms, so defining the following dimensionless variables:

$$\xi = \frac{y}{H}, \quad \phi = \frac{v_z}{V}, \quad \theta = a(T - T_0), \tag{6}$$

the velocity profile is

$$\phi' = -\Gamma[(G\xi + M1)e^{\theta}]^{1/n}, \tag{7}$$

subjected with the following boundary conditions

$$\phi'(\xi = 0) = 0, \qquad \phi'(\xi = 1) = 1, \tag{8}$$

where

$$\Gamma = \frac{H}{V}\frac{1}{\eta_0^{1/n}}, \; G = \frac{\Delta p}{L}H, \tag{9}$$

where $M1$ is an integration constant.

In the same way the temperature profile is:

$$\theta'' + \beta[(G\xi + M1)e^{\theta}]^{1/n}(G\xi + M1) = 0, \tag{10}$$

with the corresponding boundary conditions

$$\theta'(\xi = 0) = 0, \quad \theta(\xi = 1) = \theta_w \tag{11}$$

In order to obtain approximate solutions of these differential equations the numerical method used is based on orthogonal collocation. The solution is achieved through a series of known trial functions; these series of functions are called test functions, which are studied in the differential equation and the result is called the residual. We employ orthogonal collocation using the Jacobi polynomials for the flow problem considered in this work. Therefore by applying the method of placement it is required that:

$$\theta'' = \sum_{i=1}^{N+2} B_{ji}\theta_i, \quad \phi' = \sum_{i=1}^{N+2} A_{li}\phi_i, \tag{12}$$

$$\text{where} \quad j = 1, 2, \ldots, N+2.$$

Quantities B_{ji} and A_{li} are the components of the matrix formed by the Jacobi polynomials which correspond to the discretized forms of the corresponding derivatives (Villadsen and Michelsen 1978). Convergence is accomplished by successive calculations and the use of collocation points which are similar to the mesh points or nodes in finite difference methods.

3 Results and Discussion

In this section, the numerical predictions for the PLA processing in a single screw extruder are presented. The model was solved using the programming language FORTRAN.

The proposed model is validated by comparing typical curves for the Newtonian case published in the literature, in this case the Couette flow according to Tadmor and Gogos (2006). Figure 2 shows only the contribution of the drag flow, a straight line

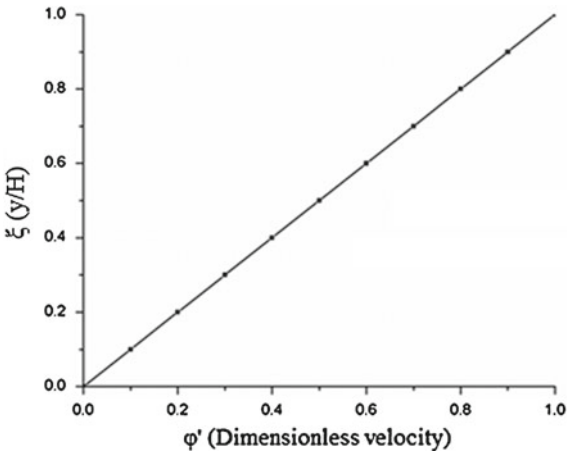

Fig. 2 Dimensionless simple shear flow

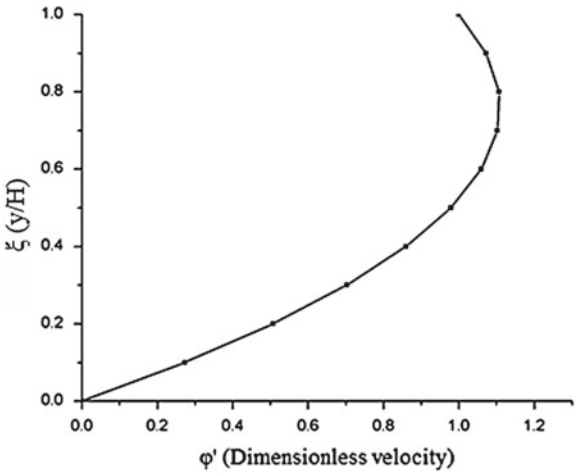

Fig. 3 Velocity profile created by combining drag flows and pressure flows with a positive pressure gradient

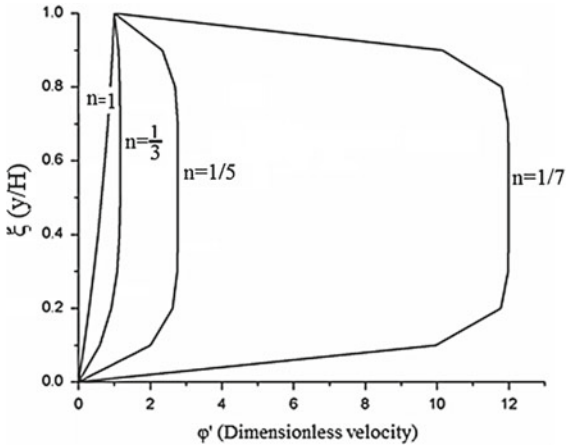

Fig. 4 Velocity profile generated by the combination of drag and pressure flows with positive pressure gradient for different values of power law index "n"

with slope equal to the viscosity is obtained, as expected. In Fig. 3 the combination of the drag flow and the pressure flow generated by a positive gradient pressure for a Newtonian fluid is shown.

Figure 4 shows the effect of the power law index "n" in the velocity profile generated by the combination of drag and pressure flows, as expected for shear thinning fluid with reducing "n" the viscosity decreases, thus having a lower resistance to flow modifying the velocity profile.

The temperature profile for different screw speeds is shown in Fig. 5. The model considers the viscous dissipation term. This implies that increasing the velocity there also increases the fluid temperature as shown in this figure. This is very important when setting the operating conditions because at high screw speeds the screw can be degraded thermally and mechanically affecting the final product.

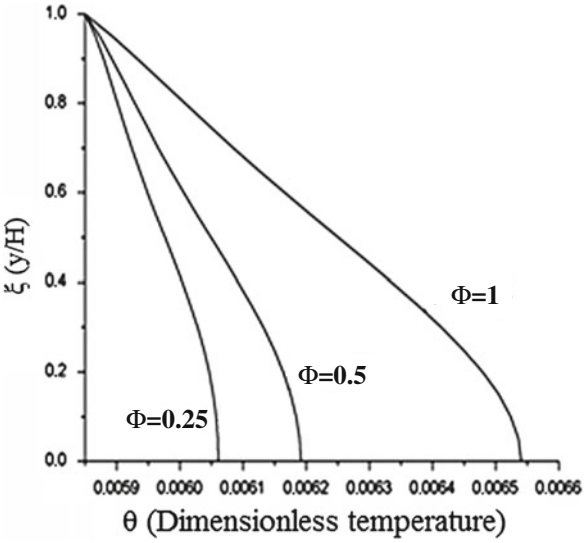

Fig. 5 Temperature profile at different screw speeds with: $\Delta P = 3{,}000$ psi, $n = 1/3$

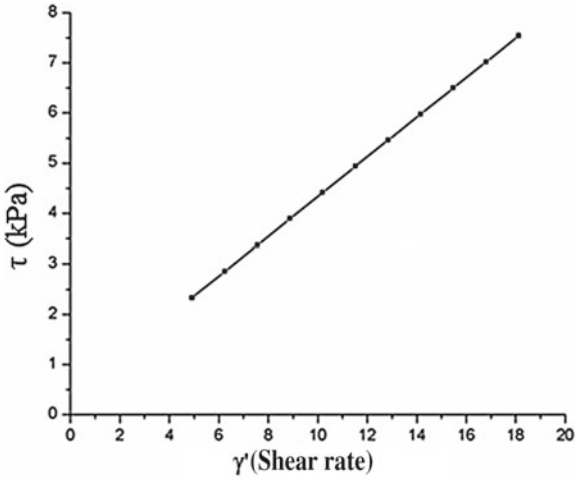

Fig. 6 Stress depending on the deformation rate for a Newtonian fluid

Figure 6 presents the flow curve for a Newtonian fluid which shows that the relationship between the stress tensor and the shear rate is linear. In this case the viscosity is independent of the shear rate according to Tadmor and Gogos (2006). For a non-Newtonian fluid the shear stress varies non-linearly with the shear rate as shown in Fig. 7. The behavior in Fig. 7 describes a pseudoplastic or shear thinning fluid, which is correct for the biopolymer considered in this work.

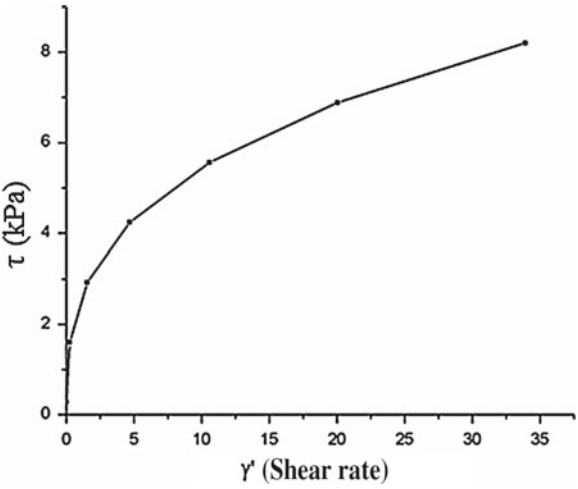

Fig. 7 Stress depending on the deformation rate for a non-Newtonian fluid n = 1/5

4 Conclusions

In this work, the modeling and simulation of a biopolymer PLA processing in a single screw extruder is performed. The development of biodegradable polymers is an option to use renewable resources and to reduce waste. PLA can be used in many applications and is proposed as a substitute for synthetic polymers.

The model is validated by comparing the Newtonian case with results from the literature, this simple model captures the Newtonian and non-Newtonian behavior shown in the flow curves of the shear stress as a function of the shear rate. The Power Law model is versatile in the processing of materials because the temperature and shear rate dependence of viscosity can be easily included. The results show that this model is simple and easy to implement for analyzing a variety of alternatives to improve this attractive sustainable process.

Acknowledgments This project is funded by the research projects 20100658 and SIP 20144085 SIP_IPN in Mexico.

References

Bird RB, Stewart WE, Lightfoot EN (1960) Transport phenomena. Wiley, New York, p 780

Jacobsen S, Friz HG, Degee P, Dubois P, Jerome R (2000) New developments on the ring-opening polymerization of polylactide. Ind Crops Prod 11(2–3):265–275

Jamshidian M, Tehrany EA, Imran M, Jacquot M, Desobry S (2010) Poly-lactic acid: production, applications, nanocomposites, and release studies. Compr Rev Food Sci Food Saf 9:552–571

Mehta R, Kumar V, Bhunia H (2005) J Macromol Sci Part C Polym Rev 45:325–349

Tadmor Z, Gogos CG (2006) Principles of polymer processing, 2nd edn. Wiley, New York

Villadsen J, Michelsen ML (1978) Solution of differential equation models by polynomial approximation. Prentice Hall, Englewood Cliffs

An Analytical Solution for Friction Stir Welding of an AISI 1018 Steel

V.H. Ferrer L., C.A. Hernández C. and R.O. Vargas Aguilar

Abstract Friction stir welding process has been usually studied from the solid mechanics point of view although the use of CFD's techniques has been increasing for the numerical treatment of the problem. In this work, a simple analytical solution using series expansions for Cauchy momentum and energy equation-set is obtained. The Power Law model takes into account the shear thinning fluid and the Arrhenius-type relationship the temperature dependent viscosity. Friction dissipation as an external heat source is considered.

1 Introduction

Friction Stir Welding (FSW) is a solid state welding process used for joining similar and dissimilar metal alloys. Thomas et al. (1991) patented this process in 1991 and developed it at The Welding Institute (TWI). Several authors have analyzed momentum and heat transfer problem in FSW. Heurtier et al. (2006) developed a kinematical model to determine material flow and temperature distribution in the stir zone. Three flow fields were solved analytically using potential flow theory (Nunes 2001). Other authors (Nandan et al. 2007; Cho et al. 2013), considered Perzyna's model (Perzyna 1966) to take into account viscoplastic response during material processing in the stir zone. Heurtier et al. (2006) also considered both viscous and friction dissipation in tool/workpiece interface and heat transfer by conduction only, for an AA2024-T351 aluminium alloy. Schmidt et al. (2004) proposed an analytical model for heat generation regarding viscous and friction dissipation, they simplified the problem by considering shear strain only.

V.H. Ferrer L. · C.A. Hernández C. (✉) · R.O. Vargas Aguilar
ESIME Azcapotzalco, Instituto Politécnico Nacional, Avenida de las Granjas No. 682, Col. Santa Catarina, Deleg. Azcapotzalco, 02250 México, D.F., Mexico
e-mail: cahernandezc@ipn.com

J. Klapp et al. (eds.), *Selected Topics of Computational and Experimental Fluid Mechanics*, Environmental Science and Engineering,
DOI 10.1007/978-3-319-11487-3_37

2 Mathematical Models

2.1 Perzyna's Model

Based on the mathematical relation of Naghdi and Murch (1963) between viscoplastic strain rate and the derivative of a potential function respect to the deviatoric stress tensor, Perzyna (1966) proposed a model in which the strain rate tensor $\dot{\varepsilon}_{ij}^{vp}$ depends on the yield stress k_1 as

$$\dot{\varepsilon}_{ij}^{vp} = \frac{1}{2\mu} S_{ij} \langle 1 - \frac{k_1}{\sqrt{J_2}} \rangle. \tag{1}$$

Here $\langle\ \rangle$ stands for Macauley brackets; m is the material shear modulus; S_{ij} is the stress deviator; and J_2 is the second invariant. Based on the expressions for effective stress and effective strain rate (Bathe 1996), Perzyna (1966) obtained a relationship for the viscosity μ in terms of the effective stress $\bar{\sigma}$ and effective strain rate $\dot{\bar{\varepsilon}}$:

$$\mu = \frac{\bar{\sigma}}{3\dot{\bar{\varepsilon}}}. \tag{2}$$

2.2 Viscosity Power Law Model

One of the simplest and most widely used equations for modelling viscosity in a non-Newtonian fluid flow with shear thickening and dilatant behaviour was devised by Ostwald (1975):

$$\mu = m\dot{\gamma}^{n-1}, \tag{3}$$

where m(N sn/m^2) and n are the consistency and index coefficients, respectively. The m parameter depends on temperature as follows:

$$m = m_0 \exp\left[\frac{\Delta E}{R}\left(\frac{1}{T} - \frac{1}{T_0}\right)\right], \tag{4}$$

where m_0 is the viscosity at T_0, ΔE is the activation energy for the process, R is the universal constant of gases, T_0 is a reference temperature and T is the process temperature. By making some arrangements the following expression is obtained:

$$m = m_0 \exp\left[-a(T - T_0)\right]. \tag{5}$$

2.3 Heat Generation Schmidt Model

Schmidt and Hattel (2008) proposed that heat generation during FSW is a function of tool geometry, tool plunge force and material yield stress. Viscous dissipation was computed in his work as $\bar{\bar{\tau}} : \nabla \bar{V}$. So, heat generation by friction q_f [W m^{-2}] in the tool/workpiece interface is:

$$q_f = \delta\, \mu_f\, P\, (\omega - U), \tag{6}$$

where μ_f is the friction coefficient, P is the pressure plunge, ω and U are the angular and weld speed, respectively. Here δ is the contact state variable or extent of slip which defines the influence of welding tool slipping in the heat generation (Deng et al. 2001):

$$\delta = 1 - \exp\left(-\frac{1}{\delta_0}\frac{\omega}{\omega_0}\frac{R_p}{R_s}\right). \tag{7}$$

In the above expression ω is the welding tool normalized angular frequency, R_p and R_s are the pin and shoulder radii, respectively; δ_0 is a constant; and ω_0 is the angular velocity of a reference welding condition.

3 Mathematical Formulation

For this problem a steady-state process is assumed. AISI 1018 steel is incompressible, thermal conductivity is constant in the mathematical domain. In the velocity vector, only the $\hat{e}_i$ component prevails, which is in x direction. Velocity and temperature are functions that depend only the y direction. Dimensionless variables are defined in Table 1. The weld speed U, the difference between shoulder and pin radii H, reference temperatures T_0 and T_1 are macroscopic variables that are established in the process.

Figure 1 depicts the mathematical domain and boundary conditions for the 1-D case. The continuity (8), momentum (9) and energy (10) equations are solved using a series expansion.

$$\frac{\partial \phi}{\partial \alpha} = 0, \tag{8}$$

Table 1 Dimensionless variables

$\phi = \frac{V_x}{U}$	$\alpha = \frac{x}{H}$	$\gamma = \frac{y}{H}$
$\theta = \frac{T - T_0}{T_1 - T_0}$	$\pi = \frac{pH^n}{m_0 U^n}$	$b = -a(T_1 - T_0)$

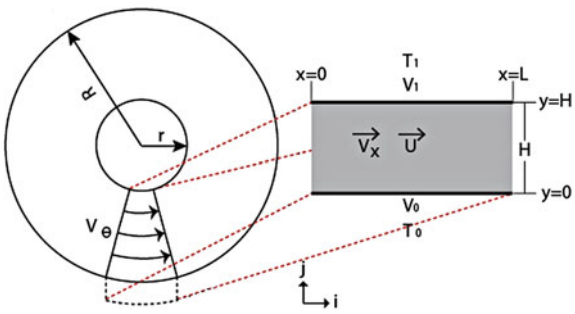

Fig. 1 Scheme and boundary conditions

$$\frac{\partial}{\partial\gamma}\left[e^{b\theta}\left(\frac{\partial\phi}{\partial\gamma}\right)^{n}\right]=\frac{\partial\pi}{\partial\alpha}, \tag{9}$$

$$\frac{\partial^2\theta}{\partial\gamma^2}+Br\cdot e^{b\theta}\left(\frac{\partial\phi}{\partial\gamma}\right)^{n+1}+A\gamma=0, \tag{10}$$

$$A=\frac{H^3\omega\,\delta\,\mu_f\,P\,(R_s^3-R_p^3)}{\lambda\,R_s^3\,k\,(T_1-T_0)}, \tag{11}$$

$$Br=\frac{U^{n+1}\,m_0}{H^{n-1}\,k\,(T_1-T_0)}, \tag{12}$$

where ϕ is a dimensionless velocity, α is the x dimensionless position, γ is the y dimensionless position, θ is the normalized temperature, π is the thermodynamic pressure, A is the heat generation term, and Br is the Brinkman number. For solving Eqs. (8)–(10) and decoupling the system series expansions for ϕ and θ with a truncation of order $\mathcal{O}(\varepsilon^2)$ is proposed:

$$\phi=\phi_0+\varepsilon\phi_1+\varepsilon^2\phi_2+\mathcal{O}(\varepsilon^3), \tag{13}$$

$$\theta=\theta_0+\varepsilon\theta_1+\varepsilon^2\theta_2+\mathcal{O}(\varepsilon^3), \tag{14}$$

$$\varepsilon=Br. \tag{15}$$

The decoupled system of equations become:

$\mathcal{O}(1)$

$$\frac{d}{d\gamma}\left[e^{b\theta_0}\left(\frac{d\phi_0}{d\gamma}\right)^{n}\right]=\frac{\partial\pi}{\partial\alpha}, \tag{16}$$

$$\frac{d^2\theta_0}{d\gamma^2}+A\,\gamma=0, \tag{17}$$

$\mathcal{O}(\varepsilon)$

$$\frac{d}{d\gamma}\left\{e^{b\theta_0}\left[b\theta_1\left(\frac{d\phi_0}{d\gamma}\right)^{n}+n\left(\frac{d\phi_0}{d\gamma}\right)^{n-1}\left(\frac{d\phi_1}{d\gamma}\right)\right]\right\}, \tag{18}$$

$$\frac{d^2\theta_0}{d\gamma^2}+e^{b\theta_0}\left(\frac{d\phi_0}{d\gamma}\right)=0, \tag{19}$$

$\mathcal{O}(\varepsilon^2)$

$$\frac{d}{d\gamma}\left\{e^{b\theta_0}\left[\left(\frac{(b\theta_1)^2}{2}+b\theta_2\right)\left(\frac{d\phi_0}{d\gamma}\right)^n+n\left(b\theta_1\frac{d\phi_0}{d\gamma}+\frac{d\phi_2}{d\gamma}\right)^{n-1}\left(\frac{d\phi_1}{d\gamma}\right)-\frac{n^2-n}{2}\left(\frac{d\phi_0}{d\gamma}\right)^{n-2}\left(\frac{d\phi_1}{d\gamma}\right)^2\right]\right\}=0, \tag{20}$$

$$\frac{d^2\theta_0}{d\gamma^2}+e^{b\theta_0}\left[b\theta_1\left(\frac{d\phi_0}{d\gamma}^{n+1}\right)+(n+1)\left(\frac{d\phi_0}{d\gamma}\right)^n\left(\frac{d\phi_1}{d\gamma}\right)\right]=0. \tag{21}$$

The above equations are subjected to the following boundary conditions:

$$\begin{aligned}
&\gamma=0;\quad \phi_0=0; && \theta_0=0;\quad \phi_1=0;\quad \theta_1=0;\quad \phi_2=0; && \theta_2=0\\
&\gamma=1;\quad \phi_0=\frac{\omega R_p(1-\delta)}{U}; && \theta_0=1;\quad \phi_1=0;\quad \theta_1=0;\quad \phi_1=0; && \theta_1=0
\end{aligned} \tag{22}$$

The solution of Eqs. (16)–(21) was carried out for $n=\frac{1}{3},\frac{1}{2},\frac{2}{3},\frac{3}{4},1$. The value of $n=1$ represents a Newtonian regime as a way to validate the solution. Furthermore a recursive solution for whatever value of $0<n\leq 1$ (Eqs. (23)–(28)) is obtained. Figure 2 shows a comparison between the analytical solution using power law model and the numerical solution using Perzyna's model, employing data given in Table 2

$$\phi_0=\frac{n\exp\left(-\frac{1}{n}b\theta_0\right)}{c_0\,(n+1)}\left[(c_0\,\gamma+c_1)^{\frac{1+n}{n}}-c_1^{\frac{1+n}{n}}\right], \tag{23}$$

$$\theta_0=\frac{A}{6}\left(\gamma-\gamma^3\right)+\gamma, \tag{24}$$

Table 2 Material's properties and data used in the calculations

Property/parameter	Value
Pin radius, mm	3.95
Shoulder radius, mm	9.50
Characteristic length H, mm	5.75
Welding speed U, mm	0.31
Workpiece material	AISI 1018
AISI 1018 density, kg m^{-3}	7860.00
Pressure plunge, MPa	65.90
Conductivity, W $m^{-1}K^{-1}$	30.00
T_0 temperature, K	1242.00
T_1 temperature, K	1552.00
m_0, Pa s^n	3.5×10^6
n	1/3, 1/2, 2/3, 3/4, 1.0

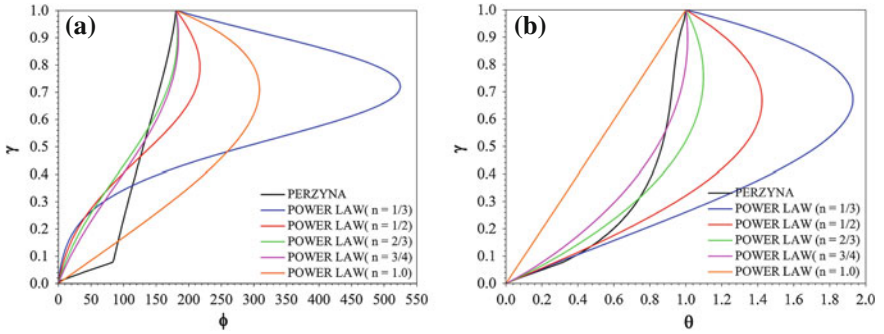

Fig. 2 Comparison between analytical non-Newtonian model with different n values to Perzyna's model (Perzyna 1966). **a** Dimensionless velocity ϕ as a function of dimensionless length γ. **b** Dimensionless temperature θ as a function of dimensionless length γ

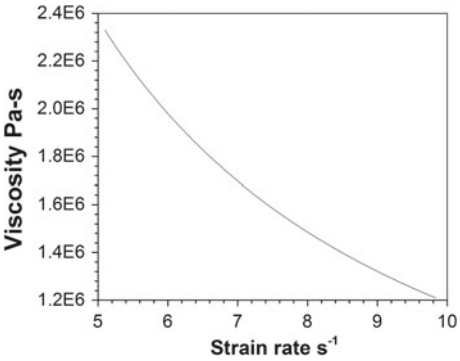

Fig. 3 Viscosity (Pa · s) as a function of the shear strain rate (s^{-1}). Dimensional parameters are recovered from dimensionless one depicted in Table 1

$$\phi_1 = -\frac{b\theta_1 \exp\left(-\frac{1}{n} b\theta_0\right)}{c_0(n+1)} (c_0\,\gamma + c_1)^{\frac{1+n}{n}}, \tag{25}$$

$$\theta_1 = -\frac{n^2 \exp\left(-\frac{1}{n}\, b\theta_0\right)}{c_0^2(1+2n)(1+3n)} \left[(c_0\,\gamma + c_1)^{\frac{1+3n}{n}} + \left(c_1^{\frac{1+3n}{n}} - (c_0 + c_1)^{\frac{1+3n}{n}}\right)\gamma - c_1^{\frac{1+3n}{n}}\right], \tag{26}$$

$$\phi_2 = \frac{\left[\frac{1}{2n}(b\theta_1)^2 - b\theta_2\right] \exp\left(-\frac{1}{n}\, b\theta_0\right)}{c_0(n+1)} (c_0\,\gamma + c_1)^{\frac{1+n}{n}}, \tag{27}$$

$$\theta_2 = \frac{n\, b\theta_1 \exp\left(-\frac{1}{n}\, b\theta_0\right)}{c_0^2(1+2n)(1+3n)} (c_0\,\gamma + c_1)^{\frac{1+3n}{n}}. \tag{28}$$

Figure 3 shows that the viscosity of the AISI 1018 steel decreases with the shear strain rate. Arora et al. (2009) reported that the strain rate during FSW is not more than 10 s^{-1} by using numerical simulations.

The Reynolds (Re) and Brinkman (Br) numbers are evaluated, using data given in Table 2 and taking a value of $n = \frac{3}{4}$. Both numbers are very low, meaning that the flow field is laminar and that viscosity has great influence in FSW (Chiumenti et al. 2013, p. 357). The results of the temperature profile for the Newtonian case are in good agreement for low Br values, i.e.,

$$\mathrm{Re} = \frac{\rho H^n}{m_0 U^{n-2}} = 1.92 \times 10^{-9}, \tag{29}$$

$$\mathrm{Br} = \frac{m_0 U^{n+1}}{k H^{n-1}(T_1 - T_0)} = 6.37 \times 10^{-5}. \tag{30}$$

4 Conclusions

An analytical solution for the AISI 1018 steel deformation under friction stir welding process has been presented. The deformed solid exhibits a non-Newtonian behavior. We found that this behavior obeys a Power Law model compared to the Perzina model. Both models had similar behavior when $n = \frac{2}{3}, \ \frac{3}{4}$. The steel dilatant behavior is more related to the temperature than to the strain rate. The low values of Re and Br numbers demonstrated that the laminar flow and the heat transfer mechanisms were by conduction. Future work will entail refining our model in 2-D for getting a more accurate solution.

References

Arora A, Zhang Z, De A, DebRoy T (2009) Strains and strain rates during friction stir welding. Scripta Mater 61:863–866

Bathe KJ (1996) Finite element procedures. Prentice Hall, New York

Chiumenti M, Cervera M, de Saracibar CA, Dialami N (2013) Numerical modeling of friction stir welding processes. Comput Method Appl Mech Eng 254:353–369

Cho HH et al (2013) Three-dimensional numerical and experimental investigation on friction stir welding processes of ferritic stainless steel. Acta Mater 61:2649–2661

Deng Z, Lovell MR, Tagavi KA (2001) Influence of material properties and forming velocity on the interfacial slip characteristics of cross wedge rolling. J Manuf Sci Eng Trans ASME 123:647–653

Heurtier P et al (2006) Mechanical and thermal modeling of friction stir welding. J Mat Proc Tech 171:348–357

Naghdi PM, Murch SA (1963) On the mechanical behavior of viscoelastic/plastic solids. J Appl Mech 30:321–328

Nandan R et al (2007) Three-dimensional heat and material flow during friction stir welding of mild steel. Acta Mater 55:883–895

Nunes AC (2001) Wiping metal transfer in friction stir welding. In: Proceedings of 2001 TMS annual meeting automotive alloys and joining aluminum symposium, pp 235–248
Ostwald W (1975) Ueber die geschwindigkeitsfunktion der viscositat disperser systeme. Kolloid-Z 36:99–117
Perzyna P (1966) Fundamental problems in viscoplasticity. Adv Appl Mech 9:244–368
Schmidt HB, Hattel JH (2008) Thermal modelling of friction stir welding. Scripta Mater 58:332–337
Schmidt HB, Hattel J, Wert J (2004) An analytical model for the heat generation in friction stir welding. Mod Sim Mat Sci Eng 12:143–157
Thomas WM et al. (1991) International patent application no. PCT/GB92/02203 and GB patent application no. 9125978.9, Dec 1991

Numerical Simulation of Water Flow in a Venturi Tube Using the Smoothed Particle Hydrodynamics Method

C.E. Alvarado-Rodríguez, A. Aviles, J. Klapp and F.I. Gomez-Castro

Abstract A numerical simulation of water flow through a Venturi tube was made with the DualSPHysics code, which uses the Smoothed Particle Hydrodynamics (SPH) method. The dimensions of the simulated system are equal to the laboratory experimental setup. The experimental data were measured in the laboratory using a rotameter and a mercury manometer. The experimental and numerical results show a similar behavior. Discharge coefficient values are obtained from the numerical results.

1 Introduction

The Venturi effect predicts that the water pressure within a close conduct decreases as the velocity increases. The velocity increment is induced by a reduction of the cross section. A Venturi tube is a device initially designed to measure pipe fluid velocities. However, it is used to accelerate the velocity of a fluid in devices where the velocity of the fluid is important as, for example, in a carburator in an oxygen mask, and in water air purifiers. The Venturi tube sections are shown in Fig. 1.

A stationary fluid flow is described by the Bernoulli equation

$$\frac{v^2\rho}{2} + P + \rho g z = \text{constant}. \tag{1}$$

C.E. Alvarado-Rodríguez (✉) · F.I. Gomez-Castro
Departamento de Ingeniería Química, DCNyE, Universidad de Guanajuato,
Noria Alta S/N, 36000 Mexico, Guanajuato, Mexico
e-mail: q_l_o@hotmail.com

A. Aviles · J. Klapp
Departamento de Matemáticas, Cinvestav Del I.P.N., 07360 Mexico, D.F., Mexico

J. Klapp
Departamento de Física, Instituto Nacional de Investigaciones Nucleares,
La Marquesa, 52750 Ocoyoacac, Estado de México, Mexico
e-mail: jaime.klapp@inin.gob.mx

J. Klapp et al. (eds.), *Selected Topics of Computational and Experimental Fluid Mechanics*, Environmental Science and Engineering,
DOI 10.1007/978-3-319-11487-3_38

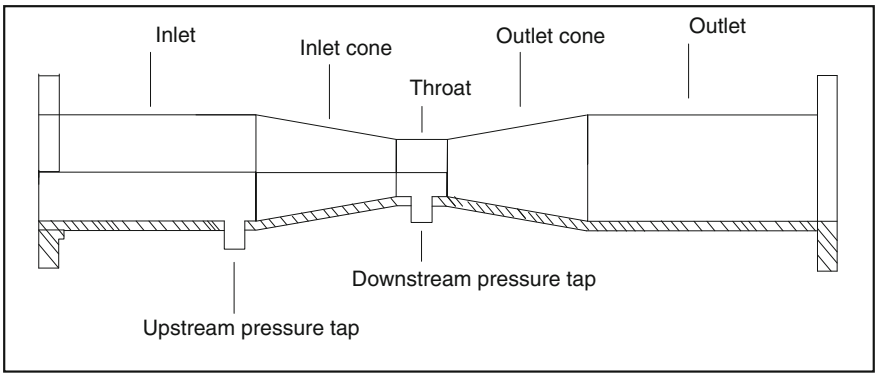

Fig. 1 Venturi tube: diagram and characteristics

From this equation, the volumetric flow Q that relates the volumetric flux with the pressure loss in the system considering an incompressible fluid is given by

$$Q = CA_0\sqrt{\frac{2g(-\Delta P)/\rho}{(D_0/D_1)^4 - 1}}, \tag{2}$$

where v is the velocity of the fluid, ρ the density, P the pressure, g the gravity acceleration, z the height of the fluid, D_1 the diameter of the straight section, D_0 the diameter of the throat, A_0 the transversal area at the throat, and C a discharge coefficient.

2 The SPH Method

Nowadays the Smoothed Particle Hydrodynamics (SPH) method has become increasingly popular to study fluid dynamics. This method uses particles to represent the domain which could contain fluid and boundaries. The particles are interpolation points where properties of the fluid such as velocity, density, pressure and others are calculated. In SPH we can easily implement complicated physics and model systems with a complex and irregular geometries.

The main characteristics of the SPH method has been described by Monaghan (1982, 1992, 2005) and Liu (2003). The fundamental principle of the SPH method consists in calculating an approximation of any function by means of an integral interpolator

$$A(r) = \int A(r')W(r - r', h)dr', \tag{3}$$

where $W(r, h)$ is a weight function or kernel, and h is the smoothing length of the weight function. Then Eq. (3) is approximated for any point with the sum

$$A(r) = \sum\nolimits_b m_b \frac{A_b}{\rho_b} W(r - r_b, h), \tag{4}$$

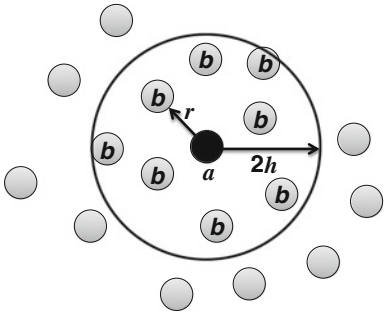

Fig. 2 *h* region where the kernel is applied

where the sum is over all particles (b) within the h region in the kernel function (see Fig. 2). The mass and density are denoted by m_b and ρ_b, respectively, such that the volume of a particle is defined by $V_b = \frac{m_b}{\rho_b}$, and for the position vector $r = r_a$, $W_{ab} = (r_a - r_b, h)$ is the kernel between particles a and b.

The momentum equation is written in the form

$$\frac{dv}{dt} = -\frac{1}{\rho}\nabla P + g + \Gamma, \tag{5}$$

where Γ is a dissipative term, and $g = -9.8$ m/s^2 is the gravity acceleration. In the DualSPHysics code it is possible to solve Eq. (5) by two options: artificial viscosity (Monaghan 1992) and laminar viscosity with sub-particle scale (Lo and Shao 2002; Gotoh et al. 2001). Artificial viscosity was used in this work. The momentum equation in SPH notation is

$$\frac{dv_a}{dt} = -\sum_b m_b \left(\frac{P_b}{\rho_b^2} + \frac{P_a}{\rho_a^2} + \Pi_{ab} \right) \nabla_a W_{ab} + g, \tag{6}$$

where Π_{ab} is a viscosity term (Gomez-Gestéira et al. 2012).

The changes in the density are calculate by

$$\frac{d\rho_a}{dt} = \sum_b m_b v_{ab} \nabla_a W_{ab}. \tag{7}$$

The equation of state is based on Monaghan (1994), where the fluid is considered as weakly compressible and Eq. (8) determines the pressure of the fluid which is written in the form

$$P = B\left[\left(\frac{\rho}{\rho_0}\right)^{\gamma} - 1\right], \tag{8}$$

where $\gamma = 7$, $B = \frac{c_0^2 \rho_0}{\gamma}$, being $\rho_0 = 1{,}000\,\text{km/m}^3$ the reference density, and c_0 the speed of sound at the reference density.

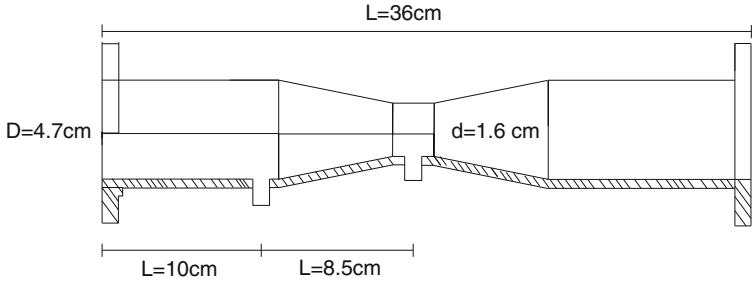

Fig. 3 Geometry and dimensions of the Venturi tube

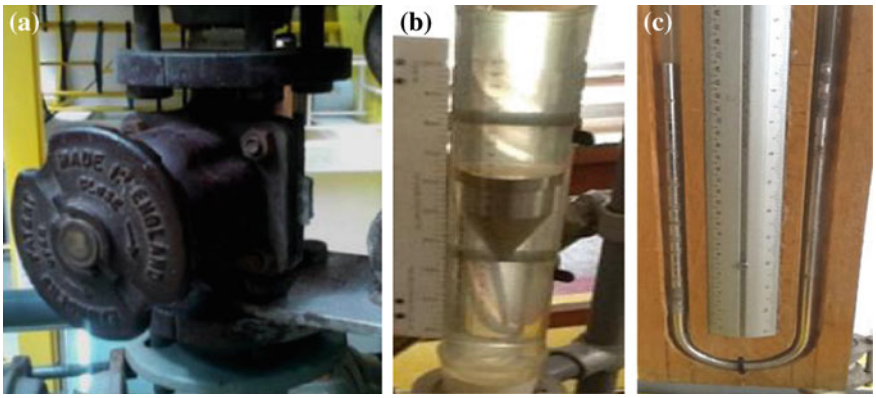

Fig. 4 **a** Flow control valve, **b** rotameter, **c** mercury manometer

3 Experimental Setup

The simulations were based in a device of the Chemical Engineering Laboratory (Universidad de Guanajuato, México), with the geometry and dimensions as shown in Fig. 3.

The pressure was measured for different volumetric fluxes. The flux was controlled with a flow control valve (Fig. 4a) and measured with a rotameter (Fig. 4b). The difference of pressure was measured with a mercury manometer evaluating the pressure in mercury millimeters (Fig. 4c). The velocity was calculated by the volumetric flow divided by the transversal area at the throat. The experiment was repeated five times.

4 Numerical Simulations

The numerical simulation was made using the DualSPHysics code that has been developed on the C++ and CUDA platform for solving the equations on the CPUs and GPUs processors. A 2D system was used in the simulation, with the same dimensions

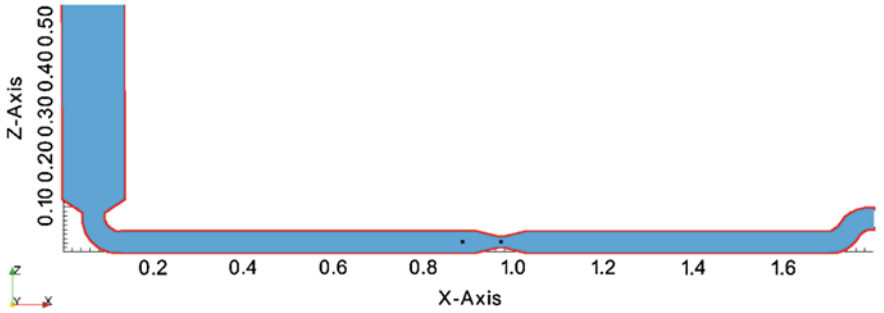

Fig. 5 Initial system configuration in the simulation, the fluid particles are painted in *blue* and the boundary particles in *red*. *Black points* indicate the places where velocities and pressure values were calculated

of the laboratory device. The image of the Venturi tube was reproduced in Blender v2.76 as a .stl file. From the .stl file a new Venturi tube was created with particles in DualSPHysics (Fig. 5).

The fluid was represented by 558,078 particles with zero initial velocity. The simulated time was 2 s, saving results each 0.01 s.

5 Results and Discussion

Numerical and experimental results were obtained and compared. The total simulation time was 2.6 h on a GeForce GTX 660M GPU card. Figure 6 shows the experimental and numerical results and the comparison of both. Numerical and experimental

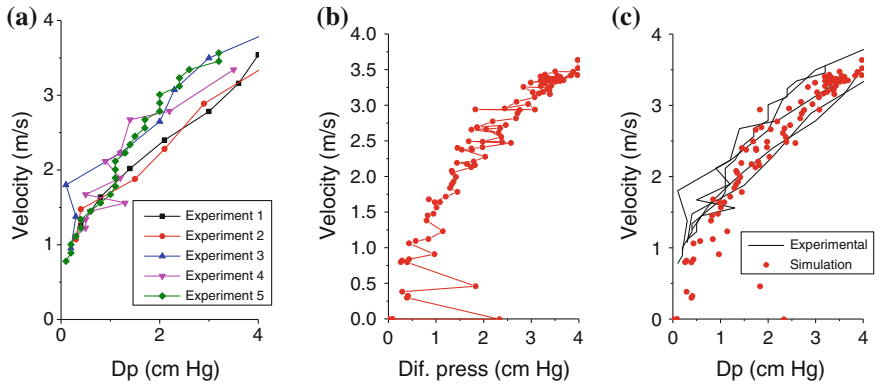

Fig. 6 **a** Experimental results obtained in the laboratory, **b** numerical results obtained from the simulation, and **c** comparison of numerical and experimental results

results are in good accordance for velocities >1.5 m/s. A pressure difference increment generate a velocity increment according to Eq. (2). The pressure difference oscillations at low velocities are produced by the initial water height.

To verify the Venturi effect in the simulation, velocities and pressures where calculated in five points across the Venturi tube (Fig. 7). Each point is separated by 17 mm. Figure 8 shows how the velocity and pressure change with time at the points of Fig. 7. The obtained results are in accordance with the Venturi effect, given that, a reduction in the transversal area produce a velocity increase and a pressure decrease. Pressure oscillations are observed at the beginning of the simulation by the water initial conditions.

From the numerical results, the discharge coefficient variation as a function of the Reynolds number in the throat was calculated (Fig. 9). Similar results were obtained by Mott (2006).

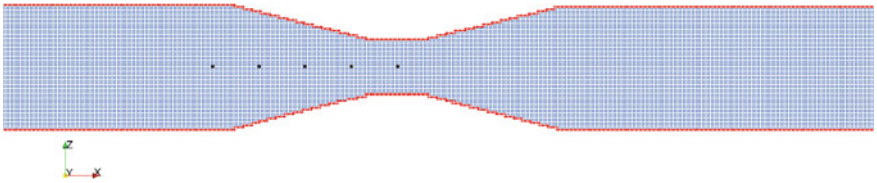

Fig. 7 Points in the Venturi tube where velocities and pressures are calculated

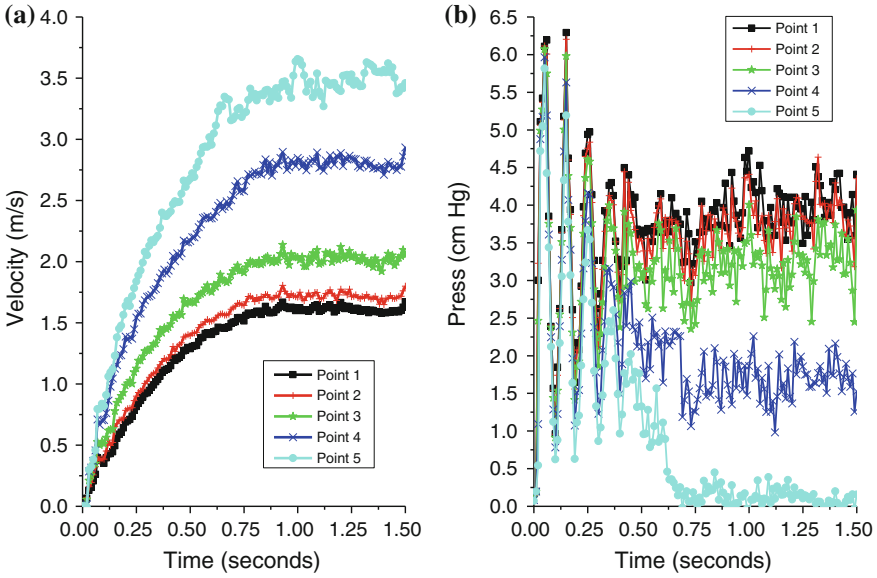

Fig. 8 Numerical results: **a** Velocity as a function of time, **b** pressure as a function of time. *Points* 1, 2, 3, 4, and 5 are indicated in Fig. 7

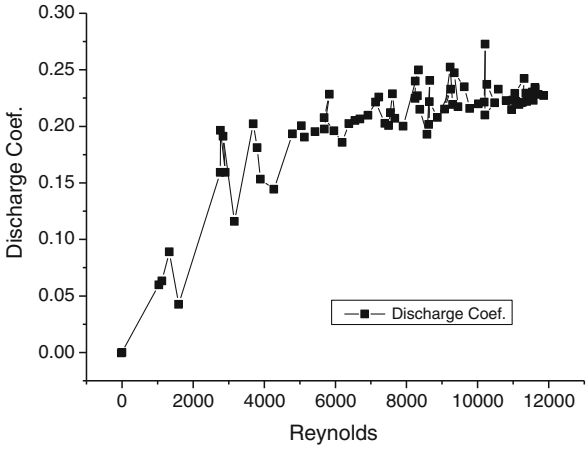

Fig. 9 Discharge coefficient as a function of the Reynolds number

6 Conclusions

With the SPH method it is possible to obtain the Venturi effect in good agreement with the experimental results. In the Venturi tube, the velocity increases as the pressure difference increases. From the numerical results it was possible to obtain the discharge coefficient as a function of the Reynolds number for $Re < 12{,}000$.

Acknowledgments CEAR thanks Conacyt for a PhD grant and support for visiting the University of Vigo, Spain. Work partially supported by ABACUS, CONACyT grant EDOMEX-2011-C01-165873.

References

Gomez-Gestéira M, Rogers BD, Crespo AJC, Dalrympe RA, Narayanaswamy M, Dominguez JM (2012) SPHysics-development of a free-surface fluid solver—part 1: theory and formulations. Comput Geosci 48:289–299

Gotoh H, Shibihara T, Hayashii M (2001) Subparticle-scale model for the Mps method-Lagrangian flow model for hydraulic engineering. Comput Fluid Dyn J 9(4):339–347

Liu GR (2003) Mesh free methods: moving beyond the finite element method. CRC Press, Boca Raton, p 692

Lo EYM, Shao S (2002) Simulation of near-shore solitary wave mechanics by an incompressible SPH method. Appl Ocean Res 24:275–286

Monaghan JJ (1982) Why particle methods work. SIAM J Sci Stat Comput 3:422–433

Monaghan JJ (1992) Smoothed particle hydrodynamics. Annu Rev Astron Astrophys 30:543–574

Monaghan JJ (1994) Simulating free surface flows with SPH. J Comput Phys 110:399–406

Monaghan JJ (2005) Smoothed particle hydrodynamics. Rep Prog Phys 68:1703–1759

Mott RL (2006) Mecánica de Fluidos, sexta edición, Editor Pearson, México, pp 479

Dynamic Behavior of a Drop on a Vertically Oscillating Surface

Fátima Flores Galicia, Flor Guadalupe Haro Velázquez, Gerardo Rangel Paredes, David Porta Zepeda, Carlos Echeverría Arjonilla and Catalina Stern Forgach

Abstract In the present paper the dynamic behavior of a drop of water subject to a vertical oscillating force is studied experimentally. A hydrophobic surface was used to maintain the form of the drop. The deformation of the drop as a response to several frequencies was analyzed by visualizing the oscillating patterns and measuring the maximum height of the drop as a function of time. The dynamic behavior has been classified in three phases: harmonic, geometric and chaotic.

1 Introduction

In the last few years, the study of the response to external forces of liquids lying on an oscillating surface has been of great interest due to its applications in industry, in geophysics and in seismology. In particular, the mixing generated by internal currents inside the drop is used in the pharmaceutical industry (Whitehill et al. 2010).

F. Flores Galicia (✉) · F.G. Haro Velázquez · G. Rangel Paredes · D. Porta Zepeda · C. Echeverría Arjonilla · C. Stern Forgach
Departamento de Física, Facultad de Ciencias, Universidad Nacional Autónoma de México, Av. Universidad 3000, Circuito Exterior S/N, Delegación Coyoacán, 04510 Ciudad Universitaria, D.F., Mexico
e-mail: ffgfcb@hotmail.com

F.G. Haro Velázquez
e-mail: avdos_podov@hotmail.com

G. Rangel Paredes
e-mail: ghiordu-pardas@hotmail.com

D. Porta Zepeda
e-mail: alviond@gmail.com

C. Echeverría Arjonilla
e-mail: carlosea1982@gmail.com

C. Stern Forgach
e-mail: catalina@ciencias.unam.mx

J. Klapp et al. (eds.), *Selected Topics of Computational and Experimental Fluid Mechanics*, Environmental Science and Engineering,
DOI 10.1007/978-3-319-11487-3_39

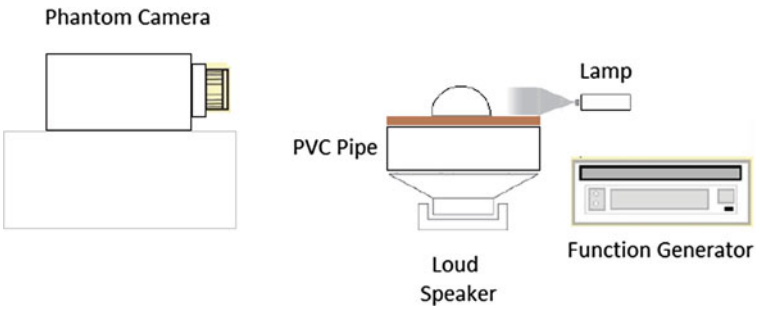

Fig. 1 Experimental set-up

2 Background

When a drop is subject to oscillating vertical forces, the changes of its geometry are strongly dependent on the frequency.

These changes have been classified by previous authors taking into account some characteristics of the pattern formation and the variation in time of its height as a response to frequency changes (Noblin et al. 2009; Sudo et al. 2010).

3 Experimental Set-Up

The experimental set-up, shown in Fig. 1, consists of a function generator connected to a speaker over which an elastic membrane is placed. The membrane is covered with Teflon, which is a hydrophobic material. A drop of water is placed on the membrane, and its response is recorded by a high speed camera (Phantom Miro M310) and the images analyzed in a computer with CINE Viewer.

4 Results

The geometry of the drop was recorded as the frequency was modified. Simultaneously, the side view of the drop was filmed and the height of its highest peak was measured as a function of time.

Different types of patterns, named phases by some authors, were observed as the frequency changed. The frequency interval for each phase is strongly dependent on the volume of the drop.

4.1 Harmonic Phase

A drop of 60 μ1 of water was placed on the membrane. In a range of frequencies between 1 and 31 Hz the drop oscillates as a whole contracting and expanding

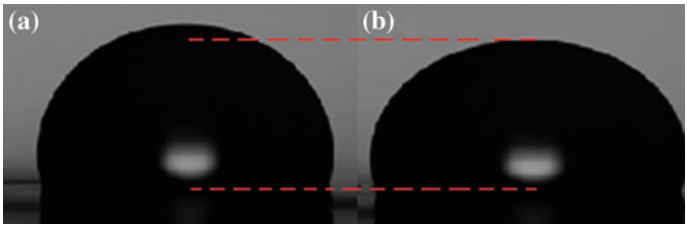

Fig. 2 Harmonic phase in a drop with 60 μl at 28 Hz **a** expansion **b** contraction

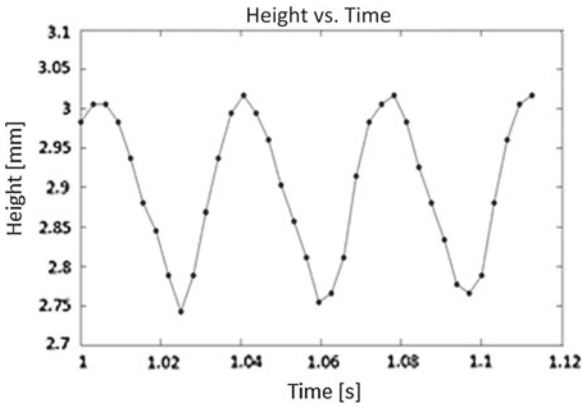

Fig. 3 Height of a 60 μl drop at subject to a frequency of 28 Hz

periodically with respect to the central axis, at the same frequency of the external force (Fig. 2).

The height of the drop was determined as a function of time (Fig. 3). The frequency of the drop is the same as the forcing frequency so the response can be considered linear.

4.2 Geometric Phase

In this phase polygonal patterns appear. Two different volumes were studied: one of 60 μl to analyze the heights as a function of time, and another of 200 μl to obtain better images.

It has been observed that as the frequency increases above the harmonic phase, the polygons increase the number of sides. Figure 4 shows two instants of a drop of 200 μl subject to a frequency of 43 Hz. A two dimensional pentagonal stationary wave is formed. The motion of the five nodes and antinodes is such that vertex and sides switch periodically in a caleidocycle.

As the frequency is slightly increased (46 Hz) the figure becomes an hexagon as can be seen in Fig. 5. The behavior is also a caleidocycle.

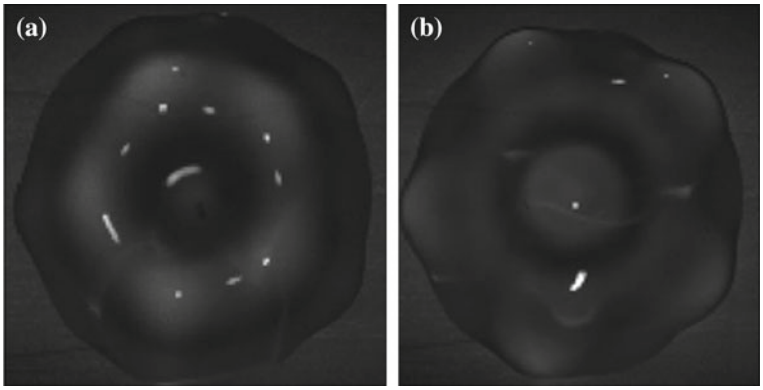

Fig. 4 **a** and **b** *Top* view, at two different times, of a drop of 200 μl of water subject to a frequency of 43 Hz

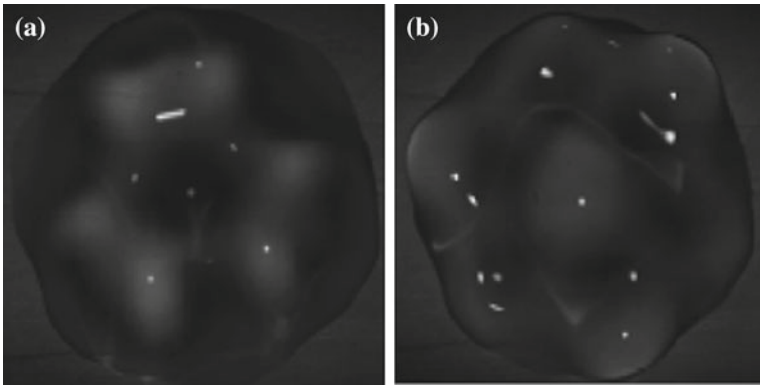

Fig. 5 **a** and **b** *Top* view, at two different times, of a drop of 200 μl of water subject to a frequency of 46 Hz

The geometric phase also has a periodic behavior. From the side view a compression-expansion cycle is observed. The height of one of the peaks has been measured as a function of time (Fig. 6).

4.3 Chaotic Phase

For a drop of 60 μl vibrating between 41 and 56 Hz a chaotic behavior can be observed. The form is irregular, nodes and antinodes do not seem to have any connection among them; the drop does not react as a whole. The variation of the height is different for each node, and there is not a unique frequency of oscillation as can be seen in Fig. 7.

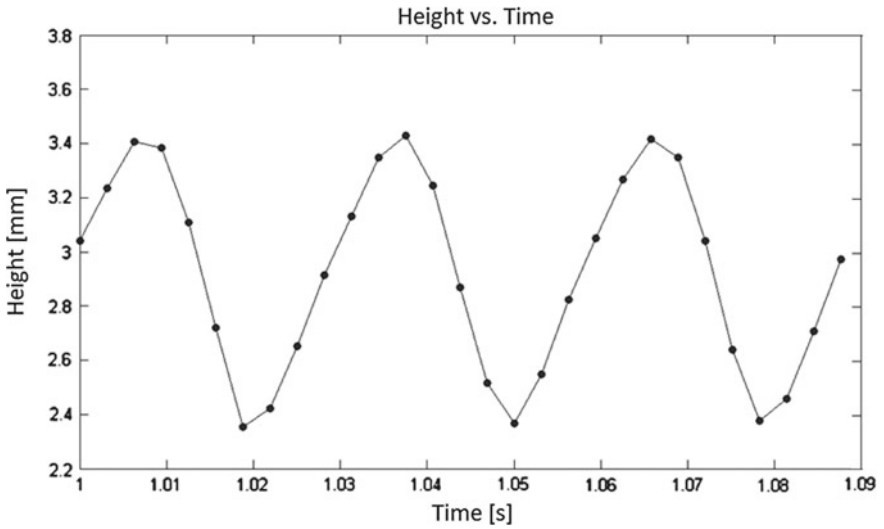

Fig. 6 Height as a function of time for a drop of 60 μl subject to a frequency of 34 Hz

Fig. 7 Images of the side view at different instants for a 60 μl drop subject to a frequency of 48 Hz, taken at a camera speed of 3,200 frames per second

However, if the height of the highest peak in each image is measured as a function of time, an almost periodic signal is obtained. Figure 8 shows a signal with a main period of about 0.21s. The non sinusoidal form of the wave corresponds to the nonlinear behavior of the drop.

The chaotic phase is metastable. The drop can be easily broken with a small perturbation, attaining an atomization stage. First, large oscillating fingers appear and small droplets are ejected from the core as is shown in Fig. 9.

For 60 μl the atomization phase is present at 56 Hz. The break up of the drop happens in two different ways:

- The energy is large enough so that the liquid in the fingers overcomes surface tension and separates. These small droplets start oscillating harmonically.
- The fingers collide and form a jet that breaks up, due to gravity, into droplets. The droplets oscillate in the harmonic phase.

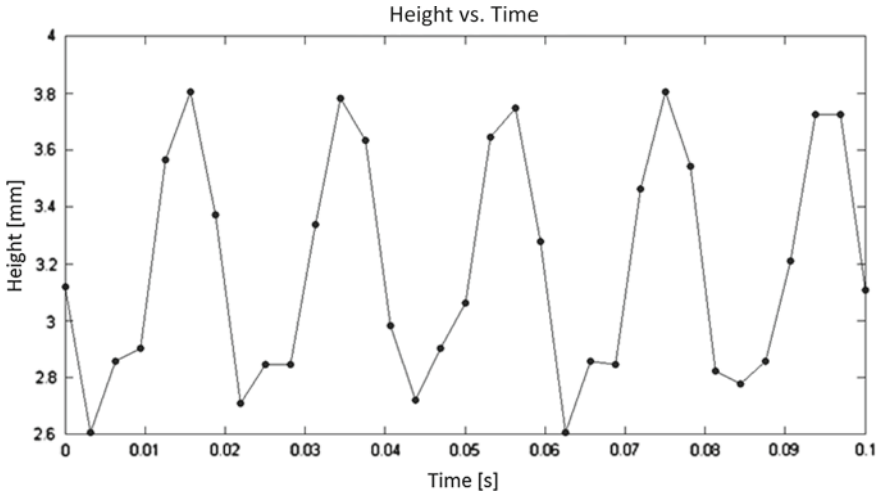

Fig. 8 Height of the highest peak as a function of time for a 60 μl drop of water to a frequency of 48 Hz

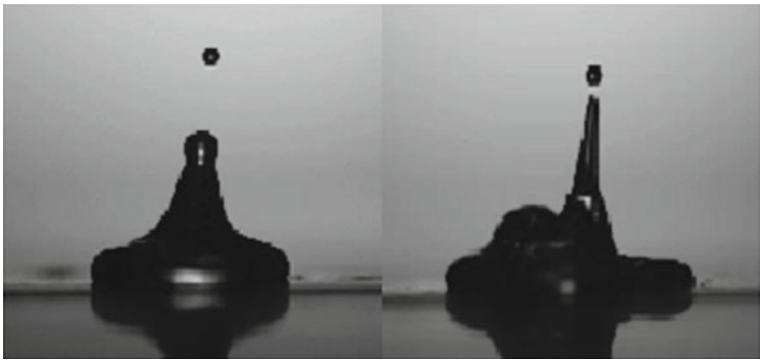

Fig. 9 Atomization of a drop of water of 60 μl at **a** 56 Hz **b** 75 Hz

The nonlinearity of the phenomenon is clearly observed when the frequency is further increased. The drop becomes stable again, and enters a geometric phase. If the change of frequency is not continuous, the atomization phase does not appear, and the drop goes from chaotic to geometric again. If the frequency is increased once again, a new chaotic phase is attained.

In Fig. 10, it can be observed that if the frequency is changed from 24 to 55 Hz, the heights increase in each phase and from one phase to the next. Just before each phase transition, the height is slightly lowered, probably due to the fact that most of the energy is used in the transition.

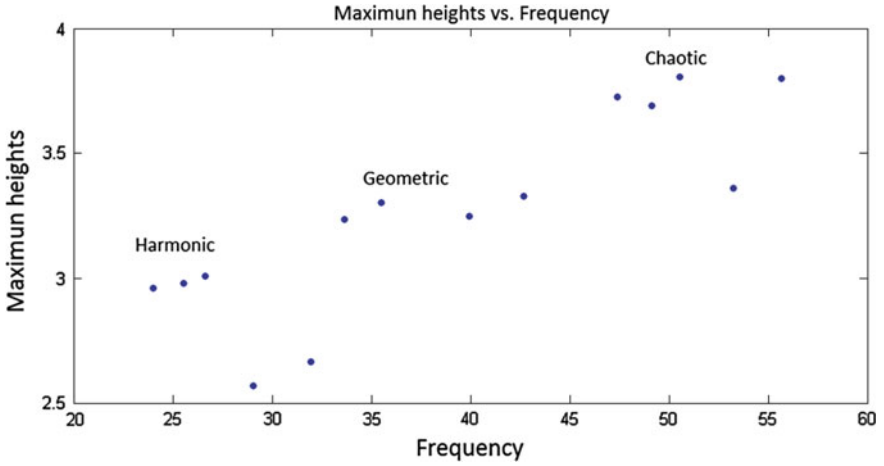

Fig. 10 Height of the peaks as a function of frequency

5 Conclusions and Future Work

It can be concluded that, as observed by previous authors, the dynamical behavior of a drop subject to vertical oscillations can be classified in three phases:

(a) harmonic: the drop deforms as a whole in periodic expansions and contractions,
(b) geometric: a two dimensional stationary wave is produced showing polygonal patterns,
(c) chaotic: the pattern is completely irregular and changes with time. There is a critical value at which atomization starts; the drop breaks into droplets.

A periodic or quasiperiodic behavior of the heights has been observed depending on the phase. However, a more detailed analysis of the frequency spectrum is required.

So far there is some information that the final state depends on the trajectory. For example, after the chaotic phase, a geometric phase can be attained following two different procedures. Future work will make a detailed study of the changes as a function of frequency to determine critical values for each phase. Hysteresis will also be searched for. These experiments will give information about the nonlinear behavior of the phenomenon, and will probably provide elements for a numerical simulation.

In particular, the spectrum of the signal in the chaotic phase should be analyzed. So far, a main frequency can be determined but the signal is not sinusoidal.

To see the video of the different phases go to the video https://www.youtube.com/watch?v=7P_c1_peG4o, or use the QR.

References

Noblin X, Buguin A, Brochard-Wyart F (2009) Vibrations of sessile drops. Eur Phys J Spec Top 166:7–10

Sudo S, Goto A, Kuwano H, Hamate Y, Yano T, Hoshika K (2010) The dynamic behavior of liquid droplets on vibrating plate. J Jpn Soc Exp Mech 10:38–45

Whitehill J, Martin S, Neild A, Wah NgT (2010) Droplet behaviour under high intensity acoustic vibration. In: Proceedings of 20th international congress on acoustics, ICA 2010, pp 1–6

Critical Phenomena of a Drop Through a Stratified Fluid

Verónica Álvarez González, Angélica Zarazúa Cruz, Carlos Echeverría Arjonilla, David Porta Zepeda and Catalina Stern Forgach

Abstract The present paper describes the dynamics of a drop as it falls through a stratified fluid with two layers. As it enters the fluid, the drop forms an annular vortex that suffers different deformation processes depending on the conditions of the experiment. In this work, the only variables that have been modified are the density of the drop and the height of the upper fluid. Images of the phenomena were taken directly with a high speed video camera and through a shadowgraph set-up. To access the videos of the experiment, a http address and a QR image are provided at the end of the paper.

1 Introduction

Stratified fluids are common in nature due to differences in density or in temperature. Probably the two examples that affect our daily lives are the atmosphere and the ocean. However, there are many industrial applications where the knowledge and control of these phenomena are crucial. It is important to understand how mixing or the dispersion of particles occur in these media. Sometimes, solid particles or vortical

V. Álvarez González · A. Zarazúa Cruz · C. Echeverría Arjonilla · D. Porta Zepeda · C. Stern Forgach (✉)
Departamento de Física, Facultad de Ciencias, Universidad Nacional Autónoma de México, Mexico, Mexico
e-mail: catalina@ciencias.unam.mx

V. Álvarez González
e-mail: vero.aag@gmail.com

A. Zarazúa Cruz
e-mail: zarknj@hotmail.com

C. Echeverría Arjonilla
e-mail: carlosea1982@gmail.com

D. Porta Zepeda
e-mail: alviond@gmail.com

J. Klapp et al. (eds.), *Selected Topics of Computational and Experimental Fluid Mechanics*, Environmental Science and Engineering,
DOI 10.1007/978-3-319-11487-3_40

structures can be trapped inside the stratification for long periods of time and the mixing process is altered (Camassa et al. 2013).

The behavior of a vortical structure of a miscible fluid as it traverses a stratified medium is not well understood. When a drop enters a fluid of lower or equal density, an annular ring is formed. The structure falls due to gravity. In this study, the interaction of such a structure with the interface between two layers of water with different concentrations of salt is observed.

In general, for this process, eight parameters have to be considered: the density of the drop, its radius, the densities of the two fluids, the height at which the drop is released, the thicknesses of the two layers and the thickness of the interface. In the present work, only the density of the drop, the height at which the drop is released and the thickness of the upper layer are varied.

There is a maximum length of penetration before the vortex becomes unstable and breaks. This length depends on initial and boundary conditions. The viscosity decelerates the structure as it travels through the fluid, a Rayleigh-Taylor instability appears and entails a collapse of the core (Camassa et al. 2013).

Four different behaviors were observed confirming results reported previously by Camassa et al. (2011): Settling, Chandelier, Bounce and Core Fallout. They will be described in the following section.

The shadowgraphs presented in this paper show better images than the ones that appear in the literature.

2 Experimental Set-Up

A large glass container was filled with the two fluids. Salt water with a density of $1.027\,g/cm^3$ is the bottom fluid; the upper fluid has a density of $0.99\,g/cm^3$. A densimeter with an uncertainty of $0.005\,g/cm^3$ was used. The drop has a radius of 2 mm and was always released at a height of 2 cm from the free surface (Fig. 1). All lengths were measured from the images with a precision of 0.01 mm. As soon as the drop touches the fluid, a toroidal vortex was formed. The thickness of the top layer was varied from 10 to 40 mm. The interface has a thickness between one and two centimeters because a density gradient was created between the two fluids. The container was filled up very carefully to avoid any mixing between the two fluids.

Two images of the phenomena were obtained simultaneously. A high speed black and white video camera was pointed directly to the container. A color video camera recorded images through a shadowgraph (Settles 2001). Figure 2 shows the position of the cameras.

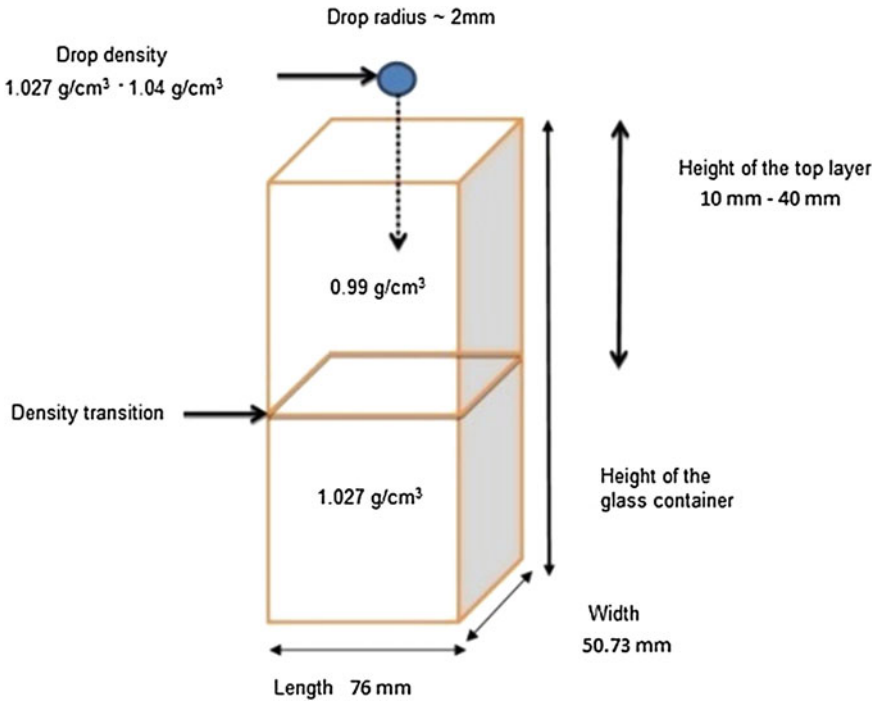

Fig. 1 Schema of the glass container

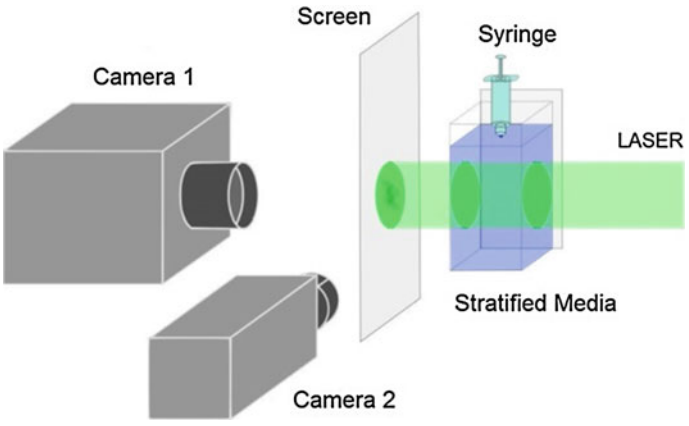

Fig. 2 Experimental set-up

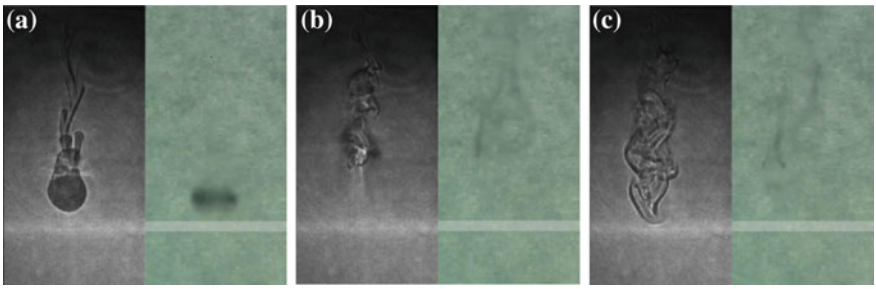

Fig. 3 Settling: Images on the *left* are shadowgraphs, images on the *right* are direct visualizations. There is an interval of 2.37 s between (**a**) and (**b**), and 3.6 s between (**b**) and (**c**)

3 Results

In most cases the image obtained through a shadowgraph is more clear than the direct image.

3.1 Settling

The densities of the drop and of the top fluid are the same. The vortex is formed as the drop enters the fluid (Fig. 3a), it touches the interface and goes up again (Fig. 3b). Then it starts to oscillate but settles on the top layer and eventually loses its form (Fig. 3c). The interface appears as a clear shadow

3.2 Chandelier

When the thickness of the top layer is increased, the vortex ring seems to crash as it enters the fluid; the core of the vortex is trapped but a slow fingering process starts on the outside (Fig. 4). After a very long time, some fingers arrive at the interface due to gravity but most of the material remains on the top layer.

In this case both types of images show the process quite clearly.

3.3 Core Fallout

In this case the drop has a bigger radius, hence more mass and is heavier. The core goes down faster than the outside material, as opposed to the previous case. The vortex ring touches the interface (Fig. 5a), rises in the form of a jellyfish (Fig. 5b)

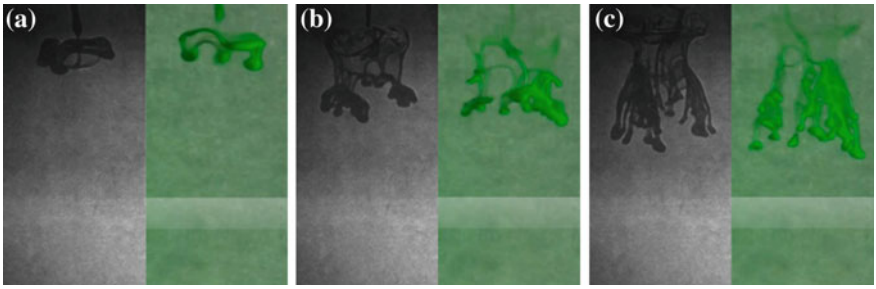

Fig. 4 Chandelier: There is an interval of 1.6 s between (**a**) and (**b**), and 1.4 s between (**b**) and (**c**)

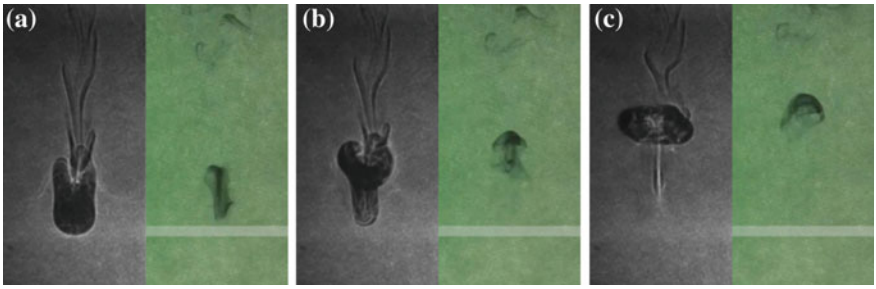

Fig. 5 Core Fallout: The wake can be seen very clearly on panel (**a**). The vortex touches the interface in (**b**), and a bubble in the middle of the core seems to make the vortex rise again

and stays floating in the middle of the top layer (Fig. 5c). A bubble is formed in the middle of the core before the material rises from the interface.

3.4 Rebound

Both the radius of the drop and the thickness of the top layer are reduced. This time the vortex ring touches (Fig. 6a) and traverses (Fig. 6b) the interface, then a bubble is formed and the material rebounds (Fig. 6c).

All results are summarized on Table 1.

Camassa et al. (2013) present a graph of stability, shown in Fig. 7, that relates experimental to theoretical data. The experimental data of this work are presented in the same figure.

The blue line shows the theoretical limit of stability. The green line shows the experimental results presented in Camassa et al. (2011). The experimental results of this work remain mostly in the trapped region, except for the rebound.

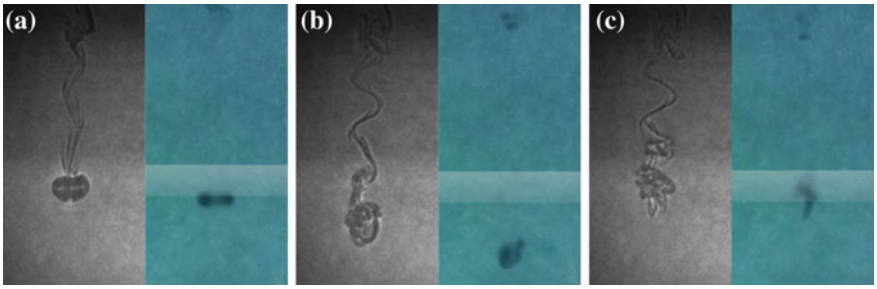

Fig. 6 Rebound: The material traverses the interface. There is an interval of 1.21 s between (**a**) and (**b**), and of 0.5 s between (**b**) and (**c**)

Table 1 Summary of results

Densities of the layers g/cm^3	Phenomenon	Density of the drop (g/cm^3) ±0.0005	Thickness of the top layer (cm) ±0.005	Height of release of the drop (cm) ±0.005	Radius of the drop (mm) ±0.05
Top 0.990	Rebound	1.027	1	1	1.95
	Settling	1.027	4	2	2.06
Lower 1.027	Core Fallout	1.040	3.5	At the free surface	1.89
	Chandelier	1.030	3	At the free surface	1.77

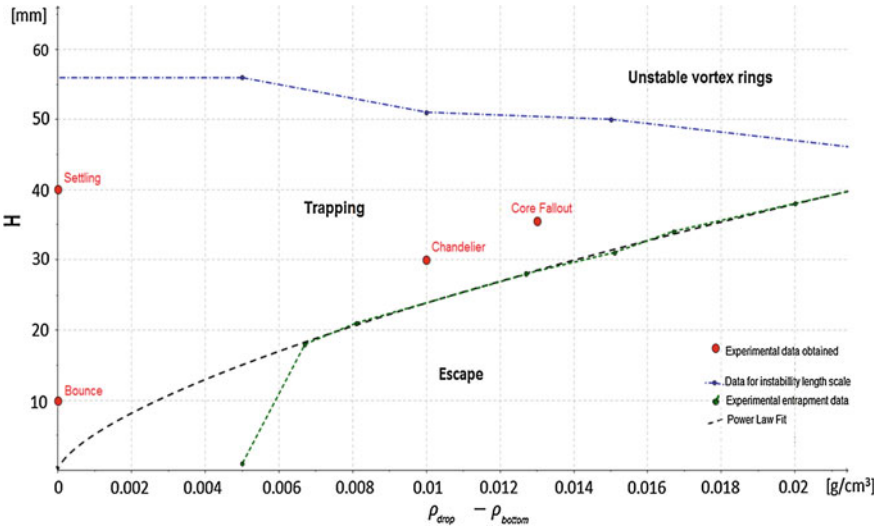

Fig. 7 Stability diagram: the thickness of the top layer is on the vertical axis while the density difference between the drop and the bottom layer appears on the horizontal axis. The *blue line* is theoretical, the *green line* are Camassa's results and the reults from this work are shown in *red*

4 Conclusions and Future Work

The four phenomena reported by Camassa et al. were reproduced and observed with a better visualization technique. Besides, in this paper the exact value of the initial and boundary conditions are reported for each case.

Through the shadowgraphs the density gradient can be clearly observed, in particular the interface, the wake behind the vortex and the bubble.

From the experiments it can be concluded that the evolution and stability of a vortex ring that moves through a stratified fluid is strongly dependent on the initial and boundary conditions. This is typical of nonlinear systems. The process is difficult to study theoretically and even numerically.

The transitions between different regions of stability will be studied in more detail. The effect of changes in the parameters in the behavior of the vortex ring will be recorded. Also, the behavior of a drop of a fluid immiscible in the other two, will be analyzed.

To see the video of the experiments described in this paper go to the video: https://www.youtube.com/watch?v=Txsw2NcUW2A or use the following QR:

References

Camassa R, Khatri S, McLaughlin R, Mertens K, Monbureau E, Nenon D, White B (2011) The trapping and escape of buoyant vortex rings in sharply stratified fluids. arXiv:1110.3435

Camassa R, Khatri S, McLaughlin R, Mertens K, Nenon D, Smith C, Viotti C (2013) Numerical simulations and experimental measurements of dense-core vortex rings in a sharply stratified environment. Comput Sci Discov 6(1):014001

Settles GS (2001) Schlieren and shadowgraph techniques. Springer, Berlin

Accretion Centers Induced in a Molecular Cloud Core After a Penetrating Collision

G. Arreaga-García and J. Klapp

Abstract The aim of this paper is to present a set of numerical simulations of a penetrating collision, in which a small gas core (the bullet) penetrates a larger gas core (the target). In the target core, the gravitational collapse is supposed to be ongoing before the collision. Each colliding core has a uniform density profile and rigid body rotation; besides the mass and size of the target core have been chosen to represent the observed molecular cloud core L1544. We modified the Lagrangian code *Gagdet*2 to identify when a gas particle can become an accretion center, and to inherit the mass and momentum of all the very close neighboring particles. Three collision models are here considered for pre-collision velocities $v/c_0 = 2.5$, 5.0, and 10 Mach. The outcome of these collision models are presented only for two different values of the bullet's radius, that is for $R_0/4$, and $R_0/2$ where R_0 is the radius of the target core. Such collision models reveal how accretion centers are formed, with a spatial distribution that strongly depends on the pre-collision velocity. We thus show hereby that penetrating collisions may have a major and favorable influence in the star formation process.

1 Introduction

Gas cloud collisions may play an important role in the star formation process by altering the physical processes in the involved clouds, including their gravitational

G. Arreaga-García (✉)
Departamento de Investigación En Física de la Universidad de Sonora,
Apdo. Postal 14740, 83000 Hermosillo, Sonora, Mexico
e-mail: garreaga@cifus.uson.mx

J. Klapp
Instituto Nacional de Investigaciones Nucleares, ININ, Km. 36.5 Carretera
Mexico-Toluca, La Marquesa, 52750 Mexico, Estado de Mexico, Mexico
e-mail: jaime.klapp@inin.gob.mx

J. Klapp
Departamento de Matemáticas, Cinvestav Del I.P.N., 07360 Mexico, D.F., Mexico

J. Klapp et al. (eds.), *Selected Topics of Computational and Experimental Fluid Mechanics*, Environmental Science and Engineering,
DOI 10.1007/978-3-319-11487-3_41

collapse, see for instance Arreaga-Garcia et al. (2014) and references there in. Recently, Higuchi et al. (2014) presented line emission observations of the core G.0253+0.016 with the Atacama Large Millimeter Array (ALMA) and proposed that this dense cloud may have formed due to a collision between two dissimilar clouds.

In this paper we consider a system of two gas spheres, the first one being the target core and is constructed in a similar way to that originally suggested by Whitworth and Ward-Thompson (2001), as an empirical model to study the collapse of the well observed core L1544. The latter is unstable and would collapse toward a binary system of protostars. The second and smaller gas sphere that we will call the bullet is directed towards the target core. We are interested in investigating what happens in this case.

Whether a penetrating collision does or does not help the fragmentation of the target gas core is the main aim of this study. The target core is additionally considered to be in counterclockwise rigid body rotation around the Z axis.

There are three physical processes participating in a gas collision: (i) the self-gravity of the target core; (ii) the flow of particles of the bullet core, which tend to diffuse within the target core, and (iii) the friction due to the viscosity of the gas. The pre-collision velocity determines which of these physical process is more important than another in a particular simulation, and therefore it determines the fate of the collision system.

It is noteworthy that Anathpindika (2009) has also simulated collisions between two clouds, considering an impact velocity within the Mach 25–35 range, and also that dissimilar collision models were also considered by Anathpindika (2010). But all their pre-collision clouds are initially in hydrodynamical equilibrium since they were modeled as Bonnor-Ebert spheres.

2 The Colliding Cores

We consider two dissimilar spherical cores which undergo a head-on collision, as illustrated in Fig. 1. The initial position (in rectangular coordinates (X, Y, Z)) of the mass center (MC) of the target core is located at $\mathbf{X}_{TC} = (0, -R_0, R_0)$, while the MC for the onrushing core is located at $\mathbf{X}_{OC} = (0, R_0, R_0)$. As previously mentioned, R_0 is the initial radius of the target core.

The pre-collision velocity V_{app} (or impact velocity) is defined as the translational velocity given to all the particles of the bullet core, in such a manner that its MC moves with the velocity $\mathbf{V}_{OC} = (0, -V_{app}, 0)$. The target core MC is initially at rest, that is $\mathbf{V}_{TC} = (0, 0, 0)$.

All the models of this paper deal with a gas sphere of radius $R_0 = 8.0 \times 10^{16}$ cm, and with an average density $\rho_{ave} = 3.0 \times 10^{-18}$ g/cm^3. The total mass in the target core is $M_0 = 8\ M_\odot$. It should be emphasized that Whitworth and Ward-Thompson (2001) suggested these parameters for investigating the L1544 core's fate.

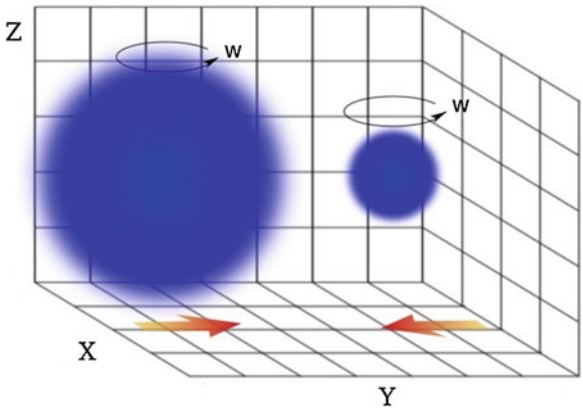

Fig. 1 The initial geometry of the colliding cores

The dynamical properties of the initial distribution of particles are commonly characterized by the thermal and kinetic energy ratios with respect to the gravitational energy, denoted by α and β, respectively, whose values are here given by

$$\begin{aligned} \alpha &\equiv \frac{E_{therm}}{|E_{grav}|} \approx 0.3, \\ \beta &\equiv \frac{E_{rot}}{|E_{grav}|} \approx 0.1. \end{aligned} \tag{1}$$

The sound speed c_0 and the rotational angular velocity Ω_0 have been calculated in this paper to fulfill the energy ratios given by Eq. (1); they are given the following numerical values

$$\begin{aligned} c_0 &\equiv 39956.8\,\mathrm{cm\,s^{-1}}, \\ \Omega_0 &\equiv 8.09\ \times 10^{-13}\ \mathrm{rad/s}. \end{aligned} \tag{2}$$

As is commonly done in papers devoted to simulate binary formation of protostars, we here implement a mass perturbation m_i on every particle of mass m_0 according to

$$m_i = m_0 + m_0 a \cos\left(m\,\phi_i\right), \tag{3}$$

where the perturbation amplitude is set to $a = 0.1$ and the mode is fixed to $m = 2$.

The onrushing core radius is given by $R_0/4$, or $R_0/2$, as can be seen in Table 1, where we show the collision models considered in this paper. The collision system has an average density $\rho_0 = 9.2 \times 10^{-18}\,\mathrm{g/cm^3}$; a fictitious gas sphere having this mass density would have a free fall time $t_{ff} = 6.925 \times 10^{11}$ s. It should be noticed that these ρ_0 and t_{ff} are only used to normalize density and time, both in the forthcoming plots as well as some results given in Table 1.

The entries of Table 1 are as follows. The first column shows the label of the models. The second column is the bullet's radius R_c given in terms of the target's radius R_0. The third column shows the pre-collision velocity in terms of the core's sound

Table 1 Collision models and detected accretion centers

Model	R_c	$\frac{V_{app}}{c_0}$	$log_{10}\left(\frac{\rho_{max}}{\rho_0}\right)$	$\frac{t_{max}}{t_{ff}}$	N_{acc}	Np_{acc}	$M_{av}/M_{\odot}$
P1	$R_0/4$	2.5	7.62	0.44	30	6	6.24×10^{-6}
P2	$R_0/4$	5.0	7.78	0.48	43	5	4.39×10^{-6}
P3	$R_0/4$	10.0	7.89	0.51	26	6	5.61×10^{-6}
P4	$R_0/2$	2.5	6.30	0.26	37	5	4.07×10^{-6}
P5	$R_0/2$	5.0	7.90	0.26	26	7	5.62×10^{-6}
P6	$R_0/2$	10.0	2.26	0.35	–	–	–

The density and time are normalized by $\rho_0 = 9.2 \times 10^{-18}\,\mathrm{g/cm^3}$ and $t_{ff} = 6.925 \times 10^{11}\,\mathrm{s}$, respectively

speed. As a way of comparing our simulations with other simulations elsewhere, in the fourth and fifth columns we show the peak density ρ_{max} reached in each run and the evolution time, respectively. In the sixth column we show the number N_{acc} of accretion centers found for each system. In the seventh column we show the average number of *SPH* particles Np_{acc} per accretion center formed in each model while in the eight column we show the accretion center average mass M_{av}/M_{sun}.

3 The Computational Method

We carry out the time evolution of the initial distribution of particles with the fully parallel *Gadget*2 code, which is described in detail by Springel (2005). *Gadget*2 is based on the *treePM* method for computing the gravitational forces and on the standard *SPH* method for solving the Euler equations of hydrodynamics. *Gadget*2 incorporates the following standard features: (i) each particle i has its own smoothing length h_i; (ii) particles are also allowed to have individual gravitational softening lengths ε_i, whose values are adjusted such that for every time step $\varepsilon_i\, h_i$ is of order unity. *Gadget*2 fixes the value of ε_i for each time-step using the minimum value of the smoothing length of all particles, that is, if $h_{min} = min(h_i)$ for $i = 1, 2...N$, then $\varepsilon_i = h_{min}$.

The *Gadget*2 code has an implementation of a Monaghan-Balsara form for the artificial viscosity, see Monaghan and Gingold (1983), and Balsara (1995). The strength of the viscosity is regulated by setting the parameter $\alpha_v = 0.75$ and $\beta_v = \frac{3}{2} \times \alpha_v$, see Eq. (14) in Springel (2005). We here fix the Courant factor to 0.1.

Let us now briefly describe the modifications implemented into the *Gadget*2 code for detecting accretion centers. Any gas particle with density higher than ρ_s is a candidate to be an accretion center. We localize all candidate particles for a given time t. We then test the separation between candidates: if there is one candidate with no other candidate closer than $10 \times r_{acc}$, then this particle is identified as an accretion center at time t. We define r_{acc} as the neighbor radius for an accretion center, given by $r_{acc} = 1.5 \times h_{min}$. In this way r_{acc} determines a set of particles

which are within the sphere of radius r_{acc}, and whose center is the accretion center itself. All those particles will give up their masses and momenta to the accretion center. We then change the *Gadget*2 type for all those particles, and therefore, they will not be advanced in time anymore.

We run our implementation to locate accretion centers in the *Gadget*2 code by using only one value for the threshold density, that is $\rho_s = 5.0 \times 10^{-14}\,\mathrm{g/cm^3}$.

Finally, let us mention that in order to take into account the increase in temperature due to non-adiabatic core contraction during the gravitational collapse, in this paper we carry out the simulations using the barotropic equation of state:

$$p = c_0^2\,\rho\left[1 + \left(\frac{\rho}{\rho_{crit}}\right)^{\gamma-1}\right], \tag{4}$$

as proposed by Boss et al. (2000), where $\gamma \equiv 5/3$ and for the critical density we assume the value $\rho_{crit} = 5.0 \times 10^{-14}\,\mathrm{g\,cm^{-3}}$.

4 Results

Although the penetrating collisions are clearly a $3D$ phenomenon, we here show the main simulation results using $2D$ iso-density plots for a thin slice of matter parallel to the XY plane. A color scale to distinguish the iso-density regions is set once the *SPH* particles defining the slice have been selected. Two numerical values to illustrate the different stages of the evolution process are included at the bottom of each iso-density panel: the time t and corresponding peak density ρ_{max}. It should be noted that there is no relation between the density colors associated with different panels, not even in the same figure.

The collision between the bullet and the target initially generates an agglomerate of dense particles in the contact region. As the bullet penetrates into the target core, this agglomerate is thickened by a snowplow effect, as seen as a small filament oriented perpendicular to the pre-collision velocity direction. At the ends of the filament, two gas arms develop due to the flow of particles emitted by the collision front, see for instance the first panels of Figs. 2, 3, and 4.

The depth of penetration of the bullet is proportional to the pre-collision velocity. For example, in model $P3$, the target core gets evenly separated in two parts, as can be seen in Fig. 4. However, we note that in models $P1$, $P2$, and $P3$, the viscosity and self-gravity manage to slow down the penetration and to re-start the gravitational collapse of the entire collided gas system. We then note that the densest gas region of the collided system takes the form of a bending filament, which is closely aligned with the pre-collision velocity direction, see the last panels of Figs. 2, 3, and 4. It is then likely that these models will still end up as a binary or multiple system of proto-stars.

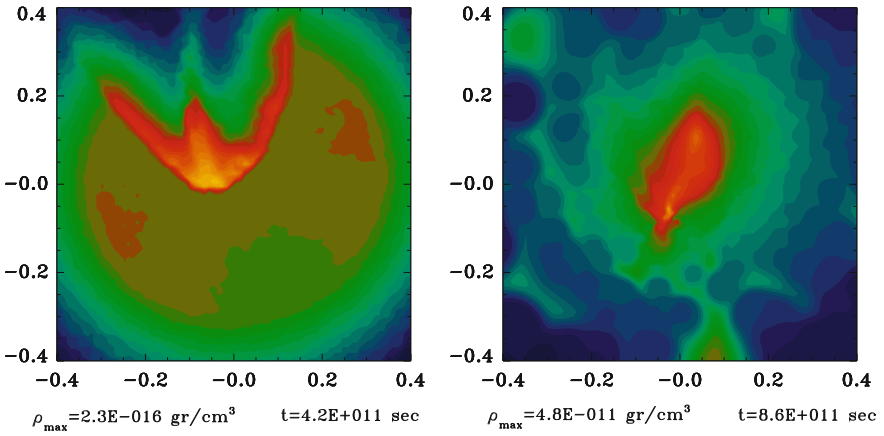

Fig. 2 Iso-density plot illustrating the collision process of model $P1$

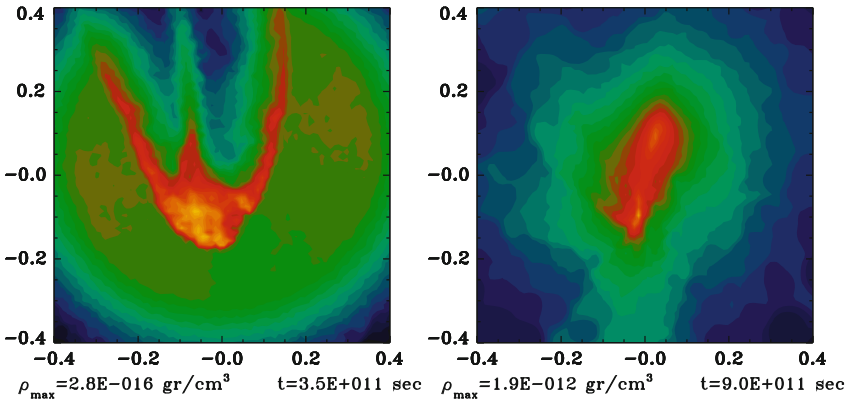

Fig. 3 Iso-density plot illustrating the collision process of model $P2$

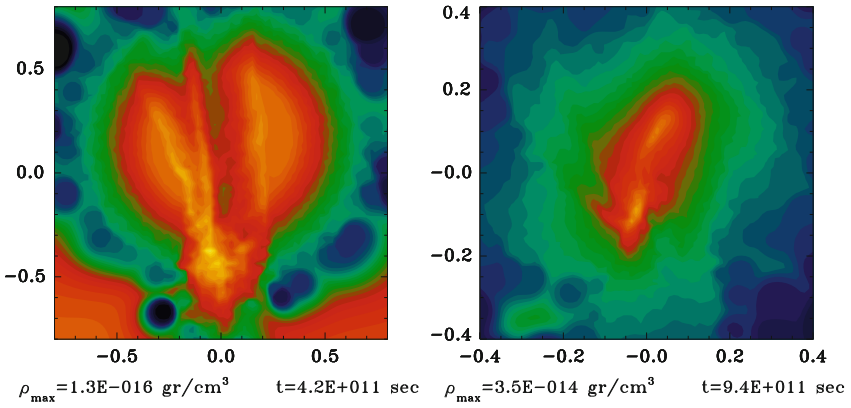

Fig. 4 Iso-density plot illustrating the collision process of model $P3$

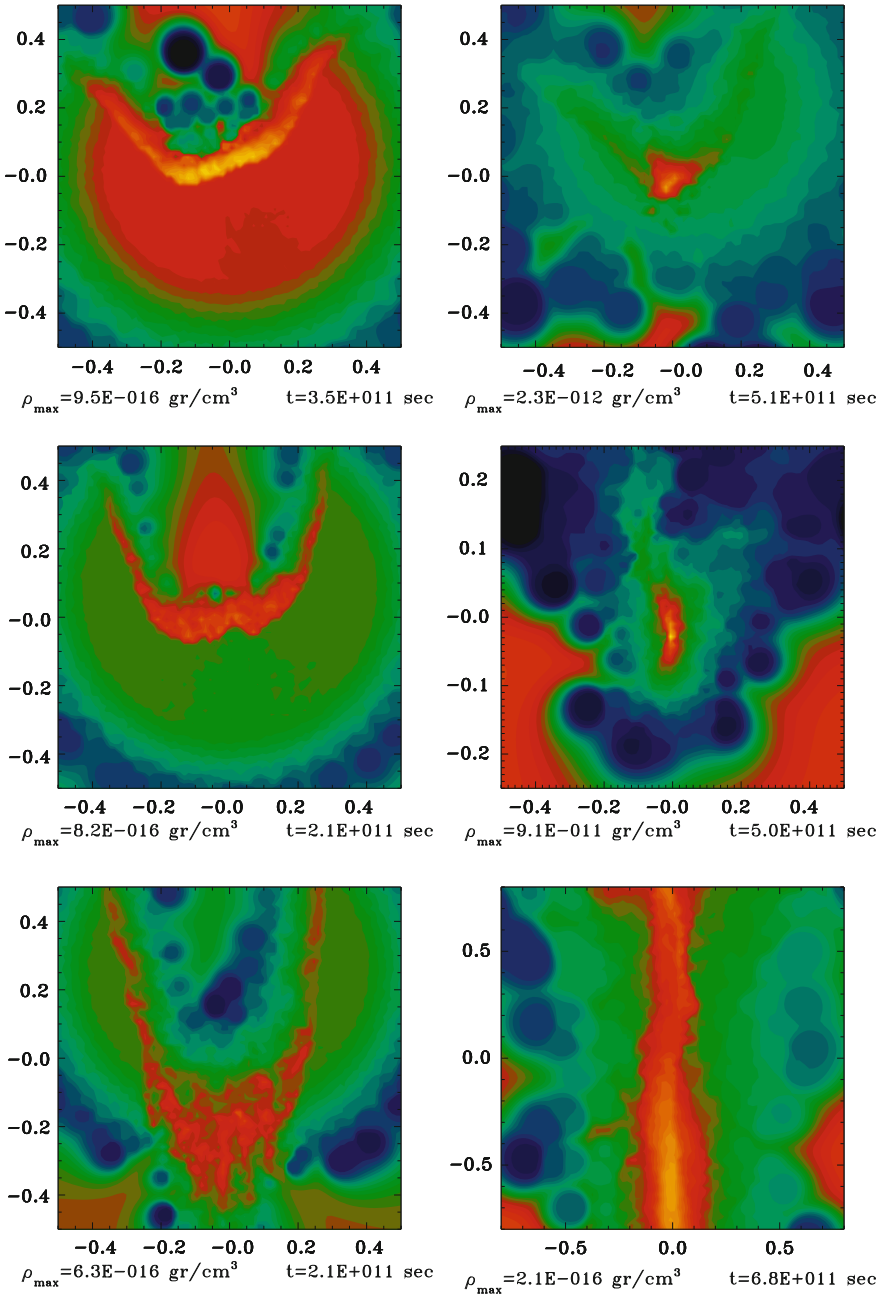

Fig. 5 Iso-density plot illustrating the collision process of model *P*4 (*top panels*), *P*5 (*middle panels*), and *P*6 (*bottom panels*)

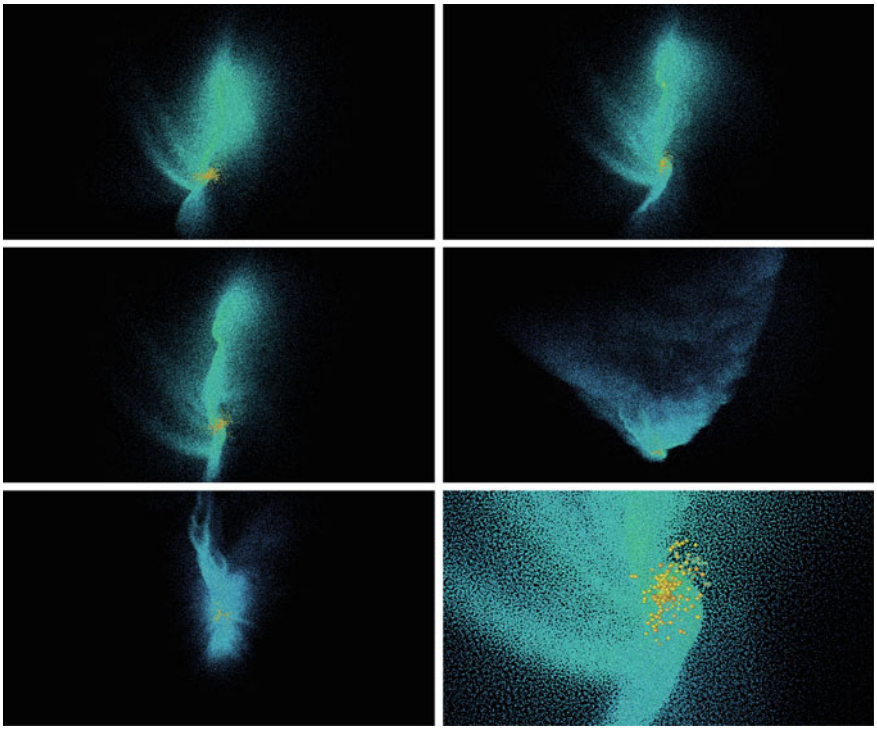

Fig. 6 Freely rotated view of the collided system to show the formed accretion centers observed as *yellow dots* for models: $P1$ (*top left panel*), $P2$ (*top right panel*), $P3$ (*middle left panel*), $P4$ (*middle right panel*), $P5$ (*bottom left panel*), and a zoom of $P2$ (*bottom right panel*, this is a zoom of the *top right panel*)

When the radius of the bullet increases from $R0/4$ to $R0/2$, the effects on the target core are more severe. For example, in Fig. 5 we can see that even for the low and intermediate pre-collision velocity models, the target core is almost divided entirely into two parts and it fully breaks for the high velocity model, see the bottom panels of Fig. 5.

In fact, for model $P6$, self-gravity and gas viscosity do manage to slow down the penetration of the bullet, and the two separated core parts coalescence, such that the system becomes a long and expanding filament, as can be seen in the last panel of Fig. 5.

In Fig. 6 we show a freely rotated $3D$ view of some models, with the purpose of better appreciating the formed accretion centers. It should be noticed that most accretion centers grow from the gas agglomeration formed around the bullet, as the densest gas particles are located at the interaction region. As an example, for model P2 we zoom in the top right panel of Fig. 6 to get the bottom right panel of Fig. 6 where we observe the spatial distribution of the accretion centers. There are no accretion

centers detected in model $P6$, while those detected in model $P5$ are less visible than for the other models.

5 Conclusions

Even though this paper has been limited to considering only highly idealized collision systems, it has been possible to capture and display some of the essential physics of a collapsing core (the target), that is penetrated by a denser gas core (the bullet).

We here observe that small over-densities are formed behind the perturbation front left by the bullet along its way digging into the target core. There is still the chance that these gas condensations may grow to end up as proto-stars. We also observe that the number and spatial distribution of the accretion centers strongly depends on the pre-collision velocity. The average mass of the accretion centers do not change appreciably in the simulations.

Acknowledgments We would like to thank ACARUS-UNISON for the use of their computing facilities. This work has been partially supported by the Consejo Nacional de Ciencia y Tecnología of Mexico (CONACyT) under the project CONACyT-EDOMEX-2011-C01-165873.

References

Anathpindika S (2009) Supersonic cloud collision. Astron Astrophys 504:437–450

Anathpindika S (2010) Collision between dissimilar clouds: stability of the bow-shock, and the formation of prestellar cores. Mon Not Roy Astron Soc 405:1431–1443

Arreaga-Garcia G, Klapp J, Saucedo-Morales J (2014) Simulations of colliding uniform density H2 clouds. Int J Astron Astrophys 4:192–220

Balsara DS (1995) von Neumann stability analysis of smooth particle hydrodynamics: suggestions for optimal algorithms. J Comput Phys 121:357–372

Boss AP, Fisher RT, Klein R, McKee CF (2000) The Jeans condition and collapsing molecular cloud cores: filament or binaries? Astrophys J 528:325–335

Higuchi AE, Chibueze-Asao JO, Tasker EJ, Ken-Takahira K, Takano S (2014) ALMA view of GO.25+0.016: can cloud-cloud collision form the cloud? Astrophys J 147(6):7

Monaghan JJ, Gingold RA (1983) On the fragmentation of differentially rotating clouds. Mon Not Roy Astron Soc 204:715–733

Springel V (2005) The cosmological simulation code Gadget-2. Mon Not Roy Astron Soc 364:1105–1134

Whitworth AP, Ward-Thompson D (2001) An empirical model for protostellar collapse. Astrophys J 547:317–322

Numerical Simulations of Interacting Galaxies: Bar Morphology

J.C. Luna Sánchez, M.A. Rodríguez Meza, A. Arrieta and R. Gabbasov

Abstract We present several numerical simulations of the collision of two spiral galaxies. A spiral galaxy is modelled with a spherical bulge and halo and a Freeman disc. The bulge is composed of a collisionless collection of stars; the halo is composed of a set of collisionless particles of unknown nature, we only need to know their gravitational influence and that the halo particles do not collide among them; and the disc is composed of stars only, gas or dust are not considered in this work. A bar is usually formed due to tidal effects after the first encounter of the spirals and we have found that this was the case in all the numerical experiments we did. The bar morphology is then studied during the evolution of the collision process. Here the morphology is the bar formation in the spiral discs, its geometry, i.e., minor and major axis length; and also we show how one of the collision galaxy partners change its disc geometry due to impact of the other galaxy. We show finally how the morphology of spiral galaxies changes due to collision geometrical parameters: impact parameter or the angle between symmetry axes of the spiral discs.

J.C. Luna Sánchez
Departamento de Física, Instituto Nacional de Investigaciones Nucleares,
Apdo. Postal 18-1027, 11801 Mexico, D.F., Mexico

J.C. Luna Sánchez · A. Arrieta
Departamento de Física y Matemáticas, Universidad Iberoamericana,
Prolongación Paseo de la Reforma 880, Lomas de Santa Fe, 01210 Mexico, D.F., Mexico

M.A. Rodríguez Meza (✉)
Instituto Nacional de Investigaciones Nucleares, Carretera México-Toluca S/N, La Marquesa,
52750 Estado de Mexico, Ocoyoacac, Mexico
e-mail: marioalberto.rodriguez@inin.gob.mx

R. Gabbasov
Instituto de Ciencias Básicas E Ingenierías, Universidad Autónoma de Pachuca, Ciudad
Universitaria, Carr. Pachuca-Tulancingo Km. 4.5 S/N, 42184 Pachuca, Hidalgo, Mexico

J. Klapp et al. (eds.), *Selected Topics of Computational and Experimental Fluid Mechanics*, Environmental Science and Engineering,
DOI 10.1007/978-3-319-11487-3_42

1 Introduction

Galaxies are the basic building blocks of the large scale structure of the universe. They were classified according to their morphology by Hubble. There are elliptical, spiral, and irregular galaxies. Spiral galaxies are the main object in this work; they are composed of a bulge, a spherical distribution of stars at the center of the galaxy; a disc of stars, gas and dust; and a halo of dark matter, of unknown particles, that only acts gravitationally on the other components. Recently Sellwood has published a review (Sellwood 2014) that discusses several aspects of current interest in the research of disc galaxies.

In the present work, we study bars in interacting spiral galaxies. Observations of spiral galaxies indicate that the presence of a bar is a common feature (Elmegreen and Elmegreen 1983; Master et al. 2011). In particular Master et al. (2011) have found that 29.4 % of the galaxies in the sample they analyse have a bar. The bar formation in isolated models has been widely studied both analytically and numerically (Hohl 1971; Sellwood 1981; Sellwood and Carlberg 1984; Athanassoula and Sellwood 1986; Weinberg 1985; Debattista and Sellwood 2000; Weinberg and Katz 2002). In this paper we consider the dynamical effects of non-isolated systems which are found in clusters of galaxies. In this sense, it has been suggested that the observed bar in many spirals is the result of the gravitational interaction between two or more nearby galaxies. For instance, Nogushi (1987) has found that during the collision of two galaxies and between the first and the second closest approaches, the disc develops a transient bar shape. The gravitational interaction between the two galaxies gives rise to perturbations in the orbits of the stars that results in the formation of the bar.

Bar formation in stellar discs depends upon various simultaneous effects. In the case of collisions, simulations have shown that these factors are (Salo 1990): rotation curve shape, disc-halo mass ratio, perturbation force and geometry. Additionally, simulations suffer from numerical effects such as low spatial and temporal resolution, too few particles representing the system, and an approximate force model. These effects were studied by Gabbasov (2006) and Gabbasov et al. (2006) where it was shown that specific parameter choices may change bar properties. Once numerical effects are controlled, we may investigate all the other model parameters, which in our case are: geometric parameters such as impact parameter and the angle between the disc planes.

In this work we study the morphology of bars that forms as a product of instabilities that result of the collision of two spiral galaxies. Morphology is given by finding major and minor axes evolution after the first encounter of the spirals.

Our work is organised in the following form: In the next section we present how to build a galaxy model by following the Hernquist method (Hernquist 1990) and explain how to set up the parabolic collision geometry. Next, we discuss our results for various collision cases such as off-axis impacts and for two different angles of collision of the disc galaxies and show the resultant morphological properties of tidally formed bars. Conclusions are shown in the final section.

2 Initial Conditions and Geometry of the Collision

We use the standard procedure to construct a galaxy model with a Newtonian potential described in Gabbasov (2006) and Gabbasov et al. (2006). An individual galaxy consists of a disc, halo, and bulge and its initial condition is constructed using a bulge and a Freeman disc composed of stars embedded in a Hernquist halo model (a Dehnen's family member with $\gamma = 1$, where γ is the power characterising the member; see Rodríguez-Meza and Cervantes-Cota (2004)) that acts on them gravitationally. We does not consider gas.

The spatial distribution of particles are constructed using density profiles: The bulge density profile is a spherical distribution of stars and is given by (Hernquist 1990):

$$\rho_{\rm b}(r) = \frac{M_{\rm b} a_{\rm b}}{2\pi} \frac{1}{r(r+a_{\rm b})^3}, \tag{1}$$

and for the halo we use a Dehnen density profile with $\gamma = 0$ (Dehnen 1993):

$$\rho_{\rm h}(r) = \frac{3M_{\rm h}}{4\pi} \frac{a_h}{(r+a_{\rm h})^4}. \tag{2}$$

We assume that the disc follows the exponential profile (Freeman 1970):

$$\rho_{\rm d}(R,z) = \frac{M_{\rm d}\alpha^2}{4\pi z_0} e^{-\alpha R} \mathrm{sech}^2\left(\frac{z}{z_0}\right). \tag{3}$$

where R and z are the spatial cylindrical coordinates. In these equations $M_{\rm b}$, $a_{\rm b}$ and $M_{\rm h}$, $a_{\rm h}$ are the mass and length of bulge and halo respectively, and $M_{\rm d}$, α^{-1} and z_0 are the mass, length scale and the thickness length scale of the disk, respectively.

For the spherical distribution of particles, their velocities, v_r, v_ϕ, v_θ, are obtained using the Schwarzschild distribution function

$$f_{B,H}(v_r, v_\phi, v_\theta) \propto \exp\left[-\frac{v_r^2}{2\,\sigma_r^2} - \frac{v_\phi^2}{2\,\sigma_\phi^2} - \frac{v_\theta^2}{2\,\sigma_\theta^2}\right], \tag{4}$$

where σ_r, σ_ϕ, and σ_θ are the dispersion of velocities and in general they are functions of r. For an isotropic ellipsoid the above velocity distribution is the Maxwell distribution.

For a spherically symmetric mass distribution and without rotation the dispersion of velocities is obtained using Jeans' equation

$$\frac{d}{dr}\left(\rho(r)\sigma_r^2\right) + \frac{\rho(r)}{r}\left[2\sigma_r^2 - (\sigma_\theta^2 + \sigma_\phi^2)\right] = -\rho(r)\frac{d\Phi}{dr}, \tag{5}$$

where Φ is the gravitational potential. If the distribution of velocities is isotropic

$$\sigma_r^2 = \sigma_\theta^2 = \sigma_\phi^2. \tag{6}$$

The above equation can be integrated to give a general expression for the dispersion of velocities:

$$\sigma_r^2(r) = \frac{1}{\rho(r)} \int_r^\infty \rho(r') \frac{d\Phi}{dr'} dr'. \tag{7}$$

Particles velocities can be found by inverting the equation

$$f_{b,h}(v, r) = \frac{4\pi}{(2\pi\sigma^2)^{2/3}} v^2 \exp\left[-\frac{v^2}{2\sigma_r^2}\right]. \tag{8}$$

In practice it is convenient to cut the Gaussian distribution at some finite value. A natural choice is the escape velocity V_e.

For axisymmetric distribution we have that the velocity profiles for the disk are computed using the epicyclic approximation, which consists in assuming that velocity dispersions are small ($\sigma_R, \sigma_z, \sigma_\phi \ll R\,\omega$):

$$f_D(v_R, v_z, v_\phi) \propto \exp\left[-\frac{v_R^2}{2\sigma_R^2} - \frac{v_z^2}{2\sigma_z^2} - \frac{(v_\phi - V_0)^2}{2\sigma_\phi^2}\right]. \tag{9}$$

Observations in the exterior of disk galaxies suggest that the radial dispersion is proportional to the surface radial density:

$$\sigma_R^2 \propto \exp(-\alpha R). \tag{10}$$

The vertical dispersion in the isothermal shell approximation is also related to the surface density of the disk, $\Sigma(R)$:

$$\sigma_z^2 = \pi G\, z_0\, \Sigma(R). \tag{11}$$

The ratio σ_R^2/σ_z^2 is constant through the disk and is considered equal to 4, i.e.,

$$\sigma_R^2 = 4\,\sigma_z^2. \tag{12}$$

The azimuthal dispersion is simply related to radial dispersion through the epicyclic approximation for the Schwarzschild velocity distribution

$$\sigma_\phi^2 = \frac{\kappa^2}{4\omega^2}\sigma_R^2, \tag{13}$$

where ω is the angular frequency, computed from the potential

$$\omega = \frac{\partial \Phi(R)}{\partial R}, \tag{14}$$

and κ is the epicyclic frequency defined by

$$\kappa^2(R) = 4\omega^2(R) + R\frac{d}{dR}\left[\omega^2(R)\right]. \tag{15}$$

For an exponential surface density profile, the azimuthal drift velocity is given approximately by

$$V_0^2 = V_c^2 + \sigma_R^2 - \sigma_\phi^2 - 2\alpha R. \tag{16}$$

where $V_c^2 = R\,\omega$ is the azimuthal circular velocity of the disk.

Table 1 Parameters of the galaxy model

Component	Mass	Number of particles	Cutoff radius	Scale-length
Bulge	0.0025	1,024	0.308	0.008
Disc	0.1017	29,491	0.5	0.045
Halo	1.6	245,760	11.55	0.3

The system of units is such that the unit of mass, length, time, and velocity are: 2.2×10^{11} $M_\odot$, 40 kpc, 0.2558 Gyr, 153 km/s, respectively

Table 2 Geometry of the numerical experiments

ID model	Mass proportion	Impact parameter p	Collision angle (°)	Prograde/retrograde
IC 602	1:1	0.1	30	N/A
IC 60255	”	”	0	Prograde
IC 60266	”	”	0	Retrograde
IC 6027	”	”	45	N/A
IC 6028	”	”	90	N/A
IC 6034	”	0.3	30	N/A
IC 6035	”	”	0	Prograde
IC 6036	”	”	0	Retrograde
IC 6037	”	”	45	N/A
IC 6038	”	”	90	N/A
IC 6039	”	0.6	30	N/A
IC 6040	”	”	0	Prograde
IC 6041	”	”	0	Retrograde
IC 6042	”	”	45	N/A
IC 6043	”	”	90	N/A

Once velocity dispersions are computed, the velocity components of particles in the disk can be found by inverting the above Gaussian distribution which includes the drift velocity V_0.

Finally, the galaxy is built, numerically, using a Monte Carlo procedure by choosing six random numbers that when transformed according to the corresponding spatial and velocity distribution functions give us the vector position and the vector velocity of each particle. This is repeated N times with N the number of particles to use in the simulation. The number of particles in each component are assigned in proportion to their masses (see Table 1, where values for other parameters are given). This initial galaxy condition is relaxed up to a time of 3.0 in units of the code (0.7674 Gyr). The geometry of the collision is such that we set both galaxies at parabolic collision orbit defined by the impact parameter p and the angle between disc planes. All experiments were performed with smoothing lengths $\varepsilon_b = \varepsilon_h = 0.003$, $\varepsilon_d = 0.004$ (bulge, halo, and disc), time step $\delta t = 0.01$ (but this is the maximum step size, we have using an adaptive time step scheme). In Table 2 we show the experiments that we will discuss in the next section.

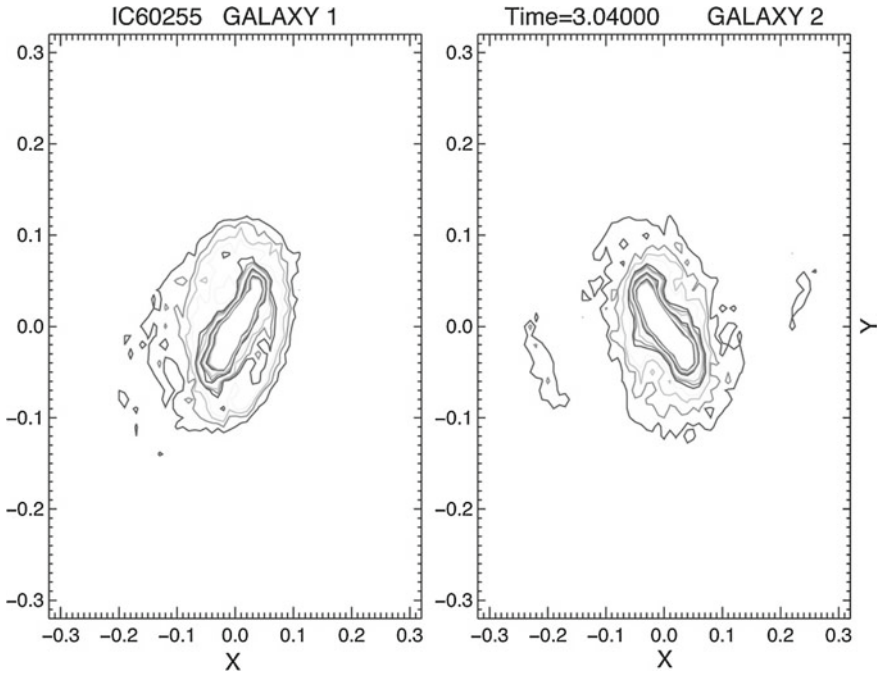

Fig. 1 Contour density map of a snapshot of the collision model IC 60255

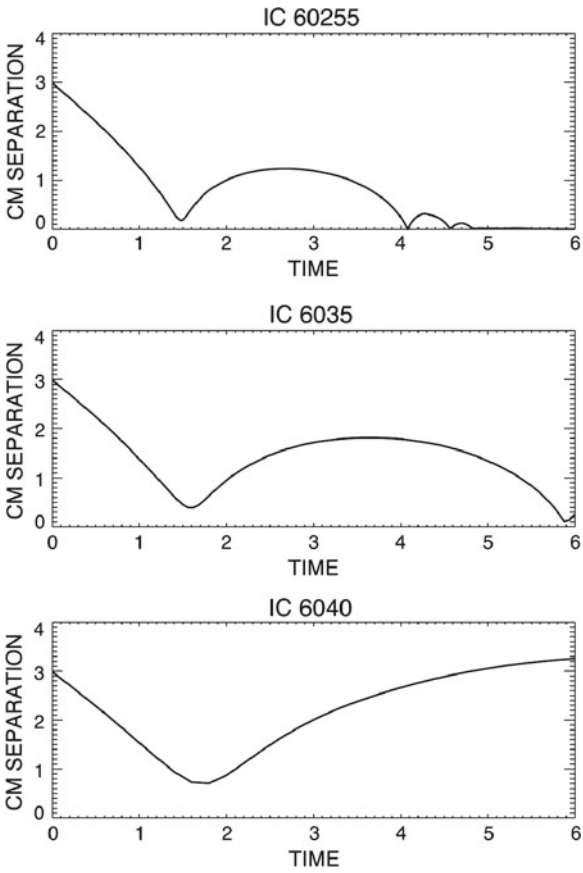

Fig. 2 Evolution of the center of mass separation. The figure corresponds to $p = 0.1$ (*top panel*), $p = 0.3$ (*middle panel*), and $p = 0.6$ (*bottom panel*)

3 Results

All collision models have $N = 552{,}550$ total particles. We consider three sets of simulations followed up to time $t = 1.56$ Gyr. The sets are defined by the impact parameter. First set is for $p = 0.1$, the second is for $p = 0.3$, and the third is for $p = 0.6$. The proportion of galaxy masses is 1:1. See Table 2 for more details. We compute the evolution of the relative differences, through the whole simulations: $|(E(t) - E_0)/E_0|$ and $|(L(t) - L_0)/L_0|$, where E_0 and L_0 are total energy and magnitude of total angular momentum at the beginning of the simulation and $E(t)$ and $L(t)$ are the corresponding quantities as functions of time. All models show a good energy and angular momentum conservation. The relative error is at most $\approx$0.4 % for the total energy and $\approx$0.8 % for the total angular momentum.

In order to detect the presence of a bar in a galaxy and to characterize quantitatively its amplitude, we use the following method. We compute isodensity curves of the disc in a 128×128 mesh, i.e., a contour map of the density field around the center of

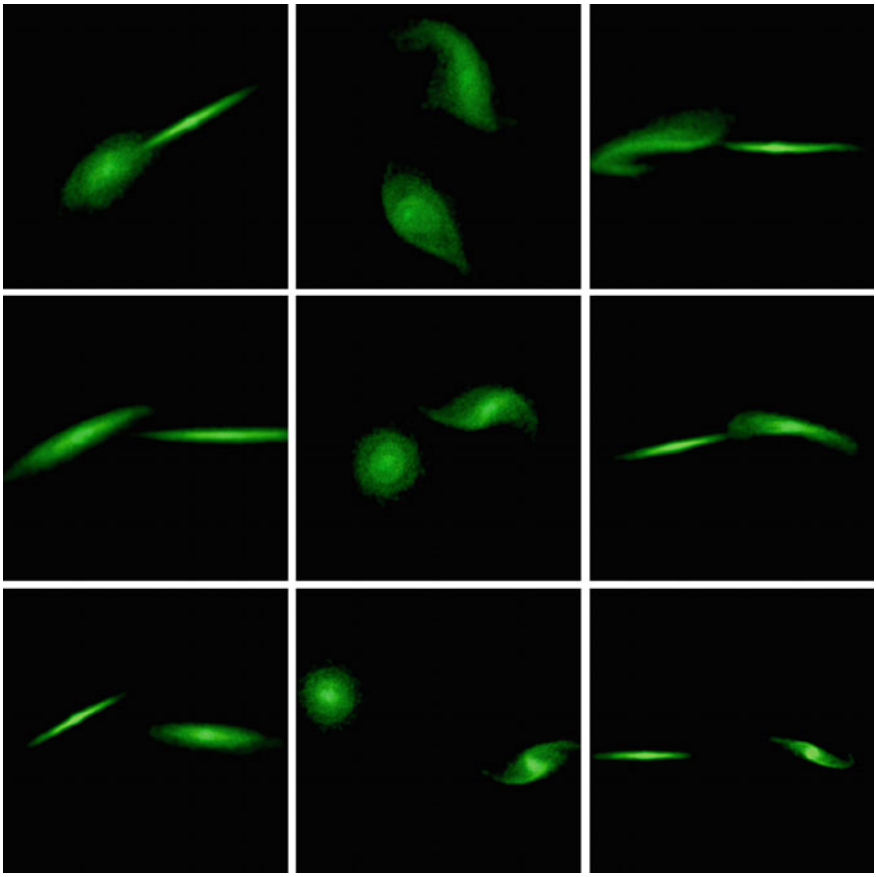

Fig. 3 Snapshots of the collisions: $p = 0.1$ *upper row*; $p = 0.3$ *middle row*; and $p = 0.6$, *lower row*. The shown area has a length side of 28 kpc. The *left column* shows snapshots before the first encounter; the *right column* shows snapshots after the collision; the *middle column* is another view of the same snapshots on the *right column*. Galaxy 1 in the first column is on the *right side* of the snapshot and on the *right column* snapshots is the one that has a well defined disc shape. After the first encounter, disc of galaxy 2 turns to a warped disc shape

mass of the disc. We tune the contour map to have a good resolution map (see Fig. 1). With this contour map we scan the contour lines following several radial trajectories starting at the center of mass. The longest trajectory which intersects the first set of contour lines and which is in the same direction of the gradient at that point is the major axis. The size of this trajectory is the size of the major axis. Now, assuming the bar is rectangular in shape we follow a trajectory perpendicular to the one that defines the major axis, and the intersection with the same set of contour lines will define the minor axis and we will obtain its size. This method allows us to detect any non-axisymmetric deformations such as bars in the disc plane. We have found traces

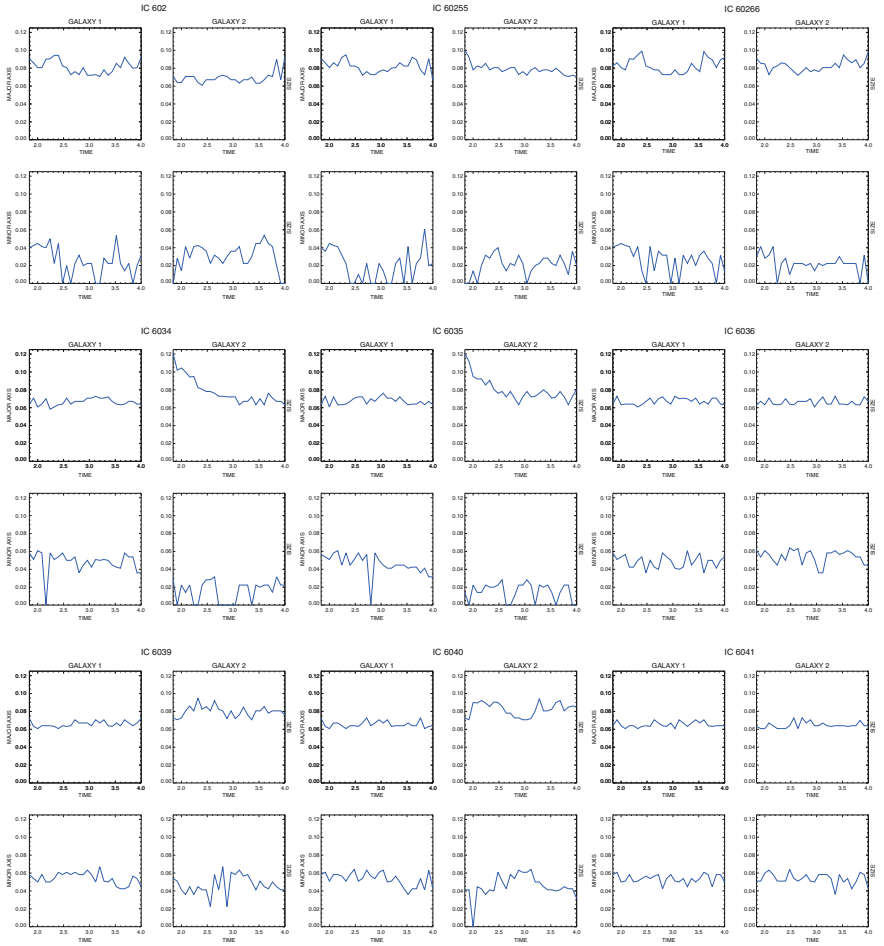

Fig. 4 Morphology of the bar formed in the galaxies. Shown are the sizes of minor and major axes of both galaxies. The *upper row* is for $p = 0.1$; the *middle row* is for $p = 0.3$; and the *lower row* is for $p = 0.6$. *First column* (galaxy 1 and galaxy 2) are morphologies for a collision angle of 30° between symmetry axes of discs of the collision galaxies. The *second column* (galaxy 1 and galaxy 2) if for a collision angle of 0°, prograde. Retrogade collisions show similar behaviour, in the *last column* (galaxy 1 and galaxy 2), showing a decreasing major axis of galaxy 2 for prograde collisions

of a bar for times between the first and second encounters. In this time interval we have computed the size of major and minor axes following the above method.

Figure 2 shows the evolution of the center of mass separation for the three impact parameter values. The behaviour of this curve is the same for all simulations for a given impact parameter. That is because the dominant component is the halo, which is spherically symmetric and the same for each galaxy. The first and second

encounters, for $p = 0.1$, are, approximately, at time 0.38 Gyr and at 1.05 Gyr, respectively. Increasing impact parameter increases the times of the first and second encounters. For all the numerical experiments we look for a bar formation in each of the galaxies for times between the first and second encounter and we analyse the morphology of these bars at times chosen uniformly in that time interval.

Figure 3 shows snapshots of the collisions for the three values of the impact parameter and a collision angle of 30°. Morphology of galaxy 2 for a 0° angle of collision is similar as the one of galaxy 1. Galaxy 2 for a collision angle different from 0° turns to warped disc shape, this is due to that galaxy 1 collides with it crossing its disc very dramatically, but, in spite of this, the bar is formed as it is shown in Fig. 4. The disc of galaxy 1 does not change its shape because it collides like a knife. In this figure we show the morphology of the bars formed in galaxy 1 and galaxy 2, i.e., the sizes of minor and major axes as function of time found with the method we described above. Morphology of the bar is almost the same for $p = 0.3$ and $p = 0.6$. For $p = 0.1$ the major (minor) axis is longer (smaller) than the ones for $p = 0.3$ and $p = 0.6$. Whereas changing the angle between disc planes does not change morphology for $p = 0.1$.

4 Conclusions

Our simulations have shown that tidal forces are an efficient mechanism to generate bars in spirals. In all our numerical experiments a bar is formed in both colliding galaxies after the first encounter. The morphology of the barred spirals that result from the collision does not show strong dependence on the geometry of the collision for galaxies like "galaxy 1" that is colliding like a knife. Whereas galaxies like "galaxy 2" show a decreasing, in time, major axis size for small impact parameters. This behaviour could be due to the fact that disc of galaxy 2, after first encounter acquires a warped shape.

References

Athanassoula E, Sellwood JA (1986) MNRAS 221:213
Debattista VP, Sellwood JA (2000) ApJ 543:704
Dehnen W (1993) MNRAS 265:250
Elmegreen BG, Elmegreen DM (1983) ApJ 267:31
Freeman KC (1970) ApJ 160:811
Gabbasov RF (2006) Numerical simulation of bars in interacting galaxies. Doctoral thesis, Universidad Autónoma del Estado de México, Toluca, México
Gabbasov RF, Rodríguez-Meza MA, Cervantes-Cota JL, Klapp J (2006) Astron Astrophys 449:1043
Hernquist L (1990) ApJ 356:359
Hohl F (1971) ApJ 168:343
Masters KL et al (2011) Mon Not R Astron Soc 411:2026
Nogushi M (1987) MNRAS 228:635

Rodríguez-Meza MA, Cervantes-Cota JL (2004) MNRAS 350:671
Salo H (1990) A&A 243:118
Sellwood JA (1981) A&A 99:362
Sellwood JA, Carlberg RG (1984) ApJ 282:61
Sellwood JA (2014) Rev Mod Phys 86:1
Weinberg MD (1985) MNRAS 213:451
Weinberg MD, Katz N (2002) ApJ 580:627

A Newtonian Approach to the Cosmological Dark Fluids

A. Aviles, J.L. Cervantes-Cota, J. Klapp, O. Luongo and H. Quevedo

Abstract We review the hydrodynamics of the dark sector components in Cosmology. For this purpose we use the approach of Newtonian gravitational instability, and thereafter we add corrections to arrive to a full relativistic description. In Cosmology and Astrophysics, it is usual to decompose the dark sector into two species, dark matter and dark energy. We will use instead a unified approach by describing a single unified dark fluid with very simple assumptions, namely that the dark fluid is barotropic and that its sound speed vanishes.

A. Aviles (✉) · J. Klapp
Departamento de Matemáticas, Cinvestav Del Instituto Politécnico Nacional (IPN), 07360 Mexico, D.F., Mexico
e-mail: aviles@ciencias.unam.mx

J. Klapp
e-mail: jaime.klapp@inin.gob.mx

J.L. Cervantes-Cota · J. Klapp
Instituto Nacional de Investigaciones Nucleares, ININ, Km. 36.5 Carretera Mexico-Toluca, La Marquesa, 52750 Mexico, Mexico
e-mail: jorge.cervantes@inin.gob.mx

O. Luongo · H. Quevedo
Instituto de Ciencias Nucleares, Universidad Nacional Autónoma de México (UNAM), 04510 Mexico, D.F., Mexico
e-mail: orlando.luongo@na.infn.it

H. Quevedo
e-mail: quevedo@nucleares.unam.mx

O. Luongo
Dipartimento di Fisica, Università di Napoli Federico II, Via Cinthia, 80126 Naples, Italy

O. Luongo
Istituto Nazionale di Fisica Nucleare (INFN), Sezione di Napoli, Via Cinthia, 80126 Naples, Italy

H. Quevedo
Dipartimento di Fisica and ICRA, Università di Roma La Sapienza, Piazzale Aldo Moro 5, 00185 Rome, Italy

J. Klapp et al. (eds.), *Selected Topics of Computational and Experimental Fluid Mechanics*, Environmental Science and Engineering,
DOI 10.1007/978-3-319-11487-3_43

1 Introduction

Currently, the most accepted picture for the study of our Universe as a whole is given by the so called Λ-Cold Dark Matter (ΛCDM) model of Cosmology. The first pillar of this model is Einstein's theory of General Relativity (GR) (Einstein 1916), in which the spacetime itself and the matter-energy fields that live in there are related by second order partial differential equations, thus any distribution of matter will effectively *curve* the arena where these matter fields evolve. Despite this fact, many features of the evolution of the Universe can be well understood in the context of Newtonian gravity; qualitatively, consider the spacetime as a curved four dimensional manifold with some characteristic curvature scale l_H, well below this scale the effects of curvature could be neglected and the Newtonian limit of GR becomes a good approximation to the whole, complete description. In the cosmic epochs that are relevant in this short review the characteristic scale is given by the inverse of the rate of expansion of the Universe, that is, the inverse of the Hubble factor H, thus we expect the Newtonian results to be valid up to the length scale cH^{-1}, where c is the speed of light. In this work we derive the relevant equations that govern the cosmic fluids evolution in Newtonian gravity and once we have done this we will add relativistic corrections in order to reach the complete set of equations.

A second pillar of the ΛCDM model is the Standard Model of Particles. The *known* matter fields of the Universe are essentially baryons,[1] neutrinos and photons. These components can be approximated as fluids as long as the mean free path of their microscopic entities are much smaller than the typical smallest macroscopic scale of the structure of interest. In this review we will follow this approach by considering the matter fields as fluids that evolve according to hydrodynamical equations. This approximation is also valid for incoherent electromagnetic radiation, while coherency requires a detailed analysis of their distribution functions through the coupled Boltzmann and Einstein equations; for such a treatment see for example Ma and Bertschinger (1994).

It turns out that to describe the Universe we observe it does not suffice with the ingredients mentioned in the two previous paragraphs. Several independent cosmological probes show that nowadays the nature of about 96 % of the energy content of the Universe is unknown to us (Cervantes-Cota and Smoot 2011). As far as today all our knowledge of these components comes from their gravitational interaction with the standard matter fields, in this sense we refer to them as dark. This *dark sector* is usually decomposed into dark matter and dark energy, from which the ΛCDM model inherits its name. The dark matter component has the property that clumps at all scales and it is responsible for the formation of the cosmic structures we observe, while dark energy fills the space homogeneously and provides a negative pressure which counteracts gravitational attraction and ultimately accelerates the Universe. Nevertheless, we will show—as it is done in Ref. Aviles and Cervantes-Cota (2011)—that

[1] In the jargon of Cosmology we refer to any particle of the standard model that is not relativistic as a baryon, referring mainly to protons and neutrons. In contrast, in particle physics a baryon is a composite subatomic particle made up of three quarks.

the dark sector can be described by just one dark fluid which can be characterized with very simple assumptions, and that there is no observation relying on zero and first order cosmological perturbation theory that can distinguish it from the ΛCDM model, concluding that the standard decomposition of the dark sector is arbitrary (Kunz 2009).

The paper is organized as follows, in Sect. 2 we develop the background evolution of the Universe in Newtonian theory, where arguments are supplemented to understand the results in a curved relativistic framework. In Sect. 3 we study the theory of small perturbations to the background evolution, which thereafter are generalized to curved spacetimes. In Sect. 4 we introduce the dark fluid and show explicitly that it is degenerated with the ΛCDM model. Finally in Sect. 5 we summarize our results.

2 Homogeneous and Isotropic Cosmology in Newtonian Gravity

One of the cornerstones of Modern Cosmology is that the Universe is homogeneous and isotropic at very large scales (from above about 150 Mpc), and this paradigm is called the Cosmological Principle. We observe essentially the same structures on the sky, a uniformly random field of distribution, type and composition of galaxies; moreover, as we look in any direction we detect the same background of cosmic microwave background radiation with a blackbody spectrum at a temperature of 2.725 K with slight differences of the order of 10^{-5} K. Assuming that we do not live in a privileged position in the Universe, the foundations of the Cosmological Principle relies on firm grounds.

To properly discuss this large scale scenario in a Newtonian framework, consider a spherical region of the space and the total mass M contained in it, and denote the radius of that sphere by $R(t)$, which is in general a function of time. Take a small region over the sphere with mass m. Ignoring all other forces except for gravity, the homogeneity of the Universe allows us to write the conservation of energy E as

$$\left(\frac{\dot{R}}{R}\right)^2 = \frac{8\pi G}{3}\rho_M + \frac{2E}{mR^2} \tag{1}$$

where we defined the mass density $\rho_M \equiv 3M/(4\pi G R^3)$ and a dot means derivative with respect to time t. We can write $R(t) = c\tau_0 a(t)$ where c is the speed of light, τ_0 an arbitrary time scale and $a(t)$ a dimensionless function of time called the scale factor, then we define $K \equiv -2E/mc^2R_0^2$, and we choose τ_0 such that K can take one of the three values -1, 0 or 1, thus we obtain the Friedmann equation

$$H^2 \equiv \left(\frac{\dot{a}}{a}\right)^2 = \frac{8\pi G}{3}\rho - \frac{Kc^2}{a^2}, \tag{2}$$

where we have used the Einstein mass-energy relation to write the energy density $\rho = \rho_M c^2$ and redefined the time $t \to ct$. In GR all forms of energy gravitate, therefore the use of the energy density instead of the matter density allow us to consider other forms of energy besides matter as sources of gravity. One interesting point is that Eq. (2) is the same that the obtained in GR. The root of this apparent coincidence is the equivalence principle: In GR Eq. (2) is obtained in a specific chosen coordinates, in these coordinates the free fall observers have fixed space coordinates and as a consequence, about these observers there is a neighborhood where the laws of Special Relativity hold.

Note that we can solve Eq. (2) for $a(t)$ once we know $\rho(t)$, or alternatively $\rho(a)$. Then, we need at least one more equation to close the system. Consider an adiabatic expansion of the same configuration, the thermodynamical Gibbs equation is then $dE = -PdV$, where P is the pressure of the considered fluid and $V = 4\pi G R(t)^3/3$ the volume enclosed by the sphere. Giving the dependence on time t we can write $\dot{E} = \dot{\rho}V + \rho\dot{V} = -P\dot{V}$, or

$$\dot{\rho} + 3H(\rho + P) = 0, \tag{3}$$

which is the continuity equation. To finally solve the system of equations (2) and (3) we need an Equation of State (EoS) that relates the energy density with the pressure. In general this can be written as $P = P(\rho, S)$, where S is the entropy of the fluid. But since in this scenario we are restricted to adiabatic processes, the EoS can take the barotropic form $P = w(\rho)\rho$, where $w(\rho)$ is called the EoS parameter function. Consider for the moment the case of constant w, in such a situation the continuity equation can be integrated to give

$$\rho(a) = \rho_0 a^{-3(1+w)} \tag{4}$$

where $\rho_0 \equiv \rho(a_0)$ and we have normalized $a_0 \equiv a(t_0) = 1$; in this work, as usually, t_0 denotes the present time. For example, the case $w = 0$ corresponds to a very dilute fluid (*dust*) for which the energy density decays as the inverse of the volume, $\rho_m = \rho_{m0} a^{-3}$; the case $P = \rho/3$ corresponds to radiation for which the energy density decays as the fourth power of the scale factor, $\rho_r = \rho_{r0} a^{-4}$—three powers for the dilution of the photons and one more for their redshift.

In GR the constant K is related to the curvature of spacetime, and due to the assumption of homogeneity and anisotropy of space, there are only three possibilities that correspond to flat space which is the case of $K = 0$, spherical space ($K = 1$) and hyperbolic space for ($K = -1$). Consider the case in which K equals zero, we can insert the solution given by Eq. (4) into Eq. (2) to obtain

$$\dot{a} = \left(\frac{8\pi G}{3}\rho_0\right)^{1/2} a^{-3(1+w)/2+1}, \tag{5}$$

which can be integrated yielding

$$a(t) \propto t^{2/3(1+w)}, \tag{6}$$

for $w \neq -1$. $w = -1$ corresponds to non-evolving dark energy and the growth of the scale factor as a function of time t becomes exponential while its energy density remains constant. In general, the situation is more complicated and an analytic expression for the scale factor cannot be found. There are several fluids which must be considered, namely matter, incoherent electromagnetic radiation, massive neutrinos and possibly dark energy, and therefore, the energy density of each one of them must contribute to the Friedmann equation. At this point it is convenient to introduce the redshift z through $a = (1+z)^{-1}$, which is commonly used instead of the scale factor. Consider a Universe filled with matter (m), radiation (r), dark energy with EoS parameter $w = -1$ (Λ) and with a possible non-zero curvature, the Friedmann equation can be written as

$$H(z) = \left(\Omega_\Lambda + \Omega_K (1+z)^2 + \Omega_M (1+z)^3 + \Omega_r (1+z)^4\right)^{1/2}, \tag{7}$$

where $\Omega_i = 8\pi G\rho_{i0}/3H_0^2$ for matter, radiation and dark energy and $\Omega_K = -Kc^2/H_0^2$, are the energy contents parameters at present time—Note that $\sum \Omega_j = 1$.

Several independent probes of the expansion history of the Universe which include redshift-distance measurements of Supernovae type Ia (Riess et al. 1998, 1999; Perlmutter et al. 1999) and observations of Baryon Acoustic Oscillations (Percival et al. 2010) agree in the fact that nowadays the Universe is spatially very flat ($\Omega_K \simeq 0$) and the dominant components to the energy content are dark energy $\Omega_{de} \simeq 0.7$ (with $w_{de} \simeq -1$) and matter $\Omega_M \simeq 0.3$ (with $w_M = 0$), and additional tiny contributions of radiation are also present. The question whether all this matter can be provided by the standard model of particles arises, it turns out that the answer is no for several reasons: The theory of Big Bang Nucleosynthesis (Gamow 1948; Olive et al. 2000) is very accurate in predicting the relative abundances of light nuclei of atoms, these results are very dependent in the quantity of baryons b present at that time, and to obtain the observed abundances it is necessary that $\Omega_b \simeq 0.04$; other constrictions to this parameter arise when one consider observations of the perturbed Universe, for example, measurements of the anisotropies in the temperature of the Cosmic Microwave Background Radiation (Ade et al. 2013) and large scale structure observations (Reid et al. 2015), both agreeing on similar values to the above quoted for Ω_b. Moreover, analysis of virialized cosmic structures as clusters of galaxies and rotation curves in spiral galaxies show that there is a lot of missing matter that we do not observe; for a review see Roos and Mod (2012). Therefore, the matter sector that fills the Universe must be split into two components, $\Omega_M = \Omega_b + \Omega_{dm}$, one is the contribution of the standard model of particles, and the other is the dark matter, which comprises about 80 % of the total matter and whose fundamental nature is still unknown.

We conclude that the origin of about 96 % of the energy content of the Universe is unknown to us. In Sect. 4 we will consider the possibility that the whole dark sector is composed by just one dark fluid.

We finally rewrite the Friedmann equation (Eq. 2) for a flat space Universe as

$$H^2 = \frac{8\pi G}{3}\left(\rho_{r0}\frac{1}{a^4} + \rho_{b0}\frac{1}{a^3} + \rho_{dm0}\frac{1}{a^3} + \rho_\Lambda\right), \tag{8}$$

where possible contribution of massive neutrinos were omitted. Note that the first two terms on the right hand side of the above equation correspond to the "light" sector, while the last two to the dark sector.

3 Small Perturbations in Newtonian Cosmology

In the study of the Universe at small scales, the homogeneous and isotropic description is no longer valid. Strictly, this situation can only be completely confronted into the framework of GR. The problem to study the Universe at these scales is that all the symmetries present in the homogeneous and isotropic description are not present. A possible solution, the one we adopt, is to treat only with small departures to the background evolution.

Thus, we want to study the evolution of a fluid with energy density $\rho = \rho(\mathbf{r}, t)$ and velocity field $\dot{\mathbf{r}} = \mathbf{u} = \mathbf{u}(\mathbf{r}, t)$ in the presence of a gravitational field $\Phi(\mathbf{r}, t)$. The continuity, Euler and Poisson equations are

$$\frac{D\rho}{Dt} + \nabla_{\mathbf{r}} \cdot (\rho \mathbf{u}) = 0, \tag{9}$$

$$\frac{D\mathbf{u}}{Dt} = -\frac{\nabla_{\mathbf{r}} P}{\rho} - \nabla_{\mathbf{r}}\Phi = 0, \tag{10}$$

and

$$\nabla^2_{\mathbf{r}}\Phi = 4\pi G\rho, \tag{11}$$

respectively. We have used the convective derivative $D/Dt \equiv \partial/\partial t + \mathbf{u} \cdot \nabla_{\mathbf{r}}$ which describes the time derivative of a quantity at rest in the comoving fluid frame. Adding an equation of state $P = P(\rho, S)$ the problem is solvable in principle, but in practice such a situation is intractable. The alternative studied here is to treat only small departures from the background description introduced in the previous section. To this end, let us first consider coordinates $\mathbf{x}$ which are comoving with the background evolution, these are defined by

$$\mathbf{x} \equiv \frac{1}{a(t)}\mathbf{r}, \tag{12}$$

and the peculiar velocity $\mathbf{v} = a(t)\dot{\mathbf{x}}$, such that $\mathbf{u} = \dot{a}(t)\mathbf{x} + \mathbf{v}$; that is, $\mathbf{v}$ is the velocity of the fluid with respect to the background comoving (*Hubble*-)flow. By the chain rule, the derivatives transform as $\nabla_{\mathbf{r}} \to a^{-1}\nabla_{\mathbf{x}}$ and $(\partial/\partial t)_{\mathbf{r}} \to (\partial/\partial t)_{\mathbf{x}} - H\mathbf{x}\cdot\nabla_{\mathbf{x}}$. (In what follows we will omit the subindex $\mathbf{x}$ from the spatial gradients and $\partial/\partial t$ should be understood as being taken at fixed $\mathbf{x}$.)

We now consider perturbations to the quantities ρ, P and Φ,

$$\rho(\mathbf{x}, t) = \bar{\rho}(t)(1 + \delta(\mathbf{x}, t)) \tag{13}$$

$$\delta P = c_s^2 \delta\rho + \sigma \delta S \tag{14}$$

$$\Phi(\mathbf{x}, t) = \bar{\Phi}(t) + \phi(\mathbf{x}, t) \tag{15}$$

where a *bar* denotes background quantities that only depend on the time coordinate. We introduced also $c_s^2 = (\partial P/\partial\rho)_S$, the squared adiabatic sound speed and $\sigma \equiv (\partial P/\partial S)_\rho$. Note also that the perturbation to the energy density is $\delta\rho = \bar{\rho}\delta$. In terms of the perturbed variables, the continuity, Euler and Poisson equation become

$$\frac{\partial\delta}{\partial t} + \frac{1}{a}\nabla\cdot\big((1+\delta)\mathbf{v}\big) = 0, \tag{16}$$

$$\frac{\partial\mathbf{v}}{\partial t} + H\mathbf{v} + \frac{1}{a}(\mathbf{v}\cdot\nabla)\mathbf{v} = -\frac{1}{a}\nabla\phi - \frac{\nabla\delta P}{a\bar{\rho}(1+\delta)}, \tag{17}$$

and

$$\nabla^2\phi = 4\pi G a^2 \bar{\rho}\delta. \tag{18}$$

The first two equations are quadratic in the perturbed variables, therefore, in the following we treat them as small and linearize Eqs. (16) and (17) to obtain

$$\frac{\partial\delta}{\partial t} + \frac{1}{a}\nabla\cdot\mathbf{v} = 0, \tag{19}$$

$$\frac{\partial\mathbf{v}}{\partial t} + H\mathbf{v} + \frac{1}{a}\nabla\phi + \frac{1}{a}\nabla c_s^2\delta = 0. \tag{20}$$

Note that in the last equation we used Eq. (14) and considered adiabatic perturbations only. By appealing the conservation of angular moment in an expanding universe, it is expected that the divergence-free piece of the peculiar velocity should decays quickly with time. This can be easily seen by taking the rotational of Eq. (20), arriving at $\nabla\times\mathbf{v} \propto a^{-1}$, which means that in the absence of sources of vector perturbations these modes are not relevant in first order perturbed cosmology, allowing us to consider only the curl-free piece of the velocity in the following discussion; moreover, any initial large vector perturbation would break the isotropy of the background, and thus it is not compatible with the Cosmological Principle.

Now, we are in position to give a closed linear second order equation for the density contrast δ, taking the partial time derivative of Eq. (19) and using Eqs. (18)

and (20) we arrive at

$$\frac{\partial^2\delta}{\partial t^2} + 2H\frac{\partial\delta}{\partial t} - 4\pi G\bar{\rho}\delta - \frac{c_s^2}{a^2}\nabla^2\delta = 0. \tag{21}$$

In this equation the second term is a *friction* component due to the background expansion, the third term implies gravitational attraction, while the fourth is a pressure term. Thus, it shows the important aspect of the competition between gravitational attraction and pressure support.

Being the set of partial differential equations linear in the perturbations it is convenient to work instead in Fourier space,[2] arriving to ordinary differential equation for which each Fourier mode evolve independently.

We define the variable θ as the divergence of the velocity in Fourier space, that is

$$\theta \equiv -\frac{i}{a}\mathbf{k}\cdot\mathbf{v}. \tag{22}$$

The factor a^{-1} is a convention used since the size of a perturbation $\lambda \sim k^{-1}$ grows with a, and thus k/a becomes a comoving wave number.

In Fourier Space $\nabla \to -i\mathbf{k}$, and Eqs. (18)–(20) can be written as

$$k^2\phi = -4\pi G a^2\bar{\rho}\delta, \tag{23}$$

$$\frac{d\delta}{dt} + \theta = 0, \tag{24}$$

$$\frac{d\theta}{dt} + 2H\theta - \frac{k^2}{a^2}\phi - \frac{k^2}{a^2}c_s^2\delta = 0. \tag{25}$$

To obtain the last equation we have taken the dot product of $i\mathbf{k}/a$ with the Fourier transform of Eq. (20) and used the definition (22). Note that in arriving at Eq. (25) we have isolated the curl-free piece of the fluid peculiar velocity.

In Fourier space the Jeans equation for an expanding Universe (Eq. 21) becomes

$$\frac{d^2\delta}{dt^2} + 2H\frac{d\delta}{dt} + \left(\frac{k^2}{a^2}c_s^2 - 4\pi G\bar{\rho}\right)\delta = 0. \tag{26}$$

From this last equation it should be clear the interplay between gravitational instability and pressure support. There exist a threshold scale, called the Jeans length

[2] Our convention for a Fourier transform of a vector or a scalar function f is

$$\tilde{f}(\mathbf{k}) = \int d^3x f(\mathbf{x}) e^{i\mathbf{k}\cdot\mathbf{x}}.$$

In this work, without worrying about confusions, we omit the tilde on Fourier transform quantities.

$\lambda_J = ac_s\sqrt{\pi/G\rho}$, for which perturbations with comoving size $L \sim ak^{-1} > \lambda_J$ grow while those with $L < \lambda_J$ oscillate and decay.

From Eq. (26) we can infer the behavior of dark matter perturbations in the different epochs of the cosmic evolution. Let us first consider a matter dominated Universe, from the Friedmann equation and since $\rho_M \propto a^{-3}$ and $a \propto t^{2/3}$, it follows that $H = 2/3t$ and $4\pi G\bar{\rho} = 2/3t^2$. In this case, Eq. (26) has two independent solutions $\delta_{dm} \propto t^{-1}$ and $\delta_{dm} \propto t^{2/3} \propto a$. The growing mode of the density contrast grows linearly with the scale factor and from Eq. (23) it follows that the gravitational potential ϕ is constant in this case. Similar analysis for the growth of the density contrast of the dark matter in the epochs dominated by radiation and dark energy show that in the first case the growing mode is logarithmic while for the second case does not exist, but it remains constant, suppressing the formation of structure. Therefore, in order for matter perturbations to grow enough to form the structures we observe today, it must have elapsed a sufficiently long epoch in which the expansion of the universe was driven by matter (either baryonic or dark).

The equations for the perturbed variables developed so far are valid for non-relativistic matter fields and for scales which are smaller than the curvature length scale cH^{-1}, as discussed in the Introduction. To obtain the complete equations it is mandatory to use the theory of General Relativity and hydrodynamics in curved spacetimes. For completeness we present here the equations for a collection of fluids with equation of state $P = w(\rho)\rho$ and that do not posses anisotropic stresses. These are the Poisson equation

$$k^2\phi = -4\pi G \sum \bar{\rho}_i \Delta_i, \tag{27}$$

where

$$\Delta_i = \delta_i + 3H(1 + w_i)\theta/k^2, \tag{28}$$

the continuity equation

$$\frac{d\delta}{dt} + (1 + w)\left(\theta - 3\frac{d\phi}{dt}\right) + 3H\left(\frac{\delta P}{\delta\rho} - w\right)\delta = 0, \tag{29}$$

and the Euler equation

$$\frac{d\theta}{dt} + 2H(1 - 3w)\theta + \frac{\dot{w}}{1 + w}\theta - \frac{k^2c_s^2}{a^2(1 + w)}\delta - \frac{k^2}{a^2}\phi = 0. \tag{30}$$

First we want to make note that for perturbations with wavelengths well bellow the Hubble scale, i.e. $k \gg H$, the Poisson equation reduces to the one found in the non relativistic treatment. Moreover, for non relativistic matter $w = \dot{w} = 0$ and $d\phi/dt = 0$, recovering the Newtonian Euler and continuity equations.

Now, consider the case of dark energy with EoS parameter $w = -1$. At any epoch of the cosmic evolution from the continuity equation follows that the density contrast is a constant. This feature and the fact that its energy density remains also constant,

as shown in Sect. 2, implies that this fluid permeates all the space homogeneously, giving it the *alias* of non-evolving dark energy. Any departure of $w = -1$ would imply that their perturbations evolve and hence possibly give rise to the formation of dark energy structure.

4 The Dark Fluid

Is it possible that the properties of dark energy and dark matter to be different manifestations of the same dark fluid? Several unified dark models of the dark sector have appeared in the literature, the prototype of these is the generalized Chaplygin gas (Kamenshchik et al. 2001; Bento et al. 2002), which is defined as a barotropic fluid with EoS $P_{Chap} = -A/\rho^{\alpha}_{Chap}$ with $0 < \alpha \leq 1$. Integrating the continuity equation (3) we obtain

$$\rho_{Chap}(a) = \left(A + \frac{B}{a^{3(1+\alpha)}}\right)^{\frac{1}{1+\alpha}} \tag{31}$$

where B is an integration constant. This model describes a smooth interpolation between an early phase dominated by *dust*, with $\rho \propto a^{-3}$ and an asymptotical future with $\rho =$ constant. The intermediate phase is well described by an EoS $P = \alpha\rho$. The tightest constraints on the parameter α come from comparisons to the observed large scale matter power spectrum obtaining $\alpha < 10^{-5}$ (Gorini et al. 2008), and therefore making the model effectively indistinguishable from ΛCDM model.

Other unified models that have recently attracted the attention of the cosmological community includes scalar fields, modifications to Einstein's theory of gravity, among others; see, for example Aviles and Cervantes-Cota (2011), De-Santiago and Cervantes-Cota (2011) and Khoury (2014).

We now specialize to a specific model that is totally degenerated with ΛCDM at least at zero and first order in cosmological perturbation theory, the *dark fluid* which was introduced in Ref. Hu and Eisenstein (1999) and further studied in Aviles and Cervantes-Cota (2011), Luongo and Quevedo (2014) and Aviles et al. (2012).

We define the dark fluid as in Aviles and Cervantes-Cota (2011), that is, a barotropic perfect fluid with adiabatic speed of sound equal to zero.[3] Gravitational instability is driven by the competition between gravitational attraction and pressure support. From Eq. (26) it follows that the condition for vanishing sound speed allows perturbations of the fluid to grow at all scales, as cold dark matter does. For the dark fluid we can write the equation of state without loss of generality as

$$P_d = w_d(\rho)\rho_d, \tag{32}$$

[3] Other definitions are possible. In Hu and Eisenstein (1999) the barotropic condition is not considered but additional conditions on its EoS are imposed. In Luongo and Quevedo (2012, 2014) it is defined as an ideal gas with vanishing speed of sound.

where the subscript d stands for $dark$. Giving $c_s^2 = dP/d\rho = 0$ one obtains that

$$w_d = \frac{P_0}{\rho_d}, \qquad P_d = P_0, \tag{33}$$

obtaining that the pressure is constant. For cold dark matter, this pressure is equal to zero, but astronomical observations allow this pressure to be non vanishing, and in fact, it could be as large as the critical density of the Universe ($\rho_c \equiv 3H_0^2/8\pi G$). For example, a recent analysis of rotation curves in LSB galaxies has shown that $|w_{dm}| < 10^{-6}$ at the center of the galaxies (Barranco et al. 2013). This allows us to think the pressure as a source of the cosmic accelerated expansion. To see how this is possible, consider the continuity equation for the background evolution

$$\dot{\rho}_d + 3\frac{\dot{a}}{a}(\rho_d + P_0) = 0. \tag{34}$$

This equation can be integrated to give

$$\rho_d(a) = \frac{\rho_{d\,0}}{1+\mathscr{K}}\left(1 + \frac{\mathscr{K}}{a^3}\right), \tag{35}$$

where $\mathscr{K} = -(\rho_{d0} + P_0)/P_0$ is an integration constant fitted such that ρ_{d0} is the value of the dark fluid energy density at a scale factor $a(t_0) \equiv a_0 = 1$. Equation (35) is what one expects for a unified dark sector fluid, that is, a component that decays with the third power of the scale factor plus a component that remains constant. In order for the energy density to be positive at all times, $\mathscr{K}$ must be positive and therefore the pressure is negative and lies in the interval $-\rho_{d0} \leq P_0 \leq 0$, allowing the dark fluid to accelerate the Universe. Equation (35) shows that the dark fluid model gives the same phenomenology as the ΛCDM at the background cosmology. Its EoS parameter can be written as

$$w_d(a) = -\frac{1}{1+\mathscr{K}a^{-3}}, \tag{36}$$

which should be compared to the corresponding for the dark sector of the standard model of Cosmology,

$$w_{\Lambda+dm}(a) = -\frac{1}{1+\frac{\Omega_{dm}}{\Omega_\Lambda}a^{-3}}. \tag{37}$$

One can go back and forth between the two models with the identifications

$$\mathscr{K} = \frac{\Omega_{dm}}{\Omega_\Lambda}, \qquad \text{and} \qquad \Omega_d = \Omega_{dm} + \Omega_\Lambda. \tag{38}$$

The first of the two equations above can be written in the suggestive form $P_0 = -\rho_c \Omega_\Lambda$. In Ref. Aviles and Cervantes-Cota (2011) it has been shown explicitly that the degeneracy persist at the linear cosmological perturbed level, and heuristic arguments are given that point to the degeneracy is present at all orders in perturbation theory.

We notice an important physical difference between the ΛCDM and dark fluid models. To describe the observed late acceleration of the Universe, in Eq. (37) it is necessary to include the cosmological constant which is then interpreted as the vacuum energy. This identification gives rise to the well-known cosmological constant problem, probably the most serious inconsistency in theoretical physics. The dark fluid model offers a possibility to avoid this problem. In fact, in Eq. (36) the term $\mathscr{K}$ does not contain any cosmological information which should be associated with the vacuum energy, but of course it remains the problem to explain $\mathscr{K}$. This problem is however in the arena of the microscopical theory of the dark fluid, that is not developed yet. The dynamics of the dark fluid naturally leads to an accelerated universe, mimicking the exact behavior of the ΛCDM model, without any cosmological constant. Nevertheless, the final decision about this possibility requires a more detailed investigation.

5 Conclusions

In this pedagogical short review we have developed the theory of cosmological perturbations at the background and linear levels within the framework of Newtonian gravity for matter-energy fields in the fluid approximation. It is remarkable that some of the important aspects of the cosmic evolution of the Universe can be understood without the use of Einstein's theory of General Relativity. Despite this fact, once we have derived the Newtonian evolution equations we proceeded to add relativistic corrections to arrive to the complete set of equations, and special emphasis has been done in finding the solutions for the evolution of dark matter and dark energy perturbations.

Due to equivalence principle and that the dark sector components—in its more radical definition—only interact with the "visible" forms of energy through gravity, it is arbitrary to decompose the dark sector into dark matter and dark energy. In this work we also reviewed a model, namely the dark fluid, that is indistinguishable from the ΛCDM. This description results very appealing because it is based on a very simple assumption, that is, the speed of sound of the dark fluid vanishes identically. We explicitly show that both models are degenerated and therefore, it does not exist any observation based on the background and linear perturbed cosmology that can tell the correct description.

In addition, we noticed that the dark fluid model opens the possibility of avoiding the cosmological constant problem because it can explain the late acceleration of the Universe, without necessarily demanding the presence of a cosmological constant.

The problem now is to understand the value of the parameter $\mathscr{K}$, as a fundamental property of the dark fluid.

Acknowledgments AA and JK gratefully acknowledge support from the project CONACyT-EDOMEX-2011-C01-165873 (ABACUS-CINVESTAV). OL is supported by the European PONa3 00038F1 KM3NET (INFN) Project and wants to thank Prof. Salvatore Capozziello for useful discussions. HQ is supported from DGAPA-UNAM, grant No. 113514, and CONACyT-Mexico, grant No. 166391.

References

Ade PAR et al. Planck Collaboration (2014) Astron Astrophys 571:A23. arXiv:1303.5083
Aviles A, Bastarrachea-Almodovar A, Campuzano L, Quevedo H (2012) Phys Rev D86:063508. arXiv:1203.4637
Aviles A, Cervantes-Cota JL (2011) Phys Rev D83:023510. arXiv:1012.3203
Aviles A, Cervantes-Cota JL (2011) Phys Rev D84:083515. arXiv:1108.2457
Barranco J, Bernal A, Nunez D (2013) arXiv:1301.6785
Bento M, Bertolami O, Sen A (2002) Phys Rev D66:043507. arXiv:gr-qc/0202064
Cervantes-Cota JL, Smoot G (2011) AIP Conf Proc 1396:28–52. arxiv 1107.1789
De-Santiago J, Cervantes-Cota JL (2011) Phys Rev D83:063502. arXiv:1102.1777
Einstein A (1916) Ann der Phys 49:769–822
Gamow G (1948) Phys Rev 74:505
Gorini V, Kamenshchki A, Moschella U, Piatella O, Starobinsky A (2008) JCAP 0802:016. arXiv:0711.4242
Hu W, Eisenstein DJ (1999) Phys Rev D59:083509. arXiv:astro-ph/9809368
Kamenshchik AY, Moschella U, Pasquier V (2001) Phys Lett B511:265–268. arXiv:gr-qc/0103004
Khoury J (2014) An alternative to particle dark matter. arXiv:1409.0012
Kunz M (2009) Phys Rev D80:123001. arXiv:astro-ph/0702615
Luongo O, Quevedo H (2012) Astrophys Space Sci 338(2):345
Luongo O, Quevedo H (2014) Int J Mod Phys D 23:1450012
Ma C-P, Bertschinger E (1994) Astrophys J 429:22
Olive KA, Steigman G, Walker TP (2000) Phys Rep 333:389–407. arXiv:astro-ph/9905320
Percival WJ et al (2010) SDSS Collaboration. Mon Not Roy Astron Soc 401:2148–2168. arXiv:0907.1660
Perlmutter S et al (1999) Astrophys J 517:565
Reid BA et al (2010) Mon Not Roy Astron Soc 404:60–85. arXiv:0907.1659
Riess AG et al (1998) Astron J 116:1009
Riess AG et al (1999) Astron J 117:707
Roos M (2012) J Mod Phys 3:1152. arXiv:1208.3662

Capillary Rise in a Taylor-Hauksbee Cell with a Tilted Edge

A. Jara, S. de Santiago, F.J. Higuera, M. Pliego, A. Medina and C.A. Vargas

Abstract In this work we discuss a series of experiments to get the equilibrium profiles when a viscous liquid rises spontaneously in the wedge-shaped gap between two vertical plates intersecting at a tight angle $\alpha \ll 1$. We contrast the differences between the case with vertical edge and those where the aristae is tilted to the vertical. Our theoretical model agrees very well with the experimental data.

1 Introduction

The problem of the spontaneous capillary rise of a liquid into a vertical cell made by two plates touching on an edge and having a small angle among them (wedge) was initially studied experimentally by Taylor (1712) and Hauksbee (1712). In both experiments the equilibrium profiles were rectangular hyperbolas with a very important particularity: near the edge, liquid can reach an infinite height, which for purposes of fractured oil fields it may be a huge problem because due to this dispersion the oil recovery may be limited. Conversely, in the process of feeding of trees this mechanism is very suitable to transport liquids as water and sap (which contains the

A. Jara · S. de Santiago · A. Medina (✉)
ESIME Azcapotzalco, Instituto Politécnico Nacional, Av. de Las Granjas 682, Col. Sta. Catarina Azcapotzalco, 02550 Mexico, D.F., Mexico
e-mail: amedinao@ipn.mx

F.J. Higuera
ETSI Aeronáuticos, Universidad Politécnica de Madrid, Plaza Cardenal Cisneros 3, 28040 Madrid, Spain

M. Pliego
Dpto. CB, ITQ Av. Tecnológico Esq. Gral. M. Escobedo, Col. Centro, 7600 Querétaro, QRO, Mexico
e-mail: mpliego@mail.itq.edu.mx

C.A. Vargas
Departamento de Ciencias Básicas, Universidad Autónoma Metropolitana-Azcapotzalco, Av. San Pablo 180, Col. Reynosa Azcapotzalco, 02200 Mexico, D.F., Mexico
e-mail: cvargas@correo.azc.uam.mx

J. Klapp et al. (eds.), *Selected Topics of Computational and Experimental Fluid Mechanics*, Environmental Science and Engineering,
DOI 10.1007/978-3-319-11487-3_44

nutrients) because the equilibrium heights attained through the xylem are unlimited and it promotes photosynthesis and transpiration in the leaves.

Historically, for nearly three hundred years the dynamic problem, to the time evolution liquid's free surface, towards the equilibrium, remained unresolved until by 2008 our group published a paper with the solution to this problem (Higuera et al. 2008).

In this work we report a series of experiments where the wedge's arista is tilted with to the vertical. This slope changes the shape of the equilibrium and dynamical profiles with respect to cases with vertical edges. Particularly, we are interested in finding the equilibrium shapes of the free surfaces, theoretically and experimentally. To reach such a goal, this work is divided as follows: in the next section we reviewed the problem of the capillary rise in the Taylor-Hauksbee cell. Later on, in the same section, we proposed a theoretical description of the equilibrium profiles in cells with tilted edges. Experimental data yield that such description is a suitable way to show such profiles. In Sect. 3 we show a set of dynamical profiles. Finally in Sect. 4 we present the main conclusions for this work.

2 Capillary Rise in the Taylor-Hauksbee Cell

2.1 Cell with a Vertical Edge

The wedge-shaped gap between two vertical plates intersecting at an angle $\alpha \ll 1$ is initially empty. At a certain moment, the lower edges of the plates get in touch with a liquid of density ρ, dynamic viscosity μ, and surface tension σ. The liquid wets the plates with a contact angle $\theta < \pi/2$ and therefore rises between the plates by capillary action as shown in Fig. 1a. The ratio of the two principal curvatures of the free surface of the liquid between the plates is small, on the order of α. The normal section of maximum curvature, by a plane nearly normal to the plates, is approximately a circular arc of radius $\alpha x/2\cos\theta$, where x is the distance to the line of intersection of the plates. The pressure jump across the surface is approximately

$$\Delta p = \frac{2\sigma\cos\theta}{\alpha x}. \tag{1}$$

At equilibrium, the height $H_e(x)$ of the meniscus above the level of the outer liquid is determined by the balance

$$\Delta p = \rho g H_e, \tag{2}$$

where g is the acceleration due to gravity. This balance gives the rectangular hyperbola (Concus and Finn 1969)

$$H_e = \frac{2\sigma\cos\theta}{\rho g\alpha x}. \tag{3}$$

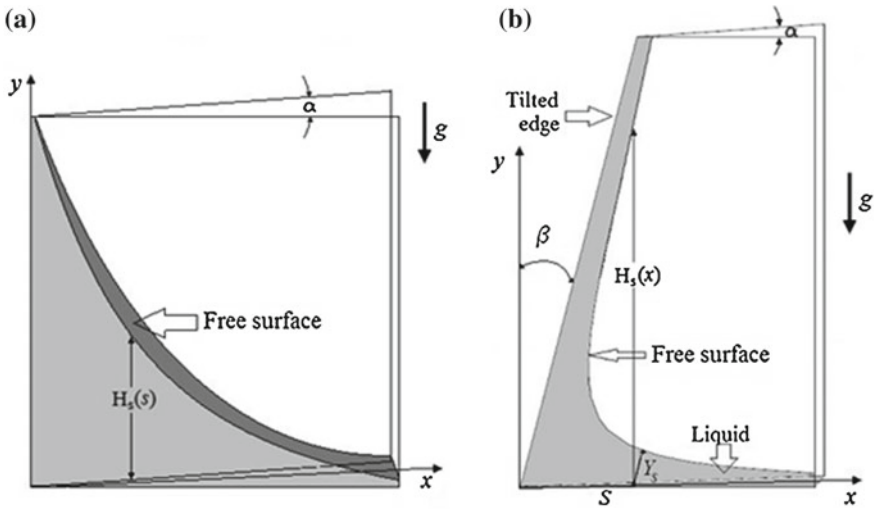

Fig. 1 **a** Scheme of the Taylor-Hauksbee cell. In this case the equilibrium profiles are given by $H_s(x)$. **b** Taylor-Hauksbee cell with a tilted edge. In this case Y_s is a distance to the equilibrium profile along the line parallel to the tilted edge and that starts at x = s and y = 0; Thus the most suitable coordinate system is given by (s, Y_s)

In order to compare the latter theoretical profile with experiments, we performed a series of experiments with silicon oil of viscosity $\mu = 100$ cP, surface tension $\sigma = 0.0215\,\text{N/m}$, density $\rho = 971\,\text{kg/m}^3$ and an aperture angle of $\alpha = 0.0166\,\text{rad}$. In experiments we used a digital Cannon Réflex T3i camera to take pictures and a video recording of the capillary rise. In Fig. 2 we show a picture with the equilibrium profile and also a comparison between the experimental data and the theoretical profile given by Eq. (3). The fit is very good assuming that $\theta = 0\,\text{rad}$.

2.2 Cell with Tilted Edge

In this part we consider the cases of cells with tilted edges with respect to the vertical, see Fig. 1b. The usual Cartesian coordinates appears no suitable to depict the equilibrium profiles because it is possible that for some values of x there are two values of $H(x)$ (the equilibrium profile). Thus, the concept of function can be lost.

Instead, we choose the rotated coordinate system (x', y') to describe the equilibrium profile. We analyze the problem for the point (s, Y_s) shown in Fig. 1b. s is the distance from the lower apex $(x' = 0, y' = 0)$ to any point along x, whereas Y_s is the distance to the equilibrium profile along the line parallel to the tilted edge (y') and that starts at the point $x' = s\cos\beta$ and $y' = s\sin\beta$; thus the equilibrium profile is given by the injective function $y'(x')$.

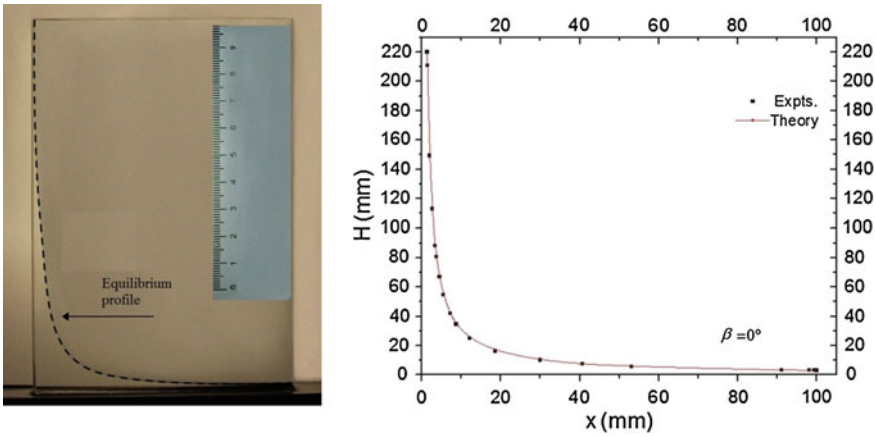

Fig. 2 *Left hand side* picture of the experimental equilibrium profile (rectangular hyperbola) for $\beta = 0$ rad. *Right hand side* theoretical profile (*curve*) and experimental data (*symbols*)

In this case the pressure jump across the surface is approximately

$$\Delta p = \frac{2\sigma\cos\theta}{\alpha s\cos\beta}, \tag{4}$$

meanwhile the equilibrium profile is determined by the balance

$$\Delta p = \rho g Y_s \cos\beta. \tag{5}$$

This balance gives the hyperbola

$$Y_s = \frac{2\sigma\cos\theta}{\rho g\alpha s\cos^2\beta}, \tag{6}$$

Another way to get the profile is by using the vertical length $H_s(s)$ but it is more complex because for some values of s could exist two values of H_s and for other ones, none. Thus, it is better to compute $s(H_s)$ (an injective function) given by

$$S = \frac{2\sigma\cos\theta}{\rho g\alpha\cos\beta H_s} + H_s\tan\beta. \tag{7}$$

Consequently, the equilibrium profile can be plotted by using Eqs. (6) or (7).

To make sure that our model is correct in the prediction of the equilibrium profiles in Fig. 3 we show the actual equilibrium profile in a Taylor-Hauskbee cell having $\beta = 0.523$ rad (30°) and $\alpha = 0.0092$ rad. The liquid of work was again silicone oil of $\mu = 100$ cP. In Fig. 4 we give an example of Fig. 3 showing other details.

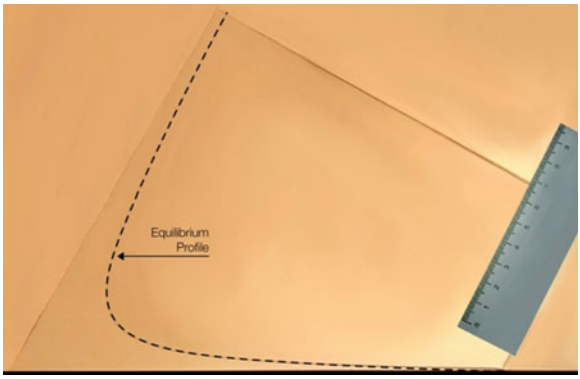

Fig. 3 Picture of the experimental equilibrium profile for $\beta = 0.523$ rad (30°) and $\alpha = 0.0092$ rad

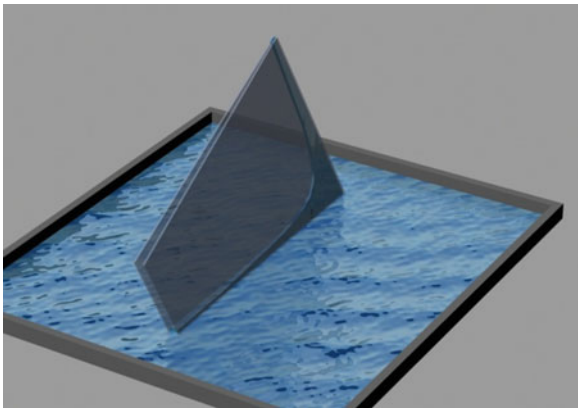

Fig. 4 Depict of the experimental equilibrium profile showing other details of the cell of Fig. 3

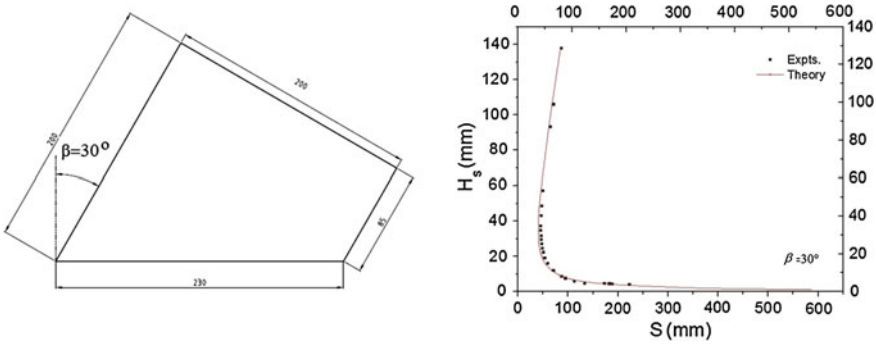

Fig. 5 *Left hand side* Scheme of the cell with its dimensions (in mm) for $\beta = 0.523$ rad (30°). *Right hand side* theoretical profile (*curve*) and experimental data (*symbols*), here $\alpha = 0.0092$ rad

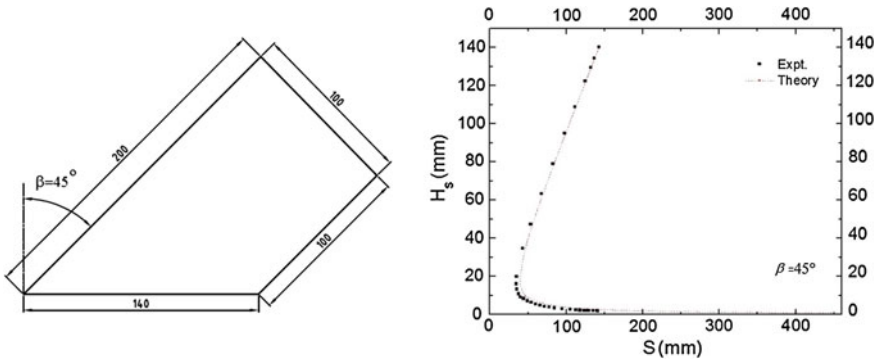

Fig. 6 *Left hand side* Scheme of the cell with its dimensions (in mm) for $\beta = 0.785$ rad (45°). *Right hand side* theoretical profile (*curve*) and experimental data (*symbols*), here $\alpha = 0.01659$ rad

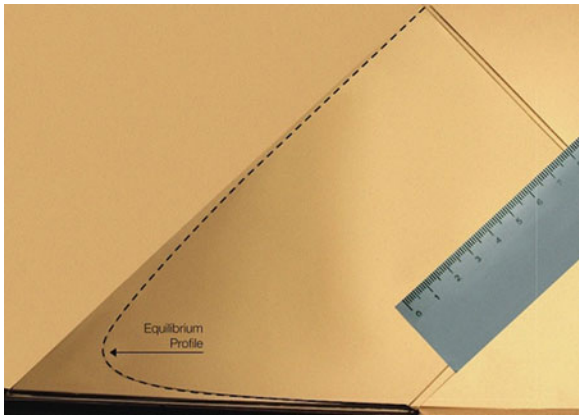

Fig. 7 Picture of the experimental equilibrium profile for $\beta = 0.785$ rad (45°) and $\alpha = 0.0166$ rad

The actual dimensions of the cell are given in Fig. 5. There, we also show the plot of the theoretical profile Eq. (7) as well as the experimental data obtained from Fig. 3. The fit is very fine.

In Fig. 6 we show a scheme of the cell and the plot of the actual equilibrium profile for $\beta = 0.785$ rad (45°) and $\alpha = 0.0166$ rad. Data were taken from Fig. 7. Clearly the fit is very good.

3 Dynamical Evolution

The equilibrium profile is attained after a succession of free surfaces. In Fig. 8 we show a plot with several free surfaces obtained at several time instants. Such a behavior is very similar to that occurring in the normal Taylor-Hauksbee cell (Higuera et al. 2008). In spite of this result, the times to reach the equilibrium between the

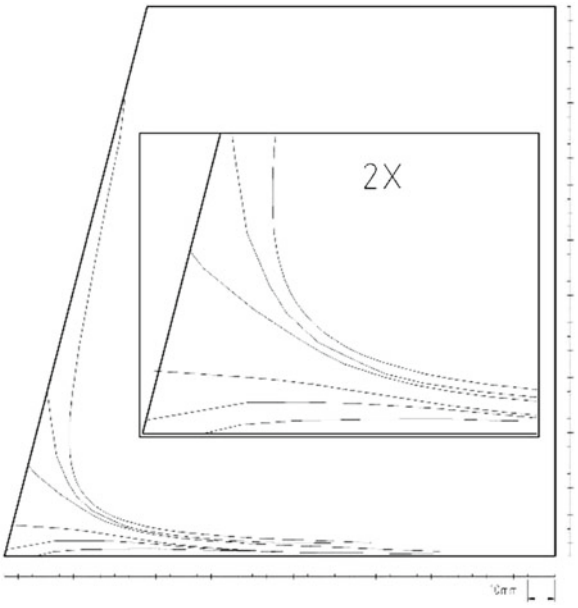

Fig. 8 Plot with the profiles at several stages (time instants) towards the equilibrium. In this case $\beta = 0.523$ rad (30°) and $\alpha = 0.0092$ rad

case with vertical edge and those where the edges are tilted was very different from each other. This is due to the intensity of the gravity field which changes with β.

4 Conclusions

In this work we have analyzed the problem of the capillary rise of a viscous liquid into vertical and tilted Taylor-Hauskbee cells. We have put forward a theoretical model to describe the actual equilibrium profiles. The model predicts pretty well the profiles in such a cell. The transition to the equilibrium profiles shows complex instantaneous profiles very similar to those occurring in a vertical cell. Further work along this line is in progress.

Acknowledgments AJ and S de S acknowledges to CONACYT for their studentships. AM acknowledges to SIP IPN for their partial support to make this work. Finally, authors acknowledge to Rodrigo Itzcoatl Pliego Suárez for his help in the digital improvement of pictures and schemes.

References

Concus P, Finn R (1969) On the behavior of a capillary free surface in a wedge. Proc Natl Acad Sci USA 63:292–299

Hauksbee F (1712) An experiment touching the ascent of water between two glass plates in an hyperbolick figure. Philos Trans R Soc Lond 27:539–540

Higuera FJ, Medina A, Liñan A (2008) Capillary rise of a liquid between two vertical plates making a small angle. Phys Fluids 20:102102

Taylor B (1712) Concerning the ascent of water between two glass plates. Philos Trans R Soc Lond 27:538